Disease Markers

The Role of Epithelial-Mesenchymal Transition (EMT)-Related Biomarkers in Disease

Lead Guest Editor: Zhen-Jian Zhuo
Guest Editors: Chia-Jung Li, Jiahui Chen, and Jian Wu

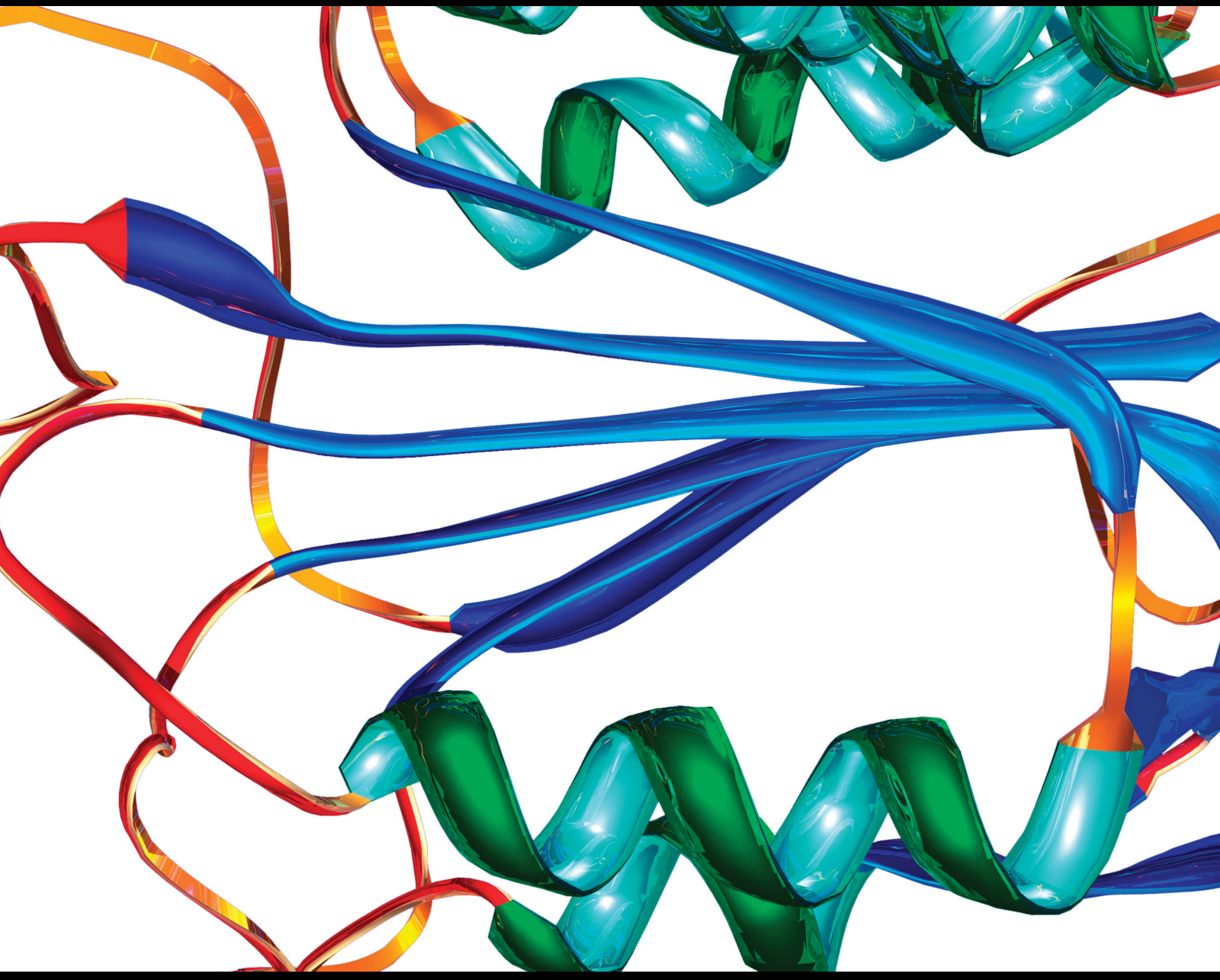

The Role of Epithelial-Mesenchymal Transition (EMT)-Related Biomarkers in Disease

Disease Markers

The Role of Epithelial-Mesenchymal Transition (EMT)-Related Biomarkers in Disease

Lead Guest Editor: Zhen-Jian Zhuo
Guest Editors: Chia-Jung Li, Jiahui Chen, and Jian Wu

Chief Editor

Paola Gazzaniga, Italy

Associate Editors

Donald H. Chace, USA
Mariann Harangi, Hungary
Hubertus Himmerich, United Kingdom
Yi-Chia Huang, Taiwan
Giuseppe Murdaca, Italy
Irene Rebelo, Portugal

Academic Editors

Muhammad Abdel Ghafar, Egypt
George Agrogiannis, Greece
Mojgan Alaeddini, Iran
Atif Ali Hashmi, Pakistan
Cornelia Amalinei, Romania
Pasquale Ambrosino, Italy
Paul Ashwood, USA
Faryal Mehwish Awan, Pakistan
Atif Baig, Malaysia
Valeria Barresi, Italy
Lalit Batra, USA
Francesca Belardinilli, Italy
Elisa Belluzzi, Italy
Laura Bergantini, Italy
Sourav Bhattacharya, USA
Anna Birková, Slovakia
Giulia Bivona, Italy
Luisella Bocchio-Chiavetto, Italy
Francesco Paolo Busardó, Italy
Andrea Cabrera-Pastor, Spain
Paolo Cameli, Italy
Chiara Caselli, Italy
Jin Chai, China
Qixing Chen, China
Shaoqiu Chen, USA
Xiangmei Chen, China
Carlo Chiarla, Italy
Marcello Ciaccio, Italy
Luciano Colangelo, Italy
Alexandru Corlateanu, Moldova
Miriana D'Alessandro, Saint Vincent and the Grenadines
Waaqo B. Daddacha, USA
Xi-jian Dai, China
Maria Dalamaga, Greece
Serena Del Turco, Italy
Jiang Du, USA
Xing Du, China
Benoit Dugue, France
Paulina Dumnicka, Poland
Nashwa El-Khazragy, Egypt
Zhe Fan, China
Rudy Foddis, Italy
Serena Fragiotta, Italy
Helge Frieling, Germany
Alain J. Gelibter, Italy
Matteo Giulietti, Italy
Damjan Glavač, Slovenia
Alvaro González, Spain
Rohit Gundamaraju, USA
Emilia Hadziyannis, Greece
Michael Hawkes, Canada
Shih-Ping Hsu, Taiwan
Menghao Huang, USA
Shu-Hong Huang, China
Xuan Huang, China
Ding-Sheng Jiang, China
Esteban Jorge Galarza, Mexico
Mohamed Gomaa Kamel, Japan
Michalis V. Karamouzis, Greece
Muhammad Babar Khawar, Pakistan
Young-Kug Kim, Republic of Korea
Mallikarjuna Korivi, China
Arun Kumar, India
Jinan Li, USA
Peng-fei Li, China
Yiping Li, China
Michael Lichtenauer, Austria
Daniela Ligi, Italy
Hui Liu, China
Jin-Hui Liu, China
Ying Liu, USA
Zhengwen Liu, China
César López-Camarillo, Mexico
Xin Luo, USA
Zhiwen Luo, China
Valentina Magri, Italy
Michele Malaguarnera, Italy
Erminia Manfrin, Italy
Upender Manne, USA

Contents

Hindawi
Disease Markers
Volume 2022, Article ID 9593039, 21 pages
https://doi.org/10.1155/2022/9593039

Research Article

Characterization of Epithelial-Mesenchymal Transition Identifies a Gene Signature for Predicting Clinical Outcomes and Therapeutic Responses in Bladder Cancer

Yicun Wang[1,2] **Hao Zhang**[1,2] **and Xiaopeng Hu**[1,2]

[1]*Department of Urology, Beijing Chao-Yang Hospital, Capital Medical University, Beijing, China*
[2]*Institute of Urology, Capital Medical University, Beijing, China*

Correspondence should be addressed to Xiaopeng Hu; xiaopeng_hu@sina.com

Received 29 April 2022; Revised 2 September 2022; Accepted 11 October 2022; Published 22 November 2022

Academic Editor: Chia-Jung Li

Purpose. The complex etiological variables and high heterogeneity of bladder cancer (BC) make prognostic prediction challenging. We aimed to develop a robust and promising gene signature using advanced machine learning methods for predicting the prognosis and therapy responses of BC patients. *Methods*. The single-sample gene set enrichment analysis (ssGSEA) algorithm and univariable Cox regression were used to identify the primary risk hallmark among the various cancer hallmarks. Machine learning methods were then combined with survival and differential gene expression analyses to construct a novel prognostic signature, which would be validated in two additional independent cohorts. Moreover, relationships between this signature and therapy responses were also identified. Functional enrichment analysis and immune cell estimation were also conducted to provide insights into the potential mechanisms of BC. *Results*. Epithelial-mesenchymal transition (EMT) was identified as the primary risk factor for the survival of BC patients (HR=1.43, 95% CI: 1.26-1.63). A novel EMT-related gene signature was constructed and validated in three independent cohorts, showing stable and accurate performance in predicting clinical outcomes. Furthermore, high-risk patients had poor prognoses and multivariable Cox regression analysis revealed this to be an independent risk factor for patient survival. CD8+ T cells, Tregs, and M2 macrophages were found abundantly in the tumor microenvironment of high-risk patients. Moreover, it was anticipated that high-risk patients would be more sensitive to chemotherapeutic drugs, while low-risk patients would benefit more from immunotherapy. *Conclusions*. We successfully identified and validated a novel EMT-related gene signature for predicting clinical outcomes and therapy responses in BC patients, which may be useful in clinical practice for risk stratification and individualized treatment.

1. Introduction

Bladder cancer (BC) is the most common type of urinary system cancer, with over 570,000 new cases and 210,000 deaths globally in 2020 [1]. Based on the tumor (T) stage, BC patients have been classified into non-muscle-invasive BC (NMIBC) and muscle-invasive BC (MIBC). After transurethral resection of bladder tumor, tumor recurrence and progression were observed in 63% and 11% of NMIBC patients, respectively [2]. Similarly, about half of MIBC patients who underwent radical cystectomy developed local recurrence or distant metastases, and 34% died within a 5-year follow-up period [3]. Individual treatment options for BC patients are currently determined primarily by cancer characteristics such as tumor-node-metastasis (TNM) staging and pathological grade [4]. However, the complex etiological variables and the high heterogeneity BC result in significantly different prognoses, making prognostic prediction difficult [5]. Therefore, a reliable and accurate biomarker in the prognosis of BC and prediction of therapy responses is highly beneficial in directing BC care.

The epithelial-mesenchymal transition (EMT) is a cellular process that allows epithelial cells to acquire mesenchymal characteristics and behaviors with down-regulated epithelial features, most notably the loss of E-cadherin [6, 7]. EMT activation is thought to enhance tumor invasiveness, metastasis,

and drug resistance, referring to aggressive tumor type [8, 9]. Several studies demonstrated an association between EMT and progression and survival outcomes in patients with BC [10, 11]. Furthermore, EMT in solid tumors has been shown to correlate with chemotherapy and immunotherapy responses [12–14]. Therefore, EMT-associated characteristics and EMT-based gene signatures have the potential to predict clinical outcomes and responses to chemotherapy and immunotherapy of BC patients.

We identified EMT as a leading risk factor for the survival of BC patients in this study. Advanced machine learning methods were then used to screen prognostic genes, resulting in constructing an EMT-related gene signature validated in multiple cohorts. Moreover, we performed comprehensive analyses of the tumor microenvironment (TME), immune cell infiltration, and therapeutic responses of BC patients to investigate their relationship with EMT and identify potential mechanisms.

2. Materials and Methods

2.1. The Collection and Pretreatment of Data. Gene expression and relevant clinicopathological data of 405 BC specimens and 19 adjacent normal specimens were obtained from TCGA (https://cancergenome.nih.gov/). After eliminating ineligible samples with overall survival (OS) of less than 30 days, the TCGA dataset including 393 BC patients was used as the training cohort. Subsequently, after screening the GEO database, two datasets were selected for this study based on the following inclusion criteria: (1) histologically confirmed BC samples with gene expression information; (2) samples with complete clinical data; (3) more than 100 samples. The GSE13507 dataset (Illumina human-6 v2.0 expression beadchip) containing 165 BC samples was utilized as validation I cohort. The GSE32894 dataset (umina HumanHT-12 V3.0 expression beadchip) comprising 221 BC samples was utilized as validation II cohort. The detailed information of the above three cohorts is shown in Table 1. All RNA-seq data involved in this study were normalized and log2 transformed.

2.2. Study Design. As illustrated in Figure 1, three phases including the discovery, training and validation, and further exploration phases were included in this research. In the discovery phase, EMT was identified as the leading risk factor for BC prognosis among various cancer hallmarks. Subsequently, prognostic differentially expressed genes (DEGs) in EMT-related genes were included for random survival forest analysis and stepwise Cox regression to construct a novel EMT-related gene signature, and its prognostic value was also validated in another two independent validation cohorts. Furthermore, we performed functional enrichment analysis, estimation of immune cell infiltration, and therapeutic responses prediction (chemotherapy and immunotherapy) in the above three cohorts.

2.3. Identification of the Leading Risk Hallmark for BC Prognosis. Briefly, the single-sample gene set enrichment analysis (ssGSEA) was employed to measure the performance of various confirmed cancer hallmarks in the training cohort using the "gsva" R package. This algorithm was based on gene expression profiles and hallmark annotation gene sets acquired from the Molecular Signatures Database (MSigDB) [15]. Then univariable Cox regression analysis identified EMT with the highest hazard ratio as the leading risk factor for the OS of BC patients and meta-analysis was also applied to compute the pooled hazard ratio of EMT among multiple cohorts to confirm its prognostic role. Moreover, we also applied gene set enrichment analysis (GSEA) to detect the significantly enriched cancer hallmarks in BC samples in comparison with adjacent normal samples using "clusterProfiler" R package [16, 17].

2.4. Generation and Verification of the EMT-Related Prognostic Gene Signature. We searched the MSigDB database using the search keyword (Epithelial-mesenchymal transition) and collected 359 EMT-related genes. DEGs between BC specimens and adjacent normal specimens were screened from EMT-related genes using the "limma" R package when the criteria $|\log FC| > 1$ and false discovery rate (FDR < 0.005) were met [18]. With a p value threshold of 0.005, we utilized univariable Cox regression analysis to detect prognostic genes among EMT-related genes. Overlapped genes between DEGs and prognostic genes were included for the random survival forest (RSFs) for further selection using the 'randomForestSRC' R package. The RSFs are an adaptation of random forests for follow-up data analysis, which are tree-based ensemble machine learning algorithms. Feature importance aligned with variable importance measure (VIMP) was applied to select real predictors [19]. Then, the genes identified by RSFs were applied for stepwise Cox regression to construct the EMT-related gene signature using the Akaike information criterion (AIC). Kaplan–Meier and time-independent receiver operating characteristic (ROC) survival assessments using "survminer" and "survivalROC" R packages were applied to comprehensively evaluate the prognostic prediction of EMT-related gene signature in BC prognosis, and two external cohorts GSE13507 and GSE32894 were used for further validation. Lastly, we demonstrated the independent prognostic value of the EMT-related gene signature based on univariable and multivariable Cox regression analysis.

2.5. Functional Enrichment Analysis. We utilized the "combat" function from R package "sva" to get rid of the batch effect across GSE13507 and GSE32894 cohorts and merged them into the merged validation cohort. BC patients in both the training and merged validation cohort were classified into high- and low-risk groups based on the optimal cutoff value of EMT-related risk score (ERS) produced by X-tile software. Then, GO and KEGG gene sets were acquired from MSigDB, which were used for the functional annotation of DEGs between risk groups. In the functional enrichment analysis, the input gene list was derived from DEGs between high- and low-risk groups divided by ERS.

2.6. TME and Immune Cell Analysis in BC. TME is mainly composed of stromal and immune cells, and it plays a crucial

Table 1: Clinical characteristics of BC patients in three independent cohorts.

Characteristics	TCGA	GSE13507	GSE32894	Overall
Total	393	165	221	779
Application	Training	Validation I	Validation II	
Age (%)				
<60	85 (21.6)	42 (25.5)	38 (17.2)	165 (21.2)
≥ 60	308 (78.4)	123 (74.5)	183 (82.8)	614 (78.8)
Sex (%)				
Female	103 (26.2)	30 (18.2)	60 (27.1)	193 (24.8)
Male	290 (73.8)	135 (81.8)	161 (72.9)	586 (75.2)
T stage (%)				
Ta		24 (14.5)	109 (49.3)	133 (17.1)
T1	3 (0.8)	80 (48.5)	61 (27.6)	144 (18.5)
T2	113 (28.8)	31 (18.8)	43 (19.5)	187 (24.0)
T3	190 (48.3)	19 (11.5)	7 (3.2)	216 (27.8)
T4	54 (13.7)	11 (6.7)	1 (0.5)	66 (8.5)
Unknown	33 (8.4)			33 (4.2)
N stage (%)				
N0	227 (57.8)	149 (90.3)		376 (67.4)
N1	44 (11.2)	8 (4.8)		52 (9.3)
N2	74 (18.8)	6 (3.6)		80 (14.3)
N3	7 (1.8)	1 (0.6)		8 (1.4)
Unknown	41 (10.4)	1 (0.6)		45 (8.1)
M stage (%)				
M0	188 (47.8)	158 (95.8)		346 (62.0)
M1	10 (2.5)	7 (4.2)		17 (3.0)
Unknown	195 (49.6)			195 (34.9)
Grade (%)				
High	372 (94.7)	60 (36.4)	91 (41.2)	523 (67.1)
Low	18 (4.6)	105 (63.6)	128 (57.9)	251 (32.2)
Unknown	3 (0.8)		2 (0.9)	5 (0.6)
Clinical outcomes				
Overall survival (%)				
Alive	219 (55.7)	96 (58.2)	196 (88.7)	511 (65.6)
Deceased	174 (44.3)	69 (41.8)	25 (11.3)	268 (34.4)
Cancer-specific (%)				
Alive	274 (69.7)	133 (80.6)		407 (72.9)
Deceased	119 (30.3)	32 (19.4)		151 (27.1)
Progression-free (%)				
Censored	222 (56.5)			222 (56.5)
Event	171 (43.5)			171 (43.5)
Follow-up time (months, mean ± SD)	27.81 (27.93)	48.38 (37.70)	40.44 (25.33)	35.75 (30.74)

role in tumor prognosis [20]. ESTIMATE algorithm was used to calculate the stromal score, immune score, ESTIMATE score, and tumor purity of each patient using the "estimate" R package [21]. Then, the scores mentioned above were compared between risk groups. Furthermore, the infiltration of various immune cell types in BC was investigated by the CIBERSORT algorithm [22]. To be specific, based on the gene expression feature set of 22 immune cell subtypes, the simulation calculation was performed 1000 times, and the relative composition ratio of the 22 immune cells in each sample was finally obtained. The abundance of 22 immune cell types across risk groups was evaluated and compared.

2.7. Evaluation of Therapy Responses. Genomics of Drug Sensitivity in Cancer (GDSC), the largest public pharmacogenomics database, contains gene expression data of many human cancer cell lines and corresponding drug response

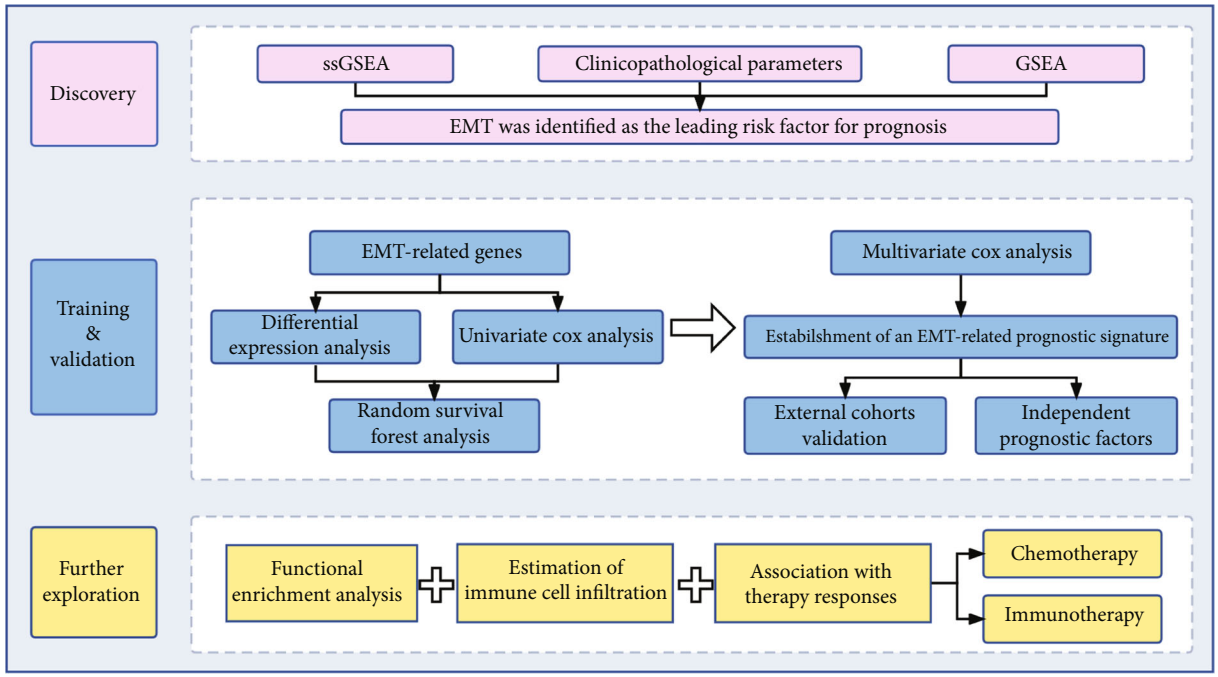

Figure 1: Flowchart of this study. GSEA: gene set enrichment analysis. EMT: epithelial-mesenchymal transition.

data [23]. We used the "oncoPredict" package to predict the responses of each patient to various chemotherapeutic drugs based on GDSC [24]. Besides, the IMvigor210 dataset [25] with metastatic urothelial cancer patients treated with anti-programmed death-ligand (PDL)-1 drug (atezolizumab) and the GSE176307 dataset with metastatic urothelial cancer patients treated with anti-PD-1 or anti-PD-ligand-1 were included in our study. According to gene expression data acquired from the above two datasets, we calculated the ERS of each patient and then divided these patients into high- and low-risk groups. Then, the differences in immunotherapy responses were evaluated.

2.8. Statistical Analysis. The D'Agostino and Pearson omnibus normality tests were applied to determine whether each comparison had a normal distribution. Once data met the assumptions of parametric tests, we conducted contrasts using a two-tailed unpaired t-test, and the Pearson correlation. The Mann–Whitney U test and Spearman correlation were employed when parameters were not normally distributed. Results are considered statistically significant at the level of 5% ($p < 0.05$) except for differential gene expression analyses and univariate Cox regression analysis.

3. Results

3.1. Identification of EMT as the Leading Risk Factor for Prognosis. In the training cohort, EMT demonstrated a higher HR for overall survival (HR = 1.281, $p = 0.002$) than other cancer hallmarks, which are glycolysis, angiogenesis, etc. (Figure 2(a)). Among all three cohorts, EMT was consistently identified as a risk factor with a pooled HR of 1.43 (Figure 2(b), Supplementary Table 1). GSEA further showed that EMT was significantly annotated in BC patients (Figure 2(c), Supplementary Table 2). Besides, we found that patients in the late clinicopathological stages (tumor stage, node stage, metastasis stage, and pathological grade) had higher ssGSEA scores than patients in the early stage (Figure 2(d)–2(e)). In addition, the Kaplan–Meier survival curves and the log-rank test demonstrated that BC patients with high ssGSEA scores had significantly worse survival outcomes, including OS (HR = 1.295, $p = 0.009$), DSS (disease-specific survival, HR = 1.276, $p = 0.017$), and DFI (disease-free interval, HR = 1.218, $p = 0.044$) (Figure 2(f)–2(h)). All findings mentioned above strongly demonstrated the great influence of EMT on the prognosis of BC patients.

3.2. Establishment of the EMT-Related Prognostic Signature. We acquired EMT-related genes ($n = 359$) from MSigDB for differential gene expression analyses. Then, the intersection of 66 DEGs (13 upregulated and 53 downregulated genes) (Figure 3(a)) and 26 prognostic genes (2 protective and 24 risk genes) (Figure 3(b)) screened 13 candidate genes for further analysis (Figure 3(c)), and the network illustrated a tight relationship among those 13 genes (Figure 3(d)). When all 13 genes were jointly considered by RSF, OS was mainly correlated with 9 genes (*EMP1*, *ANLN*, *MSX1*, *NRP2*, *ID2*, *FGFR1*, *WNT5B*, *LATS2*, and *TGFB1I1*) (Figure 3(e)). Subsequently, these 9 genes were applied to stepwise Cox regression to form the EMT-related gene signature (Figure 3(g)). Among four genes involved in the novel gene signature, three genes (*MSX1*, *ANLN*, and *EMP1*) were risk factors and the remaining one (*ID2*) was a protective factor (Figure 3(f)). The EMT-related signature was calculated as EMT-related risk score = $(-0.12119 \times ID2) + (0.33044 \times MSX1) + (0.19928 \times ANLN) + (0.24620 \times EMP1)$.

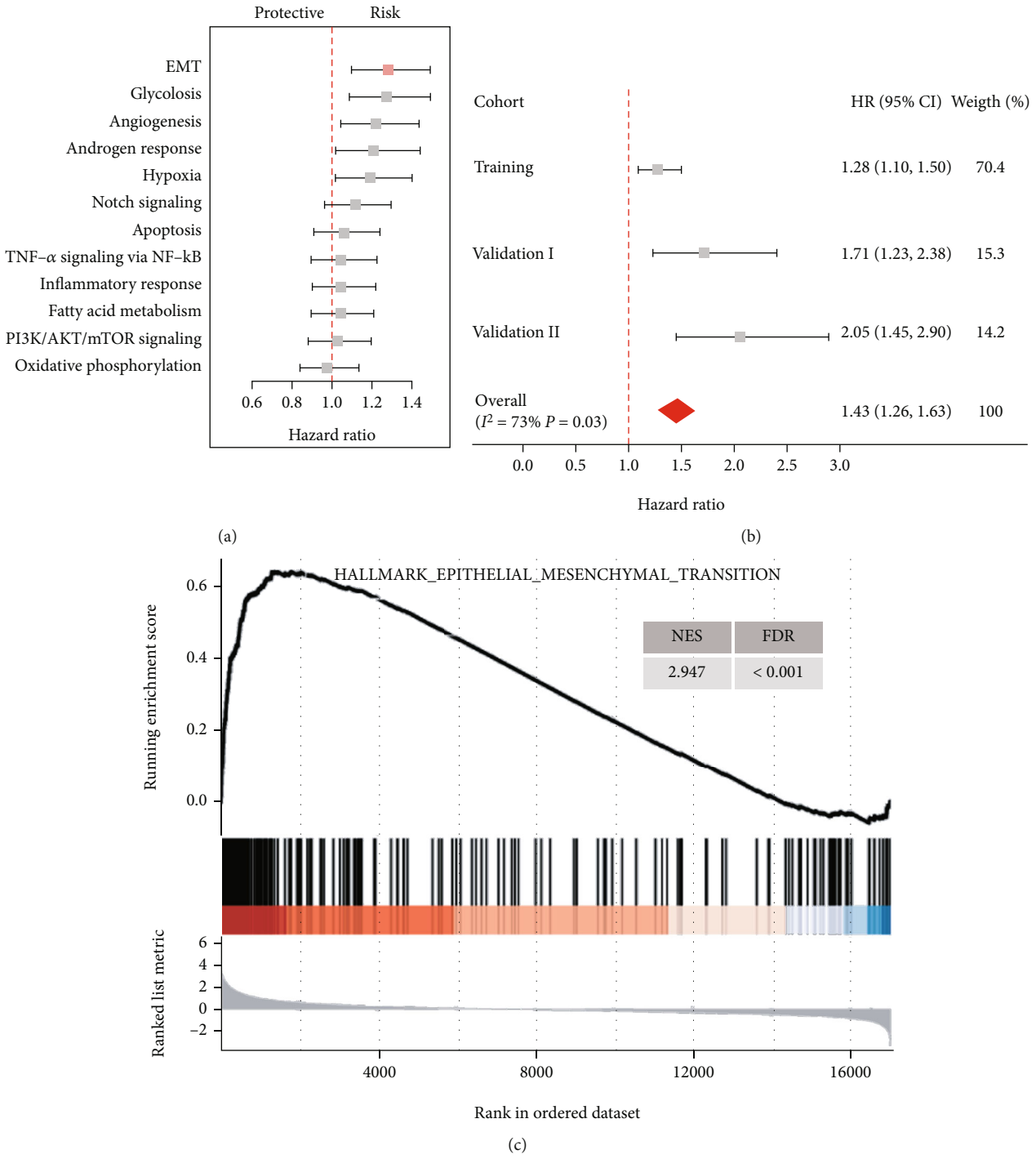

Figure 2: Continued.

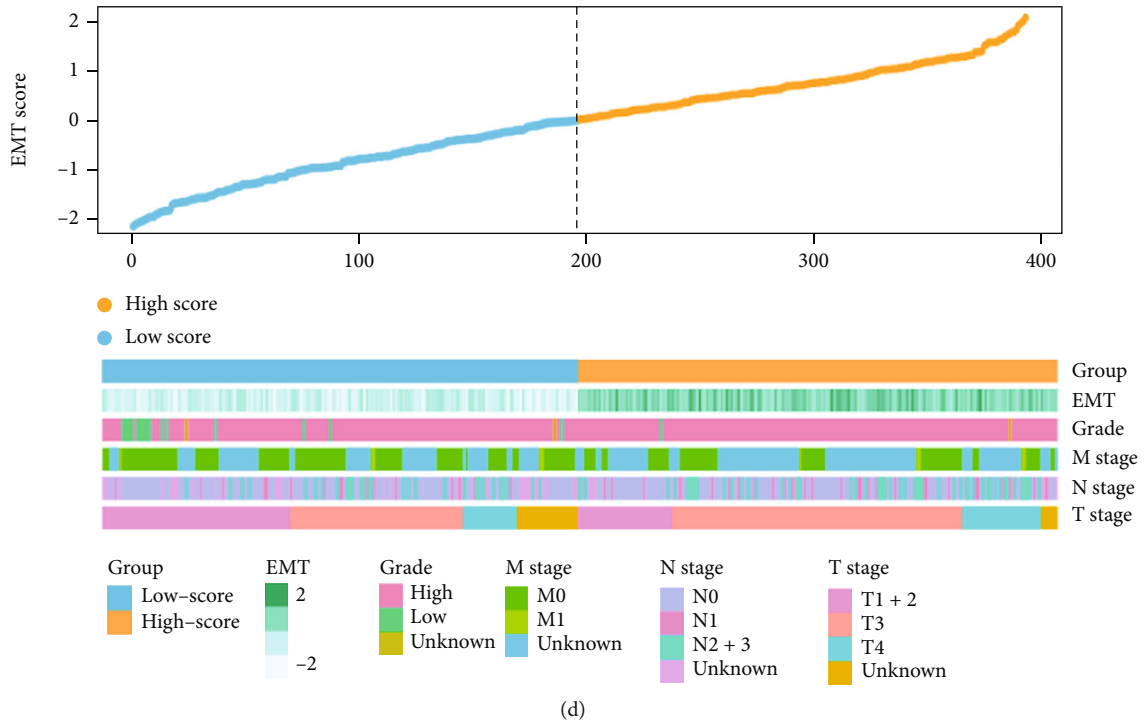

(d)

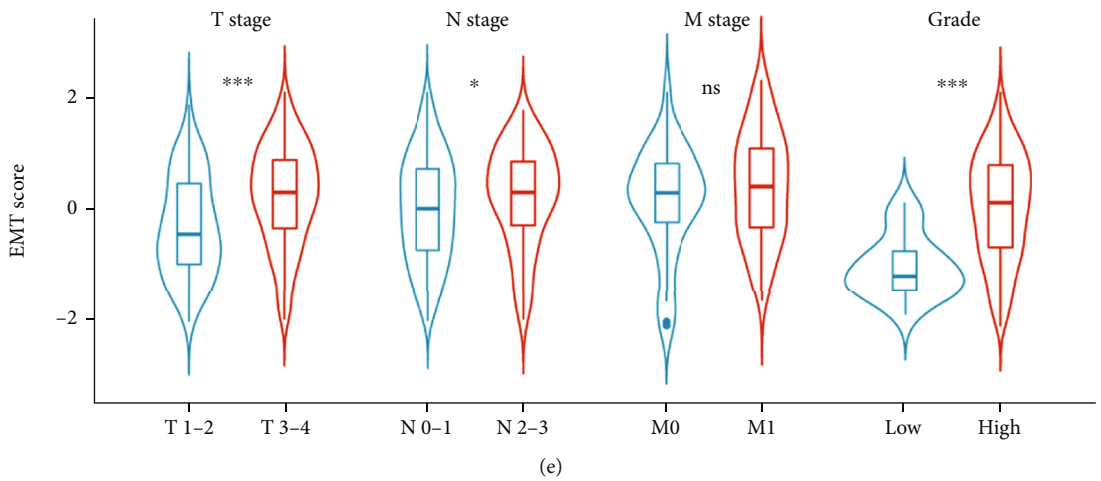

(e)

Figure 2: Continued.

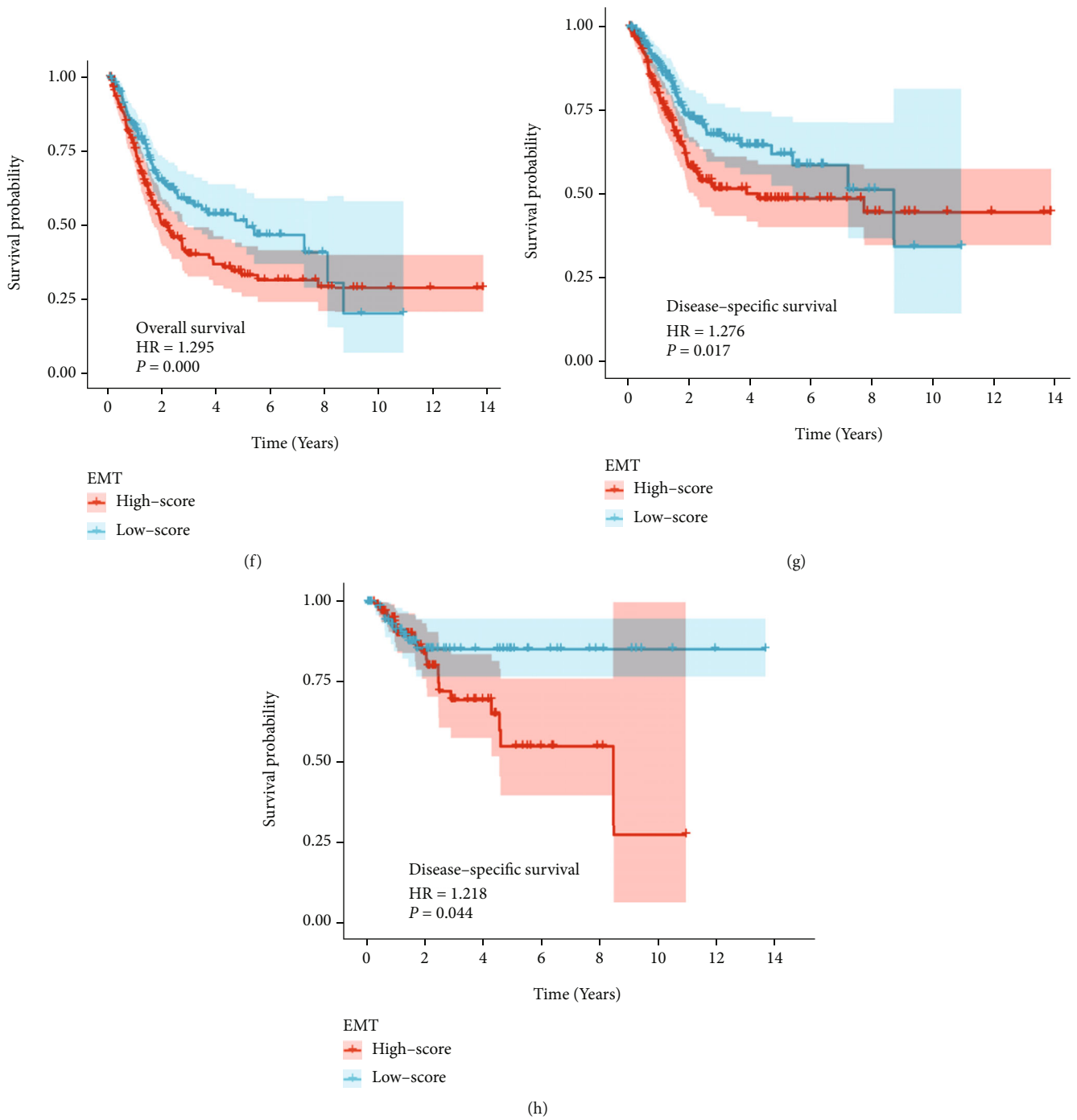

Figure 2: Identification of EMT as the leading risk factor for the prognosis of BC patients. The forest plots show that EMT has the highest HR among various cancer hallmarks in the training cohort (a) and multiple cohorts calculated by meta-analysis (b). (c) GSEA plot illustrates that EMT is significantly enriched in BC samples than adjacent normal samples. (d) The heatmap exhibits the distribution of EMT scores and the patient information of grade, M stage, N stage, and T stage in the training cohort. (e) Violin plot displays that patients with higher T stage, N stage, and pathological grade have higher EMT scores. Kaplan–Meier survival curves depict that high-risk patients divided by EMT scores have worse OS (f), DSS (g), and DFI (h) compared with low-risk patients. HR: hazard ratio. BC: bladder cancer. OS: overall survival. DSS: disease-specific survival. DFI: disease-free interval. $*p < 0.05$; $***$ $P < 0.001$; ns, no significance.

3.3. ERS Served as an Independent Prognostic Factor with Promising Value in each Cohort. Based on the optimal cutoff of ERS value produced by X-tile software, the patients were categorized into high- and low-risk groups in all three training and validation cohorts. Kaplan–Meier curves showed that high-risk patients had significantly lower survival probability in OS (HR = 4.429, $p < 0.001$), DSS (HR = 6.622, $p < 0.001$), and DFI (HR = 3.074, $p < 0.001$) (Figures 4(a), 4(c), and 4(e)). For ERS, the AUC of the predictions for 1, 3, and 5 years was illustrated in Figures 4(b), 4(d), and 4(f

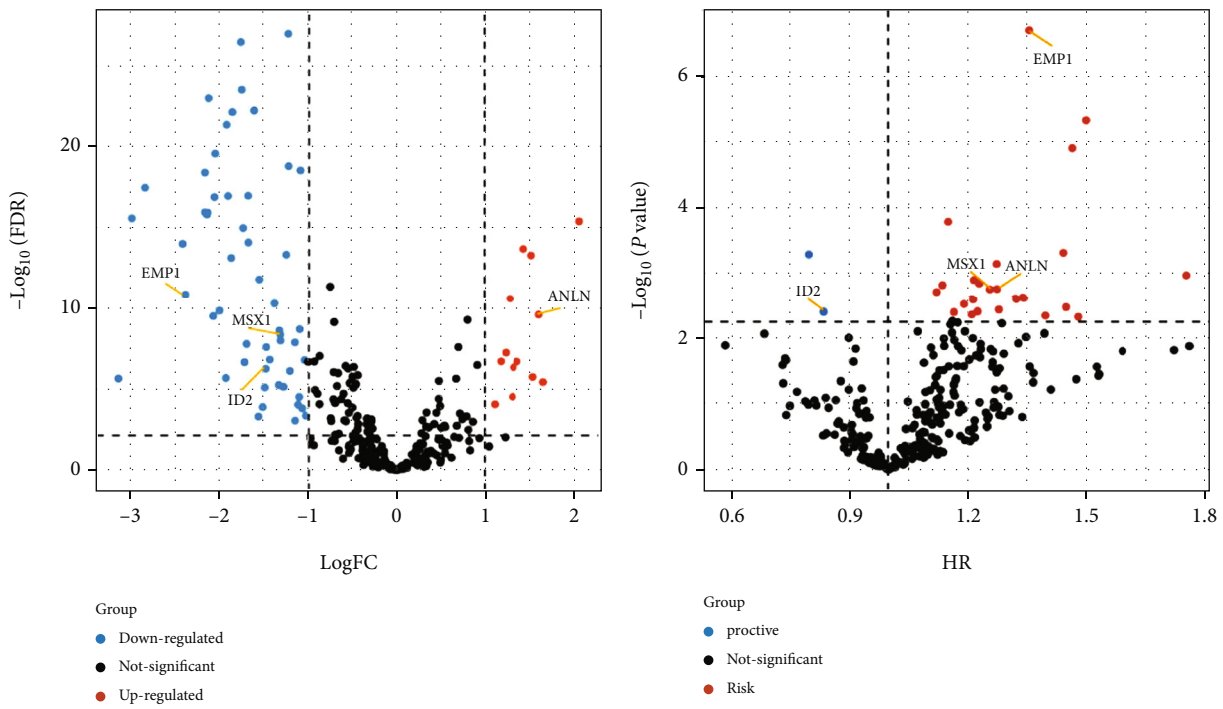

(a) (b)

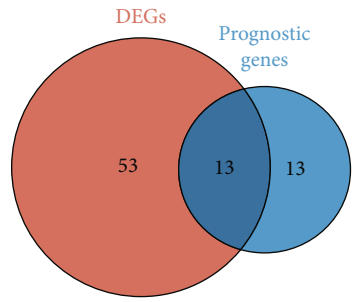

(c)

Figure 3: Continued.

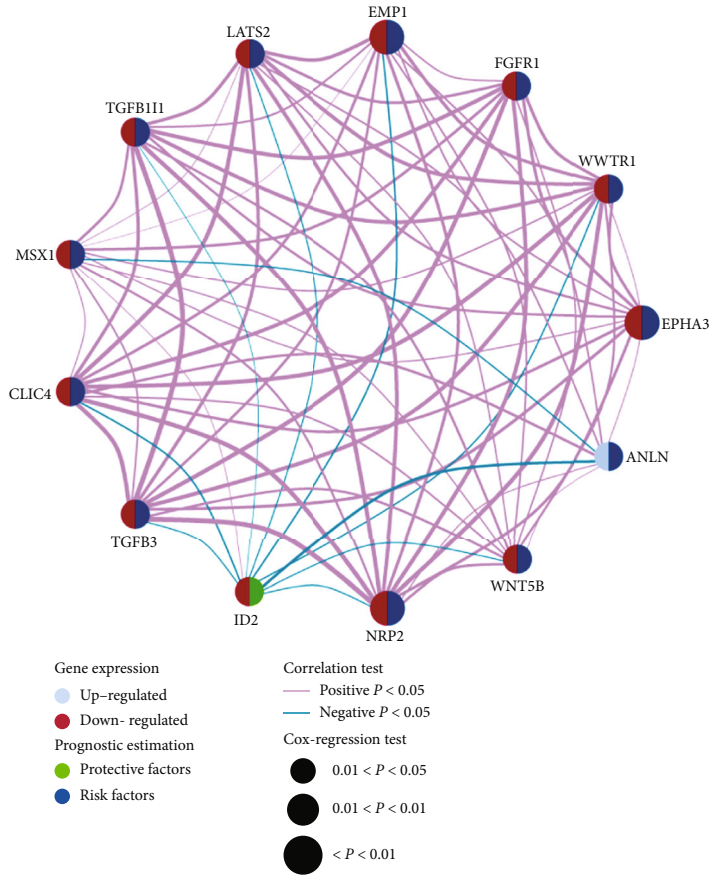

(d)

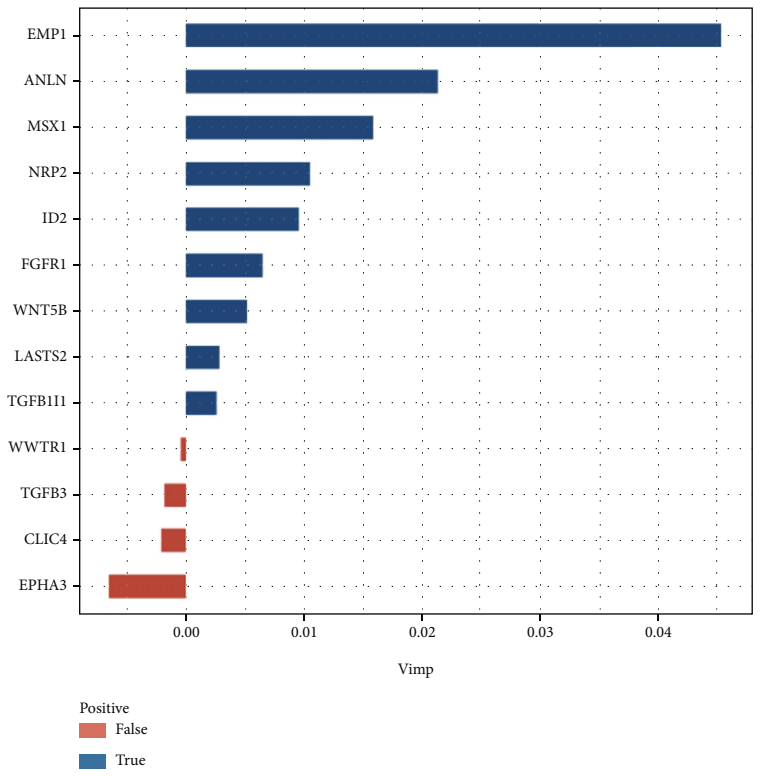

(e)

Figure 3: Continued.

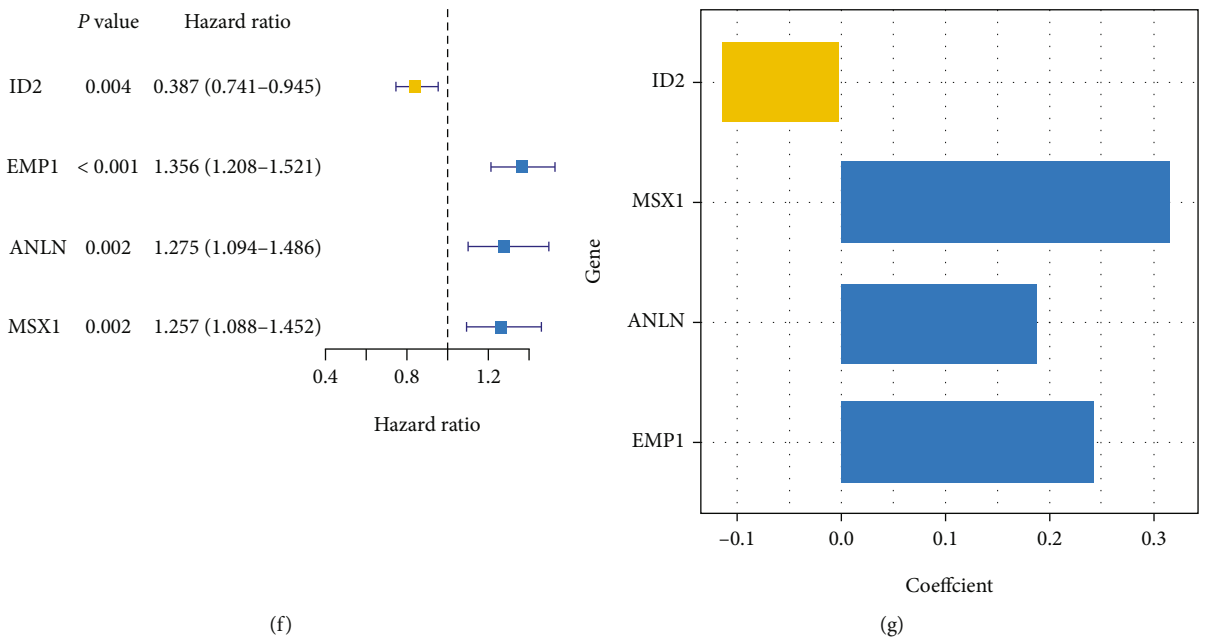

(f) (g)

Figure 3: Construction of EMT-related gene signature. Volcano plots show DEGs (a) between BC and adjacent normal samples, and prognostic genes (b) calculated by the univariable Cox regression. Red dots are upregulated genes or risk genes, and blue dots present downregulated genes or protective genes. (c) Venn diagram shows 13 intersected genes between DEGs and prognostic genes. (d) The correlation of 13 EMT-related genes in BC. Upregulated genes and downregulated genes are represented with grey and red colors. Risk genes are described in blue and protective genes are colored in green. The p values of the Cox regression test for 13 genes are represented by the size of circles. Correlation analysis is performed on 13 genes, depicted by the connecting lines between each gene. Red and blue lines present positive and negative correlations. (e) Variable importance plot based on random forest survival analysis for 13 genes. Blue color indicates predictive variables, whereas red color represents nonpredictive variables. (f) Forest plot based on univariable Cox regression analysis shows that four genes in this signature are all significantly associated with overall survival. (g) The coefficient of each gene in the gene signature is depicted by bar plots. DEGs: differentially expressed genes.

). The highest AUC values of OS, DSS, and DSI were 0.686, 0.768, and 0.687. In the validation I cohort, the survival benefits of low-risk patients were significantly better than low-risk patients (OS: HR = 1.399, $p = 0.002$; DSS: HR = 2.311, $p = 0.005$) (Figures 4(g) and 4(i)). The maximum AUC values of OS and DSS in the validation I set were 0.657 and 0.703 (Figures 4(h) and 4(j)). Similarly, ERS also performed well in prognostic prediction in the validation II cohort (HR = 10.606, $p < 0.001$, highest AUC = 0.821) (Figures 4(k) and 4(l)). Overall, ERS was accurate and robust in evaluating the prognosis of BC patients.

In univariable Cox regression analysis, the T stage, N stage, M stage, and ERS were significantly correlated with OS, while ERS was demonstrated as the only independent prognostic factor for OS by multivariable Cox regression analysis (HR = 3.831, $p < 0.001$) in the training cohort (Table 2). Similar results can also be obtained in two validation cohorts (Supplementary Table 3-5).

3.4. Functional Enrichment and Immune Cell Infiltration Analyses. According to functional enrichment analysis, DEGs between risk groups exhibited significant enrichment in EMT-associated pathways, including extracellular exosomes, epithelial cell differentiation, and wound healing (Figure 5(a)). Besides, as shown in Supplementary Figure 1, the EMT scores representing the performance of EMT process were consistently correlated with expression levels of four genes and ERS ($R = 0.59$, $p < 0.0001$). Moreover, the comparison of TME components showed that high-risk patients had significantly greater stromal scores ($p < 0.05$), immune scores ($p < 0.01$), ESTIMATE scores ($p < 0.05$), and lower tumor purity ($p < 0.01$) than the low-risk patients (Figure 5(b)). Similar results can also be observed in the merged validation cohort (Figure 5(c)). Besides, by analyzing the infiltration of immune cells, we found that CD8+ T cells, Tregs, Macrophages M1, and Macrophages M2 were higher infiltrated, and B naïve cells were lower infiltrated in the TME of high-risk patients in both training and merged validation cohorts (Figures 5(d) and 5(e)).

3.5. Role of ERS in Predicting Chemotherapeutic Sensitivity and Immunotherapeutic Response. Chemotherapies are extensively used for BC treatment in clinical practice. Therefore, we estimated the therapy responses of each patient to six commonly used drugs (Cisplatin, Vinblastine, Gemcitabine, Methotrexate, Paclitaxel, and Doxorubicin) by evaluating their IC50 values based on the GDSC database. As a result, the IC50 values of Cisplatin ($p < 0.001$), Vinblastine ($p < 0.001$), Gemcitabine ($p < 0.001$), Methotrexate ($p < 0.05$), Paclitaxel ($p < 0.001$), and Doxorubicin ($p < 0.001$) in the high-risk group was significantly lower than that in the low-risk group (Figures 6(a)–6(f)).

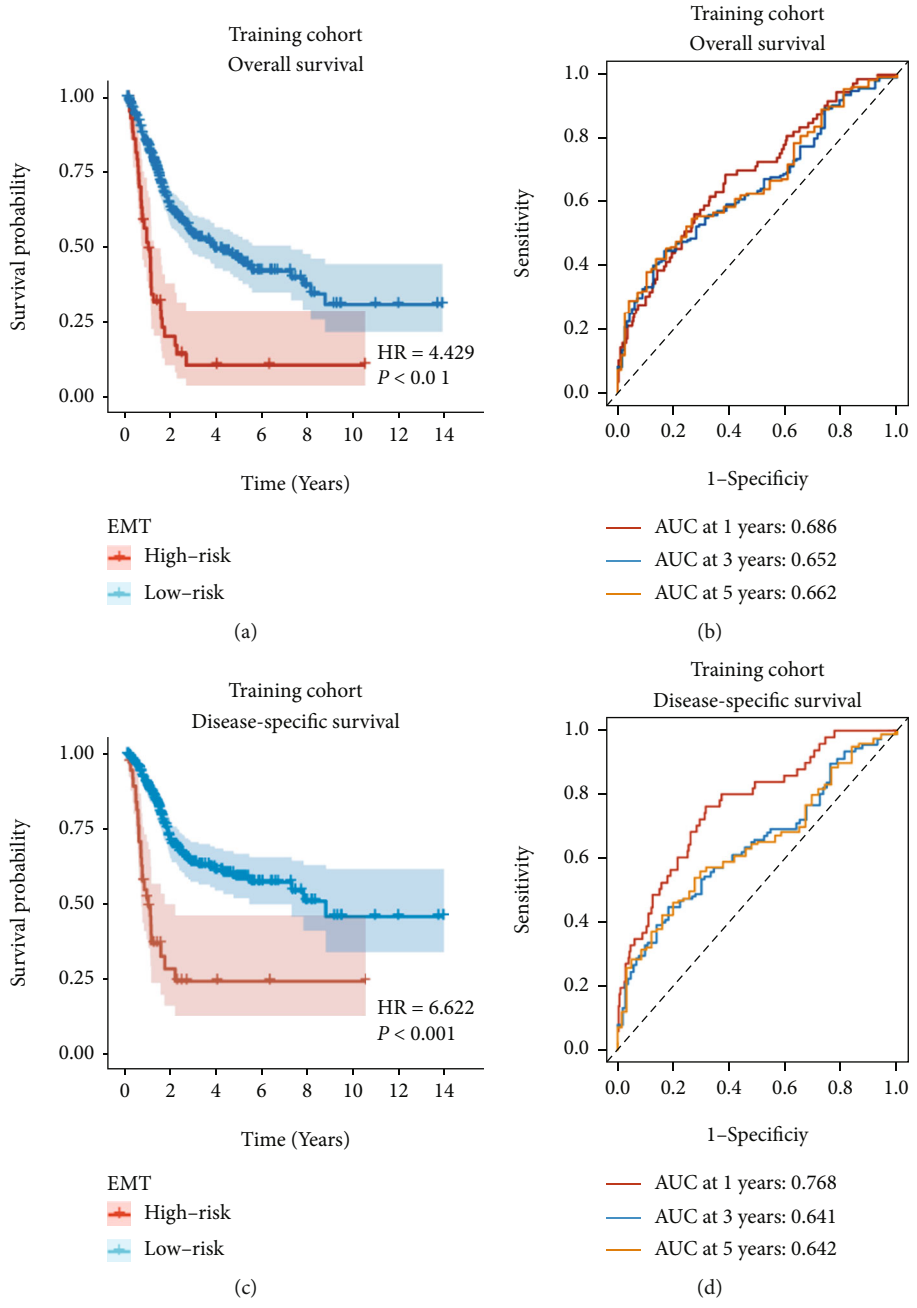

Figure 4: Continued.

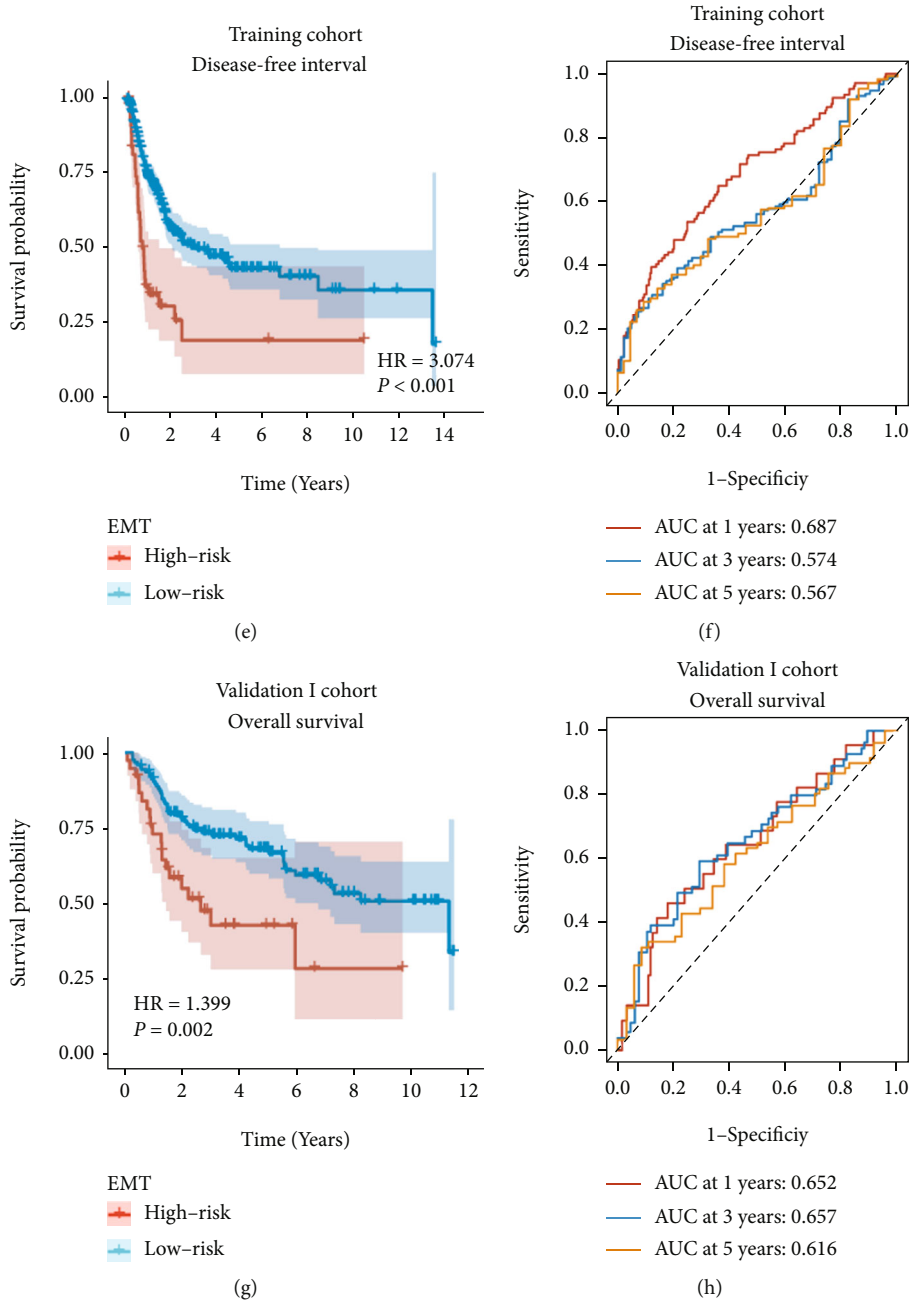

Figure 4: Continued.

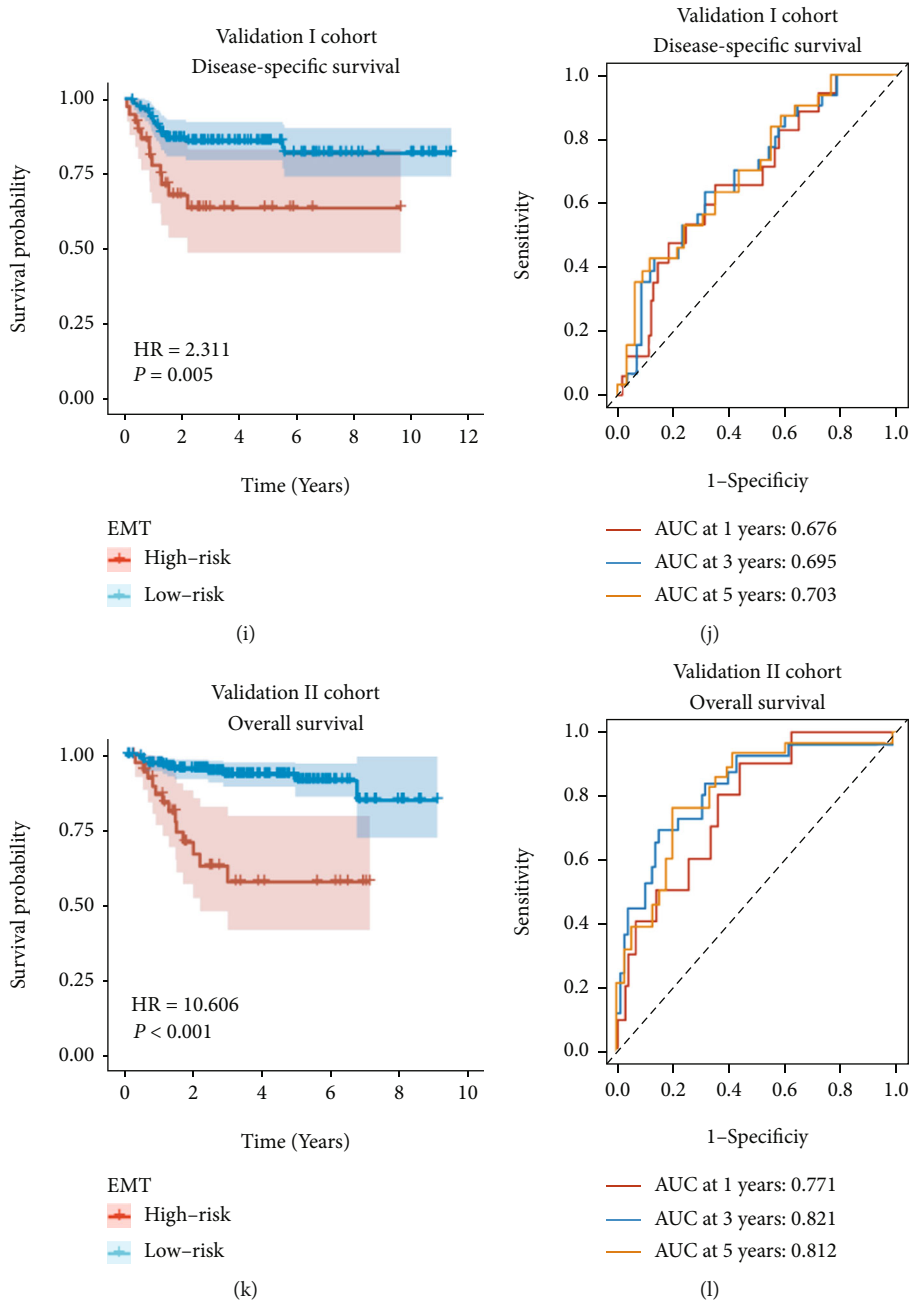

Figure 4: The gene signature serves as a robust and promising predictive factor for survival prediction. Kaplan–Meier survival curves illustrate worse survival outcomes in high-risk patients in the TCGA training cohort (a, c, e), validation I cohort (g, i), and validation II cohort (k). ROC curves for 1-year, 3-year, and 5-year survival prediction depict that this gene signature has a promising and stable predictive performance for BC patients in the training cohort (b, d, f), validation I cohort (h, j), and validation II cohort (l).

Moreover, the results of correlation analysis also showed that ERS was negatively related with the IC50 values of Cisplatin ($r = -0.19$, $p = 0.00012$), Gemcitabine ($r = -0.47$, $p < 2.2e-16$), and Doxorubicin ($r = -0.34$, $p < 3.2e-12$) (Figure 6(g)–6(i)). These results indicated that patients with higher ERS are more sensitive to chemotherapy.

Anti-PD1/PDL1 drugs were currently approved by the FDA for the treatment of BC, with 3 anti-PDL-1 drugs (atezolizumab, durvalumab, and avelumab), and 2 anti-PD-1 drugs (nivolumab and pembrolizumab). Thus, we evaluated whether the ERS might be utilized for the prediction of therapy responses to immunological checkpoint blockade (ICB) treatment based on the above two cohorts. As a result, responders displayed lower ERS compared with nonresponders in both IMvigor210 ($p < 0.01$, Figure 6(j)) and GSE176307 ($p < 0.001$, Figure 6(l)). Furthermore, through allocating patients into high- and low-risk groups based on ERS, we found that high-risk patients had significantly lower percentages of responses (complete response, CR/partial response, PR) and higher percentages of nonresponses

Table 2: Univariate and multivariate Cox regression analysis of clinical characteristics and ERS with overall survival in TCGA cohort.

Variables	No. of Patients	Univariate			Multivariate		
		HR	95% CI	p value	HR	95% CI	p value
Age	162	1.023	0.997–1.049	0.078			
Gender	162						
Female	36		Reference				
Male	126	0.61	0.363–1.022	0.061			
T stage	162						
T_{1+2}	53		Reference				
T_3	87	2.27	1.167–4.416	0.016	1.669	0.842–3.311	0.142
T_4	22	3.138	1.419–6.941	0.005	2.133	0.916–4.965	0.079
N stage	162						
N_0	112		Reference				
N_1	21	1.99	1.033–3.836	0.04	1.364	0.676–2.754	0.386
N_{2+3}	29	2.745	1.582–4.761	< 0.001	1.627	0.855–3.097	0.138
M stage	162						
M_0	155		Reference				
M_1	7	2.532	1.01–6.346	0.048	1.354	0.492–3.725	0.558
Grade	162						
High	147		Reference				
Low	15	0.272	0.037–1.979	0.199			
ERS	162	4.429	2.534–7.741	< 0.001	3.831	2.138–6.865	< 0.001

(stable disease, SD/progressive disease, PD) in both IMvigor210 ($p < 0.001$, Figure 6(k)) and GSE176307 ($p < 0.001$, Figure 6(m)) cohorts.

4. Discussion

EMT is the process by which epithelial cells transform into mesenchymal-like cells with decreased expression of epithelial markers, such as E-cadherin, and upregulation of mesenchymal markers expressions [7, 26, 27]. Decreased expression of epithelial markers in BC patients was correlated with disease progression (higher grade and stage), and EMT-related molecules (β-catenin or plakoglobin) were associated with poor DSS [9]. Sayan et al. found a link between EMT expression regulator Zeb-1 and enhanced urothelial cancer cell invasion and migration [11]. Furthermore, there was an association between EMT levels in solid tumors and their responses to chemotherapy and immunotherapy [12–14]. The above studies suggested that EMT has significant prognostic and therapeutic potential in solid tumors. However, there is a lack of EMT-related gene signatures for predicting prognosis and therapeutic response in BC.

We developed an EMT-related gene signature for predicting survival outcomes (OS, DSS, and DFI) of BC patients. The robustness and applicability of this gene signature were verified by two independent cohorts from two different RNA-seq platforms. Our findings indicated that patients designated as high-risk using the novel signature had poor survival outcomes than low-risk patients. Furthermore, multivariable Cox analysis revealed that the gene signature was the only independent predictor of OS after adjusting for clinical factors. No gene overlap was observed between these two signatures, in contrast to a previous study that used seven EMT-linked genes to predict the prognosis of patients with MIBC [28]. Our gene signature with only four genes performed well across all three cohorts, and the AUC values were higher than the previous one. Moreover, we comprehensively analyzed the relationship between EMT and chemotherapeutic and immunotherapeutic responses, providing the foundation for further research.

Functional enrichment analyses were performed to better understand the potential mechanisms of different clinical outcomes among patients. Our results revealed that DEGs between these two groups were significantly enriched in extracellular exosomes, cell proliferation, epithelial cell differentiation, wound healing, BC, and other variables. Shan et al. demonstrated that exosomes produced by cancer-associated fibroblasts might induce metastasis of BC cells by increasing their EMT [29]. Wang et al. reported that increased UCA1 expression in BC-derived exosomes promotes tumor growth via EMT [30]. McConkey et al. proposed that EMT is essential for the cell proliferation required for wound healing [31]. Moreover, the expression levels of four genes and ERS were significantly correlated with the EMT score, indicating that the novel signature was associated with the EMT process in BC. Our findings indicate that EMT-related characteristics may be closely associated with the development and progression of BC, and the EMT-related gene signature has great potential for prognostic gene-function-based prediction.

TME plays a vital role in cancer formation and treatment resistance [20]. TME dysregulation promotes BC progression and metastasis [32]. This study reported that high-risk

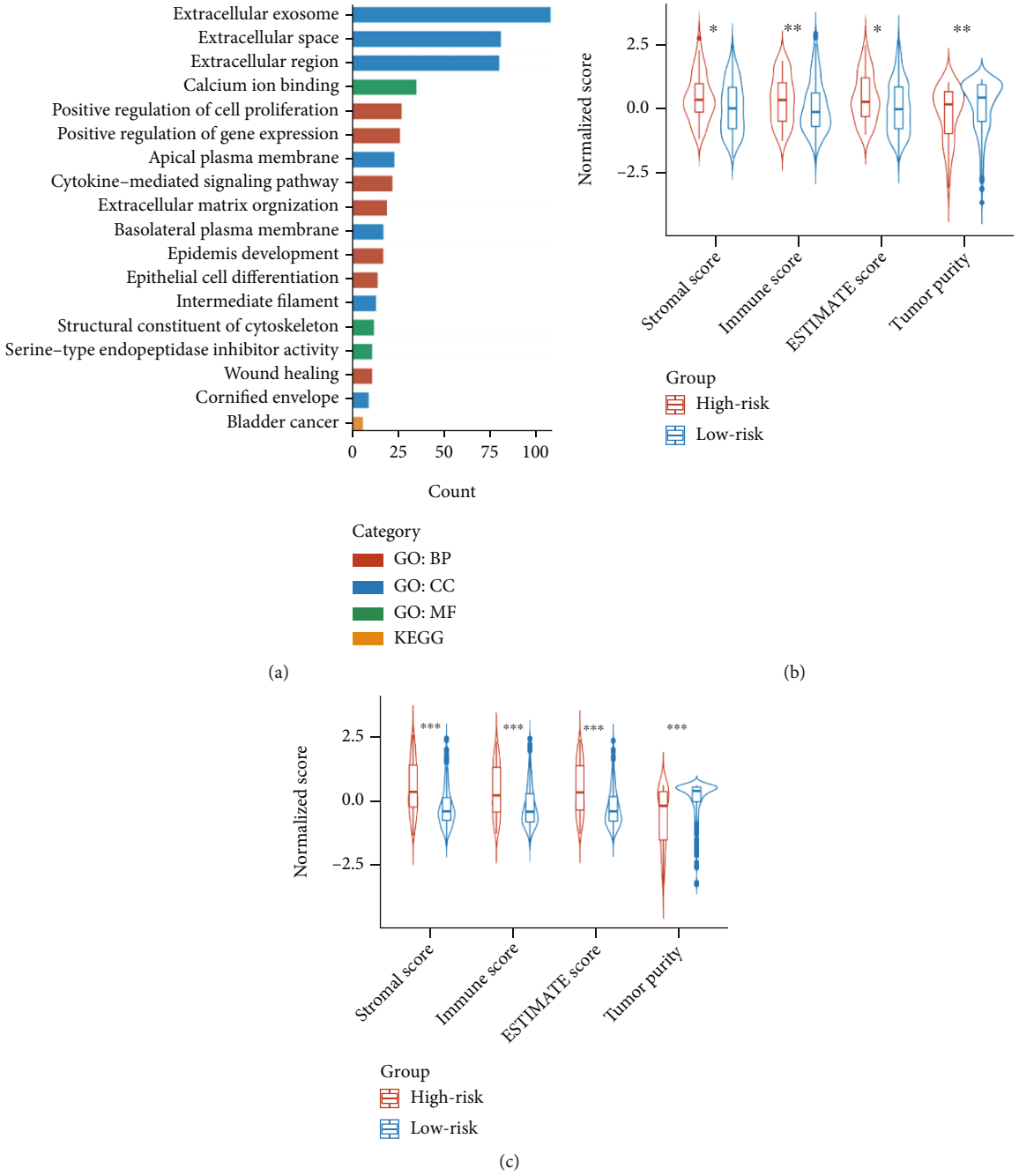

Figure 5: Continued.

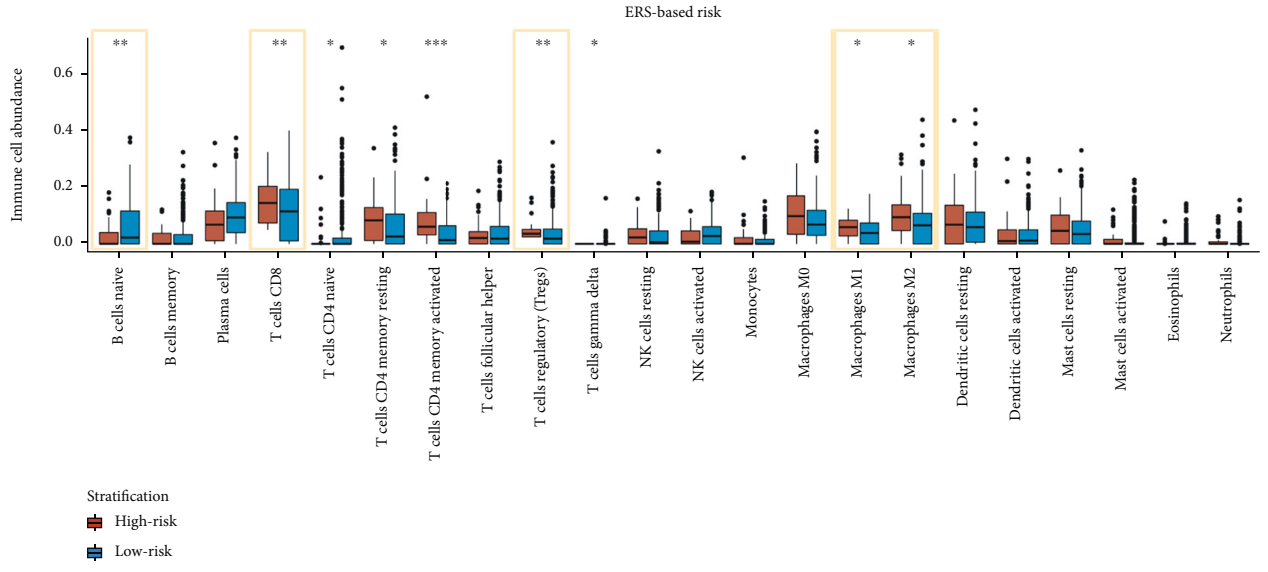

(d)

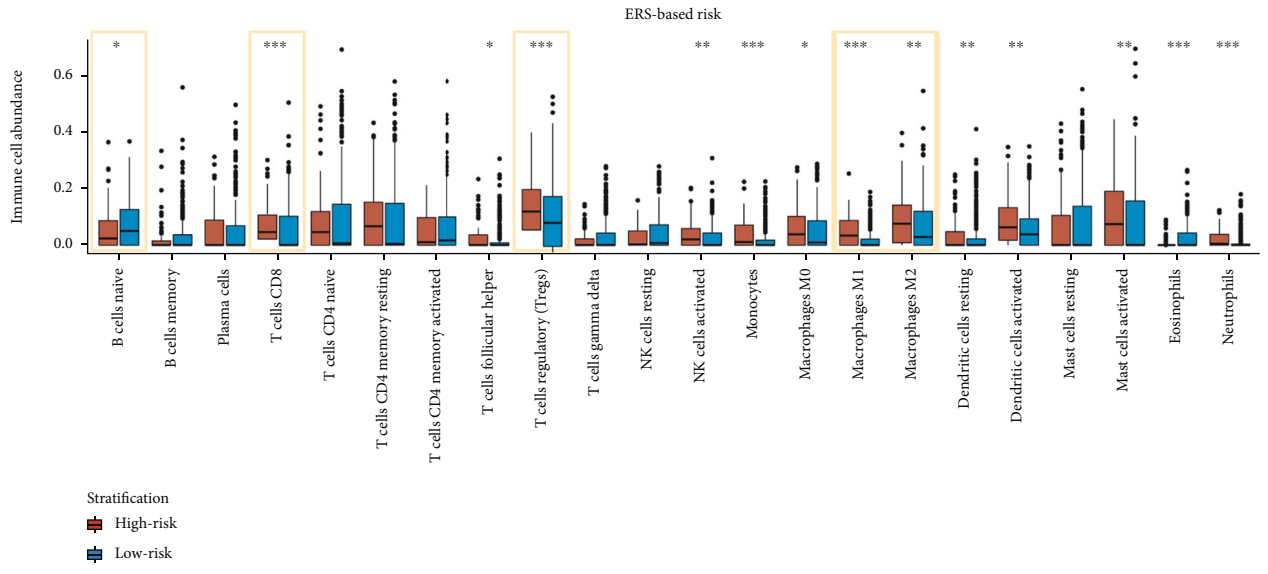

(e)

Figure 5: Functional enrichment and immune cell infiltration analyses based on the gene signature. (a) Bar graph displays significantly enriched pathways in high-risk patients. Violin plots show higher immune score, stromal score, ESTIMATE score, and lower tumor purity in the high-risk patients compared with low-risk patients in the training (b) and merged validation cohorts (c). Box plots depict that CD8+ T cells, Tregs, M1 macrophages, and M2 macrophages are higher infiltrated and B naïve cells are lower infiltrated and in high-risk patients in both training (d) and merged validation (e) cohorts. $*p < 0.05$; $**p < 0.01$; $***p < 0.001$.

patients had a higher immune score, stromal score, and lower tumor purity, suggesting a potential role of ERS in TME and was consistent with previous research [33]. The prognostic and predictive potential of immune cell infiltration in BC have been investigated, and several immunological markers have been linked with treatment outcomes [34]. Some studies reported that higher CD8+ T cell infiltration in the epithelium and invasive margin indicated a longer OS or DSI in BC patients [35–37]. However, one study reported a negative correlation between stromal CD8+ cell infiltration and survival outcomes [38]. CD8+ T cells were found to be more infiltrated in the tumors of high-risk patients, suggesting that we should pay more attention to this interesting phenomenon. Tumor-infiltrating Tregs are important suppressors of antitumor immunity. A meta-analysis study showed that Tregs were associated with poor OS in many solid tumors, consistent with our results [39]. Macrophages are essential components of innate immunity and can be classified into proinflammatory macrophages (M1) and anti-inflammatory macrophages (M2). In a previous study, the higher density of M2 macrophages was associated with higher pathological and histological grades in BC patients [40, 41]. Furthermore, there was a tendency for patients with high macrophage levels to have poor survival [34]. Our

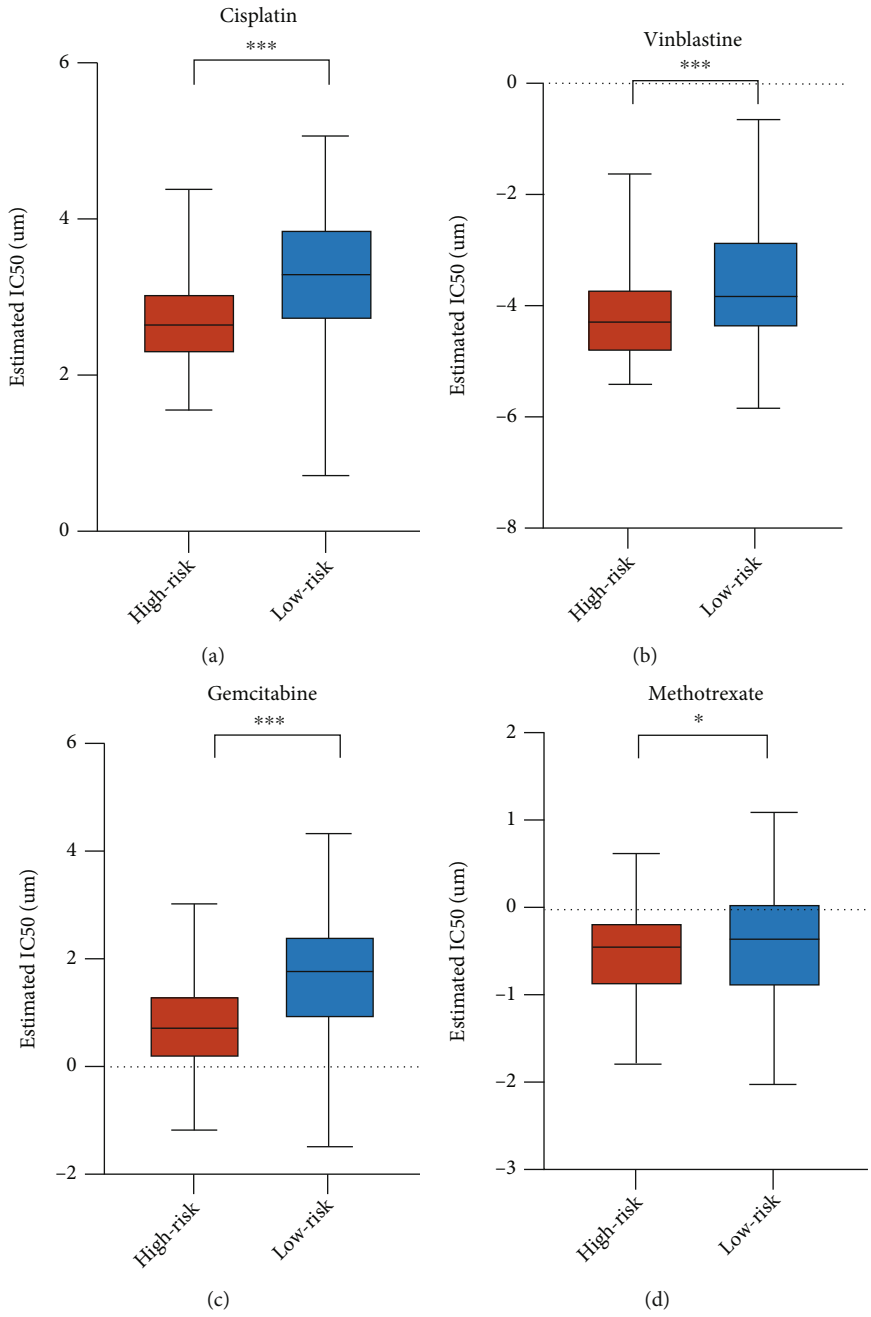

Figure 6: Continued.

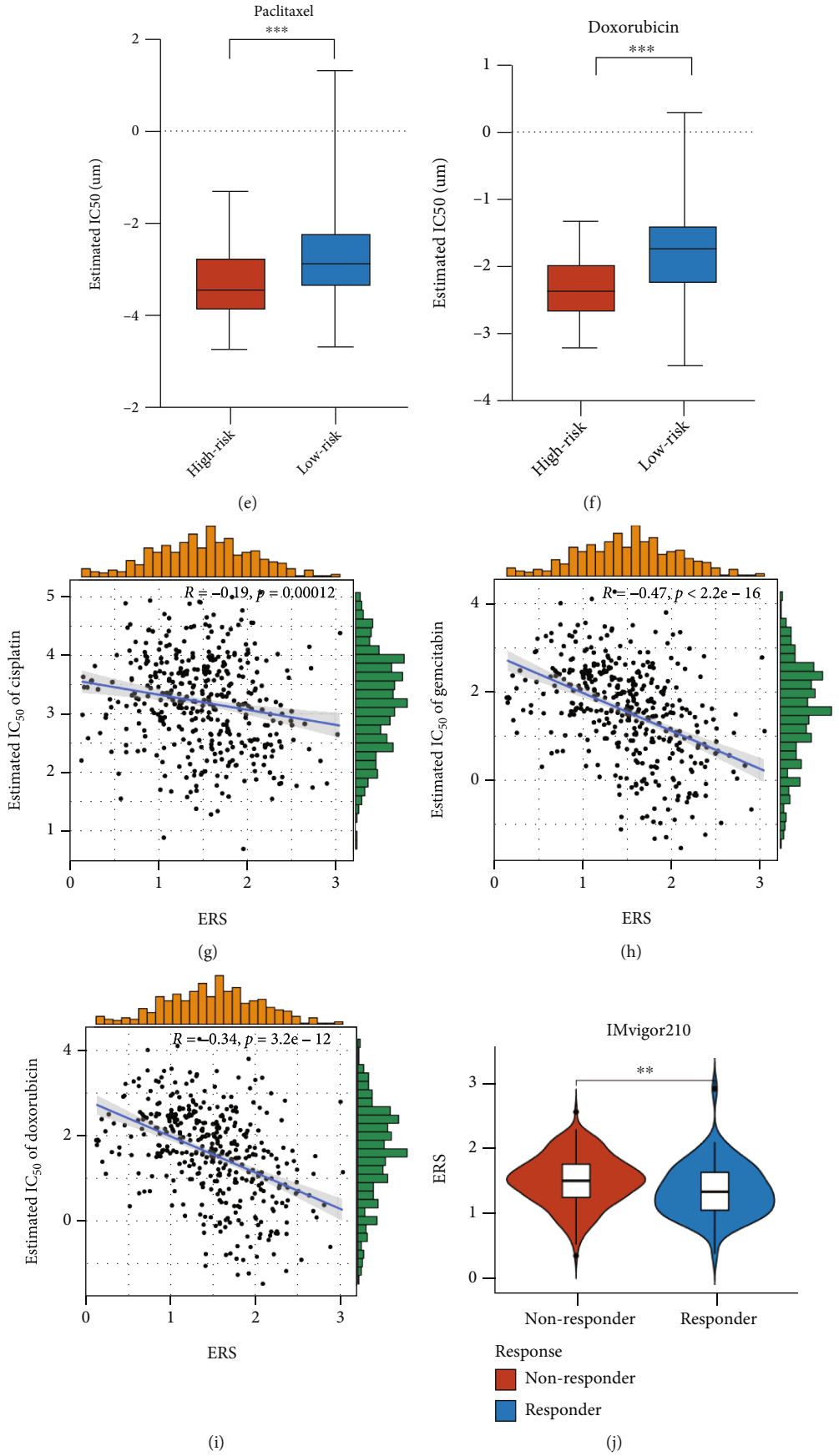

Figure 6: Continued.

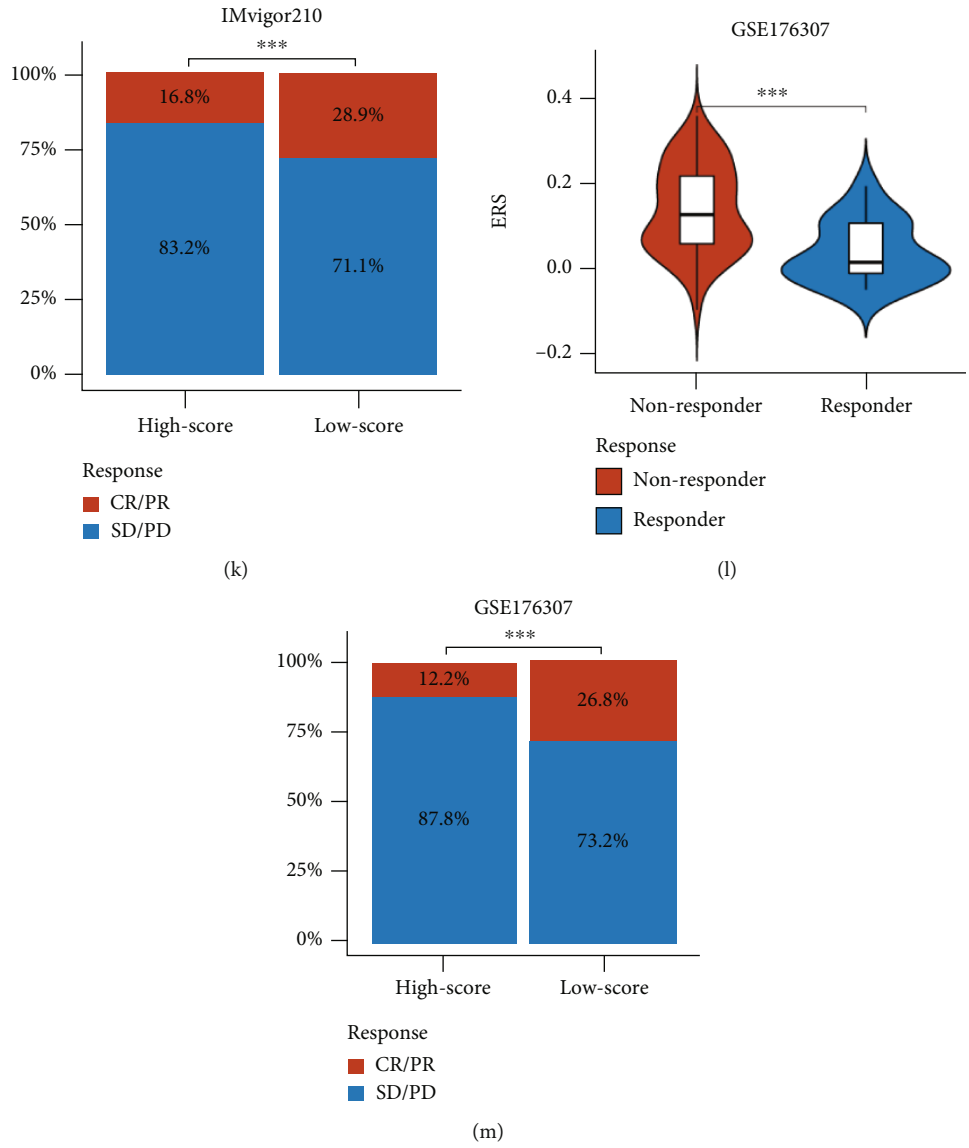

FIGURE 6: EMT-related gene signature predicts chemotherapeutic and immunotherapeutic benefits. Box plots display lower IC_{50} values of six commonly used chemical drugs in high-risk patients (a-f). Scatter plots illustrate negative correlations between ERS and the estimated IC50 values of cisplatin (g), gemcitabine (h), and doxorubicin (i). Violin plots show that ERS of nonresponders is significantly higher than that of responders in the immunotherapy cohort of IMvigor210 (j) and GSE176307 (l). High-risk patients present significantly lower percentages of responses (CR/PR) and higher percentages of nonresponses (SD/PD) in both IMvigor210 (k) and GSE176307 (m). IC_{50}: half-maximal inhibitory concentration. ERS: EMT-related risk score. CR: complete response. PR: partial response. SD: stable disease. PD: progressive disease. $*p < 0.05$; $**p < 0.01$; $***p < 0.001$.

results revealed that M2 macrophage infiltration was significantly higher in high-risk patients, consistent with previous research.

We selected six representative chemical drugs and found that high-risk patients were more sensitive to these drugs. Negative correlations between ERS and drug sensitivity were found in three chemotherapeutic drugs, including gemcitabine, cisplatin, and doxorubicin. The above results revealed that high-risk patients divided by ERS might be more likely to benefit from chemotherapy. Immune checkpoint inhibitors were approved for clinical use in metastatic BC in 2017. Unfortunately, only 21.1% of metastatic BC patients responded to ICB treatment (pembrolizumab) [42]. Therefore, predictive biomarkers are required to identify a specific subset of patients who may respond to immunotherapy. Our analysis indicated that low-risk patients showed a better response in two cohorts, suggesting that our model may be useful for identifying patients who may benefit from immunotherapy. These findings indicate that the gene signature can potentially guide clinical treatment decisions regarding chemotherapy and immunotherapy.

Although this is an original signature with promising clinical applications, this study has some limitations. Despite the robust performance of our gene signature in prognostic

prediction, more prospective studies with larger sample sizes are required to validate its general application. Moreover, an interesting phenomenon observed in this study, particularly regarding the underlying mechanisms of biological functions and immune cell infiltration, requires further experimental investigation. Furthermore, the lack of experimental and clinical evidence for verifying drug responses is also a limitation that should be addressed in the future.

5. Conclusion

In summary, we identified and verified a novel EMT-related gene signature with high prognostic prediction efficacy across multiple independent cohorts. Moreover, it was associated with the chemotherapeutic and immunotherapeutic responses of BC patients. This novel signature had great potential for predicting prognosis and guiding clinical therapies.

Data Availability

The data used to support the findings of this study are available from the corresponding author upon request.

Conflicts of Interest

The authors declare that there is no conflict of interest regarding the publication of this paper.

Authors' Contributions

Xiaopeng Hu and Yicun Wang designed the study. Yicun Wang and Hao Zhang analyzed the data and conducted the picture processing. Hao Zhang drafted the manuscript. Xiaopeng Hu and Yicun Wang revised the manuscript. All authors have read and approved the final version of manuscript. Yicun Wang and Hao Zhang contributed equally to this work.

Supplementary Materials

Supplementary Table 1. Univariate Cox analysis based on ssGSEA scores of cancer hallmarks in all three cohorts. Supplementary Table 2. GSEA of cancer hallmarks. Supplementary Table 3. Univariate and multivariate Cox regression analysis of clinical characteristics and ERS with survival outcomes (DSS, DFI) in the TCGA cohort. Supplementary Table 4. Univariate and multivariate Cox regression analysis of clinical characteristics and ERS with survival outcomes (OS, DSS) in the GSE13507 cohort. Supplementary Table 5. Univariate and multivariate Cox regression analysis of clinical characteristics and ERS with OS in the GSE32894 cohort. Supplementary Figure 1. Correlations between the EMT score and ERS, and expression levels of four genes included in the novel signature. *(Supplementary Materials)*

References

[1] H. Sung, J. Ferlay, R. L. Siegel et al., "Global cancer statistics 2020: GLOBOCAN estimates of incidence and mortality worldwide for 36 cancers in 185 countries," *CA: a Cancer Journal for Clinicians*, vol. 71, no. 3, pp. 209–249, 2021.

[2] R. T. Divrik, U. Yildirim, F. Zorlu, and H. Ozen, "The effect of repeat transurethral resection on recurrence and progression rates in patients with T1 tumors of the bladder who received intravesical mitomycin: a prospective, randomized clinical trial," *The Journal of Urology*, vol. 175, no. 5, pp. 1641–1644, 2006.

[3] W. J. Alfred, T. Lebret, E. M. Compérat et al., "Updated 2016 EAU guidelines on muscle-invasive and metastatic bladder cancer," *European Urology*, vol. 71, no. 3, pp. 462–475, 2017.

[4] P. A. Humphrey, H. Moch, A. L. Cubilla, T. M. Ulbright, and V. E. Reuter, "The 2016 WHO classification of tumours of the urinary system and male genital organs–part B: prostate and bladder tumours," *European Urology*, vol. 70, no. 1, pp. 106–119, 2016.

[5] M. Gerlinger, J. W. Catto, T. F. Orntoft, F. X. Real, E. C. Zwarthoff, and C. Swanton, "Intratumour heterogeneity in urologic cancers: from molecular evidence to clinical implications," *European Urology*, vol. 67, no. 4, pp. 729–737, 2015.

[6] J. Yang, P. Antin, G. Berx et al., "Guidelines and definitions for research on epithelial-mesenchymal transition," *Nature Reviews. Molecular Cell Biology*, vol. 21, no. 6, pp. 341–352, 2020.

[7] H. Peinado, D. Olmeda, and A. Cano, "Snail, Zeb and bHLH factors in tumour progression: an alliance against the epithelial phenotype?," *Nature Reviews. Cancer*, vol. 7, no. 6, pp. 415–428, 2007.

[8] E. Blaveri, J. P. Simko, J. E. Korkola et al., "Bladder cancer outcome and subtype classification by gene expression," *Clinical Cancer Research*, vol. 11, no. 11, pp. 4044–4055, 2005.

[9] E. Baumgart, M. S. Cohen, N. B. Silva et al., "Identification and prognostic significance of an epithelial-mesenchymal transition expression profile in human bladder tumors," *Clinical Cancer Research*, vol. 13, no. 6, pp. 1685–1694, 2007.

[10] M. Sanchez-Carbayo, N. D. Socci, J. Lozano, F. Saint, and C. Cordon-Cardo, "Defining molecular profiles of poor outcome in patients with invasive bladder cancer using oligonucleotide microarrays," *Journal of Clinical Oncology*, vol. 24, no. 5, pp. 778–789, 2006.

[11] A. E. Sayan, T. R. Griffiths, R. Pal et al., "SIP1 protein protects cells from DNA damage-induced apoptosis and has independent prognostic value in bladder cancer," *Proceedings of the National Academy of Sciences of the United States of America*, vol. 106, no. 35, pp. 14884–14889, 2009.

[12] W. Lu and Y. Kang, "Epithelial-mesenchymal plasticity in cancer progression and metastasis," *Developmental Cell*, vol. 49, no. 3, pp. 361–374, 2019.

[13] L. Chen, D. L. Gibbons, S. Goswami et al., "Metastasis is regulated via microRNA-200/ZEB1 axis control of tumour cell PD-L1 expression and intratumoral immunosuppression," *Nature Communications*, vol. 5, no. 1, p. 5241, 2014.

[14] J. L. McFaline-Figueroa, A. J. Hill, X. Qiu, D. Jackson, J. Shendure, and C. Trapnell, "A pooled single-cell genetic screen identifies regulatory checkpoints in the continuum of the epithelial-to-mesenchymal transition," *Nature Genetics*, vol. 51, no. 9, pp. 1389–1398, 2019.

[15] A. Liberzon, A. Subramanian, R. Pinchback, H. Thorvaldsdóttir, P. Tamayo, and J. P. Mesirov, "Molecular signatures database (MSigDB) 3.0," *Bioinformatics*, vol. 27, no. 12, pp. 1739-1740, 2011.

[16] A. Subramanian, P. Tamayo, V. K. Mootha et al., "Gene set enrichment analysis: a knowledge-based approach for interpreting genome-wide expression profiles," *Proceedings of the National Academy of Sciences of the United States of America*, vol. 102, no. 43, pp. 15545–15550, 2005.

[17] G. Yu, L. G. Wang, Y. Han, and Q. Y. He, "clusterProfiler: an R package for comparing biological themes among gene clusters," *OMICS*, vol. 16, no. 5, pp. 284–287, 2012.

[18] M. E. Ritchie, B. Phipson, D. Wu et al., "Limma powers differential expression analyses for RNA-sequencing and microarray studies," *Nucleic Acids Research*, vol. 43, no. 7, article e47, 2015.

[19] J. M. Taylor, "Random Survival Forests," *Journal of Thoracic Oncology*, vol. 6, no. 12, pp. 1974-1975, 2011.

[20] G. J. Koelwyn, D. F. Quail, X. Zhang, R. M. White, and L. W. Jones, "Exercise-dependent regulation of the tumour microenvironment," *Nature Reviews. Cancer*, vol. 17, no. 10, pp. 620–632, 2017.

[21] K. Yoshihara, M. Shahmoradgoli, E. Martínez et al., "Inferring tumour purity and stromal and immune cell admixture from expression data," *Nature Communications*, vol. 4, no. 1, p. 2612, 2013.

[22] A. M. Newman, C. L. Liu, M. R. Green et al., "Robust enumeration of cell subsets from tissue expression profiles," *Nature Methods*, vol. 12, no. 5, pp. 453–457, 2015.

[23] W. Yang, J. Soares, P. Greninger et al., "Genomics of drug sensitivity in cancer (GDSC): a resource for therapeutic biomarker discovery in cancer cells," *Nucleic Acids Research*, vol. 41, no. - Database issue, pp. D955–D961, 2013.

[24] D. Maeser, R. F. Gruener, and R. S. Huang, "oncoPredict: an R package for predictingin vivoor cancer patient drug response and biomarkers from cell line screening data," *Briefings in Bioinformatics*, vol. 22, no. 6, p. 22, 2021.

[25] T. Powles, I. Durán, M. S. van der Heijden et al., "Atezolizumab versus chemotherapy in patients with platinum-treated locally advanced or metastatic urothelial carcinoma (IMvigor211): a multicentre, open- label, phase 3 randomised controlled trial," *Lancet*, vol. 391, no. 10122, pp. 748–757, 2018.

[26] R. Jain, P. W. Shaul, Z. Borok, and B. C. Willis, "Endothelin-1 induces alveolar epithelial-mesenchymal transition through endothelin type a receptor-mediated production of TGF-β1," *American Journal of Respiratory Cell and Molecular Biology*, vol. 37, no. 1, pp. 38–47, 2007.

[27] R. Kalluri and E. G. Neilson, "Epithelial-mesenchymal transition and its implications for fibrosis," *The Journal of Clinical Investigation*, vol. 112, no. 12, pp. 1776–1784, 2003.

[28] R. Cao, L. Yuan, B. Ma, G. Wang, W. Qiu, and Y. Tian, "An EMT-related gene signature for the prognosis of human bladder cancer," *Journal of Cellular and Molecular Medicine*, vol. 24, no. 1, pp. 605–617, 2020.

[29] G. Shan, X. Zhou, J. Gu et al., "Downregulated exosomal microRNA-148b-3p in cancer associated fibroblasts enhance chemosensitivity of bladder cancer cells by downregulating the Wnt/β-catenin pathway and upregulating PTEN," *Cellular Oncology (Dordrecht)*, vol. 44, no. 1, pp. 45–59, 2021.

[30] M. Wang, Z. Zhang, D. Pan et al., "Circulating lncRNA UCA1 and lncRNA PGM5-AS1 act as potential diagnostic biomarkers for early-stage colorectal cancer," *Bioscience Reports*, vol. 41, no. 7, 2021.

[31] D. J. McConkey, W. Choi, L. Marquis et al., "Role of epithelial-to-mesenchymal transition (EMT) in drug sensitivity and metastasis in bladder cancer," *Cancer Metastasis Reviews*, vol. 28, no. 3-4, pp. 335–344, 2009.

[32] J. Liu, Z. Zheng, W. Zhang et al., "Dysregulation of tumor microenvironment promotes malignant progression and predicts risk of metastasis in bladder cancer," *Annals of Translational Medicine*, vol. 9, no. 18, p. 1438, 2021.

[33] L. Wang, A. Saci, P. M. Szabo et al., "EMT- and stroma-related gene expression and resistance to PD-1 blockade in urothelial cancer," *Nature Communications*, vol. 9, no. 1, p. 3503, 2018.

[34] S. van Wilpe, E. Gerretsen, A. G. van der Heijden, I. de Vries, W. R. Gerritsen, and N. Mehra, "Prognostic and predictive value of tumor-infiltrating immune cells in urothelial cancer of the bladder," *Cancers*, vol. 12, 2020.

[35] H. Fu, Y. Zhu, Y. Wang et al., "Identification and validation of stromal immunotype predict survival and benefit from adjuvant chemotherapy in patients with muscle-invasive bladder cancer," *Clinical Cancer Research*, vol. 24, no. 13, pp. 3069–3078, 2018.

[36] X. D. Li, C. W. Huang, Z. F. Liu et al., "Prognostic role of the immunoscore for patients with urothelial carcinoma of the bladder who underwent radical cystectomy," *Annals of Surgical Oncology*, vol. 26, no. 12, pp. 4148–4156, 2019.

[37] P. Sharma, Y. Shen, S. Wen et al., "CD8 tumor-infiltrating lymphocytes are predictive of survival in muscle-invasive urothelial carcinoma," *Proceedings of the National Academy of Sciences of the United States of America*, vol. 104, no. 10, pp. 3967–3972, 2007.

[38] B. Wang, W. Pan, M. Yang et al., "Programmed death ligand-1 is associated with tumor infiltrating lymphocytes and poorer survival in urothelial cell carcinoma of the bladder," *Cancer Science*, vol. 110, no. 2, pp. 489–498, 2019.

[39] B. Shang, Y. Liu, S. J. Jiang, and Y. Liu, "Prognostic value of tumor-infiltrating FoxP3$^+$ regulatory T cells in cancers: a systematic review and meta-analysis," *Scientific Reports*, vol. 5, no. 1, p. 15179, 2015.

[40] G. Sjödahl, K. Lövgren, M. Lauss et al., "Infiltration of CD3$^+$ and CD68$^+$ cells in bladder cancer is subtype specific and affects the outcome of patients with muscle-invasive tumors[1]," *Urologic Oncology*, vol. 32, no. 6, pp. 791–797, 2014.

[41] H. Takeuchi, M. Tanaka, A. Tanaka, A. Tsunemi, and H. Yamamoto, "Predominance of M2-polarized macrophages in bladder cancer affects angiogenesis, tumor grade and invasiveness," *Oncology Letters*, vol. 11, no. 5, pp. 3403–3408, 2016.

[42] Y. Fradet, J. Bellmunt, D. J. Vaughn et al., "Randomized phase III KEYNOTE-045 trial of pembrolizumab versus paclitaxel, docetaxel, or vinflunine in recurrent advanced urothelial cancer: results of >2 years of follow-up," *Annals of Oncology*, vol. 30, no. 6, pp. 970–976, 2019.

Hindawi
Disease Markers
Volume 2022, Article ID 8928282, 11 pages
https://doi.org/10.1155/2022/8928282

Research Article

A Computationally Constructed lncRNA-Associated Competing Triplet Network in Clear Cell Renal Cell Carcinoma

Hui Zhang,[1] **Qing Ye**,[2] **Zixiang Chen**,[3] **Chunyi Zhao**,[3] **Qian Wu**,[3] **Yuting Ding**,[3] **Qixiang Shao**,[4] **and Yangjing Zhao**[3]

[1]*Department of Laboratory Medicine, Affiliated Hospital of Jiangsu University, Zhenjiang 212013, China*
[2]*Department of Pathology, The First Affiliated Hospital of USTC, Division of Life Sciences and Medicine, University of Science and Technology of China, Hefei 230036, China*
[3]*Department of Laboratory Medicine, School of Medicine, Jiangsu University, Zhenjiang 212013, China*
[4]*Institute of Medical Genetics and Reproductive Immunity, School of Medical Science and Laboratory Medicine, Jiangsu College of Nursing, Huai'an 223005, China*

Correspondence should be addressed to Qixiang Shao; shao_qx@ujs.edu.cn and Yangjing Zhao; zhaoyangjing@ujs.edu.cn

Received 10 May 2022; Revised 4 October 2022; Accepted 11 October 2022; Published 17 November 2022

Academic Editor: Chia-Jung Li

Long noncoding RNAs (lncRNAs) are revealed to be involved in the tumorigenesis and progression of human malignancies mediated by microRNA (miRNA) via the competing endogenous RNA (ceRNA) mechanism, a newly proposed "RNA language." However, the lncRNA-associated competing triplet (lncACT) network among ceRNA transcripts in clear cell renal cell carcinoma (ccRCC) is currently lacking. We carried out differential expression analysis to identify aberrantly expressed lncRNAs, miRNAs, and mRNAs by analyzing the RNA-seq data of 420 ccRCC tissues and 71 noncancerous kidney tissues obtained from The Cancer Genome Atlas (TCGA). Then, a ccRCC-specific ceRNA network was built using computational algorithms, including miRcode, TargetScan, miRanda, and miRTarBase. In total, 1491 dysregulated lncRNAs were found between normal renal tissues and ccRCC (fold change > 4 and false discovery rate < 0.01). A ceRNA network that comprised of 46 DElncRNAs, 11 DEmiRNAs, and 55 DEmRNAs was established by integrating the lncRNA/miRNA and miRNA/mRNA interactions into lncACTs. Several lncRNAs were identified to be significantly associated with clinical features of ccRCC patients. Notably, four key lncRNAs (TCL6, HOTTIP, HULC, and PCGEM1) were tightly correlated with both patients' clinical characteristics and overall survival (log-rank $P < 0.05$), indicating their potential important roles in ccRCC. HOTTIP may be a potential prognostic and therapeutic molecular marker for ccRCC patients. Collectively, our results provide a comprehensive view of the lncRNA-associated ceRNA regulatory network for a better understanding of the mechanisms and prognosis biomarkers for ccRCC.

1. Introduction

Renal cell carcinoma (RCC) is the most lethal urinary system malignancy in adults with an increasing morbidity globally [1]. It is estimated that 76,080 new cases and 13,780 deaths from kidney malignancies occurred in the world in 2021 [2]. RCC, as a heterogeneous group of disease, is subdivided into several histological subtypes according to the different nephron cell types that tumors derived from, including clear cell RCC (ccRCC, ~75%), papillary RCC (pRCC, ~15%), and chromophobe RCC (chRCC, ~5%) [3]. ccRCC is the predominant and most malignant subtype of renal carcinoma. Although the diagnosis of ccRCC improved mainly due to the advanced imaging detection technologies, the clinical behaviors of ccRCC patients are aggressive, especially the high rate of metastatic progression [4]. Therefore, identification of the molecular mechanisms underlying ccRCC for developing diagnostic markers and therapeutic targets becomes urgently needed.

Noncoding RNAs (ncRNAs) are categorized into long ncRNAs and short ncRNAs according to their length. The noncoding RNA transcripts more than 200 nucleotides long

are generally termed as "long noncoding RNAs" (lncRNAs) [5]. lncRNAs have been recognized to involve in the pathogenesis of multiple cancers by disrupting various biological processes [6]. The abnormal expressions of microRNAs (miRNAs, 20-22 nucleotide in length) participate in the oncogenesis and cancer progression [7]. In recent years, lncRNAs were verified to function as competing endogenous RNAs (ceRNAs) to communicate with other RNAs via sharing miRNA-binding sites. This lncRNA-miRNA-RNA interaction was a subclass of ceRNAs, called lncRNA-associated competing triplets (lncACTs) [8]. In 2014, Xia et al. firstly constructed a lncACT cross-talk network in gastric cancer and also established a bioinformatics-based approach to predict cancer-associated ceRNA network [9]. Subsequently, several cancer-specific ceRNA networks have also been revealed in various cancers, including hepatocellular carcinoma [10], bladder cancer [11], and thyroid carcinoma [12].

However, there are only limited studies so far on lncACTs in RCC. lncRNA MALAT1 has been identified to function as a ceRNA by mediating the MALAT1/mir-200s/ZEB2 pathway to facilitate ccRCC proliferation and metastasis [13]. lncRNA HOTAIR, an oncogene in various tumors, was also reported to act as a ceRNA to promote HIF-1α/AXL cascade by binding mir-217 in RCC [14]. A drug resistance-related lncRNA lncARSR disseminated sunitinib resistance by sponging mir-34/mir-449 to increase target genes expression in RCC cells [15]. Fan et al. constructed lncRNA-related ceRNA network and discovered the nomograms and related infiltrating immune cells to predict prognosis of pRCC patients [16]. However, huge genetic heterogeneity exists among different histologic subtypes of RCC [17]. In this study, differentially expressed lncRNAs, miRNAs, and mRNAs (DElncRNAs, DEmRNAs, and DEmiRNAs) were screened out of the expression profiles of a 420 ccRCC patient cohort from The Cancer Genome Atlas (TCGA). A ccRCC specific ceRNA regulatory network was also built based on the potential competing triplets of lncRNA/miRNA/mRNA predicted by computational algorithms and databases. We also identified several key lncRNAs to be associated with ccRCC progression and prognosis.

2. Materials and Methods

2.1. Patient Dataset. TCGA is a public database providing researchers open access to the multiple cancer genomic profiles for analyses and publications [18]. This study meets the freedom-to-publish criteria announced on TCGA website (https://cancergenome.nih.gov/publications/publicationguidelines). A cohort of 537 ccRCC patients obtained from TCGA was downloaded for this study. The exclusion criteria included the following: (1) patients without complete clinicopathological data, including age, gender, race, TNM stage, and pathologic stage (12 cases); (2) patients with follow-up data over 2000 days (84 cases); and (3) patients with incomplete RNA-seq or miRNA-seq data (21 cases). In total, 420 ccRCC patients (cohort T) and 71 normal samples (cohort N) were enrolled in this study. The RNA and miRNA expression data (level 3) were produced from IlluminaHiseq_RNASeq and IlluminaHiseq_miRNASeq sequencing platform and prenormalized by TCGA archive (http://cancergenome.nih.gov).

2.2. Construction of lncACT Cross-Talk Network. We carried out differential expression analysis with edgeR package in Bioconductor [19]. Stringent filtering criteria were all set as $|\log_2 FC| > 2$ and FDR < 0.01 (FC: fold change; FDR: false discovery rate). Among these differentially expressed genes (DEGs), the putative interactions of miRNA-lncRNA were collected from miRcode [20]. Different miRNA-target prediction algorithms, including experimentally validated database TargetScan (http://www.targetscan.org/mamm_31/) [21], miRanda (http://www.microrna.org/microrna/home.do) [22], and miRTarBase (http://mirtarbase.mbc.nctu.edu.tw/) [23], were used to predict the miRNA target mRNAs. These tools provide miRNA-target interactions with comprehensive annotation and experimental validation. Finally, the lncRNA-associated ceRNA network of ccRCC was integrated and visualized based on the above competing triplets using Cytoscape v3.5.1 (http://www.cytoscape.org/) [24].

2.3. Functional Enrichment Analysis. To access functional roles of the genes in the ceRNA network, Gene Ontology (GO) was performed using Database for Annotation, Visualization and Integration Discovery (DAVID, https://david.ncifcrf.gov/) (P value < 0.05). Meanwhile, pathway analysis was conducted using Kyoto Encyclopedia of Genes and Genomes (KEGG) by KOBAS 3.0 (P value < 0.01).

2.4. Coexpression Analysis. Correlation test was conducted by the R software to figure out the coexpressed genes associated with HOTTIP ($|cor|>0.3$ and P value < 0.001).

2.5. Drug Sensitivity Analysis. Drug sensitivity analysis was carried out with pRRophetic package in Bioconductor to discover the drugs with significant differences in sensitivity between HOTTIP high and low groups (P value < 0.05).

2.6. Statistical Analysis. Unpaired t-test was applied to identify DEGs and the difference of DElnRNAs between different pathological subgroups. The associations between DElncRNAs expression and patients' overall survival (OS) were analyzed by univariate Cox proportional hazards regression (log-rank $P < 0.05$). Kaplan-Meier method was employed to generate overall survival curves.

3. Results

3.1. Patient Characteristics. A total of 420 patients who were pathologically diagnosed as ccRCC and 71 normal samples were enrolled in this study. The clinicopathological information of study population is summarized in Table 1. The median age was 60 years. Consistent with a previous report [25], white male individuals appeared to be the majority of RCC patients with the gender ratio (male/female) of 1.9/1 and white race ratio of 86.7%.

3.2. Screening Results of DEGs in ccRCC. After screening the RNA and miRNA expression profiles by the threshold of $|\log_2 FC| > 2$ and FDR < 0.01, we found 1491 DElncRNAs,

Table 1: Clinical characteristics of 420 patients with ccRCC in cohort T.

Parameter	Cohort T ($n = 420$) (%)
Age (mean ± SD[1])	60.4 ± 12.1
Gender	
Male	275 (65.5)
Female	145 (34.5)
Race	
Asian	8 (1.9)
White	364 (86.7)
Black or African American	48 (11.4)
Pathologic stage	
Stage I	199 (47.4)
Stage II	43 (10.3)
Stage III	106 (25.2)
Stage IV	72 (17.1)
Tumor size	
T1	205 (48.8)
T2	51 (12.1)
T3	153 (36.5)
T4	11 (2.6)
Lymph node	
N0	181 (43.1)
N1	14 (3.3)
NX	225 (53.6)
Metastasis status	
M0	326 (77.6)
M1	67 (16.0)
MX	27 (6.4)

[1]Standard deviation.

2368 DEmRNAs, and 53 miRNAs that aberrantly expressed between ccRCC tumor tissues and normal tissues. Among them, 989 lncRNAs, 1610 mRNAs, and 32 miRNAs were upregulated, while 502 lncRNAs, 758 mRNAs, and 21 miRNAs were downregulated in cohort T compared with cohort N. The total upregulated and downregulated lncRNAs, mRNAs, and miRNAs were listed in Table S1-6. Hierarchical clustering was further used to identify expression patterns of DEGs between two cohorts. The top 50 overexpressed and top 50 downexpressed lncRNAs were visualized in the heatmap, which showed that ccRCC tumor tissues had significantly different expression patterns from normal tissues (Figure 1 and Table S7).

3.3. lncACT Cross-Talk Network in ccRCC. The ceRNA hypothesis is described as a complex posttranscriptional regulatory mechanism between lncRNAs and other RNAs mediated by miRNAs through sharing miRNA response elements [26]. Therefore, further analysis was performed to establish lncACT cross-talk network based on the above DEGs in ccRCC. We got 11 specific DEmiRNAs that targeted on 46 DElncRNAs by miRcode online tools, which is a lncRNA-miRNA interaction prediction database (Table 2). To further analyze these DEmiRNAs, we comprehensively considered the miRNA-mRNA interactions obtained from TargetScan, miRTarBase, and miRanda databases to enhance the predictive reliability. A total of 55 targeted mRNAs were predicted to interact with 7 DEmiRNAs and were also involved in the above 2368 DEmRNAs (Table 3). By integrating these lncRNA/miRNA and miRNA/mRNA interactions into lncACTs, the ceRNA network is constructed and visualized in Figure 2, containing 46 DElncRNAs, 11 DEmiRNAs, and 55 DEmRNAs.

3.4. Functional Enrichment Analysis. To identify the functions of the 55 DEmRNAs involved in the ceRNA network, functional analysis was performed. GO analysis revealed 26 enriched GO categories in the "biological processes" (P value < 0.05), top 15 of which are visualized in Figure 3. There were two apoptotic processes significantly enriched in GO terms (GO:1902042 and GO:0043065). According to P value < 0.01, 27 KEGG categories were selected as significantly enriched KEGG pathways. The top ten enriched pathways are listed in Table 4, including four cancer-related pathways (microRNAs in cancer, bladder cancer, transcriptional misregulation in cancer, and pathways in cancer). Cyclin D1 (CCND1) was notably involved in six of the top ten pathways, indicating its complex roles in the progress of the tumor.

3.5. The Clinical Relevance of DElncRNAs in ccRCC. We next analyzed the association between the 46 DElncRNAs in the ceRNA network and clinicopathological features. A total of eight lncRNAs were discriminatively expressed in different clinical feature subgroups ($|\log_2 FC| > 2$ and $FDR < 0.01$) (Table 5). We found six downregulated lncRNAs (C12orf77, TCL6, C8orf49, PCGEM1, and ERVMER61-1), and two upregulated lncRNAs (HOTTIP and LINC00200) were significantly related to the progression of ccRCC. Both C12orf77 and TCL6 not only could inhibit tumor growth (T3 + T4 vs. T1 + T2) but also downexpressed in individuals with high levels of the pathologic stage, implying their negative roles in tumor development of ccRCC. HULC was identified to promote lymph node metastasis; however, low expression of HULC seemed to be correlated with high levels of tumor size, distant metastases, and pathologic stage.

Subsequently, the Kaplan-Meier analysis was applied to investigate overall survival time for DElncRNAs in ccRCC patients. Among the 46 DElncRNAs involved in the lncACT network, five lncRNAs (TCL6, PCGEM1, FGF12-AS2, LINC00443, and LINC00472) were found positively associated with overall survival by univariate Cox regression analysis (log-rank $P < 0.05$), while another eight lncRNAs (HOTTIP, HULC, PVT1, WT1-AS, C20orf203, NALCN-AS1, TRIM36-IT1, and LINC00299) were negatively correlated with survival. The Kaplan-Meier curves of HOTTIP, HULC, TCL6, and PCGEM1, which also differentially expressed in clinical feature comparisons, are shown in Figure 4(a). The Kaplan-Meier curve analysis was also employed to investigate overall survival for the DEmiRNAs associated with this four lncRNAs. Notably, increased expression of mir-144, which was predicted to interact with

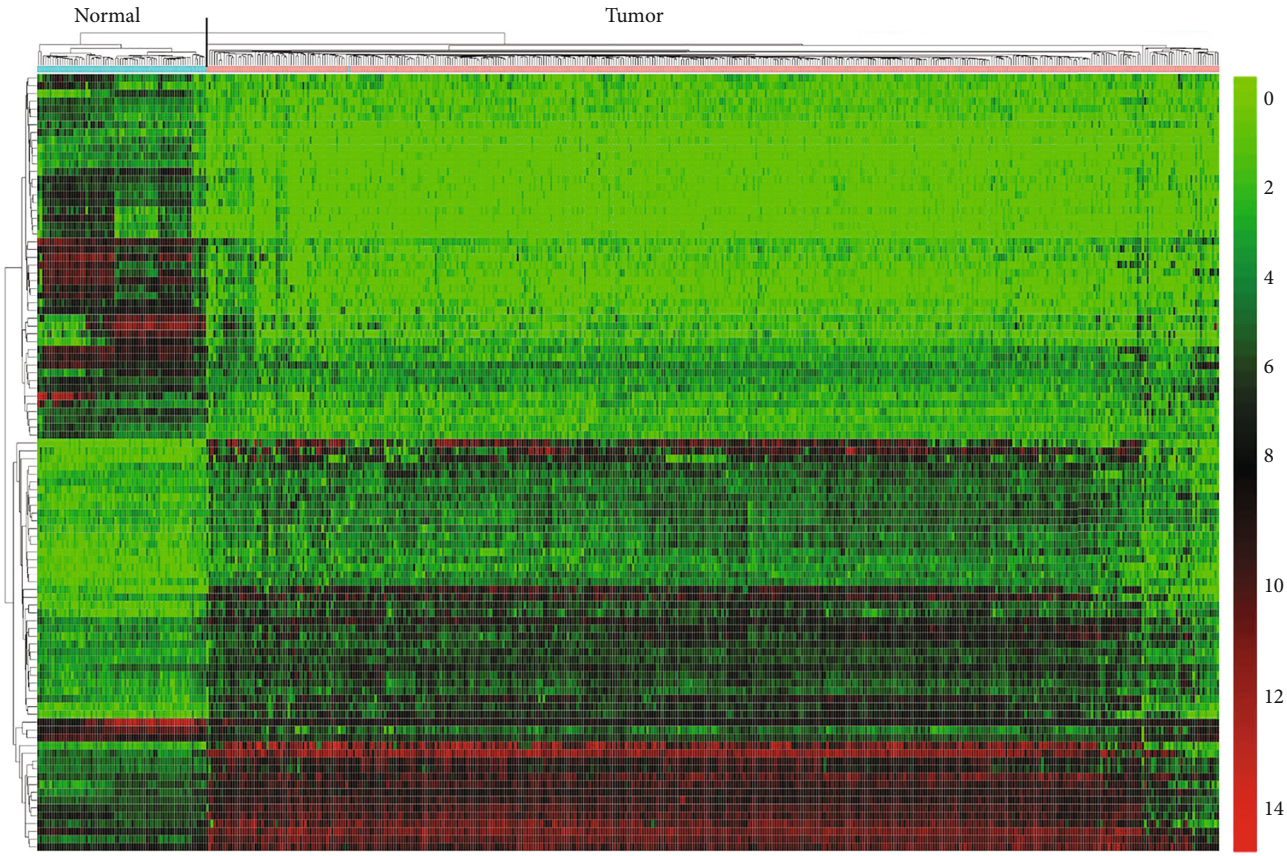

Figure 1: Heatmap of top 50 upregulated and top 50 downregulated DElncRNAs in clear cell renal cell carcinoma (ccRCC). Blue and red stripes represent normal samples and tumor samples, respectively. Descending normalized expression level is colored from red to green.

TCL6, was positively associated with prognosis. The high expression of mir-155, which potentially targeted HULC and PCGEM1, was correlated with poor prognosis (Figure 4(b)).

3.6. High Expression of HOTTIP Associated with Decreased Drug Sensitivity. To further understand the expression of HOTTIP in ccRCC patients, transcriptome sequencing data of 420 ccRCC and 71 normal samples were extracted from the TCGA database. HOTTIP expression level was significantly higher in ccRCC patients than in normal controls (Figure 5(a)). Coexpression analysis showed that 55 genes were associated with HOTTIP expression, including 7 negatively correlated genes and 48 positively correlated genes (Table S8). The correlation circle diagram showed that HOXA13, SERPIND1, ALDH1L2, AADAC, ADAM33, and OSBPL6 were positively correlated with HOTTIP, and BCL2, EDNRB, AQP1, ENPP4, and FBXL3 were negatively correlated with HOTTIP (Figure 5(b)). Drug sensitivity analysis identified that the half maximal inhibitory concentration (IC_{50}) of gemcitabine, pazopanib, sunitinib, and XL-184 in ccRCC patients with high HOTTIP expression was significantly higher than those in patients with low HOTTIP expression, indicating that patients with high HOTTIP expression were less sensitive to these treatments (Figure 6).

4. Discussion

Previous reports have shown that lncRNAs participated in tumorigenesis, cancer progression, and metastasis of RCC and functioned as oncogenes or tumor suppressors. Several studies have conducted genomic microarrays to reveal the expression patterns of lncRNAs based on small sample size [27, 28]. The tumor-specific lncACT cross-talk network has been previously described in chRCC [29]. However, different RCC histological subtypes encompass a wide diversity of molecular mechanisms for their tumorigenesis. Thus, there is an urgent to explore the lncRNA-associated ceRNA network in ccRCC. In the current study, we analyzed the expression profile data of ccRCC patient cohort in TCGA archive to comprehensively identify the landscape regarding how tumor-specific lncRNAs function in ccRCC. We successfully built the lncRNA-associated ceRNA network in ccRCC according to the predicted competing triplets among DElncRNAs, DEmRNAs, and DEmiRNAs.

Recent researches have demonstrated that lncRNAs could communicate with miRNAs and indirectly regulate miRNA targets via competing interactions. The lncACT interactions might actively function as valuable prognostic indicators in cancers [8]. Hence, we speculate that some specific lncACT cross-talks comprising lncRNA, miRNA, and mRNA may affect ccRCC progression. We utilized stringent

Table 2: The 11 specific DEmiRNAs and 46 target DElncRNAs in ccRCC.

lncRNA	miRNAs	lncRNA	miRNAs
ARAP1-AS2	mir-122	LINC00461	mir-122, mir-137, mir-141, mir-144, mir-216b, mir-508
ARHGEF26-AS1	mir-141	LINC00472	mir-155, mir-216b, mir-506
BPESC1	mir-216b, mir-506, mir-508	LINC00473	mir-142, mir-210
C12orf77	mir-137, mir-216b	LINC00487	mir-216b, mir-506
C15orf56	mir-144, mir-216b, mir-506	LINC00507	mir-216b
C20orf197	mir-122, mir-137, mir-144, mir-508	LMO7-AS1	mir-122, mir-137
C20orf203	mir-506	LY86-AS1	mir-137, mir-141, mir-142, mir-155, mir-216b, mir-506
C8orf49	mir-122	MIAT	mir-141, mir-155, mir-216b
CDRT7	mir-142	MIR155HG	mir-155
CHL1-AS1	mir-137	NALCN-AS1	mir-21, mir-508
DLEU7-AS1	mir-142	NLGN1-AS1	mir-122, mir-155
ERVMER61-1	mir-21	PCGEM1	mir-155, mir-506
FGF12-AS2	mir-506	PVT1	mir-216b
FRY-AS1	mir-122	PWRN1	mir-122
HOTTIP	mir-137, mir-506	SFTA1P	mir-122, mir-216b
HULC	mir-155	SLC25A5-AS1	mir-122, mir-144
LINC00200	mir-506	SLC6A1-AS1	mir-508
LINC00284	mir-141	SPATA13	mir-137, mir-506
LINC00299	mir-137, mir-21	TCL6	mir-122, mir-144
LINC00343	mir-142, mir-506	TRIM36-IT1	mir-155
LINC00410	mir-216b	TSSC1-IT1	mir-137
LINC00426	mir-216b	VCAN-AS1	mir-141
LINC00443	mir-141, mir-144	WT1-AS	mir-141, mir-155, mir-216b

Table 3: The 7 DEmiRNAs and 55 target DEmRNAs in ccRCC.

miRNA	mRNAs targeted by miRNA
mir-137	CIDEC, LHFPL2, LYPD6
mir-141	NR0B2, PRELID2, RASSF2
mir-142	CDC6, DEPDC1, GFI1, HMGA2, KIF5A, SCD
mir-144	BTG2, FGA, FGB, GRIK3, IL20RB, SIX4, TGFBI
mir-155	ADAMTS4, CARD11, CCND1, CD36, CTLA4, E2F2, ERMP1, GATM, GPM6B, HAL, ITK, KIF14, LY6K, MMP16, PCDH9, SPI1, TYRP1, ZIC3, ZNF98
mir-21	BTG2, CCL20, CXCL10, E2F2, FASLG, GXYLT2, HAPLN1, KLK2, MOXD1, MRAP2, NCAPG, NETO2, PPFIA4, ST6GAL1, TOP2A
mir-506	CD1D, QRFPR, SLC16A1, VIM

criteria to identify DElncRNAs, DEmiRNAs, and DEmRNAs between ccRCC tumor tissues and normal tissues and then applied several bioinformatics strategies to increase the predictive accuracy of RNA-RNA interactions. Finally, 46 DElncRNA, 11 DEmiRNAs, and 55 DEmRNAs constituted the lncACT coexpression network in ccRCC. To explore the biological functions of these ceRNA network-involved genes, KEGG pathway analysis showed that the key DEmRNAs were significantly enriched in cancer-related pathways, implicating their vital roles in tumorigenesis. Among the 46 key DElncRNAs, four lncRNA (TCL6, HOTTIP, HULC, and PCGEM1) not only had correlations with clinical features but could also affect ccRCC patients' outcome, strongly suggesting their important roles as prognostic biomarkers for ccRCC. Consistent with our results, a recent study also verified that low expression of TCL6 was correlated with advanced clinicopathological features and poor prognosis of ccRCC patients. Furthermore, preliminary

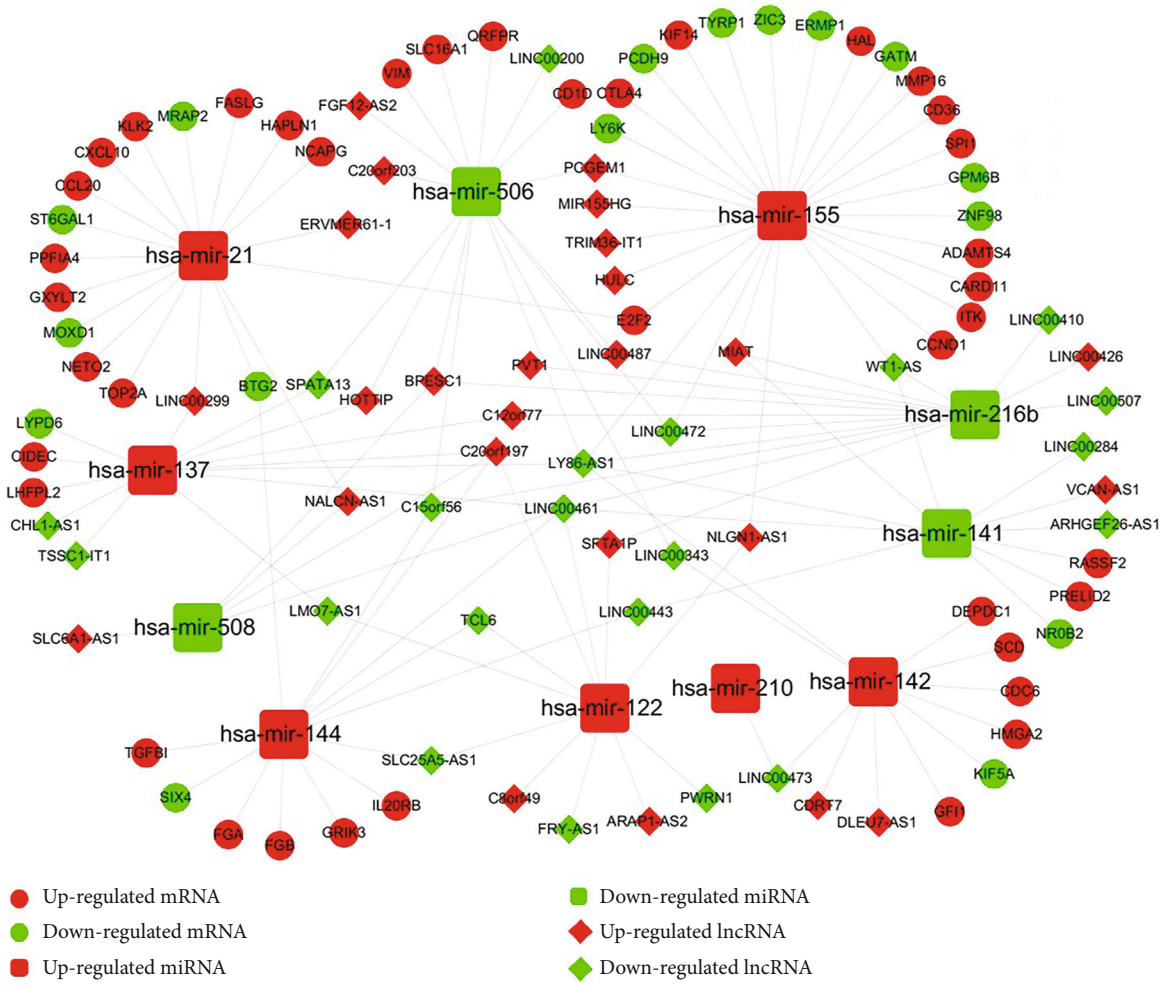

Figure 2: The ceRNA regulatory network of ccRCC. Expression levels and different RNA types are represented by different colors and different shapes, respectively. ceRNA: competitive endogenous RNA.

experiments have indicated TCL6 as a potential antioncogene by inhibiting proliferation and promoting apoptosis of ccRCC cell lines [30]. We predicted that TCL6 might interact with mir-144, of which the potential target genes included an antiproliferative gene BTG2. BTG2 was reported to participate in cell cycle regulation and subsequently involved in cell proliferation in carcinogenesis [31]. Therefore, it deserves further experiments to elucidate the mechanism underlying the effects of TCL6-associated competing triplets on ccRCC.

The upexpression of HOXA transcript at the distal tip (HOTTIP), as a critical oncogenic lncRNA, has been correlated with poor overall survival in various malignancies [32, 33]. We predicted that the high expression of HOTTIP with an approximate 12-fold change in ccRCC tumor tissues may promote tumor growth and a statistic shorter overall survival, which is consistent with previous studies [34, 35]. We found a significant positive correlation between HOTTIP and HOXA13 expression in ccRCC patients. It was demonstrated that HOTTIP transcriptionally regulates HOXA13 in esophageal squamous cell carcinoma cells to promote carcinogenesis and metastasis [36]. Because of the physical contiguity of HOTTIP with HOXA13, we hypothesized that HOTTIP and HOXA13 may closely coordinate to regulate the occurrence and development of ccRCC [37]. More importantly, we found that patients with high HOTTIP expression were less sensitive to clinical therapeutic drugs, including gemcitabine, pazopanib, sunitinib, and XL-184, than patients with low HOTTIP expression, indicating that high HOTTIP expression may lead to drug resistance in ccRCC patients.

HULC, a universal oncogenic lncRNA in human cancers, was reported to be strongly overexpressed in several cancer types, including hepatocellular carcinoma, gastric cancer, pancreatic cancer, and osteosarcoma [38]. However, the role of HULC in ccRCC still remains largely unclear. We predicted that the increased expression (~6 folds) of HULC in ccRCC tumor tissues might promote lymphatic metastasis and poor prognosis. CCND1 might be regulated by HULC through the interaction with mir-155 in ccRCC. Similarly, it has been previously revealed that HULC knockdown induced cell growth arrest and apoptosis through inhibiting CCND1 expression in diffuse large B-cell lymphoma cells [39]. The overexpression of PCGEM1, as a prostate-specific

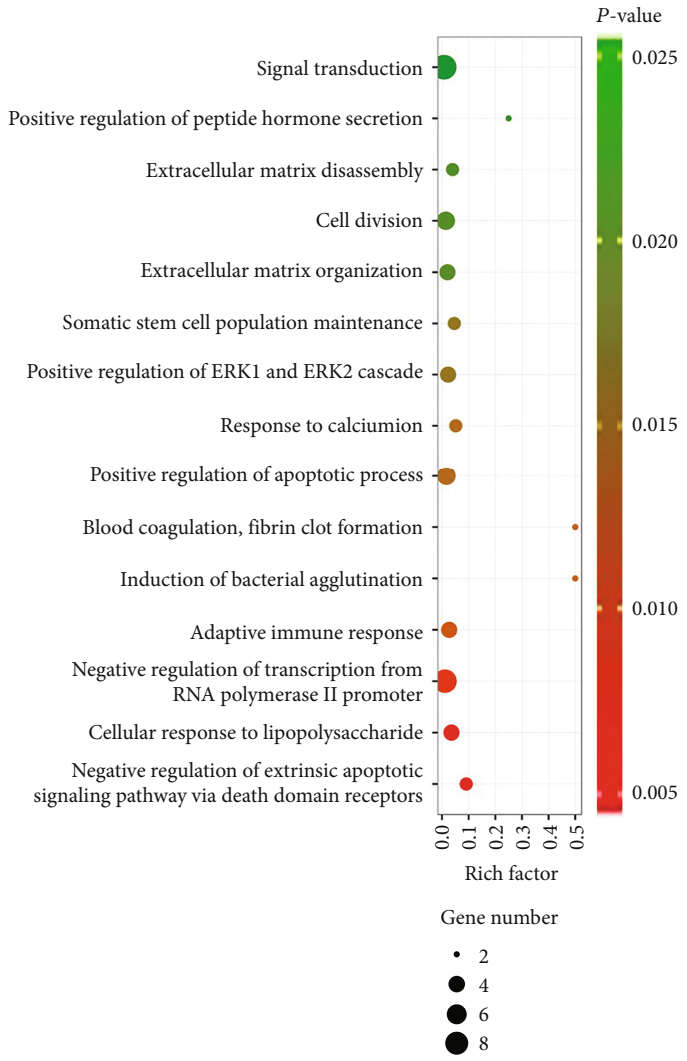

Figure 3: Top 15 enriched Gene Ontology biological process terms of DEmRNAs in the ceRNA network. The size of balls represents gene number, and different colors represent *P* value.

Table 4: KEGG[1] pathway analysis of the DEmRNAs involved in the ceRNA network.

Pathway ID	Description	*P* value	Numbers of DEmRNAs
hsa05206	MicroRNAs in cancer	6.39*E*-05	CCND1, E2F2, MMP16, VIM, HMGA2
hsa04660	T cell receptor signaling pathway	4.60*E*-04	ITK, CTLA4, CARD11
hsa04060	Cytokine-cytokine receptor interaction	5.30*E*-04	FASLG, IL20RB, CXCL10, CCL20
hsa04110	Cell cycle	7.37*E*-04	CCND1, CDC6, E2F2
hsa04152	AMPK signaling pathway	7.54*E*-04	SCD, CCND1, CD36
hsa00514	Other types of O-glycan biosynthesis	9.62*E*-04	GXYLT2, ST6GAL1
hsa05161	Hepatitis B	1.17*E*-03	FASLG, CCND1, E2F2
hsa05219	Bladder cancer	1.63*E*-03	CCND1, E2F2
hsa05202	Transcriptional misregulation in cancer	2.10*E*-03	SPI1, SIX4, HMGA2
hsa05200	Pathways in cancer	2.31*E*-03	SPI1, FASLG, CCND1, E2F2

[1]KEGG: Kyoto Encyclopedia of Genes and Genomes.

lncRNA, was correlated with high risk of prostate cancer [40, 41]. On the contrary, we found that the downregulation of PCGEM1 might prolong metastasis status and shorten survival time of ccRCC patients. To the best of our knowledge, this study firstly reported the potential functions of HULC, HOTTIP, and PCGEM1 in ccRCC to date. Furthermore,

Table 5: The lncRNAs tightly correlated with ccRCC patients' clinical characteristics.

Comparisons	Downregulated	Upregulated
Tumor size (T3 + T4 vs. T1 + T2)	C12orf77, HULC, TCL6	HOTTIP
Lymph node (N1 vs. N0)		HULC
Metastasis status (M1 vs. M0)	C8orf49, PCGEM1, HULC ERVMER61-1	LINC00200
Pathologic stage (stage III + IV vs. stage I + II)	C12orf77, HULC, TCL6	

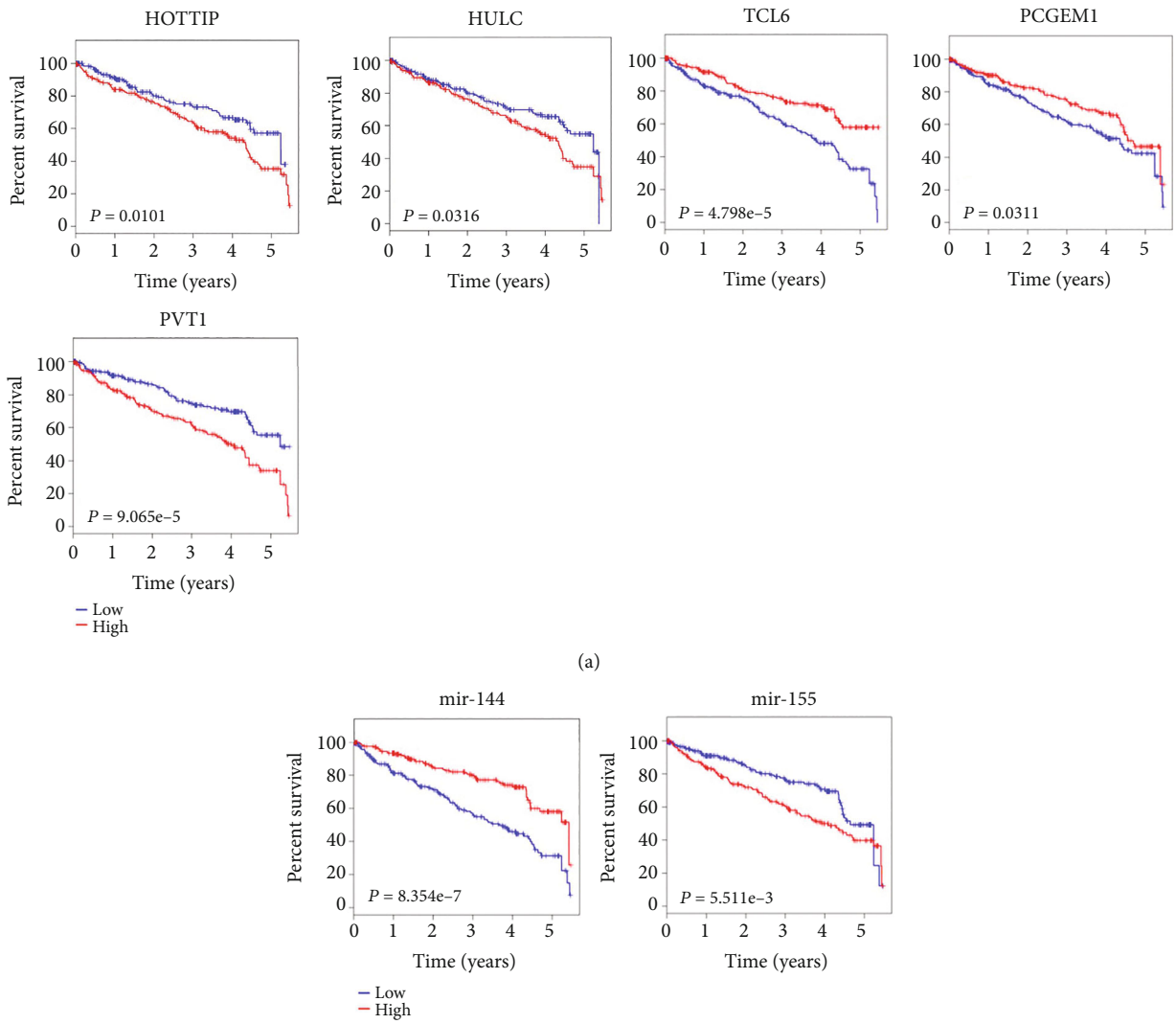

Figure 4: Kaplan-Meier curves for five DElncRNAs (a) and two DEmiRNAs (b) associated with overall survival. Horizontal axis, overall survival time (years); vertical axis, survival function. Patients were divided into "high" group (≥median) and "low" group (<median) according to the gene expression levels.

we also verified lncRNA PVT1 to be an oncogenic lncRNA in ccRCC. It has been reported that ccRCC has the strongest upregulated expression of PVT1 among all cancer types and served as a prognostic factor of renal cancer [42, 43].

However, since our study was conducted based on TCGA cohort by computational analysis, future studies should be designed to verify these lncACT cross-talks and their multiple functions in ccRCC progression. In conclusion, our study has built a newly identified ceRNA network of ccRCC based on hundreds of clinical specimens from TCGA. The ceRNA network discloses that many oncogenes and antioncogenes might contribute to ccRCC development, which can expand our understanding of the roles of lncACTs in tumorigenesis. Importantly, we have identified

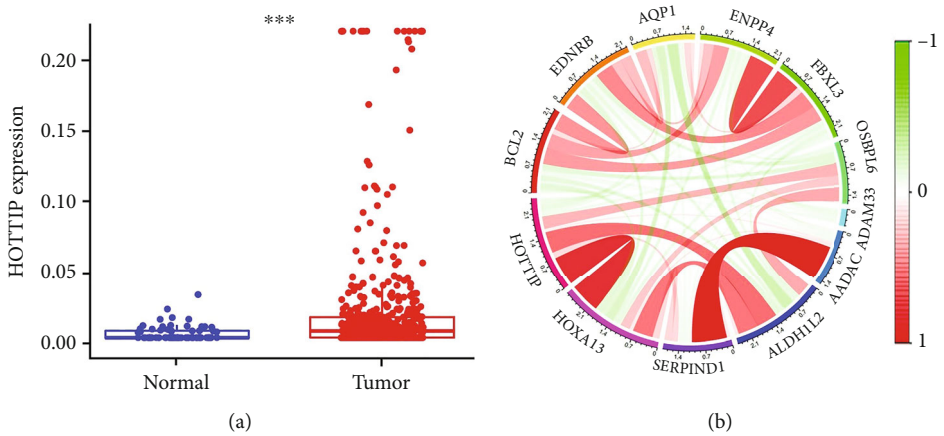

Figure 5: HOTTIP expression in ccRCC patients. (a) HOTTIP expression level in 420 ccRCC tumor and adjacent nontumor samples from the TCGA data determined by RNAseq. (b) The correlation circle diagram of the significantly correlated genes with HOTTIP in ccRCC. The gene names are labeled outside the circle, and the line colors indicate the relationships between genes. Red and green lines represent positive and negative relationships, respectively.

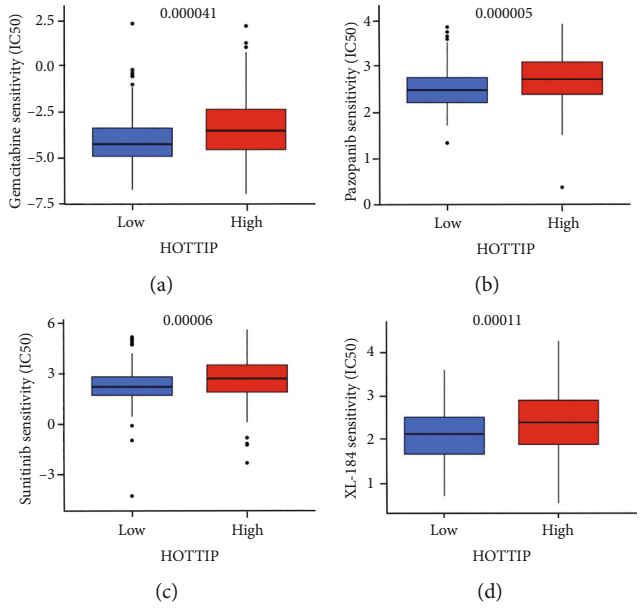

Figure 6: The half maximal inhibitory concentration (IC_{50}) of gemcitabine (a), pazopanib (b), sunitinib (c), and XL-184 (d) in "HOTTIP high" group (≥median) and "HOTTIP low" group (<median) in ccRCC patients.

several lncRNAs to be potential prognostic factors and molecular targets for ccRCC patients.

Data Availability

The data used to support the findings of this study are available from the corresponding authors upon request.

Conflicts of Interest

The authors have no conflicts of interest.

Authors' Contributions

Hui Zhang analyzed the data and wrote the main manuscript. Zixiang Chen, Chunyi Zhao, Qian Wu, and Dingyu Ting helped to analyze the data. Qixiang Shao, Yangjing Zhao, and Qing Ye designed the study and checked and revised the article. All authors read and approved the final manuscript.

Acknowledgments

This work was supported by grants from the National Natural Science Foundation of China Grant (82100183 and

82071738) and Innovation and Entrepreneurship Training Program for College Students in Jiangsu Province (2021102991051X).

Supplementary Materials

Table S1: the list of upregulated lncRNAs in ccRCC. Table S2: the list of downregulated lncRNAs in ccRCC. Table S3: the list of upregulated mRNAs in ccRCC. Table S4: the list of downregulated mRNAs in ccRCC. Table S5: the list of upregulated miRNAs in ccRCC. Table S6: the list of downregulated miRNAs in ccRCC. Table S7: the list of top 100 dysregulated (50 upregulated and 50 downregulated) lncRNAs in consistent with Figure 1. Table S8: the list of genes coexpressed with HOTTIP in ccRCC. *(Supplementary Materials)*

References

[1] A. Znaor, J. Lortet-Tieulent, M. Laversanne, A. Jemal, and F. Bray, "International variations and trends in renal cell carcinoma incidence and mortality," *European Urology*, vol. 67, no. 3, pp. 519–530, 2015.

[2] R. L. Siegel, K. D. Miller, H. E. Fuchs, and A. Jemal, "Cancer statistics, 2021," *CA: a Cancer Journal for Clinicians*, vol. 71, no. 1, pp. 7–33, 2021.

[3] L. Lipworth, A. K. Morgans, T. L. Edwards et al., "Renal cell cancer histological subtype distribution differs by race and sex," *BJU International*, vol. 117, no. 2, pp. 260–265, 2016.

[4] J. R. Bhatt and A. Finelli, "Landmarks in the diagnosis and treatment of renal cell carcinoma," *Nature Reviews. Urology*, vol. 11, no. 9, pp. 517–525, 2014.

[5] C. A. Brosnan and O. Voinnet, "The long and the short of noncoding RNAs," *Current Opinion in Cell Biology*, vol. 21, no. 3, pp. 416–425, 2009.

[6] A. Bhan, M. Soleimani, and S. S. Mandal, "Long noncoding RNA and cancer: a new paradigm," *Cancer Research*, vol. 77, no. 15, pp. 3965–3981, 2017.

[7] R. Rupaimoole and F. J. Slack, "MicroRNA therapeutics: towards a new era for the management of cancer and other diseases," *Nature Reviews. Drug Discovery*, vol. 16, no. 3, pp. 203–222, 2017.

[8] P. Wang, S. Ning, Y. Zhang et al., "Identification of lncRNA-associated competing triplets reveals global patterns and prognostic markers for cancer," *Nucleic Acids Research*, vol. 43, no. 7, pp. 3478–3489, 2015.

[9] T. Xia, Q. Liao, X. Jiang et al., "Long noncoding RNA associated-competing endogenous RNAs in gastric cancer," *Scientific Reports*, vol. 4, no. 1, 2015.

[10] J. Long, Y. Bai, X. Yang et al., "Construction and comprehensive analysis of a ceRNA network to reveal potential prognostic biomarkers for hepatocellular carcinoma," *Cancer Cell International*, vol. 19, no. 1, 2019.

[11] J. Jiang, Y. Bi, X. P. Liu et al., "To construct a ceRNA regulatory network as prognostic biomarkers for bladder cancer," *Journal of Cellular and Molecular Medicine*, vol. 24, no. 9, pp. 5375–5386, 2020.

[12] M. Lu, X. Xu, B. Xi et al., "Molecular network-based identification of competing endogenous RNAs in thyroid carcinoma," *Genes-Basel*, vol. 9, no. 1, p. 44, 2018.

[13] H. Hirata, Y. Hinoda, V. Shahryari et al., "Long noncoding RNA MALAT1 promotes aggressive renal cell carcinoma through Ezh2 and interacts with miR-205," *Cancer Research*, vol. 75, no. 7, pp. 1322–1331, 2015.

[14] Q. Hong, O. Li, W. Zheng et al., "LncRNA HOTAIR regulates HIF-1α/AXL signaling through inhibition of miR-217 in renal cell carcinoma," *Cell Death & Disease*, vol. 8, no. 5, article e2772, 2017.

[15] L. Qu, J. Ding, C. Chen et al., "Exosome-transmitted lncARSR promotes sunitinib resistance in renal cancer by ccting as a competing endogenous RNA," *Cancer Cell*, vol. 29, no. 5, pp. 653–668, 2016.

[16] Y. Fan, F. Dai, M. Yuan et al., "A construction and comprehensive analysis of ceRNA networks and infiltrating immune cells in papillary renal cell carcinoma," *Cancer Medicine*, vol. 10, no. 22, pp. 8192–8209, 2021.

[17] H. Moch, R. Montironi, A. Lopez-Beltran, L. Cheng, and A. Mischo, "Oncotargets in different renal cancer subtypes," *Current Drug Targets*, vol. 16, no. 2, pp. 125–135, 2015.

[18] P. F. Cheng, R. Dummer, M. P. Levesque, and M. P. Levesque, "Data mining The Cancer Genome Atlas in the era of precision cancer medicine," *Swiss Medical Weekly*, vol. 145, 2015.

[19] M. D. Robinson, D. J. Mccarthy, and G. K. Smyth, "edgeR: a Bioconductor package for differential expression analysis of digital gene expression data," *Bioinformatics*, vol. 26, no. 1, pp. 139-140, 2010.

[20] A. Jeggari, D. S. Marks, and E. Larsson, "miRcode: a map of putative microRNA target sites in the long non-coding transcriptome," *Bioinformatics*, vol. 28, no. 15, pp. 2062-2063, 2012.

[21] B. P. Lewis, C. B. Burge, and D. P. Bartel, "Conserved seed pairing, often flanked by adenosines, indicates that thousands of human genes are microRNA targets," *Cell*, vol. 120, no. 1, pp. 15–20, 2005.

[22] Á. Riffo-Campos, I. Riquelme, and P. Brebi-Mieville, "Tools for sequence-based miRNA target prediction: what to choose?," *International Journal of Molecular Sciences*, vol. 17, no. 12, p. 1987, 2016.

[23] C. Chou, N. Chang, S. Shrestha et al., "miRTarBase 2016: Updates to the experimentally validated miRNA-target interactions database," *Nucleic Acids Research*, vol. 44, no. D1, pp. D239–D247, 2016.

[24] P. Shannon, A. Markiel, O. Ozier et al., "Cytoscape: a software environment for integrated models of biomolecular interaction networks," *Genome Research*, vol. 13, no. 11, pp. 2498–2504, 2003.

[25] C. Jun, X. Zhishun, J. Xianzhou, F. Qiang, and W. Jin, "Association between age and clinical characteristics of renal cell carcinoma in adult patients," *International Journal of Urology*, vol. 13, no. 5, pp. 515–519, 2006.

[26] R. Sen, S. Ghosal, S. Das, S. Balti, and J. Chakrabarti, "Competing endogenous RNA: the key to posttranscriptional regulation," *The Scientific World Journal*, vol. 2014, Article ID 896206, 6 pages, 2014.

[27] G. Yu, W. Yao, J. Wang et al., "LncRNAs expression signatures of renal clear cell carcinoma revealed by microarray," *PLoS One*, vol. 7, no. 8, article e42377, 2012.

[28] C. Qin, Z. Han, J. Qian et al., "Expression pattern of long noncoding RNAs in renal cell carcinoma revealed by microarray," *PLoS One*, vol. 9, no. 6, article e99372, 2014.

[29] H. He, M. Xu, Y. Kuang, X. Han, M. Wang, and Q. Yang, "Biomarker and competing endogenous RNA potential of tumor-specific long noncoding RNA in chromophobe renal cell carcinoma," *OncoTargets and Therapy*, vol. 9, pp. 6399–6406, 2016.

[30] H. Su, T. Sun, H. Wang et al., "Decreased TCL6 expression is associated with poor prognosis in patients with clear cell renal cell carcinoma," *Oncotarget*, vol. 8, no. 4, pp. 5789–5799, 2017.

[31] B. Mao, Z. Zhang, and G. Wang, "BTG2: a rising star of tumor suppressors (review)," *International Journal of Oncology*, vol. 46, no. 2, pp. 459–464, 2015.

[32] Y. Lian, Z. Cai, H. Gong, S. Xue, D. Wu, and K. Wang, "HOTTIP: a critical oncogenic long non-coding RNA in human cancers," *Molecular BioSystems*, vol. 12, no. 11, pp. 3247–3253, 2016.

[33] Z. Chen, A. He, D. Wang, Y. Liu, and W. Huang, "Long non-coding RNA HOTTIP as a novel predictor of lymph node metastasis and survival in human cancer: a systematic review and meta-analysis," *Oncotarget*, vol. 8, no. 8, pp. 14126–14132, 2017.

[34] Q. Wang, G. Wu, Z. Zhang et al., "Long non-coding RNA HOTTIP promotes renal cell carcinoma progression through the regulation of the miR-615/IGF-2 pathway," *International Journal of Oncology*, vol. 53, no. 5, pp. 2278–2288, 2018.

[35] Z. Liu, Z. Wang, X. Wang, M. Lu, and G. Chen, "Long noncoding RNA HOTTIP serves as an independent predictive biomarker for the prognosis of patients with clear cell renal cell carcinoma," *International Journal of Genomics*, vol. 2020, Article ID 4301634, 13 pages, 2020.

[36] C. Lin, Y. Wang, Y. Wang et al., "Transcriptional and posttranscriptional regulation of HOXA13 by lncRNA HOTTIP facilitates tumorigenesis and metastasis in esophageal squamous carcinoma cells," *Oncogene*, vol. 36, no. 38, pp. 5392–5406, 2017.

[37] Y. Cui, M. Yan, C. Zhang et al., "Comprehensive analysis of the HOXA gene family identifies HOXA13 as a novel oncogenic gene in kidney renal clear cell carcinoma," *Journal of Cancer Research and Clinical Oncology*, vol. 146, no. 8, pp. 1993–2006, 2020.

[38] X. Yu, H. Zheng, M. T. V. Chan, and W. K. K. Wu, "HULC: an oncogenic long non-codingRNA in human cancer," *Journal of Cellular and Molecular Medicine*, vol. 21, no. 2, pp. 410–417, 2017.

[39] W. Peng, J. Wu, and J. Feng, "Long noncoding RNA HULC predicts poor clinical outcome and represents pro- oncogenic activity in diffuse large B-cell lymphoma," *Biomedicine & Pharmacotherapy*, vol. 79, pp. 188–193, 2016.

[40] V. Srikantan, Z. Zou, G. Petrovics et al., "PCGEM1, a prostate-specific gene, is overexpressed in prostate cancer," *Proceedings of the National Academy of Sciences - PNAS*, vol. 97, no. 22, pp. 12216–12221, 2000.

[41] G. Petrovics, W. Zhang, M. Makarem et al., "Elevated expression of PCGEM1, a prostate-specific gene with cell growth-promoting function, is associated with high-risk prostate cancer patients," *Oncogene*, vol. 23, no. 2, pp. 605–611, 2004.

[42] M. Zhang, L. Zhang, L. Fu et al., "Positive feedback regulation of lncRNA PVT1 and HIF2α contributes to clear cell renal cell carcinoma tumorigenesis and metastasis," *Oncogene*, vol. 40, no. 37, pp. 5639–5650, 2021.

[43] X. Bao, J. Duan, Y. Yan et al., "Upregulation of long noncoding RNA PVT1 predicts unfavorable prognosis in patients with clear cell renal cell carcinoma," *Cancer Biomarkers*, vol. 21, no. 1, pp. 55–63, 2017.

Hindawi
Disease Markers
Volume 2022, Article ID 7826393, 8 pages
https://doi.org/10.1155/2022/7826393

Research Article

Five EMT-Related Gene Signatures Predict Acute Myeloid Leukemia Patient Outcome

Jing Qi,[1] Jiawei Yan,[1] Muhammad Idrees,[2] Saeedah Musaed Almutairi,[3] Rabab Ahmed Rasheed,[4] Usama Ahmed Hussein,[5] Mostafa A. Abdel-Maksoud,[3] Ran Wang,[1] Jun Huang,[1] Chen Huang,[1] Nana Wang,[1] Dongping Huang,[1] Yuan Hui,[6] and Chen Li[7]

[1]*Department of Hematology, The First Affiliated Hospital of Wannan Medical College, Wuhu, Anhui 241001, China*
[2]*Primary and Secondary Health Care Department, Lahore, Pakistan*
[3]*Department of Botany and Microbiology, College of Science, King Saud University, Riyadh 11451, Saudi Arabia*
[4]*Histology & Cell Biology Department, Faculty of Medicine, King Salman International University, South Sinai, Egypt*
[5]*Anatomy Department, Faculty of Medicine, King Salman International University, South Sinai, Egypt*
[6]*Public Health Center, The First Affiliated Hospital of Xi'an Jiaotong University, Xi'an, Shanxi, China*
[7]*Department of Biology, Chemistry, Pharmacy, Free University of Berlin, Berlin 14195, Germany*

Correspondence should be addressed to Dongping Huang; hdp_9713@163.com, Yuan Hui; yuanhuiapple@163.com, and Chen Li; chen.li.scholar@gmail.com

Received 16 June 2022; Revised 7 August 2022; Accepted 23 August 2022; Published 7 October 2022

Academic Editor: Zhen-Jian Zhuo

Background. The epithelial mesenchymal transition (EMT) gene has been shown to be significantly associated with the prognosis of solid tumors; however, there is a lack of models for the EMT gene to predict the prognosis of AML patients. *Methods*. First, we downloaded clinical data and raw transcriptome sequencing data from the TCGA database of acute myeloid leukemia (AML) patients. All currently confirmed EMT-related genes were obtained from the dbEMT 2.0 database, and 30% of the TCGA data were randomly selected as the test set. Univariate Cox regression analysis, random forest, and lasso regression were used to optimize the number of genes for model construction, and multivariate Cox regression was used for model construction. Area under the ROC curve was used to assess the efficacy of the model application, and the internal validation set was used to assess the stability of the model. *Results*. A total of 173 AML samples were downloaded, and a total of 1184 EMT-related genes were downloaded. The results of univariate batch Cox regression analysis suggested that 212 genes were associated with patient prognosis, random forest and lasso regression yielded 18 and 8 prognosis-related EMT genes, respectively, and the results of multifactorial COX regression model suggested that 5 genes, CBR1, HS3ST3B1, LIMA1, MIR573, and PTP4A3, were considered as independent risk factors affecting patient prognosis. The model ROC results suggested that the area under the curve was 0.868 and the internal validation results showed that the area under the curve was 0.815. *Conclusion*. During this study, we constructed a signature model of five EMT-related genes to predict overall survival in patients with AML; it will provide a useful tool for clinical decision making.

1. Introduction

Acute myeloid leukemia (AML) is the most common type of acute leukemia in adults, characterized by a low remission rate, high relapse rate, high disease-specific mortality, and poor prognosis. The incidence of AML increases with age, and more than 20,000 cases are diagnosed per year in the United States, and over 50% of patients died from this disease [1, 2]. Although advances in immunology, cytogenetics, and molecular biology have laid the groundwork for stratified and precise treatment

Table 1: Top 20 candidate genes of univariate Cox regression analysis results.

Candidate genes	Univariate Cox regression			
	HR	95% CI		*P* value
		Low	High	
PTP4A3	1.021726223	1.014321763	1.029184734	6.96E-09
CBR1	1.03820974	1.025067827	1.051520139	7.96E-09
ROR1	8.179147658	3.372478696	19.83658384	3.33E-06
ETS2	1.005307794	1.00295453	1.00766658	9.55E-06
HIP1	1.014075523	1.007666162	1.020525653	1.56E-05
PLA2G4A	1.021276597	1.011531433	1.031115646	1.68E-05
SRC	1.041105298	1.021883572	1.060688587	2.27E-05
KRT7	2.305624508	1.5494694	3.43079016	3.80E-05
HOXB7	1.017736146	1.008665558	1.026888302	0.000118629
PEBP4	9.238964316	2.976207974	28.68027449	0.000119556
UCP2	1.001228192	1.00059024	1.001866551	0.000160359
CDK5	1.025260006	1.011990418	1.03870359	0.000174577
CCL22	1.521162335	1.219639632	1.897228318	0.000198028
RNF8	1.147867946	1.066800293	1.235096044	0.000223934
LIMA1	1.073789995	1.033493977	1.115657159	0.00026414
SPRR2A	18025860.7	2044.952808	1.58894E+11	0.000312518
BMP2	1.363657752	1.150470944	1.616348917	0.000348845
LYPD3	1.593586359	1.231965357	2.061354624	0.000387329
STIM2	1.04818812	1.021292087	1.075792468	0.000387406
BAG3	1.030482529	1.013356191	1.047898312	0.000445426

of AML, up to 50% of patients with normal karyotype have a wide range of clinical outcomes [3]. Thus, it is crucial to develop more risk standards and predictive models for predicting the prognosis and directing treatments of AML.

AML is a highly heterogeneous group of diseases with uncontrolled proliferation and differentiation of abnormally clonal myeloid stem cells. The application of next-generation sequencing (NGS) technology and bioinformatic analysis has provided systemically studies of genome and transcriptome data to unravel the mutational spectrum, epigenetic landscape, and RNA interaction network of these clonal leukemia cells [4], which help to construct different models to predict prognosis and discover potential biomarkers of AML [5, 6]. Epithelial to mesenchymal transition (EMT) is a dynamic process with the transition of epithelial cells to mesenchymal cell phenotype, which has played important roles in embryonic development and wound healing, and this process is also thought to be involved in cancer progression and therapy resistance [7, 8]. The overexpression of EMT markers and EMT transcription factors (TFs) has been proved to correlate with tumor aggressiveness and poor prognosis [9, 10]. In addition, recent studies have shown that cancer cells with the EMT process may contribute to immune escape and drug resistance, thereby reducing the effect of immunotherapy and chemotherapy [11–13]. As in hematological malignancies, previous studies already indicated a correlation between some EMT markers and poor prognosis. For example, the upregulation of vimentin, one of the EMT markers, was found associated with poor clinical outcome in AML patients [14], and downregulation of ZEB1 in AML cells can inhibit the invasive ability [15]. Taken together, all these indicate that EMT markers and EMT-TFs involve in the progression of AML, and EMT-related signatures could be used as potential target for predicting prognosis. However, more of its specific biological function still needs to be explored.

2. Materials and Methods

2.1. Data Acquisition and Preprocessing. A total of 173 AML samples were obtained from the The Cancer Genome Atlas (TCGA) database, a landmark cancer genomic program, which contains more than 20,000 primary cancer and matched normal samples spanning 33 cancer types. The corresponding transcriptome sequencing data of the AML dataset were downloaded and normalized to FPKM format. EMT-related genes were obtained from the dbEMT2.0 database, which contains a total of 1184 experimentally confirmed EMT-related genes. Then, we extracted the expression profiles of EMT-related genes from the normalized matrix based on the obtained EMT-related gene names. Finally, the expression profiles were combined with clinical information to generate a new matrix, and 30% of the data were randomly extracted from this matrix and set as the test set. For clinical data, it is necessary that the enrolled patients have a complete follow-up time, those samples with missing survival time and survival status are excluded from the cohort, and overall patient survival is defined as the endpoint event.

2.2. Batch Univariate COX Regression Screening for Prognosis-Associated EMT Genes. Not all EMT-associated genes affect patient survival; therefore, further screening of EMT-

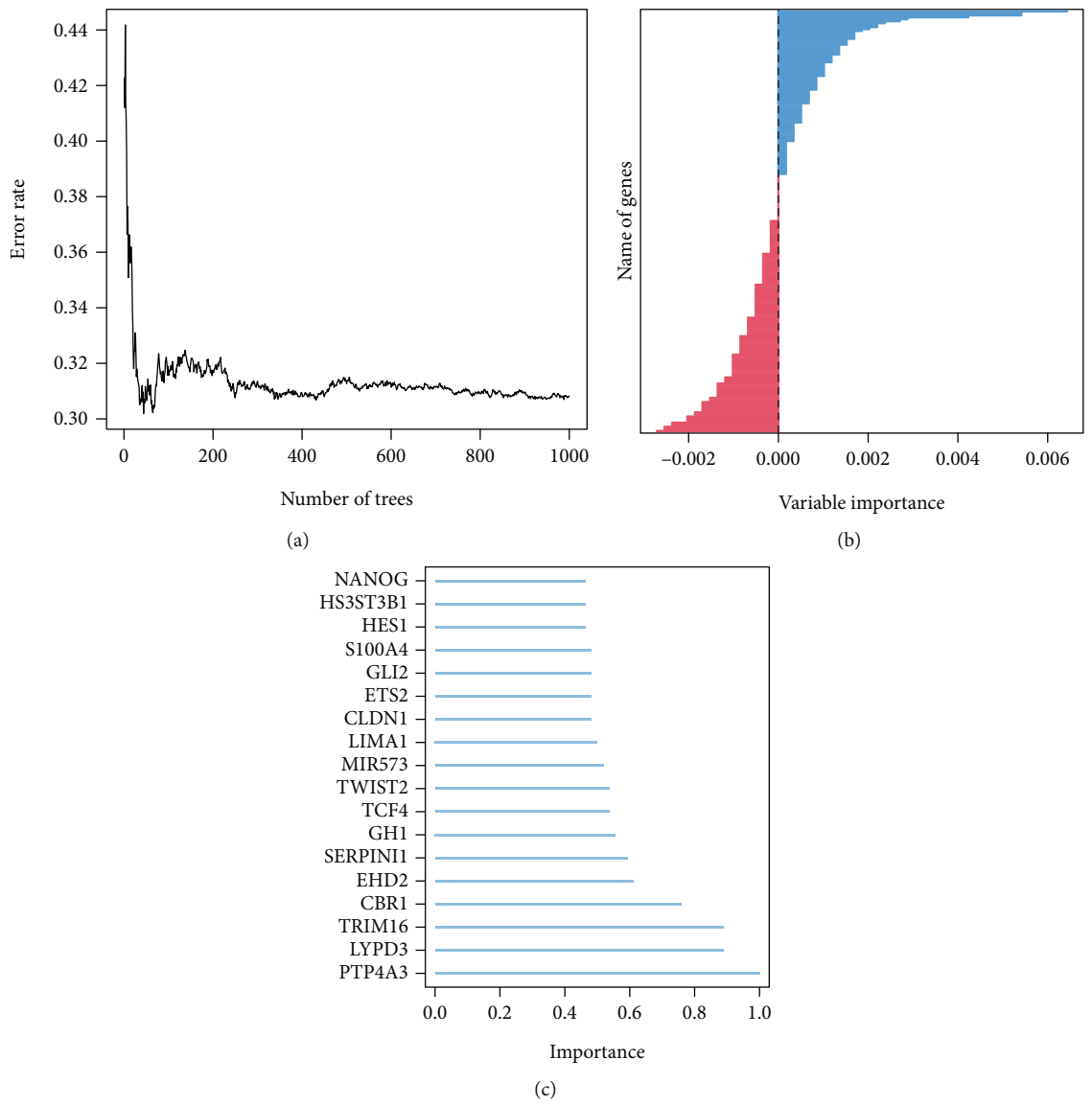

Figure 1: Random survival forest select candidate EMT-related prognosis genes. The error estimate probability (**a**), the bar plot of genes (**b**), and candidate important genes (importance >0.45) (**c**).

associated genes that affect patient prognosis is necessary. We included 1184 EMT-related genes from the EMT database in a univariate COX regression model with $p < 0.05$ as a filtering condition in order to screen for risk factors that affect the prognosis of AML patients.

2.3. Machine Learning to Screen Prognosis-Associated EMT Genes. Randomized survival forest and lasso regression are machine learning algorithms that are often used for dimensionality reduction analysis. The prognostic genes obtained from the above analyses were included in the random survival forest, which was performed by the R package "random forest", and the importance threshold of the variables was set to 0.45. Variables above this threshold were included in the lasso regression for further dimensionality reduction.

2.4. Multivariate Cox Regression and Model Construction. We first included the prognostic factors obtained from the lasso regression into the multivariate Cox regression to screen the independent risk factors affecting the prognosis of AML patients and then constructed a multigene prognostic model based on the coefficients of the regression model.

2.5. Model Efficacy Assessment and Internal Validation. We assessed whether there was a difference in the prognosis of patients in the high- and low-risk groups using the log rank test and then assessed the applied efficacy of the model using the area under the ROC curve. In addition, to validate the stability of the model, 30% of the randomly selected data from the original data were used as the test set for this evaluation.

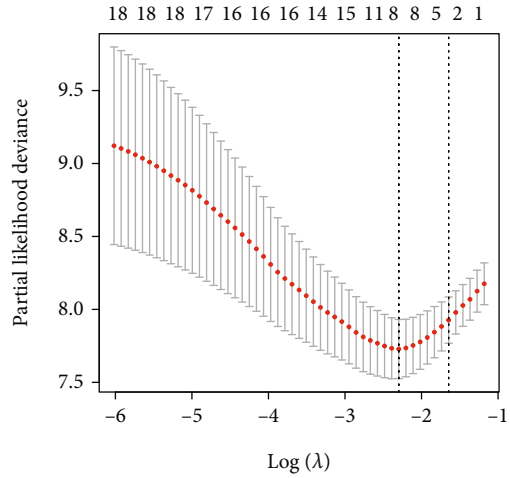

(a)

Significant genes

Gene symbol	P Value
CBR1	7.96E-09
PTP4A3	3.96E-09
LIMA1	0.00026
LYPD3	0.00039
TCF4	0.00225
MIR573	0.00304
HS3ST3B1	0.00335
SERPINI1	0.00781

p value resource from univariable

(b)

Figure 2: Lasso regression model select candidate EMT-related prognosis genes. Lambda takes the minimum value; a total of eight candidate genes are selected (**a**), and (**b**) demonstrates the prognostic value of these eight genes.

Table 2: Multivariate Cox regression analysis of candidate genes.

Candidate genes	Coef	HR	Multivariate Cox regression 95% CI		*P* value
			Low	High	
CBR1	0.0286	1.0290	1.0147	1.0436	6.62E-05
HS3ST3B1	−0.0458	0.9552	0.9131	0.9993	0.0466
LIMA1	0.0415	1.0423	1.0078	1.0781	0.0160
MIR573	−0.0134	0.9867	0.9716	1.0020	0.0888
PTP4A3	0.0145	1.0146	1.0064	1.0228	0.0004

3. Results

3.1. Training Set Prognosis-Related EMT Gene Screening and Model Construction. The results of the univariate batch COX regression analysis suggested that 212 EMT-related genes were associated with prognosis in AML patients. Top 20 prognosis-related genes are presented in Table 1. These 212 genes were included in the random survival forest model, and a total of 18 prognosis genes were selected when the gene importance was set greater than 0.45 (Figures 1(a)–1(c)), and these 18 genes were subsequently included in the lasso regression model for dimensionality reduction analysis, and a total of 8 genes were selected (Figures 2(a) and 2(b)). Further, we included these 5 genes into the multifactorial COX regression model, and a total of 5 genes were selected, and they were considered as independent risk factors affecting the prognosis of patients (Table 2). These 5 genes were CBR1, HS3ST3B1, LIMA1, MIR573, and PTP4A3. Five EMT-associated genes were further modeled for signature based on COX regression coefficients.

3.2. Performance of EMT-Associated Signature. We first calculated the risk score for each patient based on this model. To evaluate the performance of the signature model, patients were divided into high and low groups according to the median value of risk score expression, and the results suggested that the disease-specific survival rate of high-risk patients was significantly lower than that of low-risk patients, and the comparison between groups was statistically different ($p < 0.001$) (Figures 3(a)–3(c)), and the ROC results suggested that the predictive efficacy of the model was likewise. The area under the curve was 0.868 (Figure 3(d)). In addition, to verify the stability of the model, 30% of the total sample was selected for the internal validation of the test set. The results suggested that the same between-group survival differences existed in the test set (Figures 4(a)–4(c)). In addition, the results suggest that the model has strong stability with an area under the ROC curve of 0.815 (Figure 4(d)). This result suggests that the model has a strong stability.

4. Discussion

AML is a deadly and highly heterogeneous disease due to extensive genomic changes and molecular mutations, which have been incorporated in the updated 2017 European LeukemiaNet (ELN) risk stratification guidelines [16]. Breakthroughs in NGS technology have not only explored the molecular mechanisms of this disease but also bring the AML into the era of small molecule inhibitor therapy. More studies are devoted to exploring new prognostic models based on the genetic and molecular profiling to uncover more potential therapeutic targets [4–6]. In the present study, we constructed a predictive model based on the

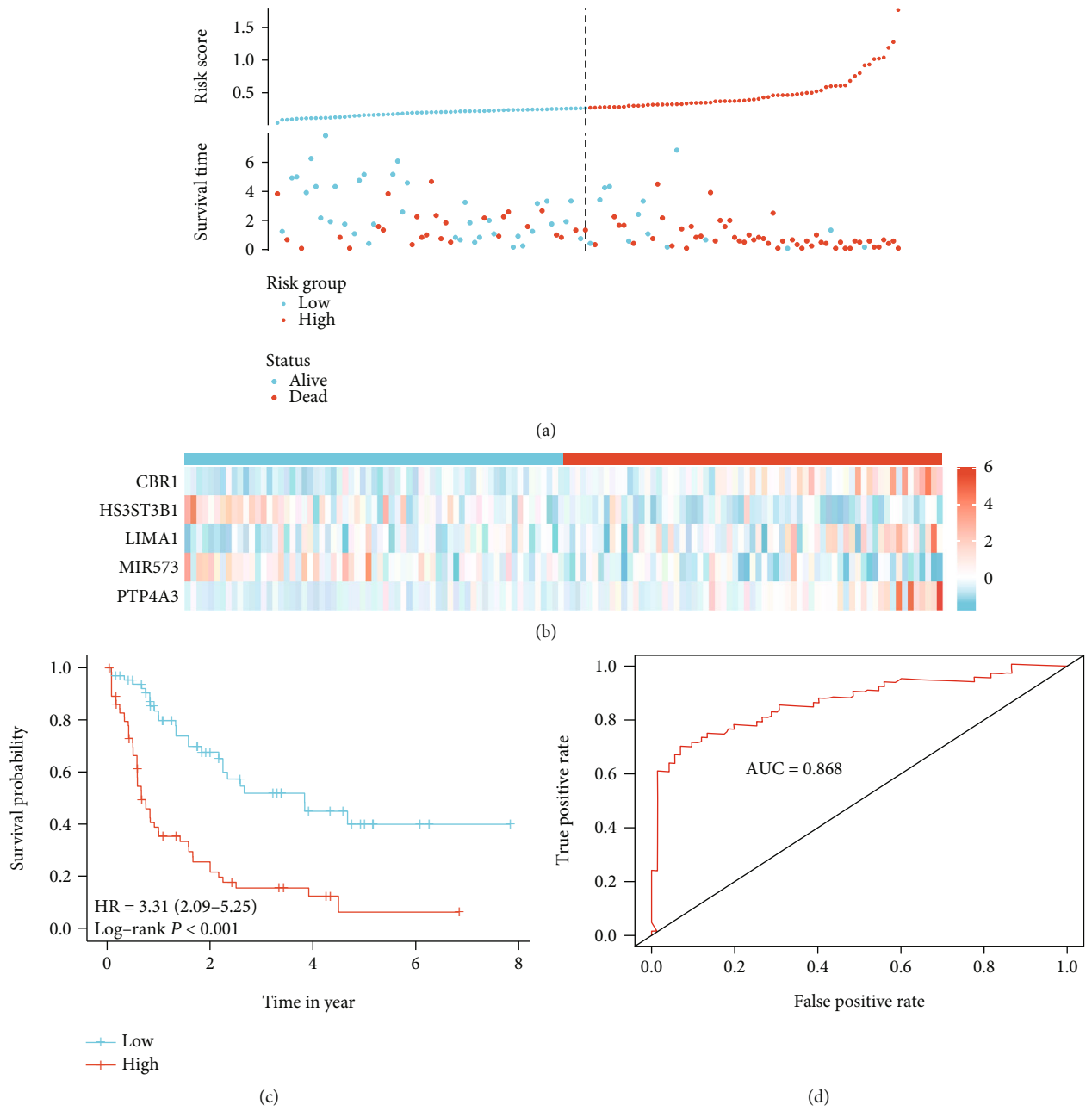

FIGURE 3: Construct model in training data set, based on the Cox regulation model, a five EMT-related gene signature was constructed: the risk score and the survival status distribution (**a**) and the heat map of five genes in high- and low-risk group (**b**). The survival curve show high-risk score patients with a worse outcome, compared with low-risk score patients (**c**). The area under the receiver operating characteristic of model was 0.868 (**d**).

EMT-related signature to provide a visual predictive tool for AML, which might lay the foundation for exploring the role of EMT in hematological malignancies.

Epithelial cells provide intercellular adhesion by cell-cell cohesion and are essential for maintaining the integrity and barrier function of multicellular structures. However, epithelial cells transform into mesenchymal cells to acquire more complex structures and functions of organs during embryonic development and wound healing, which is termed EMT [17, 18]. The quiescent epithelial cells in adults reactivated and primed for the EMT under various internal and external changes, which facilitate tumor cells to invade the extracellular matrix and evade the immune elimination [19]. The downregulation of the cell adhesion protein E-cadherin and cytoskeletal rearrangements, including downregulation of keratin and upregulation of vimentin, are the main features of EMT, which cause ultimately tumor progression and metastasis. Several EMT-TFs have been well identified to coordinate the process,

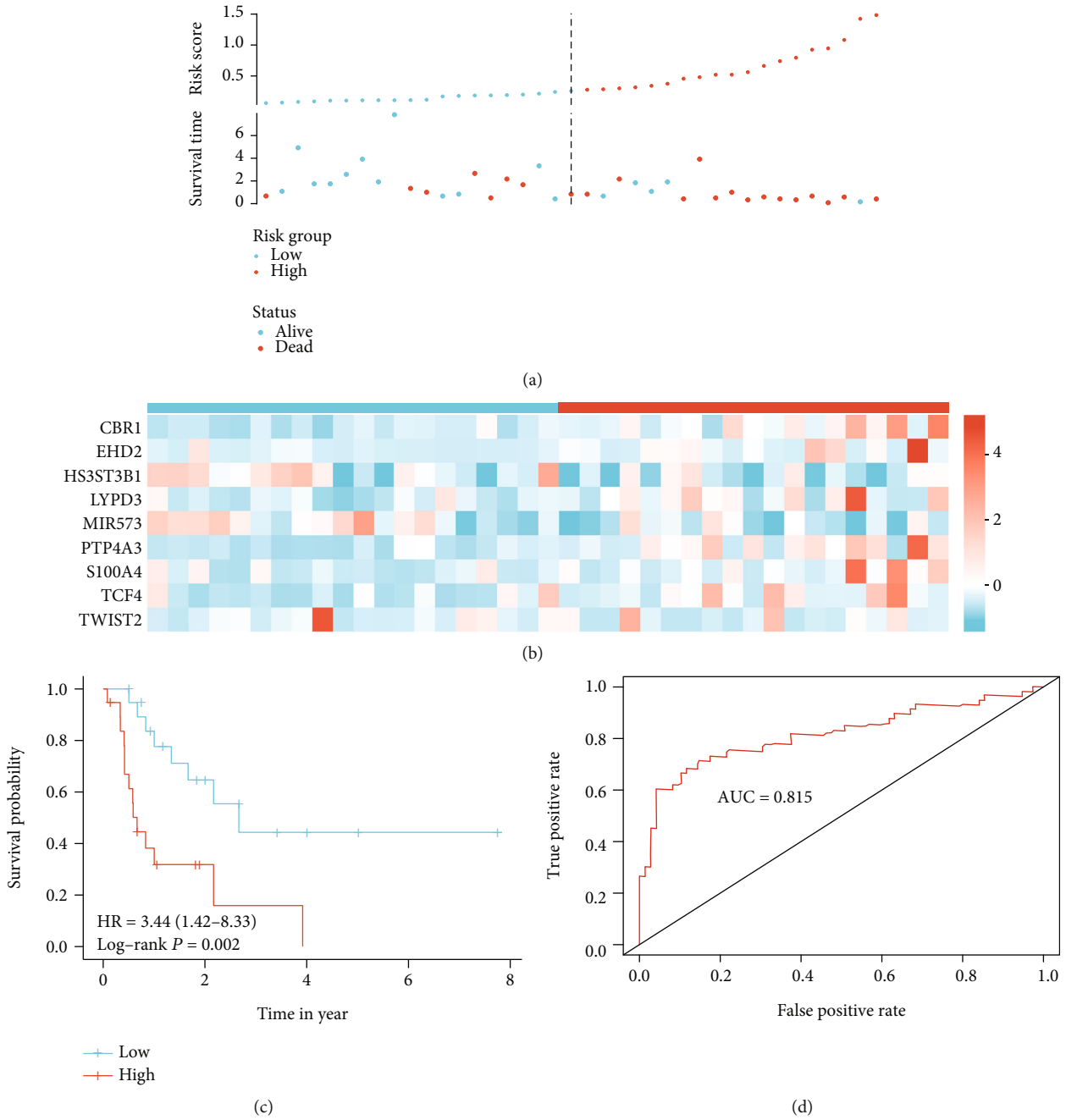

Figure 4: Validate model in test data set, a five EMT-related gene signature was validated: the risk score and the survival status distribution (**a**) and the heat map of five genes in high- and low-risk group (**b**). The survival curve show high-risk score patients with a worse outcome, compared with low-risk score patients (**c**). The area under the receiver operating characteristic of model was 0.815 (**d**).

such as SNAIL/SNAI1, SLUG/SNAI2, and TFs of the TWIST and ZEB families [20]. Given that EMT is associated with tumor invasiveness and metastasis, as well as its molecular properties, some EMT-related signatures have been developed to predict the prognosis of cancers and the response to immunotherapy. A recent study reported an EMT-related gene signature for the prognosis of human bladder cancer [21], and Chae et al. [22] analyzed the immune landscape of NSCLC (nonsmall cell lung cancer) patients based on EMT scores to predict the response of patients to immunotherapy. Although some previous studies have shown the role of EMT makers and EMT-TFs in AML, no EMT signature has been applied to predict the prognosis of AML [14, 15].

As shown in our study, five EMT-related genes (CBR1, HS3ST3B1, LIMA1, MIR573, PTP4A3) were selected by random forest algorithm as the prognostic in TCGA-LAML cohort as a training set. Then, AML patients were divided into high-risk and low-risk groups based on the EMT-related signature risk score. The results demonstrated that patients in the low-risk group have longer OS than in the high-risk group, which were also validated in internal datasets. Carbonyl reductase 1 (CBR1) belongs to the short dehydrogenase (SDR) family,

which could promote AML cell resistance to daunorubicin and be a risk gene in AML patients [23]. However, it is still unclear whether CBR1 can lead to progression and drug resistance through EMT in AML. A previous study has shown that heparan sulfate D-glucosamine 3-O-sulfotransferase 3B1 (HS3ST3B1) participates in the biosynthetic steps of heparan sulfate (HS) and positively contributed to acute AML progression by induction of VEGF expression, which also involves in the regulation TGF-beta-mediated EMT in NSCLC [24, 25]. LIMA1 (LIM domain and actin binding 1), also known as epithelial protein lost in neoplasm (EPLIN), has been known to play differential roles in the progression and metastasis of certain cancers [26, 27]. Downregulation or phosphorylation of EPLIN can alter the expression of some EMT elements such as E-cadherin and ZEB1 via Wnt-catenin signaling pathway, thus promotes the EMT process. While the exact mechanism of LIMA1 in AML remains unknown [27]. The role of MIR573 in EMT of tumors is still controversial. Wang et al. [28]. revealed that MIR573 can inhibit TGFβ1-induced EMT in prostate cancer, while another study indicated MIR573 associated with the EMT in cervical cancer cell growth and metastasis [29]. As so far, the expression of MIR573 has been confirmed in AML cell line (HL-60) and thought as a regulator in responsiveness to inorganic substances [30]. Protein tyrosine phosphatase of regenerating liver 3 (PRL-3), encoded by PTP4A3 gene, has been proved to promote EMT through PI3K/AKT pathway and Src-ERK1/2 pathways in a variety of tumors [31, 32], which is also a hazard factor with poor survival in AML [33]. All these hint the prognostic role of EMT-related gene signature in AML. Furthermore, given that the general condition of the patients is also included in the risk stratification of the disease in addition to the genomic profile [16], a predictive model was constructed based on the EMT-related genes, which demonstrated powerful predictivity.

5. Conclusion

During this study, we constructed a signature model of five EMT-related genes to predict overall survival in patients with AML; it will provide a useful tool for clinical decision making. However, our study still has some limitations. First, more datasets need to be included for better validation. Second, further function experiments regarding of the core genes are required to clarify the role of EMT-related genes in AML.

Data Availability

All data used in the study were from the publicly available The Cancer Genome Atlas (TCGA) (https://portal.gdc.cancer.gov/).

Consent

Informed consent forms are not required for patient data extracted from public databases.

Conflicts of Interest

The authors declare that the research was conducted in the absence of any commercial or financial relationships that could be construed as a potential conflict of interest.

Authors' Contributions

Dongping Huang, Yuan Hui, and Chen Li conceived and designed the study. Jing Qi and Jiawei Yan analyzed the data. Ran Wang, Jun Huang, Chen Huang, and Nana Wang joined the analysis and discussed the results. All the authors approved the submitted version. Muhammad Idrees, Saeedah Musaed Almutairi, Rabab Ahmed Rasheed, Usama Ahmed Hussein, and Mostafa A. Abdel-Maksoud contributed to the revision and language editing. Jing Qi and Jiawei Yan contributed equally to this work.

Acknowledgments

We sincerely acknowledged the TCGA database for proving publicly available genomic, epigenomic, transcriptomic, and proteomic data for researches. The authors extend their appreciation to the Researchers Supporting Project number (RSP2022R470), King Saud University, Riyadh, Saudi Arabia.

References

[1] I. De Kouchkovsky and M. Abdul-Hay, "Acute myeloid leukemia: a comprehensive review and 2016 update," *Blood Cancer Journal*, vol. 6, no. 7, pp. e441–e441, 2016.

[2] M. R. O'Donnell, C. N. Abboud, J. Altman et al., "Acute myeloid leukemia," *Journal of the National Comprehensive Cancer Network*, vol. 10, no. 8, pp. 984–1021, 2012.

[3] H. Döhner, D. J. Weisdorf, and C. D. Bloomfield, "Acute myeloid leukemia," *New England Journal of Medicine*, vol. 373, no. 12, pp. 1136–1152, 2015.

[4] M. Leisch, B. Jansko, N. Zaborsky, R. Greil, and L. Pleyer, "Next generation sequencing in AML—on the way to becoming a new standard for treatment initiation and/or modulation?," *Cancers*, vol. 11, no. 2, p. 252, 2019.

[5] L. Bullinger, K. Döhner, R. Kranz et al., "An FLT3 gene-expression signature predicts clinical outcome in normal karyotype AML," *Blood, The Journal of the American Society of Hematology*, vol. 111, no. 9, pp. 4490–4495, 2008.

[6] T. Yagi, A. Morimoto, M. Eguchi et al., "Identification of a gene expression signature associated with pediatric AML prognosis," *Blood*, vol. 102, no. 5, pp. 1849–1856, 2003.

[7] T. Brabletz, R. Kalluri, M. A. Nieto, and R. A. Weinberg, "EMT in cancer," *Nature Reviews Cancer*, vol. 18, no. 2, pp. 128–134, 2018.

[8] A. Singh and J. Settleman, "EMT, cancer stem cells and drug resistance: an emerging axis of evil in the war on cancer," *Oncogene*, vol. 29, no. 34, pp. 4741–4751, 2010.

[9] M. Sato, D. S. Shames, and Y. Hasegawa, "Emerging evidence of epithelial-to-mesenchymal transition in lung carcinogenesis," *Respirology*, vol. 17, no. 7, pp. 1048–1059, 2012.

[10] U. D. Kahlert, J. V. Joseph, and F. A. Kruyt, "EMT- and MET-related processes in nonepithelial tumors: importance for disease progression, prognosis, and therapeutic opportunities," *Molecular Oncology*, vol. 11, no. 7, pp. 860–877, 2017.

[11] S. Terry, P. Savagner, S. Ortiz-Cuaran et al., "New insights into the role of EMT in tumor immune escape," *Molecular Oncology*, vol. 11, no. 7, pp. 824–846, 2017.

[12] Y. Jiang and H. Zhan, "Communication between EMT and PD-L1 signaling: new insights into tumor immune evasion," *Cancer Letters*, vol. 468, pp. 72–81, 2020.

[13] J. Sha, Y. Bai, H. X. Ngo, T. Okui, and T. Kanno, "Overview of evidence-based chemotherapy for oral cancer: focus on drug resistance related to the epithelial-mesenchymal transition," *Biomolecules*, vol. 11, no. 6, p. 893, 2021.

[14] S. Wu, Y. du, J. Beckford, and H. Alachkar, "Upregulation of the EMT marker vimentin is associated with poor clinical outcome in acute myeloid leukemia," *Journal of Translational Medicine*, vol. 16, no. 1, pp. 1–9, 2018.

[15] V. Stavropoulou, S. Kaspar, L. Brault et al., "_MLL-AF9_ expression in hematopoietic stem cells drives a highly invasive AML expressing EMT-related genes linked to poor outcome," *Cancer Cell*, vol. 30, no. 1, pp. 43–58, 2016.

[16] H. Döhner, E. Estey, D. Grimwade et al., "Diagnosis and management of AML in adults: 2017 ELN recommendations from an international expert panel," *Blood, The Journal of the American Society of Hematology*, vol. 129, no. 4, pp. 424–447, 2017.

[17] D. S. Micalizzi, S. M. Farabaugh, and H. L. Ford, "Epithelial-mesenchymal transition in cancer: parallels between normal development and tumor progression," *Journal of Mammary Gland Biology and Neoplasia*, vol. 15, no. 2, pp. 117–134, 2010.

[18] R. Kalluri, "EMT: when epithelial cells decide to become mesenchymal-like cells," *The Journal of Clinical Investigation*, vol. 119, no. 6, pp. 1417–1419, 2009.

[19] S. Heerboth, G. Housman, M. Leary et al., "EMT and tumor metastasis," *Clinical and Translational Medicine*, vol. 4, no. 1, pp. 1–13, 2015.

[20] D. Greaves and Y. Calle, "Epithelial mesenchymal transition (EMT) and associated invasive adhesions in solid and Haematological Tumours," *Cell*, vol. 11, no. 4, p. 649, 2022.

[21] R. Cao, L. Yuan, B. Ma, G. Wang, W. Qiu, and Y. Tian, "An EMT-related gene signature for the prognosis of human bladder cancer," *Journal of Cellular and Molecular Medicine*, vol. 24, no. 1, pp. 605–617, 2020.

[22] Y. K. Chae, S. Chang, T. Ko et al., "Epithelial-mesenchymal transition (EMT) signature is inversely associated with T-cell infiltration in non-small cell lung cancer (NSCLC)," *Scientific Reports*, vol. 8, no. 1, pp. 1–8, 2018.

[23] S. Varatharajan, A. Abraham, W. Zhang et al., "Carbonyl reductase 1 expression influences daunorubicin metabolism in acute myeloid leukemia," *European Journal of Clinical Pharmacology*, vol. 68, no. 12, pp. 1577–1586, 2012.

[24] L. Zhang, K. Song, L. Zhou et al., "Heparan sulfate D-Glucosaminyl 3-O-sulfotransferase-3B1 (HS3ST3B1) promotes angiogenesis and proliferation by induction of VEGF in acute myeloid leukemia cells," *Journal of Cellular Biochemistry*, vol. 116, no. 6, pp. 1101–1112, 2015.

[25] Z. Zhang, H. Jiang, Y. Wang, and M. Shi, "Heparan sulfate D-glucosamine 3-O-sulfotransferase 3B1 is a novel regulator of transforming growth factor-beta-mediated epithelial-to-mesenchymal transition and regulated by miR-218 in non-small cell lung cancer," *Journal of Cancer Research and Therapeutics*, vol. 14, no. 1, pp. 24–29, 2018.

[26] S. Zhang, X. Wang, A. O. Osunkoya et al., "EPLIN downregulation promotes epithelial-mesenchymal transition in prostate cancer cells and correlates with clinical lymph node metastasis," *Oncogene*, vol. 30, no. 50, pp. 4941–4952, 2011.

[27] R. J. Collins, W. G. Jiang, R. Hargest, M. D. Mason, and A. J. Sanders, "EPLIN: a fundamental actin regulator in cancer metastasis?," *Cancer and Metastasis Reviews*, vol. 34, no. 4, pp. 753–764, 2015.

[28] L. Wang, G. Song, W. Tan et al., "MiR-573 inhibits prostate cancer metastasis by regulating epithelial-mesenchymal transition," *Oncotarget*, vol. 6, no. 34, pp. 35978–35990, 2015.

[29] P. Chen, R. Wang, Q. Yue, and M. Hao, "Long non-coding RNA TTN-AS1 promotes cell growth and metastasis in cervical cancer via miR-573/E2F3," *Biochemical and Biophysical Research Communications*, vol. 503, no. 4, pp. 2956–2962, 2018.

[30] Q. Xiong, Y. Yang, H. Wang et al., "Characterization of miRNomes in acute and chronic myeloid leukemia cell lines," *Genomics, Proteomics & Bioinformatics*, vol. 12, no. 2, pp. 79–91, 2014.

[31] H. Wang, S. Y. Quah, J. M. Dong, E. Manser, J. P. Tang, and Q. Zeng, "PRL-3 down-regulates PTEN expression and signals through PI3K to promote epithelial-mesenchymal transition," *Cancer Research*, vol. 67, no. 7, pp. 2922–2926, 2007.

[32] J. Ming, N. Liu, Y. Gu, X. Qiu, and E. H. Wang, "PRL-3 facilitates angiogenesis and metastasis by increasing ERK phosphorylation and up-regulating the levels and activities of rho-a/C in lung cancer," *Pathology*, vol. 41, no. 2, pp. 118–126, 2009.

[33] R. Beekman, M. Valkhof, S. J. Erkeland et al., "Retroviral integration mutagenesis in mice and comparative analysis in human AML identify reduced PTP4A3 expression as a prognostic indicator," *PLoS One*, vol. 6, no. 10, article e26537, 2011.

Hindawi
Disease Markers
Volume 2022, Article ID 3534433, 14 pages
https://doi.org/10.1155/2022/3534433

Research Article

Epithelial-Mesenchymal Transition Gene Signature Is Associated with Neoadjuvant Chemoradiotherapy Resistance and Prognosis of Esophageal Squamous Cell Carcinoma

Kewei Song,[1] Baohong Gu,[1] Chenhui Ma,[1] Bofang Wang,[1] Na Wang,[1] Rong Yu,[1] and Hao Chen[2,3]

[1]*The Second Clinical Medical College, Lanzhou University, Lanzhou 730030, China*
[2]*Department of Tumor Surgery, Lanzhou University Second Hospital, Lanzhou 730030, China*
[3]*Key Laboratory of Digestive System Tumors of Gansu Province, Lanzhou 730030, China*

Correspondence should be addressed to Hao Chen; ery_chenh@lzu.edu.cn

Received 28 May 2022; Accepted 2 August 2022; Published 27 August 2022

Academic Editor: Zhen-Jian Zhuo

Background. Neoadjuvant chemoradiotherapy (neo-CRT) in combination with surgery increases survival compared to surgery alone, as indicated by the esophageal squamous cell carcinoma (ESCC) treatment recommendations. However, the benefits of neo-CRT are diverse among patients. Consequently, the development of new biomarkers that correlate with neo-CRT might be important for the treatment of ESCC. *Methods*. The differentially expressed genes (DEG) between responsive and resistant samples from the GSE45670 dataset were obtained. On the TCGA dataset, survival analysis was performed to identify prognosis-related-EMT-genes. For EMT score model construction, lasso regression analysis in the TCGA cohort was used to identify the genes. In the TCGA-ESCC cohort, age, stage, and EMT score were used to construct a nomogram. *Results*. In total, 10 prognosis-related-EMT-genes were obtained. These 10 genes consisted of 6 risky genes and 4 protective genes. Based on the lasso analysis and univariate Cox regression, an EMT score model consisting of 7 genes (CLEC18A, PIR, KCNN4, MST1R, CAPG, ALDH5A1, and COX7B) was identified. ESCC patients with a high EMT score have a worse prognosis. These genes were differentially expressed between responsive and resistant patients and had a high accuracy for distinguishing resistant and responsive patients. *Conclusions*. The identified genes have the potential to function as molecular biomarkers for predicting ESCC patients' resistance to neo-CRT. This research may aid in the elucidation of the molecular processes driving resistance and the identification of targets for improving the prognosis for ESCC.

1. Introduction

There will be 20,640 new cases of esophageal cancer diagnosed in the United States in 2022, and 16410 people will die from esophageal cancer, according to the 2022 Cancer Statistics for the United States [1]. ESCC, a major histological subtype of EC, accounts for roughly 90% of EC occurrences [2, 3]. A number of factors contribute towards the development of ESCC, including smoking, alcohol abuse, and hot water [4, 5]. ECSS can be difficult to diagnose because there are no specific symptoms and a lack of early detection methods that allow an early diagnosis [6]. Only 15-25% of patients with ESCC survive five years after they were initially diagnosed with the disease [7]. To increase the survival time of ESCC, it is urgently necessary to discover the genetic changes of ESCC and identify new biomarkers.

The most common treatment for locally advanced ESCCs is surgery [7]. It is important to note that disease recurrences are common after surgery, and that the prognosis has not changed significantly over the past few decades [8]. The use of neo-CRT in conjunction with surgery improves prognosis greatly as compared to surgery alone, and it is suggested in treatment recommendations [9]. In a trial including 113 patients with esophageal cancer, the addition of neo-CRT increased the 3-year survival rate from 6% to 32% [10]. It should be mentioned, however, that neo-CRT had two major disadvantages. Initially,

the outcomes of neo-CRT treatment are variable. Some patients could be resistant to neo-CRT and have a worse prognosis in terms of survival [11]. In addition, studies have revealed that neo-CRT is linked with an increased risk of postoperative complications [12]. Therefore, it would be beneficial to ESCC patients if novel biomarkers could be identified that would predict their response to neo-CRT.

It is quite common for cancer cells to activate diverse signaling pathways and develop chemotherapy resistance, which helps them stay alive in spite of chemotherapy [13]. In studies, it has been observed that chemotherapy resistance can be caused by the epithelial–mesenchymal transition (EMT) [14–16]. EMT is generally defined as the loss of epithelial characteristics in a cell and the acquisition of mesenchymal characteristics in that same cell [17]. There is increasing evidence that EMT is linked to tumorigenesis, cancer invasion, and drug resistance [18, 19]. It has been found that there is a significant association between EMT genes and metastatic disease, as well as the clinical stage of ESCC [20]. However, more studies are needed to investigate the role of EMT in ESCC.

The expression data of responsive and resistant samples was obtained from different databases. The differentially expressed EMT-related genes that are correlated with neo-CRT responsiveness were identified. Using lasso regression analysis, 7 genes (CLEC18A, PIR, KCNN4, MST1R, CAPG, ALDH5A1, and COX7B) were used to obtain the EMT score for estimating the ESCC prognosis. Besides, EMT score, age, and stage were used for the construction of a nomogram for predicting the 1-, 3-, and 5-year overall survival (OS) of ESCC. For diagnosis (resistant and responsive), the EMT score showed a more accurate value than genes.

2. Patients and Methods

2.1. Gene Expression Data. GSE45670 expression data was downloaded from the GEO [21] by the GEOquery package [22]. This dataset consisted of 28 esophageal squamous cell carcinoma (ESCC) samples and 10 normal samples. In those 28 patients who had ESCCs, neoadjuvant chemoradiation therapy (neo-CRT) that included cisplatin and vinorelbine was given. 11 of them responded completely to the therapy, while 17 others were resistant to treatment. Aside from that, the TCGAbiolinks package was used to download expression information and clinical records of 185 ESCC patients from the TCGA database [23]. GSE86099 used paclitaxel resistant cells and used mRNA transcription files to identify the crucial genes for developing paclitaxel resistance [24]. The detailed information of samples from GSE45670 and TCGA-ESCC is shown in Supplementary Table 1 and Supplementary Table 2.

2.2. DEG Identification and Enrichment Analysis. In order to more clearly illustrate the distribution of 11 responsive and 17 resistant samples, a principal component analysis was applied. In order to increase the quality of samples and the number of DEG, the low-quality samples were then removed by the PCA results. We used the edgeR package to detect DEG between responsive and resistant samples based on log2-foldchange (FC) > 0.5 and p value < 0.05 as cutoff criteria [25]. The enrichment analysis was conducted using the R package "clusterProfiler" [26]. The p value < 0.05 was used to distinguish significantly enriched terms.

2.3. Survival-Related EMT Gene Identification. A total of 3600 EMT-related genes were retrieved from EMTome [27]. We determined the genes that were substantially linked with prognosis by samples from TCGA-ESCC. Among these survival-related genes, genes with "Coef > 0" were defined as risky genes, and genes with "Coef < 0" were defined as protective genes. A Venn diagram was used to show the overlap of DEGs, EMT genes, and survival-related genes. The overlapped genes were selected as the survival-related EMT genes.

2.4. Construction of EMT Score Model. We have determined the candidate prognostic genes by applying lasso regression analysis in the TCGA-ESCC cohort by using the glmnet package [28]. We then used univariate Cox regression analysis to calculate the coefficients for each gene. The mRNA expression and the coefficients associated with these genes were used in the calculation of the EMT score. ESCC patients from the TCGA dataset were divided into low and high subgroups based on the median value. The prognosis difference between low and high groups was compared, and the prognosis prediction ability of the EMT score was calculated.

2.5. Development of Nomogram. The TCGA-ESCC cohort included data on age, stage, and EMT score, which were used to construct a nomogram. Calibration curves were generated so that the concordance between the actual survival rate, and the anticipated survival rate could be evaluated. Additionally, the concordance index (C-index) was calculated to assess the capacity of models to forecast prognosis. These analyses were conducted by the package rms.

2.6. Immune Score and Immune Cell Infiltration Analyses. By expression profiles, the immune score and the stromal score were calculated using the "estimate" package [29]. By package GSVA [30], the infiltration levels of immune cell populations were determined.

2.7. Diagnostic Ability in the Classification of Resistant and Responsive Patients. In this study, we used the pROC package to estimate the area under curve (AUC) to evaluate the prediction ability of drug response to therapy. Then, we also calculated the AUC values of EMT score and genes in classifying ESCC and normal samples.

3. Results

3.1. DEG Identification. The flowchart of this study was shown in Figure 1(a). Principal component analysis (PCA) was applied to classify 11 responsive and 17 resistant samples in Figure 1(b). Then, 4 responsive samples (GSM1111699, GSM1111694, GSM1111695, and GSM1111693) and 4 resistant samples (GSM1111677, GSM1111680, GSM1111682, and GSM1111688) were removed since they were outliers (Figure 1(c)). We compared the gene expression between the 7 responsive and 13 resistant samples using the edgeR package. The log2foldchange (FC) > 0.5 and p value < 0.05 accepted to

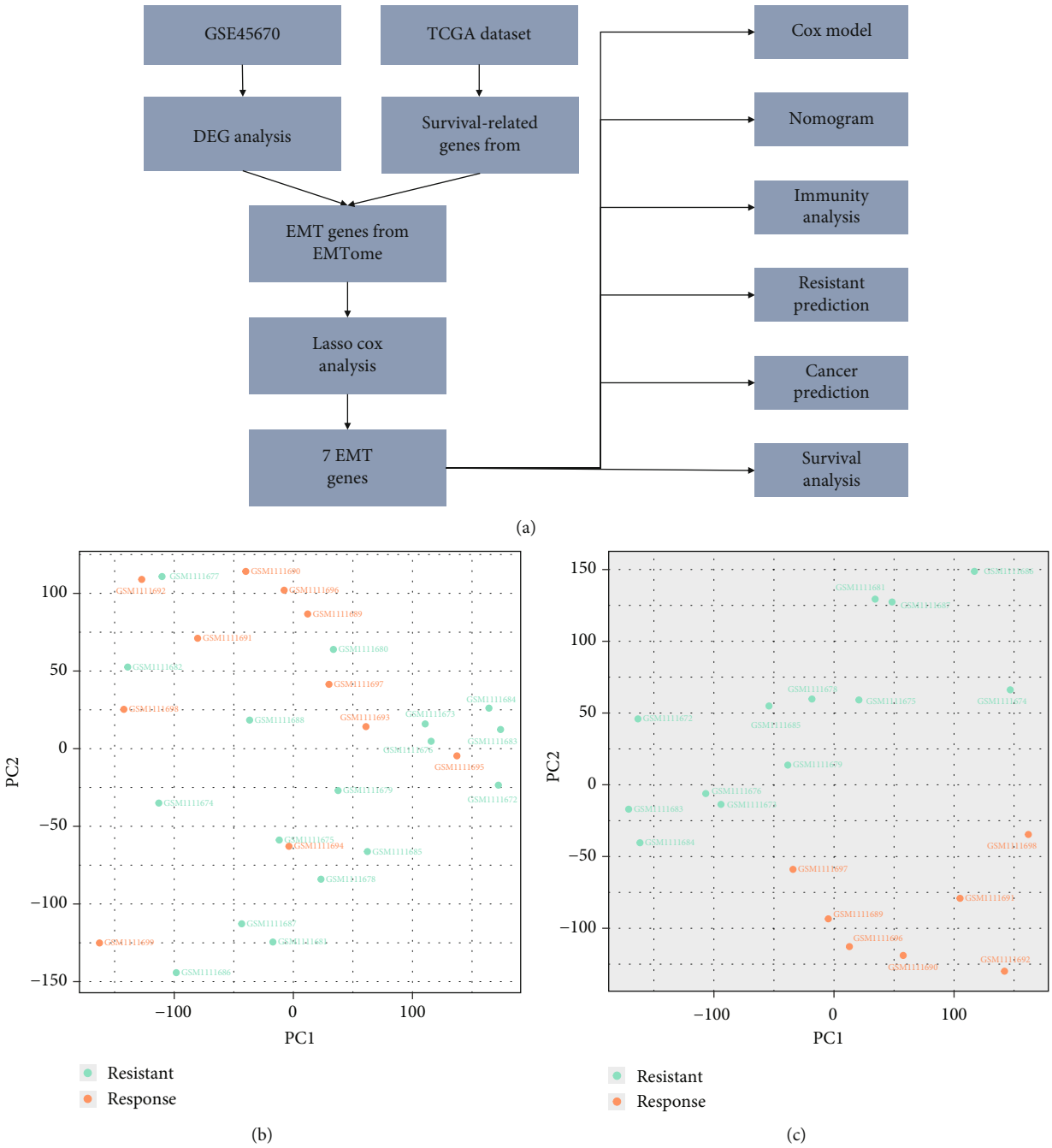

Figure 1: Continued.

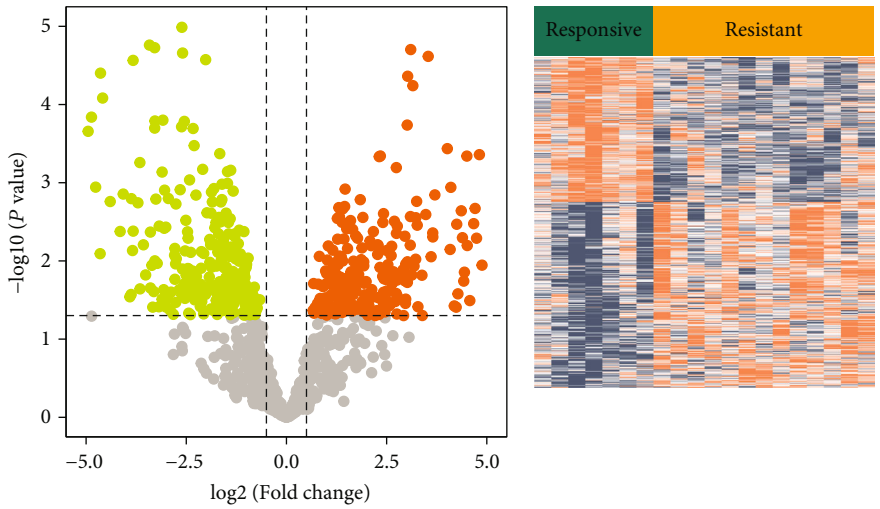

(d) (e)

Figure 1: Principal component analysis (PCA) in resistant versus responsive samples. (a) The flowchart of this study. (b) Before removing the outliers, the PCA was performed on the gene expression data. (c) After removing the outliers, the PCA was performed on the gene expression. (d) Volcano plot of DEG by log2 foldchange (FC) > 0.5 and p value < 0.05. (e) Clustering heat map of the DEG. The expression data for DEG was normalized.

Table 1: The GO enrichment analysis results of DEG.

ID	Description	p value	Count
GO: 0045229	External encapsulating structure organization	<0.01	118
GO: 0030198	Extracellular matrix organization	<0.01	117
GO: 0043062	Extracellular structure organization	<0.01	117
GO: 0006023	Aminoglycan biosynthetic process	<0.01	40
GO: 0031589	Cell-substrate adhesion	<0.01	86
GO: 0042476	Odontogenesis	<0.01	41
GO: 1903034	Regulation of response to wounding	<0.01	49
GO: 0006024	Glycosaminoglycan biosynthetic process	<0.01	37
GO: 0061041	Regulation of wound healing	<0.01	42
GO: 0001503	Ossification	<0.01	90
GO: 0001667	Ameboidal-type cell migration	<0.01	100
GO: 0050818	Regulation of coagulation	<0.01	27
GO: 0042493	Response to drug	<0.01	81
GO: 0010810	Regulation of cell-substrate adhesion	<0.01	56
GO: 0001501	Skeletal system development	<0.01	101
GO: 0034329	Cell junction assembly	<0.01	91
GO: 0060348	Bone development	<0.01	51
GO: 0022612	Gland morphogenesis	<0.01	35
GO: 0002576	Platelet degranulation	<0.01	38
GO: 0006022	Aminoglycan metabolic process	<0.01	46

consider genes to be differentially expressed, identifying a total of 2604 genes (1142 upregulated and 1462 downregulated in the resistant group) above this cut-off (Figures 1(d) and 1(e)). Then, we investigated the biological processes and pathways by enrichment analysis. External encapsulating structure organization (GO: 0045229), extracellular matrix organization (GO: 0030198), and extracellular structure organization (GO: 0043062) are the main biological processes in DEGs (Table 1). Besides, ECM-receptor interaction (hsa04512), human papillomavirus infection (hsa05165), glycosaminoglycan biosynthesis-

Table 2: The KEGG enrichment analysis results of DEG.

ID	Description	p value	Count
hsa04512	ECM-receptor interaction	<0.01	28
hsa05165	Human papillomavirus infection	<0.01	73
hsa00532	Glycosaminoglycan biosynthesis-chondroitin sulfate dermatan sulfate	<0.01	11
hsa04510	Focal adhesion	<0.01	49
hsa04974	Protein digestion and absorption	<0.01	29
hsa04933	AGE-RAGE signaling pathway in diabetic complications	<0.01	28
hsa05222	Small cell lung cancer	<0.01	26
hsa05146	Amoebiasis	<0.01	27
hsa00480	Glutathione metabolism	<0.01	18
hsa05205	Proteoglycans in cancer	<0.01	45
hsa04151	PI3K-Akt signaling pathway	<0.01	69
hsa04621	NOD-like receptor signaling pathway	<0.01	40
hsa05144	Malaria	<0.01	15
hsa05169	Epstein-Barr virus infection	<0.01	42
hsa00620	Pyruvate metabolism	<0.01	14
hsa05225	Hepatocellular carcinoma	<0.01	36
hsa04360	Axon guidance	<0.01	38
hsa05204	Chemical carcinogenesis - DNA adducts	<0.01	18
hsa04068	FoxO signaling pathway	<0.01	29
hsa05230	Central carbon metabolism in cancer	<0.01	18

chondroitin sulfate dermatan sulfate (hsa00532), and focal adhesion (hsa04510) were the main pathways in DEGs (Table 2).

3.2. Survival-Related EMT Gene Identification. Based on the survival analysis that was conducted on an R loop, among all 17468 genes, 939 genes were significantly related to survival. Among 939 survival-related genes, 118 were protective genes, and 821 were risky genes. The Venn map shows that 6 EMT genes (PIR, EID3, COX7B, CLEC18A, ALDH5A1, and DYNC1I1) are generally upregulated in resistant samples and are risky genes (Figure 2(a)). Besides, the Venn map shows that 4 EMT genes (CAPG, MST1R, KCNN4, and VDR) are generally downregulated in resistant samples and are protective genes (Figure 2(b)). These ten genes were defined as prognosis-related EMT genes (PREMTs).

3.3. Construction of EMT Score. After that, we performed a lasso analysis on the TCGA-ESCC samples to analyze these ten PREMTs (Figure 2(c)). Via the process of cross-validation, it was shown that 7 PREMTs were capable of producing a superior effect in the model (Figure 2(d)). Then, the univariate Cox regression method was adopted to obtain the coefficient values of genes. An EMT model consisting of 7 genes (CLEC18A, PIR, KCNN4, MST1R, CAPG, ALDH5A1, and COX7B) was identified. The EMT score of individuals using coefficients and gene expression was $(4.96) * \text{CLEC18A} + (0.36) * \text{PIR} + (-0.18) * \text{KCNN4} + (-0.24) * \text{MST1R} + (-0.50) * \text{CAPG} + (0.39) * \text{ALDH5A1} + (0.54) * \text{COX7B}$.

Patients with ESCC who were included in the TCGA were classified as having either a high or low EMT score based on the median value. In the course of our research, we examined the rates of mortality in two different EMT groups. We made the startling discovery that the group at high EMT had a survivability that was much lower than the group at low EMT (Figure 3(a)). The expression values of CLEC18A, PIR, KCNN4, MST1R, CAPG, ALDH5A1, and COX7B between groups were illustrated in Figure 3(b). The expression values of CLEC18A, PIR, ALDH5A1, and COX7B were higher in the group at high EMT. The expression values of KCNN4, MST1R, and CAPG were lower in the group at high EMT. There is a substantial difference in OS between groups (p value < 0.001, Figure 3(c)). In addition, the AUC value was displayed to assess the EMT signature's predictive abilities. AUC values of the EMT score for 1, 3, and 5 years of survival were 0.662, 0.729, and 0.760, respectively (Figure 3(d)).

3.4. The Nomogram for OS Prediction. Typically, a nomogram is used to quantify the risk of people in a therapeutic environment by combining various variables. By combining the EMT score, age, and stage, we developed a nomogram to estimate the survival rates of 1-, 3-, and 5-year OS of ESCC (Figure 4(a)). Each component in the nomogram is assigned points according to its contribution. The majority of contributions came from the EMT score, and the C-index for the nomogram was 0.70. Calibration curves of 1-, 3-, and 5-years were used to evaluate the accuracy of the model predictions (Figures 4(b)–4(d)). And the findings suggested that actual and anticipated survival were highly concordant, particularly for three-year survival (Figure 4(b)).

3.5. Estimation of the EMT Score with Immunity. Using ESTIMATE, the immune and stromal scores were calculated in order to examine the influence of EMT score on tumor

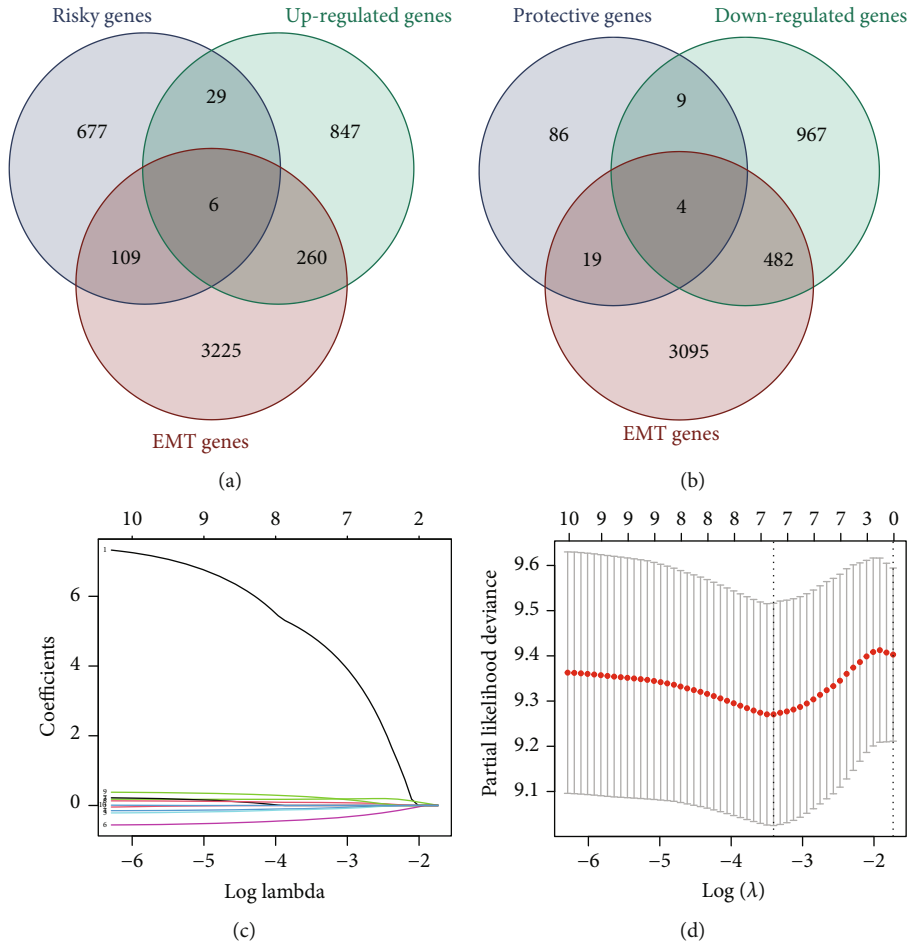

Figure 2: Identification of PREMTs in ESCC. (a, b) Venn diagrams for identifying PREMTs. (c) Lasso coefficient profiles of the 10 PREMTs. (d) Selection of the number of genes for EMT score by lasso analysis.

immunity. According to the data, the immune score of those with a low EMT score was noticeably higher than those with a high EMT score (p value = 0.011, Supplementary Figure 1A). There was an inverse relationship between the EMT score and the tumor immunity ($R = -0.22$, $p < 0.0001$, Supplementary Figure 1B). Patients with a high EMT score, on the other hand, tended to have tumor purity that was greater (Supplementary Figure 1A), but the difference was not significant (p value = 0.14).

In addition, the proportions of immune cells were compared across groups (Supplementary Figure 2). The fraction of immune cells such as CD8-T cells, dendritic cells, and natural-killer cells in the low EMT score subgroup was higher than those in the high EMT score subgroup.

3.6. Evaluate the Power of Signatures for Distinguishing Resistant and Responsive Patients. The expression values of genes were compared between resistant and responsive patients (Figure 5(a)). To evaluate the power to distinguish resistant and responsive patients, we measured the AUC of genes and EMT score (Figures 5(b)–5(i)). For diagnosis (resistant and responsive), the EMT score showed the highest AUC value (AUC = 0.89) than genes.

An independent dataset (GSE86099) contains the expression profiles of the cells associated with paclitaxel resistance. For diagnosis (resistant and responsive), all genes and EMT score showed perfect AUC values (AUC = 1.0) (Supplementary Figure 3A–3H).

3.7. Evaluate the Power of Signatures for Distinguishing ESCC and Normal Samples. The gene expression levels of CAPG, CLEC18A, and MST1R were higher in the tumor samples (Figure 6(a)). We drew the ROC curve of survival-related ECM genes to clarify the diagnostic value for distinguishing ESCC and normal samples (Figures 6(b)–6(i)). The results showed MST1R (AUC = 0.811), CAPG (AUC 0.743), CLEC18A (AUC = 0.714), and EMT score (AUC = 0.700) had significant diagnostic values.

3.8. Validates Prognostic Feature Genes. Then, the correlation between EMT genes expression and patient survival was confirmed (Supplementary Figure 4A–4J). The findings demonstrated that patients with elevated levels of ALDH5A1, PIR, and COX7B had a significantly lower OS.

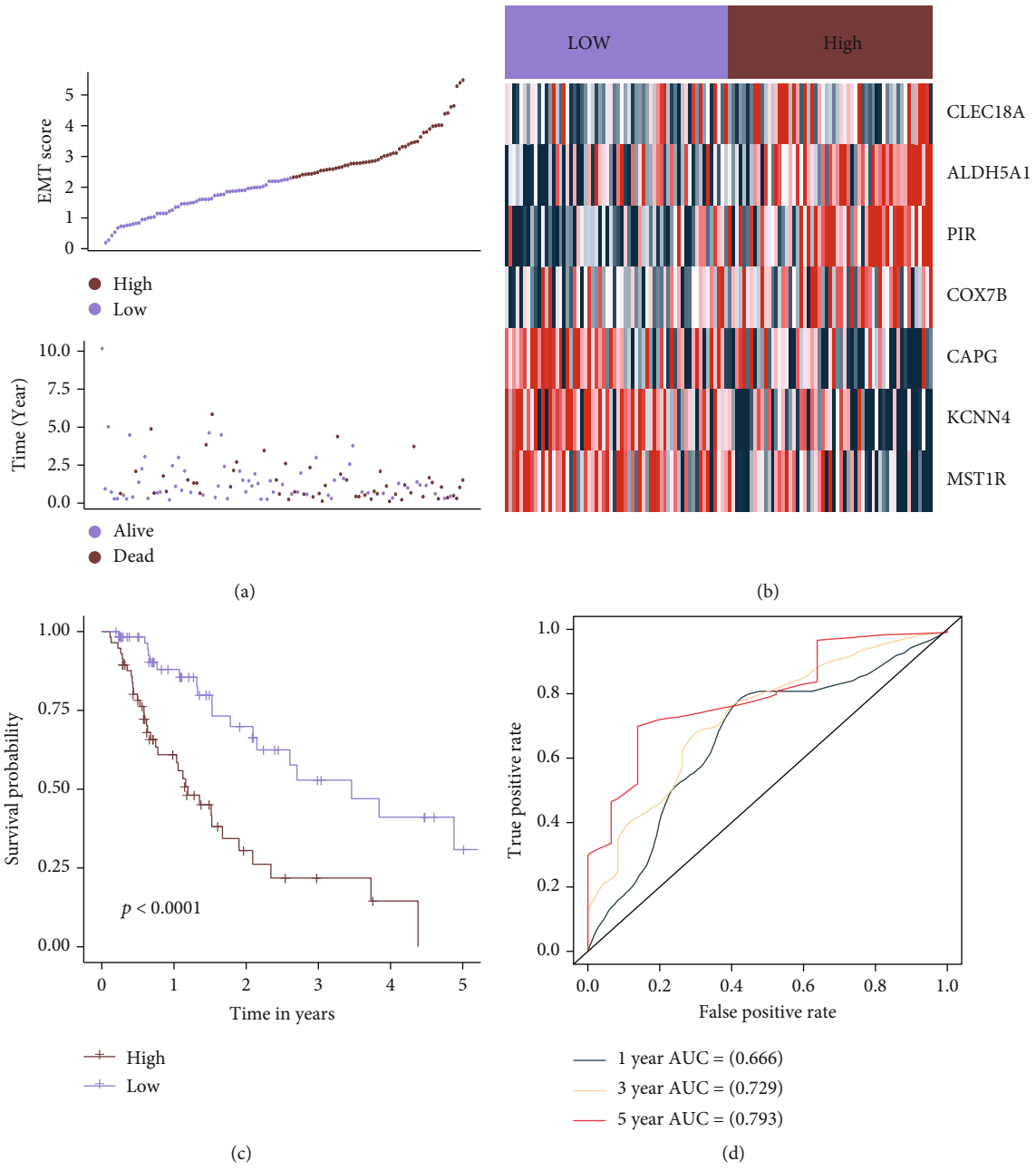

Figure 3: EMT score based on 7 EMT genes. EMT score distribution, survival overview (a), and heat map (b) for patients in the different groups. (c) The survival curves differentiate between groups. (d) The predictive accuracy of the EMT signature for TCGA patients was shown using ROC curves.

4. Discussion

ESCC is a kind of cancer that is aggressive and poses a significant threat to human health as a result of its high incidence rate as well as its low survival rate after 5 years [31]. Currently, there are few effective biomarkers that can be used to diagnose, prognosis, and treatment of ESCC. Expression data was utilized to discover EMT genes linked with chemoradiotherapy resistance, as well as their connection with ESCC prognosis. Finally, 6 risky genes (PIR, EID3, COX7B, CLEC18A, ALDH5A1, and DYNC1I1) and 4 protective genes (CAPG, MST1R, KCNN4, and VDR) were identified. Based on lasso analysis, an EMT score model was constructed by the expression values of 7 genes (CLEC18A, PIR, KCNN4, MST1R, CAPG, ALDH5A1, and COX7B). Patients with an elevated EMT score for ESCC had a worse prognosis.

Earlier research has analyzed the difference in gene expression between nCRT responder and nonresponder samples in order to predict nCRT response [32]. Among the identified genes, five genes could accurately predict the response to nCRT. In our study, among the 7 identified genes, ALDH5A1, CLEC18A, COX7B, and PIR were upregulated in resistant

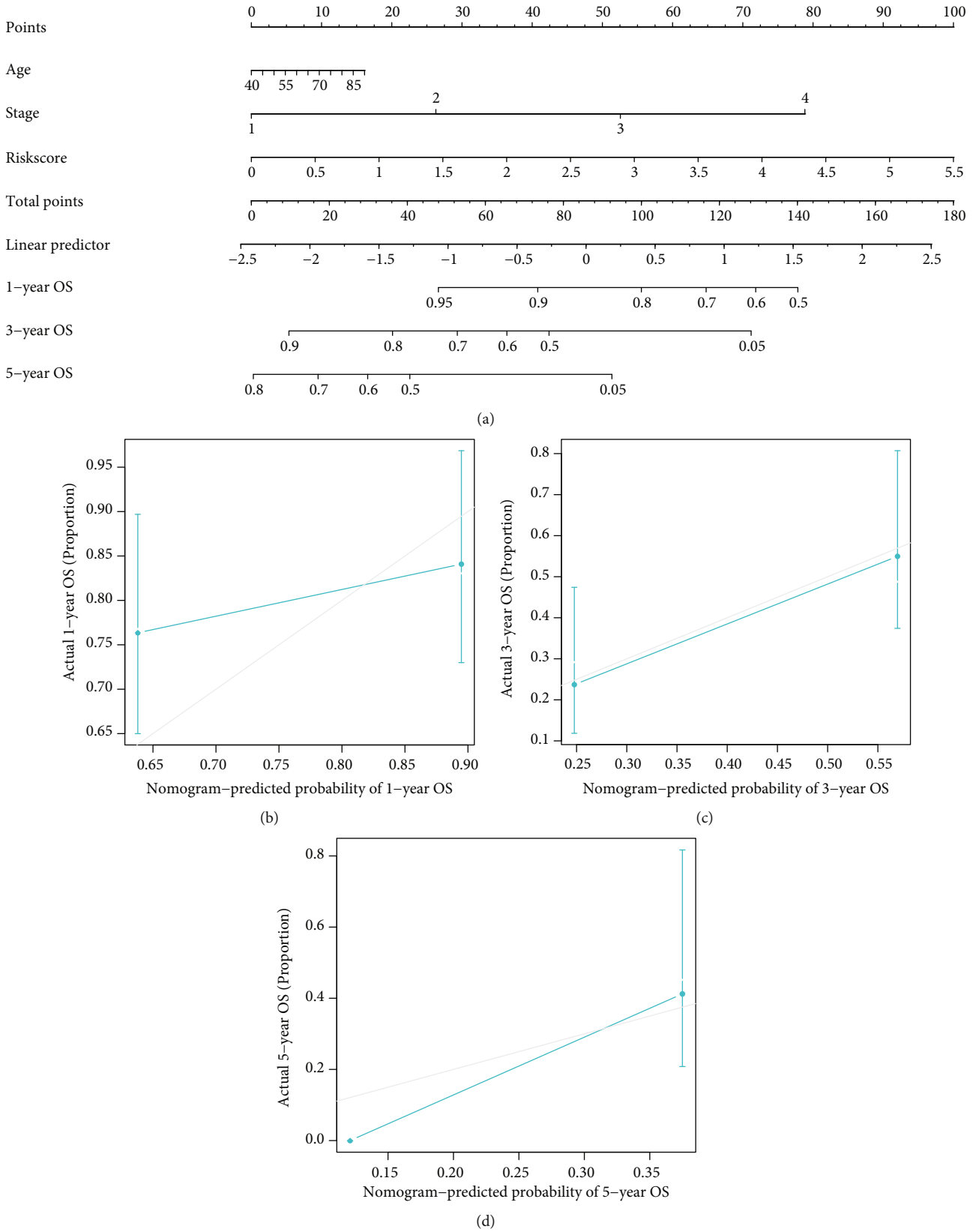

Figure 4: The nomogram constructed in the TCGA-ESCC. (a) The nomogram for predicting OS. The calibration plots for predicting 1-year (b), 3-year (c), and 5-year (d) OS.

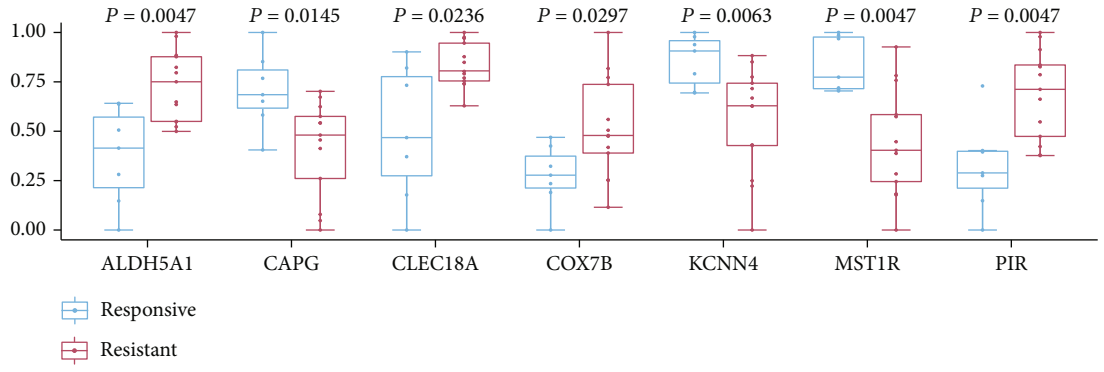

(a)

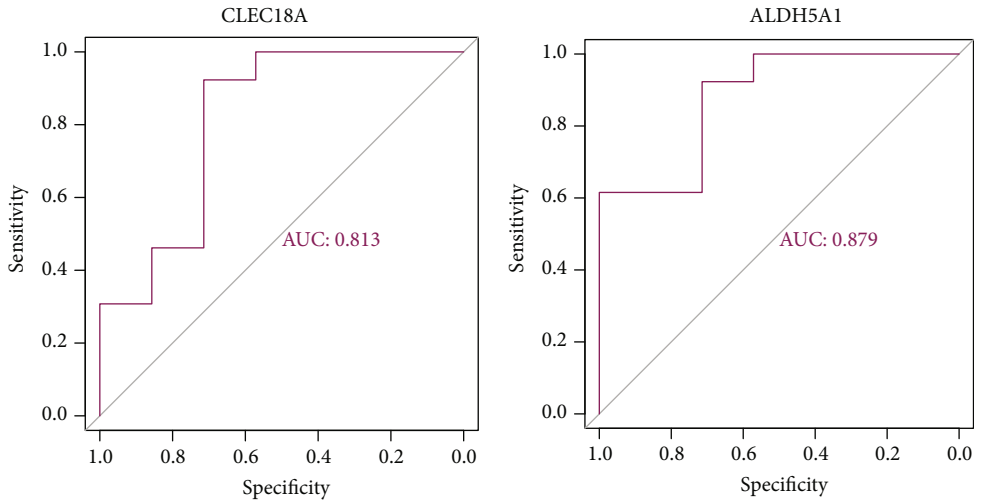

(b)

(c)

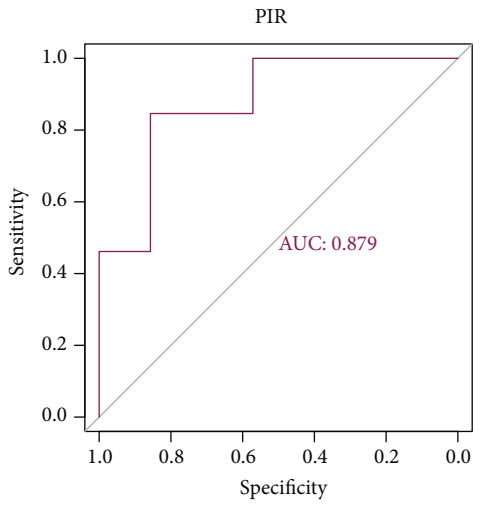

(d)

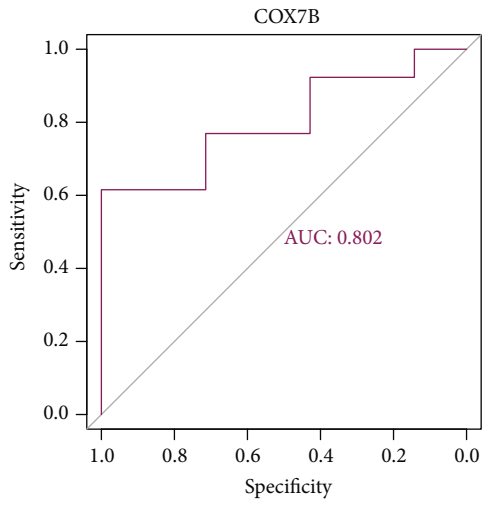

(e)

Figure 5: Continued.

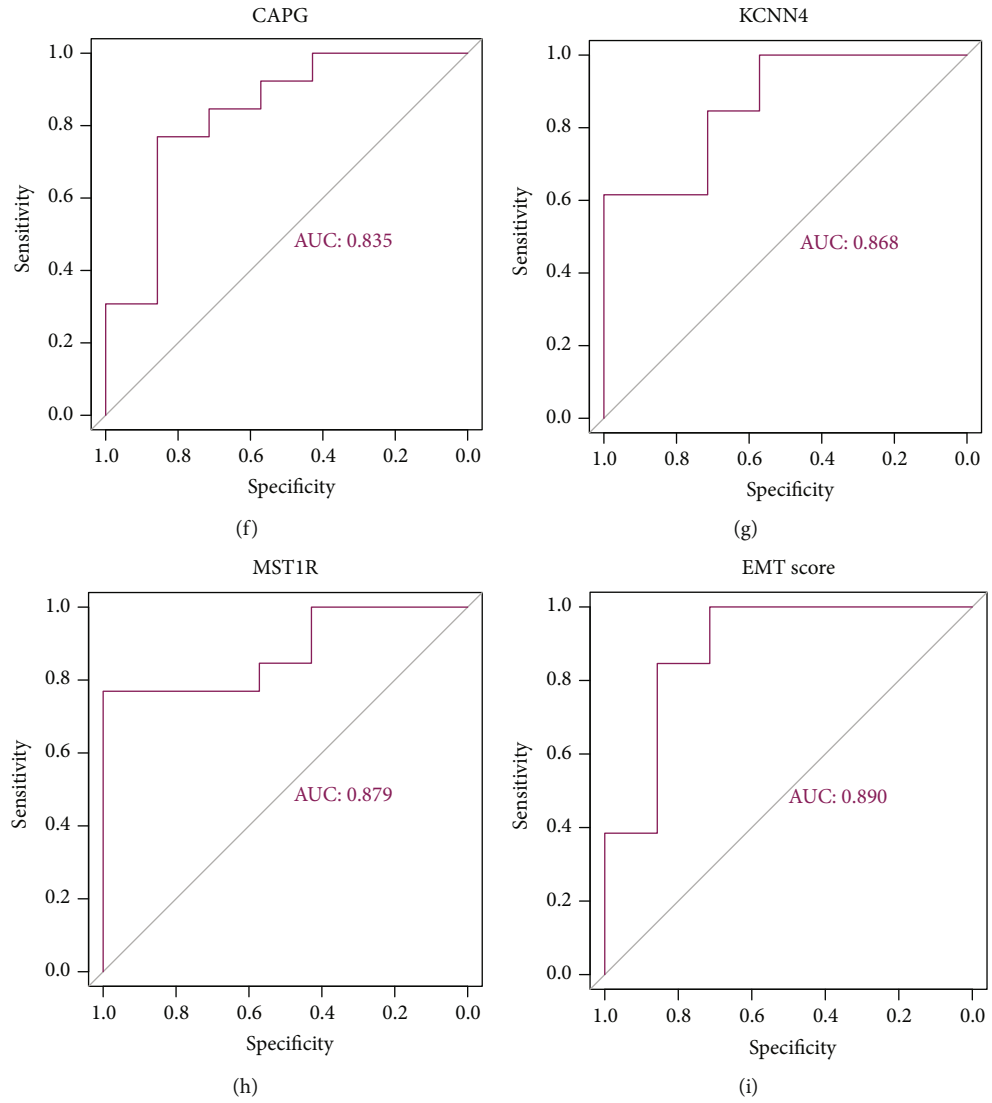

Figure 5: (a) The expression pattern of genes between responsive and resistant patients. ROC curves of genes and EMT score. (b) ROC curve of CLEC18A. (c) ROC curve of ALDH5A1. (d) ROC curve of PIR. (e) ROC curve of COX7B. (f) ROC curve of CAPG. (g) ROC curve of KCNN4. (h) ROC curve of MST1R. (i) ROC curve of EMT score. AUC > 0.7 indicates good effect.

patients. CAPG, KCNN4, and MST1R were upregulated in responsive patients. In the predictive models, all seven genes and EMT score could achieve a high accuracy (>80%) in predicting the response to therapy of patients. Besides, MST1R (AUC = 0.811), CAPG (AUC = 0.743), CLEC18A (AUC = 0.714), and EMT score (AUC = 0.700) also had significant diagnostic accuracy in distinguishing tumor and normal samples.

By analyzing expression profiles, we predicted the immune score and the values of immune subpopulations. According to the findings, the group with the high EMT score had a considerable reduction in the number of immune cells. It is possible that this is the reason why people with high EMT scores have a poorer prognosis. EMT may interact with immunosuppression either directly or indirectly, as shown by the results of a prior study [33]. Since immune cells are important biomarkers for immunotherapy, the influence of EMT on immunity is important and needs more studies.

MST1R was related to cellular motility and matrix invasion that are the predictive indications of a tumor phenotype with the ability to metastasize [34]. MST1R was significantly highly expressed in 74% of gastroesophageal samples, and overexpression predicted poor survival [34]. For other genes, their roles in ESCC need more studies.

There were some limitations to our study. These seven key EMT genes have the potential to be used not only in ESCC resistance prediction but also as possible prognostic biomarkers. However, the association between seven important EMT

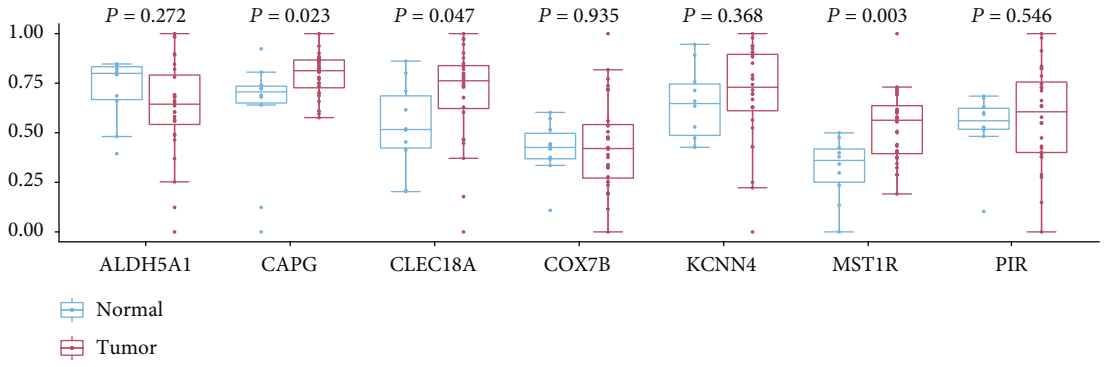

(a)

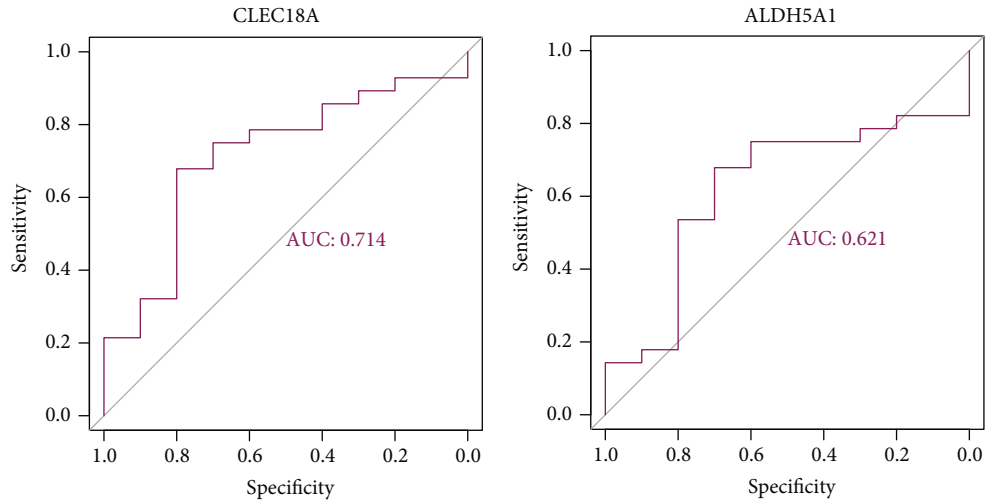

(b)

(c)

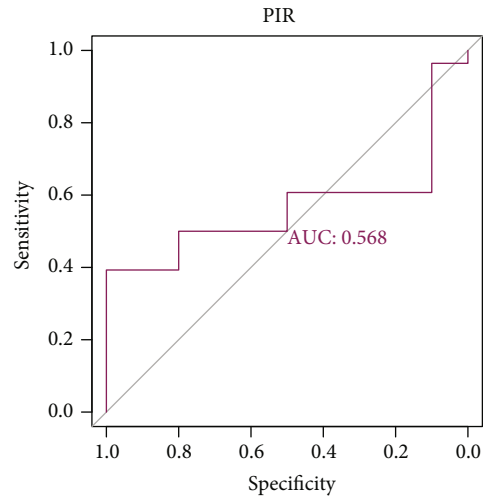

(d)

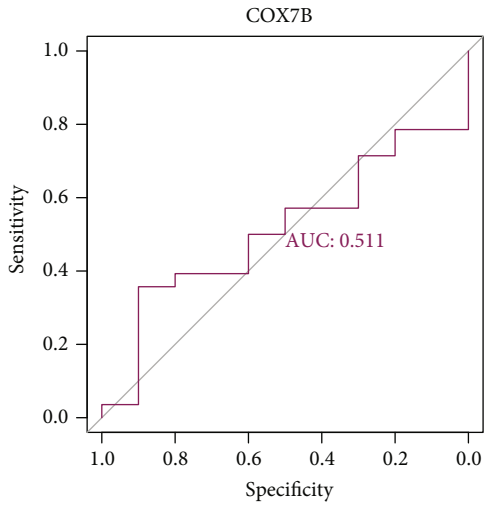

(e)

Figure 6: Continued.

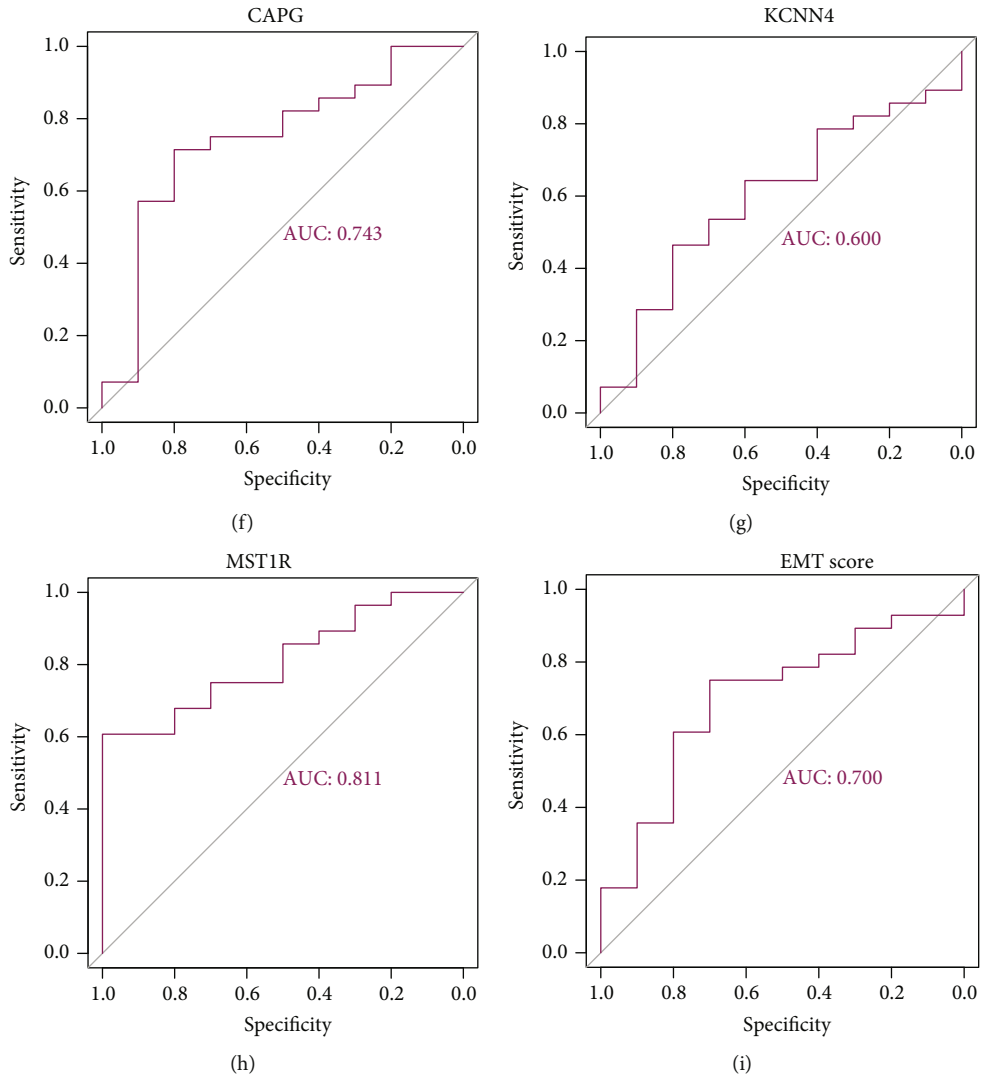

Figure 6: (a) The expression pattern of genes between normal and tumor samples. ROC curves of genes and EMT score. (b) ROC curves of CLEC18A. (c) ROC curves of ALDH5A1. (d) ROC curves of PIR. (e) ROC curves of COX7B. (f) ROC curves of CAPG. (g) ROC curves of KCNN4. (h) ROC curves of MST1R. (i) ROC curves of EMT score. AUC > 0.7 indicates good effect.

genes and ESCC prognosis may not be robust. Therefore, in order to discover the precise biological behaviors of these seven genes (CLEC18A, PIR, KCNN4, MST1R, CAPG, ALDH5A1, and COX7B) that are involved in the formation of ESCC, experimental validation has to be carried out. Meanwhile, there were just a few ESCC specimens available. In order to evaluate the potential predictive utility of these genes for illness, more validation in more samples is required.

5. Conclusions

Using different datasets, 7 genes that play essential roles in ESCC chemotherapy resistance, namely, CLEC18A, PIR, KCNN4, MST1R, CAPG, ALDH5A1, and COX7B, were selected. The findings of this research may help to clarify the molecular processes of chemotherapy resistance in ESCC and assist us in identifying prospective targets for predicting chemotherapy resistance.

Data Availability

The following information was supplied regarding data availability: data is available at the TCGA (https://portal.gdc.cancer.gov/) and GEO (https://www.ncbi.nlm.nih.gov/geo/).

Conflicts of Interest

The authors declare that they have no conflicts of interest.

Authors' Contributions

Kewei Song and Hao Chen conceived and designed the study. Kewei Song, Baohong Gu, and Chenhui Ma analyzed the data and plotted the figures. Kewei Song and Bofang Wang drafted the article. Na wang, Rong Yu, and Hao Chen revised the article critically. All authors had final approval of the submitted versions.

Acknowledgments

This study was supported by National Natural Science Foundation of China (no. 82160129), Key Talents Project of Gansu Province (no. 2019RCXM020), Key Project of Science and Technology in Gansu Province (19ZD2WA001), COVID-19 Prevention and Control Technology Research Project of Lanzhou City (2020-XG-54), Science and Technology Project of Chengguan District of Lanzhou City (2020SHFZ0039), Science and Technology Project of Chengguan District of Lanzhou City (2020JSCX0073), and Cuiying Scientific and Technological Innovation Program of Lanzhou University Second Hospital (no. CY2017-ZD01).

Supplementary Materials

Supplementary 1. Supplementary Figure 1: estimation of the EMT score with tumor immunity. (a) Distribution of stromal scores, immune scores, and tumor purity in the low and high EMT score subgroups of the TCGA data cohort. (b) Association between the EMT score and immune score.

Supplementary 2. Supplementary Figure 2: association of the EMT score with the immune subpopulations.

Supplementary 3. Supplementary Figure 3: diagnosis values of (a) CLEC18A, (b) ALDH5A1, (c) PIR, (d) COX7B, (e) CAPG, (f) KCNN4, (g) MST1R, and (h) EMT score for paclitaxel resistance.

Supplementary 4. Supplementary Figure 4: Kaplan–Meier survival curves for genes for ALDH5A1 (a), CAPG (b), CLEC18A (c), COX7B (d), DYNC1I1 (e), EID3 (f), KCNN4 (g), MST1R (h), PIR (i), and VDR (j).

Supplementary 5. Supplementary Table 1: the detailed information of samples from the GSE45670 dataset. Supplementary Table 2: the detailed information of samples from the TCGA-ESCC dataset.

References

[1] R. L. Siegel, K. D. Miller, H. E. Fuchs, and A. Jemal, "Cancer statistics," *CA: a Cancer Journal for Clinicians*, vol. 72, no. 1, pp. 7–33, 2022.

[2] W. Chen, R. Zheng, P. D. Baade et al., "Cancer statistics in China, 2015," *CA: a Cancer Journal for Clinicians*, vol. 66, no. 2, pp. 115–132, 2016.

[3] M. Arnold, I. Soerjomataram, J. Ferlay, and D. Forman, "Global incidence of oesophageal cancer by histological subtype in 2012," *Gut*, vol. 64, no. 3, pp. 381–387, 2015.

[4] C. C. Abnet, M. Arnold, and W. Q. Wei, "Epidemiology of esophageal squamous cell carcinoma," *Gastroenterology*, vol. 154, no. 2, pp. 360–373, 2018.

[5] F. Islami, H. Poustchi, A. Pourshams et al., "A prospective study of tea drinking temperature and risk of esophageal squamous cell carcinoma," *International Journal of Cancer*, vol. 146, no. 1, pp. 18–25, 2020.

[6] F. Z. Li and W. Q. Zang, "Knockdown of lncRNAXLOC_001659 inhibits proliferation and invasion of esophageal squamous cell carcinoma cells," *World Journal of Gastroenterology*, vol. 25, no. 42, pp. 6299–6310, 2019.

[7] A. Pennathur, M. K. Gibson, B. A. Jobe, and J. D. Luketich, "Oesophageal Carcinoma," *Lancet*, vol. 381, no. 9864, pp. 400–412, 2013.

[8] A. Herskovic, W. Russell, M. Liptay, M. J. Fidler, and M. al-Sarraf, "Esophageal carcinoma advances in treatment results for locally advanced disease: review," *Annals of Oncology*, vol. 23, no. 5, pp. 1095–1103, 2012.

[9] W. H. Allum, J. M. Blazeby, S. M. Griffin et al., "Guidelines for the management of oesophageal and gastric cancer," *Gut*, vol. 60, no. 11, pp. 1449–1472, 2011.

[10] T. N. Walsh, N. Noonan, D. Hollywood, A. Kelly, N. Keeling, and T. P. J. Hennessy, "A comparison of multimodal therapy and surgery for esophageal adenocarcinoma," *The New England Journal of Medicine*, vol. 335, no. 7, pp. 462–467, 1996.

[11] A. C. Berger, J. Farma, W. J. Scott et al., "Complete response to neoadjuvant chemoradiotherapy in esophageal carcinoma is associated with significantly improved survival," *Journal of Clinical Oncology*, vol. 23, no. 19, pp. 4330–4337, 2005.

[12] W. Yang, X. Xing, S. J. Yeung et al., "Neoadjuvant programmed cell death 1 blockade combined with chemotherapy for resectable esophageal squamous cell carcinoma," *Journal for Immunotherapy of Cancer*, vol. 10, no. 1, p. e003497, 2022.

[13] C. A. Martz, K. A. Ottina, K. R. Singleton et al., "Systematic identification of signaling pathways with potential to confer anticancer drug resistance," *Science Signaling*, vol. 7, article a121, 2014.

[14] D. Basu, T. T. Nguyen, K. T. Montone et al., "Evidence for mesenchymal-like sub-populations within squamous cell carcinomas possessing chemoresistance and phenotypic plasticity," *Oncogene*, vol. 29, no. 29, pp. 4170–4182, 2010.

[15] K. A. Whelan, P. M. Chandramouleeswaran, K. Tanaka et al., "Autophagy supports generation of cells with high CD44 expression via modulation of oxidative stress and Parkin-mediated mitochondrial clearance," *Oncogene*, vol. 36, no. 34, pp. 4843–4858, 2017.

[16] J. Liu, H. Fan, Y. Ma et al., "Notch1 is a 5-fluorouracil resistant and poor survival marker in human esophagus squamous cell carcinomas," *PLoS One*, vol. 8, no. 2, article e56141, 2013.

[17] I. Pastushenko, A. Brisebarre, A. Sifrim et al., "Identification of the tumour transition states occurring during EMT," *Nature*, vol. 556, no. 7702, pp. 463–468, 2018.

[18] N. Matsuura, K. Tanaka, M. Yamasaki et al., "NOTCH3 limits the epithelial–mesenchymal transition and predicts a favorable clinical outcome in esophageal cancer," *Cancer Medicine*, vol. 10, no. 12, pp. 3986–3996, 2021.

[19] D. Stefania and D. Vergara, "The many-faced program of epithelial-mesenchymal transition: a system biology-based view," *Frontiers in Oncology*, vol. 7, p. 274, 2017.

[20] M. M. Forghanifard, O. Moaven, M. Farshchian et al., "Expression analysis elucidates the roles of MAML1 and Twist1 in esophageal squamous cell carcinoma aggressiveness and metastasis," *Annals of Surgical Oncology*, vol. 19, no. 3, pp. 743–749, 2012.

[21] J. Wen, H. Yang, M. Z. Liu et al., "Gene expression analysis of pretreatment biopsies predicts the pathological response of esophageal squamous cell carcinomas to neo-chemoradiotherapy," *Annals of Oncology*, vol. 25, no. 9, pp. 1769–1774, 2014.

[22] S. Davis and P. S. Meltzer, "GEOquery: a bridge between the gene expression omnibus (GEO) and BioConductor," *Bioinformatics*, vol. 23, no. 14, pp. 1846-1847, 2007.

[23] A. Colaprico, T. C. Silva, C. Olsen et al., "TCGAbiolinks: an R/Bioconductor package for integrative analysis of TCGA data," *Nucleic Acids Research*, vol. 44, no. 8, article e71, 2016.

[24] R. Wang, A. Sumarpo, Y. Saiki, N. Chen, M. Sunamura, and A. Horii, "ABCB1 is upregulated in acquisition of taxane resistance: lessons from esophageal squamous cell carcinoma cell lines," *The Tohoku Journal of Experimental Medicine*, vol. 240, no. 4, pp. 295–301, 2016.

[25] M. D. Robinson, D. J. McCarthy, and G. K. Smyth, "Edger: a bioconductor package for differential expression analysis of digital gene expression data," *Bioinformatics*, vol. 26, no. 1, pp. 139-140, 2010.

[26] G. Yu, L. G. Wang, Y. Han, and Q. Y. He, "clusterProfiler: an R package for comparing biological themes among gene clusters," *OMICS*, vol. 16, no. 5, pp. 284–287, 2012.

[27] S. V. Vasaikar, A. P. Deshmukh, P. den Hollander et al., "EMTome: a resource for pan-cancer analysis of epithelial-mesenchymal transition genes and signatures," *British Journal of Cancer*, vol. 124, no. 1, pp. 259–269, 2021.

[28] J. Friedman, T. Hastie, and R. Tibshirani, "Regularization paths for generalized linear models via coordinate descent," *Journal of Statistical Software*, vol. 33, no. 1, pp. 1–22, 2010.

[29] K. Yoshihara, M. Shahmoradgoli, E. Martínez et al., "Inferring tumour purity and stromal and immune cell admixture from expression data," *Nature Communications*, vol. 4, no. 1, p. 2612, 2013.

[30] S. Hanzelmann, R. Castelo, and J. Guinney, "GSVA: gene set variation analysis for microarray and RNA-seq data," *BMC Bioinformatics*, vol. 14, no. 1, p. 7, 2013.

[31] Y. Song, X. Wang, F. Wang et al., "Identification of four genes and biological characteristics of esophageal squamous cell carcinoma by integrated bioinformatics analysis," *Cancer Cell International*, vol. 21, no. 1, p. 123, 2021.

[32] S. G. Maher, C. M. Gillham, S. P. Duggan et al., "Gene expression analysis of diagnostic biopsies predicts pathological response to neoadjuvant chemoradiotherapy of esophageal cancer," *Annals of Surgery*, vol. 250, no. 5, pp. 729–737, 2009.

[33] N. Kang, X. Xie, X. Zhou et al., "Identification and validation of EMT-immune-related prognostic biomarkers CDKN2A, CMTM8 and ILK in colon cancer," *BMC Gastroenterology*, vol. 22, no. 1, p. 190, 2022.

[34] D. V. Catenacci, G. Cervantes, S. Yala et al., "RON (MST1R) is a novel prognostic marker and therapeutic target for gastro-esophageal adenocarcinoma," *Cancer Biology & Therapy*, vol. 12, no. 1, pp. 9–46, 2011.

Hindawi
Disease Markers
Volume 2022, Article ID 3780391, 15 pages
https://doi.org/10.1155/2022/3780391

Research Article

Construction of an Epithelial-Mesenchymal Transition-Related Model for Clear Cell Renal Cell Carcinoma Prognosis Prediction

Shimiao Zhu,[1] Tao Wu,[1,2] Ziliang Ji,[2] Zhouliang Wu,[1] Hao Lin,[2] Chong Shen,[1] Yinggui Yang,[2] Qingyou Zheng,[2] and Hailong Hu[1]

[1]*Department of Urology, Tianjin Institute of Urology, The Second Hospital of Tianjin Medical University, Tianjin 300211, China*
[2]*Department of Urology, Shenzhen Hospital, Southern Medical University, Shenzhen 518100, China*

Correspondence should be addressed to Qingyou Zheng; zhengqingyou@smu.edu.cn and Hailong Hu; huhailong@tmu.edu.cn

Received 1 May 2022; Accepted 6 July 2022; Published 9 August 2022

Academic Editor: Zhen-Jian Zhuo

Background. A rising amount of data demonstrates that the epithelial-mesenchymal transition (EMT) in clear cell renal cell carcinomas (ccRCC) is connected with the advancement of the cancer. In order to understand the role of EMT in ccRCC, it is critical to integrate molecules involved in EMT into prognosis prediction. The objective of this project was to establish a prognosis prediction model using genes associated with EMT in ccRCC. *Methods*. We acquired the mRNA expression profiles and clinical information about ccRCC from TCGA database. In this study, we measured differentially expressed EMT-related genes (DEEGs) by two comparison groups (tumor versus normal tissues; "stages I-II" versus "stages III-IV" tumor tissues). Based on classification and regression random forest models, we identified the most important DEEGs in predicting prognosis. Afterwards, a risk-score model was created using the identified important DEEGs. The prediction ability of the risk-score model was calculated by the area under the curve (AUC). A nomogram for prognosis prediction was built using the risk-score in combination with clinical factors. *Results*. Among the 72 DEEGs, the classification and regression random forest models identified six hub genes (DKK1, DLX4, IL6, KCNN4, RPL22L1, and SPDEF), which exhibited the highest importance values in both models. Through the expression of these six hub genes, a novel risk-score was developed for the prognosis prediction of ccRCC. ROC curves showed the risk-score performed well in both the training (0.749) and testing (0.777) datasets. According to the survival analysis, individuals who were separated into high/low-risk groups had statistically different outcomes in terms of prognosis. Besides, the risk-score model also showed outstanding ability in assessing the progression of ccRCC after treatment. In terms of nomogram, the concordance index (C-index) was 0.79. Additionally, we predicted the differences in response to chemotherapy drugs among patients from low- and high-risk groups. *Conclusion*. Gene signatures related to EMT could be useful in predicting ccRCC prognosis.

1. Introduction

RCC accounts for 2 to 3% of all cancers worldwide [1]. Almost 403,000 people are diagnosed with RCC each year, and 175,000 people die from it [2]. There is a range of histological classification groups, but kidney renal clear cell carcinoma (KIRC, ccRCC) is the most prevalent and contributes to the majority of renal cancer-related deaths. KIRC can remain clinically occult in the absence of significant clinical symptoms, and patients are initially diagnosed when they are already at a late stage of the TNM. In general, cases of late diagnosis are associated with lower survival rates, which results in a lower five-year survival rate for KIRC patients. In stage I, the five-year disease-specific survival for RCC patients ranges from 80 to 95 percent, but it will drop to less than 10% for stage IV patients [3]. For these RCC patients who had a lower survival rate and high risk, more elaborate and customized treatment plans were necessary. As a result, prognostic models that are capable of accurately identifying patients at high risk are urgently needed.

The EMT process describes the transition of epithelial cells to mesenchymal cells in a series of steps, and it is characterized by a loss of polarity, a breakdown in the integrity barrier, and an increase in invasion [4]. Many studies have highlighted the significance of EMT in cancer metastasis

and pharmaceutical resistance [5]. The abnormal EMT signature is associated with various acquired capabilities, such as resistance to chemotherapy and immunotherapy, in addition to migration and invasion [6]. Recently, an EMT signature was shown to be linked to immune cell signaling, providing novel insights into the link between EMT and immune activation [7]. There are potential therapeutic opportunities because of the association between EMT and immune cells. Although EMT-related signatures have been linked to ccRCC metastasis and prognosis, limited studies have been conducted to determine if they can be employed as indicators for early detection and prognosis assessment.

In the current study, random forest models were developed to identify the most important genes associated with KIRC patient survival time and survival status. A prognostic risk-score model for KIRC was developed by the expression of six important genes. The AUC values and survival analysis results demonstrated the feasibility and accuracy of the risk-score model. A nomogram was constructed to predict overall survival (OS) in KIRC after incorporating the risk-score and clinical data parameters. Together, our findings demonstrate the importance of risk-score and nomogram for the prediction of survival for patients with KIRC.

2. Materials and Methods

2.1. Data Collection. Level three of mRNA sequencing data of cancer patients with KIRC was collected from TCGA (https://tcga-data.nci.nih.gov/tcga/). The expression data of 539 KIRC and 72 normal kidney samples were chosen for further investigation. The form of the downloaded gene expression data was "fragments-per-kilobase-million" (FPKM). The original data was then converted into "transcript-per-million" (TPM). Among 539 KIRC samples, the numbers of stage I, stage II, stage III, and stage IV were 268, 57, 123, and 83.

2.2. Identification of Differentially Expressed Genes (DEGs). The R package "edgeR" was chosen to obtain DEGs between KIRC and normal tissues [8]. The DEGs filtering criteria were established at a p value of less than 0.05 and a |log 2 FoldChange| greater than 0.5. Similarly, DEGs between early stage ("stages I-II") and advanced stage ("stage III-IV") tumor tissues were obtained by the same method and screening criteria. We downloaded 1184 genes related to EMT from the dbEMT online database [9], and then we obtained the DEEGs by integrating the DEGs and EMT-related genes through the R package "VennDiagram" [10].

2.3. Analysis of Pathways. Enrichr (https://maayanlab.cloud/enrichr/enrich) [11] was performed to identify significantly enriched pathways. Results from modules, including "GO_Biological_Process_2021," "GO_Molecular_Function_2021," "GO_Cellular_Component_2021," "KEGG_2021_Human," and "MSigDB_Hallmark_2020" were downloaded and presented in this work. Pathways with a p value of less than 0.05 were recognized as significant pathways.

2.4. Selection of Biomarkers by Machine Learning. In order to construct a model that has perfect prediction performance, we used machine learning models to select the genes that are significantly correlated with prognosis. The expression values of DEEGs were normalized by the "$\log2(x+1)$" and "min-max" normalization methods. A classification and a regression model were constructed by the random forest (RF) algorithm. The classification RF (cRF) was built for the assessment of the survival status of KIRC patients. The regression RF (rRF) was built for the prediction of the survival time of KIRC patients. The importance values of genes in two models were calculated, and the six genes with the greatest importance values were chosen for further study as hub genes.

2.5. Construction of the Risk Model. The expression profiles of TCGA-KIRC were separated randomly into training (70%) and testing (30%) datasets. In the training of KIRC patients, univariate Cox analysis was performed to assess the coefficients of genes. The risk-score was evaluated by the equation: $\text{risk} - \text{score} = (\text{coefficient} \times \text{expression of gene } 1) + (\text{coefficient} \times \text{expression of gene } 2) + \cdots + (\text{coefficient} \times \text{expression of gene } X)$. KIRC individuals were separated into low and high groups by the median risk-score, respectively. With the log-rank test, survival curves for low- and high-risk individuals were compared, including OS and progression-free interval events (PFI). The "survivalROC" R package was selected to calculate the AUC value to evaluate the predictive ability.

2.6. Stratification Analysis. TCGA-KIRC individuals were stratified into subgroups by age (≥60 years vs. <60 years), gender (female vs. male), and TNM stages (T1/T2 vs. T3/T4, N0 vs. N1, and M0 vs. M1). The "Wilcoxon rank-sum" test was selected to discover the risk-score distribution with the R package "ggpubr."

2.7. Nomogram Development. A nomogram including clinical variables (age and stage) and the risk-score was designed to estimate the likelihood of one, three, and five-year OS. C-index values vary between 0.5 and 1.0, representing no discriminating ability and excellent discriminating capacity, respectively. The fit of the generated and reference lines indicates the high accuracy of the nomogram model.

2.8. Chemotherapeutic Response Prediction. The responses to chemotherapeutic drugs were predicted for samples by the R package "pRRophetic" [12]. With a prediction model based on Genomics of Drug Sensitivity in Cancer (GDSC) data and expression profiles of TCGA-KIRC samples, the package could predict the IC50 of each drug for each patient. The IC50 refers to the dosage required for halving the number of viable cells, and it is a measure of the drug's therapeutic effectiveness and can also be used for assessing the tolerance of tumor cells to drugs.

2.9. Evaluation of the Tumor Microenvironment (TME). ESTIMATE [13] and CIBERSORT [14] were utilized in R to determine each KIRC sample's TME status. For example, ESTIMATE predicted the level of stromal, immune, and tumor is scored based on the expression profiles of TCGA-KIRC samples. The relative levels of 22 tumor-infiltrating lymphocytes (TILs) in KIRC samples were predicted by the CIBERSORT

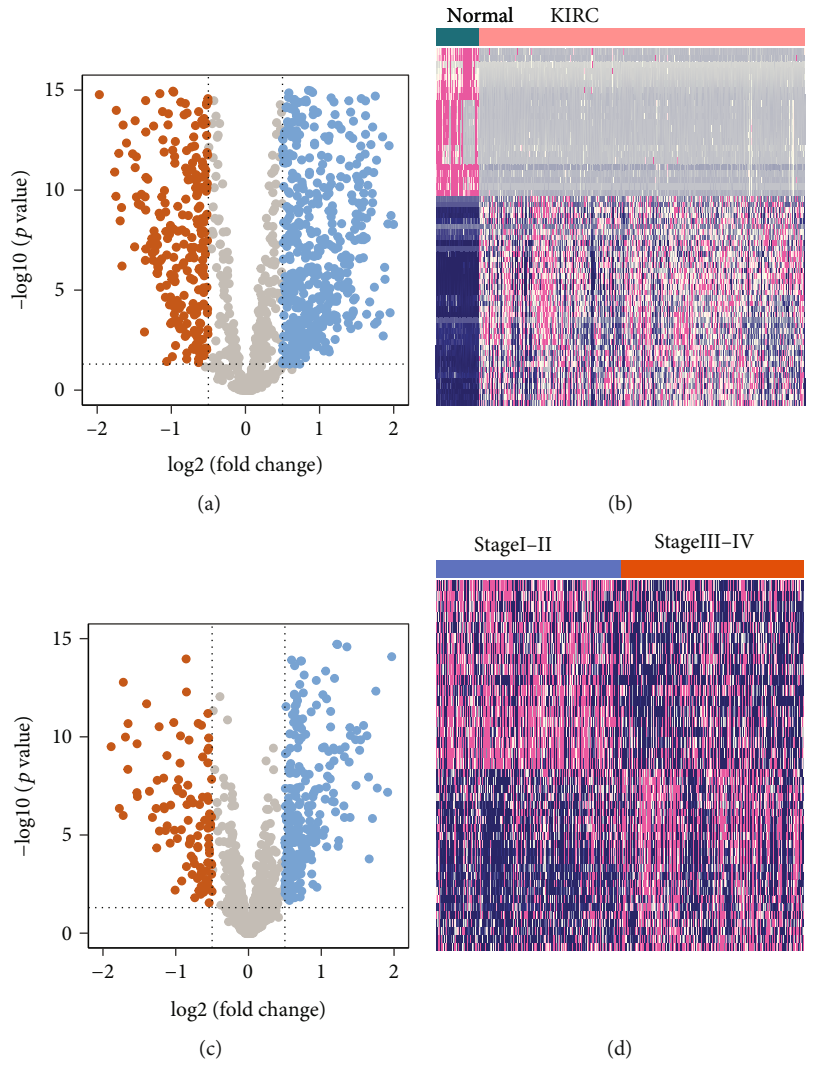

Figure 1: Identification of DEGs in TCGA-KIRC cohort. (a) The volcano of DEGs between KIRC and normal kidney samples. (b) The heatmap of DEGs between KIRC and normal kidney samples. (c) The volcano of DEGs between "stages I-II" and "stages III-IV" tumor tissues. (d) The heatmap of DEGs between "stages I-II" and "stages III-IV" tumor tissues. In volcano plots, red dots indicate downregulation genes in KIRC or "stages III-IV," whereas blue dots indicate upregulation genes. In heatmap plots, red indicates high-expression values, whereas blue indicates low-expression values.

algorithm. To ensure the prediction results are credible, p value < 0.05 was used as the selection criterion.

3. Results

3.1. Identification of DEEGs and Functional Enrichment Analysis. A total of 8905 significantly DEGs were identified between KIRC and normal kidney samples, of which 5660 were upregulated and 3245 were downregulated in KIRC samples than in normal samples (Figures 1(a) and 1(b)). Similarly, 2052 significantly DEGs were found between early stage ("stages I-II") and advanced stage ("stages III-IV") tumor tissues, of which 1453 were upregulated and 599 were downregulated in the advanced stage than in early stage KIRC samples (Figures 1(b) and 1(c)). After an intersection of EMT-related genes and DEGs by Venn diagram, 72 DEEGs were found (Figure 2(a)).

Following that, functional enrichment analysis was used to investigate the probable molecular processes behind DEEGs. The enriched biological process (BP) terms were "inflammatory_response" and "cytokine_mediated_signaling_pathway" (Supplementary Table 1). The enriched molecular function (MF) was the terms of "cytokine_activity" and "receptor_ligand_activity" (Supplementary Table 2). The significant cellular component (CC) terms were "collagen_containing_extracellular_matrix" and "secretory_granule_lumen" (Supplementary Table 3). Furthermore, the KEGG analysis indicated that DEEGs were strongly linked to pathways in "IL17_signaling" and "viral_protein_interaction_with_cytokine_and_cytokine_receptor" (Supplementary Table 4). Besides, the hallmark pathway analysis showed that

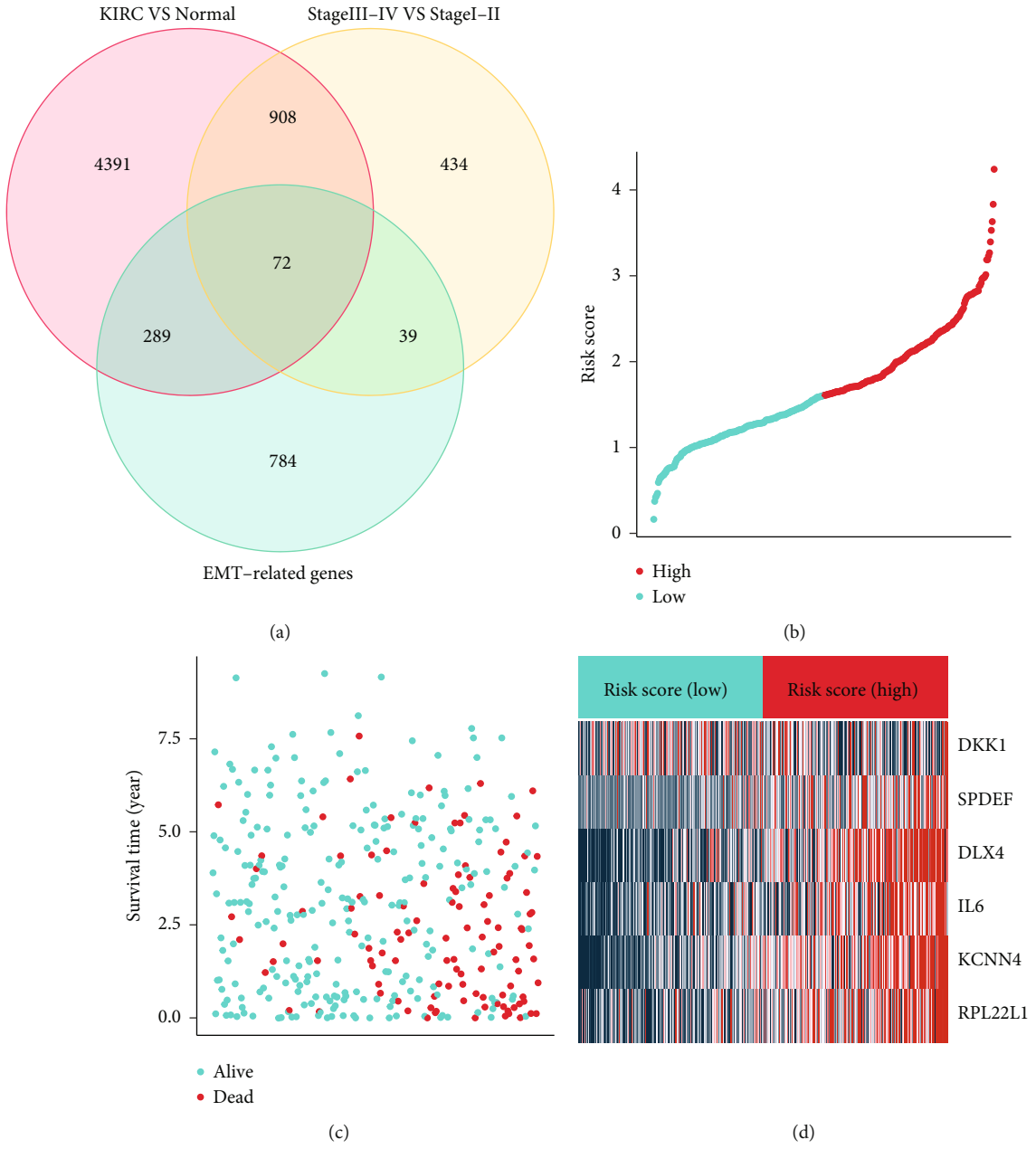

Figure 2: Continued.

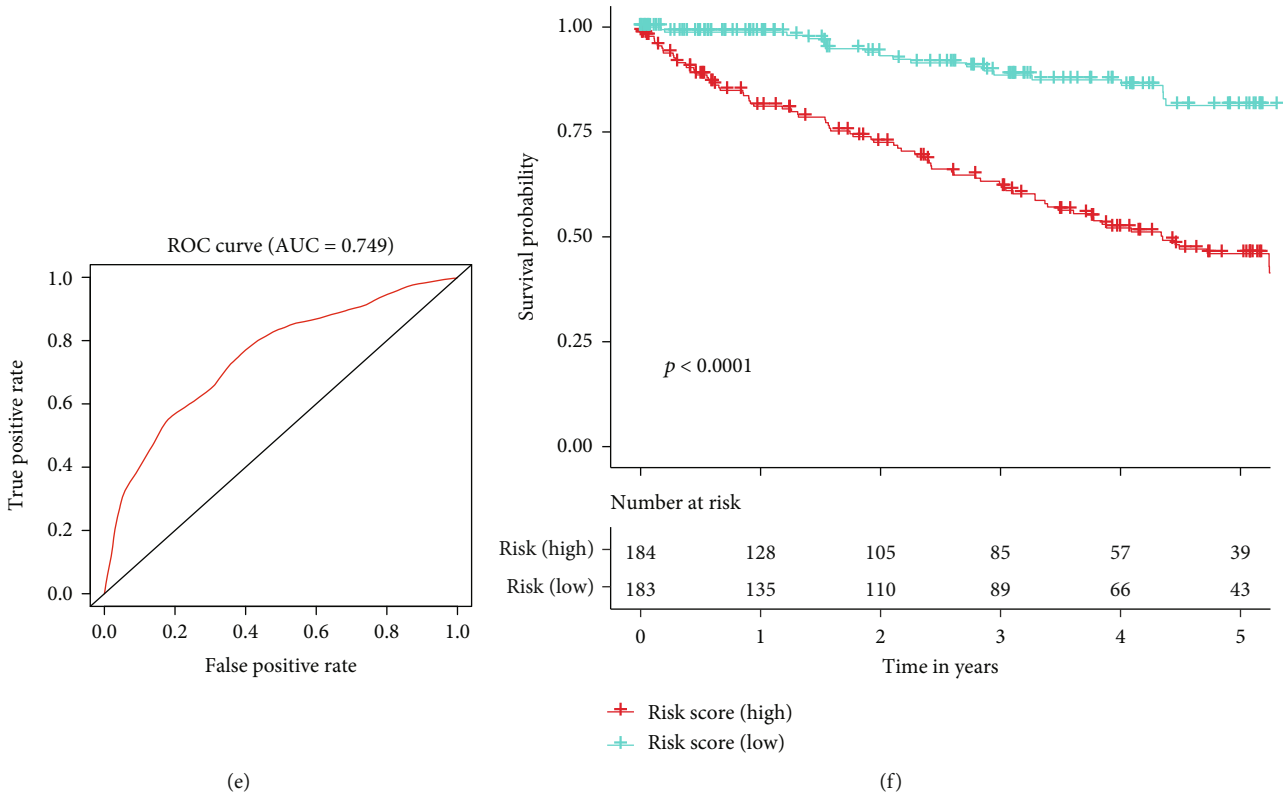

Figure 2: Assessment and DEEGs signature in the training dataset. (a) Intersection of DEGs and EMT-related genes by the Venn plot. (b) Risk-score distributions, (c) survival time/statuses, and (d) heatmap of the hub DEEGs expression in the training dataset. (e) The AUC value of the risk-score in the training dataset. (f) Survival curves (OS) of risk-score groups in the training dataset.

"epithelial_mesenchymal_transition" and "inflammatory_response" (Supplementary Table 5).

3.2. Selection of EMT-Related Genes by Machine Learning Models. We built a classification and a regression model to identify the appropriate biomarkers. The classification random forest (cRF) model was built to predict the survival status (dead or alive) of KIRC patients. The importance values of genes in the cRF are shown in Table 1. Similarly, a regression random forest (rRF) model was built to predict the survival time of KIRC patients. The importance values of genes in two models were calculated (Table 1). The six genes with the highest importance values were selected as hub genes for further analysis. Among those 72 DEEGs, KCNN4, DKK1, DLX4, SPDEF, IL6, and RPL22L1 were considered hub genes since they have the highest importance values.

3.3. Construction of Risk-Score for KIRC. The datasets were then separated into training (70%) and testing (30%) datasets. Based on coefficients from the multivariate Cox analysis, we established the risk-score by the expression of the 6 genes by the equation: $\text{risk} - \text{score} = (2.57 \times \text{KCNN4}) + (0.14 \times \text{DKK1}) + (1.27 \times \text{DLX4}) + (1.0 \times \text{SPDEF}) + (0.69 \times \text{IL6}) + (0.92 \times \text{RPL22L1})$. The risk-score distributions, survival status, survival time, and transcriptomic levels of individuals were ordered using the risk-score (Figures 2(b)–2(d)). KIRC patients were classified as the high or low group, respectively. The AUC of the risk-score was 0.749, suggesting a high prognostic prediction ability (Figure 2(e)). According to the survival curve (OS), there was a substantial difference in OS between groups (p value < 0.001) (Figure 2(f)).

Table 1: The selected hub differentially expressed EMT-related genes (DEEGs) by importance values.

Gene	Importance (cRF)	Importance (rRF)	Importance
KCNN4	57.1	80.5	137.6
DKK1	26.2	100	126.2
DLX4	73.3	52.5	125.8
SPDEF	100	18.2	118.2
IL6	49.5	65.4	114.9
RPL22L1	83.7	25.6	109.3

We then validated the 6 gene model in the testing dataset. The risk-score distributions, survival status, survival time, and transcriptomic levels of individuals were ordered using the risk-score (Supplementary Figure 1A-C). 79 and 80 KIRC individuals were classified as high or low-risk, and the AUC value was 0.777 (Supplementary Figure 1D). According to the survival curve (OS), there was a substantial difference in OS between groups (p value = 0.0011) (Supplementary Figure 1E).

We then validated the 6 genes to predict the progression of KIRC patients. The distributions of risk-scores, prognosis,

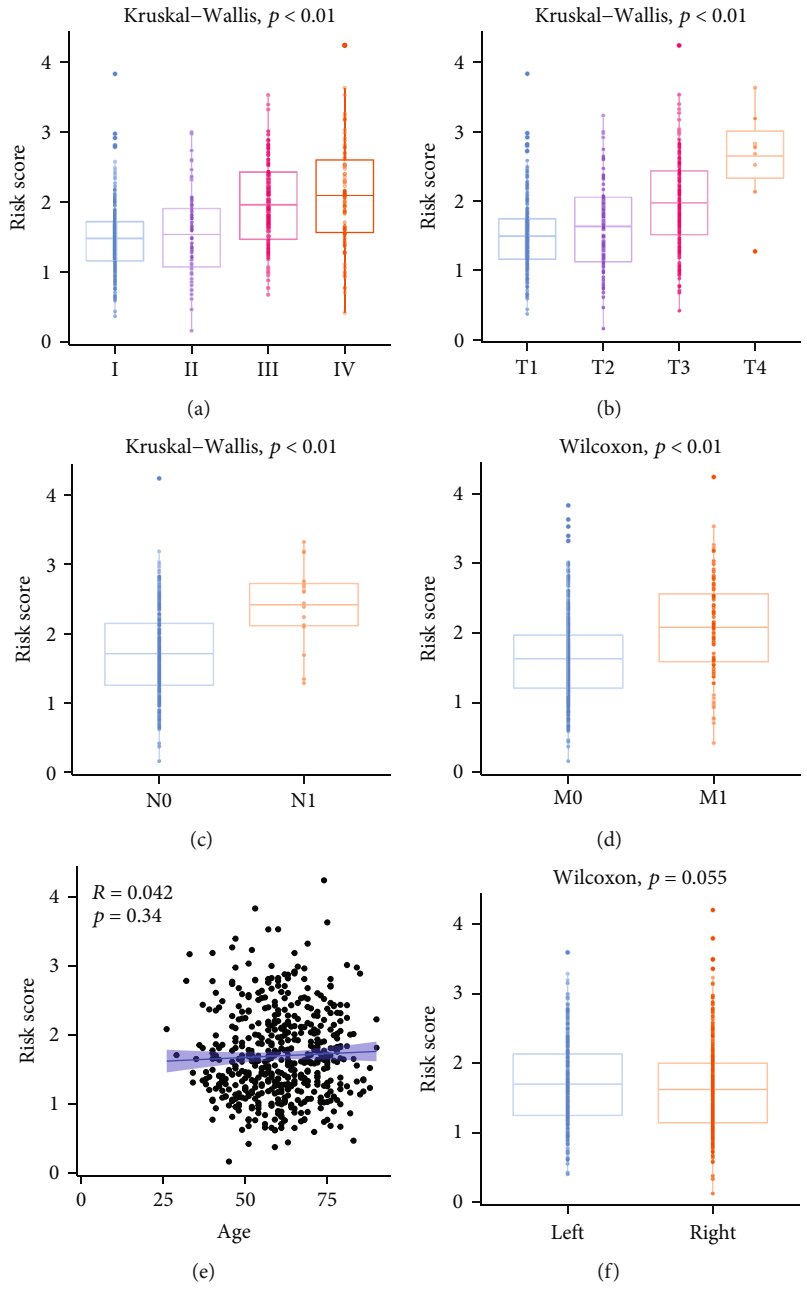

Figure 3: Relationship between risk-score and clinical factors, including (a) stage IV, (b) T stage, (c) N stage, (d) M stage, (e) Age, and (f) laterality.

and gene expression values of patients were ranked by risk-scores (Supplementary Figure 2A-C). 254 and 255 KIRC patients were labeled as high or low risk, respectively, and the AUC was 0.722 (Supplementary Figure 2D). Discrepancies in PFI were found between high and low groups (p value < 0.001) (Supplementary Figure 2E). These results suggest that our risk-score model could be an accurate indicator for OS and PFI prediction.

3.4. Relationship between Prognostic Signature and Clinicopathological Features. A correlation between the prognostic signature and clinical and pathological characteristics was then examined. The results indicated a positive correlation between the risk core and poor prognosis. For example, risk-score was found in the advanced stages of KIRC, such as stage IV (Figure 3(a)), T4 (Figure 3(b)), N1 (Figure 3(c)), and M1 (Figure 3(d)). In contrast, the correlations of the risk-score with age (Figure 3(e)) and laterality (Figure 3(f)) were not significant.

3.5. Stratification Analysis. In the groups of "stages I-II" and "stages III-IV," patients with higher risk had worse OS (Supplementary Figure 3A-B). Similarly, we demonstrated that risk-score could predict the OS of T1-T2 or T3-T4 patients

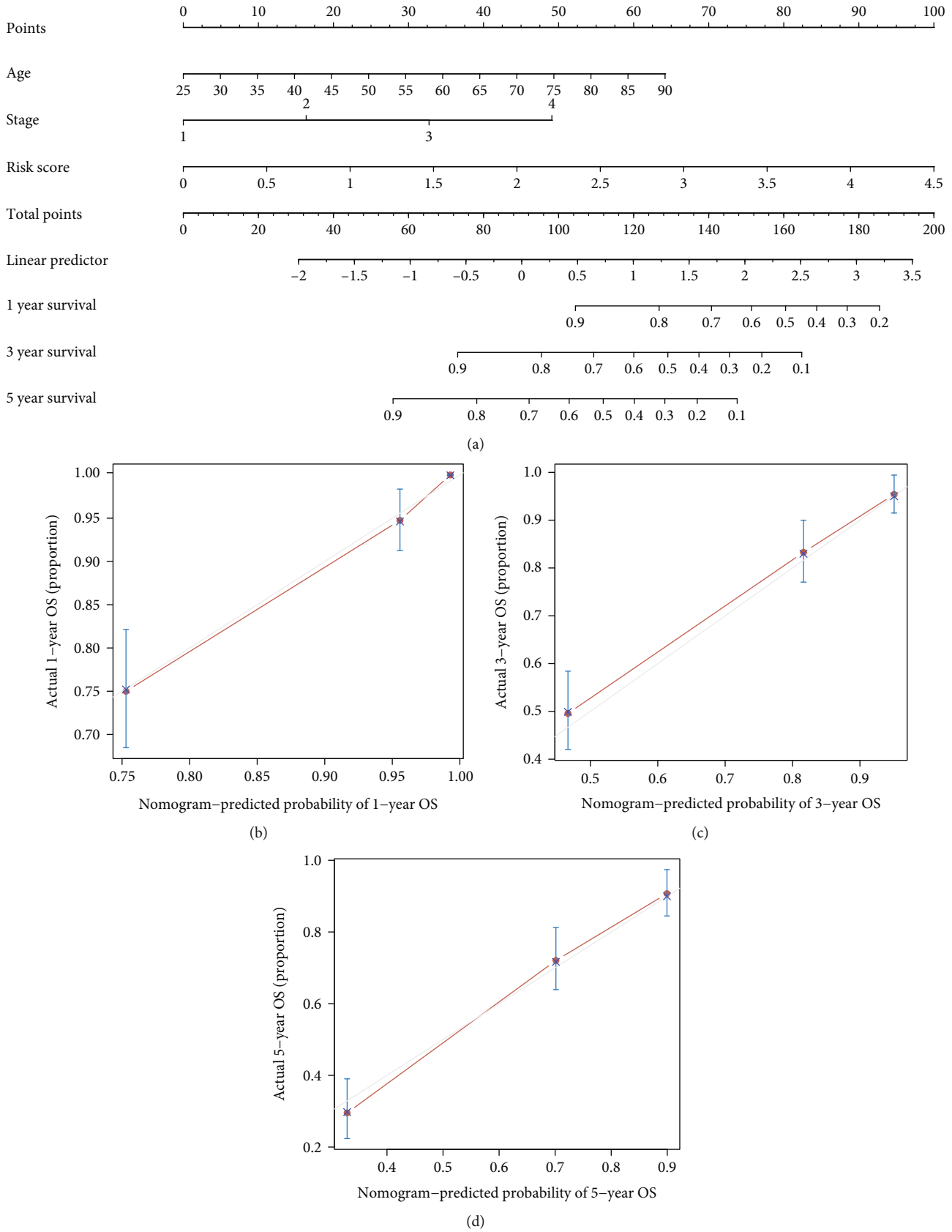

Figure 4: (a) The prognostic nomogram was constructed by age, stage, and risk-score. The calibration curve diagrams for (b) 1-year, (c) 3-year, and (d) 5-year had good agreement between the predicted probability and the actual probability.

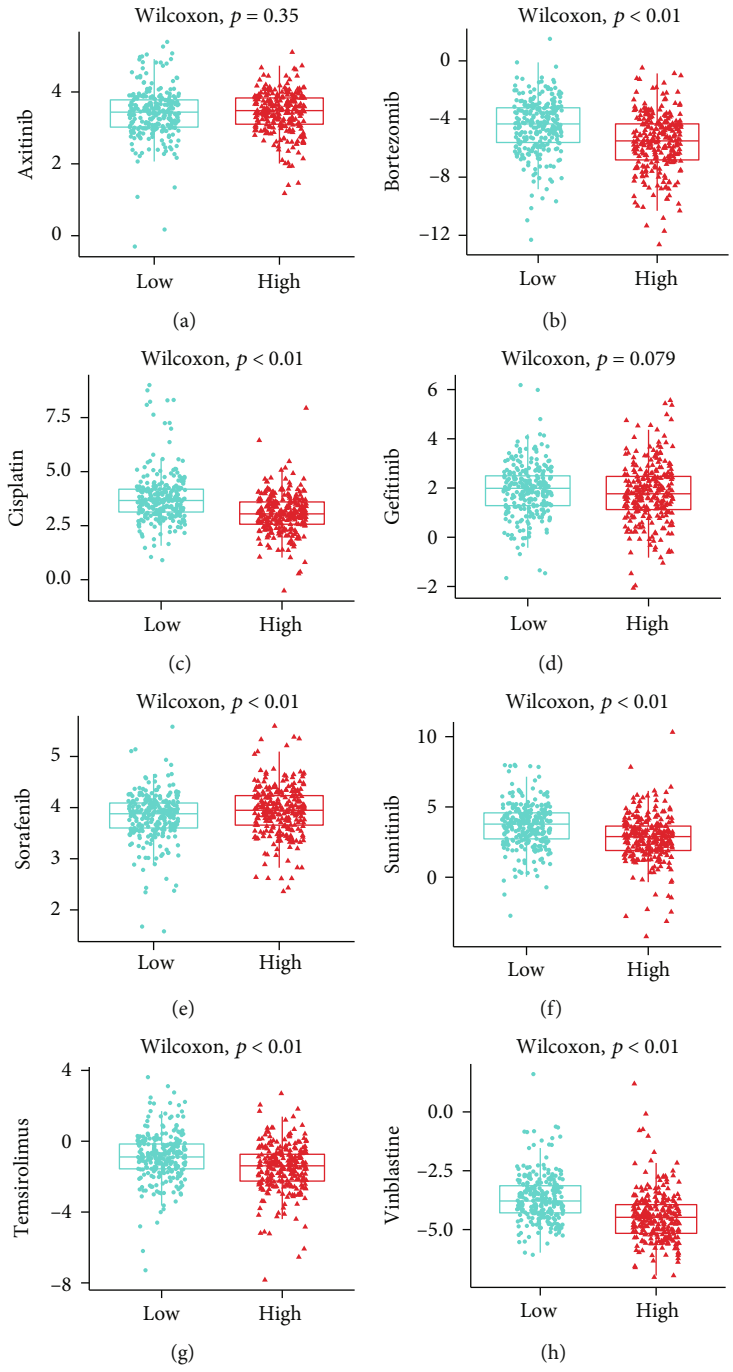

Figure 5: Box plot of estimated IC50 values for (a) axitinib, (b) bortezomib, (c) cisplatin, (d) gefitinib, (e) sorafenib, (f) sunitinib, (g) temsirolimus, and (h) Vinblastine in low and high risk-score groups.

(Supplementary Figure 3C-D), patients with TNM stage N0 (Supplementary Figure 3E), KIRC individuals with TNM stage M0 and M1 (Supplementary Figure 3G-H), patients with laterality of "left" and "right" (Supplementary Figure 3I-J), and patients with ">60" and "<60" (Supplementary Figure 3K-L). The difference in risk groups in patients with TNM stage N1 was not significant since the number of patients is low (Supplementary Figure 3F).

Afterward, we conducted the univariate/multivariate Cox regression to validate the independent prognostic role of risk-score. Univariate analysis calculated the p values of age (p value < 0.01), laterality (p value = 0.994), stage (p value < 0.01), and risk-score (p value < 0.01). Subsequent multivariate analysis demonstrated that age (coefficients: 0.037, p value < 0.01), stage (coefficients: 0.52, p value < 0.01), and risk-score (coefficients: 0.76, p value < 0.01) were

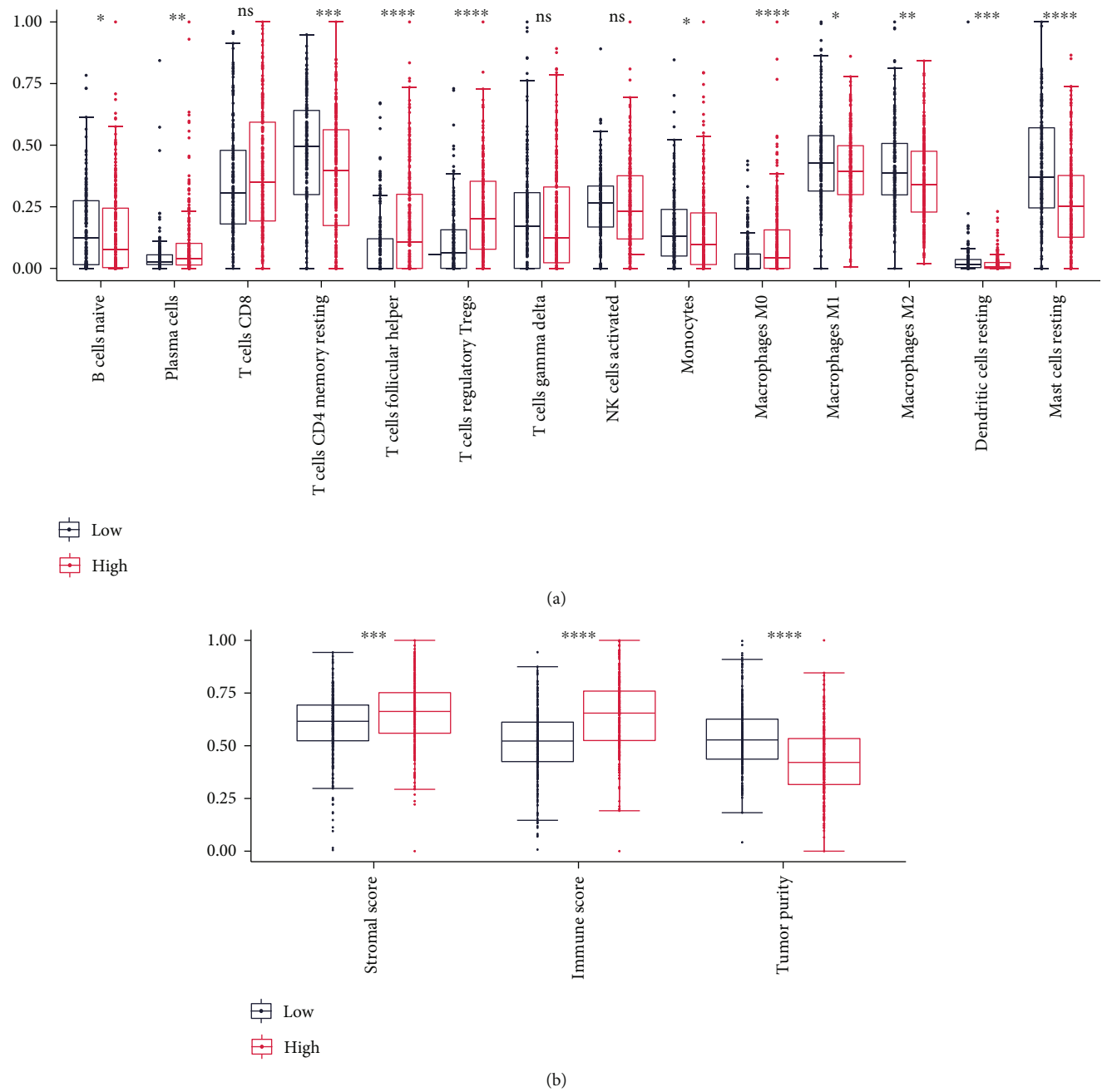

Figure 6: (a) Differential analysis of 14 immune fractions (CIBERSORT algorithm) between risk-score groups. (b) Differential analysis of stromal, immune, and tumor purity (ESTIMATE algorithm) between risk-score groups.

negatively correlated with OS. These findings suggest that the risk-score is an independent predictor of survival in KIRC patients.

3.6. Construction of a Predictive Nomogram. By combining the risk-score and various clinical indicators, a nomogram was created to assess the survival rate (Figure 4(a)). The nomogram has a C-index of 0.79, and the risk-score clearly demonstrated greater importance than age and stage did. The prediction and reference calibration curves showed a great fit in predicting one, three, and five years of OS (Figures 4(b)–4(d)), which proves the prediction ability of the nomogram.

3.7. Difference in Sensitivity to Chemotherapies. The responsive predictive values of the risk-score for chemotherapy drugs (Figures 5(a)–5(h)) were calculated by IC50 values. Bortezomib, cisplatin, sunitinib, temsirolimus, and vinblastine all had lower IC50 values in the high-risk group, indicating that patients with a higher risk-score were more responsive to these medications. In the low-risk group, however, the IC50 value of sorafenib was much lower, indicating that individuals with a lower risk-score were more susceptible to it.

3.8. Correlation between the Risk-Score and TME. The CIBERSORT method was used to determine the percentage

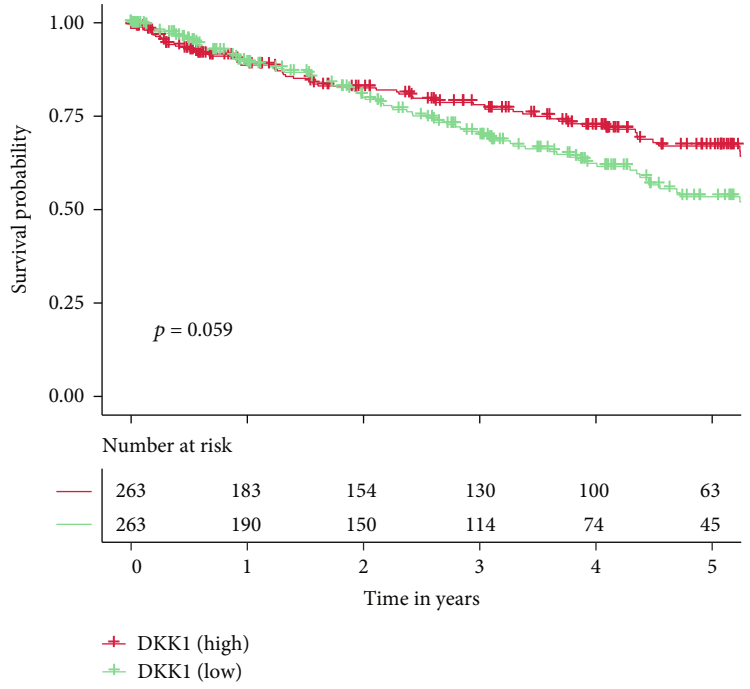

(a)

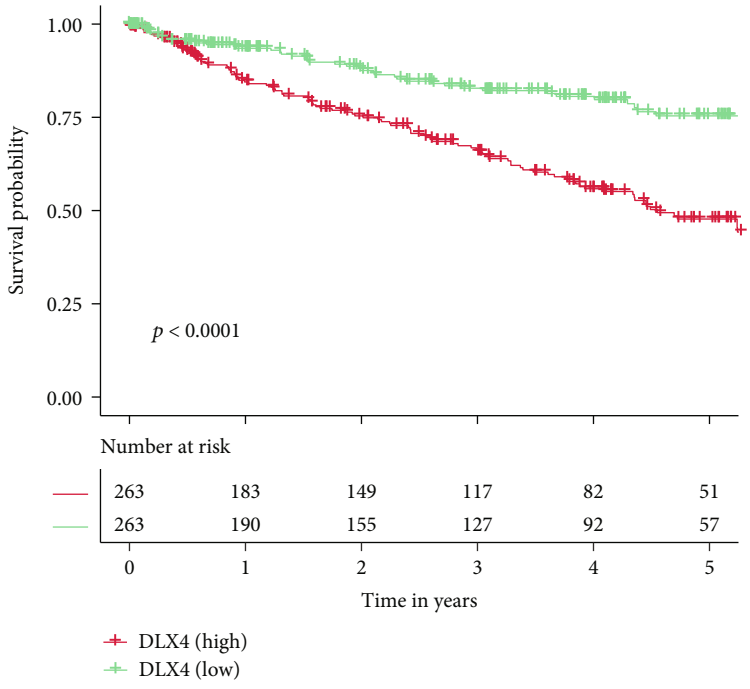

(b)

Figure 7: Continued.

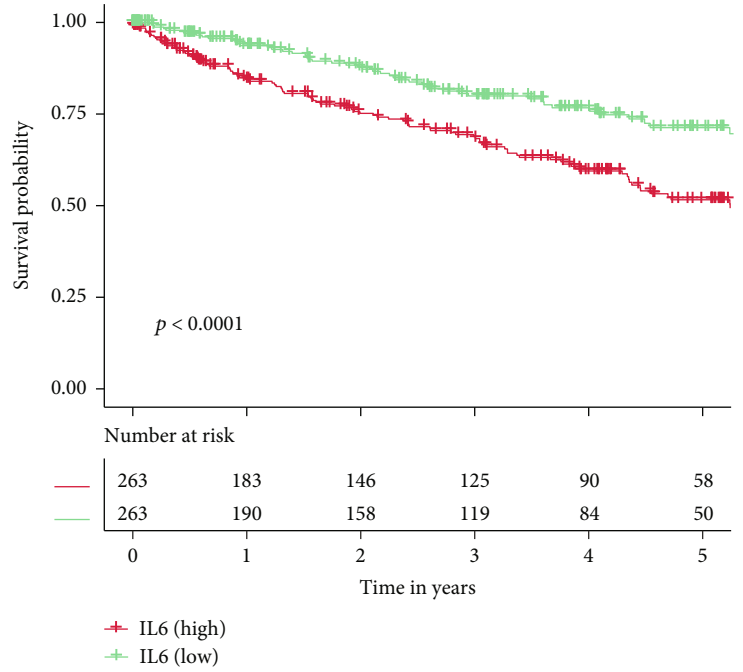

(c)

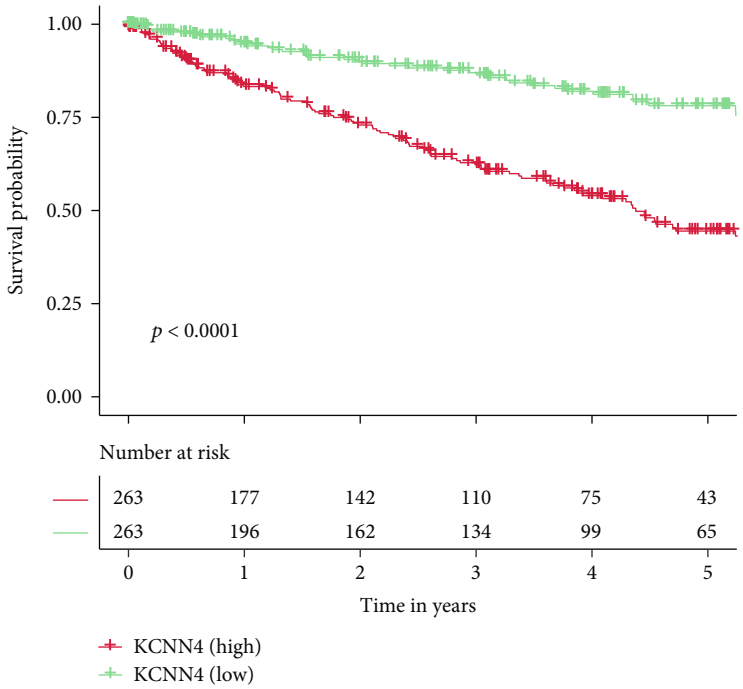

(d)

Figure 7: Continued.

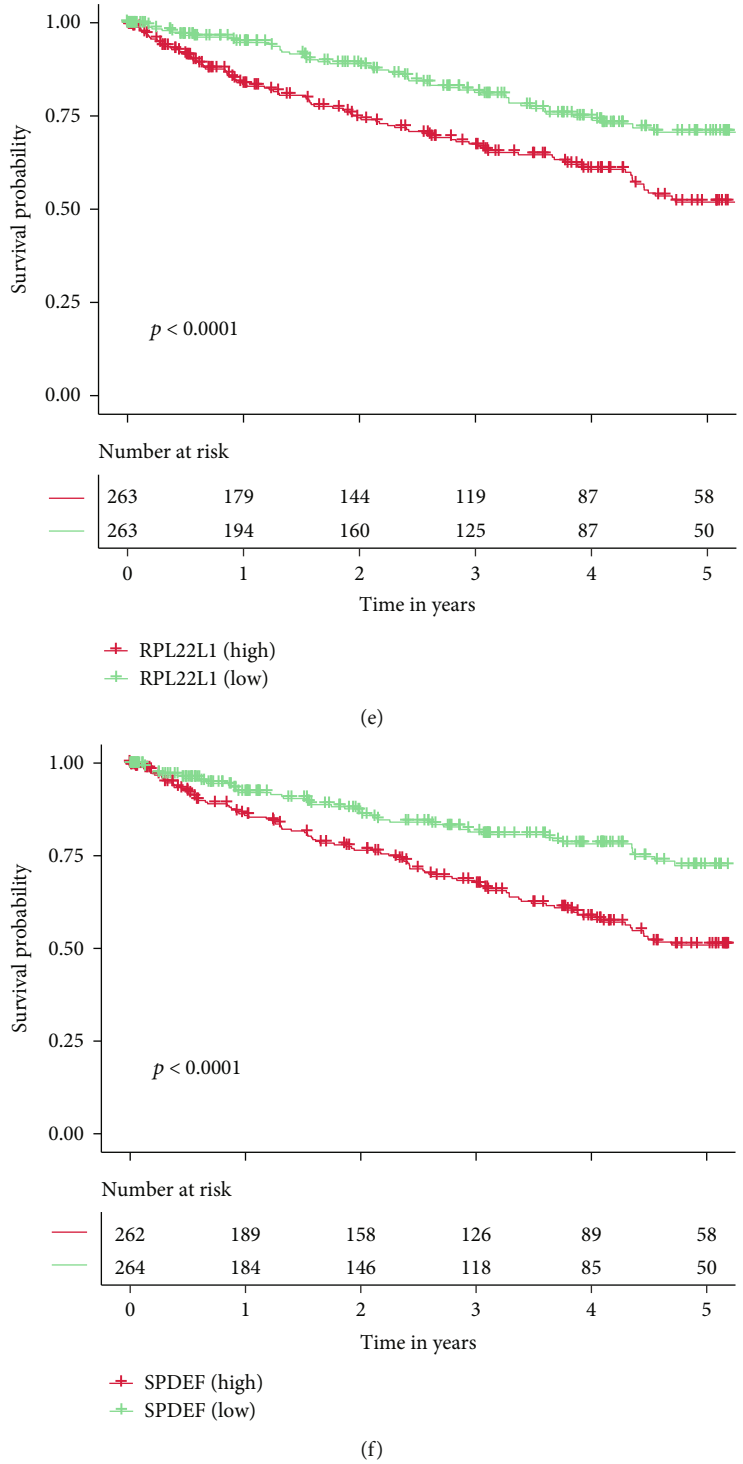

Figure 7: Overall survival analyses of the identified genes, including (a) DKK1, (b) DLX4, (c) IL6, (d) KCNN4, (e) RPL22L1, and (f) SPDEF in TCGA dataset. Red lines indicate patients with the high expression, whereas blue lines indicate patients with the low expression.

of 22 immune cells in each TCGA-KIRC sample. The cells with low mean values were deleted, and 14 cells were selected for the plot. A total of 423 samples were analyzed and found to be statistically significant. Fractions of "follicular_helper_T" and "Tregs" were higher among high-risk TCGA-KIRC samples (Figure 6(a)), while the values of "CD4_memory_T" and "NK" cells were higher among low-risk TCGA-KIRC samples (Figure 6(b)). Using the ESTIMATE technique, we also examined the differences between risk categories in terms of TME scores (Figure 6(b)). The Wilcoxon rank-sum test suggested that the immune and stromal scores in TCGA-KIRC samples were significantly higher, while the tumor purity was higher in the lower risk-score TCGA-KIRC samples. Using the Kaplan-Meier method, the prognosis of

patients with higher DKK1 (Figure 7(a)) or lower DLX4 (Figure 7(b)), IL6 (Figure 7(c)), KCNN4 (Figure 7(d)), RPL22L1 (Figure 7(e)), and SPDEF (Figure 7(f)) was greatly lower.

4. Discussion

KIRC is particularly prone to invasion and metastasis, which may explain its poor prognosis. About 25-30% of KIRC patients have metastases at the time of diagnosis [15], and about 60% have metastases within the initial 2–3 years after diagnosis [16]. EMT is critical for tumor invasion, tumor metastasis, and tumor cell proliferation [17]. As a result, we developed a prognostic risk model for six EMT-related genes and evaluated its reliability and relationship with survival. Additionally, we checked the link between risk and response to the pharmacological therapy.

Currently, Cox regression [18] and LASSO regression [19] analyses are prevalent for identifying prognostic genes and constructing prediction models. In our study, we used machine learning models to identify the prognostic genes. Machine learning has many advantages since it can achieve a higher accuracy value with fewer genes, and it also gains the prevalence of in multiple studies [20–22]. For example, in breast cancer, a machine learning model was provided to predict the immune subtype of breast cancer [21]. The major obstacle to using machine learning models on survival data is that it contains two variables: survival status and time. Thus, we built a classification model and a regression model for predicting the survival status and time, respectively. The necessary data for these two models were the expression values of DEEGs after normalization. Based on the prediction results of these two models, we could precisely plot the survival curve for each patient. Through this method, we also successfully identified the most important genes for predicting the prognosis of KIRC.

Through the EMT process, tumors including kidney cancer could gain the potential for aggressiveness and metastasis. The activation of the EMT process is complex, but our study found that immune cells may make a significant contribution to EMT in a variety of ways. For example, some kinds of immune cells may secrete immunosuppressive molecules, hence promoting cancer progression. In our study, we discovered that Tregs were more abundant in high-risk than in low-risk samples. Tregs have been shown to impair anticancer immunity by impairing protective immunosurveillance and thwarting efficient antitumor immune responses [23]. Among high-risk samples that were linked to invasion and negative prognosis, we found that immune and stromal cells were increased but tumor purity was decreased. These results suggest that the number of immune and stromal cells might exert crucial roles in tumor development. Together, we suppose that the stromal cells and Tregs among TME increase the migration of tumor cells, which leads to a worse prognosis.

DKK1 is a Wnt signaling pathway suppressor, and its dysregulation has recently been identified as a possible biomarker for cancer development and prognosis in a variety of malignancies [24]. The amount of DKK1 expression is inversely related to the number of CD8+ T cells. DLX4, often referred to as BP1, may play a crucial role in tumor development by supporting proliferation and EMT [25]. A previous study confirmed that DLX4 contributed to the proliferation and migration of KIRC [25]. In RCC patients, high levels of interleukin-6 (IL-6) are linked to a poor prognosis [26]. IL-6 is a key diver that promotes EMT and enhances migration and invasion in KIRC tissues [27]. KCNN4 expression is higher in KIRC than in normal tissues, and its level is linked to the tumor stage and grade [28]. RPL22L1 is a ribosomal protein, and previous studies have confirmed that RPL22L1 expression is greater in cancer tissue and is linked to a worse prognosis [29, 30]. SPDEF has a complex correlation with the prognosis of cancer patients. For example, upregulation of SPDEF is associated with poor prognosis in prostate cancer [31], but it could also serve as a suppressor in colorectal cancer [32].

There are some strengths in this study. Firstly, DEEGs were derived from two comparison groups (tumor versus normal tissues; "stages I-II" versus "stages III-IV" tumor tissues) and EMT-related genes, which guarantee the clinical significance of DEEGs. Secondly, machine learning models have the ability to predict both survival time and status. Thirdly, we selected the hub DEEGs by machine learning, which increased the prediction ability of these DEEGs. For example, ROC curves showed the risk-score performed well in both the training (0.749) and testing (0.777) datasets. In terms of nomogram, the concordance index (C-index) was 0.79. Numerous limitations should be noted in our research as well. To begin with, the risk-score and nomogram were constructed using a publicly available dataset. More datasets that contain the expression data and clinical information of KIRC samples are needed to validate our results. Then, the underlying mechanisms between 6 DEEGs and KIRC progression should be clarified. Prior to clinical usage, further laboratory experiments on the six-gene signature are required.

5. Conclusion

In summary, EMT is critical for the advancement of cancer and is linked with worse survival in individuals with KIRC. We developed a risk-score model and a nomogram using the EMT-related genes for predicting OS in KIRC, which might enable tailored therapy and clinical decision-making for KIRC patients.

Data Availability

The datasets generated for this study can be found in TCGA. Further inquiries can be directed to the corresponding authors.

Conflicts of Interest

The authors state that they have no conflicts of interest.

Authors' Contributions

Shimiao Zhu, Tao Wu, and Ziliang Ji contributed equally to this work. Shimiao Zhu, Tao Wu, and Ziliang Ji designed and wrote the paper. Shimiao Zhu, Tao Wu, and Ziliang Ji collected the related studies and data. Zhouliang Wu and Hao Lin analyzed the data. Chong Shen and Yinggui Yang

made the figures and tables. Qingyou Zheng and Hailong Hu revised and approved the manuscript.

Acknowledgments

The present study received financial support from the Natural Science Foundation Project of Tianjin (grant no. 18PTLCSY00010), the Tianjin Urological Key Laboratory Foundation (grant no. 2017ZDSYS13), and the Youth Fund of Tianjin Medical University Second Hospital (grant no. 2020ydey09).

Supplementary Materials

Supplementary 1. Assessment of DEEGs signature with overall survival (OS) in testing dataset. Risk-score distributions (A), overall survival time/statuses (B), and heatmap (C) of the DEEGs expression in the testing dataset. (D) AUC values of the risk-score model in the testing dataset. (E) Kaplan-Meier estimates of OS based on the risk-score groups in the testing dataset. Supplementary 2. Assessment of risk-score model with progression-free interval (PFI). Risk-score distributions (A), PFI survival time/statuses (B), and heatmap (C) of DEEGs expression. (D) AUC values of the risk-score model. (E) Kaplan-Meier estimates of PFI based on the risk-score groups. Supplementary 3. Survival analysis of high and low risk patients in subgroups: "stages I-II" (A), "stages III-IV" (B), T1-T2 (C), T3-T4 (D), N0 (E), N1 (F), M0 (G), M1 (H), laterality of "left" (I) and "right" (J), ">60" (K), and "<60" (L). Supplementary 4. Table S1: enriched GO-BP terms from "GO Biological Process 2021" module of Enrichr webserver for all differentially expressed EMT-related genes (DEEGs). Table S2: enriched GO-MF terms from "GO Molecular Function 2021" module of Enrichr webserver for all differentially expressed EMT-related genes (DEEGs). Table S3: enriched GO-CC terms from "GO Cellular Component 2021" module of Enrichr webserver for all differentially expressed EMT-related genes (DEEGs). Table S4: enriched KEGG pathways from "KEGG 2021 Human" module of Enrichr webserver for all differentially expressed EMT-related genes (DEEGs). Table S5: enriched hallmark pathways from "MSigDB Hallmark 2020" module of Enrichr webserver for all differentially expressed EMT-related genes (DEEGs). *(Supplementary Materials)*

References

[1] W. H. Chow, S. S. Devesa, J. L. Warren, and J. F. Fraumeni Jr., "Rising incidence of renal cell cancer in the United States," *Journal of the American Medical Association*, vol. 281, no. 17, pp. 1628–1631, 1999.

[2] F. Bray, J. Ferlay, I. Soerjomataram, R. L. Siegel, L. A. Torre, and A. Jemal, "Global cancer statistics 2018: GLOBOCAN estimates of incidence and mortality worldwide for 36 cancers in 185 countries," *CA: a Cancer Journal for Clinicians*, vol. 68, no. 6, pp. 394–424, 2018.

[3] E. Jonasch, J. Gao, and W. K. Rathmell, "Renal cell carcinoma," *BMJ*, vol. 349, article g4797, 2014.

[4] J. P. Thiery and J. P. Sleeman, "Complex networks orchestrate epithelial-mesenchymal transitions," *Nature Reviews. Molecular Cell Biology*, vol. 7, no. 2, pp. 131–142, 2006.

[5] T. Ruan, J. Wan, Q. Song, P. Chen, and X. Li, "Identification of a novel epithelial-mesenchymal transition-related gene signature for endometrial carcinoma prognosis," *Genes (Basel)*, vol. 13, no. 2, article 216, 2022.

[6] B. De Craene and G. Berx, "Regulatory networks defining EMT during cancer initiation and progression," *Nature Reviews. Cancer*, vol. 13, no. 2, pp. 97–110, 2013.

[7] M. P. Mak, P. Tong, L. Diao et al., "A patient-derived, Pan-cancer EMT signature identifies global molecular alterations and immune target enrichment following epithelial-to-mesenchymal transition," *Clinical Cancer Research*, vol. 22, no. 3, pp. 609–620, 2016.

[8] M. D. Robinson, D. J. McCarthy, and G. K. Smyth, "edgeR: a bioconductor package for differential expression analysis of digital gene expression data," *Bioinformatics*, vol. 26, no. 1, pp. 139-140, 2010.

[9] M. Zhao, Y. Liu, C. Zheng, and H. Qu, "dbEMT 2.0: an updated database for epithelial-mesenchymal transition genes with experimentally verified information and precalculated regulation information for cancer metastasis," *Journal of Genetics and Genomics*, vol. 46, no. 12, pp. 595–597, 2019.

[10] H. Chen and P. C. Boutros, "VennDiagram: a package for the generation of highly-customizable Venn and Euler diagrams in R," *BMC Bioinformatics*, vol. 12, pp. 1–7, 2011.

[11] M. V. Kuleshov, M. R. Jones, A. D. Rouillard et al., "Enrichr: a comprehensive gene set enrichment analysis web server 2016 update," *Nucleic Acids Research*, vol. 44, no. W1, pp. W90–W97, 2016.

[12] P. Geeleher, N. Cox, and R. S. Huang, "pRRophetic: an R package for prediction of clinical chemotherapeutic response from tumor gene expression levels," *PLoS One*, vol. 9, no. 9, article e107468, 2014.

[13] K. Yoshihara, M. Shahmoradgoli, E. Martínez et al., "Inferring tumour purity and stromal and immune cell admixture from expression data," *Nature Communications*, vol. 4, no. 1, article 3612, 2013.

[14] B. Chen, M. S. Khodadoust, C. L. Liu, A. M. Newman, and A. A. Alizadeh, "Profiling tumor infiltrating immune cells with CIBERSORT," *Methods in Molecular Biology*, vol. 1711, pp. 243–259, 2018.

[15] K. Gupta, J. D. Miller, J. Z. Li, M. W. Russell, and C. Charbonneau, "Epidemiologic and socioeconomic burden of metastatic renal cell carcinoma (mRCC): a literature review," *Cancer Treatment Reviews*, vol. 34, no. 3, pp. 193–205, 2008.

[16] A. Mendoza-Alvarez, B. Guillen-Guio, A. Baez-Ortega et al., "Whole-exome sequencing identifies somatic mutations associated with mortality in metastatic clear cell kidney carcinoma," *Frontiers in Genetics*, vol. 10, article 439, 2019.

[17] J. Winkler, A. Abisoye-Ogunniyan, K. J. Metcalf, and Z. Werb, "Concepts of extracellular matrix remodelling in tumour progression and metastasis," *Nature Communications*, vol. 11, no. 1, pp. 1–19, 2020.

[18] Z. Chen, G. Liu, A. Hossain et al., "A co-expression network for differentially expressed genes in bladder cancer and a risk score model for predicting survival," *Hereditas*, vol. 156, no. 1, pp. 1–11, 2019.

[19] S. H. Yu, J. H. Cai, D. L. Chen et al., "LASSO and bioinformatics analysis in the identification of key genes for prognostic

genes of gynecologic cancer," *Journal Of Personalized Medicine*, vol. 11, no. 11, article 1177, 2021.

[20] Z. Wang, Z. Chen, H. Zhao et al., "ISPRF: a machine learning model to predict the immune subtype of kidney cancer samples by four genes," *Translational Andrology and Urology*, vol. 10, no. 10, pp. 3773–3786, 2021.

[21] Z. Chen, M. Wang, R. L. De Wilde et al., "A machine learning model to predict the triple negative breast cancer immune subtype," *Frontiers in Immunology*, vol. 12, article 749459, 2021.

[22] M. Mohammed, H. Mwambi, I. B. Mboya, M. K. Elbashir, and B. Omolo, "A stacking ensemble deep learning approach to cancer type classification based on TCGA data," *Scientific Reports*, vol. 11, no. 1, pp. 1–22, 2021.

[23] C. Li, P. Jiang, S. Wei, X. Xu, and J. Wang, "Regulatory T cells in tumor microenvironment: new mechanisms, potential therapeutic strategies and future prospects," *Molecular Cancer*, vol. 19, no. 1, pp. 1–23, 2020.

[24] H. Y. Chu, Z. Chen, L. Wang et al., "Dickkopf-1: a promising target for cancer immunotherapy," *Frontiers in Immunology*, vol. 12, article 658097, 2021.

[25] G. Sun, Y. Ge, Y. Zhang et al., "Transcription factors BARX1 and DLX4 contribute to progression of clear cell renal cell carcinoma via promoting proliferation and epithelial-mesenchymal transition," *Frontiers in Molecular Biosciences*, vol. 8, article 626328, 2021.

[26] Y. Wang and Y. Zhang, "Prognostic role of interleukin-6 in renal cell carcinoma: a meta-analysis," *Clinical & Translational Oncology*, vol. 22, no. 6, pp. 835–843, 2020.

[27] Q. Chen, D. Yang, H. Zong et al., "Growth-induced stress enhances epithelial-mesenchymal transition induced by IL-6 in clear cell renal cell carcinoma via the Akt/GSK-3β/β-catenin signaling pathway," *Oncogenesis*, vol. 6, no. 8, article e375, 2017.

[28] S. Chen, C. Wang, X. Su, X. Dai, S. Li, and Z. Mo, "KCNN4 is a potential prognostic marker and critical factor affecting the immune status of the tumor microenvironment in kidney renal clear cell carcinoma," *Translational Andrology and Urology*, vol. 10, no. 6, pp. 2454–2470, 2021.

[29] Z. Liang, Q. Mou, Z. Pan et al., "Identification of candidate diagnostic and prognostic biomarkers for human prostate cancer: RPL22L1 and RPS21," *Medical Oncology*, vol. 36, no. 6, pp. 1–10, 2019.

[30] J. Ma, X. Jing, Z. Chen, Z. Duan, and Y. Zhang, "MiR-361-5p decreases the tumorigenicity of epithelial ovarian cancer cells by targeting at RPL22L1 and c-Met signaling," *International Journal of Clinical and Experimental Pathology*, vol. 11, no. 5, pp. 2588–2596, 2018.

[31] J. Meiners, K. Schulz, K. Möller et al., "Upregulation of SPDEF is associated with poor prognosis in prostate cancer," *Oncology Letters*, vol. 18, pp. 5107–5118, 2019.

[32] T. K. Noah, Y. H. Lo, A. Price et al., "SPDEF functions as a colorectal tumor suppressor by inhibiting β-catenin activity," *Gastroenterology*, vol. 144, no. 5, pp. 1012–1023, 2013.

Hindawi
Disease Markers
Volume 2022, Article ID 1289445, 15 pages
https://doi.org/10.1155/2022/1289445

Research Article

Establishment and Analysis of an Individualized EMT-Related Gene Signature for the Prognosis of Breast Cancer in Female Patients

Wei Xue,[1,2,3] **Chenyu Sun**,[4] **Hui Yuan**,[5] **Xin Yang**,[2] **Qiuping Zhang**,[2,6] **Yunnuo Liao**,[1,2] **and Hongwei Guo**[1,2]

[1]*Guangxi Key Laboratory for Research and Evaluation of Bioactive Molecules& College of Pharmacy, Guangxi Medical University, Nanning 530021, China*
[2]*Key Laboratory of Longevity and Aging-Related Diseases of Chinese Ministry of Education & Center for Translational Medicine, Guangxi Medical University, Nanning 530021, China*
[3]*Department of Pharmacy, Ruikang Hospital Affiliated to Guangxi University of Chinese Medicine, Nanning 530011, China*
[4]*AMITA Health Saint Joseph Hospital Chicago, 2900 N. Lake Shore Drive, Chicago, 60657 Illinois, USA*
[5]*Public Health Center, The First Affiliated Hospital of Xi'an Jiaotong University, Xi'an, 710061, China*
[6]*The First Affiliated Hospital of Guangxi Medical University, Guangxi Medical University, Nanning 530021, China*

Correspondence should be addressed to Hongwei Guo; hongweiguo@gxmu.edu.cn

Received 6 May 2022; Revised 6 July 2022; Accepted 15 July 2022; Published 28 July 2022

Academic Editor: Zhen-Jian Zhuo

Background. The current high mortality rate of female breast cancer (BC) patients emphasizes the necessity of identifying powerful and reliable prognostic signatures in BC patients. Epithelial-mesenchymal transition (EMT) was reported to be associated with the development of BC. The purpose of this study was to identify prognostic biomarkers that predict overall survival (OS) in female BC patients by integrating data from TCGA database. *Method*. We first downloaded the dataset in TCGA and identified gene signatures by overlapping candidate genes. Differential analysis was performed to find differential EMT-related genes. Univariate regression analysis was then performed to identify candidate prognostic variables. We then developed a prognostic model by multivariate analysis to predict OS. Calibration curves, receiver operating characteristics (ROC) curves, *C*-index, and decision curve analysis (DCA) were used to test the veracity of the prognostic model. *Result*. In this study, we identified and validated a prognostic model integrating age and six genes (CD44, P3H1, SDC1, COL4A1, TGFβ1, and SERPINE1). *C*-index values for BC patients were 0.672 (95% CI 0.611–0.732) and 0.692 (95% CI 0.586–0.798) in the training cohort and test set, respectively. The calibration curve and the DCA curve show the good predictive performance of the model. *Conclusion*. This study offered a robust predictive model for OS prediction in female BC patients and may provide a more accurate treatment strategy and personalized therapy in the future.

1. Introduction

Breast cancer is one of the most prevalent malignancies in women worldwide and the leading cause of most cancer-related deaths, although early-stage BC is considered curable [1, 2]. In 2018, BC was the most commonly diagnosed cancer (24.2% of all cancer cases) and the leading cause of cancer-related deaths (15% of all cancer deaths) in women worldwide. Among these, metastatic BC accounted for more than 90% of BC-related deaths [3]. At present, the main treatment strategies for BC include surgery, chemotherapy, radiotherapy, immunotherapy, and hormonal therapy [4]. Although nanomedicine has been developed this year to target progesterone and estrogen receptors (PR and ER), human epidermal growth factor receptor 2 (HER2), and microRNA (miRNAs) and long chain non-coding RNAs, the incidence of BC remains high, with previous studies suggesting that the number of new cases worldwide will be

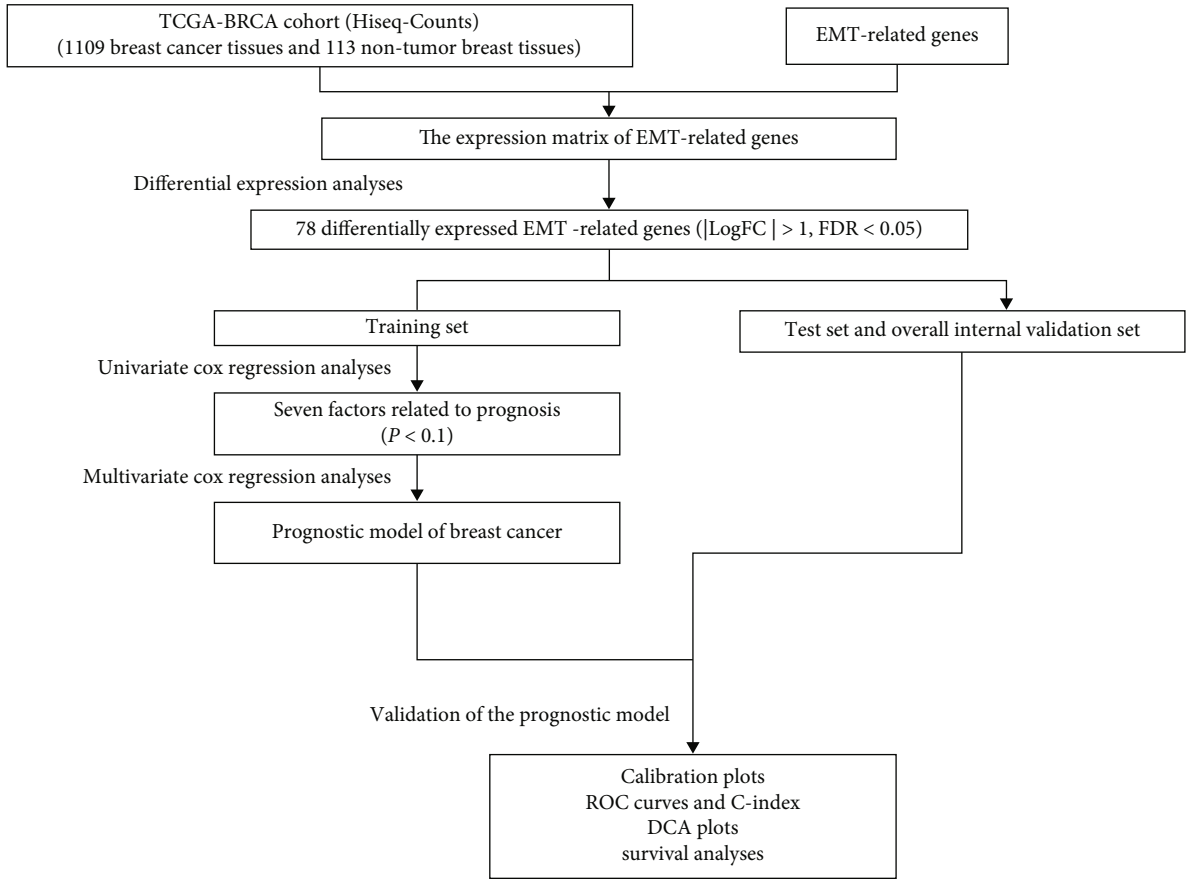

Figure 1: Flow chart of this study.

2,261,419 women in 2020, and this number is expected to increase to 30.2 million by 2040 [5, 6].

Epithelial-mesenchymal transition (EMT) is widely known to occur during mammalian development, wound healing, and cancer metastasis [7]. In recent years, EMT has received increasing attention for its role in cancer drug resistance [8]. Many studies have shown that EMT is associated with tumorigenesis, invasion, metastasis, and resistance to treatment, especially in BC [9, 10]. Saotome et al. demonstrated that GATA3 truncation mutants affected ductal BC development by altering EMT-related gene expression through partial motif recognition in luminal BC cells [11]. Parthasarathi and his colleagues found that EMT-related genes were associated with dysregulated ion channels in BC-associated tumorigenesis and could potentially be used to determine the prognosis of BC patients. Therefore, in this study, we evaluated the relevance of the EMT genes in female BC patients to explore the mechanisms of EMT in BC [12].

The new 8th edition of a related Union for International Cancer Control (UICC) and American Joint Committee on Cancer (AJCC) publication updates the description of BC staging for tumor lymph node metastasis (TNM) [13]. Yet, it is not sufficient to simply predict the prognosis of BC based on the TNM staging system. Some of the factors that influence BC include age, genes, reproductive factors, estrogen, and lifestyle [14]. Hence, a multifactorial predictive model is essential. Predictive modeling is a more advanced approach as it can be visualized using a nomogram and it can estimate individualized risk based on a more comprehensive set of gene signatures and clinical characteristics. In previous studies, we constructed a clinical prediction model based on the clinical data of metastatic colon cancer patients extracted from the SEER database. The nomogram developed with high prognosis prediction accuracy to evaluate the 1-, 3-, and 5-year survival of metastatic colon cancer patients, which will help clinical decision-making of metastatic colon cancer patients after surgery and individualized treatment [15].

In this study, we identified EMT-related genes with independent prognostic value to establish a prognostic model for predicting the overall survival (OS) at 1-, 3-, and 5-year of female BC patients and generating new insights about BC progression.

2. Materials and Methods

2.1. Data Collection. We downloaded gene expression data from The Cancer Genome Atlas (TCGA) database (https://cancergenome.nih.gov) of 1109 BC patients and 113 nontumor breast tissues. Clinical data were also acquired, but the clinical data of 12 male BC patients were removed because the study population in this paper was female. EMT-related genes were collected from the Molecular Signature

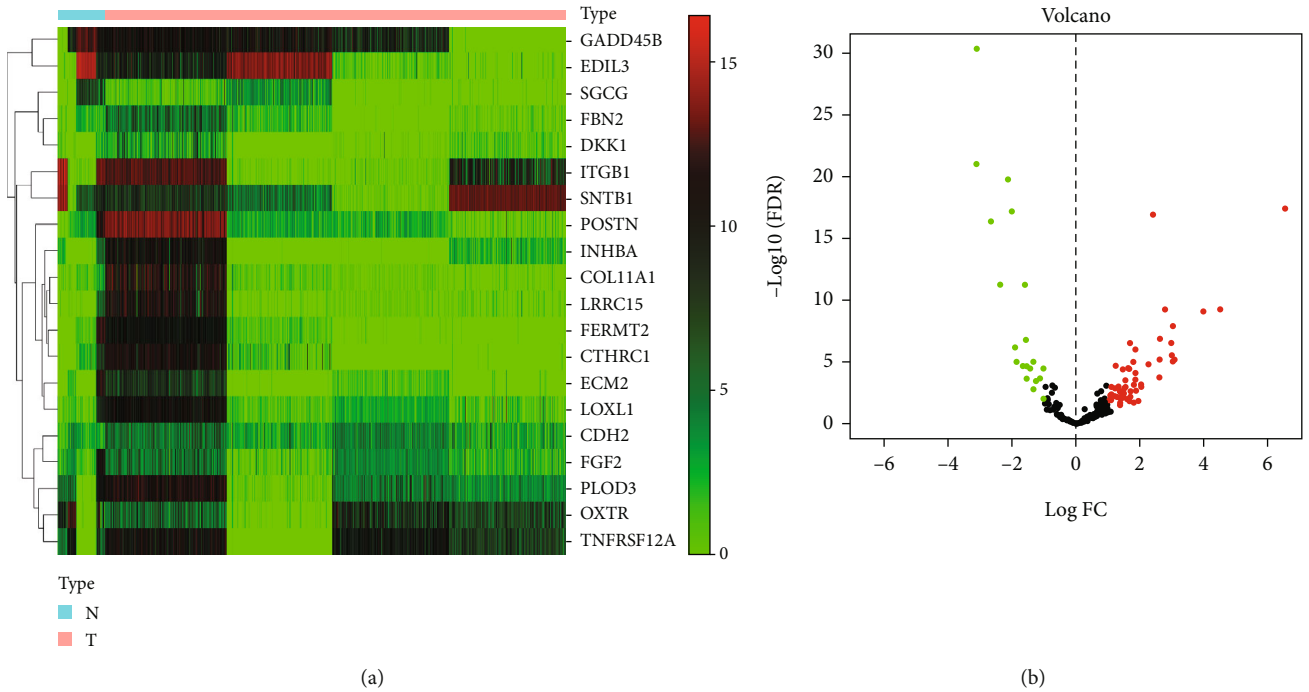

(a) (b)

Figure 2: Heat map (a) and volcano map (b) of differentially expressed gene related to EMT.

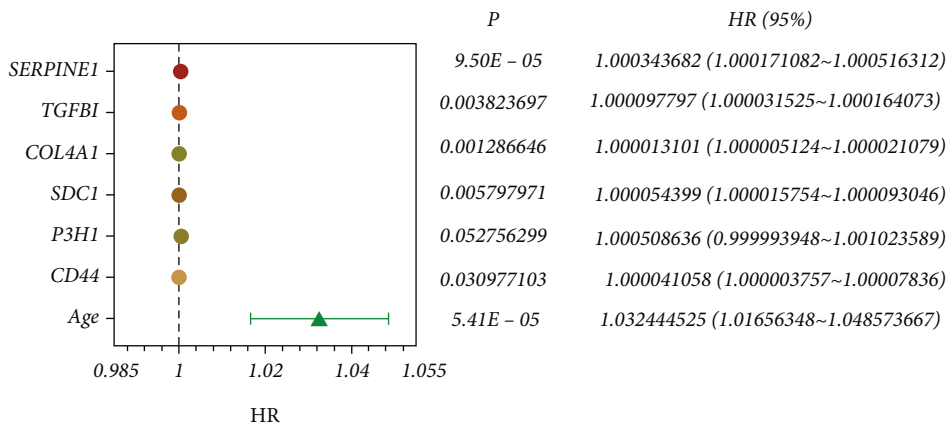

Figure 3: Forest plot analyzed by univariate Cox regression.

Table 1: Genes contained in the prognostic model of breast cancer.

Factors	coef	HR	HR_95L	HR_95U	*P*
Age	0.030655	1.031129	1.015051	1.047463	0.000132
CD44	$3.35E-05$	1.000033	0.999994	1.000073	0.098155
P3H1	0.000142	1.000142	0.999283	1.001002	0.74605
SDC1	$3.76E-05$	1.000038	0.999966	1.000109	0.304272
COL4A1	$1.60E-05$	1.000016	1.000008	1.000024	0.000149
TGFBI	$2.04E-05$	1.00002	0.999884	1.000156	0.768605
SERPINE1	0.000247	1.000247	0.999911	1.000583	0.149765

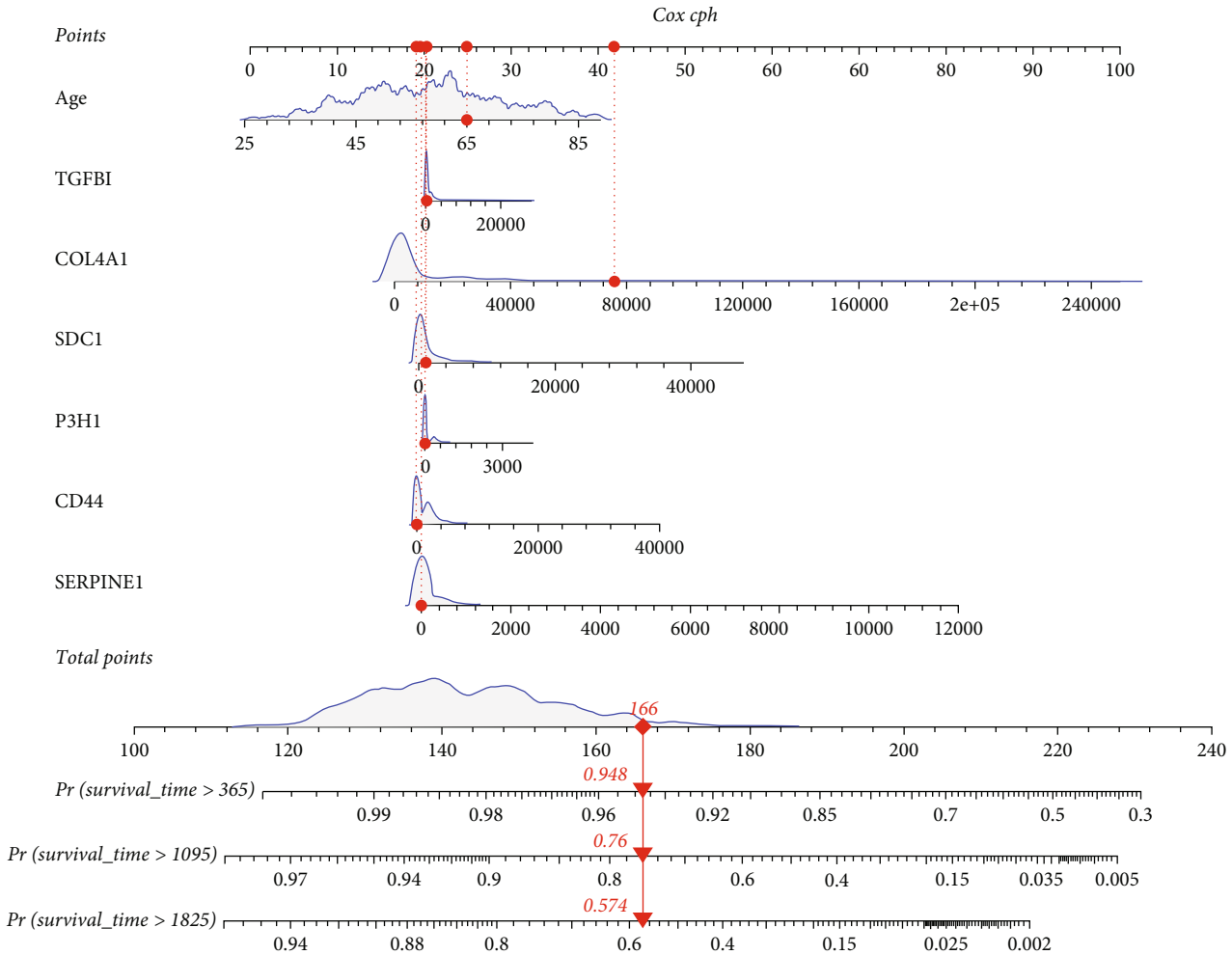

Figure 4: Nomogram for predicting 1-, 3-, and 5-year overall survival (OS) for BC patients in the training cohort.

database v7.1 (MSigDB) (http://www.broad.mit.edu/gsea/msigdb/).

2.2. Identification of Differentially Expressed EMT-Related Genes. Combining the gene expression data obtained from TCGA database with EMT-related genes by using the "edgeR" package of R software, the expression data of the target genes could be obtained. After that, the "limma" package was utilized to derive differentially expressed EMT-related genes according to False Discovery Rate (FDR) values less than 0.05 and the absolute value of fold change above 1.

2.3. Statistical Analysis

2.3.1. Univariate Cox Regression Analysis for Independent Prognostic Factors. The expression matrix of the obtained EMT-related genes was further analyzed by incorporating the matrix with the survival time and survival status. Based on previous studies, age had an impact on the prognosis of female BC patients, so we included age as a study variable [16]. Using the "caret" package in R software (version 4.1.0) to randomly divide the overall cohort into two groups in the ratio of 7 : 3. The subgroup containing 70% of female BC patients was used to construct the prediction model, while the remaining 30% of patients were examined for the accuracy and reliability of the model. Also, the whole cohort was used as the overall internal validation set. The basic values of patients were listed (Table S1).

Univariate Cox regression analysis was used to screen for independent prognostic factors. Factors with a cutoff value of $P < 0.1$ were defined as candidates associated with OS.

2.3.2. Prognostic Nomogram Construction. The genes filtered by univariate Cox regression were then analyzed in the multivariate Cox regression for the risk scoring model. The risk score for each patient can be calculated by the following formula: risk score = $\mathrm{Exp}(x1) * \beta 1 + \mathrm{Exp}(x2) * \beta 2 + \cdots + \mathrm{Exp}(xn) * \beta n$, where n is the number of selected variables, Exp is the expression level of the variable, and β is the regression coefficient of the variable. Then, the nomogram was developed using R software. According to the scores calculated from the nomogram, the patient's OS at 1, 3, and 5 years can be predicted. Subsequently, according to the median risk scores, patients with risk scores greater than the median value were divided into the high-risk group and otherwise into the low-risk group.

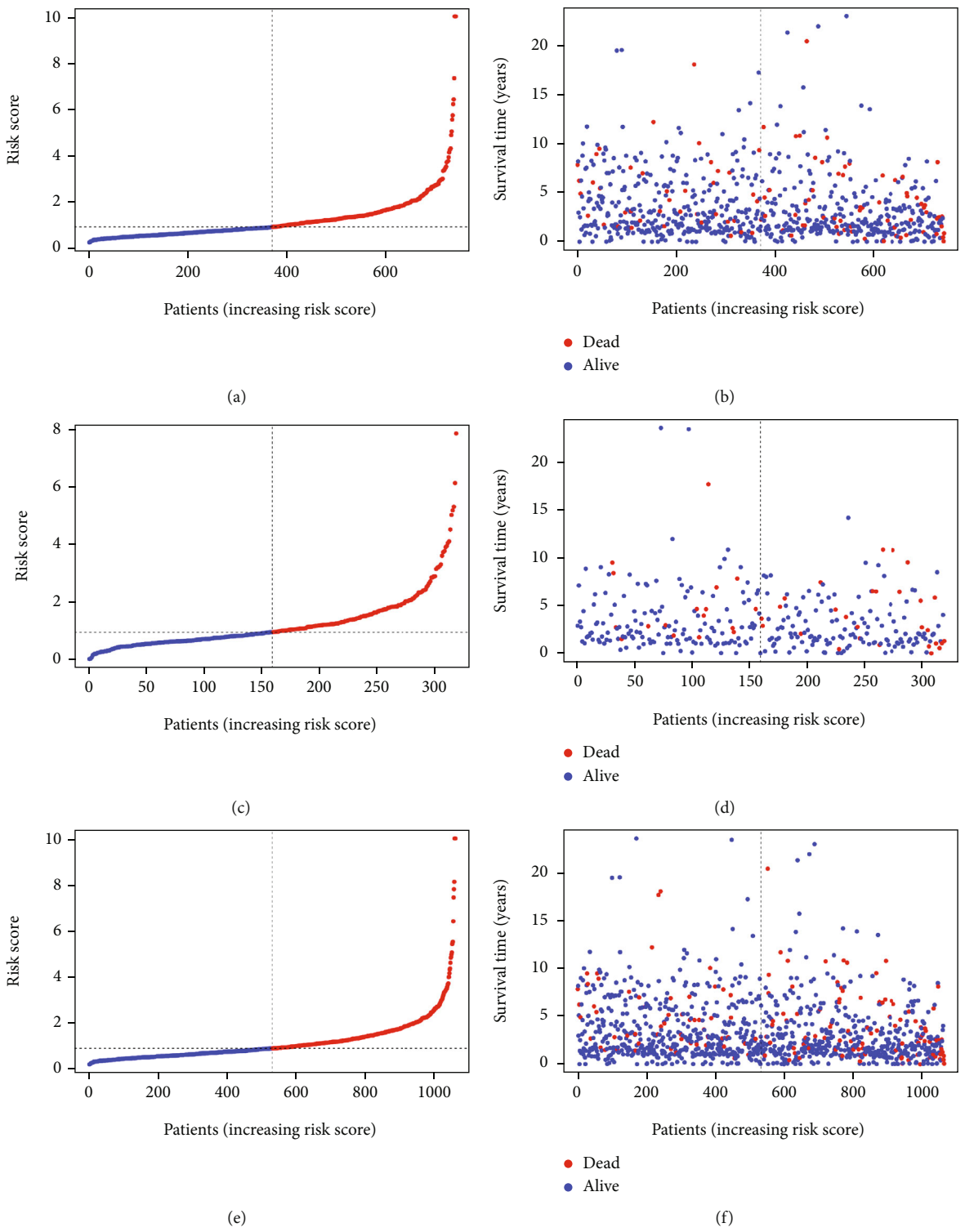

Figure 5: (a, c, e) Distribution of risk score in patients with BC. The black dotted line serves as the dividing line between the high-risk group and the low-risk group. (b, d, f) Diagram of the relationship between risk score and patient survival time. The result of (a, b) is based on training set, the result of (c, d) is based on test set, and the result of (e, f) is based on the overall internal validation set.

2.3.3. Prognostic Nomogram Evaluation and Validation. In order to improve the reliability of the prediction model and thus its clinical application, 30% of the patients and the overall cohort were used as an internal validation cohort to test the validity of the prediction model.

The discriminative power of the nomogram was calculated using the concordance index (*C*-index). We also measured the area under the curve (AUC) at 1, 3, and 5 years, which was derived from a ROC analysis. The *C*-indexes and AUCs take values ranging from 0.5 to 1.0, where 1.0

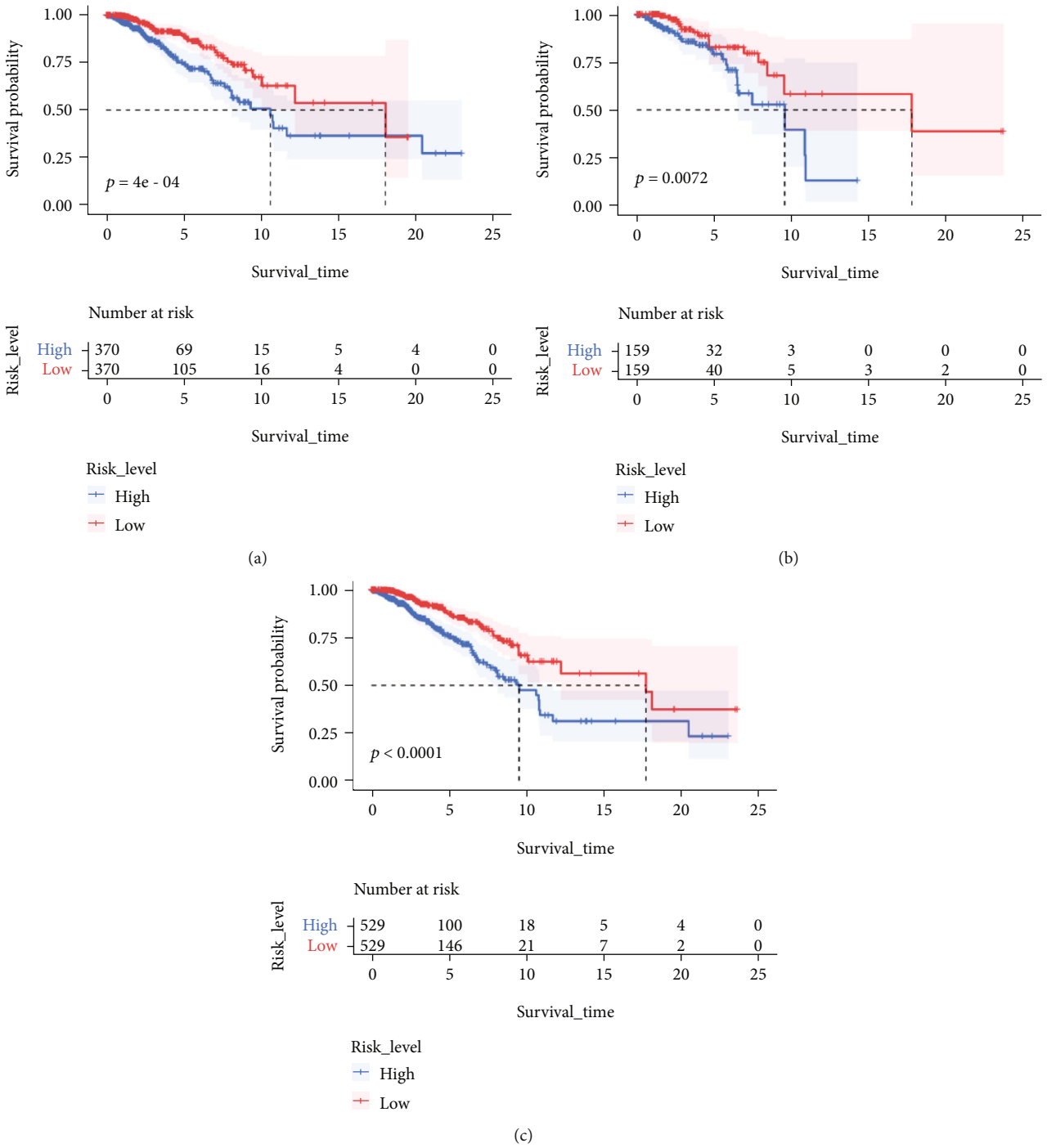

Figure 6: Overall survival (OS) Kaplan-Meier curves for patients in the low- and high-risk groups: (a) training set; (b) test set; (c) overall internal validation set.

represents the perfect ability to correctly distinguish the results from the model and 0.5 represents random chance. The calibration curve of the nomogram was evaluated graphically by plotting the ratio of the predicted probability to the observed ratio of the nomogram. Overlapping with the reference line indicated that the model was perfectly consistent. Finally, decision curve analysis was performed to evaluate the clinical benefits. A flow chart of the study process of this article was presented (Figure 1).

3. Results

3.1. Identification of Differentially Expressed EMT-Related Genes. To describe our study more clearly, we developed a flowchart of the analysis procedure. First, we obtained data from TCGA database for 1109 tumor tissues and 113 nontumor tissues. After taking intersection with EMT-related genes, a matrix of 200 EMT-related genes (Table S2) expression values was acquired. Then, after differential

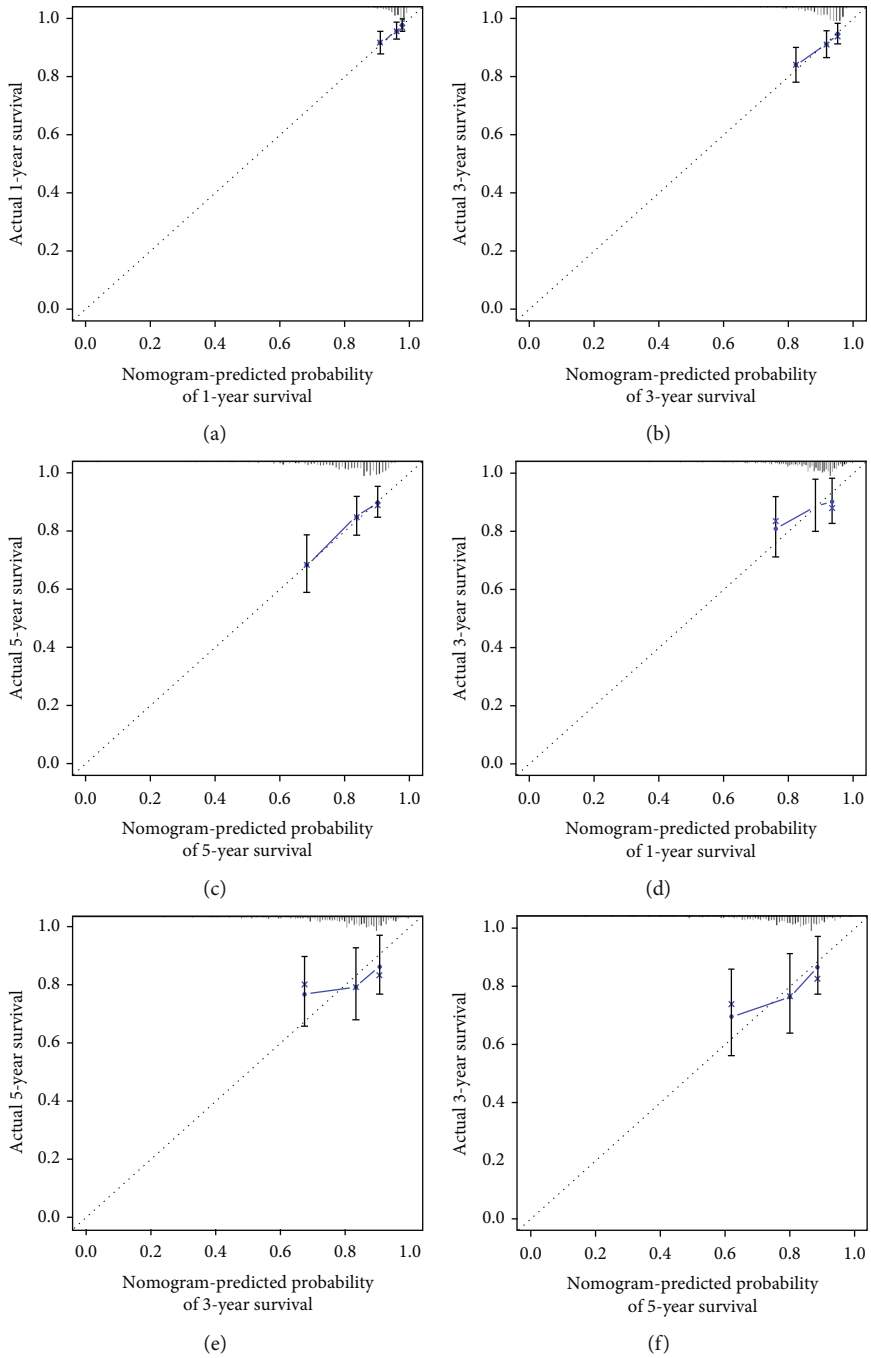

Figure 7: Continued.

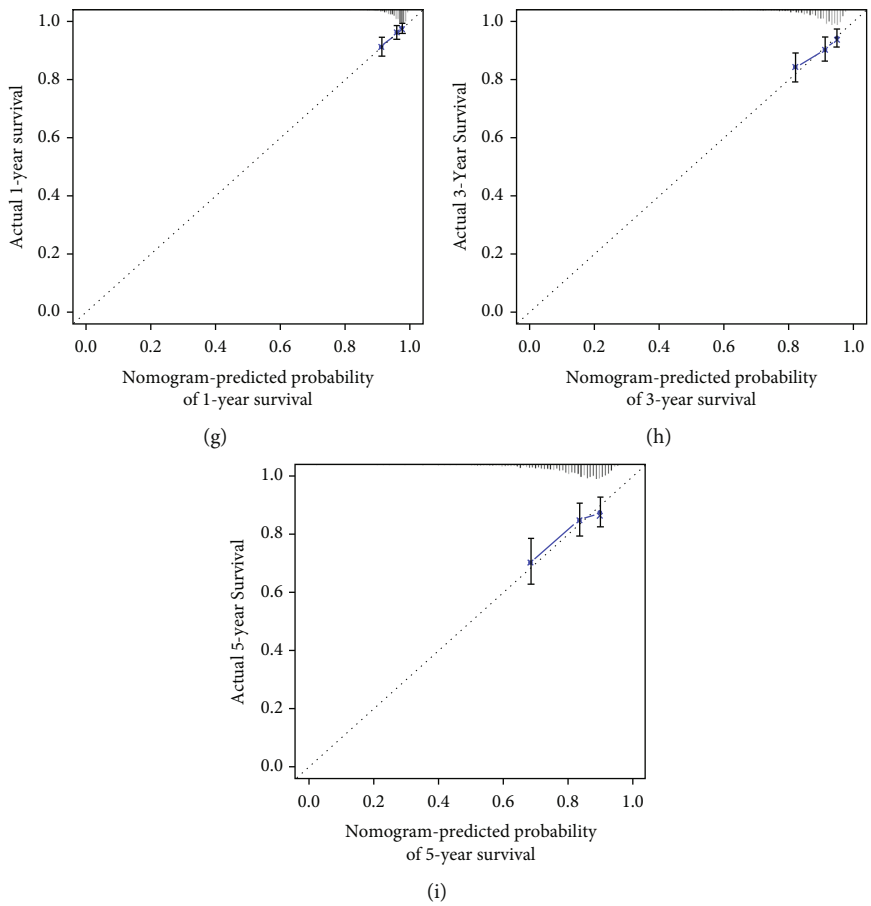

Figure 7: (a–c) Calibration plots to predict 1-, 3-, and 5-year overall survival (OS) in the training set; (d–f) calibration plots to predict 1-, 3-, and 5-year; overall survival (OS) in the test set; (g–i) calibration plots to predict 1-, 3-, and 5-year overall survival (OS) in the overall internal validation set.

analyses, a total of 78 differentially expressed EMT-related genes were identified. (logFC > 1 or logFC < −1, FDR < 0.05). The results were expressed in heat maps and volcano plots (Figures 2(a) and 2(b)).

3.2. Prognostic Nomogram Construction. Since age is associated with prognosis in female BC patients, we included age and 78 differentially expressed genes in univariate Cox regression to investigate the correlation between the included variables and prognostic value in BC patients and finally identified seven variables significantly associated with OS in BC patients at P value < 0.1 (Figure 3). The model was then constructed with age, CD44, P3H1, SDC1, COL4A1, TGFβ1, and SERPINE1 by multivariate Cox regression: risk score = $(0.030655 * \text{age level}) + (3.35E-05 * \text{expression level of CD44}) + (0.000142 * \text{expression level of P3H1}) + (3.76E-05 * \text{expression level of SDC1}) + (1.60E-05 * \text{COL4A1 expression level}) + (2.04E-05 * \text{TGF}\beta 1 \text{ expression level}) + (0.000247 * \text{SERPINE1 expression level})$ (Table 1).

The nomogram was then constructed and consisted of a total of seven variables (Figure 4), and the total score could be obtained by summing the scores of each variable. The total score can be used to predict the survival rate of individual patients at 1, 3, and 5 years. For example, a BC patient aged 65 years (20 points) with CD44 expression of 0 (20 points), P3H1 expression of 0 (21 points), SDC1 expression of 0 (20 points), COL4A1 expression of 80000 (43 points), TGFβ1 expression of 0 (21 points), and SERPINE1 expression of 0 (21 points) gets a sum-point of 166, corresponding to predicted 1-, 3-, and 5-year OS of 94.8%, 76.0%, and 57.4%, respectively.

Patients in TCGA group were divided into a low-risk group and a high-risk group using the median risk score as the threshold value. Figures 5(a), 5(c), and 5(e) show the distribution of the risk scores of BC patients from high to low in the training set, the internal validation set, and the overall internal validation set. The relationship between risk score and patient survival time in the training set, test set, and overall internal validation set is also shown (Figures 5(b), 5(d), and 5(f)). Patients with high-risk scores tended to have poorer clinical outcomes compared with those with low-risk scores. The survival analyses indicated the high-risk group had worse OS than that of the high-risk group ($P < 0.05$) (Figures 6(a)–6(c)).

3.3. Nomogram Calibration and Validation. The small angle between the survival probability and the actual survival outcome in the calibration curve indicates a strong agreement between them (Figure 7).

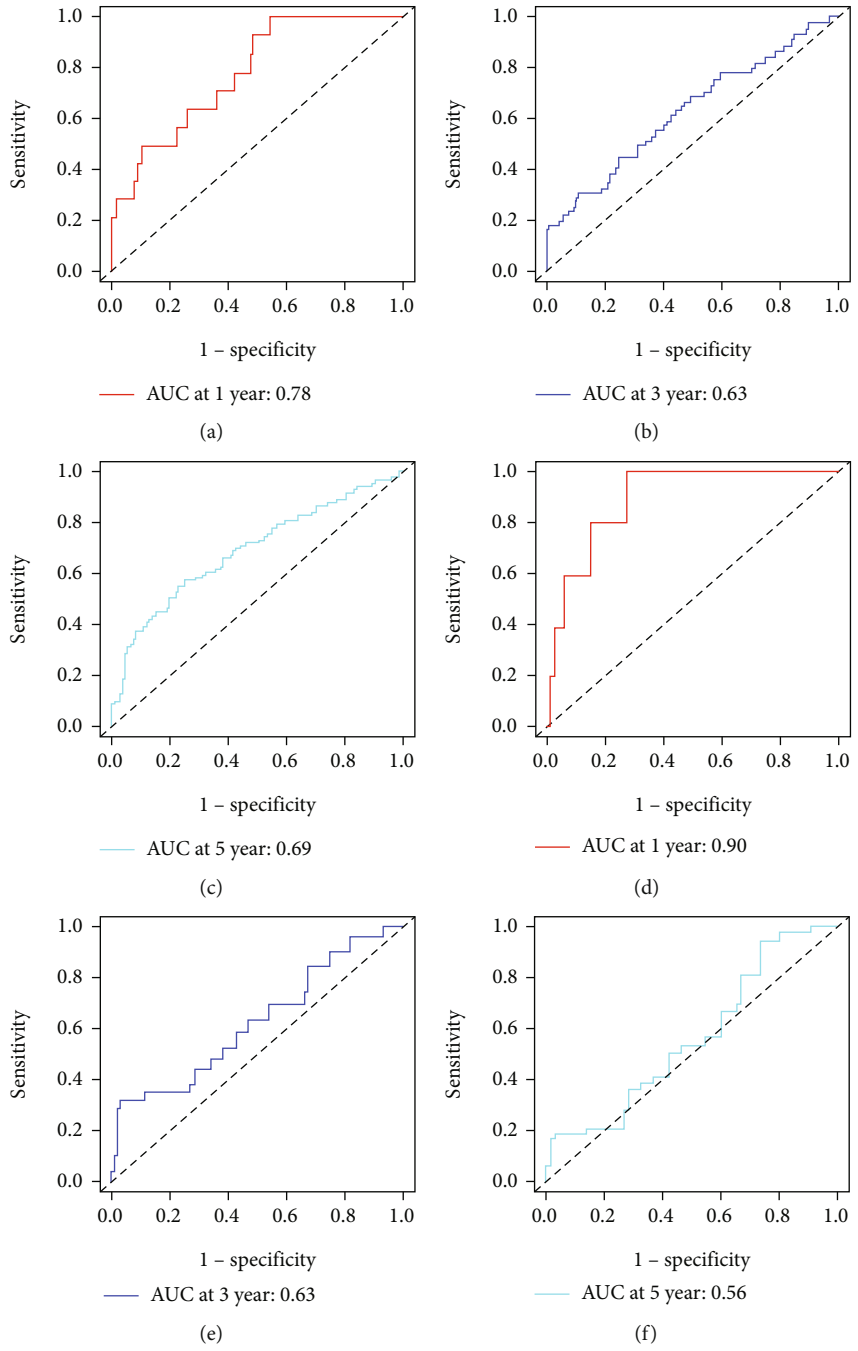

Figure 8: Continued.

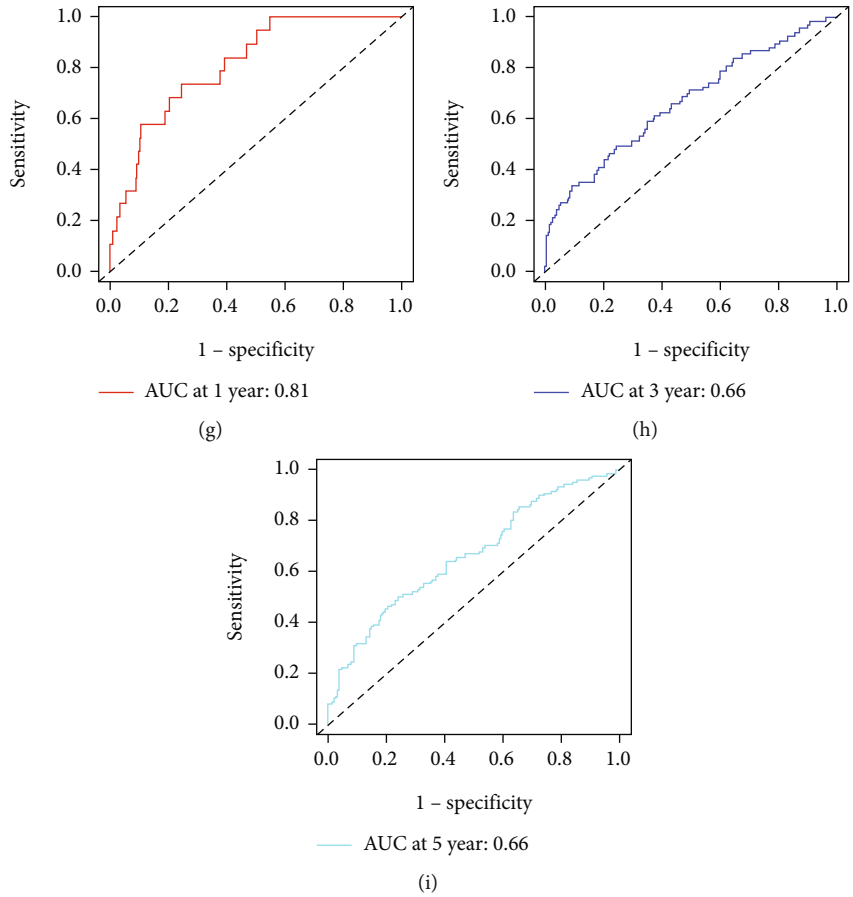

Figure 8: (a–c) ROC curves to predict 1-, 3-, and 5-year overall survival (OS) in the training set; (d–f) ROC curves to predict 1-, 3-, and 5-year; overall survival (OS) in the test set; (g–i) ROC curves to predict 1-, 3-, and 5-year overall survival (OS) in the overall internal validation set.

The *C*-index values for BC patients were 0.672 (95% CI 0.611–0.732), 0.692 (95% CI 0.586–0.798), and 0.679 (95% CI 0.626–0.732) in the training cohort, test set, and overall internal validation set, respectively. The time-dependent ROC curves were used to measure the sensitivity and specificity of the prediction model for predicting OS. Significantly, the AUC values were all greater than 0.63, except for the overall internal validation set with a 5-year predicted survival rate of 0.56, indicating that the model has high survival outcome prediction performance (Figure 8). The DCA curves also revealed better clinical applications for the risk scoring model (Figure 9).

The results based on C-index, ROC curves, calibration curves, and DCA curves indicated that the nomogram in our study demonstrated favorable predictive accuracy for the survival prognosis of female BC patients.

4. Discussion

BC is one of the most common cancers in females, with over 1,300,000 new cases and 450,000 deaths worldwide each year [16, 17]. Treatment of BC has advanced considerably, mainly through surgery, neoadjuvant chemotherapy, adjuvant chemotherapy, radiotherapy, systemic therapy, targeted therapy, and so on, with initial conventional surgery no longer being the best option for all patients [1]. However, BC remains one of the leading causes of cancer deaths in women worldwide, largely due to delayed diagnosis and unsuccessful treatment strategies [18]. Therefore, it is crucial to diagnose BC at an early stage and propose a personalized treatment plan based on the characteristics of the women patient's condition to predict their prognosis.

The TNM staging system is still the most widely used prognosis method to predict the survival of patients with BC. Although the American Joint Committee on Cancer (AJCC) updated BC staging in 2016 to include T, N, M, tumor grade, and expression of estrogen and progesterone receptors and HER2 [19], the current TNM staging system still has its undeniable deficiencies. For instance, it does not take into account other pathophysiological characteristics of the patient that have an impact on the prognosis of the tumor: age, gender, exercise, and overweight [20–22]. In addition, gene signature is an important factor in determining the prognosis of BC patients, as BC is a highly heterogeneous disease with different subtypes with different biological, molecular, and clinical processes. Gene expression profiling can identify genetic features to predict prognosis and guide the use of adjuvant therapy [23]. Among others, EMT genes regulate tumor proliferation, invasion, and metastasis [24, 25]. There are many prognostic models

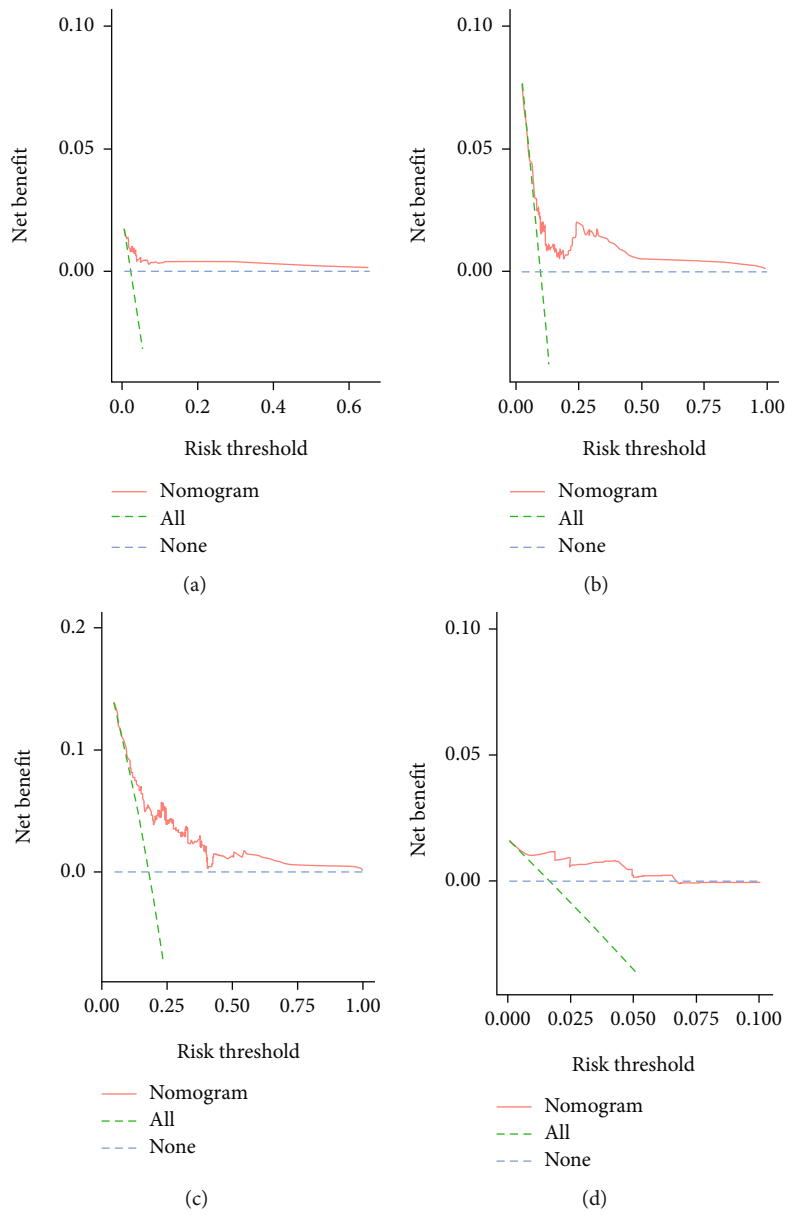

Figure 9: Continued.

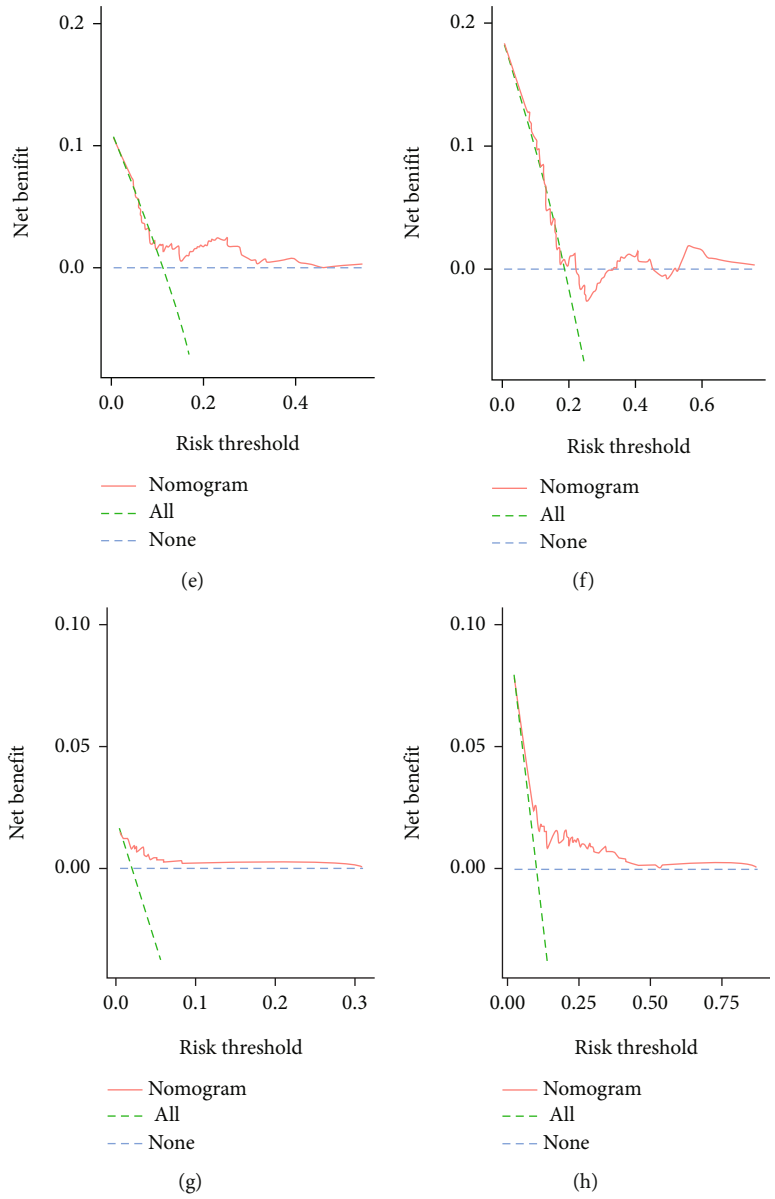

Figure 9: Continued.

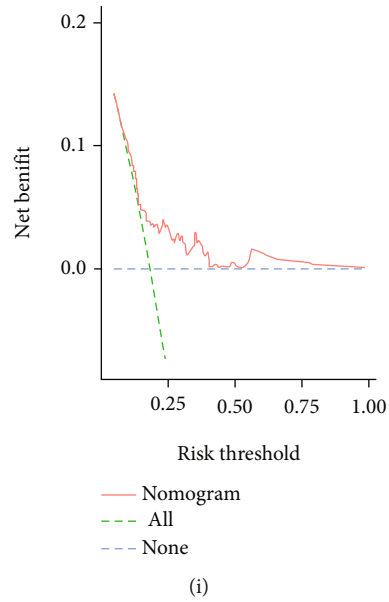

Figure 9: (a–c) DCA analysis predicting 1-, 3-, and 5-year overall survival (OS) in the training set; (d–f) DCA analysis predicting 1-, 3-, and 5-year; overall survival (OS) in the test set; (g–i) DCA analysis predicting 1-, 3-, and 5-year overall survival (OS) in the overall internal validation set.

on BC; however, this is the first gene signature constructed by EMT-related genes. Moreover, considering the role of age and gender in the onset and progression of BC, we chose to study the prognosis of patients in women and used age as one of the predictors. Compared to previous studies, this nomogram was more accurate.

EMT is a cellular process in which cells lose their epithelial characteristics and acquire mesenchymal characteristics, such as quiescent adnexal cells gaining the ability to migrate [26]. EMT has been associated with a variety of tumor functions, including tumor initiation, malignant progression, tumor stemness, tumor cell migration, intravascular infiltration, metastasis, and resistance to therapy [9]. Most notably in this context, previous studies have shown that both cancer stem cell-like properties and drug resistance are associated with EMT [27]. Given the close link between oncogenic signaling and EMT blockers, EMT has emerged as a therapeutic target or goal in cancer therapy [28]. The relationship between EMT-related genes and breast cancer is also increasingly being investigated by researchers. The major focus of current studies is the regulatory mechanisms and therapeutic approaches of EMT for breast cancer in metastasis and invasion, mainly including miRNA and signaling pathways such as Wnt, Notch, TNF-α, NF-κB, and RTK. Investigators suppress breast cancer by attempting to therapeutically target or inhibit key/auxiliary players in these pathways [8, 29–31]. Most notably, upregulation of programmed death ligand 1 (PD-L1) expression is associated with EMT cell phenotype activation, and the control of the interaction between p53 and EMT master regulators is of importance in breast cancer. These two mechanisms have also been studied in other types of cancer and play a key role in the development and metastasis of cancer [30, 32].

This study was based on TCGA database. Differential analysis was firstly performed to find differential EMT-related genes. Univariate regression analysis was then conducted to identify candidate prognostic variables. We then developed a prognostic model by multivariate analysis to predict OS. Calibration curves, receiver operating characteristics (ROC) curves, *C*-index, and decision curve analysis (DCA) were used to test the veracity of the prognostic model. In addition to the training cohort of 70% BC patients, the remained cohort was treated as the test set. In the end, we derived that patient's age, CD44, P3H1, SDC1, COL4A1, TGFβ1, and SERPINE1 were independent prognostic factors for overall survival in female BC patients and constructed predictive models. The accuracy of the model has also been verified using various methods.

In accordance with our findings, in stage I and IV BC tumors, excess mortality increased linearly with age [33]. Recent studies have shown that a novel positive feedback loop between IL1β and CD44 promoted malignant progression in triple-negative BC (TNBC) and that CD44 was a potential target for inhibiting PD-L1 function in TNBC [34, 35]. Sayyad et al. demonstrated the role of Sdc1 in promoting brain metastasis in BC [36]. Several studies have demonstrated that COL4A1 expression could be used as a biomarker for superior prognosis in BC patients receiving neoadjuvant chemotherapy [37], while epigallocatechin-3-gallate (EGCG) exerted antitumor effects by restoring nine key genes, including COL4A1, in myeloid-derived suppressor cells (MDSCs) [37]. TGFβ1-activated cancer-associated fibroblasts (CAFs) promote BC growth and metastasis in part through autophagy [38]. The evolutionary branch E member 1 (SERPINE1) is a molecule involved in a variety of human malignancies. Zhang et al. showed that SERPINE1 served as an oncogene for PTX resistance in BC, and Xu et al. identified a functional pathway linking miR-1185-2-3p, GOLPH3L, and SERPINE1, which played an essential role in glucose metabolism in BC. Both of their studies

revealed that it may serve as a possible target for the treatment of BC [39, 40]. No studies have yet explored the mechanisms by which P3H1 affects BC development, progression, and metastasis, but an algorithm-based meta-analysis of genome-wide and proteomic data identified P3H1 as a potential biomarker for CRC. Our study indicates a direction of research for subsequent basic studies [41].

In this endeavor, some limitations need to be acknowledged. To begin with, the population races in TCGA database are primarily limited to whites and blacks, and extrapolation of findings to other racial groups needs to be validated. Second, a robust nomogram should be externally validated across cohorts; therefore, our nomogram needs to be further validated in multicenter clinical trials and prospective studies. Finally, some of the genes identified in this paper are relatively rarely reported in the academic literature. Therefore, more evidence including sample collection with complete experimental and clinical information should be performed for future validation is needed to elucidate the intrinsic association between age and six-gene signature and prognosis of BC patients.

However, our study also has some advantages. To our knowledge, this is the first study to additionally combine age as a prognostic variable with EMT-related genes to predict the prognosis of BC patients. Prognostic models may predict patient prognosis more accurately than conventional indicators.

In conclusion, we have developed and validated a relatively effective predictive model to predict the survival outcome of female BC patients at 1, 3, and 5 years. The accuracy and reliability of the prognostic model have also been verified. The results of our research need to be further validated in subsequent clinical practice.

Data Availability

The research article data used to support the findings of this study are included within the article.

Conflicts of Interest

The authors declare that they have no conflicts of interest.

Authors' Contributions

Wei Xue and Chenyu Sun performed the study, collected data, and wrote the manuscript. Hui Yuan, Xin Yang, Qiuping Zhang, and Yunnuo Liao participated in analyzing data and prepared the tables and figures. Hongwei Guo designed the research study and revised the manuscript. All authors read and approved the final manuscript. Wei Xue and Chenyu Sun contributed equally to this work.

Acknowledgments

This work was supported by the National Natural Science Foundation of China (No. 82074347) and the Innovation Project of Guangxi Graduate Education (No. YCBZ2021048).

Supplementary Materials

Supplementary Table S1: basic values of patients. Supplementary Table S2: EMT-related gene list. *(Supplementary Materials)*

References

[1] N. Harbeck and M. Gnant, "Breast cancer," *Lancet*, vol. 389, no. 10074, article S0140673616318918, pp. 1134–1150, 2017.

[2] Y. Liang, H. Zhang, X. Song, and Q. Yang, "Metastatic heterogeneity of breast cancer: molecular mechanism and potential therapeutic targets," *Seminars in Cancer Biology*, vol. 60, article S1044579X1930063X, pp. 14–27, 2020.

[3] X. Xu, M. Zhang, F. Xu, and S. Jiang, "Wnt signaling in breast cancer: biological mechanisms, challenges and opportunities," *Molecular Cancer*, vol. 19, no. 1, article 1276, p. 165, 2020.

[4] G. Cui, J. Wu, J. Lin et al., "Graphene-based nanomaterials for breast cancer treatment: promising therapeutic strategies," *Journal of Nanobiotechnology*, vol. 19, no. 1, p. 211, 2021.

[5] P. Boix-Montesinos, P. M. Soriano-Teruel, A. Armiñán, M. Orzáez, and M. J. Vicent, "The past, present, and future of breast cancer models for nanomedicine development," *Advanced Drug Delivery Reviews*, vol. 173, article S0169409X2100096X, pp. 306–330, 2021.

[6] S. Yardım-Akaydin, B. Karahalil, and S. N. Baytas, "New therapy strategies in the management of breast cancer," *Drug Discovery Today*, vol. 27, no. 6, pp. S1359–S6446, 2022.

[7] B. Bakir, A. M. Chiarella, J. R. Pitarresi, and A. K. Rustgi, "EMT, MET, plasticity, and tumor metastasis," *Trends in Cell Biology*, vol. 30, no. 10, article S0962892420301446, pp. 764–776, 2020.

[8] J. Luo, J. F. Yao, X. F. Deng et al., "14, 15-EET induces breast cancer cell EMT and cisplatin resistance by up-regulating integrin $\alpha v\beta 3$ and activating FAK/PI3K/AKT signaling," *Journal of Experimental & Clinical Cancer Research: CR*, vol. 37, no. 1, article 694, p. 23, 2018.

[9] I. Pastushenko and C. Blanpain, "EMT transition states during tumor progression and metastasis," *Trends in Cell Biology*, vol. 29, no. 3, article S0962892418302010, pp. 212–226, 2019.

[10] M. Saotome, D. B. Poduval, R. Nair, M. Cooper, and M. Takaku, "GATA3 truncation mutants Alter EMT related gene expression via partial motif recognition in luminal breast cancer cells," *Frontiers in Genetics*, vol. 13, p. 820532, 2022.

[11] K. Parthasarathi, S. Mandal, S. Singh et al., "In silico analysis of ion channels and their correlation with epithelial to mesenchymal transition in breast cancer," *Cancers*, vol. 14, no. 6, p. 1444, 2022.

[12] G. Cserni, E. Chmielik, B. Cserni, and T. Tot, "The new TNM-based staging of breast cancer," *Virchows Archiv: an International Journal of Pathology*, vol. 472, no. 5, article 2301, pp. 697–703, 2018.

[13] Y. S. Sun, Z. Zhao, Z. N. Yang et al., "Risk factors and preventions of breast cancer," *International Journal of Biological Sciences*, vol. 13, no. 11, pp. 1387–1397, 2017.

[14] L. Cao, C. W. Towe, R. Shenk, N. Stabellini, A. L. Amin, and A. J. Montero, "A comparison of local therapy alone with local plus systemic therapy for stage I pT1aN0M0 HER2+ breast cancer: a National Cancer Database analysis," *Cancer*, vol. 128, no. 13, pp. 2433–2440, 2022.

[15] Q. Tai, W. Xue, M. Li et al., "Survival nomogram for metastasis colon cancer patients based on SEER database," *Frontiers in Genetics*, vol. 13, p. 832060, 2022.

[16] N. A. Bagegni and L. L. Peterson, "Age-related disparities in older women with breast cancer," *Advances in Cancer Research*, vol. 146, pp. 23–56, 2020.

[17] Y. Huang, S. Du, J. Liu et al., "Diagnosis and prognosis of breast cancer by high-performance serum metabolic fingerprints," *Proceedings of the National Academy of Sciences of the United States of America*, vol. 119, no. 12, article e2122245119, 2022.

[18] N. Jokar, I. Velikyan, H. Ahmadzadehfar et al., "Theranostic approach in breast cancer," *Clinical Nuclear Medicine*, vol. 46, no. 8, pp. e410–e420, 2021.

[19] S. B. Edge, G. N. Hortobagyi, and A. E. Giuliano, "New and important changes in breast cancer TNM: incorporation of biologic factors into staging," *Expert Review of Anticancer Therapy*, vol. 19, no. 4, pp. 309–318, 2019.

[20] N. R. Latha, A. Rajan, R. Nadhan et al., "Gene expression signatures: a tool for analysis of breast cancer prognosis and therapy," *Critical Reviews in Oncology/Hematology*, vol. 151, article S1040842820301025, p. 102964, 2020.

[21] M. de Roon, A. M. May, A. McTiernan et al., "Effect of exercise and/or reduced calorie dietary interventions on breast cancer-related endogenous sex hormones in healthy postmenopausal women," *Breast Cancer Research: BCR*, vol. 20, no. 1, article 1009, p. 81, 2018.

[22] S. Jiralerspong and P. J. Goodwin, "Obesity and breast cancer prognosis: evidence, challenges, and opportunities," *Journal of Clinical Oncology: Official Journal of the American Society of Clinical Oncology*, vol. 34, no. 35, pp. 4203–4216, 2016.

[23] M. Kwa, A. Makris, and F. J. Esteva, "Clinical utility of gene-expression signatures in early stage breast cancer," *Clinical Oncology*, vol. 14, no. 10, pp. 595–610, 2017.

[24] L. Sun, C. Shi, S. Liu et al., "Overexpression of NuSAP1 is predictive of an unfavourable prognosis and promotes proliferation and invasion of triple-negative breast cancer cells via the Wnt/β-catenin/EMT signalling axis," *Gene*, vol. 747, article S0378111920303267, p. 144657, 2020.

[25] H. Wang, S. Guo, S. J. Kim et al., "Cisplatin prevents breast cancer metastasis through blocking early EMT and retards cancer growth together with paclitaxel," *Theranostics*, vol. 11, no. 5, pp. 2442–2459, 2021.

[26] N. M. Aiello and Y. Kang, "Context-dependent EMT programs in cancer metastasis," *The Journal of Experimental Medicine*, vol. 216, no. 5, pp. 1016–1026, 2019.

[27] G. Pan, Y. Liu, L. Shang, F. Zhou, and S. Yang, "EMT-associated microRNAs and their roles in cancer stemness and drug resistance," *Cancer communications (London, England)*, vol. 41, no. 3, pp. 199–217, 2021.

[28] E. S. Cho, H. E. Kang, N. H. Kim, and J. I. Yook, "Therapeutic implications of cancer epithelial-mesenchymal transition (EMT)," *Archives of Pharmacal Research*, vol. 42, no. 1, article 1108, pp. 14–24, 2019.

[29] S. Kotiyal and S. Bhattacharya, "Breast cancer stem cells, EMT and therapeutic targets," *Biochemical and Biophysical Research Communications*, vol. 453, no. 1, article S0006291X14016957, pp. 112–116, 2014.

[30] S. S. Messeha, N. O. Zarmouh, and K. Soliman, "Polyphenols modulating effects of PD-L1/PD-1 checkpoint and EMT-mediated PD-L1 overexpression in breast cancer," *Nutrients*, vol. 13, no. 5, article nu13051718, p. 1718, 2021.

[31] Y. Li, Y. W. Wang, X. Chen et al., "MicroRNA-4472 promotes tumor proliferation and aggressiveness in breast cancer by targeting RGMA and inducing EMT," *Clinical Breast Cancer*, vol. 20, no. 2, article S152682091930669X, pp. e113–e126, 2020.

[32] S. Parfenyev, A. Singh, O. Fedorova, A. Daks, R. Kulshreshtha, and N. A. Barlev, "Interplay between p53 and non-coding RNAs in the regulation of EMT in breast cancer," *Cell Death & Disease*, vol. 12, no. 1, article 3327, p. 17, 2021.

[33] C. Cluze, M. Colonna, L. Remontet et al., "Analysis of the effect of age on the prognosis of breast cancer," *Breast Cancer Research and Treatment*, vol. 117, no. 1, article 222, pp. 121–129, 2009.

[34] J. H. Jang, D. H. Kim, J. M. Lim et al., "Breast cancer cell-derived soluble CD44 promotes tumor progression by triggering macrophage IL1β production," *Cancer Research*, vol. 80, no. 6, pp. 1342–1356, 2020.

[35] T. Kong, R. Ahn, K. Yang et al., "CD44 promotes PD-L1 expression and its tumor-intrinsic function in breast and lung cancers," *Cancer Research*, vol. 80, no. 3, pp. 444–457, 2020.

[36] M. R. Sayyad, M. Puchalapalli, N. G. Vergara et al., "Syndecan-1 facilitates breast cancer metastasis to the brain," *Breast Cancer Research and Treatment*, vol. 178, no. 1, article 5347, pp. 35–49, 2019.

[37] S. M. Wang, P. M. Chen, Y. W. Sung, W. C. Huang, H. S. Huang, and P. Y. Chu, "Effect of COL4A1 expression on the survival of neoadjuvant chemotherapy breast cancer patients," *Journal of Oncology*, vol. 2020, Article ID 5209695, 8 pages, 2020.

[38] M. Huang, M. Fu, J. Wang et al., "TGF-β1-activated cancer-associated fibroblasts promote breast cancer invasion, metastasis and epithelial-mesenchymal transition by autophagy or overexpression of FAP-α," *Biochemical Pharmacology*, vol. 188, article S0006295221001234, p. 114527, 2021.

[39] Q. Zhang, L. Lei, and D. Jing, "Knockdown of SERPINE1 reverses resistance of triple-negative breast cancer to paclitaxel via suppression of VEGFA," *Oncology Reports*, vol. 44, no. 5, pp. 1875–1884, 2020.

[40] Y. Xu, W. Chen, J. Liang et al., "The miR-1185-2-3p-GOLPH3L pathway promotes glucose metabolism in breast cancer by stabilizing p53-induced SERPINE1," *Journal of Experimental & Clinical Cancer Research: CR*, vol. 40, no. 1, article 1767, p. 47, 2021.

[41] D. R. Gawel, E. J. Lee, X. Li et al., "An algorithm-based meta-analysis of genome- and proteome-wide data identifies a combination of potential plasma biomarkers for colorectal cancer," *Scientific Reports*, vol. 9, no. 1, article 51999, p. 15575, 2019.

Hindawi
Disease Markers
Volume 2022, Article ID 7594489, 9 pages
https://doi.org/10.1155/2022/7594489

Research Article

COPS3 Promotes Proliferation, Invasion, and EMT of Colorectal Cancer Cells by MEK/ERK Pathway

Yanchao Xie, Zhijiang Wei, and Chi Cheng

Department of Gastroenterology, Cangzhou Central Hospital, Cangzhou, Hebei 061000, China

Correspondence should be addressed to Yanchao Xie; xyc0810_dr@163.com

Received 12 May 2022; Accepted 1 July 2022; Published 19 July 2022

Academic Editor: Chia-Jung Li

Colorectal cancer (CRC) is one of the most aggressive cancers with poor prognosis and high mortality. The study of the pathogenesis of CRC is a top priority in providing effective diagnostic and prognostic strategies for CRC. COPS3 protein is a subunit of the COP9 signaling body (CSN), which is closely associated with the development of multiple types of tumors. However, there are few studies on the role of COPS3 in colon adenocarcinoma (COAD). This study investigated the effects of COPS3 on proliferation, motility, and EMT of colorectal cancer cells and related mechanisms. COPS3 was highly expressed in COAD. The depletion of COPS3 suppressed the viability and stimulated the apoptosis of COAD cells. Depletion of COPS3 suppressed the motility and EMT process of COAD cells. Mechanically, we found that COPS3 could mediate MEK/ERK pathway and therefore affected the process of COAD cells. We thought that COPS3 could serve as a promising COAD target.

1. Introduction

Colorectal cancer (CRC), as one of the most aggressive cancers with poor prognosis, causes a large number of deaths worldwide and affects millions of people every year [1, 2]. CRC mainly affects the distal rectum, sigmoid colon, and descending colon [3]. More and more CRC risk factors have been reported recently, such as ageing, unhealthy diet, smoking, obesity, physical inactivity, inflammatory bowel disease, and genetic factors [4]. Treatment for CRC includes surgery, chemotherapy, and radiotherapy [5, 6]. However, because the detailed mechanism of CRC development is not fully understood, the 5-year survival rate for CRC is low, especially in the later stages [7]. Therefore, a better understanding of the pathogenesis of CRC is a top priority in providing effective diagnostic and prognostic strategies for patients with CRC.

COPS3 protein is a subunit of the COP9 signaling body [8], located in chromosome region 17p11.2 and plays a role in deubiquitination and protein kinase activity in a variety of processes [9]. COPS3 is closely associated with tumor development [10, 11]. Knockdown of COPS3 significantly reduced lung metastasis of osteosarcoma cells in mouse models, downregulated MEK and ERK signaling, and inhibited EMT by 90 kDa ribosomal S6 kinase (RSK), reducing metastasis of osteosarcoma cells [12]. In addition, COPS3 depletion inhibited tumor growth in nude mice by blocking cell cycle progression [13]. However, there are few studies on the role of COPS3 in colorectal cancer, particularly colon adenocarcinoma (COAD).

MEK/ERK cell signaling pathway plays an important role in various human tumors and is involved in cell proliferation, survival, metabolism, and cell migration [14]. For example, sophorine inhibits tumorigenesis in colorectal cancer by downregulating the MEK/ERK/VEGF pathway [15]. Epithelial mesenchymal transformation (EMT) is a biological process in which cancer cells lose their epithelial features and acquire mesenchymal markers, which make tumor cells more mobile and invasive [16]. EMT is marked by decreased E-cadherin expression and increased N-cadherin or Vimentin expression [17]. The process of EMT is controlled by transcription factors and certain pathways.

This study investigated the effects of COPS3 on proliferation, migration, invasion, and EMT of colorectal cancer cells and related mechanisms. Our data revealed that COPS3 was highly expressed in human COAD cells and affected the

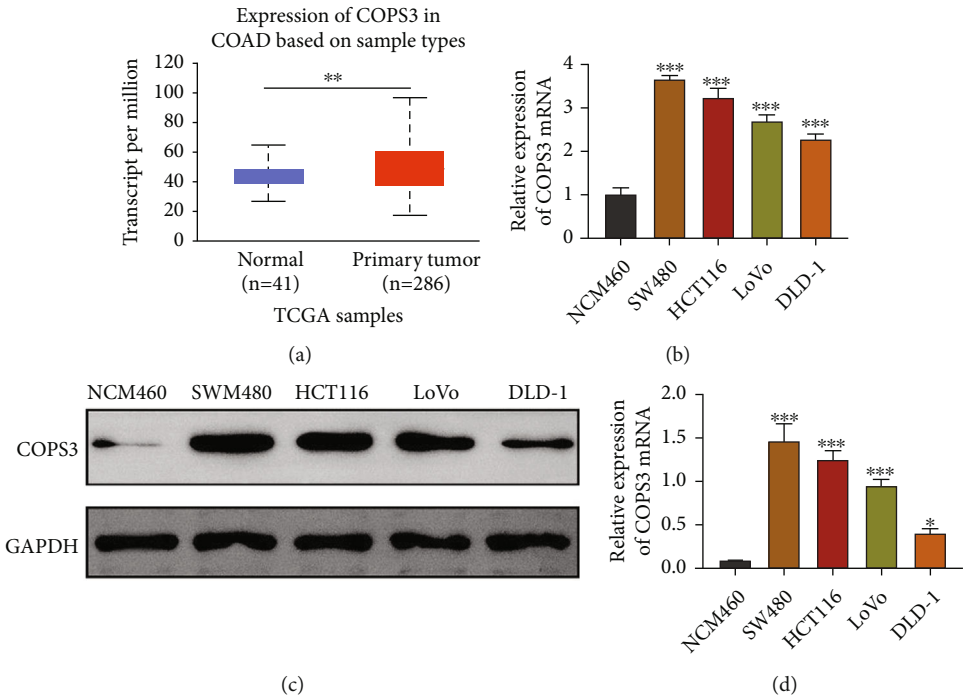

Figure 1: COPS3 was highly expressed in COAD tissues and cell lines. (a) TCGA database showed the levels of transcript per million (TPM) in 286 tumor tissues compared to the 41 normal tissues. (b) qPCR assays showed the mRNA levels of COPS3 in normal cell line NCM460 and 4 COAD cell lines, including SW480, HCT116, LoVo, and DLD-1. (c and d) Immunoblot assays showed the protein levels of COPS3 in normal cell line NCM460 and 4 COAD cell lines, including SW480, HCT116, LoVo, and DLD-1. Data are presented as mean ± SD. $^{**}p < 0.01$ and $^{***}p < 0.001$.

viability, motility, and EMT of COAD cells via MEK/ERK pathway. We thought that COPS3 could serve as a promising COAD target.

2. Materials and Methods

2.1. Antibodies, Primers, and Plasmids. The antibodies used were anti-COPS3 (1 : 500 dilution, ab231344, Abcam), anti-E-cadherin (1 : 1000 dilution, ab76055, Abcam), anti-N-cadherin (1 : 1000 dilution, ab76011, Abcam), anti-Vimentin (1 : 500 dilution, ab8978, Abcam), anti-MEK (1 : 1000 dilution, 178876, Abcam), anti-p-MEK (1 : 1000 dilution, ab278564, Abcam), anti-ERK (1 : 1000 dilution, ab184699, Abcam), anti-p-ERK (1 : 500 dilution, ab201015, Abcam), and anti-β-actin (1 : 2000 dilution, 60008-1-Ig, Proteintech).

The quantitative PCR primer sequences of COPS3 are forward, 5′-GCGAGGAAUUGGCAUCCUUTT-3′ and reverse, 5′-AAGGAUGCCAAUUCCUCGCTT-3′. The quantitative PCR primer sequences of GAPDH are 5′-TCCGCCGTGTG TACGTCATT-3′ and 5′-TCCGCCGTGTGTACGTCATT-3′.

siRNA of COPS3 and control siRNA was bought from Riobio (China).

2.2. Cell Culture. The normal cell line NCM460 and 4 COAD cell lines, including SW480, HCT116, LoVo, and DLD-1, were all purchased from ATCC. Both of the cells were maintained in DMEM, supplemented with 10% of fetal bovine serum, and incubated at 37°C in a 5% CO_2 incubator.

2.3. Immunoblot Assay. The samples were lysed with the lysis buffer (RIPA, Beyotime, China) and then separated by a 10% SDS-PAGE experiment; sequentially, the total proteins were transferred onto PVDF membranes (Millipore, USA). Then, the PVDF membranes were blocked by the use of 5% dry milk in TBST buffer and antibodies. After washing with TBST for 3 times, the membranes were treated with the secondary antibodies for 45 min. Each blot was then visualized using the ECL kit (GE, SA).

2.4. Cell Viability Assays. For CCK-8, COAD cells were plated into the 96-well plates (1000 cell per well) and maintained in complete growth media for 24 h at 37°C. The cells were exposed to CCK-8 reagent at 37°C for 1.5 h. The relative cell viability was assessed with microplate spectrophotometer at 450 nm (Bio-Rad, U.S.A.).

For colony formation assay, COAD cells were plated into 24-well plates (1000 cell per well) and maintained in complete growth media for 14 d at 37°C. Subsequently, the cells were incubated with 0.2% crystal violet and washed, and then, the cells were photographed by a fluorescence microscope (Zeiss, Germany).

2.5. Cell Apoptosis Assay. The cells after transfection for 48 h were washed with PBS. Subsequently, the cells were fixed with precooled 70% ethanol at -20°C for 1 h. Subsequently, the cells were stained with propidium iodide (PI) and FITC-labelled Annexin V at 4°C for 10 min, and the apoptosis levels were measured by BD FACS caliber.

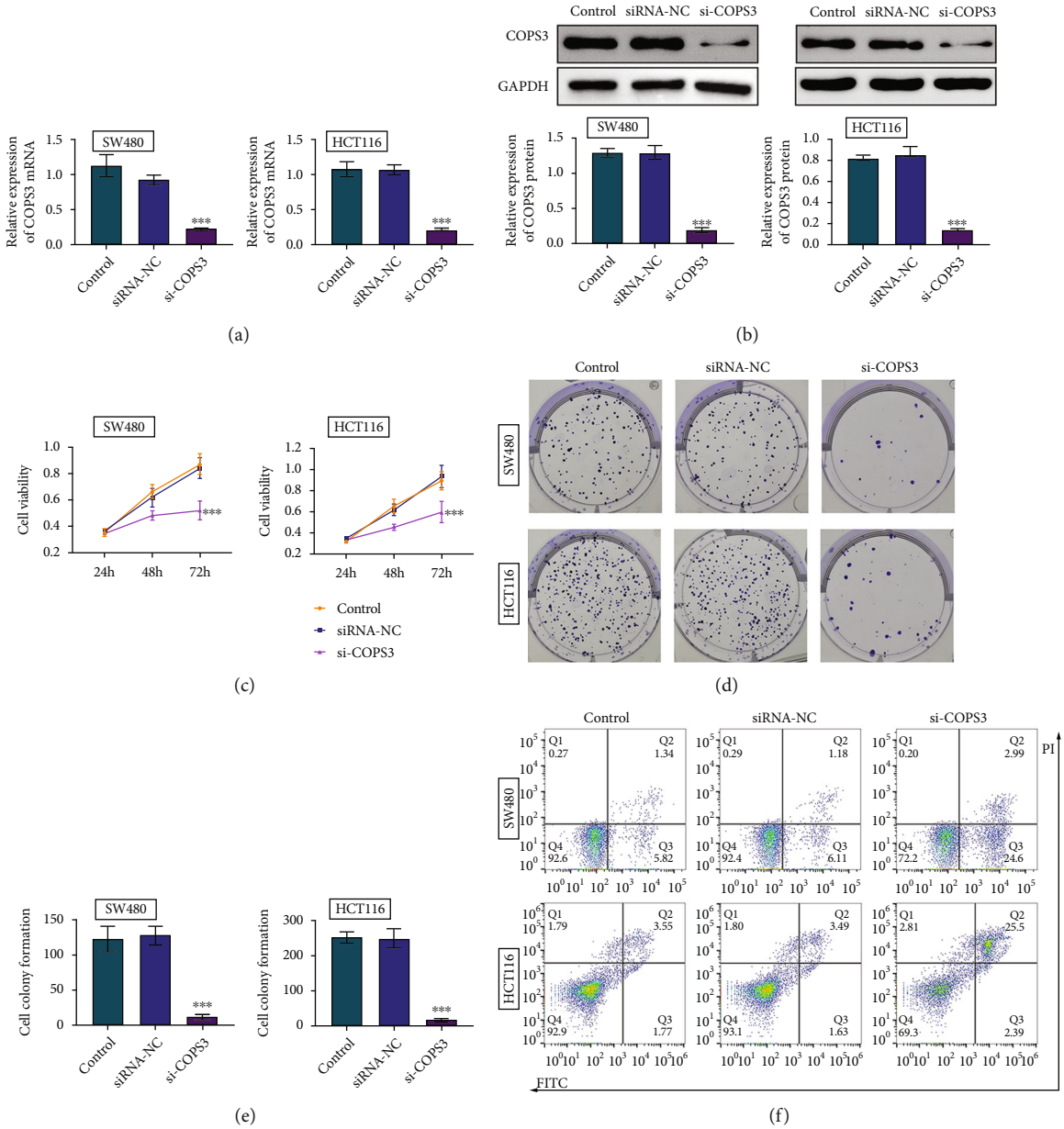

FIGURE 2: Continued.

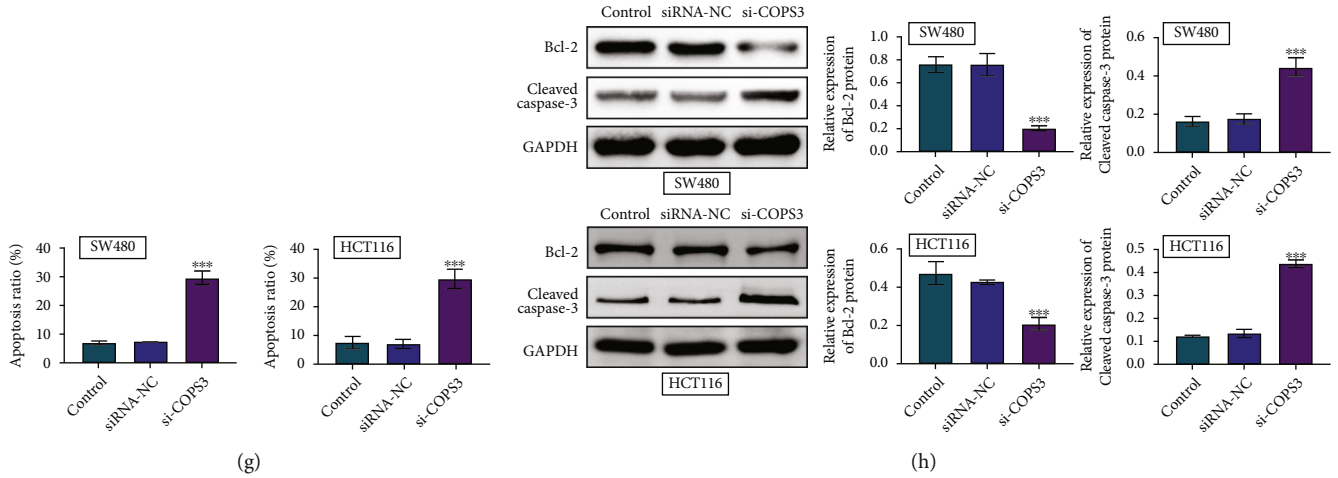

Figure 2: COPS3 ablation suppressed the viability of COAD cells and stimulated apoptosis. (a) qPCR assays showed the mRNA levels of COPS3 in SW480 and HCT116 cells upon the transfection of control or COPS3 siRNAs or without transfection (control). (b) Immunoblot showed the expression of COPS3 in SW480 and HCT116 cells upon the transfection of control or COPS3 siRNAs or without transfection (control). (c) CCK-8 assays showed the OD value at 450 nm wavelength of SW480 and HCT116 cells upon the transfection of control or COPS3 siRNAs or without transfection (control). (d and e). Colony formation assays showed the colony number of SW480 and HCT116 cells upon the transfection of control or COPS3 siRNAs or without transfection (control). The quantification was in panel (e). (f and g). Flow cytometry (FCM) assays showed the apoptosis percentage of SW480 and HCT116 cells upon the transfection of control or COPS3 siRNAs or without transfection (control). The quantification was in panel (g). (h) Immunoblot showed the expression of the indicated proteins in control or COPS3 siRNAs or without transfection (control). Data are presented as mean ± SD. $^{***}p < 0.001$, siCOPS3 vs. siControl.

2.6. Tumor Growth In Vivo Assay. All experimental procedures were according to the criteria outlined in the Regulations of Experimental Animal Administration (http://www.most.gov.cn). Female BALB/c nude mice (8-week-old; weight, ~20 g) were obtained from Beijing Vital River Laboratory Animal Technology Co., Ltd. None of the mice died during the study. A total of 10 athymic nude mice were randomly divided into control ($n = 5$) and transfection ($n = 5$) groups. HCT116 cells which were stably transfected with shRNA plasmids were injected into the right flank of female nude mice. After 2 weeks, the volume of tumors was estimated every week, and the tumor growth curves of 7 consecutive weeks were calculated. The final tumor volume was calculated according to the equation: Tumor volume (mm^3) = tumor length (mm) × tumor width (mm)2/2.

2.7. Statistics. Data were represented as mean ± SD. The statistical significance of the difference was evaluated by Student's t test, and $p < 0.05$ was considered significant.

3. Results

3.1. COPS3 Was Highly Expressed in COAD. We first detected the expression levels of COPS3 in COAD tissues through the analysis in TCGA database. We noticed that the transcript per million of COPS3 in primary tumor tissues ($n = 286$) was higher than normal ($n = 41$), suggesting the high expression in COAD (Figure 1(a)). COPS3 mRNA level increased, indicating that COPS3 high expression may be transcriptional. We then detected the expression of COPS3 in normal cell line NCM460 and 4 COAD cell lines, including SW480, HCT116, LoVo, and DLD-1, through qPCR and immunoblot assays. We found that COPS3 was highly expressed in COAD cell lines at mRNA and protein levels (Figures 1(b) and 1(d)). We therefore thought that COPS3 was highly expressed in COAD.

3.2. COPS3 Depletion Suppressed the Viability of COAD Cells and Stimulated Apoptosis. Then, the effects of COPS3 on the viability and apoptosis of COAD cells were evaluated by the transfection of its siRNA in COAD cells including SW480 and HCT116. qPCR and immunoblot confirmed that the transfection of its siRNA decreased the expression of COPS3, compared to the control and NC-siRNA groups in these cells at mRNA and protein levels (Figures 2(a) and 2(b)). Through CCK-8 assays, we found that COPS3 ablation decreased the OD value at 450 nm wavelength, suggesting the inhibition of cell viability (Figure 2(c)). Further through colony formation, we found that the knockdown of COPS3 also decreased colony number in SW480 and HCT116 cells (Figures 2(d) and 2(e)). In addition, FCM assays showed that the depletion of COPS3 contributed to the apoptosis of SW480 and HCT116 cells, with the increased percentage of apoptosis cells (Figures 2(f) and 2(g)). We further detected the expression of cleaved caspase-3 and Bcl-2 in control and COPS3 siRNA cells and further confirmed the previous conclusion (Figure 2(h)). Therefore, COPS3 depletion suppressed the viability of COAD cells and stimulated apoptosis.

3.3. The Knockdown of COPS3 Suppressed the Motility of COAD Cells. We then detected the effects of COPS3 on the motility of COAD cells. We found that its ablation increased the wound width at 24th hour time point, in SW480 and

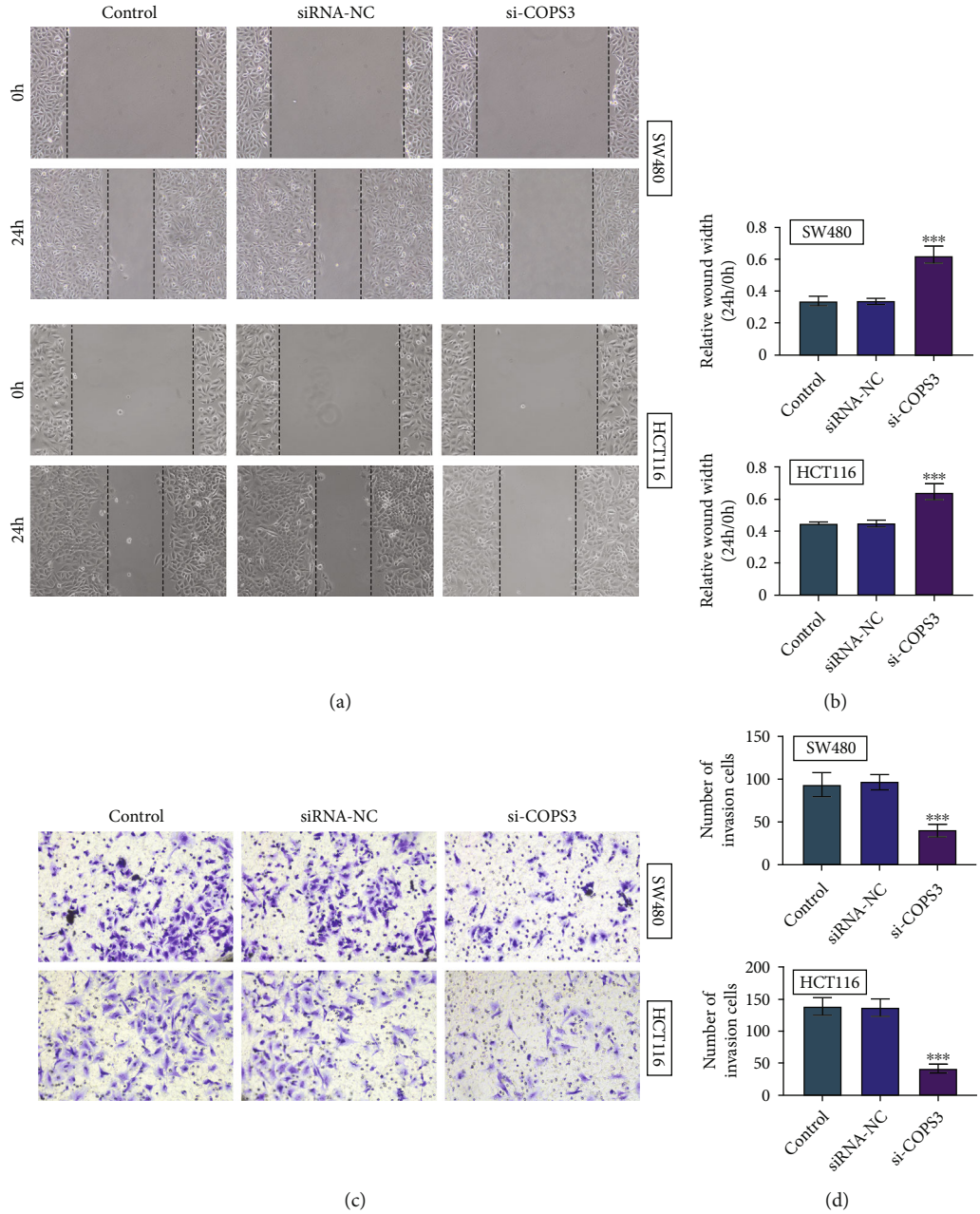

Figure 3: COPS3 knockdown inhibited the migration as well as invasion of COAD cells. (a and b) Wound closure assays showed the wound healing degree of SW480 and HCT116 cells upon the transfection of control or COPS3 siRNAs or without transfection (control). The representative images were shown in (a). The wound width was shown in (b). (c and d). Transwell assays showed the invasive SW480 and HCT116 cells upon the transfection of control or COPS3 siRNAs or without transfection (control). The representative images were shown in (c). The invasive cell number was shown in (d). Data are presented as mean ± SD. $^{**}p < 0.01$ and $^{***}p < 0.001$, siCOPS3 vs. siControl.

HCT116 cells (Figures 3(a) and 3(b)). We therefore thought depletion of COPS3 suppressed COAD cell migration. Further, we found its knockdown suppressed the invasion of SW480 and HCT116 cells, with the decreased number of invasive cells (Figures 3(c) and 3(d)). Therefore, COAD3 knockdown inhibited the motility of COAD cells.

3.4. Knockdown of COPS3 Suppressed the EMT in COAD Cells. Since previously we showed the effects of COPS3 on COAD3 cell viability and migration, we then investigated its role in the COAD cell EMT process. We detected the expression of several EMT markers. Through immunoblot assays, we found that COPS3 knockdown increased the protein levels of E-cadherin and downregulation of N-cadherin and Vimentin, in both SW480 and HCT116 cells (Figure 4). Therefore, depletion of COPS3 suppressed the EMT process in COAD cells.

3.5. COPS3 Mediated the MEK/ERK Pathway in COAD Cells. Then, we investigated the possible mechanism underlying

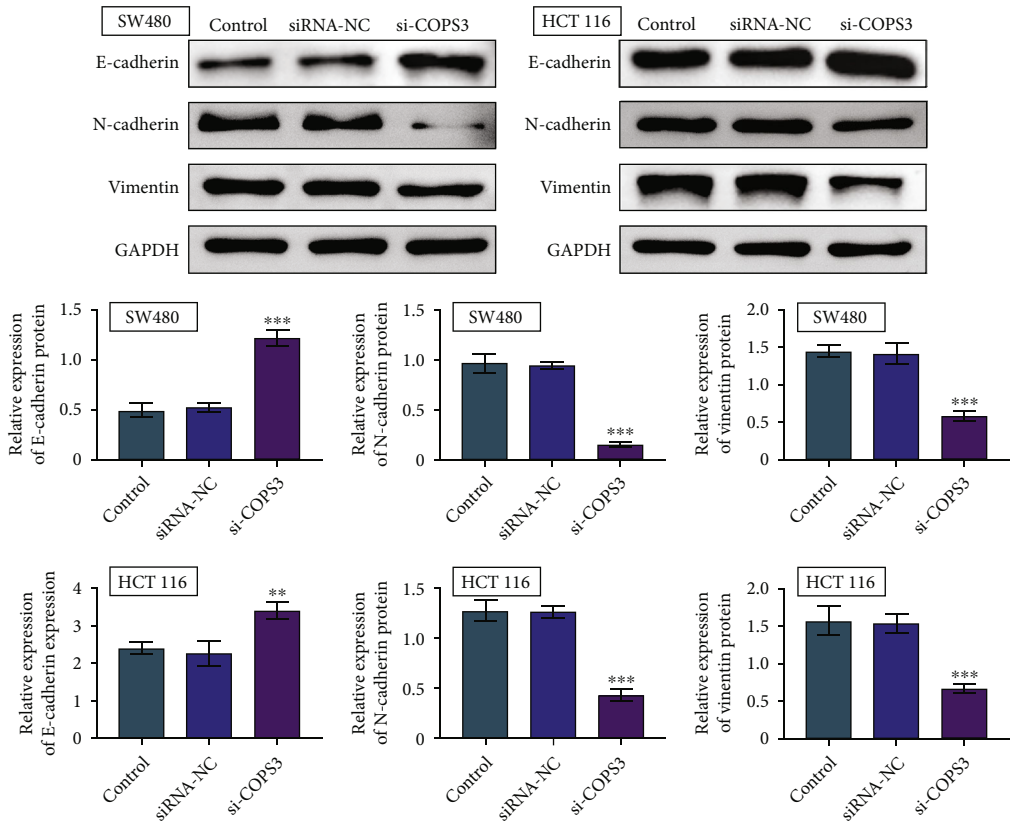

Figure 4: Depletion of COPS3 suppressed the EMT process in COAD cells. Immunoblot assays showed the expression of E-cadherin, N-cadherin, and Vimentin in SW480 and HCT116 cells upon the transfection of control or COPS3 siRNAs or without transfection (control). Data are presented as mean ± SD. $^{**}p < 0.01$ and $^{***}p < 0.001$, siCOPS3 vs. siControl.

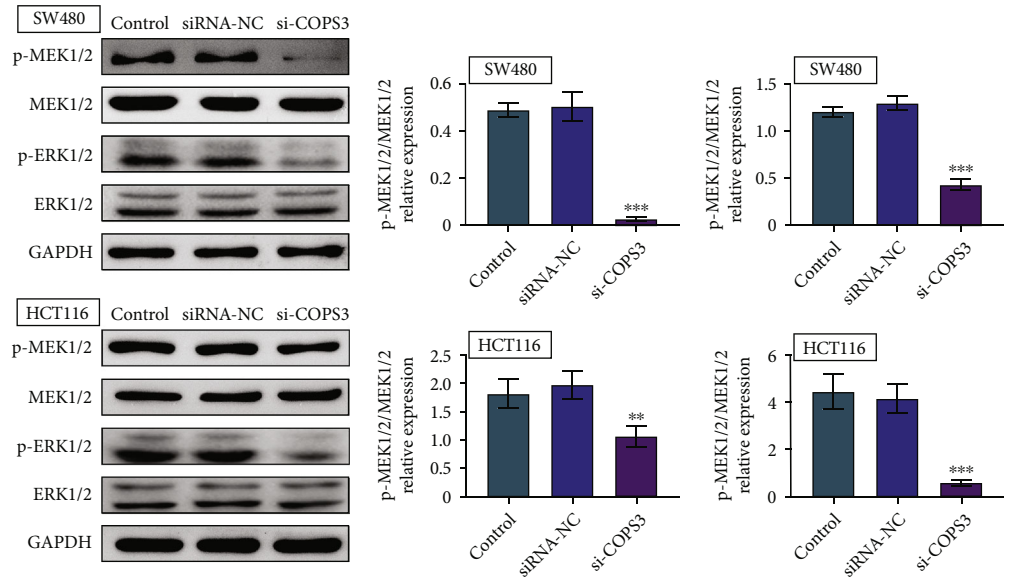

Figure 5: COPS3 mediated the MEK/ERK pathway in COAD cells. Immunoblot assays showed the expression of phosphorylated MEK and ERK and expression of these proteins in SW480 and HCT116 cells upon the transfection of control or COPS3 siRNAs or without transfection (control). Data are presented as mean ± SD. $^{**}p < 0.01$ and $^{***}p < 0.001$, siCOPS3 vs. siControl.

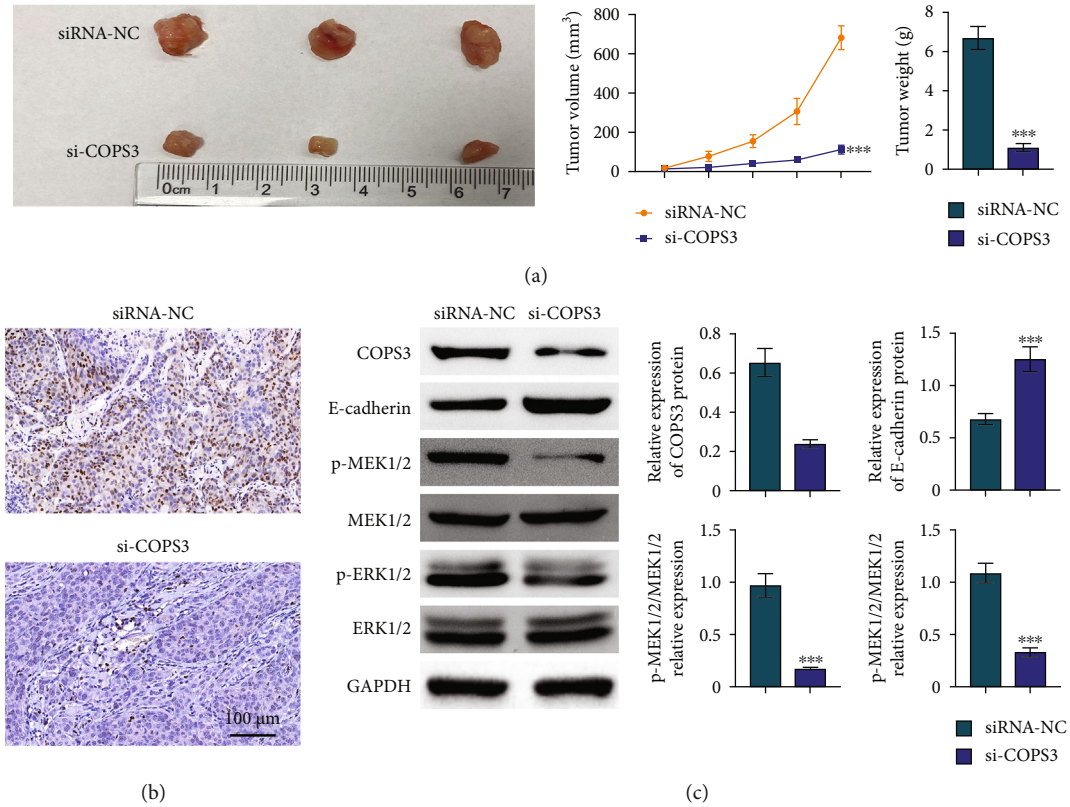

Figure 6: COPS3 depletion suppressed tumor growth *in vivo*. (a) The representative images of tumors in control and COPS2 siRNA transfection mice and the tumor growth curve. (b) IHC assays showed the expression of COPS2 in tumors in control and COPS2 siRNA transfection mice. (c) Immunoblot showed the expression of COPS2, E-cadherin, Erk, p-Erk, Mek, and p-Mek in tumors from control and COPS2 siRNA transfection mice. Data are presented as mean ± SD. $^{***}p < 0.001$, siCOPS3 vs. siControl.

COPS3 affecting COAD progression. The previous study indicated the effects of COPS3 on the MEK/ERK pathway, which could mediate the proliferation, motility, and EMT in several types of tumor cells [12]. We then detected whether COPS3 could mediate this pathway in COAD cells. Through immunoblot assays, the knockdown of COPS3 decreased the phosphorylation levels of MEK and ERK in both SW480 and HCT116 cells (Figure 5). Therefore, we thought COPS3 could mediate the MEK/ERK in COAD cells.

3.6. COPS3 Depletion Suppressed Tumor Growth In Vivo. To further confirm whether COPS3 deficiency was able to repress tumor growth, the in vivo assays were constructed. Through injection of COPS3 deficiency HCT116 cells into nude mice, we measured and calculated the growth curves of tumors. Consistent with our hypothesis, the volumes of tumors in COPS3-depleted groups were markedly smaller than the negative control groups (Figure 6(a)). To ulteriorly identify the silencing efficiency of COPS3 siRNA, we detected the expression of COPS3 in tumor tissues of mice via IHC and immunoblot assays, and the data revealed that compared with the negative groups, the protein levels of COPS3 were efficiently restrained by COPS3 siRNA in the COPS3 depletion groups (Figures 6(b) and 6(c)). We further detected the expression of E-cadherin, Erk, p-Erk, Mek, and p-Mek through immunoblot, and the data further confirmed our previous conclusion (Figure 6(d)). Therefore, COPS3 depletion suppressed tumor growth in vivo.

4. Discussion

CRC is a common gastrointestinal malignancy occurring in the colon [18]. CRC inchoate symptom is more not apparent and often already was in progress period when seeing a doctor, right now commonly used remedial measure [2]. To improve the resection rate, reduce the recurrence rate, and improve the survival rate, the treatment of intermediate and advanced CRC is based on surgery, supplemented by chemotherapy, immunotherapy, traditional Chinese medicine, and other supportive therapies [18]. Recently, targeted therapy has made a series of positive progress and has great potential to improve the survival rate of patients with advanced colorectal cancer [19]. However, there are new and more therapeutic targets for the CRC treatment. Here, we noticed that COPS3 was highly expressed in COAD. It affected the viability, motility, and EMT of COAD cells. We thought it could act as a target of COAD.

Through a series of in vitro assays, we concluded that COPS3 was highly expressed in human COAD cells. We further confirmed its effects on the viability, motility, and the process of EMT in COAD cells. COPS3 is an important oncogene involved in metastasis of osteosarcoma [9]. COPS3 depletion could inhibit the growth of lung cancer

and liver cancer cells and induce apoptosis [13, 20]. A previous study also revealed that COPS3 played a vital role in linking Raf-1/MEK/ERK pathway and autophagic regulation in osteosarcoma [12]. Depletion of COPS3 could suppress the progression of prostate cancer through reducing phosphorylated p38 MAPK and impairs the EMT [21]. In addition, the overexpression of COPS3 could contribute to the progression of clear cell renal cell carcinoma (ccRCC) via regulation of phospho-AKT, Cyclin D1, and Caspase-3 [22]. The ablation of COPS3 suppressed the proliferation of lung cancer cells via induction of cell cycle arrest and stimulation of apoptosis [13]. These studies with our findings confirmed that COPS3 could serve as a promising target of cancers.

The multiple biological functions of COPS3 have been widely revealed [10]. COP9S3 played a role in regulating mouse oocytes meiosis by regulating MPF activity and securing degradation [23]. The COPS3 is necessary for early embryo survival by way of a stable protein deposit in mouse oocytes [24]. COPS3 is also poised to facilitate communication between the extracellular matrix and the nucleus [25]. Therefore, we guess that COPS3 could induce the deubiquitination of the downstream proteins or the protein kinase activity and therefore mediate the progression of COAD. However, the precise mechanism needs further study.

MEK/ERK signaling pathway can promote the progression of multiple types of cancers, including COAD [26]. The MEK/ERK pathway has been revealed to affect the proliferation, apoptosis, and motility of tumors and affect the EMT progression [12]. Multiple proteins or drugs affected COAD progression via this pathway. For example, Verticillin A could increase the BIM/MCL-1 ratio to overcome ABT-737 resistance in COAD cells by this pathway [27]. These studies all confirmed that MEK/ERK pathway could serve as a promising target of COAD.

In summary, we noticed the high expression of COPS3 in COAD cells. COPS3 contributed to the viability, motility, and EMT of COAD cells via MEK/ERK pathway. We therefore thought COPS3 could serve as a target of COAD.

Data Availability

All data generated or analyzed during this study are included in this published article.

Conflicts of Interest

The authors state that there are no conflicts of interest to disclose.

Authors' Contributions

Yanchao Xie designed the study and supervised the data collection, Zhijiang Wei analyzed the data and interpreted the data, and Chi Cheng prepared the manuscript for publication and reviewed the draft of the manuscript. All authors have read and approved the manuscript.

References

[1] Y. Jin, L. Meng, H. Yang et al., "The *IL-22* gene rs2227478 polymorphism significantly decreases the risk of colorectal cancer in a Han Chinese population," *Pathology, research and practice*, vol. 228, article 153690, 2021.

[2] D. Lucchetti, I. V. Zurlo, F. Colella et al., "Mutational status of plasma exosomal KRAS predicts outcome in patients with metastatic colorectal cancer," *Scientific Reports*, vol. 11, no. 1, p. 22686, 2021.

[3] A. Zuhan, I. Riwanto, D. E. Listiana, F. Djannah, and R. M. Rosyidi, "The extent of distal intramural spread of colorectal cancer cell study of it's relationship with histological grading, stage of disease and CEA level," *Annals of medicine and surgery*, vol. 64, p. 102227, 2021.

[4] A. Ottaiano, L. Circelli, M. Santorsola et al., "Metastatic colorectal cancer and type 2 diabetes: prognostic and genetic interactions," *Molecular oncology*, vol. 16, no. 2, pp. 319–332, 2022.

[5] V. Lago, L. Sala Climent, B. Segarra-Vidal, M. Frasson, B. Flor, and S. Domingo, "Ghost ileostomy: prevention, diagnosis, and early treatment of colorectal anastomosis leakage in advanced ovarian cancer," *International journal of gynecological cancer*, vol. 32, no. 1, pp. 109-110, 2022.

[6] Y. Luan, M. Li, Y. Zhao et al., "Centrosomal-associated proteins: potential therapeutic targets for solid tumors?," *Biomedicine & pharmacotherapy*, vol. 144, article 112292, 2021.

[7] J. Nian, L. Tao, and W. Zhou, "Prior endoscopic resection does not affect the outcome of secondary surgery for T1 colorectal cancer, a systematic review and meta-analysis," *International journal of colorectal disease*, vol. 37, no. 2, pp. 273–281, 2022.

[8] E. Oron, M. Mannervik, S. Rencus et al., "COP9 signalosome subunits 4 and 5 regulate multiple pleiotropic pathways in Drosophila melanogaster," *Development*, vol. 129, no. 19, pp. 4399–4409, 2002.

[9] T. Yan, J. S. Wunder, N. Gokgoz et al., "COPS3 amplification and clinical outcome in osteosarcoma," *Cancer*, vol. 109, no. 9, pp. 1870–1876, 2007.

[10] M. van Dartel and T. J. Hulsebos, "Amplification and overexpression of genes in 17p11.2 ~ p12 in osteosarcoma," *Cancer genetics and cytogenetics*, vol. 153, no. 1, pp. 77–80, 2004.

[11] J. Both, T. Wu, A. L. Ten Asbroek, F. Baas, and T. J. Hulsebos, "Oncogenic properties of candidate oncogenes in chromosome region 17p11.2p12 in human osteosarcoma," *Cytogenetic and genome research*, vol. 150, no. 1, pp. 52–59, 2017.

[12] F. Zhang, T. Yan, W. Guo et al., "Novel oncogene COPS3 interacts with Beclin1 and Raf-1 to regulate metastasis of osteosarcoma through autophagy," *Journal of experimental & clinical cancer research : CR.*, vol. 37, no. 1, p. 135, 2018.

[13] J. Pang, X. Yan, H. Cao et al., "Knockdown of COPS3 inhibits lung cancer tumor growth in nude mice by blocking cell cycle progression," *Journal of Cancer*, vol. 8, no. 7, pp. 1129–1136, 2017.

[14] J. Xue, Y. Li, J. Yi, and H. Jiang, "HAVCR1 affects the MEK/ERK pathway in gastric adenocarcinomas and influences tumor progression and patient outcome," *Gastroenterology research and practice*, vol. 2019, Article ID 6746970, 10 pages, 2019.

[15] P. Zhang, H. Kawakami, W. Liu et al., "Targeting CDK1 and MEK/ERK overcomes apoptotic resistance in BRAF-mutant human colorectal cancer," *Molecular cancer research : MCR*, vol. 16, no. 3, pp. 378–389, 2018.

[16] N. L. Tran, R. B. Nagle, A. E. Cress, and R. L. Heimark, "N-cadherin expression in human prostate carcinoma cell lines. An epithelial-mesenchymal transformation mediating adhesion with stromal cells," *The American journal of pathology*, vol. 155, no. 3, pp. 787–798, 1999.

[17] X. Zhang, G. Liu, Y. Kang, Z. Dong, Q. Qian, and X. Ma, "N-cadherin expression is associated with acquisition of EMT phenotype and with enhanced invasion in erlotinib-resistant lung cancer cell lines," *PLoS One*, vol. 8, no. 3, article e57692, 2013.

[18] W. Song, J. Ren, R. Xiang, C. Kong, and T. Fu, "Identification of pyroptosis-related subtypes, the development of a prognosis model, and characterization of tumor microenvironment infiltration in colorectal cancer," *Oncoimmunology*, vol. 10, no. 1, p. 1987636, 2021.

[19] H. H. Hasbullah and M. Musa, "Gene therapy targeting p53 and KRAS for colorectal cancer treatment: a myth or the way forward?," *International journal of molecular sciences*, vol. 22, no. 21, article 11941, 2021.

[20] Y. S. Yu, Z. H. Tang, Q. C. Pan, X. H. Chen, X. N. Liu, and G. Q. Zang, "Inhibition of Csn3 expression induces growth arrest and apoptosis of hepatocellular carcinoma cells," *Cancer Chemotherapy and Pharmacology*, vol. 69, no. 5, pp. 1173–1180, 2012.

[21] Z. Zhu, Y. Hong, F. Zhang et al., "Knockdown of COPS3 inhibits the progress of prostate cancer through reducing phosphorylated p38 MAPK expression and impairs the epithelial-mesenchymal transition process," *The Prostate*, vol. 79, no. 16, pp. 1823–1831, 2019.

[22] Y. Hong, X. Huang, L. An et al., "Overexpression of COPS3 promotes clear cell renal cell carcinoma progression via regulation of phospho-AKT(Thr308), cyclin D1 and caspase-3," *Experimental cell research*, vol. 365, no. 2, pp. 163–170, 2018.

[23] E. Kim, S. J. Yoon, E. Y. Kim et al., "Function of COP9 signalosome in regulation of mouse oocytes meiosis by regulating MPF activity and securing degradation," *PLoS One*, vol. 6, no. 10, article e25870, 2011.

[24] S. Israel, H. C. A. Drexler, G. Fuellen, and M. Boiani, "The COP9 signalosome subunit 3 is necessary for early embryo survival by way of a stable protein deposit in mouse oocytes," *Molecular human reproduction*, vol. 27, no. 8, 2021.

[25] C. Hunter, J. Evans, and M. L. Valencik, "Subunit 3 of the COP9 signalosome is poised to facilitate communication between the extracellular matrix and the nucleus through the muscle-specific beta1D integrin," *Cell communication & adhesion*, vol. 15, no. 3, pp. 247–260, 2008.

[26] N. Cui, L. Li, Q. Feng, H. M. Ma, D. Lei, and P. S. Zheng, "Hexokinase 2 promotes cell growth and tumor formation through the Raf/MEK/ERK signaling pathway in cervical cancer," *Frontiers in oncology*, vol. 10, p. 581208, 2020.

[27] Y. Guan, K. Tu, Q. Huang, and F. Liu, "Verticillin A increases the BIMEL/MCL-1 ratio to overcome ABT-737-resistance in human colon cancer cells by targeting the MEK/ERK pathway," *Biochemical and biophysical research communications*, vol. 567, pp. 22–28, 2021.

Hindawi
Disease Markers
Volume 2022, Article ID 4399334, 20 pages
https://doi.org/10.1155/2022/4399334

Research Article

Evodiamine as the Active Compound of Evodiae fructus to Inhibit Proliferation and Migration of Prostate Cancer through PI3K/AKT/NF-κB Signaling Pathway

Yuhe Lei,[1] **Meiching Chan**,[2] **Haiyan Liu**,[3] **Wenyu Lyu**,[4] **Lei Chen**,[1] **Yinqin Zhong**,[1] **Hua Gan**,[2] **Mei Wang**,[2] **Ming Qi**,[4] **Yu Guo**,[5] **Junshan Liu**,[6,7,8] **and Enxin Zhang**[1]

[1]*Shenzhen Hospital of Guangzhou University of Chinese Medicine, Shenzhen, 518034 Guangdong, China*
[2]*Formula-Pattern Research Center, School of Traditional Chinese Medicine, Jinan University, Guangzhou, 510632 Guangdong, China*
[3]*Second Clinical Medical College of Guangzhou University of Traditional Chinese Medicine, Guangzhou, 510006 Guangdong, China*
[4]*College of Pharmacy, Jinan University, Guangzhou, 510632 Guangdong, China*
[5]*School of Traditional Chinese Medicine, Jinan University, Guangzhou, 510632 Guangdong, China*
[6]*School of Traditional Chinese Medicine, Southern Medical University, Guangzhou, 510510 Guangdong, China*
[7]*Department of Pharmacy, Zhujiang Hospital, Southern Medical University, Guangzhou, 510280 Guangdong, China*
[8]*Guangdong Provincial Key Laboratory of Chinese Medicine Pharmaceutics, Southern Medical University, Guangzhou 510510, China*

Correspondence should be addressed to Enxin Zhang; ergep53@126.com

Received 7 April 2022; Accepted 30 June 2022; Published 18 July 2022

Academic Editor: Jian Wu

Evodiae fructus (EF) is a traditional Chinese medicine which is widely used for the treatment of obesity, inflammation, cardiovascular disease, and diseases of the central nervous system. Recent studies have demonstrated the anticancer property of EF, but the active compounds of EF against prostate cancer and its underlying mechanism remain unknown. In this study, a network pharmacology-based approach was used to explore the multiple ingredients and targets of EF. Through protein-protein interaction (PPI), Gene Ontology (GO) enrichment, and Kyoto Encyclopedia of Genes and Genomes (KEGG) pathway enrichment analyses, the potential targets and corresponding ingredients of EF against prostate cancer cells were obtained. CCK8 and colony formation assays were performed to evaluate the antiproliferative effect of the active compounds on DU145 cells. Cell cycle analysis, Annexin V-FITC/PI staining assay, and Hoechst 33258 staining assay were used to explore the way of evodiamine-induced cell death. The capacities of cell migration after evodiamine treatment were evaluated by wound-healing assay. PharmMapper database was used to predict the potential targets of evodiamine against cancer cell migration. Western blot assay was performed to investigate the signaling pathway through which evodiamine inhibits cell proliferation and migration. The binding of evodiamine to PI3K and AKT was verified by molecular docking. As a consequence, 24 active compounds and 141 corresponding targets were obtained through a network pharmacology-based approach. The results of PPI analysis, GO enrichment, and KEGG pathway enrichment indicated that molecules in the PI3K/AKT/NF-κB signaling pathway were the potential targets of EF against prostate cancer, and evodiamine was the potential active compound. *In vitro* study demonstrated that evodiamine displays antiproliferative effect on DU145 cells obviously. Evodiamine induces G_2/M cell cycle arrest by Cdc25c/CDK1/cyclin B1 signaling. Additionally, evodiamine also promotes mitochondrial apoptosis and inhibits cell migration through PI3K/AKT/NF-κB signaling in DU145 cells. In conclusion, evodiamine is the active compound of EF to inhibit proliferation and migration of prostate cancer through PI3K/AKT/NF-κB signaling pathway, indicating that evodiamine may serve as a potential lead drug for prostate cancer treatment.

1. Introduction

Prostate cancer remains a huge challenge to men's health worldwide. It is reported that the incidence and mortality of prostate cancer ranks the second in males [1]. The treatments of prostate cancer include radiotherapy, chemotherapy, surgery, and hormonal therapy [2]. However, these treatments, particularly the standard androgen deprivation therapy (ADT), are not curative and easily result in resistance to therapeutic interventions [3]. Therefore, seeking efficient drugs with low toxicity is an urgent task for prostate cancer treatment.

Herbal medicine plays a major role in the prevention and treatment of cancers and other diseases worldwide, especially in Asian countries [4]. Numerous studies have demonstrated that a wide spectrum of traditional Chinese medicines (TCMs) possess anticancer properties, such as Scutellariae Barbatae Herba, Andrographis Herba, and Panax Ginseng C. A. Mey [5]. Screening natural compounds from TCM has attracted extensive attention. More and more promising compounds with potential anticancer activity, such as podophyllotoxin, camptothecin, and berberine, have been isolated from TCM [6, 7]. In recent years, "integrated pharmacology" (IP) has come into sight. It uses a network pharmacology approach to explore the synergistic effects of multiple ingredients, targets, and mechanisms of diseases based on multiple databases, which is perfect for TCM research [8]. Evodiae fructus (EF), a fruit of Tetradium ruticarpum, has been used in traditional Chinese herbal formulas for a long time. Numerous studies have revealed the therapeutic potential of EF on various diseases including obesity, inflammation, cardiovascular disease, cancers, and diseases of the central nervous system [9]. However, the active compounds of EF against prostate cancer and its underlying mechanism remain unknown.

Inhibiting cancer cell growth and metastasis constitute the major aspects in anticancer strategies. Cell migration is essential for tumor metastasis to colonize remote sites, frequently resulting in cancer deaths [10]. The phosphoinositide-3-kinase/protein kinase B (PI3K/AKT) signaling pathway participates in various biological processes including cell growth, survival, metabolism, invasion, and migration [11, 12]. PI3K/AKT signaling is aberrantly activated in a high proportion of prostate cancer patients [13]. PI3Ks are a class of heterodimers consisting of a catalytic subunit and a regulatory subunit [14]. AKT, a serine/threonine kinase, modulates the function of multiple substrates such as mTOR, NF-κB, MDM2, and Bad [15]. Nuclear factor kappaB (NF-κB), a transcription factor, translocates to the nucleus to facilitate oncogene transcription after activation in response to various stimuli [16]. Augmented phosphorylation of PI3K/AKT/NF-κB signaling pathway has been confirmed to correlate to prostate cancer progression [17].

In this study, we identified evodiamine as the active compound of EF through a network pharmacology approach and evaluated the antiproliferative effects of evodiamine on prostate cancer DU145 cells. Further mechanistic study demonstrated that evodiamine induces mitochondrial apoptosis and inhibits migration of prostate cancer cells through PI3K/AKT/NF-κB signaling pathway. This study will provide a rationale for using evodiamine as the potential lead drug for prostate cancer treatment.

2. Materials and Methods

2.1. Reagents and Antibodies. The chemical compounds evodiamine, rutaecarpine, berberine, quercetin, and β-sitosterol were purchased from Baoji Herbest Bio-Tech Co., Ltd. (Baoji, Shanxi, China). The Cell Counting Kit-8 (CCK8) was obtained from Good Laboratory Practice Bioscience (California, Montclair, USA). The Hoechst 33258 was supplied by Beijing Solarbio Science & Technology Co., Ltd. (Beijing, China). The Annexin V-FITC/PI staining assay kit was purchased from Dalian Meilun Biotechnology Co., Ltd. (Dalian, Liaoning, China). Propidium iodide, crystal violet, and RNase were obtained from Sigma-Aldrich (St. Louis, MO, USA). The BCA protein quantitation assay kit was supplied by KeyGEN BioTECH (Nanjing, Jiangsu, China). The primary antibodies against CDK1, p-CDK1^{Thr14}, cyclin B1, p-Cdc25C^{Ser216}, Bax, Bcl-2, AKT, β-actin, p-AKT^{Ser473}, NF-κB, PARP, and PI3K were purchased from Proteintech (Wuhan, Hubei, China). The anti-PI3K p85 (phospho Y458)+PI3 kinase p55 (phospho Y199) antibody [PI3KY458-1A11] was supplied by Abcam (Shanghai, China). The primary antibodies against pro- and cleaved-caspase 3/9 were obtained from Abscitech (Shanghai, China). The primary antibodies against p-NF-κB^{Ser536} and the secondary antibodies anti-rabbit IgG and antimouse IgG were obtained from Cell Signaling Technology (Danvers, MA, USA). Other reagents were obtained from Sigma-Aldrich (St. Louis, MO, USA).

2.2. Compounds and Targets Screening of EF. The traditional Chinese medicine system pharmacology (TCMSP) database, a unique system pharmacology platform of Chinese herbal medicines [18], was used to search for the ingredients and targets of EF. To obtain the active compounds of all the ingredients according to ADME (absorption, distribution, metabolism, and excretion) properties, we selected the compounds which meet the requirements of both oral bioavailability $\geq 30\%$ [15] and drug – likeness $(DL) \geq 0.18$. The information of the active compounds and their related targets was collected for further research. UniProt (https://www.uniprot.org) was used to convert protein names to gene symbols.

2.3. Prediction of Potential Targets of EF on Prostate Cancer. The known therapeutic targets of prostate cancer were obtained from the GeneCards database (https://www.genecards.org). Key terms "prostate cancer," "prostate adenocarcinoma," and "prostatic cancer" were retrieved, and the requirement of relevance score ≥ 5 was set. After getting the disease-related genes, we selected the target genes at the intersection of EF and prostate cancer (E&P), which were regarded as potential target genes of EF against prostate cancer. The chemical compounds corresponding to E&P targets were considered as therapeutic components of EF against prostate cancer.

2.4. Drug-Compound-Target-Disease Network Construction. Based on the active compounds and corresponding targets of E&P, we employed cytoscape (v3.8.0, Agilent Technologies Company, USA) to visualize the drug-compound-target-disease network. Each node in the network represents a drug, disease, target, or compound. Each line in the network represents the connection of drug-compound, compound-target, and target-disease.

2.5. Protein-Protein Interaction (PPI) Network Analysis. The PPI network of E&P targets was obtained from the STRING database (https://string-db.org/). Gene symbols of the targets were submitted to the STRING database, and the required interaction score is high confidence (≥0.700). The bitmap image and simple tabular text output were downloaded from this website. After enrichment of all the nodes, the top 20 targets, which were considered to be of significance in the PPI network, were selected.

2.6. Gene Ontology (GO) Enrichment and KEGG Pathway Enrichment. GO enrichment and KEGG pathway enrichment analyses were based on the Bioconductor software (http://bioconductor.org/). We used the R statistical programming language (cluster-profiler version 4.1) to load the Bioconductor source and gene symbols of E&P. The results of GO enrichment and KEGG enrichment were considered significant when P value < 0.05. The top 20 targets in GO and KEGG enrichment were displayed in barplot and dotplot.

2.7. Cell Line and Cell Culture. The human prostate cancer cell line DU145 was obtained from the Chinese Academy of Sciences Cell Bank (Shanghai, China). Cells were cultured in RPMI 1640 supplemented with 10% fetal bovine serum (FBS) and 1% penicillin-streptomycin (PS) in 5% CO_2 containing incubator at 37°C. The DU145 cell line was identified by short tandem repeat (STR) profiling and tested for mycoplasma (Genetic Testing Biotechnology Inc., Suzhou, Jiangsu, China).

2.8. Cell Viability Assay. Viability of DU145 cells was measured using the Cell Counting Kit-8 (CCK8) assay. Cells (5,000/well) were seeded into 96-well plates and cultured overnight. After treatment with different concentrations of evodiamine, rutaecarpine, berberine, quercetin, and β-sitosterol for 72 h, the cells were exposed to 100 μL/well-diluted CCK8 solution. Then, the light absorbance was detected at 450 nm by a microplate reader (Beckman Coulter Inc., USA).

2.9. Colony Formation Assay. DU145 cells were cultured in 6-well plates (2000 cells/well) for 24 h. Then, the cells were exposed to evodiamine at the concentrations of 0, 1.25, 2.5, and 5.0 μM for 48 h. After washing with phosphate-buffered saline (PBS), cells were cultured in the fresh medium which was replaced every three days. After ten days, the cells were fixed in 75% alcohol for 10 min at 4°C and stained with 1% crystal violet for 30 min. After washing twice with PBS, the number of colonies > 0.5 mm in diameter was counted manually, and the images of colonies were photographed.

2.10. Cell Cycle Analysis. DU145 cells (2×10^5/well) were seeded in 6-well plates and cultured overnight. After treatment with evodiamine at the concentrations of 0, 1.25, 2.5, and 5.0 μM for 24 h, cells were fixed and permeabilized with precooled 75% ethanol at 4°C overnight. Then, cells were incubated with PI (0.2 mg/mL) and RNase (0.1 mg/ml) for 15 min in the dark at room temperature. The Epics XL Flow cytometry (Beckman Coulter, USA) was used to detect the PI fluorescence. The phase distribution of cell cycle was analyzed by the ModFit LT v3.1 software (Verity Software House, Inc.)

2.11. Annexin V-FITC/PI Staining Assay. Cell apoptotic rate was measured by Annexin V-FITC/PI staining assay. Cells (1×10^5/well) were seeded in 6-well plates and cultured overnight. After treatment with evodiamine at the concentrations of 0, 1.25, 2.5, and 5.0 μM for 24 h, DU145 cells were collected and stained with Annexin V-FITC for 15 min and PI for 5 min in darkness at room temperature. Then, Epics XL flow cytometer (Beckman Coulter Inc.) was used to measure the cell apoptotic rates (excitation = 488 nm and emission = 525 nm for Annexin V-FITC; excitation = 488 nm and emission = 620 nm for PI). The data was quantified using the FlowJo v7.6 software (FlowJo LLC).

2.12. Hoechst 33258 Staining Assay. DU145 cells (2×10^5 /well) were seeded into 6-well plates. After culture for 24 h, cells were treated with evodiamine at the concentrations of 0, 1.25, 2.5, and 5.0 μM for 24 h. Then, PBS was added to wash the cells. After fix for 30 min, the cells were stained with Hoechst 33258 (1 mg/mL) for 30 min at 37°C. A fluorescence microscope (Carl Zeiss, Jena, Germany) was applied to observe the nuclear morphology of DU145 cells.

2.13. Western Blot Analysis. Following treatment with different concentrations of evodiamine for 24 h, DU145 cells were collected using trypsin. Then, the RIPA lysis buffer (containing 1 mM PMSF, 1× phosphatase inhibitor, and 1× protease inhibitor) was added to obtain the total cellular protein. The BCA assay was performed to quantify the protein concentration. Proteins (30 μg/lane) were separated by 12% SDS-PAGE gels and then transferred to PVDF membranes. The membranes were blocked with 5% skimmed milk at room temperature for 1 h. After incubation with primary antibody overnight at 4°C and secondary antibody for 1 h at room temperature, the protein bands were visualized by ECL detection kit (Millipore, Merck KGaA) and quantified using the ImageJ software v1.8.0 (National Institutes of Health). β-Actin was used as the loading control.

2.14. Wound-Healing Assay. DU145 cells (2×10^5/well) were seeded into 6-well plates and cultured. After reaching 80% confluency, cells were scratched in a straight line with 200 μL pipette tips. Then, different concentrations of evodiamine (0.5 and 1.0 μM) in serum-free medium were added. Images of cells treated with different time (0, 6, 12, and

24 h) were acquired with an Olympus IX70 inverted microscope (Shinjuku, Tokyo, Japan).

2.15. Prediction of Potential Targets of Evodiamine on Cell Migration. The potential targets of evodiamine were obtained from PharmMapper database (http://www.lilabecust.cn/pharmmapper/), an updated integrated pharmacophore matching platform that can be used to identify potential target candidates for given small molecules using a pharmacophore mapping approach [19]. The chemical structure of evodiamine submitted to the PharmMapper website was downloaded from the PubChem database (https://pubchem.ncbi.nlm.nih.gov). The known therapeutic targets of cancer metastasis were obtained from the GeneCards database. Key term "cancer cell migration" was retrieved, and the requirement of relevance score ≥ 20 was set. After getting the cell migration-related genes, we selected the targets at the intersection of evodiamine and cell migration (E&M), which were regarded as potential target genes of evodiamine against cell migration.

2.16. Molecular Docking. PDB database (https://www.pdbus.org/) was used to search for the conformational information of PIK3CG (PDB ID: 6AUD) and AKT1 (PDB ID: 4GV1). After removing irrelevant small molecules in the crystal structure by the Pymol 2.1 software and adding with Kollman atom charges, solvation parameters, and polar hydrogens by AutoDock Tools (1.5.6 software), PIK3CG and AKT1 were used as the receptors. The PubChem database (https://pubchem.ncbi.nlm.nih.gov) was used to obtain the chemical structure of evodiamine. Then, we minimized the energy of evodiamine by Chem3D and converted it into mol2 format. After adding with atomic charge and assigning an atomic type by AutoDock Tools, evodiamine was used as the ligand. Then, the ligand and receptors were imported into AutoDock 4.2 to start the docking process. The free energy of binding in the receptor was calculated through Lamarckian genetic algorithm. Then, Pymol 2.1 was used to visualize the binding of evodiamine to PIK3CG and AKT1.

2.17. Statistical Analysis. All experiments were performed in triplicate. Results are presented as the mean ± standard deviation (SD). For the statistical analysis, GraphPad Prism 7.0 (GraphPad Software Inc.) was used to evaluate one-way analysis of variance (ANOVA) followed by Tukey's post hoc test. $P < 0.05$ was considered statistically significant.

3. Results

3.1. Screening of Active Compounds and Potential Targets of EF against Prostate Cancer. After retrieval in TCMSP, 176 compounds of EF and 1504 related targets were obtained. We selected 30 active compounds that met the requirements of both oral bioavailability $\geq 30\%$ [15] and drug − likeness (DL) ≥ 0.18, as well as 197 corresponding targets. They form 501 compound-target connections. After retrieval in the GeneCards database, 11719 prostate cancer-related targets were collected and 2340 of them met the requirement of relevance score ≥ 5. We obtained the intersections between 197 drug targets and 2340 disease targets, resulting in 141 E&P targets corresponding to 24 compounds (Figure 1(a)). These 141 genes were regarded as potential targets through which EF exerts its antiprostate cancer effects, and 24 compounds were regarded as candidate components. Then, the cytoscape software was used to establish drug-compound-target-disease network. As shown in Figure 1(b), 24 drug-compound, 346 compound-target, and 141 target-disease connections were created in a network, which integrally illustrated the anticancer activity of EF characterized by multi-ingredients, multitargets, and synergistic effects. The PPI analysis of E&P targets was performed by STRING. Totally, 141 target genes of E&P were searched in the STRING database, and a total of 1126 PPI connections were generated (Figure 1(c)). According to the frequency of each node and the combined score between two nodes, the top 30 enriched targets were displayed in a barplot (Figure 1(d)). The results demonstrated that AKT1, TP53, MAPK1, and other targets are associated with the antiprostate cancer effects of EF.

3.2. Prediction of Antiprostate Cancer Mechanism by GO and KEGG Enrichment. The results of GO functional enrichment were displayed in a barplot (Figure 2(a)) and a dotplot (Figure 2(b)). According to the results, the main molecular functions of the targets include DNA-binding transcription factor, nuclear receptor, and ligand-activated transcription factor. The results of KEGG pathway enrichment in a barplot (Figure 2(c)) and a dotplot (Figure 2(d)) showed that PI3K/AKT and AGE-RAGE signaling pathways were the potential pathways mediating the antiprostate cancer effects of EF. The "prostate cancer" listed in the second in Figure 2(c) and the seventh in Figure 2(d) also confirmed the cancer type which EF is more likely to influence on. Since AKT is the most significant target protein in the PPI network (Figure 1(d)), we focused on the PI3K/AKT signaling pathway, which is closely related to prostate cancer initiation and progression [20]. From the results of PI3K/AKT signaling pathway enriched in KEGG (Figure 2(e)), we predicted that PI3K/AKT/NF-κB signaling pathway may participate in the inhibitory effects of EF on prostate cancer since NF-κB is a key transcription factor downstream of PI3K/AKT to mediate prostate carcinogenesis [21], which is also consistent with the results of GO enrichment featuring transcription factor binding (Figures 2(a) and 2(b)). Based on these results, we suggested that evodiamine, which targets PI3K, may be the active ingredient of EF for prostate cancer treatment.

3.3. Evodiamine Displays Obvious Antiproliferative Effect on DU145 Cells. Among the 24 potential active compounds of EF against prostate cancer, 5 of them were selected to evaluate their cytotoxicity on DU145 cells. As shown in Figure 3(a), evodiamine (chemical structure in Figure 3(b)) displays more potent antiproliferative effect than rutaecarpine, berberine, quercetin, and β-sitosterol on DU145 cells. Evodiamine, an indoloquinazoline alkaloid isolated from EF, was reported to display cytotoxicity on various types of cancers [22, 23]. Subsequently, the antiproliferative effect

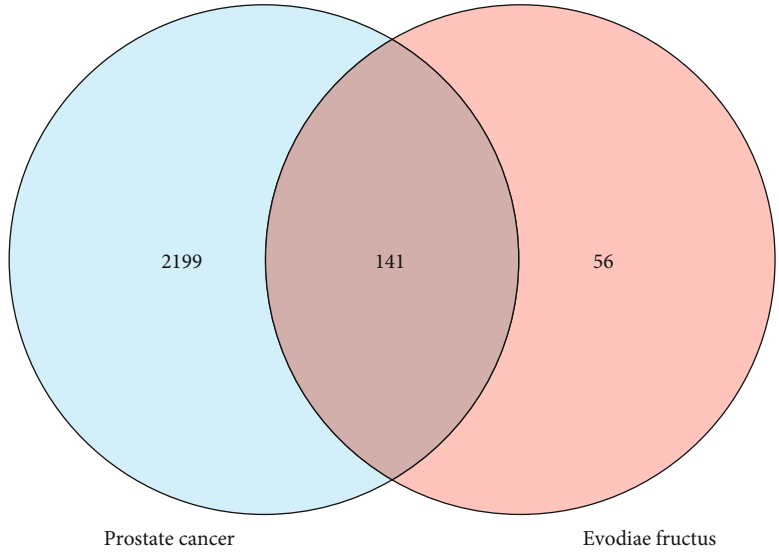

(a)

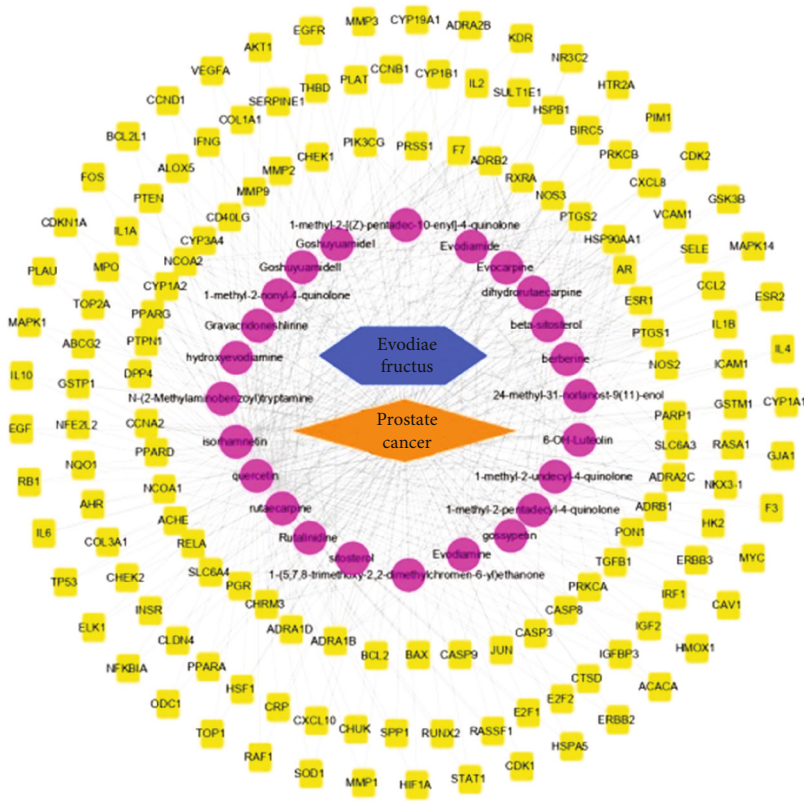

(b)

Figure 1: Continued.

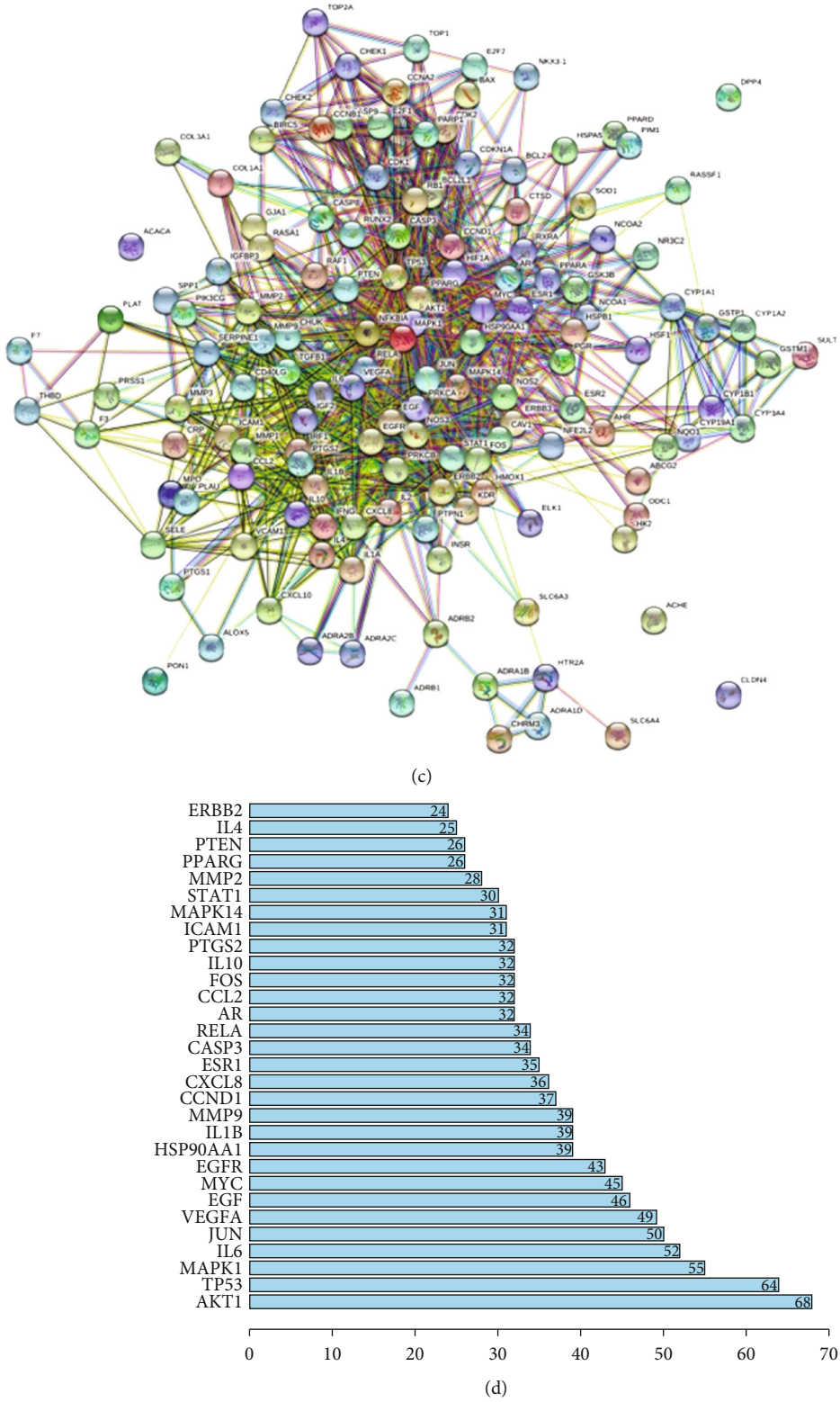

Figure 1: The construction of drug-compound-target-disease network and PPI network. (a) Venn diagram displays the overlap between the prostate cancer-related targets and the potential targets of EF. (b) The construction of drug-compound-target-disease network. The orange rhombus represents diseases. The blue hexagon represents drugs. The purple ovals represent active compounds. The yellow rectangles represent target genes. (c) PPI network of 141 target genes of E&P. Each node represents the E&P targets. Each line represents the interaction between two targets. (d) The top 30 enriched targets in the PPI network were displayed in a barplot.

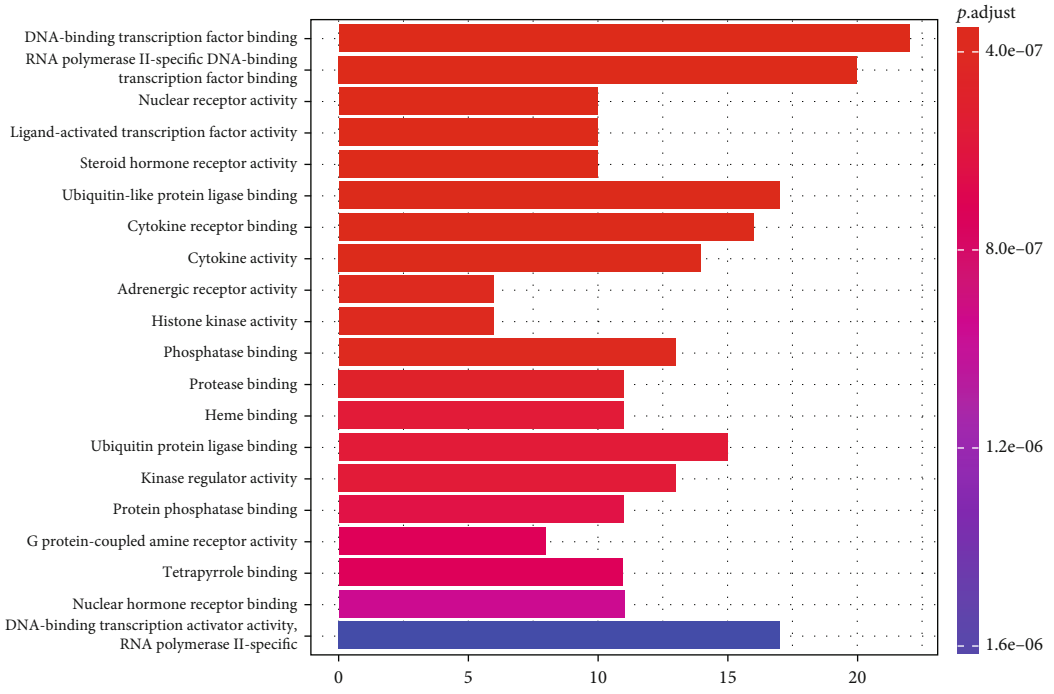

(a)

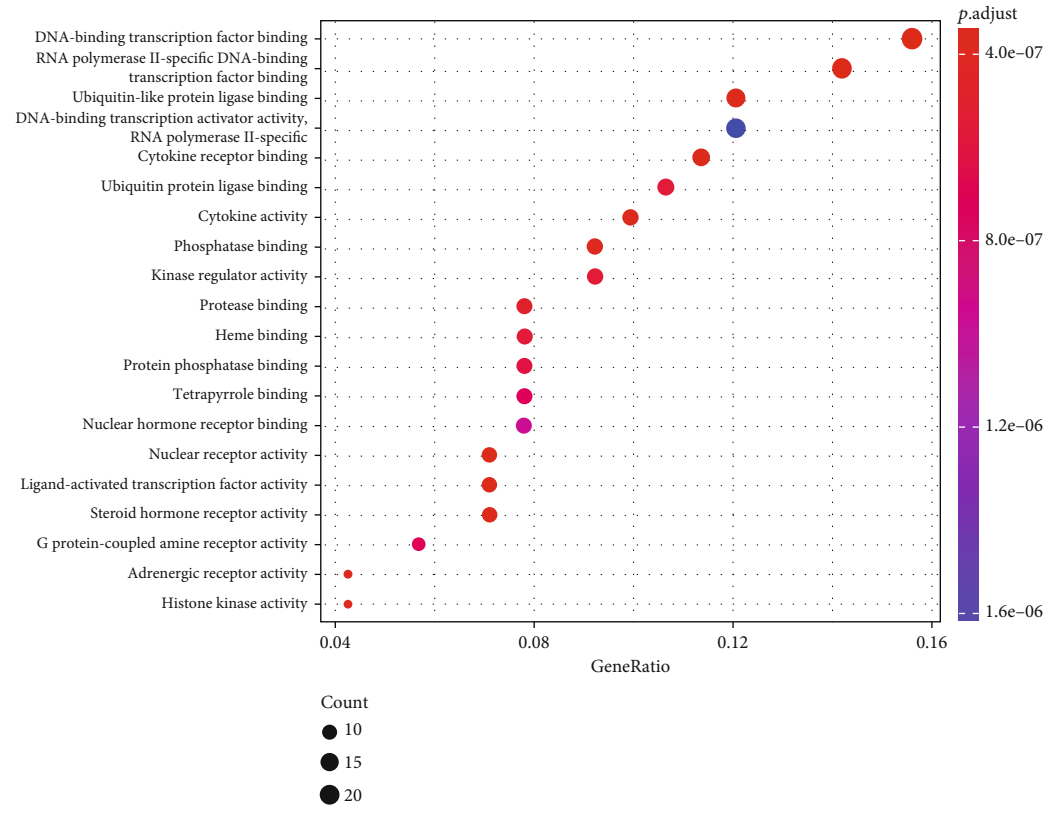

(b)

Figure 2: Continued.

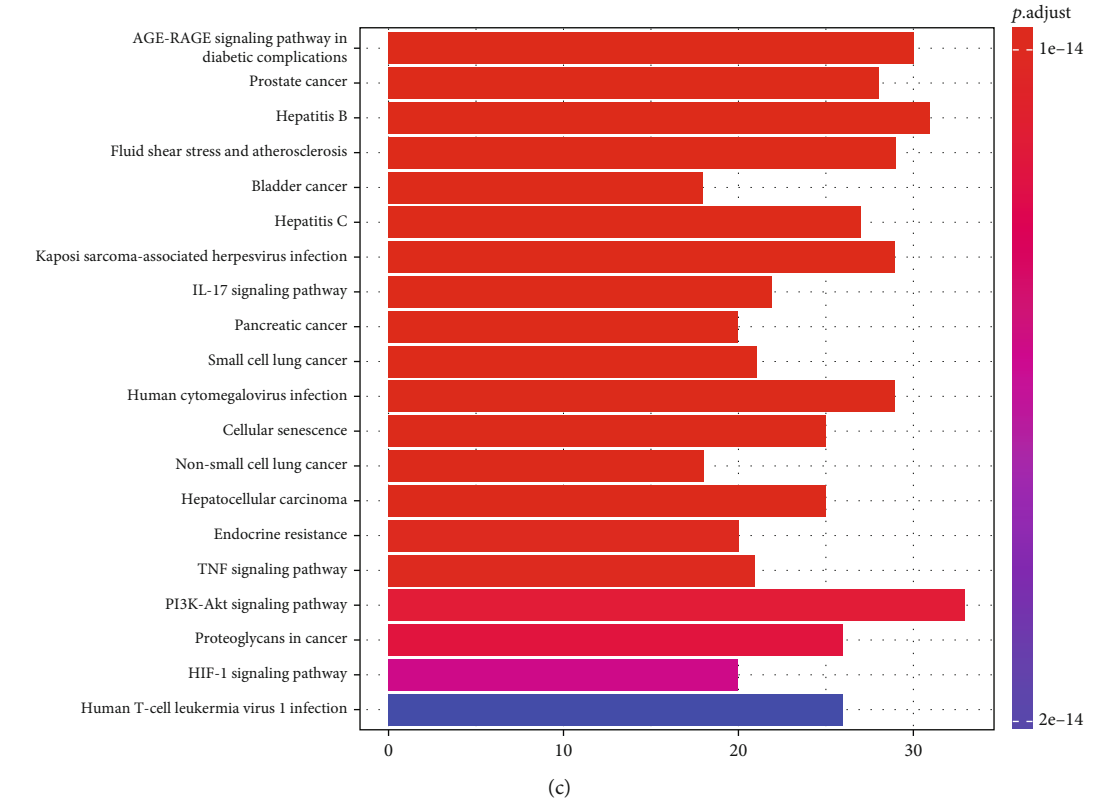

(c)

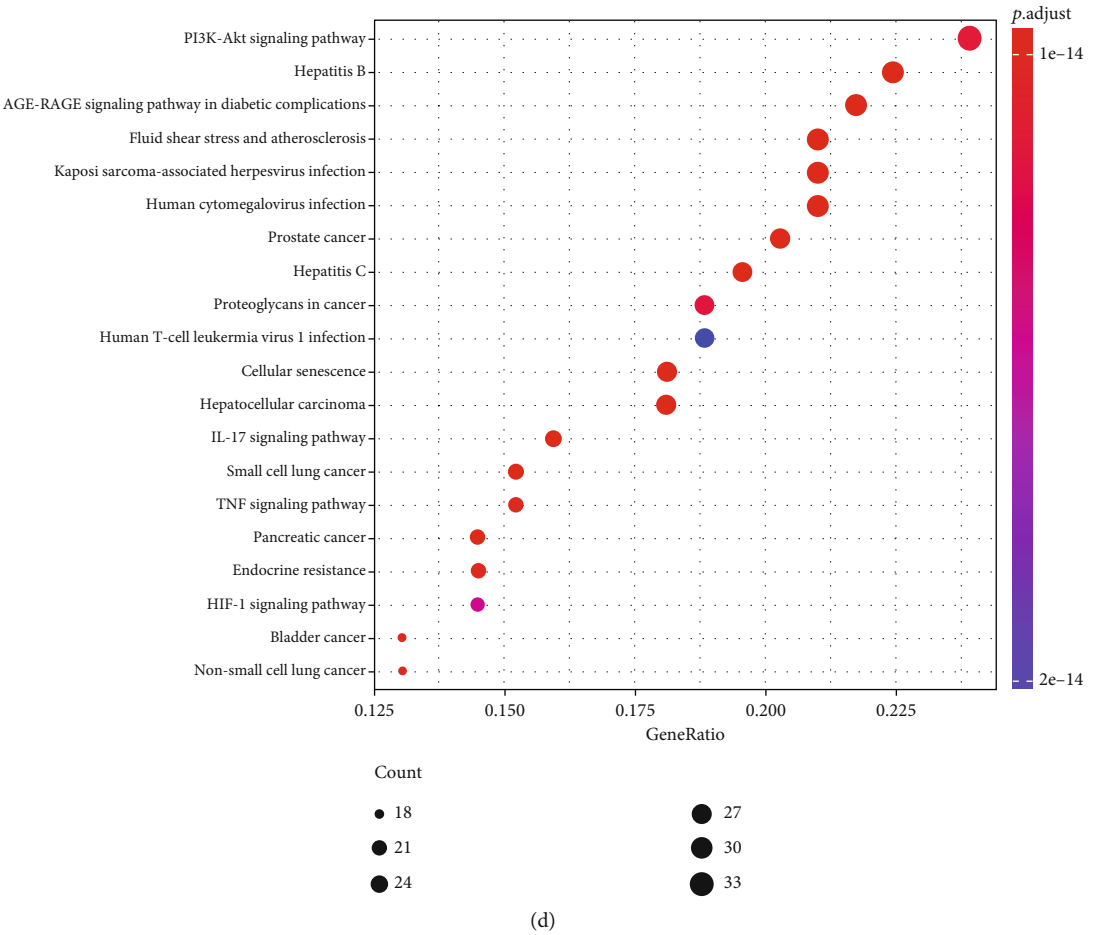

(d)

Figure 2: Continued.

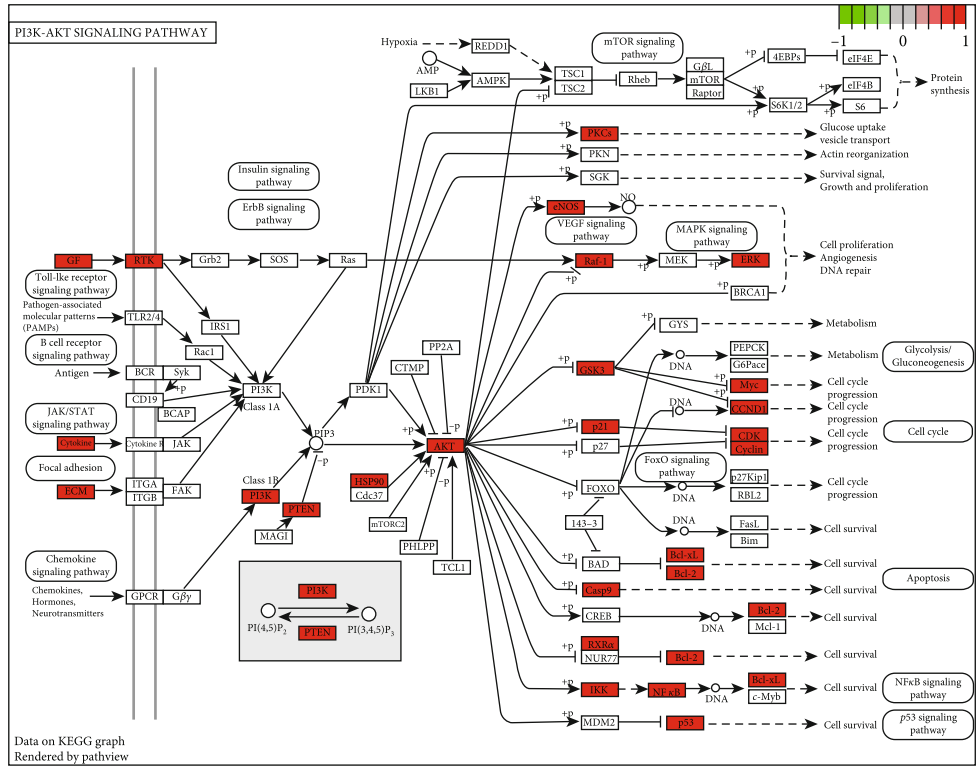

(e)

Figure 2: The GO functional enrichment and KEGG pathway enrichment. (a) The barplot of top 20 items identified by GO functional enrichment. (b) The dotplot of top 20 items identified by GO functional enrichment. (c) The barplot of top 20 items identified by KEGG pathway enrichment. (d) The dotplot of top 20 items identified by KEGG pathway enrichment. The color of the bubble and column is associated with the P value, and the size of bubble is related to the ratio of target gene. (e) PI3K/AKT signaling pathway enriched in KEGG pathway analysis.

of evodiamine on DU145 cells was further examined. As shown in Figure 3(c), the viability of DU145 cells was significantly inhibited in a dose-dependent manner after treatment with evodiamine for 24 h, with the IC_{50} value of $1.94 \pm 0.23\,\mu M$. The evodiamine-induced cell morphology changes under the microscope were presented in Figure 3(d), which indicated that evodiamine has potent cytotoxicity on DU145 cells. In addition, the long-term efficacy of evodiamine on DU145 cell survival was evaluated by colony formation assay. The results demonstrated that evodiamine inhibits the cell proliferation in a dose-dependent way (Figures 3(e) and 3(f)).

3.4. Evodiamine Induces G_2/M Cell Cycle Arrest in DU145 Cells. To determine whether the inhibitory effect of evodiamine on DU145 cells is related to cell cycle arrest, flow cytometry was used to analyze the content of DNA in various stages of DU145 cells. As shown in Figures 4(a) and 4(b), compared with the control group, the cell population in G_2/M phase significantly increased from 24.48% to 44.61% following 5 μM evodiamine treatment, suggesting that evodiamine induces G_2/M cell cycle arrest in DU145 cells. CDK1 and cyclin B1 are key regulators involved in the G_2/M transition by forming the CDK1/cyclin B1 complex [24]. Cdc25C activates the CDK1 complex through $CDK1^{Tyr15}$ and $CDK1^{Thr14}$ dephosphorylation [25]. As shown in Figures 4(c) and 4(d), evodiamine decreased the level of p-$Cdc25C^{Ser216}$ in a dose-dependent manner, indicating that the activation of Cdc25c is inhibited by evodiamine. As a consequence, the inactive Cdc25C can no longer dephosphorylate p-$CDK1^{Thr14}$, which makes p-$CDK1^{Thr14}$ and cyclin B1 accumulation to block the G_2/M transition. These results indicated that evodiamine induces G_2/M cell cycle arrest in DU145 cells through regulating Cdc25c/CDK1/cyclin B1 signaling pathway.

3.5. Evodiamine Induces Mitochondrial Apoptosis in DU145 Cells. To investigate whether evodiamine-induced cell death is attributed to cell apoptosis, the Annexin V-FITC/PI staining assay was performed using flow cytometry. Figures 5(a) and 5(b) demonstrated that evodiamine treatments at different concentrations (1.25, 2.5, and 5.0 μM) increased the number of apoptotic cells. The apoptotic cell ratio (early apoptotic stage plus late stage) in the 5.0 μM treatment group is almost 4 times of that of the control group. In addition, the Hoechst 33258 staining assay was performed to observe nuclear morphological changes in DU145 cells. As shown in Figure 5(c), following different concentrations of evodiamine treatment for 24 h, cells emit bright blue fluorescence representing nuclear condensation and DNA fragmentation which are the typical characteristics of cell apoptosis. The fluorescence intensity in evodiamine-treated

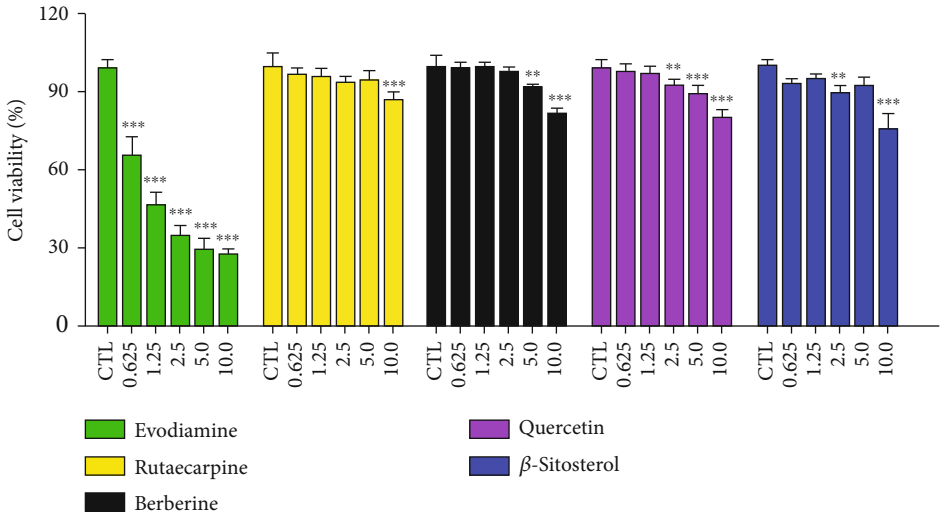

(a)

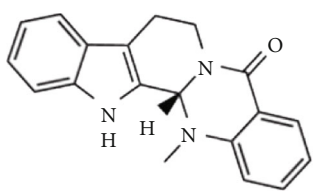

Evodiamine

(b)

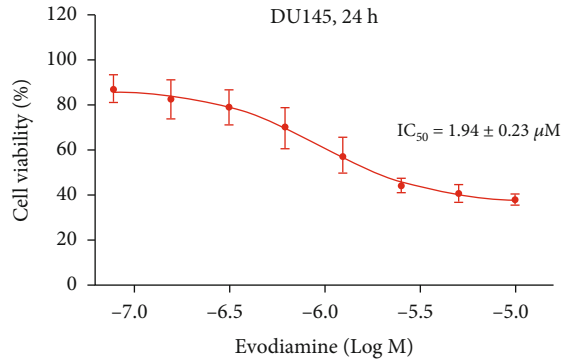

(c)

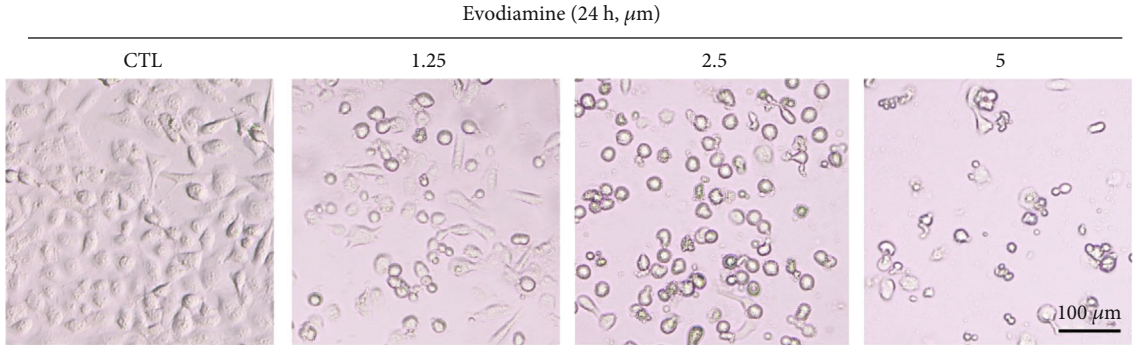

(d)

Figure 3: Continued.

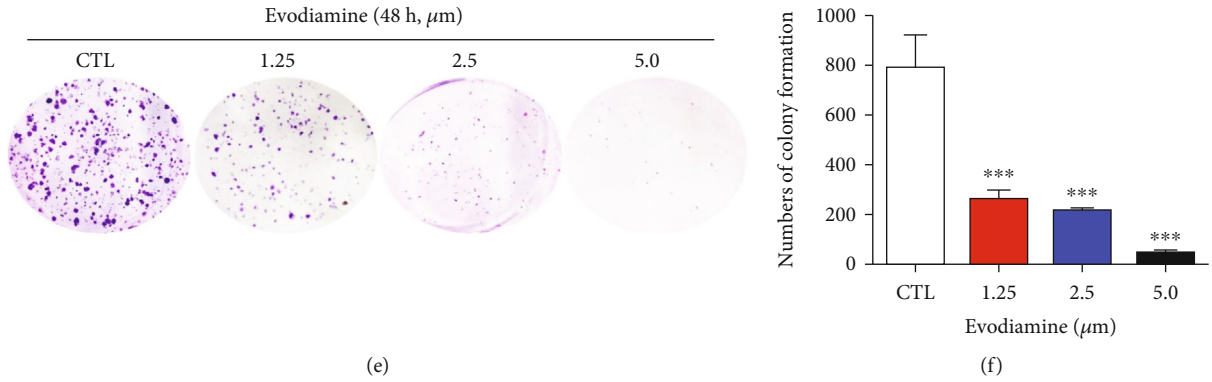

Figure 3: Evodiamine displays antiproliferative effect on DU145 cells. (a) DU145 cells were treated with 5 potential active compounds at different concentrations (0, 0.625, 1.25, 2.5, 5.0, and 10.0 μM) for 72 h. The cell viability was detected by CCK8 assay. Among these compounds, evodiamine (chemical structure in Figure 3(b)) displays the most potent cytotoxicity. Data are presented as mean ± SD ($n = 3$). $^{**}P < 0.01$ and $^{***}P < 0.001$ versus the control group. (c) DU145 cells were treated with different concentrations of evodiamine for 24 h. The cell viability was detected by CCK8 assay. The curve indicated that E2 exerts antiproliferative effect on DU145 cells in a dose-dependent manner. (d) Representative images of CCK8 assay. Original magnification: 100x; scale bar: 100 μm. (e) DU145 cells were exposed to evodiamine at the concentrations of 0, 1.25, 2.5, and 5.0 μM for 48 h and then cultured in fresh medium which was replaced every three days. After ten days, the colonies of DU145 cells were visualized by crystal violet staining. (f) The numbers of colonies of DU145 cells were counted and presented as mean ± SD ($n = 3$). $^{***}P < 0.001$ versus the control group.

cells is significantly higher than that of the control group. These results provided evidence for the induction of apoptosis by evodiamine. A Western blotting assay was applied to detect the expression levels of apoptosis-related proteins. Figures 5(d) and 5(e) displayed that evodiamine upregulates the ratio of cleaved-caspase 3/procaspase 3, cleaved-caspase 9/procaspase 9, and cleaved PARP/PARP. Moreover, evodiamine significantly changed the ratio of Bax/Bcl-2. It is well recognized that the interaction between apoptotic promotor Bax and apoptotic inhibitor Bcl-2 determines the fate of cell towards mitochondrial apoptosis [26]. These results demonstrated that evodiamine induces mitochondrial apoptosis in DU145 cells.

3.6. Evodiamine May Inhibit DU145 Cell Migration through PI3K Signaling Pathway. To evaluate the capacity of cell migration, the wound-healing assay was applied. As shown in Figures 6(a) and 6(b), evodiamine treatments at different concentrations (0.5 and 1.0 μM) inhibited wound closure in a time-dependent manner. To further predict the targets of evodiamine against cell migration, we used PharmMapper database to obtain targets of evodiamine and GeneCards database to obtain cell migration-related targets. As a result, 170 drug targets and 1774 cancer cell migration targets which met the requirement of relevance score ≥ 20 were collected. The 85 targets (E&M) at the intersection between drug targets and migration targets were regarded as potential antimigration targets of evodiamine (Figure 6(c)). The PPI analysis of E&M targets was performed by STRING. Totally, 85 gene symbols of E&M were searched in the STRING database, and a total of 844 PPI connections were generated (Figure 6(d)). According to the frequency of each node and the combined score between two nodes, the top 20 enriched targets were displayed in a barplot (Figure 6(e)), which represent the most probable antimigration targets of evodiamine. Since PI3K turned out to be both antiprostate cancer and antimigration targets of evodiamine, we predicted that evodiamine may inhibit DU145 cell migration through PI3K signaling pathway.

3.7. Evodiamine Exerts Antiprostate Cancer Effects through PI3K/AKT/NF-κB Signaling Pathway. Previous studies demonstrated that AKT plays a central role in mediating the antiprostate cancer effect of EF, and PI3K was predicted to be the potential target of evodiamine to inhibit proliferation and migration of prostate cancer. In addition, the activation of PI3K/AKT/NF-κB signaling pathway was confirmed to be closely related to pathogenesis of prostate cancer [21]. Therefore, the molecular docking of evodiamine to PI3K and AKT was performed. As shown in Figure 7(a), the binding free energy of evodiamine to PI3K is -6.77 kcal/mol, indicating a good binding affinity. The interaction type includes hydrogen bonds, hydrophobic interactive, and π-stacking. Evodiamine binds to active amino acid residues of PI3K including ILE-963, MET-953, and VAL-882. Evodiamine belongs to a type of polycyclic compound with potent hydrophobic property, which interacts with hydrophobic residues of PI3K including ILE-963, ILE-879, MET-804, TRP-812, and ILE-831 through hydrophobic effect. Moreover, evodiamine binds to MET-953 and VAL-882 residues of PI3K through hydrogen bond interaction. The average hydrogen bond distance is 3.4 Å and 2.4 Å, which is lower than the conventional hydrogen bond distance 3.5 Å. As shown in Figure 7(b), the binding free energy of evodiamine to AKT is -6.82 kcal/mol, indicating a good binding affinity. Evodiamine binds to active amino acid residues of AKT including LYS-179, PHE-161, and ASP-292. Evodiamine is an indoloquinazoline alkaloid with six-membered rings that can form strong hydrophobic interactions with the pocket amino acids of AKT such as ILE-963, ILE-879, MET-804, TRP-812, and ILE-831. Additionally, evodiamine can bond to ASP-292 residues of AKT through hydrogen bond

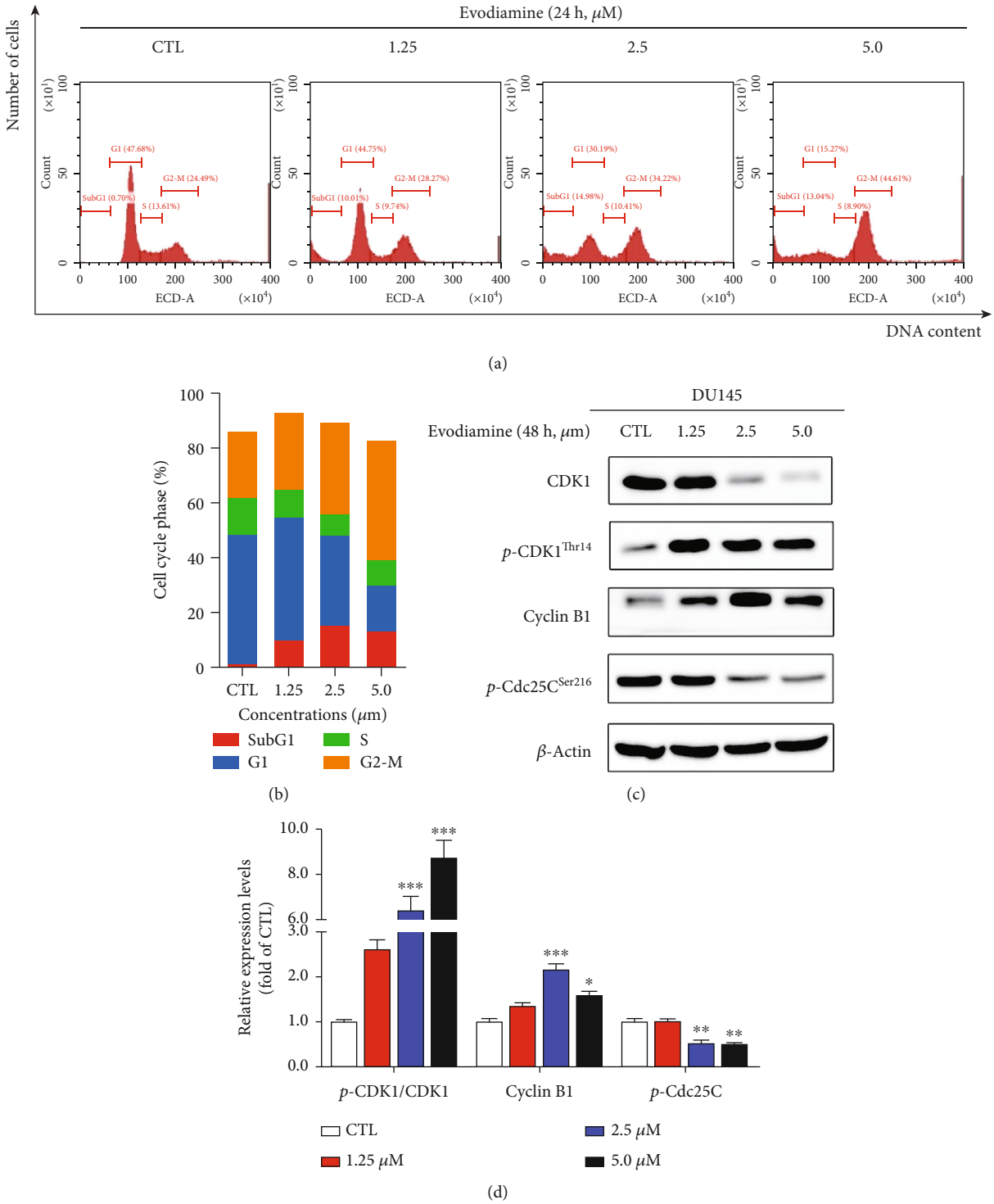

Figure 4: Evodiamine induces G_2/M cell cycle arrest in DU145 cells. (a) After treatment with evodiamine (0, 1.25, 2.5, and 5.0 μM) for 24 h, the cell cycle distributions were analyzed by flow cytometry. The cell population in the G_2/M phase significantly augmented in a dose-dependent manner. (b) The cell populations were quantified using Prism. Each column represents the cell population in different phases ($n = 3$). (c) DU145 cells were treated with evodiamine (0, 1.25, 2.5, and 5.0 μM) for 24 h. The protein expression levels of CDK1, p-CDK1^{Thr14}, cyclin B1, and p-Cdc25C^{Ser216} were detected by Western blot. β-Actin was used as the loading control. Evodiamine-induced G_2/M cell cycle arrest is associated with upregulation of p-CDK1^{Thr14}/CDK1 and cyclin B1 and downregulation of p-Cdc25C^{Ser216}. (d) Quantitative analysis of the relative protein expression. Data are presented as the mean ± SD ($n = 3$). $^{*}P < 0.05$, $^{**}P < 0.01$, and $^{***}P < 0.001$ versus the control group.

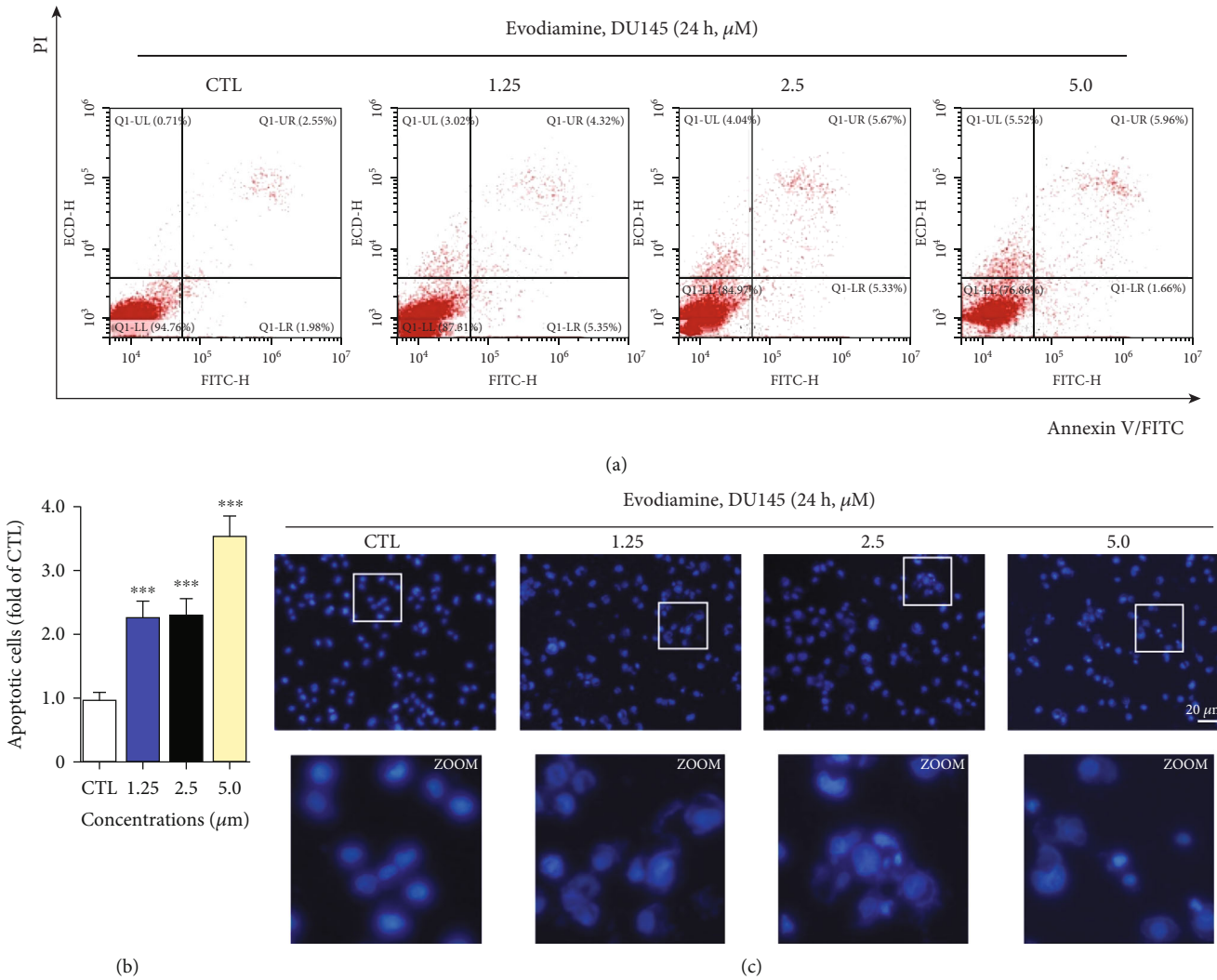

Figure 5: Continued.

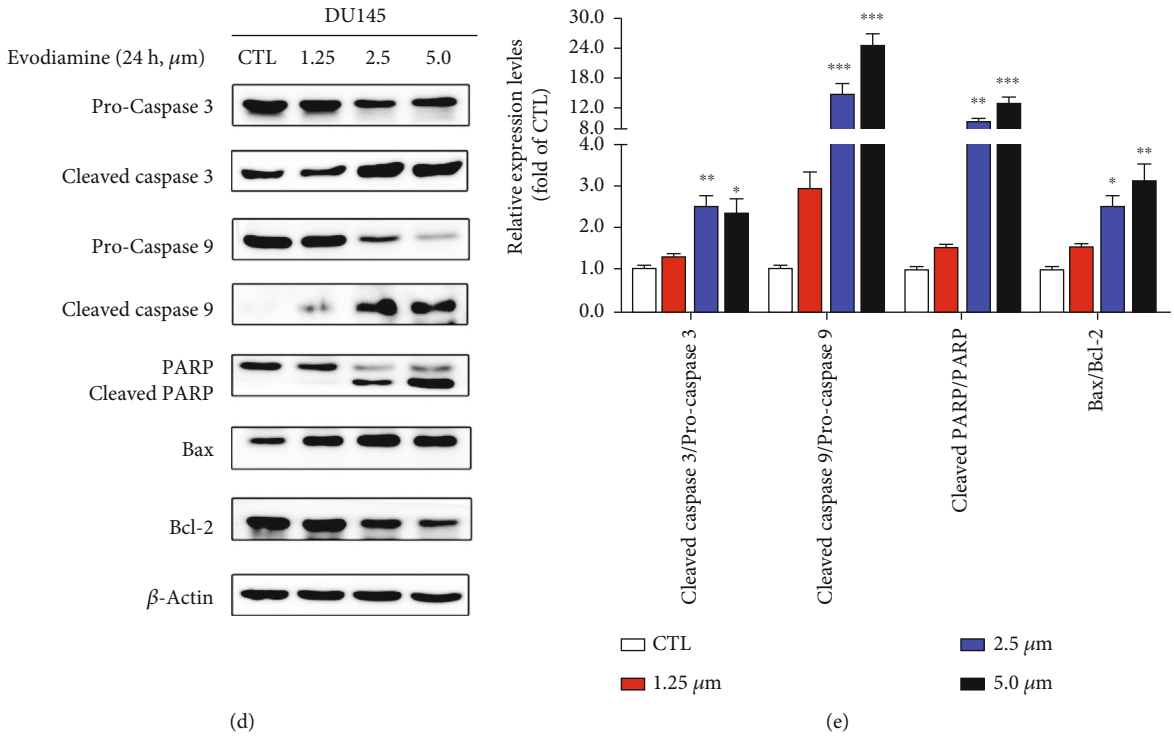

Figure 5: Evodiamine induces mitochondrial apoptosis in DU145 cells. (a) After evodiamine treatment (0, 1.25, 2.5, and 5.0 μM) for 24 h, the apoptotic rate of DU145 cells was measured by PI/Annexin V-FITC staining assay. Representative images are shown. Evodiamine induces cell apoptosis in a dose-dependent manner. (b) Quantitative data of evodiamine-induced apoptotic cells. Data are presented as the mean ± SD ($n = 3$). $^{***}P < 0.001$ versus the control group. (c) Apoptotic morphological changes observed by Hoechst 33258 staining assay after evodiamine treatment (0, 1.25, 2.5, and 5.0 μM) for 24 h. Original magnification: 200x; scale bar: 20 μm. (d) After evodiamine treatment (0, 1.25, 2.5, and 5.0 μM) for 24 h, the expression levels of apoptosis-related proteins including pro- and cleaved-caspases 3/9, PARP, cleaved-PARP, Bax, and Bcl-2 were detected by Western blotting. β-Actin was used as the loading control. (e) The quantitative data of relative protein expression shown as the mean ± SD ($n = 3$). $^{*}P < 0.05$, $^{**}P < 0.01$, and $^{***}P < 0.001$ versus the control group.

interaction. The average hydrogen bond distance is 2.92, which is much lower than the conventional hydrogen bond distance 3.5 Å. The results of molecular docking demonstrated that evodiamine is a potential active molecule targeting PI3K and AKT. The results of Western blot also confirmed the inhibition of PI3K/AKT/NF-κB signaling pathway by evodiamine. As shown in Figures 7(c) and 7(d), the expression levels of p-PI3K/PI3K, p-AKT^{Ser473}/AKT, and p-NF-κB^{Ser536}/NF-κB were decreased following evodiamine treatment, indicating that inhibition of PI3K/AKT/NF-κB signaling by evodiamine may result in proliferation and migration inhibition of DU145 cells.

4. Discussion

TCM, which is widely used in clinics especially in Asia and Africa, has displayed the great potential in the prevention and treatment of cancers and other diseases [4]. Isolation of active compounds from TCM is an important strategy for drug discovery [27]. The discovery of vinblastine and vincristine was the beginning of developing anticancer drugs from natural resources [28]. It has been reported that approximately 80% of small molecule anticancer drugs are natural products and their derivatives [29]. The multiple pharmacological properties of natural compounds provided a basis for the mechanistic study of their biological functions. TCMSP is a unique system pharmacology platform of Chinese herbal medicine that captures the relationships among drugs, targets, and diseases [18]. Through target prediction in TCMSP and PPI analysis in STRING database, AKT was identified as the most central target in antiprostate cancer effects of EF. Through GO and KEGG enrichment, PI3K/AKT was predicted as the most likely signaling pathway by which EF displays its antiprostate cancer effects. From 5 potential active compounds of EF, evodiamine was verified to possess the most potent cytotoxicity against DU145 cells. In addition, the results of target prediction showed that PI3K is the potential target of evodiamine against prostate cancer and cell migration. Hence, we suggested that evodiamine is the active compound of EF to inhibit proliferation and migration of prostate cancer through PI3K/AKT signaling pathway. To predict the downstream substrates of AKT, we focused on the transcription factor NF-κB, which is closely related to tumorigenesis and tumor progression [30]. The results of molecular docking demonstrated a good binding affinity between evodiamine and PI3K, as well as evodiamine and AKT. The inhibition of PI3K/AKT/NF-κB by evodiamine *in vitro* was also verified by Western blot. However, evodiamine was selected as the

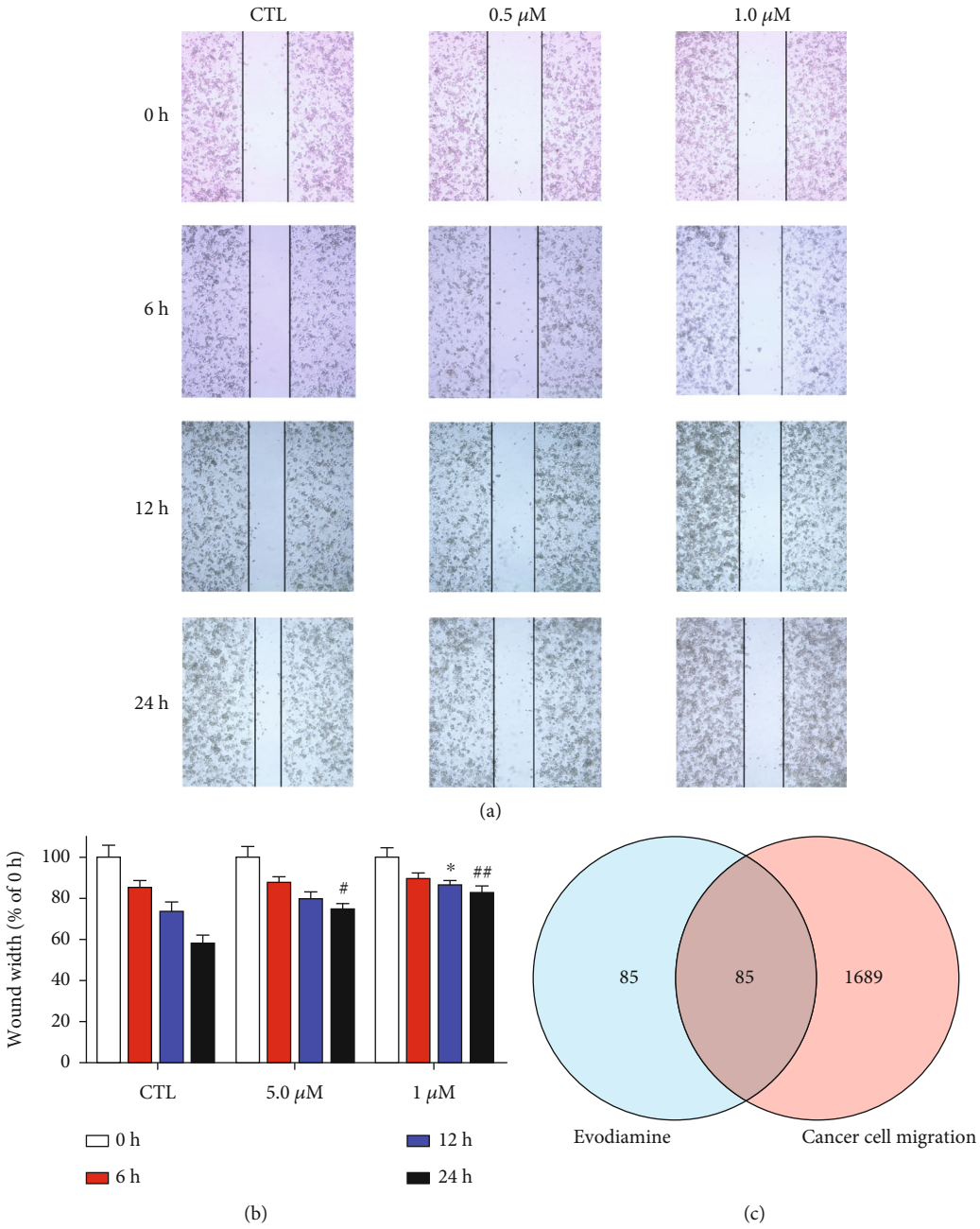

Figure 6: Continued.

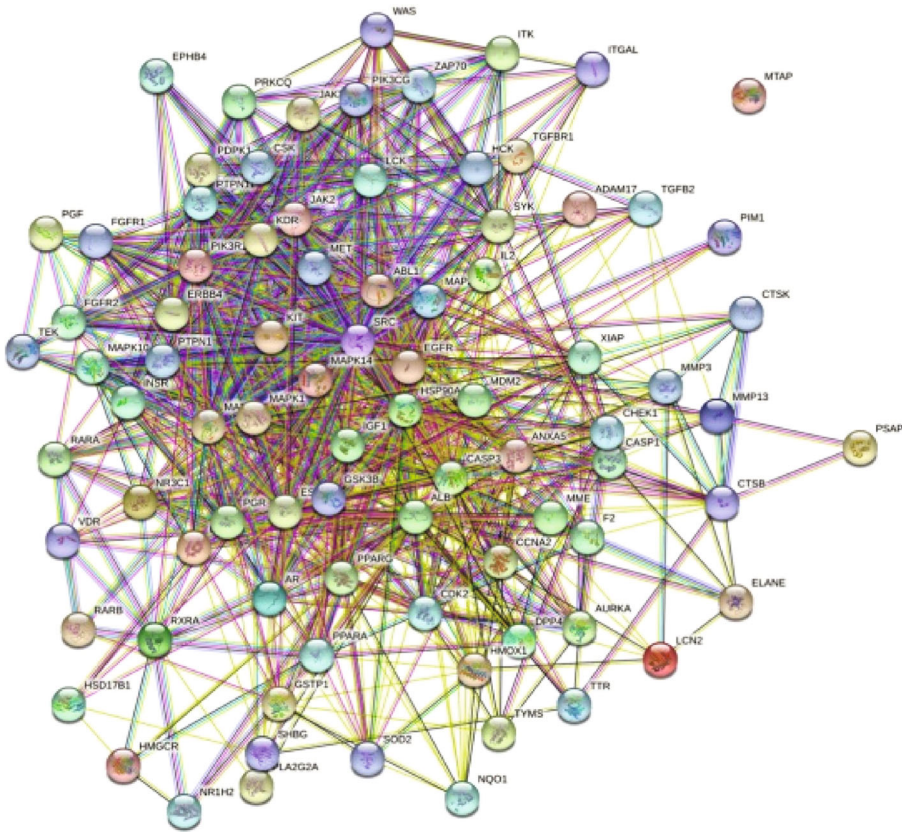

(d)

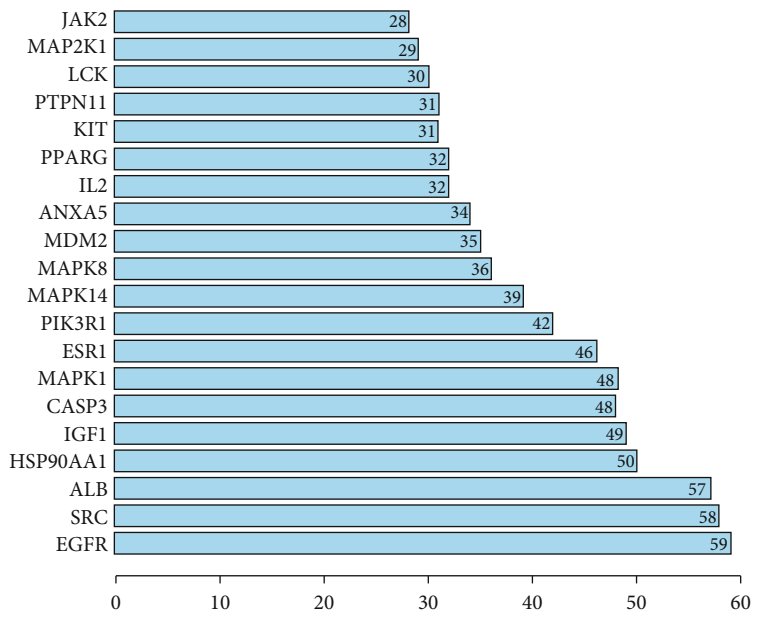

(e)

Figure 6: Evodiamine may inhibit DU145 cell migration through PI3K signaling pathway. (a) The migratory properties of DU145 cells were analyzed by wound-healing assays. Original magnification: 100x. (b) The relative wound width was analyzed using GraphPad Prism 7.0. Data are presented as the mean ± SD ($n = 3$). $^{*}P < 0.05$, $^{\#}P < 0.05$, and $^{\#\#}P < 0.01$ versus the control group. (c) Venn diagram displays the overlap between the migration-related targets and the potential targets of evodiamine. (d) PPI network of 85 target genes of E&M. Each node represents the E&M targets. Each line represents the interaction between two targets. (e) The top 20 enriched targets in the PPI network were displayed in a barplot.

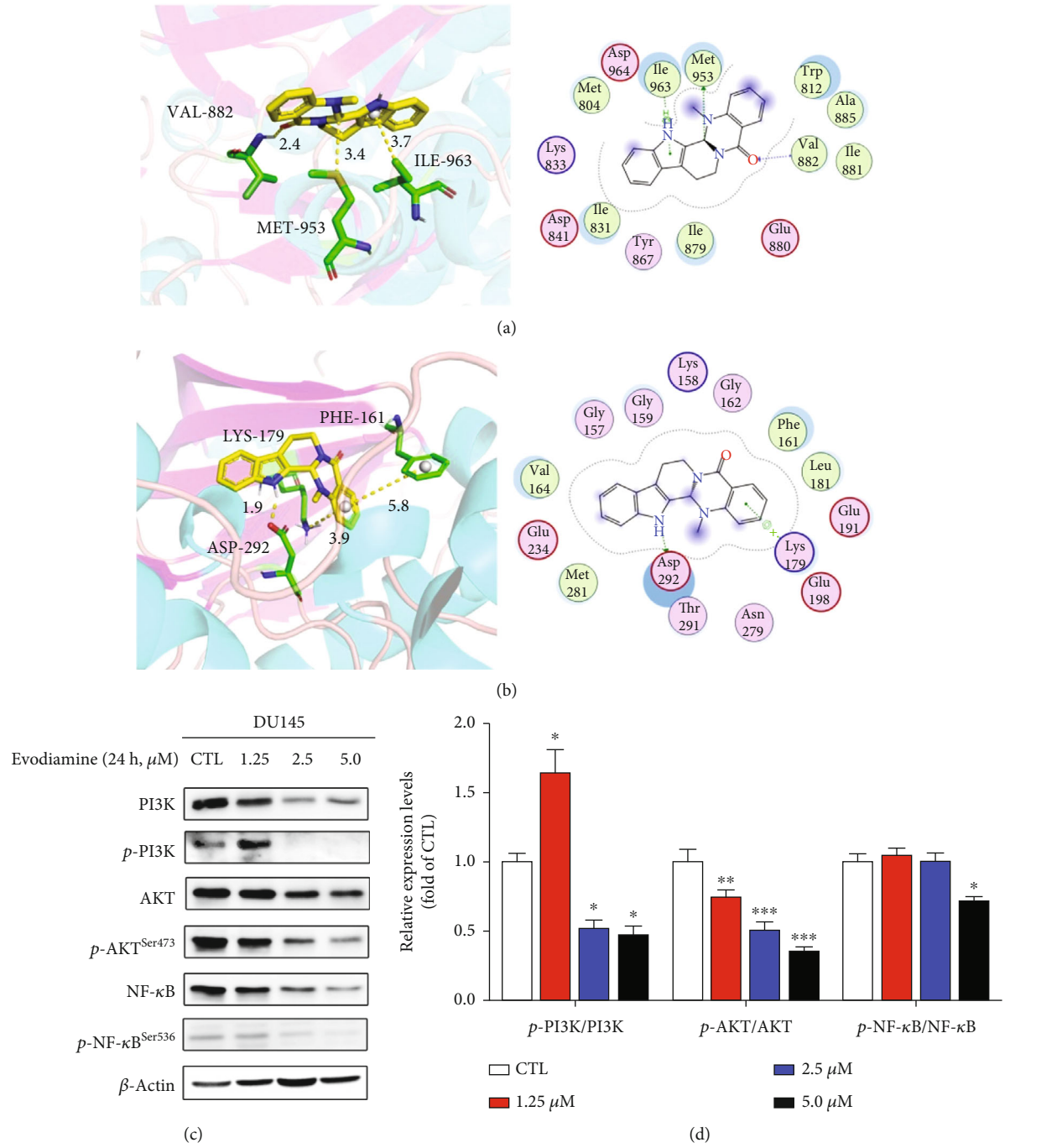

Figure 7: Evodiamine exerts antiprostate cancer effects through PI3K/AKT/NF-κB signaling pathway. (a) The binding mode of evodiamine with PI3K (left: 3D structure; right: 2D structure). The yellow structure is evodiamine, and the green structure represents the binding site of PI3K. (b) The binding mode of evodiamine with AKT (left: 3D structure; right: 2D structure). The yellow structure is evodiamine, and the green structure represents the binding site of AKT. (c) After evodiamine treatment (0, 1.25, 2.5, and 5.0 μM) for 24 h, the expression levels of p-PI3K, PI3K, p-AKT^{Ser473}, AKT, p-NF-κB^{Ser536}, and NF-κB were detected by Western blotting. β-Actin was used as the loading control. (d) The quantitative data of relative protein expression shown as the mean ± SD ($n = 3$). $^{*}P < 0.05$, $^{**}P < 0.01$, and $^{***}P < 0.001$ versus the control group.

most active ingredient of EF against prostate cancer but not the only one. The active ingredients of herbal medicine are multiple and complex. TCM exerts effects on disease through multi-ingredients, multitargets, and synergetic way. Hence, the complex connections between EF and prostate cancer indicate that multiple possible mechanism participate in this process, which need further investigation. This research provides an example for the exploration of pharmacological mechanism of TCM. However, *in vivo* studies are needed to further confirm the inhibitory effects of evodiamine on tumor growth and tumor metastasis through PI3K/AKT/NF-κB signaling pathway.

Natural compounds and their derivatives exert anticancer effects via multiple mechanisms. In traditional herbal medicine, EF has been used for the treatment of headaches, abdominal pain, and menorrhalgia [31]. Through activity screening and mechanistic study, evodiamine was identified as one of the major bioactive components of EF against various types of cancers including colon cancer [32], hepatocellular carcinoma (HCC) [33], lung cancer [34], and melanoma [35]. It is reported that different mechanisms are involved in the anticancer effects of evodiamine such as induction of apoptosis, cell cycle arrest, inhibition of invasion and metastasis [36]. The targets of evodiamine include topoisomerases, aryl hydrocarbon receptor (AhR), and transient receptor potential cation channel subfamily V member 1 (TRPV1) in the treatment of different types of cancers [37]. Various signaling pathways participate in the evodiamine-induced cancer cell apoptosis such as mTOR signaling [38], STAT3 signaling [39], and Bax/Bcl-2 [40]. Meanwhile, evodiamine repressed the EMT of gastric cancer stem cells by inhibiting Wnt pathway [41]. The inactivation of the PI3K/AKT signaling pathway induced by evodiamine was previously verified to result in cell apoptosis in pancreatic cancer [42, 43], glioma [44], and melanoma [45], which is consistent with our present study. This is the first time to report that inhibition of PI3K/AKT/NF-κB signaling pathway is associated with the antiprostate cancer effect of evodiamine, making it a promising therapeutic lead drug for prostate cancer treatment. Currently, numerous efforts have been made to explore small molecular inhibitors targeting the PI3K/AKT signaling pathway to block cancer growth and metastasis. However, the clinical efficacies of these inhibitors are limited since the activation of the PI3K family occurs through complex mechanisms [46]. Hence, combination of PI3K/AKT inhibitors and other cancer treatments has been proposed to solve the therapeutic dilemma [47]. Future research may focus on the combination of evodiamine and other cancer therapies to improve the treatment efficacy.

However, the poor bioavailability and potential toxicity limit the clinical application of evodiamine. Evodiamine inhibits the activities of metabolic enzymes such as cytochrome P450, leading to cytotoxic effects [48]. Moreover, the safety concern exists as the precise target of evodiamine is unknown and the excessive inhibition of PI3K/AKT/NF-κB pathway may bring about side effects. Hence, evodiamine treatment may be more potent but not necessarily more effective than EF treatment, which needs further evaluation. Currently, a number of novel drug delivery systems have been designed to improve the bioavailability and minimize side effects of low-solubility natural medicines [49]. Further research aiming to enhance the anticancer effects of evodiamine would prove beneficial.

5. Conclusion

In conclusion, this study demonstrated that evodiamine is the active compound of Evodiae fructus to inhibit proliferation and migration of prostate cancer through PI3K/AKT/NF-κB signaling pathway. This study provides a rationale of using evodiamine as the potential lead drug for prostate cancer treatment.

Data Availability

The data supporting the conclusions of this article are included within the article.

Ethical Approval

The ethical approval was waived since this study is based on previously archived data that are publicly available.

Conflicts of Interest

The authors declare there are no conflicts of interest.

Authors' Contributions

Y. L., M. C., and H. L. contributed equally to this work and shared the first authorship.

Acknowledgments

This study was supported by the National Natural Science Foundation of China (no. 82074382) and the Natural Science Foundation of Guangdong Province (no. 2021A1515011232).

References

[1] F. Bray, J. Ferlay, I. Soerjomataram, R. L. Siegel, L. A. Torre, and A. Jemal, "Global cancer statistics 2018: GLOBOCAN estimates of incidence and mortality worldwide for 36 cancers in 185 countries," *CA: Cancer Journal for Clinicians*, vol. 68, no. 6, pp. 394–424, 2018.

[2] J. C. Wu, C. T. Wang, H. C. Hung et al., "Heteronemin is a novel c-Met/STAT3 inhibitor against advanced prostate cancer cells," *Prostate*, vol. 76, no. 16, pp. 1469–1483, 2016.

[3] T. Liu, D. E. Mendes, and C. E. Berkman, "From AR to c-Met: androgen deprivation leads to a signaling pathway switch in prostate cancer cells," *International Journal of Oncology*, vol. 43, no. 4, pp. 1125–1130, 2013.

[4] A. Tariq, S. Sadia, K. Pan et al., "A systematic review on ethnomedicines of anti-cancer plants," *Phytotherapy Research*, vol. 31, no. 2, pp. 202–264, 2017.

[5] F. Chen, Z. Zhong, H. Y. Tan et al., "Uncovering the anticancer mechanisms of Chinese herbal medicine formulas: therapeutic alternatives for liver cancer," *Frontiers in Pharmacology*, vol. 11, p. 293, 2020.

[6] A. K. Mukherjee, S. Basu, N. Sarkar, and A. C. Ghosh, "Advances in cancer therapy with plant based natural products," *Current Medicinal Chemistry*, vol. 8, no. 12, pp. 1467–1486, 2001.

[7] N. Wang, H. Y. Tan, L. Li, M. F. Yuen, and Y. Feng, "Berberine and Coptidis Rhizoma as potential anticancer agents: recent updates and future perspectives," *Journal of Ethnopharmacology*, vol. 176, pp. 35–48, 2015.

[8] S. Li and B. Zhang, "Traditional Chinese medicine network pharmacology: theory, methodology and application," *Chinese Journal of Natural Medicines*, vol. 11, no. 2, pp. 110–120, 2013.

[9] M. Li and C. Wang, "Traditional uses, phytochemistry, pharmacology, pharmacokinetics and toxicology of the fruit of Tetradium ruticarpum: A review," *ournal of Ethnopharmacology*, vol. 263, article 113231, 2020.

[10] A. S. Hammad and K. Machaca, "Store operated calcium entry in cell migration and cancer metastasis," *Cells*, vol. 10, no. 5, 2021.

[11] S. A. Danielsen, P. W. Eide, A. Nesbakken, T. Guren, E. Leithe, and R. A. Lothe, "Portrait of the PI3K/AKT pathway in colorectal cancer," *Biochimica et Biophysica Acta (BBA) - Reviews on Cancer*, vol. 1855, no. 1, pp. 104–121, 2014.

[12] M. Yu, B. Qi, W. Xiaoxiang, J. Xu, and X. Liu, "Baicalein increases cisplatin sensitivity of A549 lung adenocarcinoma cells via PI3K/Akt/NF-kappaB pathway," *Biomedicine & Pharmacotherapy*, vol. 90, pp. 677–685, 2017.

[13] M. Crumbaker, L. Khoja, and A. M. Joshua, "AR signaling and the PI3K pathway in prostate cancer," *Cancers (Basel)*, vol. 9, no. 4, 2017.

[14] L. M. Thorpe, H. Yuzugullu, and J. J. Zhao, "PI3K in cancer: divergent roles of isoforms, modes of activation and therapeutic targeting," *Nature Reviews Cancer*, vol. 15, no. 1, pp. 7–24, 2015.

[15] P. Liu, H. Cheng, T. M. Roberts, and J. J. Zhao, "Targeting the phosphoinositide 3-kinase pathway in cancer," *Nature Reviews Drug Discovery*, vol. 8, no. 8, pp. 627–644, 2009.

[16] A. G. Vaiopoulos, K. Athanasoula, and A. G. Papavassiliou, "NF-κB in colorectal cancer," *Journal of Molecular Medicine*, vol. 91, no. 9, pp. 1029–1037, 2013.

[17] S. I. Sutherland, R. Pe Benito, S. M. Henshall, L. G. Horvath, and J. G. Kench, "Expression of phosphorylated-mTOR during the development of prostate cancer," *Prostate*, vol. 74, no. 12, pp. 1231–1239, 2014.

[18] J. Ru, P. Li, J. Wang et al., "TCMSP: a database of systems pharmacology for drug discovery from herbal medicines," *Journal of Cheminformatics*, vol. 6, p. 13, 2014.

[19] X. Wang, Y. Shen, S. Wang et al., "PharmMapper 2017 update: a web server for potential drug target identification with a comprehensive target pharmacophore database," *Nucleic Acids Research*, vol. 45, no. W1, pp. W356–W360, 2017.

[20] A. Gasmi, G. Roubaud, C. Dariane et al., "Overview of the development and use of Akt inhibitors in prostate cancer," *Journal of Clinical Medicine*, vol. 11, no. 1, 2021.

[21] H. Chen, L. Zhou, X. Wu et al., "The PI3K/AKT pathway in the pathogenesis of prostate cancer," *Frontiers in Bioscience-Landmark*, vol. 21, pp. 1084–1091, 2016.

[22] L. Shi, F. Yang, F. Luo et al., "Evodiamine exerts anti-tumor effects against hepatocellular carcinoma through inhibiting beta-catenin-mediated angiogenesis," *Tumor Biology*, vol. 37, no. 9, pp. 12791–12803, 2016.

[23] S. T. Hwang, J. Y. Um, A. Chinnathambi et al., "Evodiamine mitigates cellular growth and promotes apoptosis by targeting the c-Met pathway in prostate cancer cells," *Molecules*, vol. 25, no. 6, 2020.

[24] Y. Lei, H. Gan, Y. Huang et al., "Digitoxin inhibits proliferation of multidrug-resistant HepG2 cells through G2/M cell cycle arrest and apoptosis," *Oncology Letters*, vol. 20, no. 4, p. 71, 2020.

[25] L. J. Deng, L. P. Hu, Q. L. Peng et al., "Hellebrigenin induces cell cycle arrest and apoptosis in human hepatocellular carcinoma HepG2 cells through inhibition of Akt," *Chemico-Biological Interactions*, vol. 219, pp. 184–194, 2014.

[26] L. J. Deng, Y. H. Lei, J. Y. Quan et al., "1beta-OH-arenobufagin induces mitochondrial apoptosis in hepatocellular carcinoma through the suppression of mTOR signaling pathway," *Journal of Ethnopharmacology*, vol. 266, article 113443, 2020.

[27] N. Yao, C. Wang, N. Hu et al., "Inhibition of PINK1/Parkin-dependent mitophagy sensitizes multidrug-resistant cancer cells to B5G1, a new betulinic acid analog," *Cell Death & Disease*, vol. 10, no. 3, p. 232, 2019.

[28] G. M. Cragg and D. J. Newman, "Plants as a source of anti-cancer agents," *Journal of Ethnopharmacology*, vol. 100, no. 1-2, pp. 72–79, 2005.

[29] D. J. Newman and G. M. Cragg, "Natural products as sources of new drugs from 1981 to 2014," *Journal of Natural Products*, vol. 79, no. 3, pp. 629–661, 2016.

[30] E. Pikarsky, R. M. Porat, I. Stein et al., "NF-κB functions as a tumour promoter in inflammation-associated cancer," *Nature*, vol. 431, no. 7007, pp. 461–466, 2004.

[31] C. Luo, J. Ai, E. Ren et al., "Research progress on evodiamine, a bioactive alkaloid of *Evodiae fructus*: focus on its anti-cancer activity and bioavailability (Review)," *Experimental and Therapeutic Medicine*, vol. 22, no. 5, p. 1327, 2021.

[32] F. S. Li, J. Huang, M. Z. Cui et al., "BMP9 mediates the anticancer activity of evodiamine through HIF1alpha/p53 in human colon cancer cells," *Oncology Reports*, vol. 43, no. 2, pp. 415–426, 2019.

[33] F. Yang, L. Shi, T. Liang et al., "Anti-tumor effect of evodiamine by inducing Akt-mediated apoptosis in hepatocellular carcinoma," *Biochemical and Biophysical Research Communications*, vol. 485, no. 1, pp. 54–61, 2017.

[34] Y. Zou, X. Qin, H. Xiong, F. Zhu, T. Chen, and H. Wu, "Apoptosis of human non-small-cell lung cancer A549 cells triggered by evodiamine through MTDH-dependent signaling pathway," *Tumor Biology*, vol. 36, no. 7, pp. 5187–5193, 2015.

[35] N. Liu, Y. Li, G. Chen, and K. Ge, "Evodiamine induces reactive oxygen species-dependent apoptosis and necroptosis in human melanoma A-375 cells," *Oncology Letters*, vol. 20, no. 4, p. 121, 2020.

[36] X. Hu, D. Li, C. Chu et al., "Antiproliferative effects of alkaloid evodiamine and its derivatives," *International Journal of Molecular Sciences*, vol. 19, no. 11, 2018.

[37] H. Yu, H. Jin, W. Gong, Z. Wang, and H. Liang, "Pharmacological actions of multi-target-directed evodiamine," *Molecules*, vol. 18, no. 2, pp. 1826–1843, 2013.

[38] X. Liu, L. Yang, Y. Bi, L. H. Wang, and H. Huang, "Effect of evodiamine in inducing apoptosis of gastric cancer SGC-7901 cells through mTOR signal pathway," *Zhongguo Zhong yao za zhi= Zhongguo Zhongyao Zazhi= China Journal of Chinese Materia Medica*, vol. 40, no. 16, pp. 3262–3266, 2015.

[39] B. Zhu, L. Zhao, Y. Liu et al., "Induction of phosphatase shatterproof 2 by evodiamine suppresses the proliferation and invasion of human cholangiocarcinoma," *he International Journal of Biochemistry & Cell Biology*, vol. 108, pp. 98–110, 2019.

[40] X. X. Guo, X. P. Li, P. Zhou et al., "Evodiamine induces apoptosis in SMMC-7721 and HepG2 cells by suppressing NOD1 signal pathway,," *International Journal of Molecular Sciences*, vol. 19, no. 11, 2018.

[41] Z. Wen, S. Feng, L. Wei, Z. Wang, D. Hong, and Q. Wang, "Evodiamine, a novel inhibitor of the Wnt pathway, inhibits the self-renewal of gastric cancer stem cells," *International journal of molecular medicine*, vol. 36, no. 6, pp. 1657–1663, 2015.

[42] W. T. Wei, H. Chen, Z. H. Wang et al., "Enhanced antitumor efficacy of gemcitabine by evodiamine on pancreatic cancer via regulating PI3K/Akt pathway," *International journal of biological sciences*, vol. 8, no. 1, pp. 1–14, 2012.

[43] Z. Hong, Z. Wang, B. Zhou et al., "Effects of evodiamine on PI3K/Akt and MAPK/ERK signaling pathways in pancreatic cancer cells," *International Journal of Oncology*, vol. 56, no. 3, pp. 783–793, 2020.

[44] R. Wang, D. Deng, N. Shao et al., "Evodiamine activates cellular apoptosis through suppressing PI3K/AKT and activating MAPK in glioma," *OncoTargets and Therapy*, vol. 11, pp. 1183–1192, 2018.

[45] C. Wang, S. Li, and M. W. Wang, "Evodiamine-induced human melanoma A375-S2 cell death was mediated by PI3K/Akt/caspase and Fas-L/NF-kappaB signaling pathways and augmented by ubiquitin-proteasome inhibition," *Toxicol In Vitro*, vol. 24, no. 3, pp. 898–904, 2020.

[46] Y. He, M. M. Sun, G. G. Zhang et al., "Targeting PI3K/Akt signal transduction for cancer therapy," *Signal Transduction and Targeted Therapy*, vol. 6, no. 1, p. 425, 2021.

[47] M. C. De Santis, F. Gulluni, C. C. Campa, M. Martini, and E. Hirsch, "Targeting PI3K signaling in cancer: challenges and advances," *Biochimica et Biophysica Acta (BBA)-Reviews on Cancer*, vol. 1871, no. 2, pp. 361–366, 2019.

[48] B. Wen, V. Roongta, L. Liu, and D. J. Moore, "Metabolic activation of the indoloquinazoline alkaloids evodiamine and rutaecarpine by human liver microsomes: dehydrogenation and inactivation of cytochrome P450 3A4," *Drug Metabolism and Disposition*, vol. 42, no. 6, pp. 1044–1054, 2014.

[49] S. Yan, Y. Liu, J. Feng et al., "Difference and alteration in pharmacokinetic and metabolic characteristics of low-solubility natural medicines," *Drug Metabolism Reviews*, vol. 50, no. 2, pp. 140–160, 2018.

Hindawi
Disease Markers
Volume 2022, Article ID 9312971, 10 pages
https://doi.org/10.1155/2022/9312971

Research Article

Inhibition of DEK Enhances Doxorubicin-Induced Apoptosis and Cell Cycle Arrest in T-Cell Acute Lymphoblastic Leukemia Cells

Xiaoxue Tian,[1] **Zeyu Zhu**,[1] **Guangming Wang**,[1] **Jun Xu**,[2] **Aibin Liang**,[1] **and Wenjun Zhang**[1]

[1]*Department of Hematology, Tongji Hospital, Tongji University School of Medicine, 1239 Siping Road, Shanghai 200092, China*
[2]*East Hospital, Tongji University School of Medicine, 1239 Siping Road, Shanghai 200092, China*

Correspondence should be addressed to Wenjun Zhang; zhangwenjun@tongji.edu.cn

Received 14 March 2022; Revised 19 May 2022; Accepted 21 May 2022; Published 20 June 2022

Academic Editor: Jian Wu

T-cell acute lymphoblastic leukemia (T-ALL) is a serious hematological tumor derived from early T-cell progenitors, which is extremely resistant to chemotherapy. Classically, doxorubicin (DOX) is an effective first-line drug for the treatment of T-ALL; however, DOX resistance limits its clinical effect. The DEK proto-oncogene (DEK) has been involved in neoplasms but remains unexplored in T-ALL. We silenced DEK on Jurkat cells and detected cell proliferation with cell counting and colony formation assay. Then, we detected DEK's drug sensitivity to DOX with CCK-8, cell cycle, and apoptosis with DOX treatment. Western blot analysis was performed to determine protein expression of apoptosis and cell cycle-related genes, including BCL2L1, caspase-3, and cyclin-dependent kinases (CDK). Finally, the tumorigenic ability of DEK was analyzed using a BALB/C nude mouse model. In this study, DEK was highly expressed in Jurkat cells. Inhibition of DEK can lead to decreased cell proliferation and proportion of S-phase cells in the cell cycle and more cell apoptosis, and the effect is more obvious after DOX treatment. Western blot results showed that DOX treatment leads to cell cycle arrest, reduction of cyclin-dependent kinase 6 (CDK6) protein, accumulation of CDKN1A protein, and DOX-induced apoptosis accompanied by reductions in protein levels of BCL2L1, as well as increases in protein level of caspase-3. Furthermore, DEK-silenced Jurkat cells generated a significantly smaller tumor mass in mice. Our study found that DEK is a novel, potential therapeutic target for overcoming DOX resistance in T-ALL.

1. Introduction

T-cell acute lymphoblastic leukemia (T-ALL) is a serious hematological tumor that is metastatic, aggressive, and resistant to chemotherapy [1], accounting for approximately 15% of ALL cases in children and 25% in adults [2]. With the advances in induction therapy, the event-free survivals of T-ALL patients have exceeded 85% in recent clinical trials [3]. However, about 20% of children and 40% of adults with T-ALL will relapse after intensive chemotherapy, leading to a 5-year overall survival of 50%–60% [4]. Chemoresistance is considered a major cause of recurrence and death of T-ALL [5]. Thus, resensitizing drug-resistant leukemia cells to chemotherapy may improve the prognosis of T-ALL patients.

Recently, the systematic gene expression has been emphasized [6]. The DEK proto-oncogene (DEK) is preferentially expressed in malignant cells [7]. DEK facilitates the tumorigenesis of different types of cancer cells by promoting cell proliferation and modulating cell cycle transition, as well as inhibiting cell apoptosis and senescence [8]. Furthermore, apoptosis induced by DEK deletion was accompanied by an increase in TP53 activity and its upregulation of CDKN1A and Bax [9]; this effect may be related to growth retardation and activation of TP53 function. CDKN1A mediates cell cycle arrest in the G1 and G2 phase and leads to cell apoptosis, and it can effectively inhibit CDK2, CDK3, CDK4, and CDK6 [10–12]. In melanoma, the downregulation of DEK significantly increased cell apoptosis and senescence through DOX treatment and had no effect on TP53 and CDKN2A

levels but had a significant effect on CDKN1A and caspase-3 levels [13]. DEK overexpression has been seen in many neoplasms, including chronic lymphocytic leukemia and acute myeloid leukemia [14, 15]. However, the involvement of DEK in T-ALL remains unexplored. It has been reported that DEK silencing may increase cancer cell sensitivity to DOX treatment in nonsmall cell lung cancer and metastatic colorectal cancer [16, 17]. Thus, we hypothesized that DEK silencing might enhance the sensitivity of leukemia cells.

Doxorubicin (DOX) is an anthracycline chemotherapeutic agent that is commonly used to treat ALL [18, 19]. Anthracyclines such as DOX, a topoisomerase II, kill leukemia cells by inhibiting cellular RNA and DNA synthesis [20, 21]. However, the efficacy of DOX is limited by the development of chemoresistance in leukemia cells [22]. DEK deficiency in different tumor cells has been shown to increase their sensitivity to DOX [13, 20]. Based on these studies, we supposed that the downregulation of DEK can enhance the sensitivity of Jurkat cells to DOX chemotherapy in T-ALL cells.

In this study, we determined DEK expression in different leukemia cell lines and found that DEK is highly expressed in Jurkat cells. Thus, we inhibited DEK expression in Jurkat cells to investigate the role and the underlying mechanism of DEK in the cellular response to DOX. We also explored the role of DEK in the tumorigenicity of Jurkat cells in a murine model. Our results suggest that DEK silencing may increase the sensitivity of Jurkat cells to DOX treatment, serving as a promising therapeutic approach for the management of DOX-resistant T-ALL.

2. Materials and Methods

2.1. Cell Lines. 293T, Raji, SU-DHL-4, Daudi, Nalm6, Jurkat, Panc-1,U937, PC-3, and MCF-7 cell lines (Shanghai Cell Bank). High glucose DMEM (SH30022.01B, Hyclone) was used to culture the 293T, Panc-1, and MCF-7 cell line. The remaining hematological tumor cell lines were cultured in RPMI-1640 medium (SH30809.01B, Hyclone). All cell lines were incubated at 37°C with 5% CO_2.

2.2. Gene Knockdown. shRNAs targeting DEK and negative control (scramble, SCR) vectors were purchased from Genomeditech. The shRNA sequences were as follows: shDEK-1, 5′-GCCAGTGCTAACTTGGAAGAA-3′; shDEK-2, 5′-GCCTGAAATTCTGTCAGATGAA-3′; and Scramble, 5′-GTTCTCCGAACGTGTCACGT-3′. The Jurkat cell line was infected with lentiviral supernatant and then analyzed *in vitro* for proliferation, cell viability, colony formation, cell cycle, and apoptosis.

2.3. RT-PCR. Total RNA was extracted from Jurkat cells at 48 h after transduction, using a Quick-RNA™ Microprep Kit (Zymo, Irvine, CA, USA). PCR was performed on a LightCycler 96 PCR system (Roche Life Science, Indianapolis, IN, USA). The primers were as follows: GAPDH, forward, 5′-CTCTGATTTGGTCGTATTGGG-3′, and reverse, 5′-TGGAAGATGGTGATGGGATT-3′; DEK, forward, 5′-AACTGCTTTACAACAGGCCAG-3′, and reverse, 5′-ATGGTTTGCCAGAAGGCTTTG-3′. The relative expression of DEK was calculated using the $2^{-\Delta\Delta Ct}$ method [24].

2.4. Colony Formation Assay. Jurkat cells were seeded into a 12-well plate coated with agarose (1.2% at the bottom and 0.6% on the top) at a density of 1×10^3 cells per well and transduced with lentiviral vectors expressing scramble shRNA or shDEK. After 14 days of culture, the number of colonies was counted at a magnification of 4x using an inverted microscope (AE2000; Motic, China).

2.5. Cell Counting Kit-8 (CCK-8) Assay. Jurkat cells were seeded in a 96-well plate at 5×10^3 cells per well and transduced with lentiviral vectors expressing scramble shRNA or shDEK. Cell viability was determined at 72 h after transduction using CCK-8 (Dojindo, Japan). Then, a microplate reader was used at an optical density of 450 nm.

2.6. Cell Apoptosis Analysis. We seed 1×10^6 cells per well in a 6-well plate and grow them at 37°C in a medium containing DOX or PBS for 4 hours. Then, the cells were washed 3 times with PBS and continued to be cultured in a cell incubator. Cells were washed 3 times with PBS and collected, then resuspended in 100 μl 1x binding buffer, stained with annexin V-APC at room temperature for ten minutes, and then stained with propidium iodide (PI) at room temperature for 5 minutes in the dark (BD Biosciences).

2.7. Cell Cycle Analysis. Bromodeoxyuridine (BrdU, BD biosciences, USA) and PI double staining was performed to detect cell cycle distribution. 1×10^6 cells were seeded and incubated with 3 μg/ml BrdU for 2 hours in 6-well plates. Cells were then harvested, mixed with 70% ethanol, and fixed overnight at -20°C. Samples were treated according to APC-BrdU antibody (BioLegend), and PI solution was added 5 minutes before flow cytometry analysis.

2.8. Western Blotting. Jurkat cells were harvested 5 days after lentiviral infection after transduction and lysed in RIPA lysis buffer (PC101, Epizyme Biotech). Then, the protein samples were mixed with 1x SDS (LT101S; Epizyme Biotech), boiled for 10 minutes, and then subjected to PAGE gel electrophoresis. The primary antibody used in the experiment includes DEK (E4S5J; Cell Signaling Technology), GAPDH (D16H11; Cell Signaling Technology), TP53 (DO-7; Cell Signaling Technology), c-Myc (ab32072; Abcam), CDK4 (A11136; ABclonal), CDK6 (13331; Cell Signaling Technology), CDKN1A (A1483; ABclonal), CDKN2A (ab151303; Abcam), caspase-3 (9662; Cell Signaling Technology), BCL2L1 (A19703; ABclonal) at 4°C, and HRP-conjugated secondary antibody (anti-rabbit,7074S, anti-mouse; 7076S,Cell Signaling Technology) at room temperature for 2 h. The target protein was detected by using Omni-ECL™-enhanced chemiluminescent liquid (SQ101; Epizyme Biotech) and quantified using ImageQuant LAS 4000 mini (GE).

2.9. Animal Model. 10^7 Jurkat cells from the SCR group or DEK knockdown (KD) group were injected into the subcutaneous tissue of female adult BALB/c nude mice in a

volume of 100 μl for *in vivo* tumor growth studies. Thirty days after transplantation, euthanizing mice in each group, the tumor volume was calculated as follows: tumor volume $= \text{length} \times (\text{width}^2)/2$, and tumor sizes were analyzed [23]. All animal experiments were performed in accordance with the standards of Tongji University School of Medicine.

2.10. Statistical Analysis. All quantitative data are displayed as mean ± SEM, and analyses were executed using Prism 8.0.

Unpaired two-tailed Student's *t*-test is used for data analysis. FCS Express 10 Flow software analyzes flow cytometry data. Differences were considered statistically significant at $P < 0.05$.

3. Results

3.1. DEK Is Highly Expressed in Jurkat Cells. To determine DEK expression in leukemia, assays were performed in different leukemia cell lines using RT-PCR and western blotting. The Raji cell line expressing the lowest DEK was selected as a control among the acute leukemia and lymphoma cell lines tested. The Jurkat cell line showed the highest level of DEK mRNA and protein (Figure 1). Of these cell lines, these results suggested that DEK is highly involved in T-ALL development. Results of the human protein analysis (https://www.proteinatlas.org/ENSG00000124795-DEK/tissue) showed the level of DEK mRNA transcripts in different cancer cell lines and normal tissues (Supplemental Figure S1). Therefore, experiments for DEK phenotypic and functional validation were performed using Jurkat cells.

3.2. shRNA-Mediated DEK Knockdown Efficiently Suppresses Cell Proliferation. We used the DEK-KD group and SCR group to conduct cell proliferation experiments in Jurkat cell. As shown in Figures 2(a) and 2(b), shDEK effectively suppressed DEK mRNA and protein expression of Jurkat cells compared with scramble shRNA. The cell proliferation assay showed that knockdown of DEK significantly inhibited Jurkat cell proliferation compared with SCR group starting 2 days after transduction (day 2: $P < 0.0001$, day 4 and day 6: $P < 0.001$; Figure 2(c)). Colony formation assay showed that the number of colonies formed by DEK-silenced cells was dramatically less than the number of colonies formed by the SCR group (28 ± 6 and 39 ± 4 vs. 135 ± 7; $P < 0.0001$; Figure 2(d)). Consistent results were observed in the size of colonies (Figure 2(e)). These data suggest that knockdown of DEK suppresses leukemia cell proliferation and colony formation. Thus, DEK is a novel target of T-ALL treatment.

3.3. DEK Inhibition in Jurkat Cells Increases the Response to DOX. We treated SCR Jurkat cells and DEK-silenced Jurkat cells with DOX and then performed cell viability, apoptosis, and cell cycle distribution. The results of CCK-8 analysis further showed that compared with the negative control, knockdown of DEK significantly reduced the cell viability of Jurkat cells in the presence of DOX ranging from 0 to 10 μM (IC50 of SCR group: 9.306 nM, IC50 of shDEK group: 3.744 nM; Figure 3(f)). The apoptotic rates of Jurkat cells in the DEK-KD groups were $13.02 \pm 0.58\%$ and $9.53 \pm 0.91\%$, compared with $4.95 \pm 0.41\%$ in the SCR group as shown in Figures 3(a) and 3(b) (shDEK-1: $P < 0.05$, shDEK-2: $P < 0.0001$). Following DOX treatment, the apoptotic rates of DEK KD groups were $19.3 \pm 0.49\%$ and $17.58 \pm 0.23\%$ compared with $10.38 \pm 0.92\%$ in the SCR group (shDEK-1: $P < 0.05$, shDEK-2: $P < 0.01$; Figures 3(a) and 3(b)). In brief, these results proved that DEK silencing increased the induction of apoptosis via DOX in Jurkat cells.

BrdU is a synthetic thymidine analog that is incorporated during the S phase of cellular DNA replication [25]. After the DNA is denatured, the cells are stained to allow BrdU incorporation, and any other target cell surfaces and/or intracellular targets are stained. The rates of S-phase cells in the DEK KD Jurkat cells were $37.67 \pm 1.53\%$ and $42.53 \pm 0.47\%$ versus $73.3 \pm 0.73\%$ in the SCR cells, the rates of G0/G1 phase cells in the DEK KD groups were $52.03 \pm 2.67\%$ and $48.93 \pm 0.83\%$ versus $21.83 \pm 0.36\%$ in the SCR cells in Figures 3(c) and 3(d) ($^{****}P < 0.0001$), and the proportions of G2/M-phase cells in the DEK KD groups were $9.06 \pm 1.53\%$ and $7.67 \pm 1.61\%$ versus $4.47 \pm 0.17\%$ in the SCR Jurkat cells (shDEK-1: $P < 0.01$, shDEK-2: $P < 0.05$). With DOX treatment, the proportions of S-phase cells were $7.41 \pm 0.47\%$ and $14.1 \pm 0.9\%$ in the KD groups and $26 \pm 2.9\%$ in the SCR group (Figures 3(c) and 3(e), shDEK-1: $P < 0.001$, shDEK-2: $P < 0.01$). These results indicate that under normal growth conditions, DEK silencing leads to reduced cell distribution in the S phase, cell arrest in the G0/G1 phase, and cell cycle arrest in the G2/M phase with DOX treatment.

3.4. DEK Regulates Apoptosis and Cell Cycle-Related Genes. The contribution of DEK in cancer progression involves the alterations in TP53, CDKN1A, c-Myc, and other apoptosis- and cell cycle-related genes [13, 26]. In melanoma, DEK silencing considerably increased cell apoptosis and senescence through DOX treatment and had no effect on TP53 and CDKN2A levels but had a significant effect on CDKN1A and caspase-3 levels [13]. As shown in Figures 4(a)–4(d), DEK silencing did not affect the protein expression of TP53, c-Myc, or CDKN2A regardless of the presence or absence of DOX, compared with SCR group. However, DEK silencing significantly suppressed BCL2L1 protein expression under normal conditions ($P < 0.001$) and further attenuated BCL2L1 protein expression repressed by DOX ($P < 0.0001$). In contrast, knockdown of DEK further enhanced DOX-induced caspase-3 protein expression ($P < 0.01$; Figures 4(a) and 4(c)). Regarding cell cycle-related genes, knockdown of DEK significantly suppressed CDK6 expression in the presence of DOX, respectively, compared with the SCR group (both $P < 0.05$). DEK silencing also further enhanced DOX-induced upregulation of CDKN1A expression ($P < 0.001$; Figures 4(b) and 4(d)). These data suggest that DEK silencing enhances the DOX sensitivity of Jurkat cells by modulating some apoptosis- and cell cycle-related genes in a TP53/CDKN2A/c-Myc-independent manner.

3.5. DEK Silencing Reduces the Tumorigenesis Ability of Jurkat Cells. To investigate the effect of DEK silencing

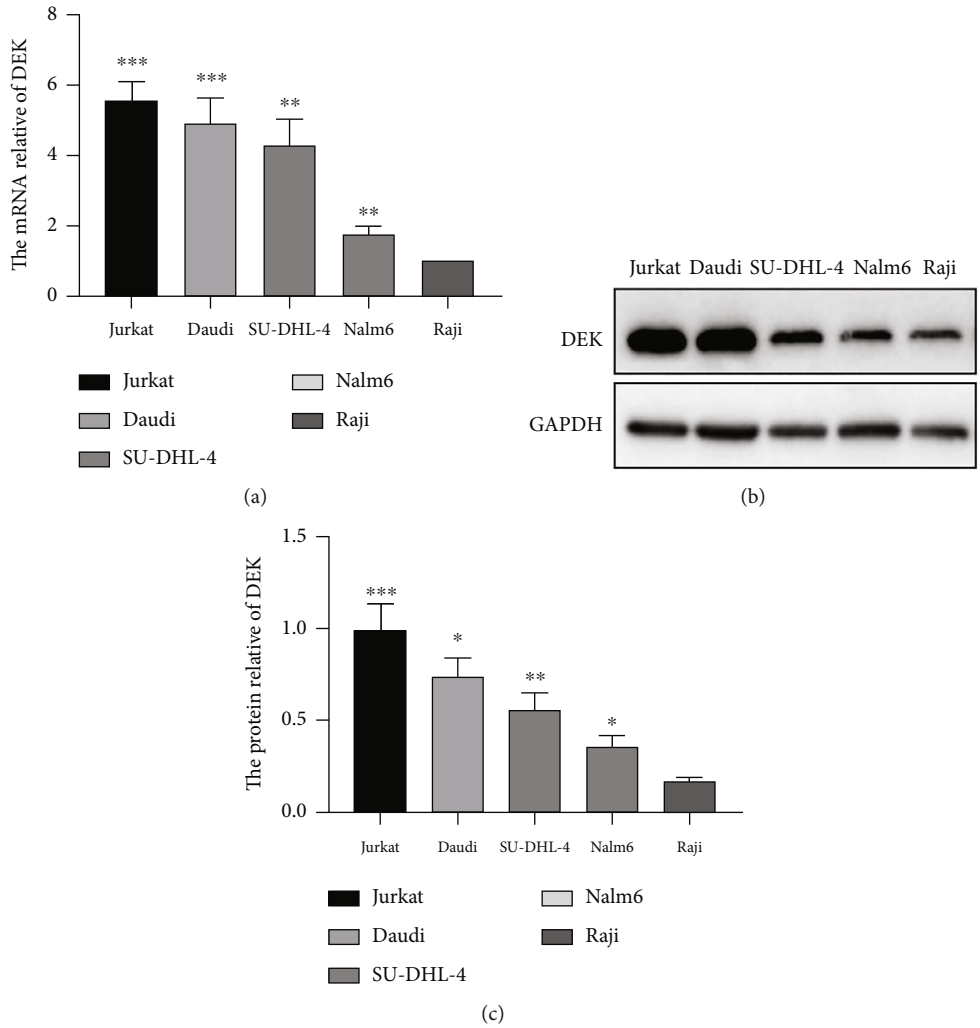

Figure 1: DEK is highly expressed in Jurkat T-ALL cells. (a) DEK mRNA expression in Jurkat, Daudi, Nalm6, SU-DHL-4, and Raji cells was analyzed by RT-PCR. (b) Protein expression levels of DEK and GAPDH in Jurkat, Daudi, Nalm6, SU-DHL-4, and Raji cells. (c) Quantification of DEK protein level by densitometric analysis. $^{*}P < 0.05$, $^{**}P < 0.01$, and $^{***}P < 0.001$.

in vivo, we established a tumor model by subcutaneously injecting DEK-silenced Jurkat cells or control cells into female adult BALB/C nude mice. The tumor volume in the DEK KD group was $82 \pm 13\,\text{mm}^3$ and the tumor weight was $0.708 \pm 0.248\,\text{g}$, whereas the tumor volume in the SCR group was $194.4 \pm 24.4\,\text{mm}^3$ and the tumor weight was $2.28 \pm 0.42\,\text{g}$ (Figures 5(a)–5(c), $****P < 0.0001$). The DEK KD mice were less aggressive and showed smaller tumor sizes than the mice we injected with SCR Jurkat cells.

4. Discussion

T-ALL is a serious hematological tumor and is highly resistant to chemotherapy, occurs in both adults and children, and has a high rate of recurrence [27, 28]. DEK plays a potential role in hematopoiesis and is dysregulated in acute myeloid leukemia and chronic lymphocytic leukemia [14, 15]; however, the involvement of DEK in T-ALL remains unknown.

Many studies have focused on the expression of cytokines [29]. Of note, it has been reported that DEK is overexpressed in most tumors of different origins, and tumorigenesis is promoted by promoting cell self-renewal and proliferation while inhibiting apoptosis, differentiation, and senescence of malignant cells [8, 9]. DEK-targeted inhibition has been considered as an effective treatment strategy of different malignancies due to its frequent upregulation in human malignancies which is considered to be an oncogene [30].

In this study, Jurkat cells were treated with DOX to induce apoptosis, decreased cell viability, and cell cycle arrest. Compared with negative control, knockdown of DEK promoted DOX-induced cell apoptosis while further reducing S-phase cells and cell proliferation of Jurkat cells with DOX, accompanied by significant alterations in the expression of apoptosis- and cell cycle-related genes. DEK silencing has no effect on TP53-related apoptosis and CDKN2A-induced senescence in Jurkat cells with DOX treatment. Therefore, DEK overexpression may inhibit the activity of TP53 and CDKN2A in Jurkat cells through alternative mechanisms. DEK acts as a transcriptional corepressor to inhibit NF-κB signaling, and NF-κB can participate

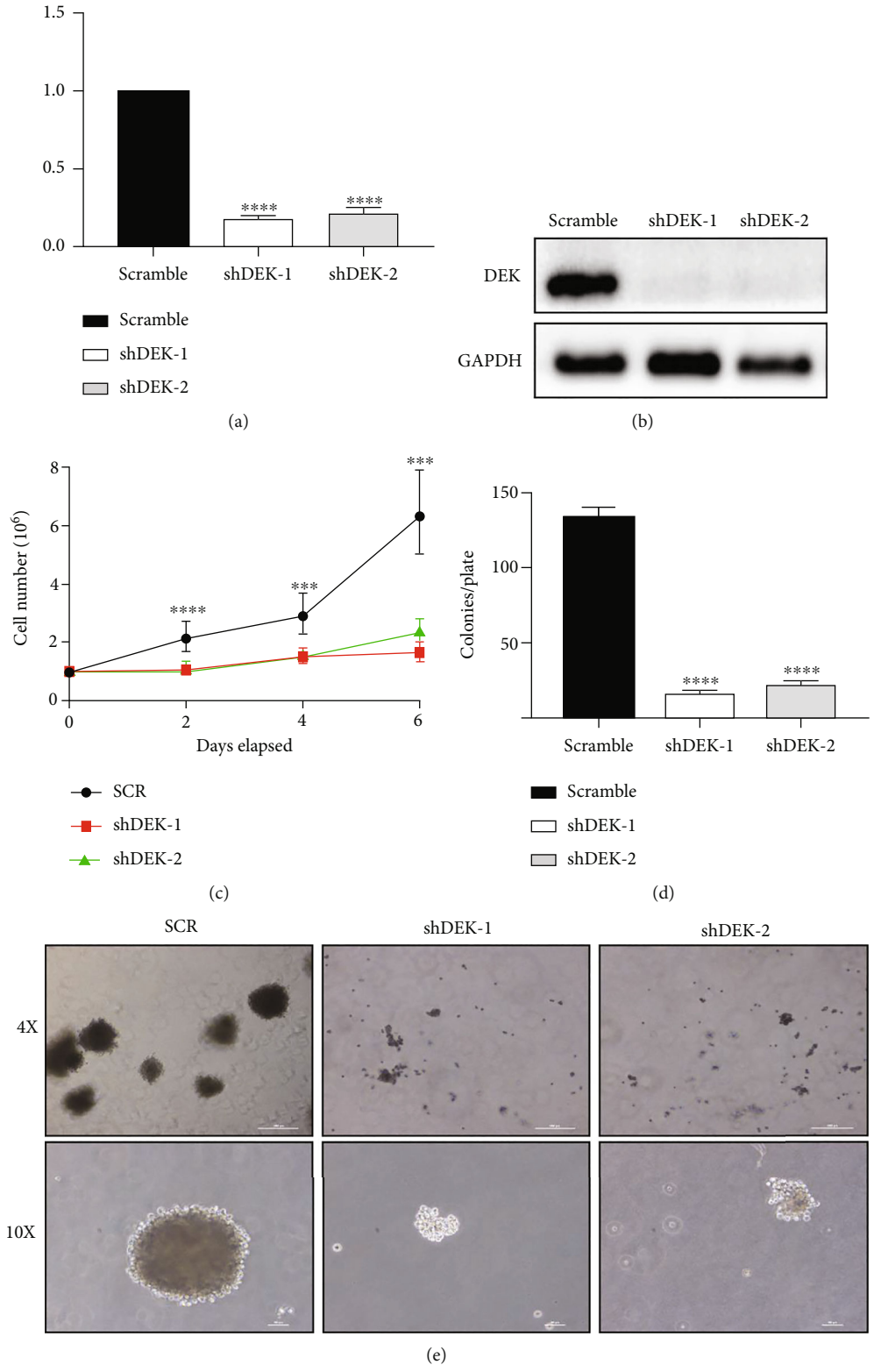

FIGURE 2: DEK silencing efficiently suppresses cell proliferation. (a) DEK mRNA levels relative to GAPDH levels in Jurkat cells infected with three different lentiviruses (SCR, shDEK-1, and shDEK-2) as detected by RT-PCR. (b) Western blotting was conducted to confirm that shDEK efficiently knocked down DEK protein expression in Jurkat cells. (c) Cell proliferation assay. Cell numbers were counted at 0, 2, 4, and 6 days after transduction. Data are expressed as the mean ± SEM. $^{***}P < 0.001$ vs. SCR; $n = 3$. (d) Colony formation assay. The number of colonies formed by Jurkat cells was counted at 14 days after transduction. (e) Representative images of colonies formed by DEK KD Jurkat cells after 14 days. $^{***}P < 0.001$ and $^{****}P < 0.0001$.

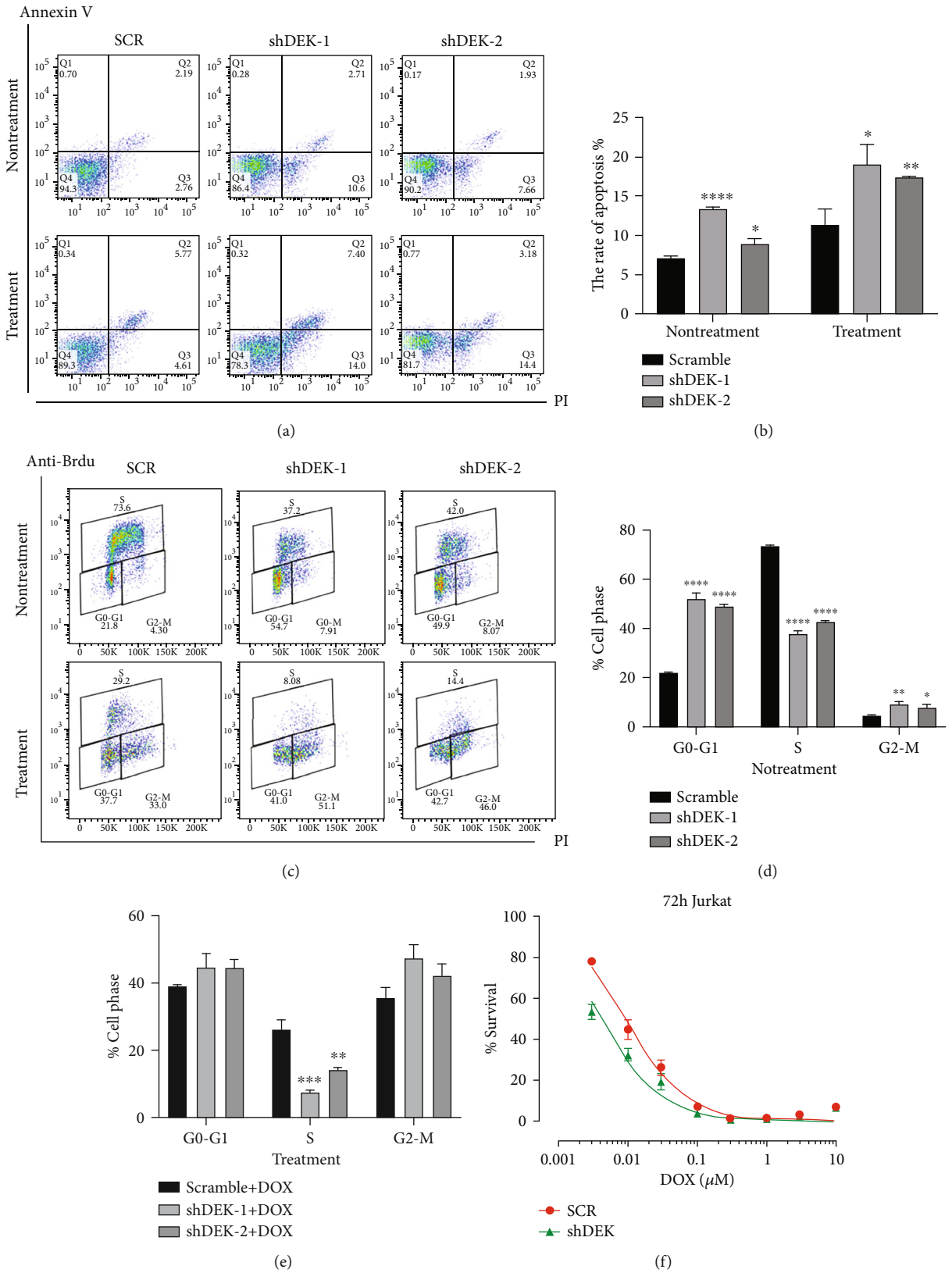

Figure 3: Knockdown of DEK promotes doxorubicin- (DOX-) induced apoptosis and cell cycle arrest of Jurkat cells. (a, b) Cells were treated with vehicle or DOX for 72 h at 5 days after lentiviral infection, and then, we examined cell apoptosis via flow cytometry. (c–e) Flow cytometry analysis was carried out to examine cell cycle phase distribution of Jurkat cells. (f) Cell viability in SCR and DEK KD groups was detected by CCK-8. Data are expressed as the mean ± SEM. $^{*}P < 0.05$, $^{**}P < 0.01$, $^{***}P < 0.001$, and $^{****}P < 0.0001$; shDEK-1 and shDEK-2 vs. SCR or shDEK-1+DOX and shDEK-2+DOX vs. SCR+DOX; $n = 3$. SCR: scramble RNA.

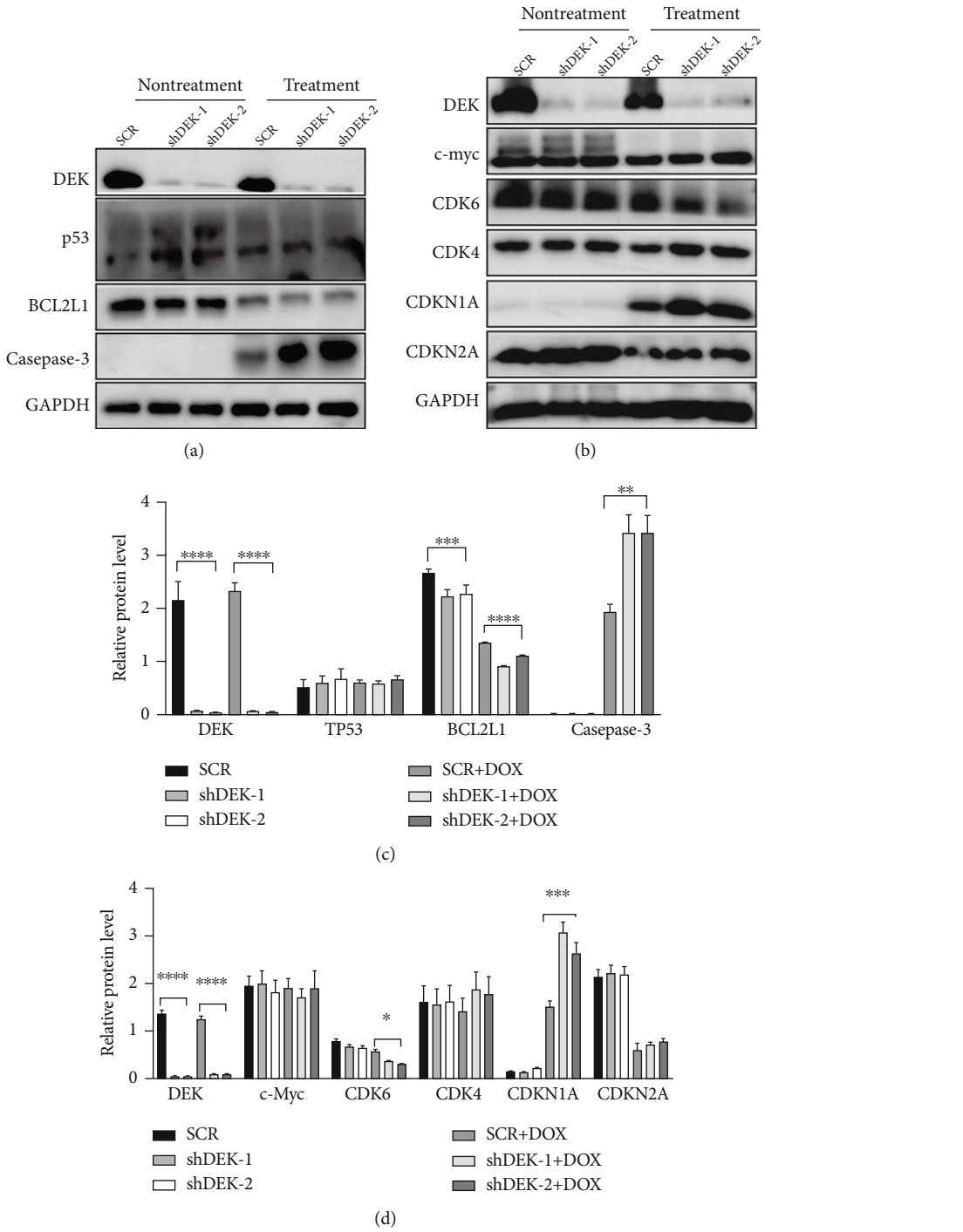

Figure 4: Expression of apoptosis- and cell cycle-related proteins in Jurkat cells. (a, b) Western blot analysis was conducted to measure the protein levels of SCR, shDEK-1, or shDEK-2 as indicated. (a, b) Representative blots are shown. (c) Quantification of (a). (d) Quantification of (b). GAPDH was used as an internal control. Data are expressed as the mean ± SEM. $^{*}P < 0.05$, $^{**}P < 0.01$, $^{***}P < 0.001$, $^{****}P < 0.0001$ vs. SCR; $n = 3$. SCR: scramble RNA.

in the apoptosis process of malignant hematopoietic cell lines by acting on CDKN1A [28]. CDKN1A effectively inhibits cyclins with direct roles in G1/S transition, including CDK2, CDK3, CDK4, and CDK6, but it inhibits other known CDKs poorly [11, 12]. Therefore, further research is needed to determine whether DEK acts on CDKN1A in Jurkat cells through NF-κB.

Apoptosis is a complex biological process, and chemotherapy drugs are often used to kill tumor cells to treat tumors. With the widespread application of anticancer drugs, dysregulation of apoptotic pathways has been shown to play an irreplaceable role in chemoresistance. Antiapoptotic protein BCL2L1 regulates apoptotic cell death through Bcl-2. Increased expression of BCL2L1 is

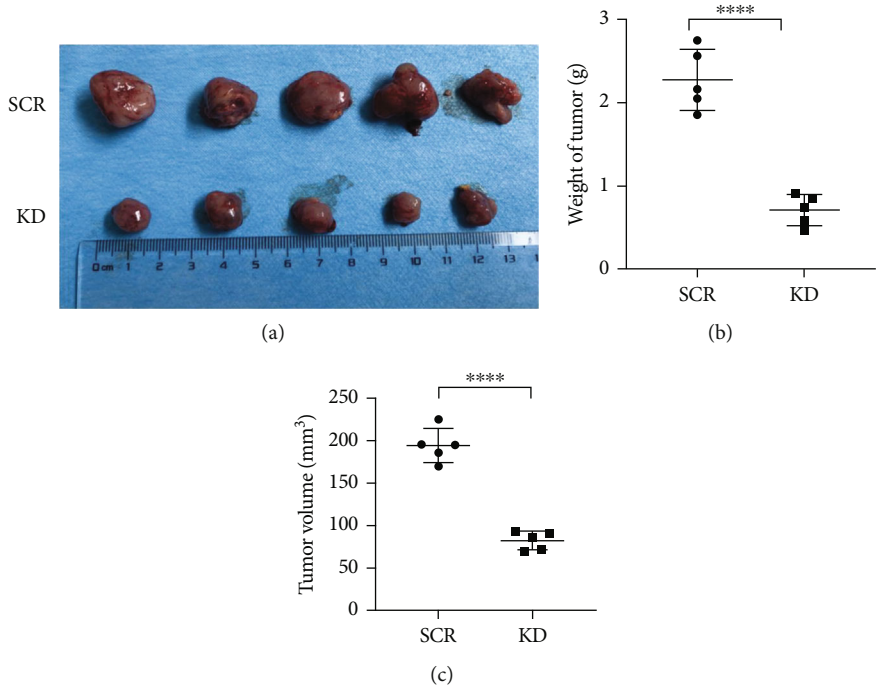

FIGURE 5: *In vivo* tumorigenesis ability study. Knockdown of DEK suppressed the growth of Jurkat cell-derived tumors in mice. (a) Image of tumors derived from Jurkat cells. (b, c) Tumor weights and volumes at 30 days after inoculating Jurkat cells transduced with negative control or shDEK. $^{****}P < 0.0001$ vs. SCR, $n = 5$. SCR: scramble RNA; KD: knockdown.

associated with chemoresistance in T-ALL [31]. Consistent with our results, knockdown of DEK attenuated the BCL2L1 expression of Jurkat cells, and the effect was more pronounced with DOX. These results suggest that DEK silencing enhances the sensitivity of Jurkat cells to chemotherapeutic drugs.

Caspase-3 is a well-known proapoptotic marker. Proapoptotic caspase-3 is frequently activated during apoptosis. DEK silencing induces apoptosis of tumor cells by activation of caspase-9 and subsequent cleavage and activation of procaspase-3, which then cleaves different cellular endogenous substrates leading to cell death [32, 33]. Therefore, DEK silencing may enhance DOX-induced apoptosis by activating the mitochondrial pathway through activating caspase-9 and then caspase-3 in Jurkat cells. Consistent with the *in vitro* data, knockdown of DEK also suppressed the growth of Jurkat cell-derived tumors in mouse model, suggesting that DEK is a promising therapeutic target in T-ALL treatment.

In brief, the deletion of DEK under DOX treatment leads to the overexpression of caspase-3 and the downregulation of BCL2L1, indicating its role in regulating cell apoptosis; the level of CDK6 decreases, and the expression of CDKN1A increases, indicating its role in regulating cell cycle. These results indicate that the inhibition of DEK expression combined with DOX treatment is a possible therapeutic strategy for T-ALL. In general, all these data suggest that DEK silencing in T-ALL cells increases their sensitivity to DOX and may work as a novel therapeutic target to T-ALL.

5. Conclusion

In summary, DEK is highly expressed in Jurkat cells and promotes cell proliferation and colony formation in vitro. DEK silencing may promote DOX-induced cell apoptosis and cell cycle arrest, thus increasing the sensitivity of Jurkat cells to DOX treatment. Although the underlying mechanisms and effects of DEK on normal cells require further study, our results suggest that knockdown of DEK is a novel, potential therapeutic approach to overcome DOX resistance in T-ALL treatment.

Data Availability

The data that support the findings of this study are available from the corresponding author upon reasonable request.

Ethical Approval

All experiments and procedures were conducted in compliance with the ethical principles of Tongji University School of Medicine and received ethical approval from the Animal Ethics Committee of Tongji University.

Consent

Written informed consent was obtained from all participants at the time of obtaining consent to participate.

Conflicts of Interest

The authors have no conflicts of interest to declare.

Authors' Contributions

WZ, AL, and JX provided biological materials and reagents, and GM and ZZ revised the manuscript. XT was responsible for designing and conducting the experiments and analyzing the data for article writing. All authors read and approved the final manuscript.

Acknowledgments

We thank the research staff at Tongji University School of Medicine for assistance in performing experiments. This study was supported by the Ministry of Science and Technology of the People's Republic of China (Grant no. 2021YFA1100800) and the National Natural Science Foundation of China (Grant no. 81770151).

Supplementary Materials

Supplemental Figure S1: DEK is highly expressed in tumor cell lines. *(Supplementary Materials)*

References

[1] E. A. Raetz and D. T. Teachey, "T-cell acute lymphoblastic leukemia," *Hematology 2014, the American Society of Hematology Education Program Book*, vol. 2016, no. 1, pp. 580–588, 2016.

[2] M. R. Litzow and A. A. Ferrando, "How I treat T-cell acute lymphoblastic leukemia in adults," *Blood*, vol. 126, no. 7, pp. 833–841, 2015.

[3] K. P. Dunsmore, S. S. Winter, M. Devidas et al., "Children's oncology group AALL0434: a phase III randomized clinical trial testing nelarabine in newly diagnosed T-cell acute lymphoblastic leukemia," *Journal of Clinical Oncology*, vol. 38, no. 28, pp. 3282–3293, 2020.

[4] A. Moricke, M. Zimmermann, M. G. Valsecchi et al., "Dexamethasone vs prednisone in induction treatment of pediatric ALL: results of the randomized trial AIEOP-BFM ALL 2000," *Blood*, vol. 127, no. 17, pp. 2101–2112, 2016.

[5] E. Follini, M. Marchesini, and G. Roti, "Strategies to overcome resistance mechanisms in T-cell acute lymphoblastic leukemia," *International Journal of Molecular Sciences*, vol. 20, no. 12, p. 3021, 2019.

[6] J. Wu, Z. P. Chen, A. Q. Shang et al., "Systemic bioinformatics analysis of recurrent aphthous stomatitis gene expression profiles," *Oncotarget*, vol. 8, no. 67, pp. 111064–111072, 2017.

[7] M. Devany, F. Kappes, K. M. Chen, D. M. Markovitz, and H. Matsuo, "Solution NMR structure of the N-terminal domain of the human DEK protein," *Protein Science*, vol. 17, no. 2, pp. 205–215, 2008.

[8] V. Alexiadis, T. Waldmann, J. Andersen, M. Mann, R. Knippers, and C. Gruss, "The protein encoded by the proto-oncogene DEK changes the topology of chromatin and reduces the efficiency of DNA replication in a chromatin-specific manner," *Genes & Development*, vol. 14, no. 11, pp. 1308–1312, 2000.

[9] T. M. Wise-Draper, H. V. Allen, E. E. Jones, K. B. Habash, H. Matsuo, and S. I. Wells, "Apoptosis inhibition by the human DEK oncoprotein involves interference with p53 functions," *Molecular and Cellular Biology*, vol. 26, no. 20, pp. 7506–7519, 2006.

[10] J. W. Harper, G. R. Adami, N. Wei, K. Keyomarsi, and S. J. Elledge, "The p21 Cdk-interacting protein Cip1 is a potent inhibitor of G1 cyclin-dependent kinases," *Cell*, vol. 75, no. 4, pp. 805–816, 1993.

[11] J. W. Harper and S. J. Elledge, "Cdk inhibitors in development and cancer," *Current Opinion in Genetics & Development*, vol. 6, no. 1, pp. 56–64, 1996.

[12] A. L. Gartel and A. L. Tyner, "Transcriptional regulation of the p21(WAF1/CIP1) gene," *Experimental Cell Research*, vol. 246, no. 2, pp. 280–289, 1999.

[13] M. S. Khodadoust, M. Verhaegen, F. Kappes et al., "Melanoma proliferation and chemoresistance controlled by the DEK oncogene," *Cancer Research*, vol. 69, no. 16, pp. 6405–6413, 2009.

[14] D. M. Wang, L. Liu, L. Fan et al., "Expression level of DEK in chronic lymphocytic leukemia is regulated by fludarabine and Nutlin-3 depending on p53 status," *Cancer Biology & Therapy*, vol. 13, no. 14, pp. 1522–1528, 2012.

[15] S. Casas, B. Nagy, E. Elonen et al., "Aberrant expression of HOXA9, DEK, CBL and CSF1R in acute myeloid leukemia," *Leukemia & Lymphoma*, vol. 44, no. 11, pp. 1935–1941, 2003.

[16] X. Liu, D. D. Qi, J. J. Qi et al., "Significance of DEK overexpression for the prognostic evaluation of non-small cell lung carcinoma," *Oncology Reports*, vol. 35, no. 1, pp. 155–162, 2016.

[17] J. Martinez-Useros, M. Rodriguez-Remirez, A. Borrero-Palacios et al., "DEK is a potential marker for aggressive phenotype and irinotecan-based therapy response in metastatic colorectal cancer," *BMC Cancer*, vol. 14, no. 1, 2014.

[18] C. F. Thorn, C. Oshiro, S. Marsh et al., "Doxorubicin pathways: pharmacodynamics and adverse effects," *Pharmacogenetics and Genomics*, vol. 21, no. 7, pp. 440–446, 2011.

[19] G. Minotti, P. Menna, E. Salvatorelli, G. Cairo, and L. Gianni, "Anthracyclines: molecular advances and pharmacologic developments in antitumor activity and cardiotoxicity," *Pharmacological Reviews*, vol. 56, no. 2, pp. 185–229, 2004.

[20] D. A. Gewirtz, "A critical evaluation of the mechanisms of action proposed for the antitumor effects of the anthracycline antibiotics adriamycin and daunorubicin," *Biochemical Pharmacology*, vol. 57, no. 7, pp. 727–741, 1999.

[21] B. X. Pang, X. H. Qiao, L. Janssen et al., "Drug-induced histone eviction from open chromatin contributes to the chemotherapeutic effects of doxorubicin," *Nature Communications*, vol. 4, no. 1, p. 1908, 2013.

[22] B. S. Sorensen, J. Sinding, A. H. Andersen, J. Alsner, P. B. Jensen, and O. Westergaard, "Mode of action of topoisomerase II-targeting agents at a specific DNA sequence: uncoupling the DNA binding, cleavage and religation events," *Journal of Molecular Biology*, vol. 228, no. 3, pp. 778–786, 1992.

[23] S. Naito, A. C. Voneschenbach, R. Giavazzi, and I. J. Fidler, "Growth and metastasis of tumor cells isolated from a human renal cell carcinoma implanted into different organs of nude mice," *Cancer Research*, vol. 46, no. 8, pp. 4109–4115, 1986.

[24] K. J. Livak and T. D. Schmittgen, "Analysis of relative gene expression data using real-time quantitative PCR and the $2^{(-\Delta\Delta C(T))}$ method," *Methods*, vol. 25, no. 4, pp. 402–408, 2001.

[25] L. Harris, O. Zalucki, and M. Piper, "BrdU/EdU dual labeling to determine the cell-cycle dynamics of defined cellular subpopulations," *Journal of Molecular Histology*, vol. 49, pp. 229–234, 2018.

[26] K. H. Kim, C. W. Han, S. H. Yoon et al., "The fruit hull of Gleditsia sinensis enhances the anti-tumor effect of cis-diammine dichloridoplatinum II (cisplatin)," *Evidence-Based Complementary and Alternative Medicine*, vol. 2016, Article ID 7480971, 10 pages, 2016.

[27] Y. Liu, J. Easton, Y. Shao et al., "The genomic landscape of pediatric and young adult T-lineage acute lymphoblastic leukemia," *Nature Genetics*, vol. 49, no. 8, pp. 1211–1218, 2017.

[28] J. Savickiene, G. Treigyte, K. E. Magnusson, and R. Navakauskiene, "p21 (Waf1/Cip1) and FasL gene activation via Sp1 and NFκB is required for leukemia cell survival but not for cell death induced by diverse stimuli," *The International Journal of Biochemistry & Cell Biology*, vol. 37, no. 4, pp. 784–796, 2005.

[29] Y. Wang, J. Wu, J. Xu, and S. Lin, "Clinical significance of high expression of stanniocalcin-2 in hepatocellular carcinoma," *Bioscience Reports*, vol. 39, no. 4, 2019.

[30] H. H. Guo, M. Prell, H. Konigs et al., "Bacterial growth inhibition screen (BGIS) identifies a loss-of-function mutant of the DEK oncogene, indicating DNA modulating activities of DEK in chromatin," *FEBS Letters*, vol. 595, no. 10, pp. 1438–1453, 2021.

[31] H. E. Broome, A. L. Yu, M. Diccianni, B. M. Camitta, B. P. Monia, and N. M. Dean, "Inhibition of Bcl-xL expression sensitizes T-cell acute lymphoblastic leukemia cells to chemotherapeutic drugs," *Leukemia Research*, vol. 26, no. 3, pp. 311–316, 2002.

[32] J. Wu, J. R. Zhang, and J. Qin, "Clinical significance of methylation of E-cadherin and p14ARF gene promoters in skin squamous cell carcinoma tissues," *International Journal of Clinical and Experimental Medicine*, vol. 7, no. 7, pp. 1808–1812, 2014.

[33] M. X. Jiang, L. Qi, L. S. Li, and Y. Li, "The caspase-3/GSDME signal pathway as a switch between apoptosis and pyroptosis in cancer," *Cell Death Discovery*, vol. 6, no. 1, p. 112, 2020.

Hindawi
Disease Markers
Volume 2022, Article ID 3451544, 17 pages
https://doi.org/10.1155/2022/3451544

Research Article

The Effect of Artificial Liver Support System on Prognosis of HBV-Derived Hepatorenal Syndrome: A Retrospective Cohort Study

Xinyu Sheng,[1] **Jiaqi Zhou**,[2] **Xiuyu Gu**,[3] **and Hong Wang**[1]

[1]*Department of Infectious Disease, Zhejiang Hospital, Hangzhou, China*
[2]*Department of Respiration, The First Hospital of Jiaxing (The Affiliated Hospital of Jiaxing University), Jiaxing, Zhejiang, China*
[3]*Department of Clinical Laboratory, The Affiliated Suzhou Hospital of Nanjing Medical University, Suzhou, Jiangsu, China*

Correspondence should be addressed to Xiuyu Gu; 1352117185@qq.com and Hong Wang; hongwang71@yahoo.com

Received 4 February 2022; Revised 23 March 2022; Accepted 25 April 2022; Published 1 June 2022

Academic Editor: Chia-Jung Li

Hepatorenal syndrome (HRS) could occur when patients get decompensated liver cirrhosis. Meanwhile, hepatitis B virus (HBV) infection raises the risk of mortality of the end-stage liver diseases. As the artificial liver support system (ALSS) has been applied in liver failure, whether ALSS could benefit HBV-derived HRS remains uncertain. We retrospectively enlisted eligible HRS patients and compared the baseline characteristics and prognosis between HBV-derived HRS and non-HBV-derived HRS. Furthermore, propensity score matching (PSM) and Cox regression analyses were used to assess the beneficial effect of ALSS on HBV-derived HRS. In addition, a stratified analysis was carried out according to the degree of acute kidney injury (AKI) and the number of organ failures to observe in which populations ALSS can obtain the most excellent therapeutic effect. 669 patients were diagnosed as HRS, including 298 HBV negative and 371 HBV positive. Baseline characteristics were different between patients with HBV positive and HBV negative. HBV-derived HRS has higher 28-day mortality, though without a statistical difference. After PSM, 50 patients treated with ALSS and 150 patients treated with standard medical treatment (SMT) constituted a new cohort for the following analysis. We found that ALSS could significantly benefit HRS patients ($P = 0.025$). Moreover, the median survival time of patients treated with ALSS was longer than those treated with SMT. INR, neutrophil percentage, and treatment with ALSS were independent predictive factors for short-term mortality in HBV-derived HRS. The stratified analysis showed that ALSS could reduce the 28-day mortality of patients with HBV-derived HRS, especially those in AKI stage 3 and with organ failure ≥ 2. Additionally, serum bilirubin was significantly lower after ALSS, and the alteration of INR and creatinine were independent predictive elements for the mortality of HBV-derived HRS. HBV-derived HRS is more severe than non-HBV-derived HRS and has a worse prognosis. ALSS could reduce the short-term mortality of patients with HBV-derived HRS, especially those in AKI stage 3 and with organ failure ≥ 2. INR and the change of creatinine and INR could predict the prognosis of HBV-derived HRS. ChiCTR2200060123.

1. Introduction

Patients with cirrhosis are more prone to acute kidney injury (AKI). According to reports, 20% of the hospitalized patients with cirrhosis may get AKI [1]. Hepatorenal syndrome (HRS) means a progressive renal dysfunction in cirrhosis patients and high mortality in a brief time, which is one of the severe complications of decompensated cirrhosis [2, 3]. The probability of patients with liver cirrhosis and ascites developing to HRS within five years is up to 40% [4]. Given the unclear diagnosis, treatment strategies for HRS are inaccurate, which may result in high mortality of HRS. Hepatitis B virus (HBV) has been threatening health for many years. There are more than 350 million HBV carriers all around the world.

Millions of people suffer from HBV-related liver diseases every year [5]. Although the number of HBV-related liver diseases has been decreasing with the prevalence of HBV vaccines, it still brings significant challenges to many countries' medical and health services, including China. HBV

infection has been proved to be associated with hepatitis, cirrhosis, and even hepatocellular carcinoma, which could cause an unwell prognosis [6–8]. A multicenter descriptive study has revealed that the original characteristics of COVID-19 cases combined with HBV infection were a higher rate of liver injury, coagulation disorders, severe/critical tendency, and increased susceptibility [9]. Considering the unique pathophysiology of HRS with extrahepatic manifestations, it is essential to pay more attention to HBV-related HRS. The most effective treatment for HRS is liver transplantation, but due to insufficient donors and economic constraints, the proportion of liver transplantation is small. Thus, finding a cost-effective treatment that can effectively improve the survival of HBV-derived HRS has become the top priority.

Various artificial liver support systems (ALSSs) have been widely used during past decades [8, 9]. ALSS could remove harmful substances from the patient's body and supplement the substances needed in the body through physical means, using the unique biofilm and the adsorption of chemical substances [10]. ALSSs have several types, and Professor Li's team launched a novel ALSS named Li's artificial liver system (Li-ALS) which includes plasma exchange, charcoal hemoperfusion, plasma bilirubin absorption, charcoal plasma perfusion, hemofiltration, and hemodialysis and has been applied in China since the 1980s [11]. Many kinds of research have proved that it could benefit patients with end-stage liver diseases, especially HBV-related acute-on-chronic liver failure. However, studies on the effect of ALSS on HRS, especially HBV-derived HRS, are not abundant and whether ALSS could benefit this part of patients has been uncertain.

We conducted a multicenter, retrospective, and long-term study to evaluate the association between ALSS and HBV-derived HRS. And we use propensity score matching (PSM) to balance confounding variables.

2. Materials and Methods

2.1. Study Population and Data Collection. In this cohort study, we screened patients from four general hospitals from January 2011 to March 2021, including the First affiliated Hospital of Zhejiang University, Shulan Hospital, People's Hospital of Zhejiang Province, and People's Hospital of Shengzhou City. The patients with decompensated cirrhosis and acute renal injury were enrolled at admission. Demographic data and vital signs were obtained from medical records. And follow-up was tracked by phone or address. Considering the rapid progress of HRS, we recorded 28-day mortality as our primary outcome and change of laboratory indexes as a secondary outcome. All assays for serum biochemical parameters were operated with the same testing equipment. The study was approved by the Ethics Committee of the First Affiliated Hospital, Zhejiang University (No. 2019-1449-1), and developed according to the ethical guidelines of the Declaration of Helsinki.

2.2. Inclusion and Exclusion Criteria. HRS was identified according to the standard from the International Club of Ascites (ICA) in 2015. An increase in sCr ≥ 26.5 mmol/L (≥0.3 mg/dL) within two days or 1.5 times the baseline was AKI. Detailed stage information was listed. AKI stage 1: increase in sCr ≥ 26.5 mmol/L (≥0.3 mg/dL) or an increase in sCr ≥ 1.5-fold to 2-fold from baseline. AKI stage 2: increase in sCr > two to threefold from baseline. AKI stage 3: increase of sCr > threefold from baseline or sCr ≥ 353.6 mmol/L (4.0 mg/dL) with an acute increase ≥ 26.5 mmol/L (≥0.3 mg/dL) or received renal replacement therapy. HBV positive was defined as HBV surface antigen positive ≥ six months, serum HBV-DNA ≥ 20000 IU/mL, or liver biopsy indicating chronic hepatitis.

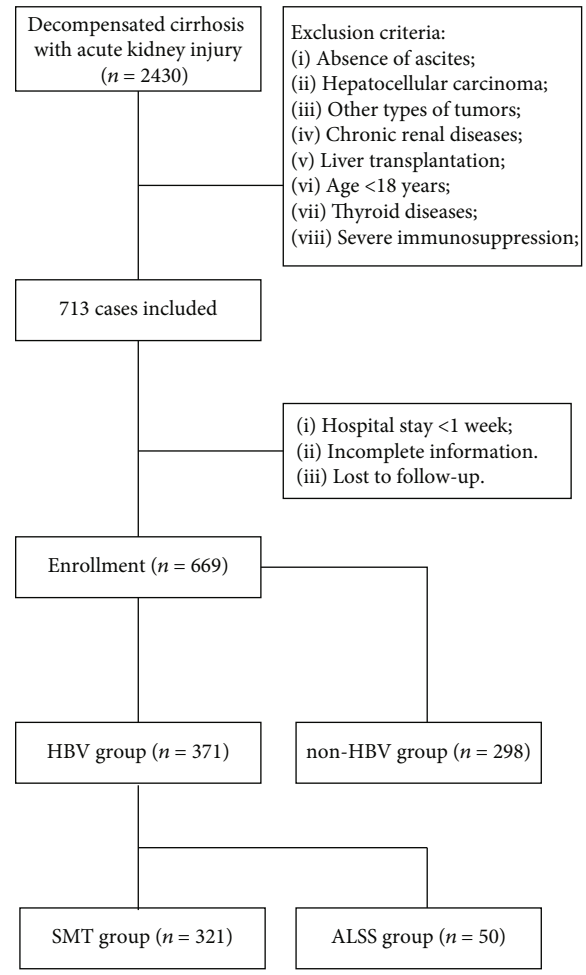

Figure 1: Screening and enrollment of patients. ALSS: artificial liver support system; SMZ: standard medical treatment.

Exclusion criteria are as follows: (1) absence of ascites, (2) any benign or malignant carcinoma (37), (3) chronic renal injury, (4) liver transplantation or severe immunosuppression, (5) age < 18 years, (6) hospital stay was less one week, and (7) incomplete information. Also, patients lost to follow-up were excluded.

For ACLF grade 1, patients include those with single organ failure, mainly coagulation, circulatory, respiratory systems or kidney failure. For ACLF grade 2, patients include those with two organ failures. ACLF grade 3: in patients include those with 3 or more organ system failures.

Table 1: Characteristics between HBV-derived HRS and non-HBV-derived HRS.

Variates	Non-HBV-derived HRS	HBV-derived HRS	*P* value
n	298	371	
Age (year)	62.54 ± 11.66	57.82 ± 12.38	<0.001
Male sex	208 (69.80)	282 (76.00)	0.086
Degree of HE			0.998
Without HE (%)	164 (55.0)	202 (54.4)	
I	42 (14.1)	55 (14.8)	
II	26 (8.7)	34 (9.2)	
III	22 (7.4)	26 (7.0)	
IV	44 (14.8)	54 (14.6)	
Ascitic (%)			0.222
Grade 1	54 (18.10)	70 (18.90)	
Grade 2	84 (28.2)	110 (29.6)	
Grade 3	120 (40.3)	122 (32.9)	
Missing data	40 (13.4)	69 (18.6)	
MAP (mmHg)	93.01 ± 16.06	95.97 ± 16.76	0.021
HR	85.43 ± 15.57	87.14 ± 16.10	0.166
INR	1.75 (1.40-1.99)	1.84 (1.51-2.42)	<0.001
Neutrophil (%)	74.27 ± 11.83	74.80 ± 11.93	0.566
Albumin (g/L)	28.50 ± 5.59	29.25 ± 5.46	0.079
Globulin (g/L)	29.44 ± 9.09	28.81 ± 8.98	0.368
ALT (U/L)	36.50 (21.00-106.00)	50.50 (24.00-125.00)	0.053
AST (U/L)	63.50 (34.50-98.75)	80.50 (41.00-164.50)	0.006
Hemoglobin (g/L)	93.41 ± 26.13	101.05 ± 26.88	<0.001
Cystatin C (mg/L)	2.16 (1.56-3.53)	1.95 (1.34-3.24)	0.197
Urea (mmol/L)	14.53 (9.05-24.40)	13.30 (7.77-23.10)	0.284
Creatinine (mg/dL)	1.83 (1.03-2.71)	1.62 (0.93-2.64)	0.656
Serum bilirubin (mg/dL)	11.75 (2.28-22.28)	13.68 (3.17-24.88)	0.073
GGT (U/L)	70.00 (32.00-152.00)	59.00 (34.00-122.00)	0.107
Potassium (mmol/L)	4.20 ± 0.81	4.63 ± 0.72	0.281
Sodium (mmol/L)	134.45 ± 6.12	133.95 ± 6.70	0.049
MELDs	26.21 ± 8.09	27.55 ± 9.21	0.742
iMELD	50.86 ± 10.24	51.14 ± 11.21	0.179
CTP	10.95 ± 1.92	11.18 ± 1.92	0.122
CLIF-ACLFs	50.57 ± 10.14	49.69 ± 10.57	0.278
CLIF-SOFAs	10.01 ± 3.49	10.14 ± 3.56	0.620
COSSH-ACLFs	7.13 ± 1.63	7.19 ± 1.85	0.648
Liver failure	146 (49.0)	198 (53.4)	0.295
Coagulation failure	42 (14.1)	84 (22.6)	0.007
Cerebral failure	66 (22.1)	80 (21.6)	0.930

ALT: alanine aminotransferase; CLIF-SOFA: Chronic Liver Failure-Sequential Organ Failure Assessment; COSSH-ACLF: Chinese Group on the Study of Severe Hepatitis B-Acute-on-Chronic Liver Failure; HBV: hepatitis B virus; INR: international normalized ratio; MAP: mean arterial pressure; MELD: Model for End-Stage Liver Disease.

Model 1 was adjusted for age and sex. Model 2 was adjusted for age, sex, neutrophils, alanine aminotransferase (ALT), albumin, serum bilirubin, COSSH-ACLFs, and international normalized ratio (INR).

Liver failure was defined as serum bilirubin ≥ 12 mg/dL, coagulation failure as INR ≥ 2.5, brain failure as hepatic encephalopathy grade ≥ 3 (West Haven criteria), and circulatory failure as the need for vasopressor therapy to maintain blood pressure [12].

2.3. Treatment. According to ICA-AKI diagnostic criteria, standard medical treatment (SMT) was applied according

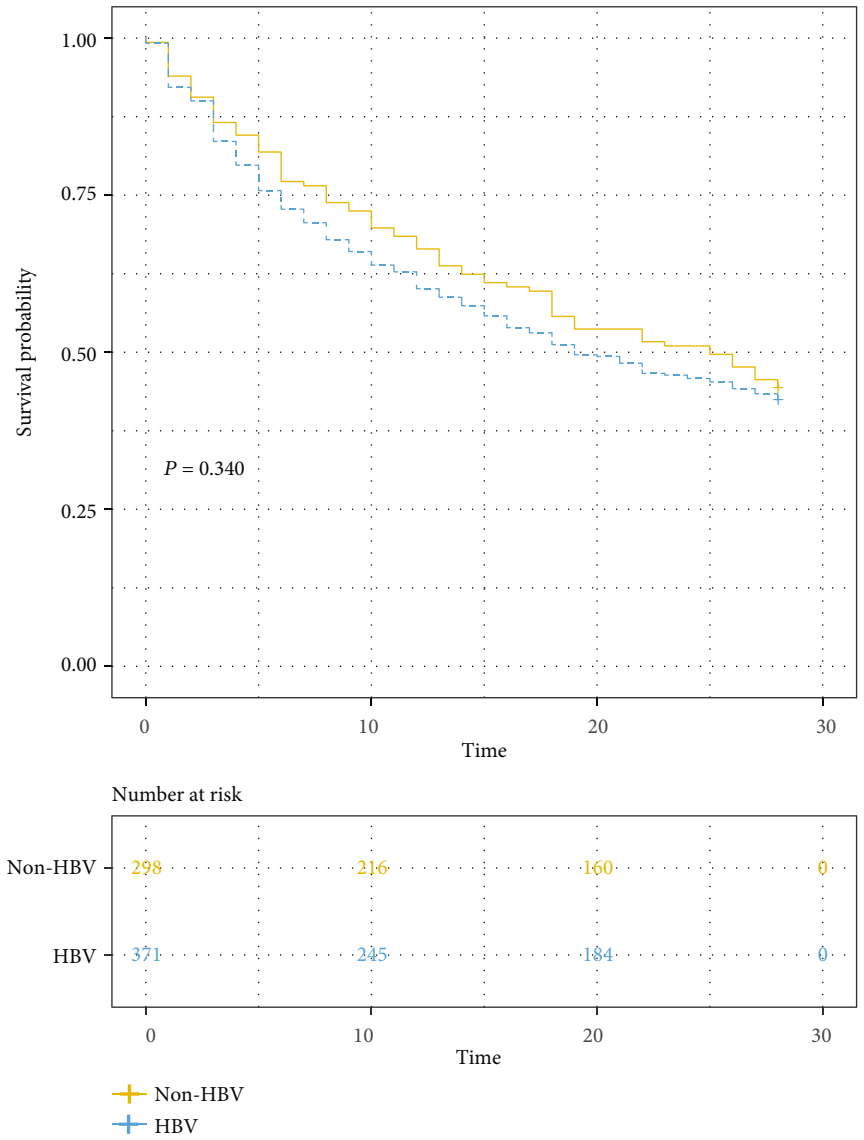

Figure 2: Kaplan–Meier curves of HBV-derived HRS and non-HBV-derived HRS. HRS: hepatorenal syndrome; HBV: hepatitis B virus.

to the stage of AKI, including treatment of infections, plasma volume expansion, withdrawal of nephrotoxic or nonsteroidal anti-inflammatory drugs, and basic life support. ALSS treatment adopted Li-ALS. Li-ALS includes plasma exchange (PE), hemodialysis (HD), hemofiltration (HF), and hemoperfusion (HP). PE uses hollow fiber membrane separation technology to filter the toxin-containing plasma components (mainly protein-binding toxins) in the blood out of the membrane and discard them and place equal amounts of fresh frozen plasma and albumin with the blood in the membrane and return to the body together. HF uses a membrane with a larger pore size and relies on the pressure difference between the liquids on both sides of the membrane as the transmembrane pressure, mimicking the principle of glomerular filtration function and removing excess water and toxic substances from the blood by convection. HP uses a cylindrical perfusion device containing special activated carbon or resin particles to remove toxins or drugs in the blood by adsorption, and the perfused blood returns to the body through a catheter. HD mainly relies on the concentration gradient dispersion on both sides of the membrane to precipitate small water-soluble substances such as blood Cr and urea nitrogen, to correct water and electrolyte disorders and acid-base balance disorders. Patients receive Li-ALS treatment approximately 1-2 times a week until TB $\leq$ 5 mg/dL or persistent hyperbilirubinemia and coagulopathy improve, or until liver transplantation. When active bleeding or circulatory failure occurs, it needs to be stopped.

2.4. Statistical Analysis. Clinicopathological features were summarized using medians with interquartile ranges (IQRs) or frequencies with percentages, and biochemical parameters were compared using the Wilcoxon rank-sum, chi-squared, and Fisher exact test. The propensity score (PS) for ALSS was estimated using a logistic regression model

Table 2: Characteristics between SMT and ALSS before PSM.

Variates	SMT	ALSS	*P* value
n	321	50	
Age (year)	58.46 ± 12.17	53.70 ± 13.05	0.011
HBV-DNA (log copies/mL)	5.1 ± 1.5	5.1 ± 1.6	0.986
Male sex	240 (74.80)	42 (84.00)	0.213
Degree of HE			0.322
Without HE	179 (55.80)	23 (46.00)	
I	49 (15.30)	6 (12.00)	
II	27 (8.40)	7 (14.00)	
III	20 (6.20)	6 (12.00)	
IV	46 (14.30)	8 (16.00)	
Ascitic (%)			0.003
Grade 1	58 (17.00)	12 (24.00)	
Grade 2	87 (27.10)	23 (46.00)	
Grade 3	115 (35.80)	7 (14.00)	
Missing data	61 (19.00)	8 (16.00)	
MAP (mmHg)	95.83 ± 17.02	96.88 ± 15.14	0.682
HR	87.40 ± 16.47	85.46 ± 13.45	0.428
INR	1.84 (1.46-2.33)	2.08 (1.74-2.63)	0.137
WBC (10^9/L)	7.40 (4.98-11.40)	6.55 (5.05-9.58)	0.072
Neutrophil (%)	75.29 ± 12.04	71.68 ± 10.79	0.047
Albumin (g/L)	29.21 ± 5.60	29.55 ± 4.54	0.686
Globulin (g/L)	28.73 ± 8.99	29.30 ± 8.97	0.677
ALT (U/L)	44.50 (22.00-104.20)	114.00 (54.75-253.50)	0.060
AST (U/L)	70.00 (39.00-154.20)	144.50 (92.50-282.00)	0.202
Hemoglobin (g/L)	98.80 ± 26.44	115.22 ± 25.51	<0.001
Cystatin C (mg/L)	2.14 (1.53-3.41)	1.24 (0.92-1.70)	0.002
Urea (mmol/L)	14.40 (8.50-23.75)	7.95 (4.23-14.50)	0.006
Creatinine (mg/dL)	1.75 (1.01-2.75)	0.93 (0.71-1.61)	0.001
Serum bilirubin (mg/dL)	12.61 (2.51-24.09)	20.07 (10.64-28.13)	0.011
GGT (U/L)	59.00 (33.00-123.00)	61.50 (45.75-99.50)	0.393
Potassium (mmol/L)	4.30 ± 0.91	4.19 ± 0.74	0.627
Sodium (mmol/L)	133.77 ± 6.91	135.06 ± 5.10	0.208
MELDs	27.55 ± 9.54	27.59 ± 6.72	0.979
iMELD	51.44 ± 11.53	49.15 ± 8.74	0.179
CTP	11.08 ± 1.96	11.82 ± 1.52	0.011
CLIF-ACLFs	49.87 ± 10.71	48.54 ± 9.65	0.408
CLIF-SOFAs	10.09 ± 3.67	10.46 ± 2.79	0.499
COSSH-ACLFs	7.19 ± 1.89	7.20 ± 1.51	0.988
Liver failure	163 (50.80)	35 (70.00)	0.017
Coagulation failure	68 (21.20)	16 (32.00)	0.129
Cerebral failure	66 (20.60)	0 (0.00)	0.315
28-day mortality	190 (59.20)	24 (48.00)	0.182

ALT: alanine aminotransferase; CLIF-SOFA: Chronic Liver Failure-Sequential Organ Failure Assessment; COSSH-ACLF: Chinese Group on the Study of Severe Hepatitis B-Acute-on-Chronic Liver Failure; HBV: hepatitis B virus; INR: International normalized ratio; MAP: Mean arterial pressure; MELD: Model for End-Stage Liver Disease.

Table 3: Characteristics between SMT and ALSS after PSM.

Variates	SMT	ALSS	*P* value
n	150	50	
Age (year)	54.21 ± 11.59	53.70 ± 13.05	0.796
HBV-DNA (log copies/mL)	5.1 ± 1.7	5.1 ± 1.6	0.990
Male sex	124 (82.70)	42 (84.00)	1.000
Degree of HE			0.109
Without HE	81 (54.00)	23 (46.00)	
I	24 (16.00)	6 (12.00)	
II	7 (4.70)	7 (14.00)	
III	9 (6.00)	6 (12.00)	
IV	29 (19.30)	8 (16.00)	
Ascitic (%)			0.007
Grade 1	30 (20.00)	12 (24.00)	
Grade 2	37 (24.70)	23 (46.00)	
Grade 3	52 (34.70)	7 (14.00)	
Missing data	31 (20.70)	8 (16.00)	
MAP (mmHg)	95.82 ± 16.05	96.88 ± 15.14	0.683
HR	87.65 ± 16.61	85.46 ± 13.45	0.399
INR	2.01 (1.68-2.82)	2.08 (1.74-2.63)	0.536
WBC (10^9/L)	7.15 (4.70-10.38)	6.55 (5.05-9.58)	0.241
Neutrophil (%)	72.88 ± 13.18	71.68 ± 10.79	0.563
Albumin (g/L)	29.30 ± 5.68	29.55 ± 4.54	0.777
Globulin (g/L)	28.66 ± 8.66	29.30 ± 8.97	0.654
ALT (U/L)	57.00 (25.50-127.00)	114.00 (54.75-253.50)	0.273
AST (U/L)	90.50 (49.75-205.00)	144.50 (92.50-282.00)	0.511
Hemoglobin (g/L)	99.82 ± 26.30	115.22 ± 25.51	<0.001
Cystatin C (mg/L)	2.14 (1.44-3.44)	1.24 (0.92-1.70)	0.007
Urea (mmol/L)	14.81 (6.75-23.82)	7.95 (4.26-14.50)	0.001
Creatinine (mg/dL)	1.80 (1.01-2.95)	0.93 (0.71-1.61)	<0.001
Serum bilirubin (mg/dL)	14.12 (3.95-25.28)	20.07 (10.64-28.13)	0.079
GGT (U/L)	50.00 (33.00-119.00)	61.50 (45.75-99.50)	0.501
Potassium (mmol/L)	4.39 ± 0.95	4.19 ± 0.74	0.480
Sodium (mmol/L)	132.97 ± 7.69	135.06 ± 5.10	0.074
MELDs	29.91 ± 9.54	27.59 ± 6.72	0.113
iMELD	53.09 ± 12.04	49.15 ± 8.74	0.034
CTP	11.47 ± 1.98	11.82 ± 1.52	0.259
CLIF-ACLFs	49.90 ± 11.41	48.54 ± 9.65	0.450
CLIF-SOFAs	10.83 ± 3.84	10.46 ± 2.79	0.527
COSSH-ACLFs	7.56 ± 2.10	7.20 ± 1.51	0.260
Liver failure	84 (56.00)	35 (70.00)	0.114
Coagulation failure	50 (33.30)	16 (32.00)	1.000
Cerebral failure	38 (25.30)	14 (28.00)	0.852
28-day mortality	96 (64.00)	24 (48.00)	0.067

ALT: alanine aminotransferase; CLIF-SOFA: Chronic Liver Failure-Sequential Organ Failure Assessment; COSSH-ACLF: Chinese Group on the Study of Severe Hepatitis B-Acute-on-Chronic Liver Failure; HBV: hepatitis B virus; INR: international normalized ratio; MAP: mean arterial pressure; MELD: Model for End-Stage Liver Disease.

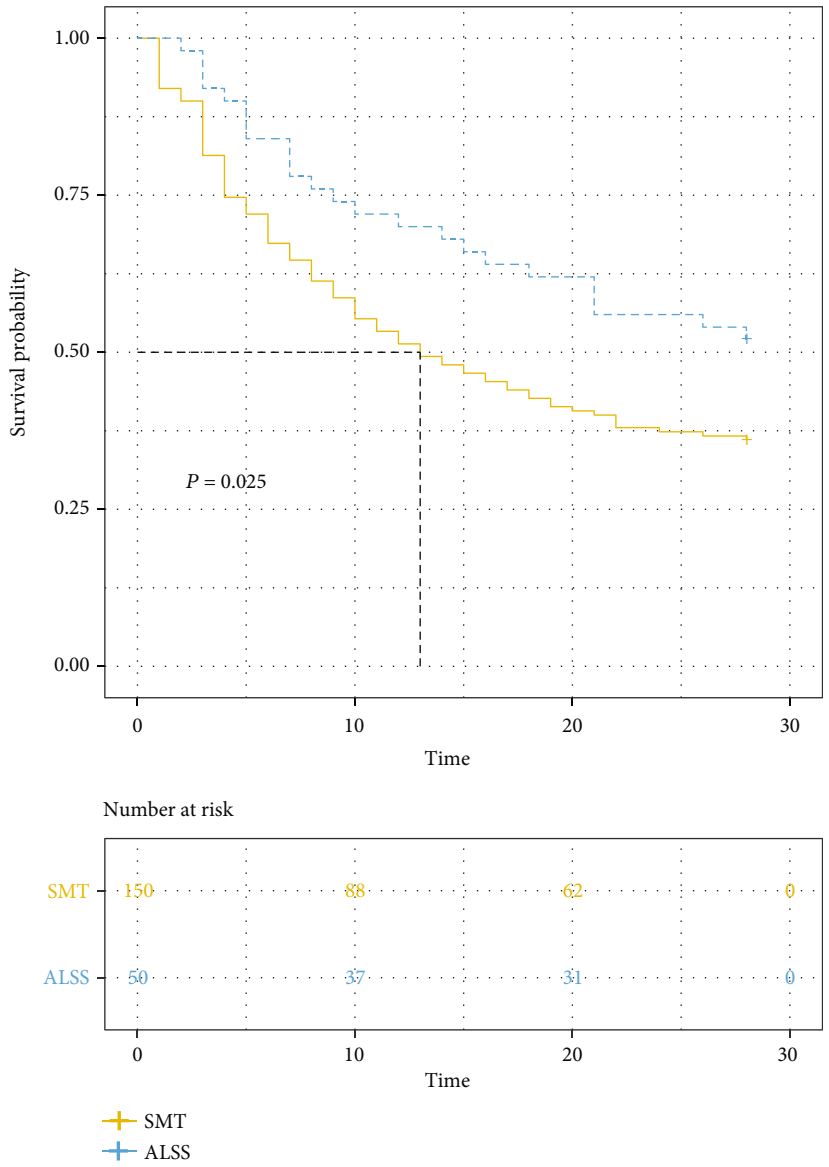

Figure 3: Kaplan–Meier curves of HBV-derived HRS treated with ALSS and SMT only after PAM. ALSS: artificial liver support system; HBV: hepatitis B virus; HRS: hepatorenal syndrome; SMZ: standard medical treatment.

with ALSS as the outcome. All 371 HBV-positive patients were included in the PS analytical cohort. The associations between ALSS and overall survival were evaluated using Cox regression models and summarized as hazard ratios (HRs) with 95% confidence intervals (CIs). The PS techniques employed propensity score matching (PSM). A propensity score matching (PSM) method was applied to compare the mortality between the patients treated with ALSS and SMT. Patients treated with ALSS were matched in a 1 : 3 ratio to patients treated with SMT only using a method based on the logit of the PS. Statistical analyses were performed with the aid of R ver. 4.0.5 (R Foundation for Statistical Computing, Vienna, Austria). All tests were two-sided, and a P value < 0.05 was considered statistically significant.

3. Results

3.1. HBV-Derived HRS Is More Severe than Non-HBV-Derived HRS. A total of 669 patients were diagnosed as HRS used by inclusion and exclusion criteria. 669 HRS patients, including 298 HBV negative and 371 HBV positive, were enrolled for the subsequent analysis (Figure 1). The baseline characteristics of both cohorts are listed in Table 1. No significant differences in the heart rate, neutrophil percentage, globulin, cystatin C, urea, potassium, kidney failure, and other indexes were found between the HBV-derived HRS and non-HBV-derived HRS groups. However, the age of onset of the HBV-derived HRS cohort was lower, and the proportion of male patients was higher. Also, the coagulation and liver function of the HBV-derived HRS

Table 4: Univariate and multivariate Cox regression.

Variates	Univariate cox regression		Multivariate cox regression	
	HR (95% CI)	*P* value	HR (95% CI)	*P* value
Age (year)	0.99 (0.99-1.02)	0.329	1.02 (1.00-1.03)	0.069
Male sex	1.01 (0.62-1.63)	0.981	1.24 (0.76-2.03)	0.396
Degree of HE				
Without HE	Ref.			
I	1.57 (0.92-2.66)	0.096		
II	1.42 (0.70-2.90)	0.329		
III	2.40 (1.28-4.52)	0.007		
IV	2.67 (1.69-4.21)	<0.001		
Ascitic (%)				
Grade 1	Ref.			
Grade 2	0.41 (0.19-0.86)	0.019		
Grade 3	0.48 (0.23-1.00)	0.051		
Missing data	0.46 (0.21-0.99)	0.049		
MAP (mmHg)	0.99 (0.98-1.00)	0.180		
HR	1.02 (1.01-1.03)	<0.001		
INR	1.82 (1.56-2.02)	<0.001	1.61 (1.37-1.89)	<0.001
WBC (10^9/L)	1.09 (1.06-1.12)	<0.001	1.03 (0.99-1.07)	0.104
Neutrophil (%)	1.05 (1.04-1.07)	<0.001	1.03 (1.01-1.05)	0.003
Albumin (g/L)	0.98 (0.94-1.01)	0.168	0.98 (0.94-1.02)	0.257
Globulin (g/L)	1.01 (0.99-1.03)	0.463		
ALT (U/L)	1.00 (1.00-1.00)	0.003		
AST (U/L)	1.00 (1.00-1.00)	0.001		
Hemoglobin (g/L)	1.00 (1.00-1.01)	0.219		
Cystatin C (mg/L)	1.25 (1.05-1.49)	0.012		
Urea (mmol/L)	1.01 (1.00-1.02)	0.012		
Creatinine (mg/dL)	1.00 (1.00-1.00)	0.046		
Serum bilirubin (mg/dL)	1.00 (1.00-1.00)	<0.001	1.00 (1.00-1.00)	0.104
GGT (U/L)	1.00 (1.00-1.00)	0.952		
Potassium (mmol/L)	0.99 (0.96-1.02)	0.535		
Sodium (mmol/L)	0.96 (0.94-0.98)	<0.001		
MELDs	1.10 (1.07-1.12)	<0.001		
iMELD	1.08 (1.06-1.10)	<0.001		
CTP	1.48 (1.32-1.67)	<0.001		
CLIF-ACLFs	1.08 (1.06-1.10)	<0.001		
CLIF-SOFAs	1.22 (1.16-1.28)	<0.001		
COSSH-ACLFs	1.47 (1.35-1.60)	<0.001		
Organ failure				
Liver failure	2.07 (1.40-3.07)	<0.001		
Coagulation failure	2.87 (1.99-4.13)	<0.001		
Cerebral failure	2.27 (1.55-3.31)	<0.001		
With ALSS	0.60 (0.39-0.95)	0.027	0.59 (0.38-0.94)	0.025

cohort were worse, along with elevated serum bilirubin, ALT, and AST levels. Thus, it could be inferred that the pathology is different between the HBV-derived HRS cohort and non-HBV-derived cohort. In this way, patients with HBV-derived HRS should be paid more attention. Moreover, KM curves showed that HBV-derived HRS has higher 28-day mortality, though with no statistical differences ($P = 0.340$) (Figure 2). Considering worse liver function and prognosis, HBV-derived HRS deserves further research.

3.2. Baseline Characteristics of Patients with HBV-Derived HRS after PSM. 321 patients received SMT, and 50 patients received ALSS treatment in the whole HBV-derived HRS cohort. Generally, there were significant differences in ascitic

Table 5: Summary of the results of multivariate analyses of 28-day mortality in HBV-derived HRS patients after PSM who received ALSS versus SMT treatment with risk stratification by number of organ failures or AKI degree.

Analysis	Treatment	Crude model		Model 1		Model 2	
		HR (95% CI)	*P* value	HR (95% CI)	*P* value	HR (95% CI)	*P* value
AKI stage 1	ALSS (SMT as reference)	1.03 (0.60-1.79)	0.908	1.04 (0.60-1.80)	0.892	0.76 (0.43-1.35)	0.352
AKI stage 2	ALSS (SMT as reference)	0.41 (0.13-1.35)	0.143	0.47 (0.14-1.64)	0.238	0.24 (0.03-1.90)	0.175
AKI stage 3	ALSS (SMT as reference)	0.37 (0.16-0.88)	0.024	0.34 (0.14-0.83)	0.018	0.29 (0.12-0.70)	0.006
Organ failure (≤ 1)	ALSS (SMT as reference)	0.72 (0.36-1.43)	0.345	0.72 (0.36-1.43)	0.344	0.68 (0.32-1.43)	0.307
Organ failure (≥ 2)	ALSS (SMT as reference)	0.41 (0.23-0.74)	0.003	0.42 (0.23-0.76)	0.004	0.52 (0.28-0.95)	0.033

Model 1 was adjusted for age and sex. Model 2 was adjusted for age, sex, neutrophils, alanine aminotransferase (ALT), albumin, serum bilirubin, COSSH-ACLFs, and international normalized ratio (INR). AKI: acute kidney injury; SMT: standard medical treatment; ALSS: artificial liver support system.

grade, urea, creatinine, serum bilirubin, CTP score, etc., between HRS patients who received SMT and ALSS treatment (Table 2). Considering the selection bias of the retrospective study, we adopted the PSM method to balance the confounding factors. Patients with SMT and ALSS treatment were matched in a ratio of 3 to 1 and then integrated into a new cohort. Several indexes were balanced between two cohorts while the other indexes still differed, indicating that the baseline characteristics are quite different (Table 3).

3.3. ALSS Reduce the Mortality of HBV-Derived HRS. To further evaluate the effect of ALSS on the prognosis of HBV-derived HRS, we conducted KM curves in a new cohort after PSM. Finally, we found ALSS could significantly benefit HRS patients ($P = 0.025$). The median survival time of patients in SMT group was 13 days, while those treated with ALSS were more than 28 days (Figure 3).

Additionally, in univariate analysis, HE degree III, ascitic, ALT, AST, cystatin C, urea, creatinine, iMELD, MELDs, CLIF-ACLFs, CLIF-SOFAs, COSSH-ACLFs, organ failures, and treated with ALSS were associated with 28-day mortality. When combined with multivariate analysis, eventually, INR, neutrophil percentage, and treated with ALSS were independent predictive factors for 28-day mortality in HBV-derived HRS. The mortality of patients treated with ALSS was 0.6 times that of those without ALSS, which could considerably prolong the life of patients (Table 4).

3.4. ALSS Could Acquire More Survival Benefit in AKI Stage 3. According to the definitions of diagnosis of HRS from the International Club of Ascites (ICA-AKI), the severity of AKI could be classified into three stages. In this way, patients could be divided into three stages, namely, AKI stage 1, AKI stage 2, and AKI stage 3. The baseline characteristics of AKI stage 1, AKI stage 2, and AKI stage 3 are shown in Table S1. Similarly, some indexes were different between patients with ALSS and those without ALSS. The Cox regression model was developed to figure out the effect of ALSS on prognosis in different AKI stages. Here, we developed three kinds of models, crude model, model 1, and model 2. Finally, in all three models, ALSS could acquire survival benefit in AKI stage 3, and the mortality of patients treated with ALSS was 0.37, 0.34, and 0.29 times that of those without ALSS in the crude model, model 1, and model 2, respectively (Table 5). In other words, ALSS could reduce the population's mortality rate by 2/3 in the AKI stage 3 cohort. Nevertheless, in other patients, the 28-day mortality remained similar between patients with/without ALSS, especially in the AKI stage 1 cohort. Both the results of KM curves and Cox regression analysis support this conclusion (Figure 4). The mortality of patients with ALSS was much lower than that of patients without ALSS in the AKI stage 3 cohort ($P = 0.006$). The median survival time was 10 days in patients without ALSS, while the median survival time was more than 28 days in patients with ALSS. In total, ALSS could greatly benefit patients in severe HBV-derived HRS.

3.5. ALSS Could Acquire More Survival Benefit with Organ Failure ≥ 2. According to the number of organ failures, patient with HBV-derived HRS could be divided into two groups; the number of organ failures ≤ 1 and ≥2. The baseline characteristics are listed in Table S2. In patients with 0 or 1 organ failure, ALT, AST, creatinine, and urea were different between patients with and without ALSS. In patients with more organ failures, those two groups differed in heart rate, cystatin C, iMELD, MELDs, and COSSH-ACLFs. Given the variety, the effect of ALSS on prognosis was evaluated in Table 5. Finally, ALSS could reduce the mortality in patients with more than two organ failures by almost half in all three models. From Figure 5, we could find that patients with more organ failures are at high risk of mortality ($P = 0.002$) but could benefit from ALSS. Combined with the results in different AKI stages, ALSS could significantly reduce the mortality of severe HBV-derived HRS patients.

3.6. Patients Treatment with ALSS Have Lower Scores and Mortality. Figure 6 displayed various score systems, including iMELD, CLIF-ACLFs, CLIF-SOFAs, and COSSH-ACLFs, after patients were treated with ALSS or SMT only. The iMELDs was much higher in patients treated with SMT rather than ALSS, while nonsurvivors were concentrated in the higher iMELD part. Consistently, this trend remained the same when patients were evaluated by CLIF-ACLFs, CLIF-SOFAs, and COSSH-ACLFs. As all the four scores were found to be associated with mortality of HBV-derived HRS, generally, it can be inferred that ALSS might help reduce the scores and benefit the prognosis of HBV-derived HRS.

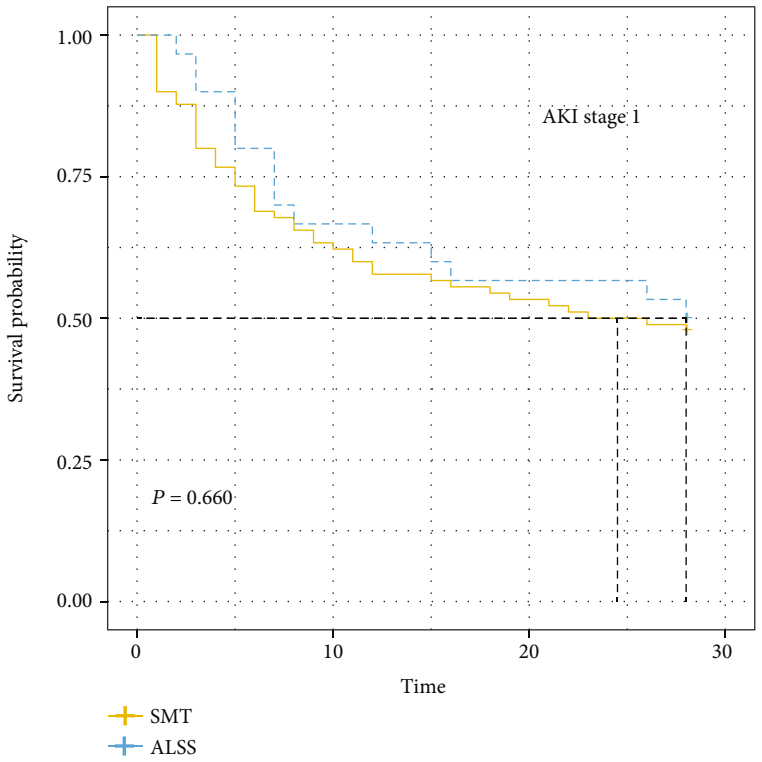

(a)

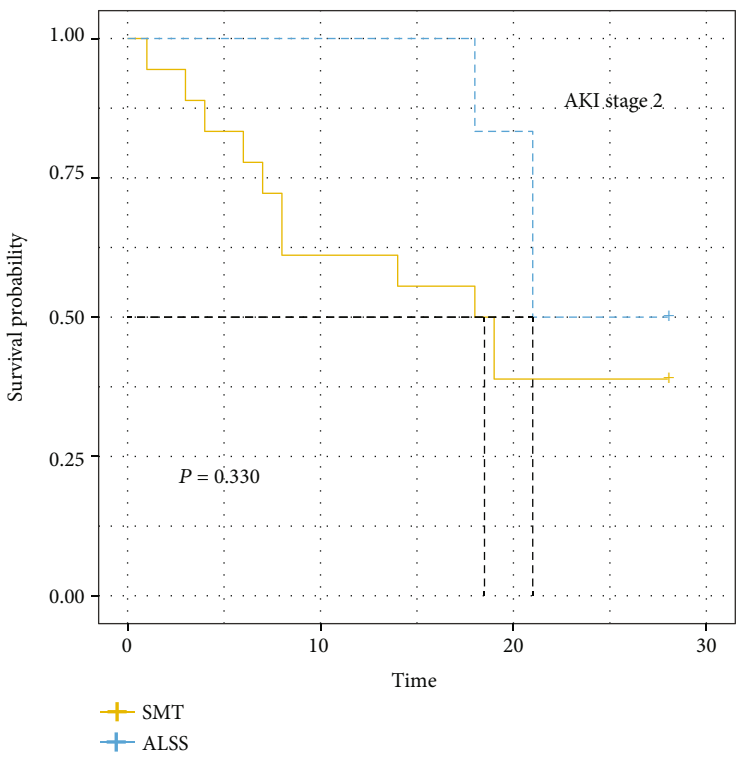

(b)

Figure 4: Continued.

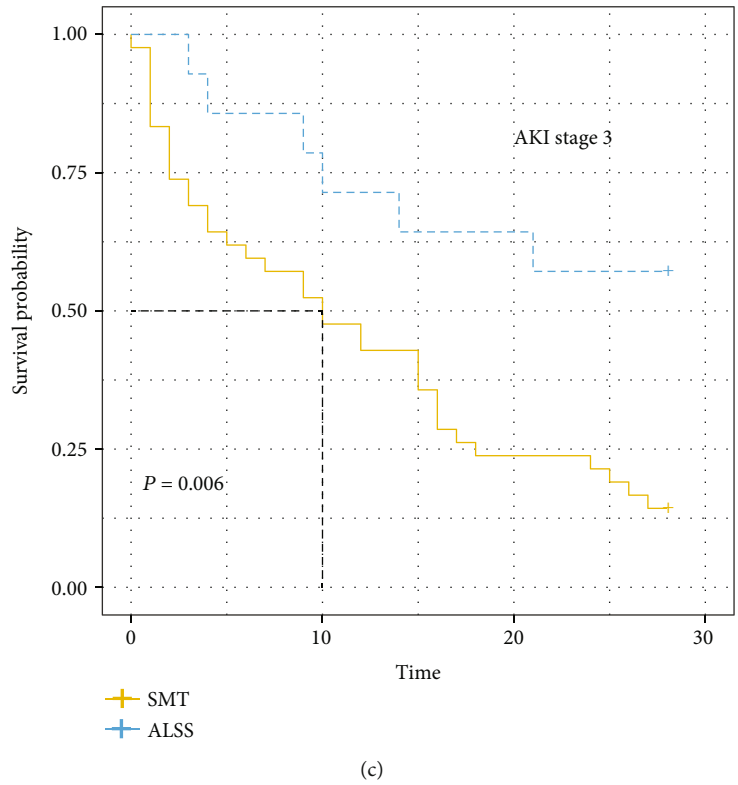

(c)

Figure 4: Kaplan–Meier curves of mortality of ALSS in different AKI degrees. (a) The effect of ALSS in AKI stage 1. (b) The effect of ALSS in AKI stage 2. (c) The effect of ALSS in AKI stage 3. ALSS: artificial liver support system; AKI: acute kidney injury.

3.7. The Change of INR and Creatinine Were Independent Predictive Factors for the Mortality of HBV-Derived HRS. The ALT, serum bilirubin, creatinine, INR, and neutrophil were monitored both pre-ALSS and post-ALSS treatment. Serum bilirubin was significantly decreased after ALSS treatment ($P = 0.004$), while ALT, creatinine, INR, and neutrophil percentage remained at the same level (Table 6). To further assess the effect of the change of indexes on 28-day mortality, we included the change of serum bilirubin, ALT, neutrophil percentage, INR, and creatinine into Cox regression analysis. We found that the change of INR and creatinine were independent predictive factors for the prognosis of HBV-derived HRS ($P = 0.020$ and 0.016, respectively) (Table 7).

4. Discussion

This study retrospectively enrolled HRS patients from multiple centers in the past ten years and obtained 28-day mortality through telephone follow-up. From the total patients, we found the distinct characteristics between HBV-derived HRS and non-HBV-derived HRS and worse prognosis in those with HBV positive. Then, we balanced the selection bias through PSM and concluded that ALSS could improve the prognosis of HBV-derived HRS whenever in various Cox regression models. As for hierarchical analysis, ALSS could greatly benefit patients in AKI stage 3 and with ≥ two organ failures. Finally, serum bilirubin was reduced after ALSS treatment, and the change of INR and creatinine could predict the 28-day mortality of HBV-derived HRS. Eventually, ALSS could improve the prognosis of HBV-derived HRS, especially severe HRS.

The HBV infection rate has been high in China [13, 14]. Although newborns are generally vaccinated against HBV, the current situation of HBV infection is still severe. Specifically, HBV infection still accounts for a large proportion of the causes of HRS; 371 out of 669 patients were HBV positive in this study. Patients with HBV positive had higher INR, ALT, AST, serum bilirubin, and proportion of coagulation failure than those with HBV negative, which is not conducive to the prognosis of the HRS. Consistent with the previous study, patients with HBV positive are at risk of higher mortality in the KM curve. The previous view believed that HRS is only a kind of renal dysfunction and the structure of the kidney is normal. However, electron microscopy studies on kidneys obtained from HRS patients shortly after death have demonstrated renal tubular tears and the presence of dark bodies in mitochondria [15]. Besides, a particular lesion involving reflux of the proximal convoluted tubule epithelium into the Bowman space has also been described in autopsy specimens from patients with HRS [16]. Like hepatitis C virus (HCV) infection, the pathogenetic role of HBV infection has been documented primarily by the demonstration of hepatitis B antigen-antibody complexes in the renal lesions via immunofluorescence microscopy [4, 17]. In this way, HBV-derived HRS is recommended for more attention.

Several indexes were different, including ascitic, hemoglobin, cystatin C, urea, creatinine, serum bilirubin, and CTP score between patients treated with ALSS and SMT

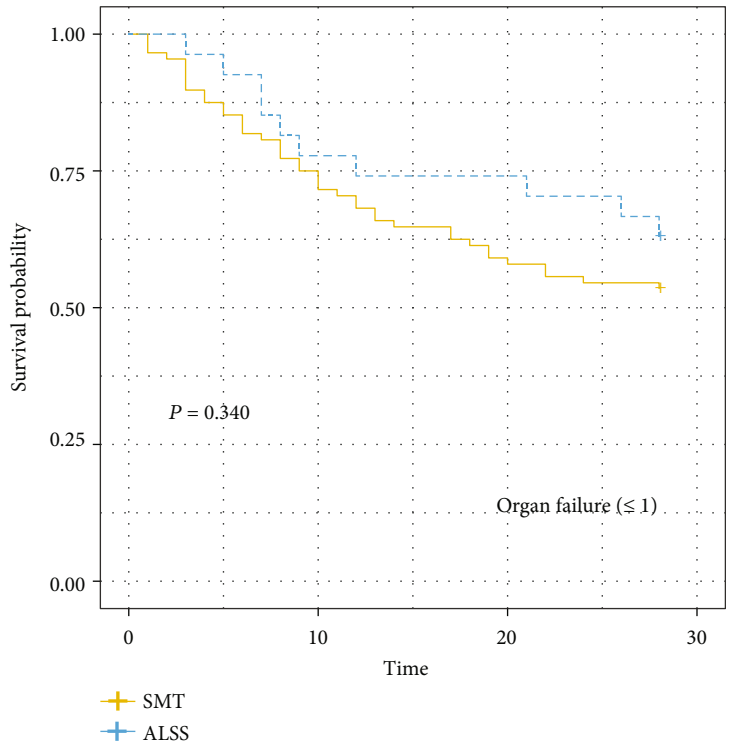

(a)

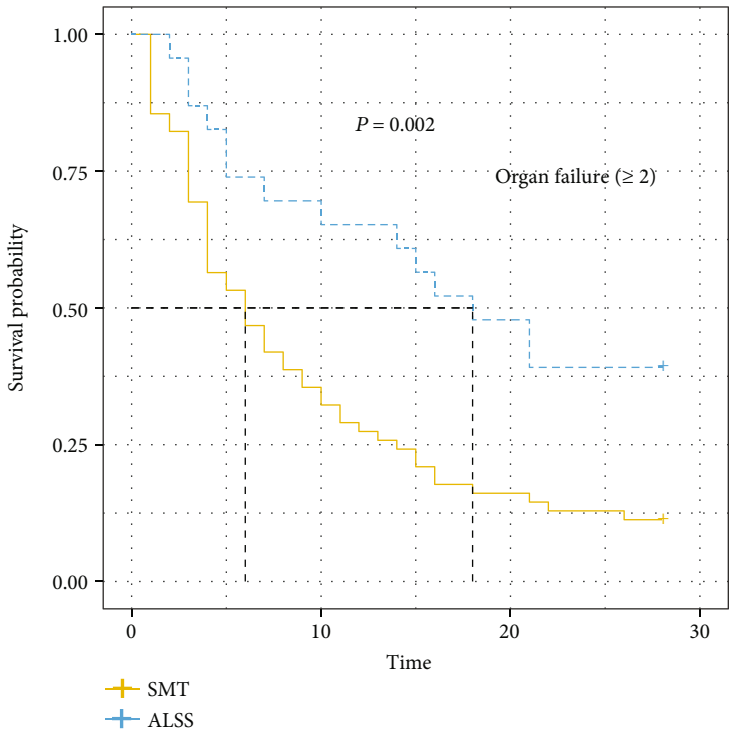

(b)

Figure 5: Continued.

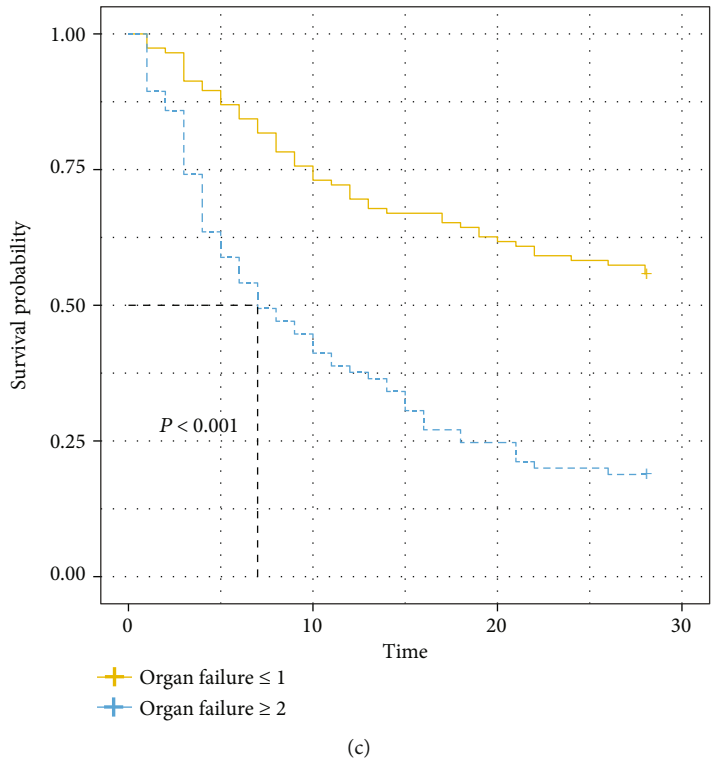

(c)

Figure 5: Kaplan–Meier curves of mortality of ALSS in patients with organ failures ≥ 2 and ≤1. (a) The effect of ALSS in patients with organ failure ≤ 1. (b) The effect of ALSS in patients with organ failure ≥ 2. (c) The effect of the number of organ failures on mortality. ALSS: artificial liver support system.

only. After being balanced by PSM, some of them remained at the same level between the two groups, indicating the PSM method's efficacy. To figure out the association between ALSS and prognosis of HBV-derived HRS, we did survival analysis, and it showed that the median survival time of patients with ALSS is longer than those treated only with SMT, and ALSS could reduce mortality.

We enrolled various indexes into univariate Cox regression analysis to further reveal ALSS and predictive factors for 28-day mortality. Then, we found different degrees of ascitic, heart rate, INR, neutrophil percentage, ALT, AST, cystatin C, urea, and creatinine were associated with the prognosis of HBV-derived HRS [18]. Liver function, including the degree of ascitic, ALT, AST, and cystatin C, and renal function, including urea and creatinine, account for the most factors related to prognosis [19]. Additionally, standard score systems, MELDs, iMELD, CTP, CLIF-ACLFs, CLIF-SOFA, and COSSH-ACLFs, were calculated according to mainly liver function. Thus, it is reasonable that these score systems are related to the prognosis [20–23]. When selected for multivariate Cox regression, INR and neutrophil percentage are independent predictive factors for 28-day mortality. One of the elements to assess the severity of advanced liver diseases is INR for decades [24]. Usually, higher INR means blood coagulation dysfunction and may result in an unwell prognosis of advanced liver diseases, including HRS. Neutrophil percentage is positively correlated with the severity of systemic inflammation. Advanced liver disease is often accompanied by bacterial infections, increasing the percentage of neutrophils [25, 26]. We found that it can predict the mortality of HRS. As it is convenient and readily available, neutrophil percentage could serve as a monitor factor. Moreover, ALSS could significantly reduce mortality. In this way, we could treat patients with ALSS and use INR and neutrophil percentage as monitor factors to give more survival benefits to patients with HBV-derived HRS.

According to the definition of AKI from the International Club of Ascites (ICA-AKI), there are three stages of AKI [12]. As the degree of AKI could influence the outcome, we wonder whether ALSS could benefit all degrees of AKI. We developed three models adjusted by various variables. Finally, ALSS greatly benefits patients in AKI stage 3. This may result from the working principle of ALSS, which can take away metabolic waste and replace it with normal plasma. This can quickly correct the fluid balance and restore liver and kidney functions. Patients in AKI stage 1 and AKI stage 2 may regulate their internal environment disorders through their adjustment ability.

ACLF is also a common advanced liver disease with rapid liver dysfunction and high mortality [27]. There are many similarities between HRS and ACLF; for example, ACLF patients often have kidney damage, continued collection of various metabolites and toxins and systemic inflammation, which means that treatment for ACLF could also help patients with HRS. Non-HBV-ACLF patients were confirmed to have a good prognosis [14, 28, 29]. The effect of ALSS on HRS has been uncertain before; however, ALSS

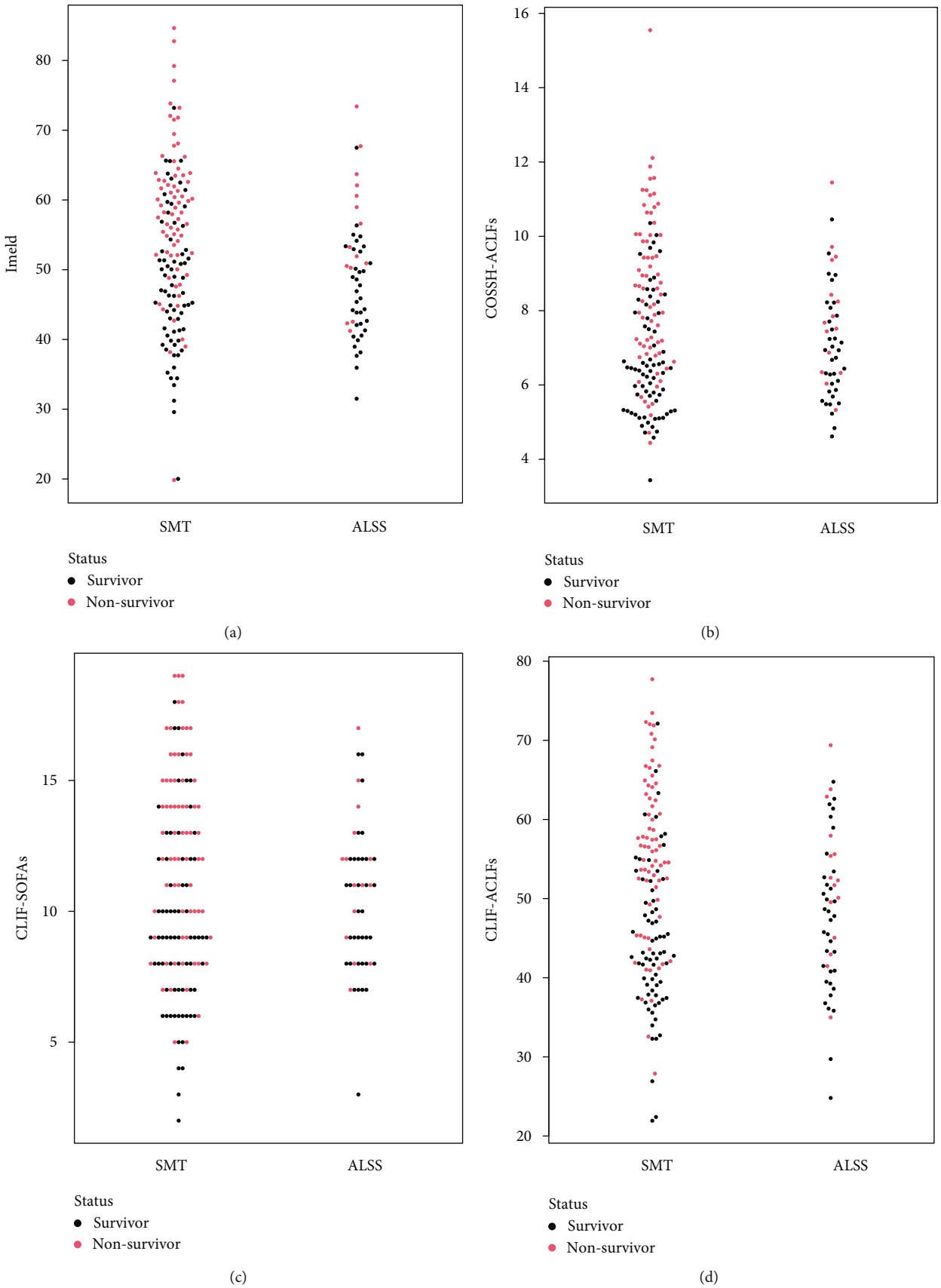

Figure 6: Score distribution in patients treated with ALSS or SMT only. ALSS: artificial liver support system; SMZ: standard medical treatment.

Table 6: Patients characteristics before and post-ALSS treatment.

Variates	Pre-ALSS	Post-ALSS	*P* value
ALT (U/L)	147.00 (73.00-377.00)	103.00 (44.50-235.00)	0.120
Serum bilirubin (mg/dL)	20.07 (10.64-28.12)	7.51 (1.47-27.75)	0.004
Creatinine (mg/dL)	0.93 (0.71-1.61)	1.51 (0.70-2.36)	0.213
INR	2.08 (1.74-2.63)	2.21 (1.55-3.26)	0.533
Neutrophil (%)	73.50 (63.58-81.15)	83.60 (76.08-86.60)	0.068

ALT: alanine aminotransferase; INR: international normalized ratio.

Table 7: Univariate and multivariate analysis of the difference of variates between post- and pre-ALSS groups as risk factors on 28-day mortality in patients treated with ALSS.

Variates	Univariate Cox regression		Multivariate Cox regression	
	HR (95% CI)	*P* value	HR (95% CI)	*P* value
ΔSerum bilirubin	1.00 (1.00-1.00)	0.301		
ΔALT	1.00 (1.00-1.00)	0.581		
ΔNeutrophil	0.99 (0.98-1.00)	0.075		
ΔINR	1.49 (1.12-1.98)	0.006	1.42 (1.06-1.90)	0.020
ΔCreatinine	1.00 (1.00-1.00)	0.003	1.00 (1.00-1.00)	0.016

ALT: alanine aminotransferase; INR: international normalized ratio.

could significantly reduce mortality of ACLF [30–33]. A study of 132 patients with HBV-ACLF revealed that ALSS could better improve the short-term survival of HBV-ACLF patients than SMT alone, especially in those with HBV-ACLF with infection [34, 35]. This is consistent with our results that ALSS could significantly promote survival of patients with HBV-derived HRS, especially those in AKI stage 3.

ACLF degree is defined mainly according to the degree of organ failures. It is artificially separated into ACLF-1, ACLF-2, and ACLF-3 according to the number of organ failures, and this classification is significantly associated with the prognosis of ACLF. Similarly, we divided our patients into 2 groups in the same way. Finally, ALSS could give great benefit to those with ≥2 organ failures. The mortality of patients treated with SMT only is about 3 times that of patients treated with ALSS. As described before, organ failures were associated with the severity and outcome of ACLF [32, 36]. Also, according to the mechanism of ALSS, it could rapidly improve organ function. The consistency of the above two stratified analyses illustrates the reliability of the results. We can conclude that ALSS can reduce the mortality of HRS patients, especially those with multiple organ failures and severe renal dysfunction.

MELDs has been developed to evaluate the liver function of liver diseases. It contains total serum bilirubin, INR, and creatinine. INR and the change of creatinine and INR could predict the prognosis of HBV-derived HRS. Patients with higher INR and creatinine may get a worse outcome. According to the bee swarm plot related to iMELD, CLIF-SOFAs, CLIF-ACLF, and COSSH-ACLF, the scores of all four systems are higher in patients treated with SMT only. Although scoring systems above could predict the mortality of HRS, the severe complication of decompensated cirrhosis, a novel predictive tool that specifically predicts the mortality of HRS is needed. Our team has launched a novel tool named GIMNS, which combines neutrophil percentage and INR, to predict mortality of HRS [37].

Indexes including ALT, serum bilirubin, creatinine, INR, and neutrophil percentage were reassessed after ALSS treatment. The level of serum bilirubin decreased while the others remained the same. The small sample size of patients could cause this as some information was missing due to retrospective data. But the change of INR and creatinine are proved to be predictive factors for 28-day mortality in patients treated with ALSS. Decreased creatinine and INR after ALSS treatment may represent a better prognosis of HBV-derived HRS. Our study also has some limitations. First, this is a retrospective cohort study, and some selection biases exist. In this way, we adopted PSM analysis to balance the confounding variables and enrolled four general hospitals to increase the sample size. Second, we diagnosed HRS according to the latest criteria from ICA-AKI to improve the accuracy of diagnosis. But definitions for the diagnosis of HRS have not been clear. The patients we enrolled may contain those with acute tubular necrosis (ATN). Thus, more clinical trials on HRS should be carried out to define HRS better. Finally, our study cohort did not adopt urine output as a diagnostic indicator. We would add this index in the following prospective cohort study.

5. Conclusions

In summary, HBV-derived HRS is more severe than non-HBV-derived HRS and has a worse prognosis. ALSS could reduce the 28-day mortality of patients with HBV-derived HRS, especially those in AKI stage 3 and with organ failure ≥ 2. INR and the change of creatinine and INR could predict the prognosis of HBV-derived HRS.

Data Availability

The original contributions presented in the study are included in the article/Supplementary Material; further inquiries can be directed to the corresponding authors.

Ethical Approval

The study was reviewed and approved by the Ethics Committee of The First Affiliated Hospital, College of Medicine, Zhejiang University (no. 2019-1449-1).

Conflicts of Interest

All authors have no conflict of interest related to the manuscript.

Authors' Contributions

Xinyu Sheng designed the research study, collected data, and wrote the manuscript. Jiaqi Zhou and Xiuyu Gu contributed to the analysis, conception, design, and manuscript writing. Hong Wang contributed to the design, study supervision, and manuscript writing. All authors read and approved the final manuscript.

Acknowledgments

We thank The First Affiliated Hospital of Zhejiang University, Shulan Hospital, People's Hospital of Zhejiang Province, and People's Hospital of Shengzhou City for providing data.

Supplementary Materials

Table S1: baseline characteristics of patients in different AKI stages. ALT: alanine aminotransferase; CLIF-SOFA: Chronic Liver Failure-Sequential Organ Failure Assessment; COSSH-ACLF: Chinese Group on the Study of Severe Hepatitis B-Acute-on-Chronic Liver Failure; HBV: hepatitis B virus; INR: international normalized ratio; MAP: mean arterial pressure; MELD: Model for End-Stage Liver Disease. Table S2: baseline characteristics of patients with organ failures. ALT: alanine aminotransferase; CLIF-SOFA: Chronic Liver Failure-Sequential Organ Failure Assessment; COSSH-ACLF: Chinese Group on the Study of Severe Hepatitis B-Acute-on-Chronic Liver Failure; HBV: hepatitis B virus; INR: international normalized ratio; MAP: mean arterial pressure; MELD: Model for End-Stage Liver Disease. *(Supplementary Materials)*

References

[1] J. M. Belcher, A. J. Sanyal, A. J. Peixoto et al., "Kidney biomarkers and differential diagnosis of patients with cirrhosis and acute kidney injury," *Hepatology*, vol. 60, no. 2, pp. 622–632, 2014.

[2] C. Francoz, F. Durand, J. A. Kahn, Y. S. Genyk, and M. K. Nadim, "Hepatorenal syndrome," *Clinical Journal of the American Society of Nephrology*, vol. 14, no. 5, pp. 774–781, 2019.

[3] J. C. Q. Velez, G. Therapondos, and L. A. Juncos, "Reappraising the spectrum of AKI and hepatorenal syndrome in patients with cirrhosis," *Nature Reviews. Nephrology*, vol. 16, no. 3, pp. 137–155, 2020.

[4] K. Lhotta, "Beyond hepatorenal syndrome: glomerulonephritis in patients with liver disease," *Seminars in Nephrology*, vol. 22, no. 4, pp. 302–308, 2002.

[5] S. T. Goldstein, F. Zhou, S. C. Hadler, B. P. Bell, E. E. Mast, and H. S. Margolis, "A mathematical model to estimate global hepatitis B disease burden and vaccination impact," *International Journal of Epidemiology*, vol. 34, no. 6, pp. 1329–1339, 2005.

[6] M. F. Yuen, D. S. Chen, G. M. Dusheiko et al., "Hepatitis B virus infection," *Nature Reviews. Disease primers*, vol. 4, article 18035, 2018.

[7] L. Tang, E. Covert, E. Wilson, and S. Kottilil, "Chronic hepatitis B infection," *JAMA*, vol. 319, no. 17, pp. 1802–1813, 2018.

[8] Y. Wang, J. Wu, J. Xu, and S. Lin, "Clinical significance of high expression of stanniocalcin-2 in hepatocellular carcinoma," *Bioscience Reports*, vol. 39, no. 4, article BSR20182057, 2019.

[9] J. Wu, J. Yu, X. Shi et al., "Epidemiological and clinical characteristics of 70 cases of coronavirus disease and concomitant hepatitis B virus infection: a multicentre descriptive study," *Journal of Viral Hepatitis*, vol. 28, no. 1, pp. 80–88, 2021.

[10] W. Bernal and J. Wendon, "Acute liver failure," *The New England Journal of Medicine*, vol. 369, no. 26, pp. 2525–2534, 2013.

[11] W. M. Lee, R. T. Stravitz, and A. M. Larson, "Introduction to the revised American Association for the Study of Liver Diseases position paper on acute liver failure 2011," *Hepatology*, vol. 55, no. 3, pp. 965–967, 2012.

[12] J. Stange, S. R. Mitzner, T. Risler et al., "Molecular adsorbent recycling system (MARS): clinical results of a new membrane-based blood purification system for bioartificial liver support," *Artificial Organs*, vol. 23, no. 4, pp. 319–330, 1999.

[13] L. Lanjuan, Y. Qian, H. Jianrong et al., "Severe hepatitis treated with an artificial liver support system," *The International Journal of Artificial Organs*, vol. 24, no. 5, pp. 297–303, 2001.

[14] P. Angeli, P. Ginès, F. Wong et al., "Diagnosis and management of acute kidney injury in patients with cirrhosis: revised consensus recommendations of the International Club of Ascites," *Journal of Hepatology*, vol. 62, no. 4, pp. 968–974, 2015.

[15] D. Y. Xie, Z. G. Ren, J. Zhou, J. Fan, and Q. Gao, "2019 Chinese clinical guidelines for the management of hepatocellular carcinoma: updates and insights," *Hepatobiliary Surgery and Nutrition*, vol. 9, no. 4, pp. 452–463, 2020.

[16] F. M. Lu, T. Li, S. Liu, and H. Zhuang, "Epidemiology and prevention of hepatitis B virus infection in China," *Journal of Viral Hepatitis*, vol. 17, Suppl 1, pp. 4–9, 2010.

[17] G. C. Kanel and R. L. Peters, "Glomerular tubular reflux–a morphologic renal lesion associated with the hepatorenal syndrome," *Hepatology*, vol. 4, no. 2, pp. 242–246, 1984.

[18] U. Kumar, R. Kumar, S. K. Jha, A. K. Jha, V. M. Dayal, and A. Kumar, "Short-term mortality in patients with cirrhosis of the liver and acute kidney injury: a prospective observational study," *Indian Journal of Gastroenterology*, vol. 39, no. 5, pp. 457–464, 2020.

[19] V. Agnello, R. T. Chung, and L. M. Kaplan, "A role for hepatitis C virus infection in type II cryoglobulinemia," *The New England Journal of Medicine*, vol. 327, no. 21, pp. 1490–1495, 1992.

[20] R. U. Saif, H. A. Dar, S. M. Sofi, M. S. Andrabi, G. Javid, and S. A. Zargar, "Noradrenaline versus terlipressin in the management of type 1 hepatorenal syndrome: a randomized

controlled study," *Indian Journal of Gastroenterology*, vol. 37, no. 5, pp. 424–429, 2018.

[21] M. Janicko, E. Veseliny, G. Senajova, and P. Jarcuska, "Predictors of hepatorenal syndrome in alcoholic liver cirrhosis," *Biomedical Papers of the Medical Faculty of the University Palacky, Olomouc, Czech Republic*, vol. 159, no. 4, pp. 661–665, 2015.

[22] M. R. Al Sibae and M. S. Cappell, "Accuracy of MELD scores in predicting mortality in decompensated cirrhosis from variceal bleeding, hepatorenal syndrome, alcoholic hepatitis, or acute liver failure as well as mortality after non-transplant surgery or TIPS," *Digestive Diseases and Sciences*, vol. 56, no. 4, pp. 977–987, 2011.

[23] M. Cavallin, P. S. Kamath, M. Merli et al., "Terlipressin plus albumin versus midodrine and octreotide plus albumin in the treatment of hepatorenal syndrome: a randomized trial," *Hepatology*, vol. 62, no. 2, pp. 567–574, 2015.

[24] P. Angeli and P. Gines, "Hepatorenal syndrome, MELD score and liver transplantation: an evolving issue with relevant implications for clinical practice," *Journal of Hepatology*, vol. 57, no. 5, pp. 1135–1140, 2012.

[25] J. W. Yu, G. Q. Wang, Y. H. Zhao, L. J. Sun, S. Q. Wang, and S. C. Li, "The MELD scoring system for predicting prognosis in patients with severe hepatitis after plasma exchange treatment," *Hepatobiliary & Pancreatic Diseases International*, vol. 6, no. 5, pp. 492–496, 2007.

[26] O. Witzke, M. Baumann, D. Patschan et al., "Which patients benefit from hemodialysis therapy in hepatorenal syndrome?," *Journal of Gastroenterology and Hepatology*, vol. 19, no. 12, pp. 1369–1373, 2004.

[27] C. Solé, E. Solà, P. Huelin et al., "Characterization of inflammatory response in hepatorenal syndrome: relationship with kidney outcome and survival," *Liver International*, vol. 39, no. 7, pp. 1246–1255, 2019.

[28] W. R. Kim, J. M. Smith, M. A. Skeans et al., "OPTN/SRTR 2012 annual data report: liver," *American Journal of Transplantation*, vol. 14, Suppl 1, pp. 69–96, 2014.

[29] T. Wu, J. Li, L. Shao et al., "Development of diagnostic criteria and a prognostic score for hepatitis B virus-related acute-on-chronic liver failure," *Gut*, vol. 67, no. 12, pp. 2181–2191, 2018.

[30] Y. Shi, Y. Yang, Y. Hu et al., "Acute-on-chronic liver failure precipitated by hepatic injury is distinct from that precipitated by extrahepatic insults," *Hepatology*, vol. 62, no. 1, pp. 232–242, 2015.

[31] S. G. Lim, C. T. Wai, A. Rajnakova, T. Kajiji, and R. Guan, "Fatal hepatitis B reactivation following discontinuation of nucleoside analogues for chronic hepatitis B," *Gut*, vol. 51, no. 4, pp. 597–599, 2002.

[32] H. Liu, Q. Zhang, L. Liu et al., "Effect of artificial liver support system on short-term prognosis of patients with hepatitis B virus-related acute-on-chronic liver failure," *Artificial Organs*, vol. 44, no. 10, pp. E434–E447, 2020.

[33] J. Yao, S. Li, L. Zhou et al., "Therapeutic effect of double plasma molecular adsorption system and sequential half-dose plasma exchange in patients with HBV-related acute-on-chronic liver failure," *Journal of Clinical Apheresis*, vol. 34, no. 4, pp. 392–398, 2019.

[34] G. Qin, J. G. Shao, B. Wang et al., "Artificial liver support system improves short- and long-term outcomes of patients with HBV-associated acute-on-chronic liver failure: a single-center experience," *Medicine (Baltimore)*, vol. 93, no. 28, article e338, 2014.

[35] L. L. Xiao, X. W. Xu, K. Z. Huang, Y. L. Zhao, L. J. Zhang, and L. J. Li, "Artificial liver support system improves short-term outcomes of patients with HBV-associated acute-on-chronic liver failure: a propensity score analysis," *BioMed Research International*, vol. 2019, Article ID 3757149, 8 pages, 2019.

[36] V. Arroyo, R. Moreau, P. S. Kamath et al., "Acute-on-chronic liver failure in cirrhosis," *Nature Reviews. Disease Primers*, vol. 2, no. 1, article 16041, 2016.

[37] X. Y. Sheng, F. Y. Lin, J. Wu, and H. C. Cao, "Development and validation of a prognostic model for patients with hepatorenal syndrome: a retrospective cohort study," *World Journal of Gastroenterology*, vol. 27, no. 20, pp. 2615–2629, 2021.

Hindawi
Disease Markers
Volume 2022, Article ID 4090346, 10 pages
https://doi.org/10.1155/2022/4090346

Research Article

Deguelin Attenuates Non-Small-Cell Lung Cancer Cell Metastasis by Upregulating PTEN/KLF4/EMT Signaling Pathway

Guohua Lu,[1] **Yinan Yao**,[1] **Xiaochen Zhang**,[2] **Dawei Cui**,[3] **and Jianying Zhou**[1]

[1]*Department of Respiratory Diseases, The First Affiliated Hospital, Zhejiang University School of Medicine, Hangzhou 310003, China*
[2]*Departments of Medical Oncology and Pathology, The First Affiliated Hospital, Zhejiang University School of Medicine, Hangzhou 310003, China*
[3]*Department of Blood Transfusion, The First Affiliated Hospital, Zhejiang University School of Medicine, Hangzhou 310003, China*

Correspondence should be addressed to Dawei Cui; daweicui@zju.edu.cn and Jianying Zhou; zjyhz@zju.edu.cn

Received 25 February 2022; Accepted 22 April 2022; Published 21 May 2022

Academic Editor: Chia-Jung Li

Non-small-cell lung cancer (NSCLC) is the most common lung cancer and a major cause of cancer mortality worldwide. Deguelin plays a vital inhibitory role in NSCLC initiation and development. However, the downstream mechanism of deguelin-suppressed metastasis of NSCLC cells is still not completely understood. Interestingly, phosphatase and tensin homologue deleted on chromosome 10 (PTEN) and Krüppel-like factor 4 (KLF4) also contribute to inhibition of metastasis in NSCLC cells. Here, we demonstrated that deguelin significantly upregulated PTEN and KLF4 expressions and PTEN positively upregulated KLF4 expression in NSCLC cells including A549 and PC9 cells. Moreover, overexpressions of PTEN and KLF4 inhibited the migration and invasion of NSCLC cells, an effect similar to that of deguelin. Furthermore, overexpressions of PTEN and KLF4 could suppress the epithelial-mesenchymal transition (EMT), an effect also similar to that of deguelin. Additionally, deguelin displayed a significant antitumor ability by upregulating PTEN and KLF4 expressions in mice model with NSCLC cells. Together, these results indicated that deguelin could be a potential therapeutic agent through upregulating PTEN and KLF4 expressions for NSCLC therapy.

1. Introduction

Lung cancer has become the leading cause of cancer-related deaths worldwide, especially in non-small-cell lung cancer (NSCLC), which accounts for about 85% of all lung cancer cases [1–4]. The burden of lung cancer has become one of the major public health problems in the world. In recent years, various studies on lung cancer and its drugs have made some progress, but the five-year survival rate of patients caused by factors such as adverse drug reactions has not been effectively improved. Thus, the treatment of lung cancer patients is still a big medical problem [3–5].

In recent years, a number of studies have shown that herbal extracts have become a new strategy for the treatment of tumors. For example, the Chinese herbal extract of deguelin, derived from *Lonchocarpus*, *Derris*, or *Tephrosia*, can effectively inhibit the proliferation, invasion, and metastasis of a variety of tumors (e.g., colon cancer, human pancreatic cancer, breast cancer, and lung cancer) [6, 7]. Importantly, deguelin can enhance the sensitivity of tumor cells to chemotherapy drugs and radiotherapy and has no obvious toxicity and inhibitory effect on the growth of normal cells [6]. The main antitumor effects of deguelin include inhibiting the proliferation, invasion, and metastasis of tumor cells; promoting the apoptosis of tumor cells; delaying the tumor cell cycle; and inducing DNA damage of tumor cells [8–13]. However, the molecular mechanisms of deguelin in antitumor effects remain completely unclear, a situation that needs to be explored in the future.

The activation of tumor suppressor genes and oncogenes, including phosphatase and tensin homologue deleted on chromosome 10 (PTEN) and Krüppel-like factor 4 (KLF4), plays a key role in regulating the occurrence and development of tumors. PTEN is a tumor suppressor gene

that is closely related to tumorigenesis, and its functional defect exists widely in many kinds of tumors [14–16]. KLF4 plays a dual role in both oncogenes and tumor suppressor genes, and its expression is tissue or cell specific [17–20]. Studies have shown that PTEN and KLF4 are less active in NSCLC, and their high expression can effectively inhibit the proliferation of NSCLC [6, 7, 17, 18]. However, the relationship between PTEN and KLF4 in NSCLC remains unclear, and whether the deguelin affect the expression of PTEN or KLF4 has not been reported.

Numerous studies have shown that epithelial-mesenchymal transition (EMT) of tumor cells plays an important role in tumorigenesis and invasion [21, 22]. In studies of pancreatic cancer, researchers found that deguelin prevented epithelial cells from transforming into mesenchymal cells by inhibiting EMT [8, 23]. Moreover, deguelin inhibited the invasion, metastasis, and EMT transformation of NSCLC, colorectal cancer, and pancreatic tumors [24–26]. Therefore, the inhibition of the EMT process is an important measure in the treatment of tumors. These findings imply that deguelin plays important roles in pathogenesis of the tumors by inhibiting the EMT level. Currently, the accumulated evidence suggests that inactivation or loss of PTEN promotes the poor prognosis and metastasis of cancers by upregulating EMT expression including lung cancer [27, 28]. Similarly, KLF4 can negatively regulate the expression of EMT that is closely associated with the proliferation, invasion, and metastasis of cancer cells including breast cancer and colorectal cancer [29, 30]. These findings imply a possible relation between PTEN and KLF4 in invasion and metastasis of cancer cells that are involved with EMT expression. However, the relation in NSCLC still was completely unclear.

Therefore, this study was done to analyze the regulation of PTEN and KLF4 expressions in NSCLC cells by deguelin in vitro and in mice and to improve the mechanism of deguelin inhibiting the proliferation of NSCLC to explore the potential value of deguelin in the treatment of NSCLC.

2. Materials and Methods

2.1. Cell Culture. Human lung cancer cell lines A549 and PC9, purchased from the Committee on Type Culture Collection of Chinese Academy of Sciences (Shanghai, China), were cultured in PRMI-1640 medium, containing 10% fetal bovine serum (FBS), 100 U penicillin, and 100 μg streptomycin, and then, the cells were cultured in cell incubator at 37°C with 5% CO_2.

2.2. Quantitative Real-Time PCR. Total cellular RNA was extracted by RNeasy Mini Kit (74106, Qiagen, Germany), based on the manufacturer's protocol, the concentration of which was measured by NanoDrop 2000 (Thermo Scientific, USA). The total RNA was reverse transcribed into complementary DNA (cDNA) by PrimeScript 1st Strand cDNA Synthesis Kit (D6110A, Takara, China); then, real-time quantitative polymer chain reaction (qPCR) for cDNA amplification was carried out by QuantiFast SYBR Green PCR Kit (Qiagen, Germany). The relative levels of messenger RNA (mRNA) expression were calculated by the comparative Ct method ($2^{-\Delta\Delta Ct}$). The glyceraldehyde 3-phosphate dehydrogenase (GAPDH) was considered as an internal control of gene expression [8]. The specific primers of real-time qPCR are shown in Table 1.

Table 1: Specific primers used for real-time PCR in this study.

Primer name	Sequences (5′ to 3′)
PTEN-F	5-TGGATTCGACTTAGACTTGACCT-3
PTEN-R	5-GGTGGGTTATGGTCTTCAAAAGG-3
KLF4-F	5-TCGGACCACCTCGCCTTACA-3
KLF4-R	5-TCGGACCACCTCGCCTTACA-3
GAPDH-F	5-GGAGCGAGATCCCTCCAAAAT-3
GAPDH-R	5-GGCTGTTGTCATACTTCTCATGG-3

2.3. Immunoblotting. Immunoblotting was performed as previously described [8]. Briefly, the cells were washed twice using cold phosphate buffered saline (PBS) and lysed with lysis buffer, supplied with protease and phosphatase inhibitors, at 4°C for 30 min. The lysate supernatants were harvested and boiled in loading buffer. Protein concentration was tested by Pierce BCA Protein Assay Kit (23227, Thermo Scientific, USA). Cell lysates were followed by SDS–PAGE gel electrophoresis and then transferred to polyvinylidene fluoride (PVDF) membrane (Millipore, USA) for immunoblotting analysis and antibody hybridization. The target protein bands were visualized by an enhanced chemiluminescence system (Bio-Rad, California, USA). The antibodies PTEN (9559), KLF4 (4038), Claudin-1 (4933), Cyclin D1 (2978), E-cadherin (3195), N-cadherin (13116), survivin (71G4B7), Vimentin (Cat#5741), and β-actin (3700) were obtained from Cell Signaling Technology (Danvers, MA, USA).

2.4. Cell Transfection. NSCLC cells were transfected with PTEN or KLF4 small interfering RNA (siRNA) sequences (or overexpression plasmids) or negative control, purchased from RiboBio (Guangzhou, China), by Lipofectamine 2000 (11668019, Invitrogen, USA), according to the protocols, to determine PTEN or KLF4 knockdown (or overexpression) in the two cell lines, respectively. After transfection, the cells were collected for further experimentation. The transfection efficiency was confirmed by immunoblotting to analyze the expression levels of PTEN or KLF4 protein.

2.5. Cell Scratch Assay. A cell scratch assay was performed to evaluate cell motility. The transfected cells were seeded and cultured in six-well plates. The wound healing was scratched by a 100 μL sterile pipette tip, and the cells were washed three times with PBS. The wound healing width was observed in five different areas at 48 h by an inversion fluorescence microscope (Olympus, Japan).

2.6. Cell Invasion Assay. The invasion experiment was carried out in a transwell. The NSCLC cells in a serum-free medium were inoculated into the upper chamber of the transwell, and the 24-well plate in the lower chamber was filled with RPMI 1640 culture medium. The cells in the

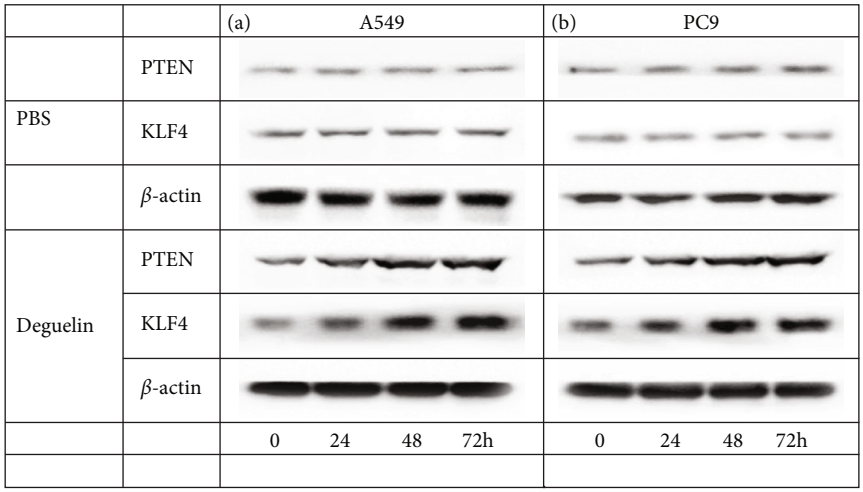

Figure 1: Deguelin upregulates PTEN and KLF4 expression in NSCLC cells. (a) The expression levels of PTEN and KLF4 in A549 cells induced by deguelin (25 μM) at different times compared to controls treated by PBS. (b) The expression levels of PTEN and KLF4 in PC9 cells induced by deguelin at different times compared to controls treated by PBS. β-Actin was used as an internal control. All experiments were repeated at least in triplicate.

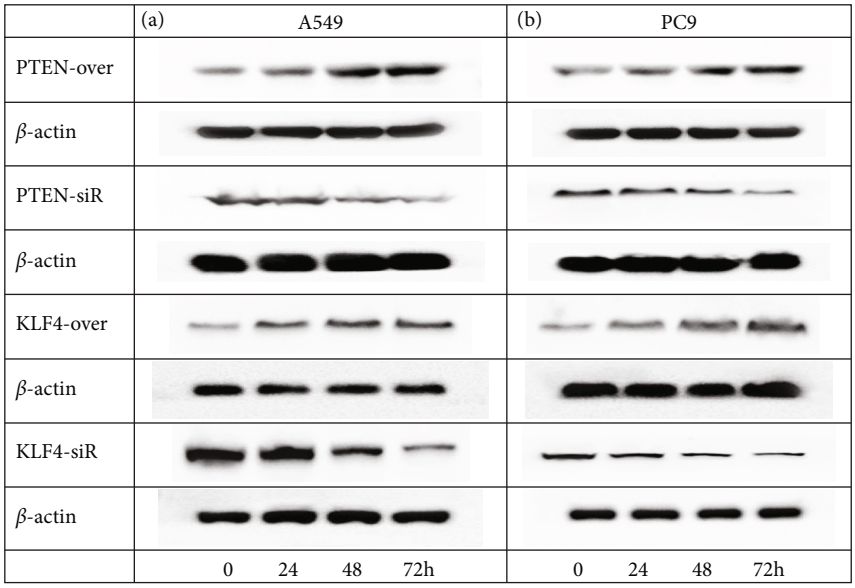

Figure 2: Determination of PTEN-siR/overexpression and KLF4-siR/overexpression in NSCLC cells at different times. (a) The expression levels of PTEN and KLF4 in A549 cells treated by PTEN-siR/overexpression and KLF4-siR/overexpression at different times compared to controls treated by PBS, respectively. (b) The expression levels of PTEN and KLF4 in PC9 cells treated by PTEN-siR/overexpression and KLF4-siR/overexpression at different times compared to controls treated by PBS, respectively. β-Actin was used as an internal control. All experiments were repeated at least in triplicate.

upper chamber were wiped out after 48 h, and those in the lower chamber were stained with 1% crystal violet. The chamber was precoated with Matrigel (BD Bioscience, USA) to evaluate cell invasion. The cells were counted in at least three random fields.

2.7. Animal Experiments. Six-week-old female BALB/c-nude mice were obtained from Shanghai Experimental Animal Center (Chinese Academy of Sciences, China) for human tumor models. After two-week acclimatization, they were randomized into groups of six mice. The control group was injected with 2×10^6/cells with PC9 cells per mouse. The experimental group were injected with an equal number of PC9 cells. When palpable tumors (~50-100 mm^3) arose, the control group was orally treated with physiological saline, and experimental group were treated with deguelin (4 mg/kg) by oral gavage on 1, 3, and 5 days of each week for three weeks. Tumor size was tested by caliper through measurements of the two perpendicular diameters every three days using the formula: Tumor Volume = (width^2 $\times$

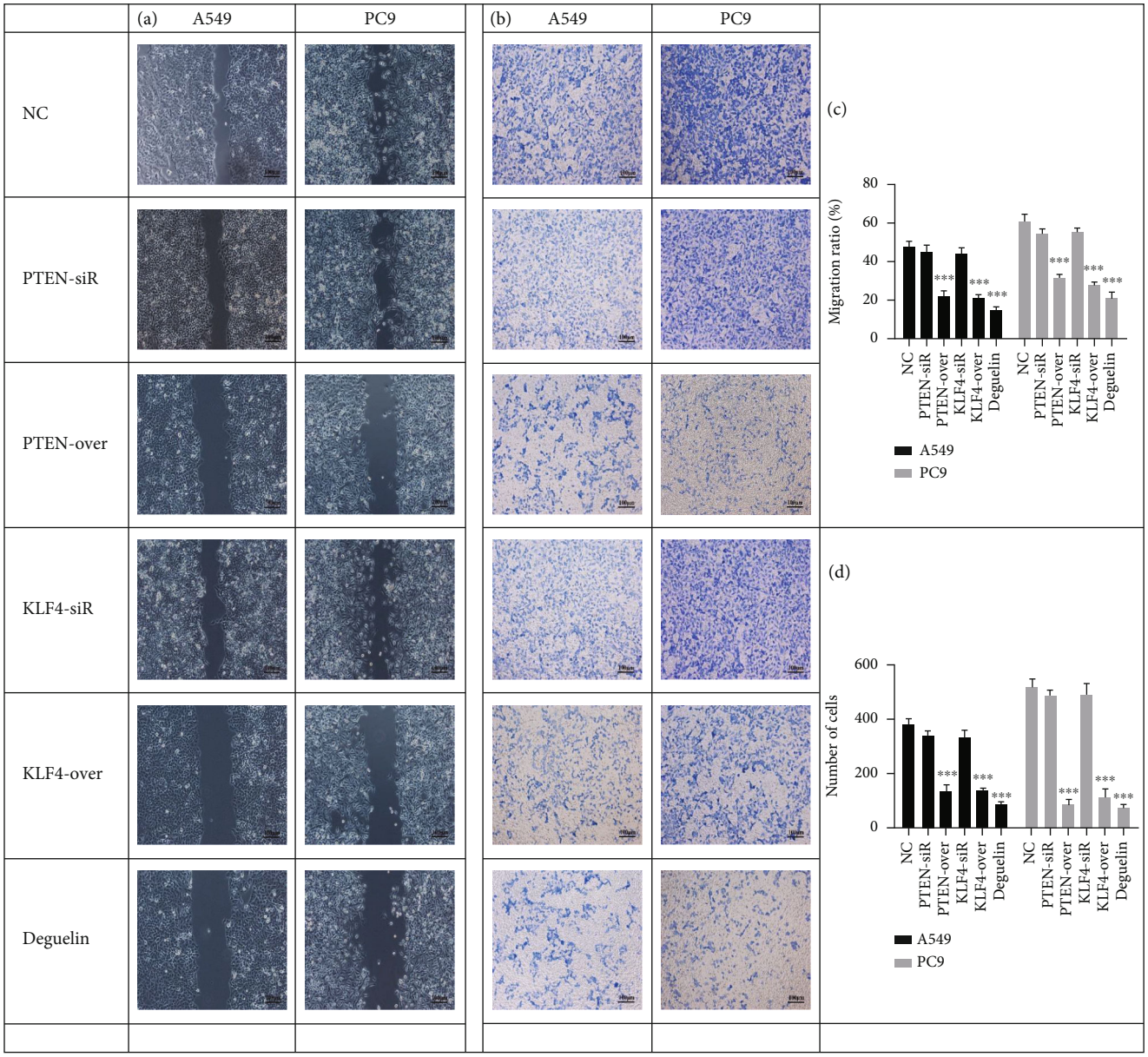

Figure 3: Deguelin inhibits migration and invasion of NSCLC. (a and c) The cell scratch assay for A549 and PC9 cell migration after cells were transfected by PTEN-siR/overexpression, KLF4-siR/overexpression, and deguelin (25 μM), respectively. The migration area was counted. (b and d) The cell invasion assay for A549 and PC9 cells after cells were transfected by PTEN-siR/overexpression, KLF4-siR/overexpression, and deguelin (25 μM), respectively. The numbers of invasion cells were counted. Scale bar represents 100 μm. All experiments were repeated at least in triplicate. The data are presented as the mean ± SD. Significant differences are indicated by $^{***}P < 0.001$.

length)/2. All procedures were performed according to the Regulations for the Administration of Affairs Concerning Experimental Animals. The experiments were approved by the Experimental Animal Ethics Committee of the First Affiliated Hospital, Zhejiang University School of Medicine.

2.8. Statistical Analysis. The experimental data were analyzed by GraphPad 6.04 software (GraphPad Software Inc., La Jolla, USA). All the experiments were independently repeated three times. The results were expressed by mean ± standard deviation (SD), *t*-test, and analysis of variance between groups of samples; *P* value < 0.05 was considered to be statistically significant.

3. Results

3.1. Deguelin Upregulates the Expressions of PTEN and KLF4. To investigate the effect of deguelin on the expressions of PTEN and KLF4, we added 25 μmol (μM) deguelin into A549 and PC9 cells and detected the changes of PTEN and KLF4 proteins by immunoblotting assay at different time points (0, 24, 48, and 72 h). The results showed that compared to controls, deguelin significantly upregulated the expressions of PTEN and KLF4 in a time-dependent manner in A549 cells and PC9 cells, respectively (Figures 1(a) and 1(b)). Moreover, significant differences of PTEN and KLF4 gene expressions were observed at 48 h by PCR assay (Fig. 1S).

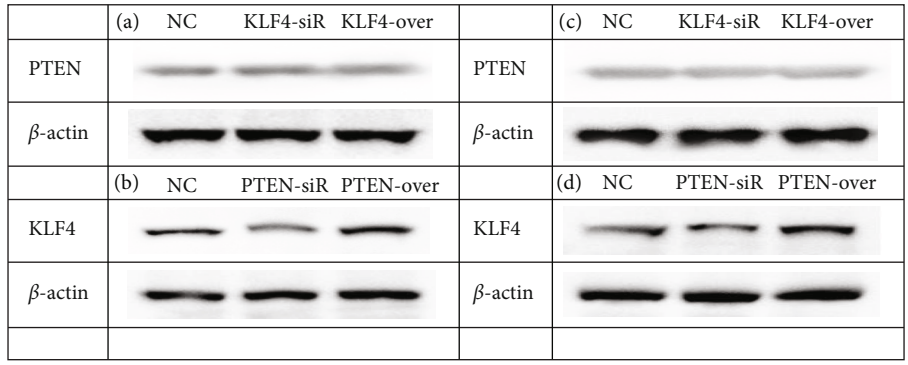

Figure 4: PTEN upregulates KLF4 expression in NSCLC cells. (a) The expression levels of PTEN in A549 cells transfected with KLF4-siR/overexpression were detected by immunoblotting assay. (b) The expression levels of KLF4 in A549 cells transfected with PTEN-siR/overexpression were detected by immunoblotting assay. (c) The expression levels of PTEN in PC9 cells transfected with KLF4-siR/overexpression were detected by immunoblotting assay. (d) The expression levels of KLF4 in PC9 cells transfected with PTEN-siR/overexpression were detected by immunoblotting assay. β-Actin was used as an internal control. All experiments were repeated at least in triplicate.

3.2. Determination of Time Point of Target Gene Overexpression and Interference Experiment. To determinate the appropriate time point of target gene expression, we determined the time point (0, 24, 48, and 72 h) of overexpression and siRNA in the experiment on PTEN and KLF4 genes in A549 cells and PC9 cells to facilitate the follow-up experiment. The best time point for overexpression and siRNA of PTEN and KLF4 genes was 48 h in A549 cells and PC9 cells, respectively (Figures 2(a) and 2(b)). Moreover, significant changes of PTEN and KLF4 gene expressions were observed at 48 h by PCR assay (Fig. 1S).

3.3. Deguelin Inhibits the Migration and Invasion of NSCLC Cells. To investigate the effect of deguelin on the migration and invasion of NSCLC cells, we added deguelin (25 μM) into A549 and PC9 cells for 48 h. The results of the scratch analysis showed that deguelin could effectively inhibit the migration of A549 and PC9 cells, the migration effect of PTEN and KLF4 induced by their overexpression was similar to that of deguelin, and the effect on siRNA of PTEN and KLF4 was similar to that of normal control (NC) but contrary to the effect on deguelin (Figures 3(a) and 3(c)). The invasive effect of PTEN and KLF4 on NSCLC cells was similar to that of deguelin, and the effect on siRNA of PTEN and KLF4 in NSCLC cells was similar to that of NC but different from that of deguelin (Figures 3(b) and 3(d)).

3.4. Relationship between PTEN and KLF4. To determine whether PTEN affects the expression of KLF4 in NSCLC cells, siRNA and overexpressions of PTEN and KLF4 were analyzed in this study. The results showed that the overexpression or siRNA of KLF4 had no significant effect on PTEN expression in A549 cells and PC9 cells (Figures 4(a) and 4(c)). Interestingly, both overexpression and siRNA of PTEN positively regulated KLF4 expression in A549 cells and PC9 cells (Figures 4(b) and 4(d)).

3.5. Effect of Deguelin on EMT Expression by PTEN and KLF4. To determine the effect of deguelin, PTEN, and KLF4 on EMT in NSCLC cells, deguelin, siRNA, and overexpressions of PTEN and KLF4 were analyzed in this study. The results showed that deguelin can effectively inhibit EMT in A549 cells and PC9 cells by decreasing vimentin protein expression and promoting E-cadherin level, an effect that was similar to that of PTEN and KLF4 overexpressions on the EMT in A549 cells and PC9 cells (Figures 5(a) and 5(b)). However, the effect of deguelin was different from that of PTEN and KLF4 siRNA, which promotes EMT expressions in A549 cells and PC9 cells (Figures 5(c) and 5(d)).

3.6. Effect of Deguelin on Tumor Size in Tumor-Bearing Mice. To further analyze the effect of deguelin on tumor size and expressions of PTEN and KLF4, we inoculated PC9 cells subcutaneously into BABL/c mice and injected deguelin. After 2 weeks, the tumor size was measured, and the expressions of PTEN and KLF4 were detected. The results showed that deguelin could effectively inhibit tumor growth and upregulate the expressions of PTEN and KLF4 in tumor tissues (Figure 6).

4. Discussion

NSCLC is the most common lung cancer and is a major cause of cancer-related deaths worldwide. The metastasis of NSCLC is the key factor for its poor prognosis [3–5, 31]. The burden of disease with NSCLC has become one of the major public health problems in the world. Here, we observed that deguelin could significantly upregulate PTEN and KLF4 expressions in NSCLC cells, including A549 and PC9 cells in this study. Interestingly, PTEN could positively upregulate KLF4 expression in A549 and PC9 cells. Moreover, overexpressions of PTEN and KLF4 or deguelin could inhibit the migration and invasion of NSCLC cells, which were involved into EMT expressions in NSCLC cells. Additionally, deguelin displayed a significant antitumor ability by upregulating PTEN and KLF4 expressions in mice model with NSCLC cells. Together, these results indicated that deguelin was considered to be a potential therapeutic target for the treatment of NSCLC.

Figure 5: EMT-associated proteins were regulated by deguelin, PTEN, and KLF4. (a) EMT-associated proteins were detected in A549 cells and PC9 cells by deguelin and PTEN-siR/overexpression. (b) EMT-associated proteins were detected in A549 cells and PC9 cells by deguelin and KLF4-siR/overexpression. β-Actin was used as an internal control. All experiments were repeated at least in triplicate.

In recent years, deguelin, a rotenoid of the flavonoid family, extracted from *Lonchocarpus*, *Derris*, or *Tephrosia*, can effectively inhibit the proliferation, invasion, and metastasis of many kinds of tumors, including colon cancer, human pancreatic cancer, breast cancer, and lung cancer, and is a promising chemopreventive agent for cancer therapy [6, 7]. Deguelin promotes apoptosis of NSCLC by inhibiting galectin-1 protein expression [8]. Deguelin derivatives block the development of NSCLC by interfering with the binding of adenosine triphosphate (ATP) to heat shock protein 90 (HSP90); its analogue SH-1242 also exerts its antitumor effect by inhibiting HSP90 [32, 33]. Researchers found that deguelin could inhibit the proliferation, invasion, metastasis, and autophagy of tumor cells by regulating many signal pathways (e.g., EGFR/IGF1R-Akt, MAPK, and mTOR). Our study also confirmed that deguelin can effectively inhibit the invasion, migration, and growth of NSCLC cells [6–10, 34, 35]. In the xenograft mouse model, orally treated with deguelin (4 mg/kg/three times a week) significantly prevented tumor growth, according to the dose conversion [36], the 4 mg/kg deguelin dose used in mouse is equivalent to the dose of 19.5 mg deguelin dose for a 60 kg person, which is certainly within the range of a number of plant extracts. These data provide a strong basis for the future clinical translational research of deguelin.

Studies show that PTEN, as a tumor suppressor gene, its functional defect plays a key role in the development of various cancers, including prostate cancer, lung cancer, hepatocellular carcinoma (HCC), and pancreatic cancer

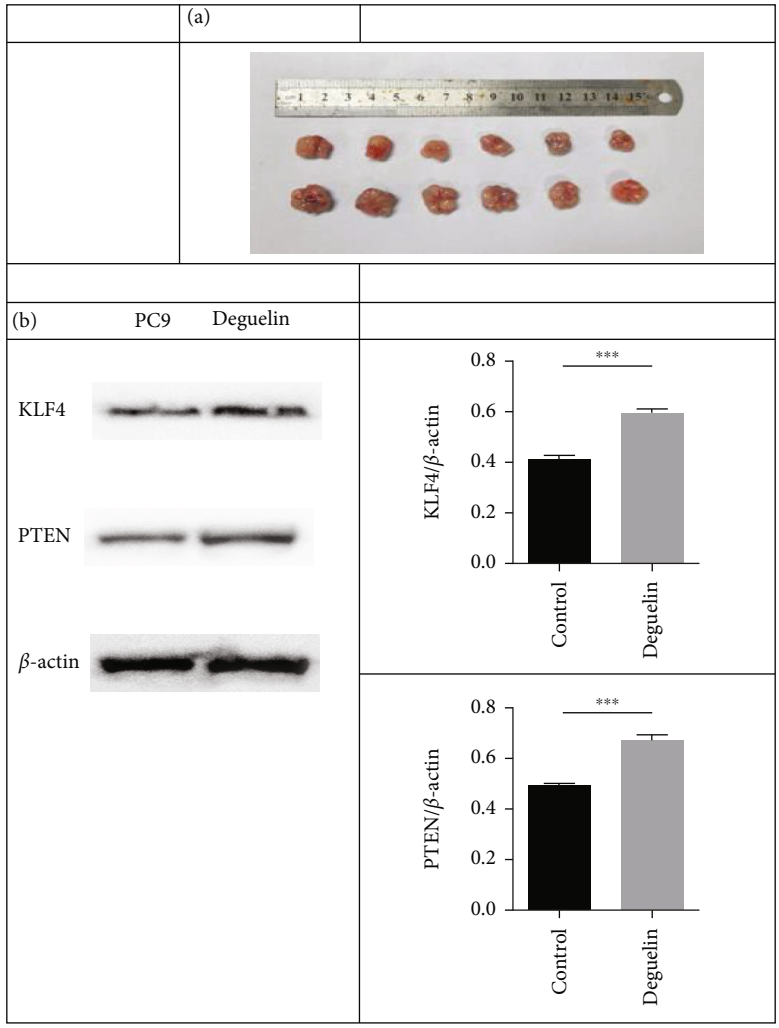

Figure 6: Deguelin inhibited tumor growth by upregulating PTEN and KLF4 expressions in mice model with NSCLC cells. (a) On day 21, the tumors were carefully dissected from the mice, and the tumor size was measured. (b) The expression levels of KLF4 and PTEN proteins in tumors were detected. (c and d) The relative band intensity of KLF4 and PTEN in tumors were detected. β-Actin was used as an internal control. All experiments were repeated at least in triplicate. $^{***}P < 0.001$ and $^{****}P < 0.0001$.

[14, 37–40]. The low expression or loss of function of PTEN in patients and animal models with NSCLC could not effectively inhibit the proliferation and migration of NSCLC [41–43]. These results indicated that increased PTEN will contribute to inhibition of tumors. Our study also showed that deguelin could effectively promote the expression of PTEN to inhibit the invasion and migration of NSCLC cells in vitro, which was associated with inhibition of EMT, and suppressed tumor growth with upregulation of PTEN expression in tumor tissue from mice model with NSCLC. These findings further confirmed the important value of deguelin as an antitumor agent for NSCLC by upregulating PTEN expression to decrease the EMT.

Previous reports showed that KLF4, a zinc finger-type transcription factor, played a pivotal and different role in the development of various cancers, including lung cancer, HCC, and pancreatic cancer [44–48]. However, low expression of KLF4 promoted the growth, invasion, and metastasis of NSCLC, but high expression of KLF4 displayed a valuable role for therapy of NSCLC [49–51]. In our study, the results showed that increased expression of KLF4 could effectively inhibit the growth, invasion, and metastasis of NSCLC, which was associated with inhibition of EMT in cell lines. Interestingly, deguelin could significantly promote the expression of KLF4 in cell lines and mouse tumor tissue of NSCLC to play an important antitumor role. These findings indicated that deguelin could effectively suppress the growth, invasion, and metastasis of NSCLC by upregulating KLF4 expression to reduce the EMT. Importantly, deguelin could suppress the invasion and metastasis of NSCLC by upregulating PTEN and KLF4 expressions to reduce the EMT, which indicated an important relation between PTEN and KLF4 in NSCLC. Our results demonstrated the value of the hypothesis about the relation between PTEN and KLF4

in NSCLC. Overexpressed PTEN could promote KLF4 expression to inhibit the EMT, and siPTEN attenuated KLF4 expression to restore the EMT. However, overexpressed KLF4 (or siKLF4) could not enhance (or decrease) PTEN expression but could affect the EMT in NSCLC cell lines. These findings confirmed that PTEN could promote KLF4 expression to suppress EMT in NSCLC and deguelin is a promising agent for NSCLC therapy. However, how does deguelin regulate the PTEN/KLF4/EMT process is explored in the future study.

5. Conclusion

In summary, deguelin effectively promoted the expression of PTEN and KLF4 in NSCLC cells in vitro, and upregulated PTEN could increase the expression of KLF4 to suppress the EMT to further attenuate the invasion and migration of NSCLC cells. In vivo experiments also showed that deguelin could upregulate the expression of PTEN and KLF4 in tumor-bearing mice and then significantly inhibit the growth of NSCLC in mice. These findings further improved the important molecular mechanism of deguelin inhibiting the invasion and migration of NSCLC and established an important foundation for exploring the potential value of deguelin as a promising drug for NSCLC therapy.

Data Availability

The data used to support the findings of this study are included within the article.

Conflicts of Interest

The authors declare no conflict of interests.

Authors' Contributions

GL and XZ performed the experiments, drafted the manuscript, and designed the figures and tables. YY revised the manuscript. JZ conceived the topic and revised the manuscript. All authors contributed to the article and approved the submitted version.

Acknowledgments

This work was supported by the National Natural Science Foundation of China (Nos. 81670017, 81472171, and 81871709) and Zhejiang Provincial Key Research and Development Program (No. 2019C03042).

Supplementary Materials

Fig. 1S: expression levels of PTEN and KLF4 mRNAs in NSCLC cells at 48 h. (A and B) The relative levels of PTEN mRNA in A549 cells and PC9 cells treated with deguelin and transfected with PTEN-siR/overexpression. (C and D) The relative levels of KLF4 mRNA in A549 cells and PC9 cells treated with deguelin and transfected with PTEN-siR/overexpression. GAPDH was used as an internal control. All experiments were repeated at least in triplicate. $^{*}P < 0.05$, $^{**}P < 0.01$, and $^{***}P < 0.001$. *(Supplementary Materials)*

References

[1] C. de Martel, D. Georges, F. Bray, J. Ferlay, and G. M. Clifford, "Global burden of cancer attributable to infections in 2018: a worldwide incidence analysis," *The Lancet Global Health*, vol. 8, no. 2, pp. e180–e190, 2020.

[2] H. Sung, J. Ferlay, R. L. Siegel et al., "Global cancer statistics 2020: GLOBOCAN estimates of incidence and mortality worldwide for 36 cancers in 185 countries," *CA: a Cancer Journal for Clinicians*, vol. 71, no. 3, pp. 209–249, 2021.

[3] W. Cao, H. D. Chen, Y. W. Yu, N. Li, and W. Q. Chen, "Changing profiles of cancer burden worldwide and in China: a secondary analysis of the global cancer statistics 2020," *Chinese Medical Journal*, vol. 134, no. 7, pp. 783–791, 2021.

[4] W. T. Iams, J. Porter, and L. Horn, "Immunotherapeutic approaches for small-cell lung cancer," *Nature Reviews. Clinical Oncology*, vol. 17, no. 5, pp. 300–312, 2020.

[5] H. Cheng and R. Perez-Soler, "Leptomeningeal metastases in non-small-cell lung cancer," *The Lancet Oncology*, vol. 19, no. 1, pp. e43–e55, 2018.

[6] Z. Y. Lin, Q. Z. Yun, L. Wu, T. W. Zhang, and T. Z. Yao, "Pharmacological basis and new insights of deguelin concerning its anticancer effects," *Pharmacological Research*, vol. 174, article 105935, 2021.

[7] H. S. Tuli, S. Mittal, M. Loka et al., "Deguelin targets multiple oncogenic signaling pathways to combat human malignancies," *Pharmacological Research*, vol. 166, article 105487, 2021.

[8] B. Yan, D. Zhao, Y. Yao, Z. Bao, G. Lu, and J. Zhou, "Deguelin induces the apoptosis of lung squamous cell carcinoma cells through regulating the expression of galectin-1," *International Journal of Biological Sciences*, vol. 12, no. 7, pp. 850–860, 2016.

[9] F. Gao, X. Yu, M. Li et al., "Deguelin suppresses non-small cell lung cancer by inhibiting EGFR signaling and promoting GSK3β/FBW7-mediated Mcl-1 destabilization," *Cell Death & Disease*, vol. 11, no. 2, p. 143, 2020.

[10] Y. Wang, W. Ma, and W. Zheng, "Deguelin, a novel antitumorigenic agent targeting apoptosis, cell cycle arrest and anti-angiogenesis for cancer chemoprevention," *Mol Clin Oncol*, vol. 1, no. 2, pp. 215–219, 2013.

[11] W. Li, X. Yu, X. Ma et al., "Deguelin attenuates non-small cell lung cancer cell metastasis through inhibiting the CtsZ/FAK signaling pathway," *Cellular Signalling*, vol. 50, pp. 131–141, 2018.

[12] K. B. Lokhande, S. Nagar, and K. V. Swamy, "Molecular interaction studies of deguelin and its derivatives with cyclin D1 and cyclin E in cancer cell signaling pathway: the computational approach," *Scientific Reports*, vol. 9, no. 1, p. 1778, 2019.

[13] W. Li, X. Yu, Z. Xia et al., "Repression of Noxa by Bmi1 contributes to deguelin-induced apoptosis in non-small cell lung cancer cells," *Journal of Cellular and Molecular Medicine*, vol. 22, no. 12, pp. 6213–6227, 2018.

[14] F. Conciatori, C. Bazzichetto, I. Falcone et al., "PTEN function at the interface between cancer and tumor microenvironment: implications for response to immunotherapy," *International Journal of Molecular Sciences*, vol. 21, no. 15, p. 5337, 2020.

[15] A. Naguib, G. Mathew, C. R. Reczek et al., "Mitochondrial complex I inhibitors expose a vulnerability for selective killing of Pten-null cells," *Cell Reports*, vol. 23, no. 1, pp. 58–67, 2018.

[16] S. Vallabhaneni, J. Liu, M. Morel, J. Wang, F. J. DeMayo, and W. Long, "Conditional ERK3 overexpression cooperates with

PTEN deletion to promote lung adenocarcinoma formation in mice," *Molecular Oncology*, vol. 16, 2022.

[17] M. C. Fadous-Khalifé, N. Aloulou, M. Jalbout et al., "Krüppel-like factor 4: a new potential biomarker of lung cancer," *Mol Clin Oncol*, vol. 5, no. 1, pp. 35–40, 2016.

[18] V. Vaira, A. Faversani, N. M. Martin et al., "Regulation of lung cancer metastasis by Klf4-Numb-like signaling," *Cancer Research*, vol. 73, no. 8, pp. 2695–2705, 2013.

[19] V. K. Xie, Z. Li, Y. Yan et al., "DNA-methyltransferase 1 induces dedifferentiation of pancreatic cancer cells through silencing of Krüppel-like factor 4 expression," *Clinical Cancer Research*, vol. 23, no. 18, pp. 5585–5597, 2017.

[20] L. Yang, P. Shi, G. Zhao et al., "Targeting cancer stem cell pathways for cancer therapy," *Signal Transduction and Targeted Therapy*, vol. 5, no. 1, p. 8, 2020.

[21] A. Dongre and R. A. Weinberg, "New insights into the mechanisms of epithelial-mesenchymal transition and implications for cancer," *Nature Reviews. Molecular Cell Biology*, vol. 20, no. 2, pp. 69–84, 2019.

[22] E. D. Williams, D. Gao, A. Redfern, and E. W. Thompson, "Controversies around epithelial-mesenchymal plasticity in cancer metastasis," vol. 19, no. 12, pp. 716–732, 2019.

[23] A. W. Lambert and R. A. Weinberg, "Linking EMT programmes to normal and neoplastic epithelial stem cells," *Nature Reviews. Cancer*, vol. 21, no. 5, pp. 325–338, 2021.

[24] D. Zhao, W. Han, X. Liu, D. Cui, and Y. Chen, "Deguelin inhibits epithelial-to-mesenchymal transition and metastasis of human non-small cell lung cancer cells by regulating NIMA-related kinase 2," *Thorac Cancer*, vol. 8, no. 4, pp. 320–327, 2017.

[25] N. Zhang, A. S. Ng, S. Cai, Q. Li, L. Yang, and D. Kerr, "Novel therapeutic strategies: targeting epithelial-mesenchymal transition in colorectal cancer," *The Lancet Oncology*, vol. 22, no. 8, pp. e358–e368, 2021.

[26] S. R. Boreddy and S. K. Srivastava, "Deguelin suppresses pancreatic tumor growth and metastasis by inhibiting epithelial-to-mesenchymal transition in an orthotopic model," *Oncogene*, vol. 32, no. 34, pp. 3980–3991, 2013.

[27] H. Rajabi, M. Hiraki, and D. Kufe, "MUC1-C activates polycomb repressive complexes and downregulates tumor suppressor genes in human cancer cells," *Oncogene*, vol. 37, no. 16, pp. 2079–2088, 2018.

[28] F. Luongo, F. Colonna, F. Calapà, S. Vitale, M. E. Fiori, and R. De Maria, "PTEN tumor-suppressor: the dam of stemness in cancer," *Cancers (Basel)*, vol. 11, no. 8, p. 1076, 2019.

[29] J. Cui, M. Shi, M. Quan, and K. Xie, "Regulation of EMT by KLF4 in gastrointestinal cancer," *Current Cancer Drug Targets*, vol. 13, no. 9, pp. 986–995, 2013.

[30] J. L. Yori, D. D. Seachrist, E. Johnson et al., "Kruppel-like factor 4 inhibits tumorigenic progression and metastasis in a mouse model of breast cancer," *Neoplasia*, vol. 13, no. 7, pp. 601–IN5, 2011.

[31] A. A. Thai, B. J. Solomon, L. V. Sequist, J. F. Gainor, and R. S. Heist, "Lung cancer," *Lancet*, vol. 398, no. 10299, pp. 535–554, 2021.

[32] S. Y. Hyun, H. T. Le, C. T. Nguyen et al., "Development of a novel Hsp90 inhibitor NCT-50 as a potential anticancer agent for the treatment of non-small cell lung cancer," *Scientific Reports*, vol. 8, no. 1, p. 13924, 2018.

[33] S. C. Lee, H. Y. Min, H. Choi et al., "Deguelin analogue SH-1242 inhibits Hsp90 activity and exerts potent anticancer efficacy with limited neurotoxicity," *Cancer Research*, vol. 76, no. 3, pp. 686–699, 2016.

[34] M. Miller and N. Hanna, "Advances in systemic therapy for non-small cell lung cancer," *BMJ*, vol. 375, article n2363, 2021.

[35] F. D. Dimitrakopoulos, A. E. Kottorou, M. Kalofonou, and H. P. Kalofonos, "The fire within: NF-κB involvement in non-small cell lung cancer," *Cancer Research*, vol. 80, no. 19, pp. 4025–4036, 2020.

[36] S. Reagan-Shaw, M. Nihal, and N. Ahmad, "Dose translation from animal to human studies revisited," *The FASEB Journal*, vol. 22, no. 3, pp. 659–661, 2008.

[37] G. Xun, W. Hu, and B. Li, "PTEN loss promotes oncogenic function of STMN1 via PI3K/AKT pathway in lung cancer," *Scientific Reports*, vol. 11, no. 1, p. 14318, 2021.

[38] D. Tang, J. He, Y. Dai et al., "Targeting KDM6A suppresses SREBP1c-dependent lipid metabolism and prostate tumorigenesis," *Cancer Research*, p. canres.1825.2021, 2021.

[39] C. Zhao, B. Wang, E. Liu, and Z. Zhang, "Loss of PTEN expression is associated with PI3K pathway-dependent metabolic reprogramming in hepatocellular carcinoma," *Cell Communication and Signaling: CCS*, vol. 18, no. 1, p. 131, 2020.

[40] Z. Niu, X. Li, S. Dong et al., "The E3 ubiquitin ligase HOIP inhibits cancer cell apoptosis via modulating PTEN stability," *Journal of Cancer*, vol. 12, no. 21, pp. 6553–6562, 2021.

[41] H. Chen, W. Wang, C. Xiao, D. Xia, F. Li, and S. Liu, "ACY1 regulating PTEN/PI3K/AKT signaling in the promotion of non-small cell lung cancer progression," *Ann Transl Med*, vol. 9, no. 17, p. 1378, 2021.

[42] Y. He, S. Jiang, C. Mao et al., "The deubiquitinase USP10 restores PTEN activity and inhibits non-small cell lung cancer cell proliferation," *The Journal of Biological Chemistry*, vol. 297, no. 3, article 101088, 2021.

[43] M. Zhao, P. Xu, Z. Liu et al., "RETRACTED ARTICLE: Dual roles of miR-374a by modulated c-Jun respectively targets CCND1-inducing PI3K/AKT signal and PTEN-suppressing Wnt/β-catenin signaling in non-small-cell lung cancer," *Cell Death & Disease*, vol. 9, no. 2, p. 78, 2018.

[44] A. Taracha-Wisniewska, G. Kotarba, S. Dworkin, and T. Wilanowski, "Recent discoveries on the involvement of Krüppel-like factor 4 in the most common cancer types," *International Journal of Molecular Sciences*, vol. 21, no. 22, p. 8843, 2020.

[45] Y. Li, S. Yu, L. Li et al., "KLF4-mediated upregulation of CD9 and CD81 suppresses hepatocellular carcinoma development via JNK signaling," *Cell Death & Disease*, vol. 11, no. 4, p. 299, 2020.

[46] M. Karabicici, S. Alptekin, Z. Fırtına Karagonlar, and E. Erdal, "Doxorubicin-induced senescence promotes stemness and tumorigenicity in EpCAM-/CD133- nonstem cell population in hepatocellular carcinoma cell line, HuH-7," *Molecular Oncology*, vol. 15, no. 8, pp. 2185–2202, 2021.

[47] L. Feng, J. Wang, J. Zhang et al., "Comprehensive analysis of E3 ubiquitin ligases reveals ring finger protein 223 as a novel oncogene activated by KLF4 in pancreatic cancer," *Frontiers in Cell and Development Biology*, vol. 9, article 738709, 2021.

[48] K. Ganguly, S. R. Krishn, S. Rachagani et al., "Secretory mucin 5AC promotes neoplastic progression by augmenting KLF4-mediated pancreatic cancer cell stemness," *Cancer Research*, vol. 81, no. 1, pp. 91–102, 2021.

[49] X. Wang, S. Xia, H. Li et al., "The deubiquitinase USP10 regulates KLF4 stability and suppresses lung tumorigenesis," *Cell Death and Differentiation*, vol. 27, no. 6, pp. 1747–1764, 2020.

[50] Y. Wu, L. Lin, X. Wang et al., "Overexpression of Krüppel-like factor 4 suppresses migration and invasion of non-small cell lung cancer through c-Jun-NH2-terminal kinase/epithelial-mesenchymal transition signaling pathway," *Frontiers in Pharmacology*, vol. 10, p. 1512, 2020.

[51] W. Feng, Q. Xie, S. Liu et al., "Krüppel-like factor 4 promotes c-met amplification-mediated gefitinib resistance in non-small-cell lung cancer," *Cancer Science*, vol. 109, no. 6, pp. 1775–1786, 2018.

Hindawi
Disease Markers
Volume 2022, Article ID 6304859, 18 pages
https://doi.org/10.1155/2022/6304859

Research Article

A Prognosis Marker Dynein Cytoplasmic 1 Heavy Chain 1 Correlates with EMT and Immune Signature in Liver Hepatocellular Carcinoma by Bioinformatics and Experimental Analysis

Yanhong Wang,[1,2] **Jiyu Han**,[1,2] **Haichao Zhou**,[1,2] **Songtao Ai**,[3] **and Daqian Wan**[1,2]

[1]*Department of Orthopedics, Tongji Hospital, School of Medicine, Tongji University, Shanghai 200065, China*
[2]*Key Laboratory of Spine and Spinal Cord Injury Repair and Regeneration, Ministry of Education, Shanghai 200065, China*
[3]*Department of Radiology, Shanghai Ninth People's Hospital, Shanghai Jiao Tong University School of Medicine, Shanghai 200011, China*

Correspondence should be addressed to Songtao Ai; aistss1024@sjtu.edu.cn and Daqian Wan; wdqwdq1986@126.com

Received 8 March 2022; Revised 17 April 2022; Accepted 25 April 2022; Published 11 May 2022

Academic Editor: Zhen-Jian Zhuo

Background. Liver hepatocellular carcinoma (LIHC) has had a continuous increase in incidence and mortality rates over the last 40 years. Dynein Cytoplasmic 1 Heavy Chain 1 (DYNC1H1) is a protein coding gene which encodes the cytoplasmic dynein heavy chain family. This is the first investigation into the expression of DYNC1H1 and its mechanisms of action in LIHC patients. *Methods*. Based on the DYNC1H1 expression data from the TCGA database, we performed the DYNC1H1 expression, clinicopathological data, gene enrichment, and immune infiltration analysis. TIMER and CIBERSORT were used to assess immune responses of DYNC1H1 in LIHC. GEPIA, K-M survival analysis, and immunohistochemical staining pictures from the THPA were used to validate the results. In order to evaluate the diagnostic value of DYNC1H1, GEO datasets were analyzed by using ROC analysis. And quantitative real-time polymerase chain reaction was also carried out to evaluate the expression of DYNC1H1. *Results*. DYNC1H1 expression levels were associated with T classification, pathologic stage, histologic grade, and serum AFP levels. DYNC1H1 is an independent factor for a poor prognosis in patients with LIHC. Further study showed that high expression of DYNC1H1 was enriched in epithelial–mesenchymal transition (EMT) and the TGF β signaling pathway by GSEA analysis enrichment, indicating that DYNC1H1 might play a key role in the progression of CRC through EMT and immune response, which also had been validated by the experimental assays. *Conclusions*. DYNC1H1 will provide a novel and important perspective for the mechanisms of LIHC by regulating EMT. This gene will be able to act as an efficacious tool for the early diagnosis and effective intervention of LIHC.

1. Introduction

LIHC is one of the few prevalent solid organ tumors in which a continuous increase in incidence and mortality rates has been observed over the last 40 years [1]. The 2020 Global Cancer Statistics showed that LIHC new cases were approximately 906,000 and the death cases were 830,000, of which more than 50% occurred in China. Hepatocellular carcinoma (HCC) represents the predominant histological subtype (75–85%) of primary liver cancer [2]. Currently, several risk factors have been indicated to contribute for developing LIHC, such as hepatitis B, hepatitis C, excessive consumption of

alcohol, exposure, tobacco use, and aflatoxin [3–5]. At present, ultrasonography (US), computed tomography (CT), magnetic resonance imaging (MRI), and the serum alpha-fetoprotein (AFP) value are the most common noninvasive methods used to detect and diagnose LIHC, but all of them are not always sufficiently sensitive in early diagnosis [6]. Therefore, the identification of a more specific biomarker and potential target for treatment is critical for improving the prognosis of LIHC.

Dynein Cytoplasmic 1 Heavy Chain 1 (DYNC1H1) is a protein coding gene which encodes the cytoplasmic dynein heavy chain family. This family links engulfment and execution of apoptosis to prevent several pathologies including cancer, neurodegenerative diseases, and autoimmune disorders [7–9]. The DYNC1H1 plays a dominant role in the assembly of the mitotic spindle and the congression of the metaphase plate [10]. DYNC1H1 also controls microtubule binding [11]. Therefore, DYNC1H1 involved in microtubule dynamics and mitotic spindle orientation could be a possible factor in the pathophysiology and progression of tumors [12]. They are closely linked to tumor pathogenesis [13, 14].

Although DYNC1H1-associated immune responses have been identified among various types of cancer, comprising gastric and lung cancer, the role of DYNC1H1 in immune infiltration and prognosis is still underexplored [11, 15]. To address this challenge, we analyzed DYNC1H1 in LIHC through using RNA expression sequencing data from The Cancer Genome Atlas (TCGA, https://cancergenome.nih.gov/) database. We used R language software to compare the interrelationship between DYNC1H1 and some clinicopathological parameters. In order to better confirm the pathogenic effect of DYNC1H1 and understand the regulatory mechanisms, we constructed protein–protein interaction (PPI) networks, Gene Ontology (GO) analyses, and gene set enrichment analysis (GSEA) analyses. The correlation between DYNC1H1 and EMT pathway scores was analyzed. Using the Tumor Immunoassay Resource (TIMER) and CIBERSORT algorithm, we further investigated the interrelationship between DYNC1H1 and Tumor-Infiltrating Immune Cells (TIICs). The association of DYNC1H1 and prognosis was subsequently analyzed by using the Gene Expression Profiling Interactive Analysis (GEPIA), Kaplan–Meier (K-M) survival analysis, and the Human Protein Atlas (THPA). In order to assess the diagnostic value of DYNC1H1, a receiver operating characteristic (ROC) curve was established. Finally, we further validated DYNC1H1 using qPCR, which will help us further elucidate the potential pathogenesis of LIHC.

Despite certain previous studies involving the potential role of this gene in LIHC [16, 17], the association of TIICs and poor prognosis did not present an exhaustive analysis and lacked an in-depth discussion. The development and pathogenesis of LIHC is an extremely complex process consisting of multiple causative aspects and risk factors involved in the etiology. Our study has suggested that higher DYNC1H1 expression is strongly associated with T classification, pathologic stage, histologic grade, AFP, and overall survival (OS) event, generally indicating a poor prognosis. In addition, the correlation between DYNC1H1 and TIICs was explored. In this paper, the function of DYNC1H1 in LIHC was analyzed in detail to explore effective molecules for LIHC diagnosis and treatment.

2. Materials and Methods

2.1. Data Acquisition and Mining. The TCGA database was utilized to find the gene expression data (workflow type: HTSeq-TPM), immune system infiltrates, and corresponding clinical information [18]. In addition, for any missing, insufficient, or unclear data source, the sample will be excluded from the research. We used both RNA-sequence and clinical data, which was used for analysis and investigation. Both RNA-sequence and relevant clinical data were used to guide further studies. Among these 424 cases, 374 cases of LIHC tissue and corresponding 50 cases of normal healthy liver tissues were included in our research. For investigation of the underlying molecular mechanism of the DYNC1H1 expression, patients with LIHC were clustered into 2 groups, the high or low expression level group based on patients' expression level and the median value of the DYNC1H1 gene. Our research was performed in conformity with the publication guidelines offered by TCGA [19]. Moreover, in order to verify the expression and diagnostic value of DYNC1H1 in LIH, we collected 2 gene expression profiling datasets (GSE14520 and GSE63898) from the Gene Expression Omnibus (GEO) database [20–22] (Table 1).

2.2. Validation of DYNC1H1 Expression. We analyzed the TCGA dataset to validate and verify the potential prognostic role of DYNC1H1 genes in LIHC. To analyze difference in DYNC1H1 genes between LIHC samples and normal liver tissues, we utilized independent sample t-tests for nonpaired samples and paired t-test for paired samples. The results were generated with boxplots. And using the ggplot2 R package [23], boxplots were plotted.

2.3. Survival Analysis Based on DYNC1H1 Expression. In short, using the R packages survival and survminer to graph K-M survival curves, survival analysis was carried out. It was the K-M survival curves that were used to represent the OS and progression-free interval (PFI) distributions between the high and low DYNC1H1 groups. By the OS and PFI time derived from TCGA, the relations of the DYNC1H1 expression level with patients' survival outcome was computed. Following that, in order to further appraise the upshots of the K-M survival analysis, receiver operating characteristic (ROC) curves were generated by using the pROC package [24] in R language [24].

2.4. Construction of the Predicted PPI Network. Using the DESeq2 R package [25], the samples were split into 2 expression groups in LIHC: low DYNC1H1 group (0–50%) and high DYNC1H1 group (50–100%). STRING, a well-known online biological tool for the prediction of PPI, comprises direct (physical) and indirect (functional) associations [26]. With the help of the version 11.0 of the PPI database STRING, we identified the differentially expressed genes (DEGs) involved in the PPI with the threshold values of $|\log 2\,\text{fold} - \text{change}(FC)| > 2.0$ and adjusted p value $(p.\text{adjust}) < 0.05$. In this PPI network, the required

Table 1: Basic information of the microarray datasets.

ID	Platform	Data type	Author	Update date	Country	Sample type	n (N)	n (LIHC)
GSE14520	GPL3921	mRNA	Xin Wei Wang et al.	Oct 06, 2021	USA	Human tissues	220	225
GSE63898	GPL13667	mRNA	Augusto Villanueva et al.	Apr 14, 2020	USA	Human tissues	168	228

interaction score for determining a significant interplay was medium confidence (0.400) as cut-off criteria. Second, the PPI network was visualized with Cytoscape (version 3.8.2) [27].

2.5. GO Pathway Enrichment Analysis of DEGs. GO analysis comprises a biological process (BP), cellular component (CC), and molecular function (MF). The GO enrichment analysis of DEGs in samples of LIHC was performed by the clusterProfiler [28] R package. Afterwards, we used the org.Hs.eg.db (version 3.4.0) and GOplot R (version 1.0.2) packages for analysis and visualization of the results by generating cluster plots [29].

2.6. Gene Set Enrichment Analysis. For GSEA, we chose normalized RNA-seq datasets from the TCGA data portal [30]. Herein, gene set permutations were set to 1000 with default parameters. Hallmark pathway enrichment analyses were performed to determine the possible biological function of DYNC1H1 by using GSEA. Enrichment results with 2 conditions (p.adjust < 0.05 and q-value <0.25) were considered as statistically significant.

2.7. Immune Infiltrate Analysis. TIMER is a comprehensive and publicly available resource for systemic analysis of immune infiltrates across various types of tumor (https://cistrome.shinyapps.io/timer/) [31]. We investigated the interrelation between the DYNC1H1 expression and the tumor using TIMER. The TIMER correlation module was also used to evaluate and visualize the interrelation between the gene and the tumor-infiltrating immune cell profile in LIHC. TIMER employs a previously released deconvolution statistical method to investigate associations among infiltrating immune cells and DYNC1H1 genes. We assessed the correlation between the expression of DYNC1H1 and the abundance of immune infiltrates (CD4+ T cells, dendritic cells, B cells, CD4+ T cells, B cells, neutrophils, and macrophages) in LIHC by the gene modules. The pictures of the gene against tumor purity were drawn using TIMER [32]. After that, to assess the relative gene expression, we chose a deconvolution algorithm called CIBERSORT (http://cibersort.stanford.edu/) on the basis of gene expression [33]. By evaluating the association between immune cell infiltration and DYNC1H1 expression in LIHC to uncover correlations between TIICs, we assessed the immune response of 24 TIICs by using CIBERSORT. We chose standard annotation files to build gene expression datasets by setting the default signature matrix at one thousand permutations. To determine the confidence of the deconvolution method, CIBERSORT derived a p value through Markov chain Monte Carlo (MCMC) methods. The three hundred and seventy-four tumor samples were classified into two groups to assess the significant effects of the DYNC1H1 expression on the microenvironment of the immune system. To identify the species of lymphocytes influenced by DYNC1H1, the p value < 0.05 was set up.

2.8. Comprehensive Analysis. The online database GEPIA analyzes the RNA-sequencing expression data of 8587 normal and 9736 tumor samples of 33 malignant tumors from TCGA and GTEx by using a standard processing pipeline [34]. OS with the DYNC1H1 expression in LIHC was analyzed by using GEPIA. Furthermore, a boxplot was generated to calculate the differential DYNC1H1 expression by using the tumor or normal state as a variable. Kaplan–Meier analysis of survival curve was performed using K-M survival analysis (http://kmplot.com/analysis/) to analyze interaction relationships between the DYNC1H1 expression and survival information with LIHC [35]. DYNC1H1 was fed into the database to graph K-M survival plots. The hazard ratio (HR) and the log-rank p value were calculated. Values with p value < 0.05 ($p < 0.05$) were considered to be statistically significant.

2.9. Immunohistochemistry-Based Validation of Hub Genes in THPA. THPA, a public database which includes over 5 million immunohistochemically stained tissues and cell distribution information for 26,000 human proteins, was a program supported by a grant from Sweden. THPA can examine normal and LIHC tissues via antibody proteomics, which is often used for the validation of the hub target genes' expressions. Therefore, we used this pathology tool to evaluate expression levels of DYNC1H1 between liver tissues and LIHC tissues from THPA.

2.10. Cell Culture. The human normal liver cell lines (L02) and hepatocellular carcinoma cell lines (Hep3B, HepG2, SMMC7721, and MHCC97H) were obtained from the Chinese Academy of Sciences (Shanghai, China). All cells were cultured in Dulbecco's modified eagle's medium (DMEM) containing 10% fetal bovine serum (FBS). Then after, cells were maintained in a humidified incubator containing 37°C and 5% CO_2.

2.11. Quantitative Reverse-Transcription Polymerase Chain Reaction. According to the manufacturer's instructions, the total amount of RNA was extracted from the cell lines using a TRIzol reagent (Invitrogen, Thermo Fisher Scientific, Inc.) and subjected to reverse transcription using the PrimeScript™ RT Reagent Kit (Takara, Shiga, Japan). Quantitative Reverse-Transcription Polymerase Chain Reaction (qRT-PCR) was analyzed and performed using the Applied Biosystems® 7500 Fast Real-Time PCR System (Thermo Fisher Scientific, Waltham, MA) and accompanying Applied Biosystems® 7500 Software (version 2.0.6) to measure the

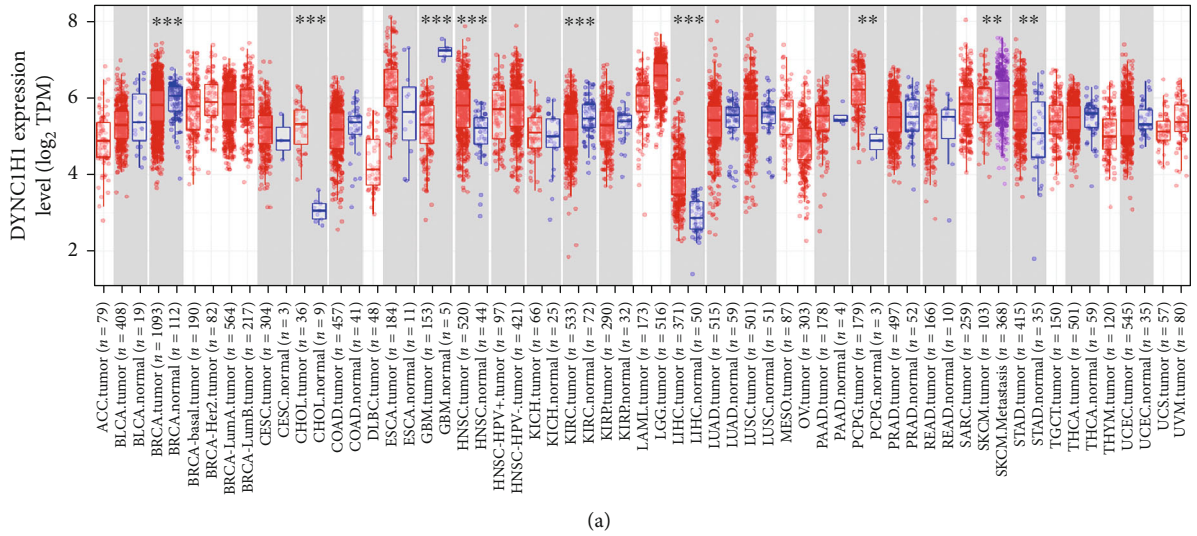

(a)

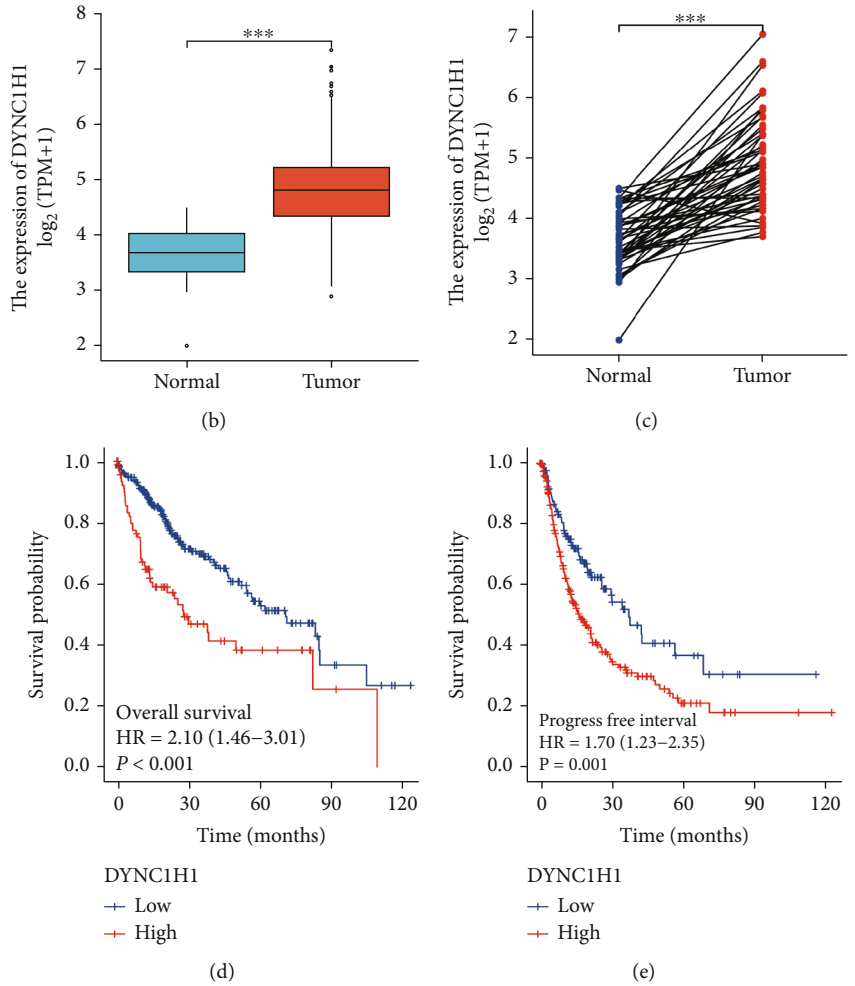

Figure 1: Continued.

Characteristics	Total (N)	HR (95% CI) multivariate analysis
Age	373	1.314 (0.809–2.132)
Gender	373	1.062 (0.637–1.773)
Histologic grade	368	1.140 (0.709–1.834)
Pathologic stage	349	0.279 (0.015–5.202)
T stage	370	9.921 (0.554–177.718)
M stage	272	2.200 (0.633–7.651)
N stage	258	3.437 (0.450–26.229)
DYNC1H1	373	1.610 (1.128–2.297)

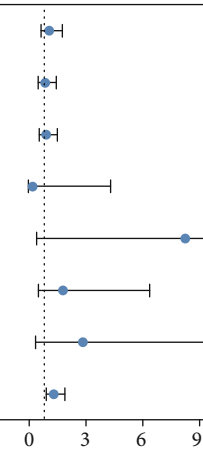

(f)

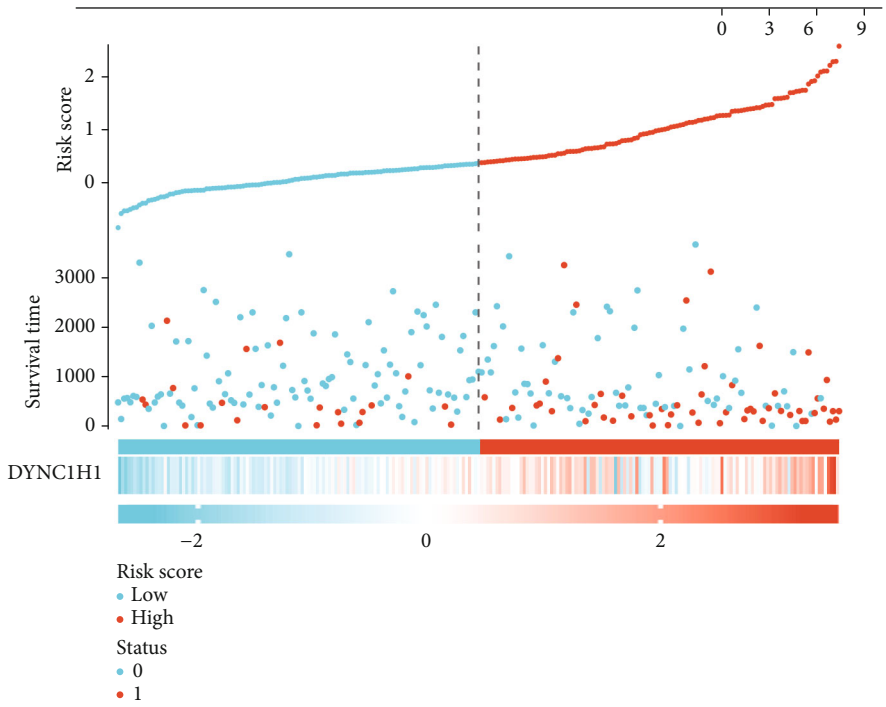

(g)

Figure 1: Continued.

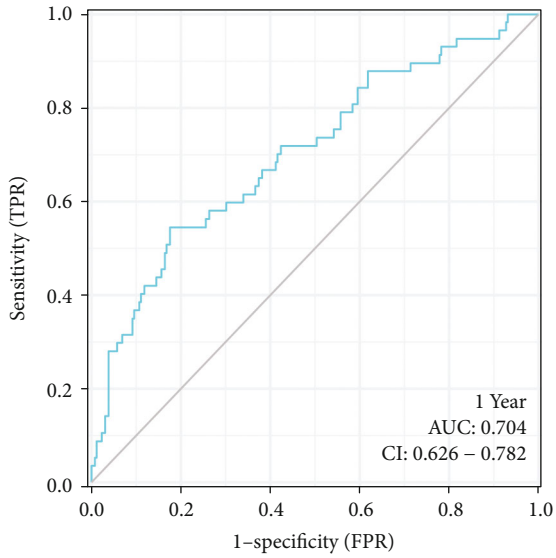

(h)

Figure 1: DYNC1H1 serves an oncogenic role in LIHC, and high DYNC1H1 expression predicts poor prognosis. (a) Human DYNC1H1 expression levels in different tumor types from TCGA database were determined by TIMER database ($^{*}p < 0.05$, $^{**}p < 0.01$, and $^{***}p < 0.001$). (b) The expression of DYNC1H1 in all LIHC samples from TCGA. (c) The expression of DYNC1H1 in paired CRC samples from TCGA. (d, e) The correlation between DYNC1H1 expression and survival status in TCGA. (f) Multivariate Cox analysis of DYNC1H1 expression and other clinicopathological variables. (g) DYNC1H1 expression distribution and survival status. (h) ROC curves of DYNC1H1.

mRNA expression levels of DYNC1H1. The following primer sequences were used: DYNC1H1 forward primer: TTGGGC ACTAGGAAATTGATGC; DYNC1H1 reverse primer: GCAGGGTTGATACGCCACA.

2.12. Statistical Analysis. All statistical analyses were conducted using R statistical software (R Core Team, version 3.6.3). The univariate and multivariate models of the Cox analysis were used to show the multivariate HR and 95% confidence intervals (95% CI). We then evaluated the DYNC1H1 expression and other clinical and pathological features affecting OS. The significance threshold was set as probability (p) value < 0.05. Logistic regression was used to evaluate the associations between the DYNC1H1 expression and clinical characteristics (T stage, pathologic stage, histologic grad, AFP, and OS event). A p value of less than 0.05 was considered to be statistically significant.

3. Results

3.1. Survival Outcomes and Variable Analysis. To confirm the expression levels of DYNC1H1 in various species of tumors, we firstly analyzed the RNA-seq data from TCGA datasets using the TIMER tools. Analysis result shows that the expression level of DYNC1H1 is upregulated in the majority of tumors involving BLCA, CESC, CHOL, COAD, ESCA, GBM, HNSC, HNSC-HPV, KICH, KIRC, KIRP, LIHC, LUAD, LUSC, PAAD, PCPG, PRAD, SKUM, STAD, THCA, and UCEC (Figure 1(a)). To further validate the expression level and prognosis role of DYNC1H1 in these tumors, we checked their expression; we again analyzed the RNA-seq datasets and characteristics of the patient from the TCGA database and discovered that DYNC1H1 was upregulated when compared to all LIHC tissues and normal liver tissues (Figure 1(b)). We acquired the same outcome in paired LIHC tissues ($N = 50$) compared with normal liver tissues (Figure 1(c)). Meanwhile, the high expression of DYNC1H1 exhibited poor survival and progression-free survival of patients with LIHC (Figures 1(d) and 1(e)). As displayed in Table 2, we performed the Cox analysis to assess the correlation between the DYNC1H1 expression and overall survival, as well as other multivariable characteristics in LIHC patients. Univariate regression analysis demonstrated that a number of factors, comprising the pathologic stage (HR = 2.504, p value < 0.001), T stage (HR = 2.598, p value < 0.001), M stage (HR = 4.077, p value = 0.017), and DYNC1H1 expression (HR = 1.709, p value < 0.001), are highly associated with overall survival. The multivariate analysis, shown with a forest diagram in Figure 1(f), uncovered that the DYNC1H1 expression (p value = 0.009) is an independent factor for a poor prognosis in patients with LIHC (Table 2). The distribution of DYNC1H1 expression, survival status of patients with LIHC, and expression profiles of DYNC1H1 are depicted in Figure 1(g). The DYNC1H1 level displayed a robust prognostic value because the ROC curve indicated that the AUC of the DYNC1H1 expression for predicting survival was 0.704 (Figure 1(h)).

3.2. Relationship between DYNC1H1 Expression and Clinicopathology. Our study appraised the association between DYNC1H1 and clinicopathological characteristics of LIHC patients. The TCGA database includes 424 LIHC tissues including gene expression data and clinical characteristics obtained from LIHC patients. LIHC with increased

Table 2: Correlation between overall survival and multivariable characteristics in TCGA patients via Cox regression and multivariate survival model.

Characteristics	Total (*N*)	Univariate analysis Hazard ratio (95% CI)	*p* value	Multivariate analysis Hazard ratio (95% CI)	*p* value
Age	373				
≤60	177	Reference			
>60	196	1.205 (0.850-1.708)	0.295	1.314 (0.809-2.132)	0.270
Gender	373				
Female	121	Reference			
Male	252	0.793 (0.557-1.130)	0.200	1.062 (0.637-1.773)	0.817
Histologic grade	368				
G1 & G2	233	Reference			
G3 & G4	135	1.091 (0.761-1.564)	0.636	1.140 (0.709-1.834)	0.589
Pathologic stage	349				
Stage I & stage II	259	Reference			
Stage III & stage IV	90	2.504 (1.727-3.631)	<0.001	0.279 (0.015-5.202)	0.392
T stage	370				
T1 & T2	277	Reference			
T3 & T4	93	2.598 (1.826-3.697)	<0.001	9.921 (0.554-177.718)	0.119
M stage	272				
M0	268	Reference			
M1	4	4.077 (1.281-12.973)	0.017	2.200 (0.633-7.651)	0.215
N stage	258				
N0	254	Reference			
N1	4	2.029 (0.497-8.281)	0.324	3.437 (0.450-26.229)	0.234
DYNC1H1	373	1.709 (1.346-2.169)	<0.001	1.610 (1.128-2.297)	0.009

DYNC1H1 expression was distinctly associated with T stage (p value < 0.05, Figure 2(a)), pathologic stage (p value < 0.01, Figure 2(b)), histologic grade (p value < 0.01, Figure 2(c)), AFP (p value < 0.01, Figure 2(d)), and OS event (p value < 0.001, Figure 2(e)). Results from this study showed that LIHC patients with high DYNC1H1 levels were more likely to present with worse T stage, worse pathologic stage, worse histologic grade, worse AFP, and worse OS event compared to those with low DYNC1H1 patients.

3.3. PPI Network Construction. In the PPI network, a total of 353 DEGs were included via the STRING database. The aim of the construction of the PPI network was to further understand the interactions of DEGs correlated with LIHC risk, including 180 nodes and 313 edges (Figure 2(f)).

3.4. GO Enrichment Analyses. In order to elucidate the mechanism of DYNC1H1 in the progression of LIHC, we performed GO enrichment analysis based on single-gene differential expression with the threshold values of $|\log 2\ FC| > 1.5$ and p.adjust value < 0.05. GO functional analyses revealed these DEGs to be involved in biological processes including detoxification of copper ion (GO:0010273), stress response to copper ion (GO:1990169), detoxification of inorganic compound (GO:0061687), and stress response to metal ion (GO:0097501). In the molecular functions, the DEGs were primarily enriched in the receptor ligand activity (GO:0048018), ligand-gated ion channel activity (GO:0015276), ligand-gated channel activity (GO:0022834), and substrate-specific channel activity (GO:0022838). The cellular components of the DEGs were significantly enriched in the intrinsic component of the synaptic membrane (GO:0099240), immunoglobulin complex (GO:0019814), postsynaptic membrane (GO:0045211), and synaptic membrane (GO:0097060) (Table 3 and Figures 2(g) and 2(h)). The biological function and molecular role of DYNC1H1 were receptor-ligand, membrane, and immunoglobulin complex.

3.5. GSEA of DYNC1H1 in LIHC. In order to elucidate the mechanism of DYNC1H1 in the progression of LIHC, we then preformed GSEA to analyze the enrichment of the Hallmark pathways in the high-expression group and the low-expression group. Based on the NES, q-value, and p .adjust, significantly enriched Hallmark pathways were selected. When using the Hallmark gene set as a reference gene set, DEGs tended to be enriched in the following Hallmark signaling pathways: Hallmark epithelial mesenchymal transition, Hallmark estrogen response early, and Hallmark UV response DN, as depicted in Table 4 and Figure 2(i).

3.6. Regulation of the Progression of LIHC through the EMT Pathway. We found that the hallmark of EMT was the top of the enriched gene signature when comparing the high-expression group and the low-expression group from TCGA

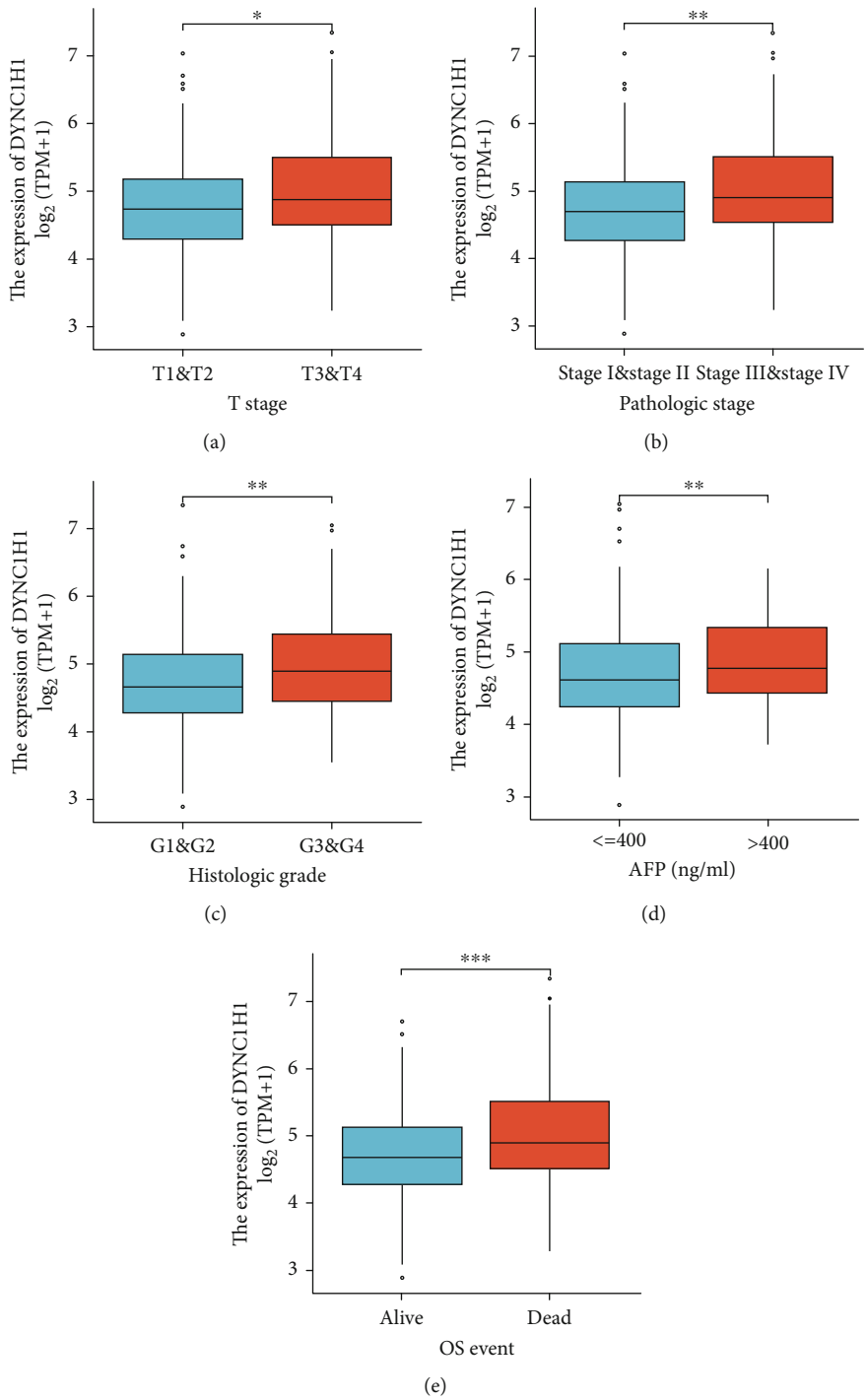

Figure 2: Continued.

(f)

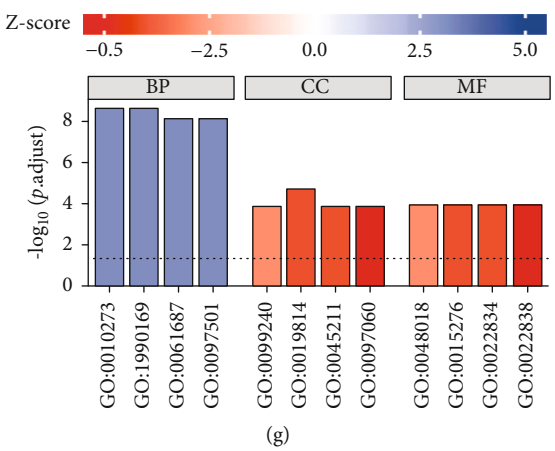

(g)

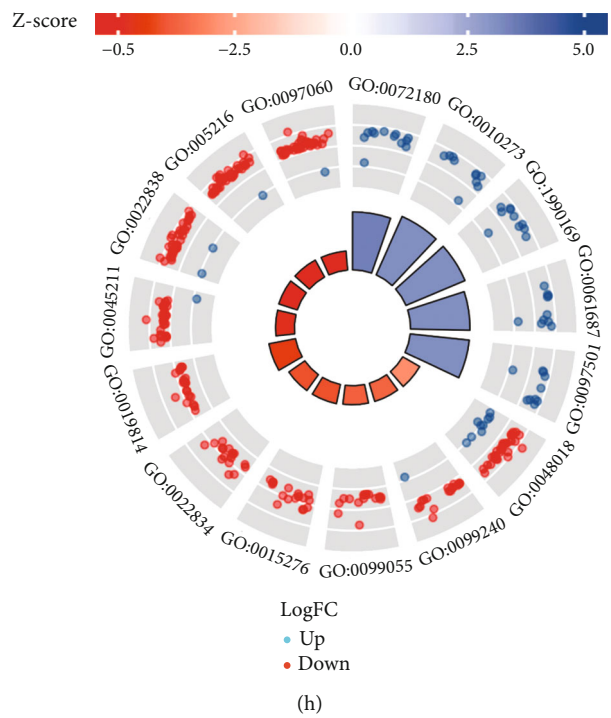

(h)

Figure 2: Continued.

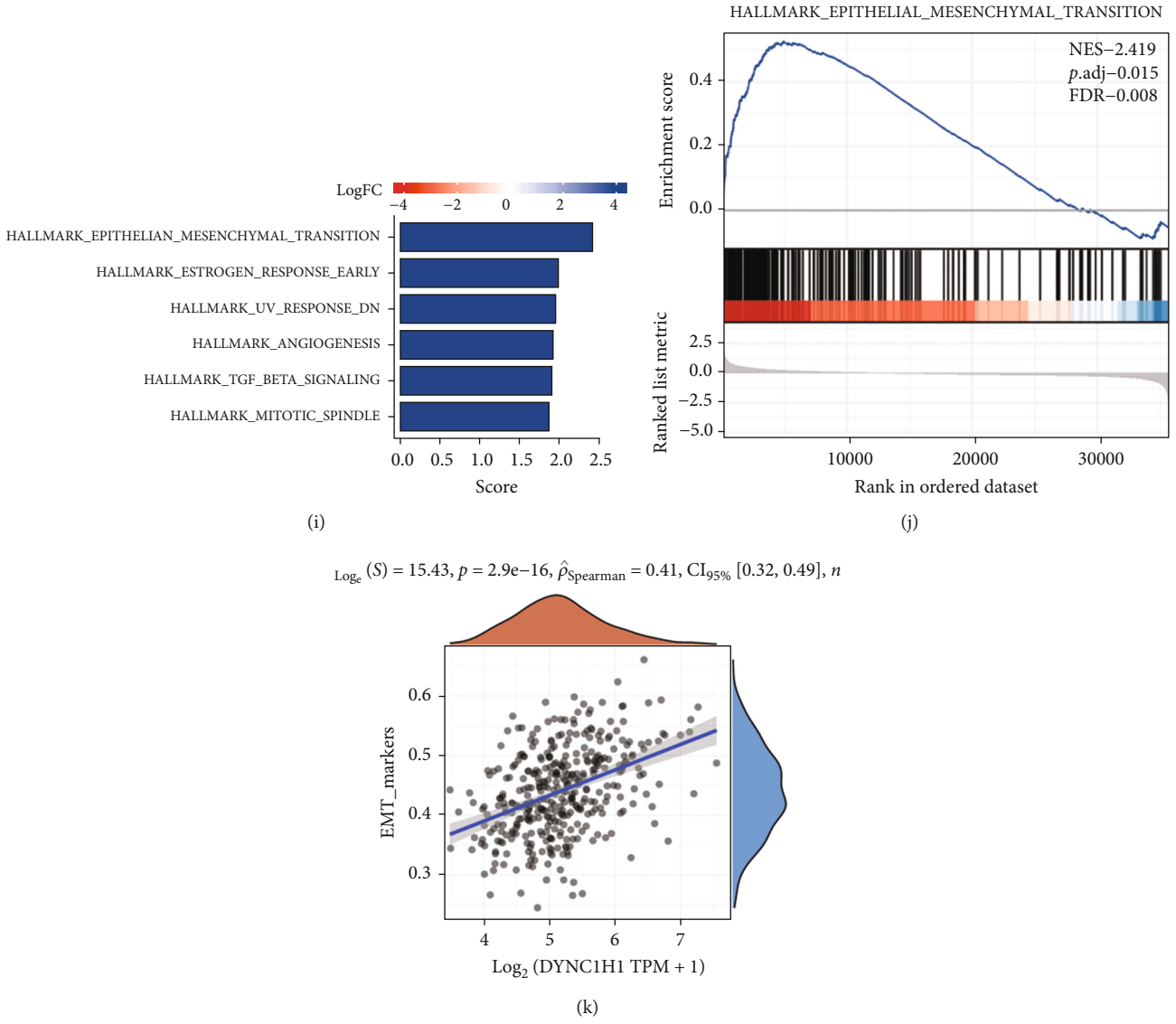

Figure 2: DYNC1H1 expression was associated with clinicopathological features of LIHC based on TCGA and GO term/GSEA pathway enrichment results. Expression of DYNC1H1 correlated significantly with T stage (a), pathologic stage (b), histologic grade (c), AFP (d), and OS event (e). (f) PPI network. (g) *Z*-score results for the top 12 GO terms, including the top 4 BPs, CCs, and MFs. (h) Enrichment results for DEGs and the top 12 GO terms. (i, j) Gene set enrichment analysis. (k) The correlations between individual gene and EMT marker score.

LIHC samples (Figure 2(j)). We next examined whether overexpression of DYNC1H1 affects EMT markers including SNAIL, SLUG, MMP9, TWIST1, and TWIST2 (Figure 2(k)). These findings suggest that DYNC1H1 might promote LIHC progression by regulating the EMT pathway.

3.7. Relationship between DYNC1H1 Expression and Tumor-Infiltrating Immune Cells. The presence of tumor-infiltrating lymphocytes (TIL) has emerged as an independent predictor of cancer sentinel lymph node status and overall survival rate (Azimi et al. 2012). We therefore chose the TIMER web tool to analyze the relationship between DYNC1H1 and the immune infiltration's level in LIHC. The results are shown in Figure 3(a). The expression levels of DYNC1H1 were positively correlated with the levels of B cells (p value = 3.51×10^{-14}), CD8+ T cell (p value = 4.82×10^{-7}), CD4+ T cell (p value = 3.91×10^{-25}), macrophage (p value = 1.30×10^{-28}), neutrophil (p value = 2.96×10^{-24}), and dendritic cell (p value = 3.88×10^{-22}). The aforesaid results showed that DYNC1H1 played a meaningful and pivotal role in immune infiltration. Furthermore, we sought to figure out whether the tumor immune microenvironment was distinct in LIHC patients with low DYNC1H1 compared to those with high DYNC1H1. According to the DYNC1H1 expression, the 424 tumor samples were classified into two groups, with 212 samples in the high expression of the DYNC1H1 group

Table 3: Functional and pathway enrichment analyses for genes.

Ontology	ID	Description	Gene ratio	Bg ratio	p value	p.adjust	q-value
BP	GO:0010273	Detoxification of copper ion	10/555	15/18670	1.31e-12	2.41e-09	2.20e-09
BP	GO:1990169	Stress response to copper ion	10/555	15/18670	1.31e-12	2.41e-09	2.20e-09
BP	GO:0061687	Detoxification of inorganic compound	10/555	17/18670	8.02e-12	7.40e-09	6.74e-09
BP	GO:0097501	Stress response to metal ion	10/555	17/18670	8.02e-12	7.40e-09	6.74e-09
MF	GO:0048018	Receptor ligand activity	36/527	482/17697	4.32e-07	1.21e-04	1.04e-04
MF	GO:0015276	Ligand-gated ion channel activity	17/527	138/17697	7.58e-07	1.21e-04	1.04e-04
MF	GO:0022834	Ligand-gated channel activity	17/527	138/17697	7.58e-07	1.21e-04	1.04e-04
MF	GO:0022838	Substrate-specific channel activity	33/527	428/17697	6.50e-07	1.21e-04	1.04e-04
CC	GO:0099240	Intrinsic component of synaptic membrane	18/583	164/19717	1.83e-06	1.42e-04	1.23e-04
CC	GO:0019814	Immunoglobulin complex	20/583	159/19717	5.18e-08	1.95e-05	1.69e-05
CC	GO:0045211	Postsynaptic membrane	27/583	323/19717	1.35e-06	1.42e-04	1.23e-04
CC	GO:0097060	Synaptic membrane	33/583	432/19717	7.14e-07	1.34e-04	1.16e-04

Table 4: Signaling pathways most significantly correlated with DYNC1H1 expression based on NES, q-value, and p.adjust.

Hallmark pathways	Enrichment score	NES	p.adjust	q-values
Hallmark_epithelial_mesenchymal_transition	0.526697402	2.419142251	0.014927601	0.008485163
Hallmark_estrogen_response_early	0.432011711	1.988225556	0.014927601	0.008485163
Hallmark_UV_response_DN	0.443524891	1.954904884	0.014927601	0.008485163
Hallmark_angiogenesis	0.569576131	1.917856809	0.014927601	0.008485163
Hallmark_TGF_beta_signaling	0.521478423	1.906591073	0.01937609	0.011013777
Hallmark_mitotic_spindle	0.407384283	1.874883995	0.014927601	0.008485163

and 212 samples in the low-expression group. In order to further explore the mechanisms of immune response and the proportion of 24 immune cell populations in downloaded samples, we used the computational deconvolution method as implemented in CIBERSORT. Using the CIBERSORT algorithm, the difference between high and low DYNC1H1 expression groups in 24 immune cells was analyzed (Figure 3(b)). Plasmacytoid dendritic cell (pDC), CD56bright NK cells, macrophages, immature dendritic cells (iDC), eosinophils, dendritic cells (DC), cytotoxic cells, activated dendritic cells (aDC), T helper cells, central memory T cell (Tcm), effector memory T cell (Tem), T follicular helper cells (TFH), helper T type 1 (Th1) cells, and helper T type 2 (Th2) cells were influenced by DYNC1H1 levels, with notable variation existing in the dendritic cell and T cell lines between the high and low DYNC1H1 groups. Th2 cells, TFH, T helper cells, aDC, macrophages, and CD56bright NK cells were increased compared to the group with the low DYNC1H1 expression (p value < 0.001). Meanwhile, pDC, DC, and cytotoxic cells were decreased in the group with a high DYNC1H1 expression (p value < 0.001). In addition, we further examined possible correlations between 24 types of immune cells (Figure 3(c)). Moderate to strong correlations existed between different subpopulations of TIICs as per the heat map.

3.8. Data Validation. We first analyzed the mRNA expression of DYNC1H1 by using the GEPIA database. The DYNC1H1 level was increased in the LIHC group when compared to the normal control (Figure 4(a)). A significant interrelation was revealed between the high DYNC1H1 level and the poor OS for LIHC (p value = 3×10^{-4}, Figure 4(b)). We further verified this finding by performing K-M survival plots. K-M survival plots showed that the high DYNC1H1 expression group was markedly correlated with poor overall survival rates (p value = 0.0049, Figure 4(c)). In addition, representative immunohistochemistry (IHC) images indicated that DYNC1H1 has higher expression levels compared to nontumor tissues from the THPA (Figure 4(d)).

3.9. DYNC1H1 Possesses a Higher Specificity than AFP for LIHC Diagnosis. Eventually, in order to evaluate the diagnostic value of DYNC1H1, GSE14520 and GSE63898 datasets were analyzed by using ROC analysis. As we know, alpha-fetoprotein (AFP) is a kind of diagnostic tumor marker that is commonly associated with LIHC. In GSE14520, the expression level of DYNC1H1 was significantly higher than that of the nontumor tissue (Figure 5(a)), and its AUC of 0.866 was higher than the AUC value of 0.685 for AFP (Figure 5(b)). In GSE63898, the expression level of DYNC1H1 was significantly higher than that of the nontumor tissue (Figure 5(c)), and its AUC of 0.796 was higher than the AUC value of 0.566 for AFP (Figure 5(d)). In Figure 5(e), the expression of DYNC1H1 was further validated by qRT-PCR in multiple cell lines.

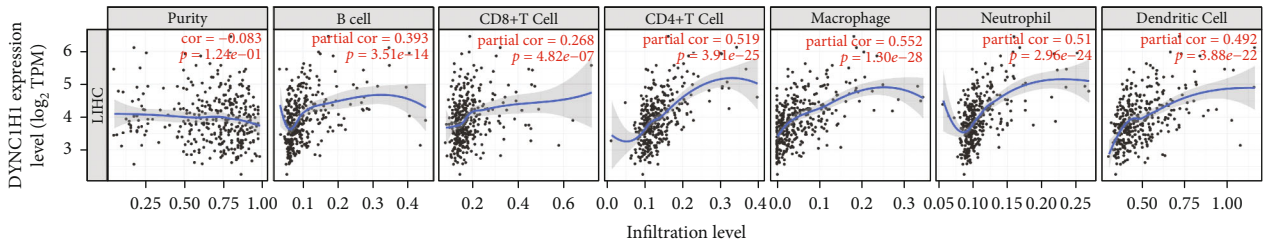

(a)

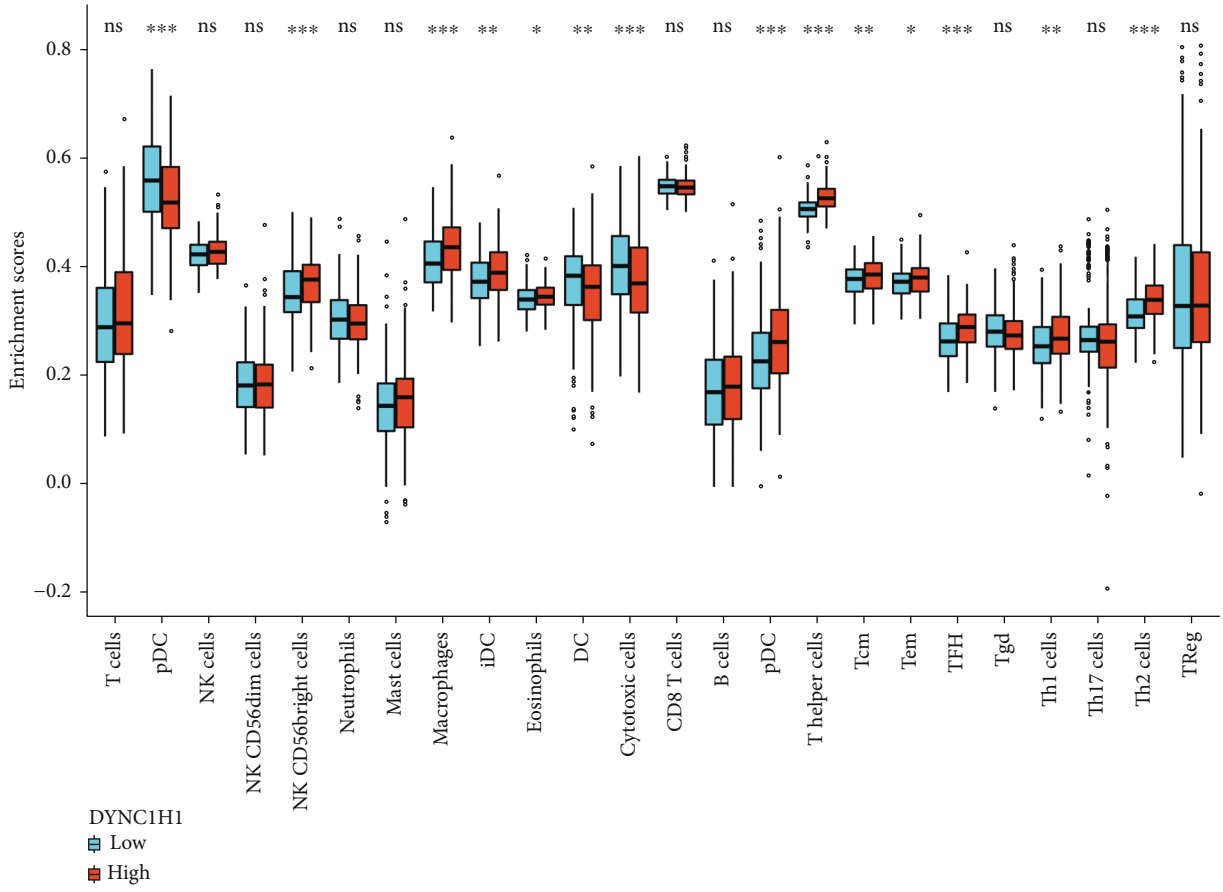

(b)

Figure 3: Continued.

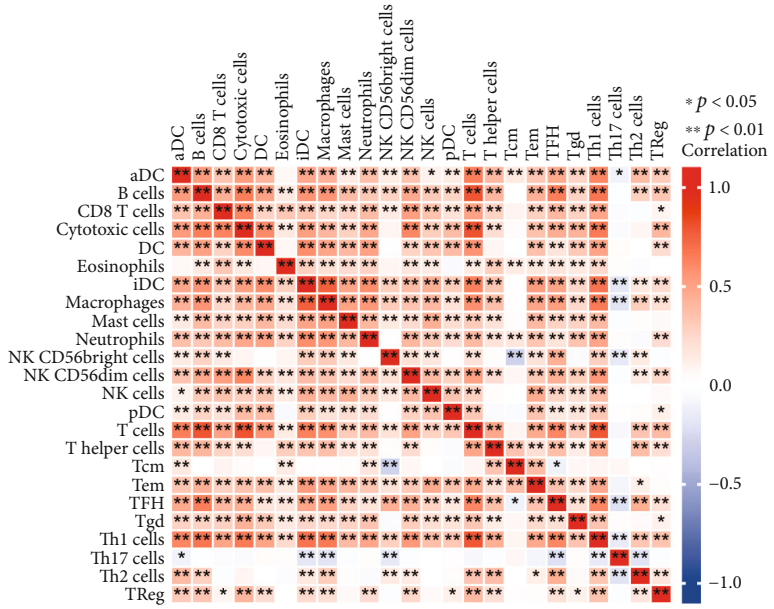

(c)

Figure 3: Correlations between DYNC1H1 expression and immune infiltration levels in LIHC by TIMER. (a) Correlations between DYNC1H1 expression and immune infiltration levels. (b) The varied proportions of 24 subtypes of immune cells in high and low DYNC1H1 expression groups in tumor samples. (c) Heat map of 24 immune infiltration cells in tumor samples.

4. Discussion

LIHC is the 3rd leading reason of cancer death and one of the five most frequently diagnosed cancer types [36]. During the past 20 years, LIHC's prevalence had been increasing persistently [37]. Cancer progression and metastasis have been implicated in a range of steps, including cell survival and proliferation, cell adhesion and migration, cell adhesion, and cell metabolism [38]. A number of previous biomarker studies have provided information on LIHC. Microtubule-associated serine and threonine kinase 2 (MAST2) was initially identified as a microtubule-associated protein. Recently, MAST2 is found to be a biomarker of diagnosis and prognosis of LIHC. The high expression level of MAST2 was correlated with advanced clinical status, for example, histological type, histologic grade, T classification, N classification, survival status, and poor prognosis of patients [39].

We assessed DYNC1H1 as a prognostic biomarker for LIHC in our current research. We evaluated the prognostic value of DYNC1H1 in patients with LIHC by analyzing the RNA-seq data from the TCGA database. Through DYNC1H1 analysis, and its interrelation to multiple tumor characteristics and immune cell responses, high DYNC1H1 expression served as an independent prognostic factor for poor OS. Furthermore, high DYNC1H1 expression levels were remarkably associated with T classification, pathologic stage, histologic grade, and serum AFP levels. Collectively, these results indicated that the DYNC1H1 expression level might influence LIHC initiation, progression, and immune microenvironment.

Subsequently, GO pathway analyses were performed. GO functional analyses revealed DYNC1H1 to be involved in biological processes including detoxification of copper ion, stress response to copper ion, detoxification of inorganic compound, and stress response to metal ion. The detoxification of inorganic compound like selenium plays a major role in tumor cell survival [40]. In parallel, these findings also indicate a close relationship between metal ions and immunity to cancer. This finding was in agreement with prior studies. Metal ion-activated immunotherapy is considered as an effective and potential approach in tumor therapy [41]. In the molecular functions, the DYNC1H1 was primarily enriched in receptor ligand activity, ligand-gated ion channel activity, ligand-gated channel activity, and substrate-specific channel activity. The family of ligand-gated channels warrants further investigation in tumor therapy [42–44]. The cellular components of the DYNC1H1 were significantly enriched in the intrinsic component of the synaptic membrane, immunoglobulin complex, postsynaptic membrane, and synaptic membrane. The synaptic membrane is complexed with tubulin which is essential for tumor cell migration [45].

GSEA was used as a method for determining pathway enrichment and functional module enrichment in the DEGs. Based on GSEA enrichment, we found that DYNC1H1 was involved in the EMT pathway and was positively correlated with EMT markers. Thus, it demonstrated that DYNC1H1 drove the EMT phenotype and regulated the EMT program in LIHC. This agreed with reality and was consistent with the importance of the EMT in HCC invasion and metastasis [46]. Additionally, the Hallmark results showed an enrichment in estrogen response early. In the literature, it is also suggested that antiestrogens or reduced estrogen levels may be linked to liver cancer [47].

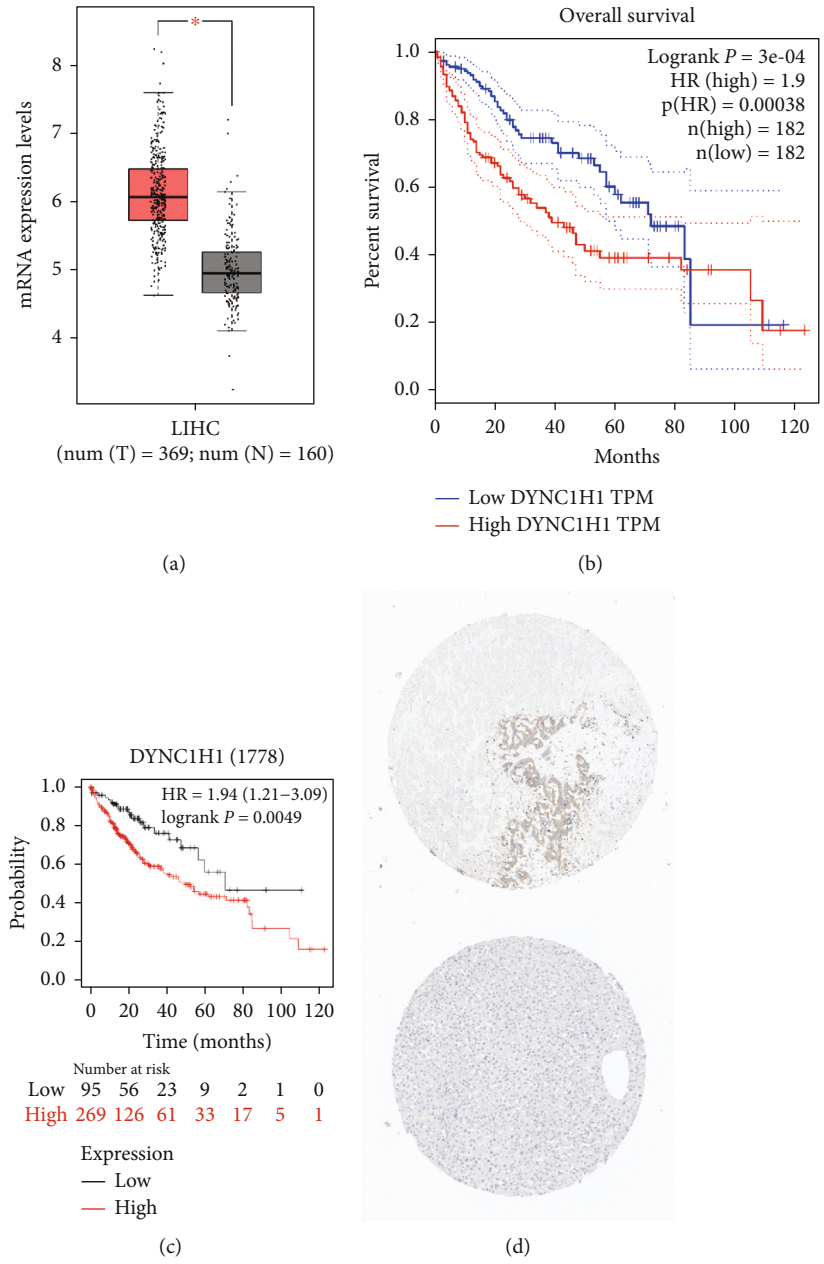

Figure 4: The synthesized analysis of DYNC1H1 mRNA expression and prognosis in patients with LIHC. (a) DYNC1H1 mRNA expression levels in normal and LIHC tissues, as obtained from GEPIA. (b) Levels of DYNC1H1 mRNA expression and overall survival based on data obtained from GEPIA. (c) Further validation of the correlation between DYNC1H1 expression and overall survival, as shown in K-M survival plot. (d) Hepatic expression of DYNC1H1 protein was visualized using immunohistochemistry via THPA.

In the present study, by using the TIMER database, we studied the connection between the DYNC1H1expression and the immune cell infiltration level in LIHC. It was found that DYNC1H1 was positively related with B cells, CD8+ T cells, CD4+ T cells, macrophages, neutrophils, and dendritic cells. Using the CIBERSORT algorithm, we confirmed that the high DYNC1H1 expression was related with the upregulation of Th2 cells, TFH, T helper cells, aDC, macrophages, and CD56bright NK cells and the downregulation of pDC, DC, and cytotoxic cells. DC serves as one of the functionally specialized antigen-presenting cells to play essential roles in initiating specific T cell responses for innate antitumor immunity [48]. It also regulated humoral immune responses to inhibit tumor development [49]. Therefore, we hypothesized that the function of DC could be suppressed by the overexpression of DYNC1H1. Summing up, these studies demonstrate that DYNC1H1 plays a critical role in modulating the immune responses of LIHC. However, randomized controlled trials (RCTs); multicenter randomized, controlled clinical trials, and mechanism researches are required for a more accurate understanding of the correlation between DYNC1H1 and LIHC in vitro and in vivo [50–52].

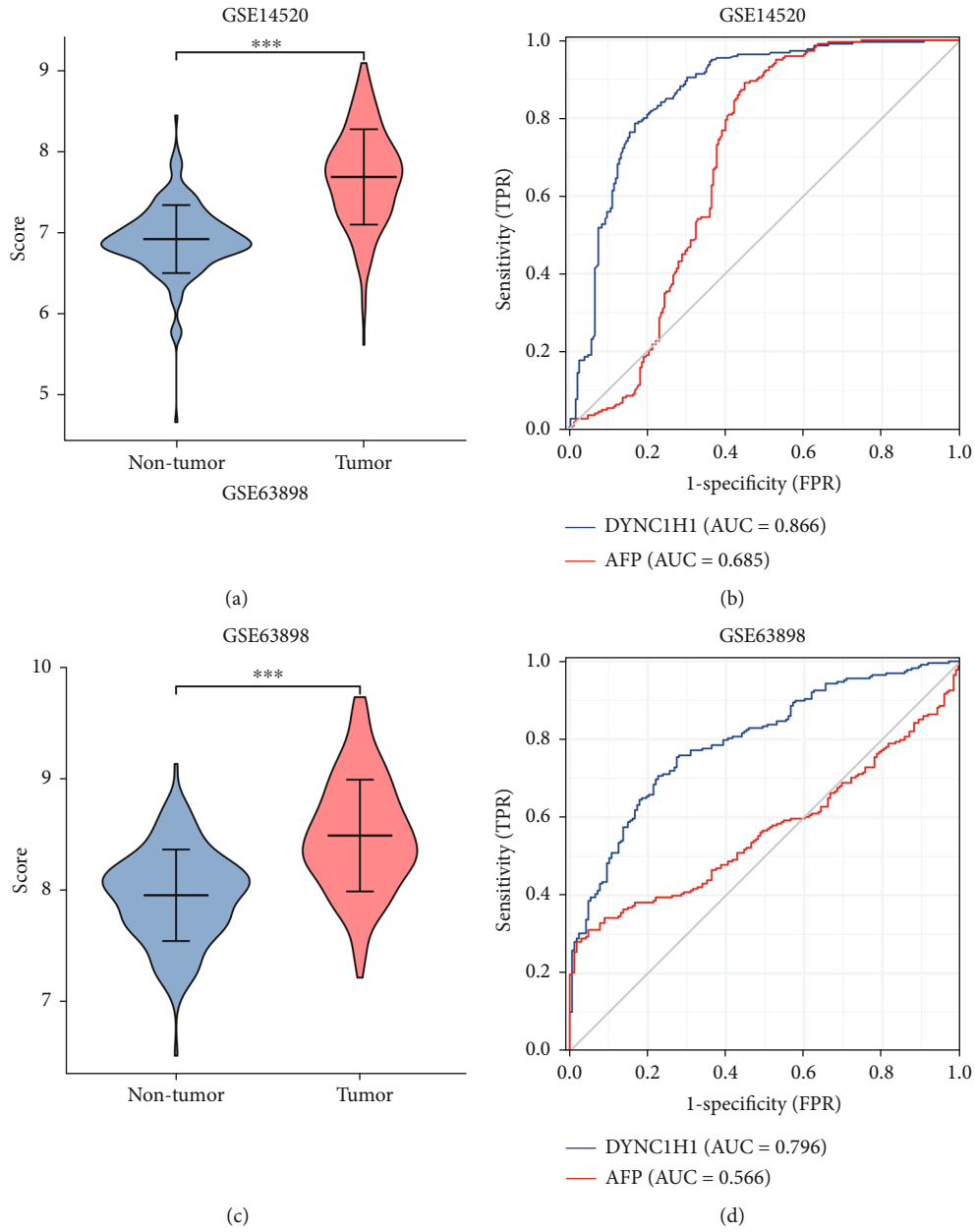

Figure 5: Continued.

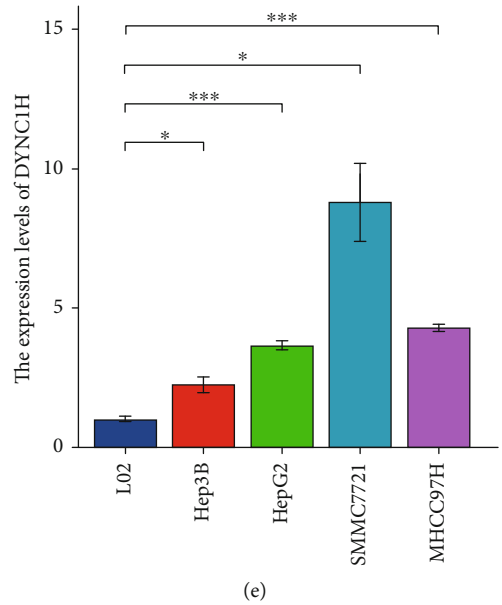

Figure 5: DYNC1H1 shows a higher positive predictive value than AFP in LIHC patients. (a) The violin plot shows DYNC1H1 mRNA levels in patients with nontumor ($n = 220$) and LIHC ($n = 225$) from the GSE14520 dataset. (b) ROC curve analysis shows the diagnostic value of DYNC1H1and AFP in nontumor and LIHC patients from the GSE14520 dataset. (c) The violin plot shows DYNC1H1 mRNA levels in patients with nontumor ($n = 168$) and LIHC ($n = 228$) from the GSE63898 dataset. (d) ROC curve analysis shows the diagnostic value of DYNC1H1 and AFP in nontumor and HCC patients from the GSE63898 dataset. (e) DYNC1H1 expression level in LIHC by using qRT-PCR.

Finally, our results are validated by GEO datasets, its ROC curve analysis, and qRT-PCR. They demonstrated that the expression level of DYNC1H1 was significantly higher than nontumor tissue and its AUC was higher than the AUC value of AFP which was the mainstream biomarker for LIHC in 2 datasets. Altogether, these results showed that DYNC1H1 was expected to be the positive predictive tumor marker for patients with LIHC.

There are still several drawbacks to our research. The first point concerns data sources which come from public databases. In the future, we need to collect as many serum samples as possible from patients with LIHC, in order to validate this biomarkers. This brings us to the second point. Because the usefulness of biomarkers is mechanism dependent, we require more experimental validation and mechanistic elucidation in cell lines and animal models.

5. Conclusion

To sum up, DYNC1H1 associated with LIHC was identified using bioinformatic analysis. DYNC1H1 is a novel prognostic biomarker and has correlation with EMT and immune infiltrates in LIHC. With further study in the future, DYNC1H1 will provide novel and important perspectives for the mechanisms of LIHC. This gene will be able to act as an efficacious tool for the early diagnosis and effective intervention of LIHC.

Data Availability

The gene expression profiling data supporting this study are from previously reported studies and datasets, which have been cited. The expression and survival data are derived from TCGA and GEO databases. TCGA and GEO belong to public databases. The patients involved in the database have obtained ethical approval. Users can download relevant data for free for research and publish relevant articles. The qRT-PCR data used to support the findings of this study have not been made available.

Conflicts of Interest

The authors declare that they have no conflicts of interest.

Authors' Contributions

Yanhong Wang and Jiyu Han contributed to the work equally and should be regarded as co-first authors. Songtao Ai and Daqian Wan contributed to the work equally and should be regarded as corresponding authors.

Acknowledgments

This study was supported by the Fundamental Research Funds for the Central Universities (grant 22120210569); the National Scientific Foundation of China (82171993); the Clinical Research Plan of SHDC (SHDC2020CR3083B); the Technology Project of the Shanghai Science and Technology Commission (19441902700); the Clinical Research Program of the Shanghai 9th People's Hospital, School of Medicine, Shanghai Jiao Tong University (JYLJ202122); and the Project of Biobank from Shanghai 9th People's Hospital, School of Medicine, Shanghai Jiao Tong University (YBKB202116).

References

[1] M. Maluccio and A. Covey, "Recent progress in understanding, diagnosing, and treating hepatocellular carcinoma," *CA: a Cancer Journal for Clinicians*, vol. 62, no. 6, pp. 394–399, 2012.

[2] R. Qiang, Z. Zhao, L. Tang, Q. Wang, Y. Wang, and Q. Huang, "Identification of 5 hub genes related to the early diagnosis, tumour stage, and poor outcomes of hepatitis B virus-related hepatocellular carcinoma by bioinformatics analysis," *Computational and Mathematical Methods in Medicine*, vol. 2021, Article ID 9991255, 20 pages, 2021.

[3] Y. Lee, H. Moon, J. Lee et al., "Association of metabolic risk factors with risks of cancer and all-cause mortality in patients with chronic hepatitis B," *Hepatology (Baltimore, Md)*, vol. 73, no. 6, pp. 2266–2277, 2021.

[4] B. McMahon, S. Nolen, M. Snowball et al., "HBV genotype: a significant risk factor in determining which patients with chronic HBV infection should undergo surveillance for HCC: the hepatitis B Alaska study," *Hepatology (Baltimore, Md)*, vol. 74, no. 6, pp. 2965–2973, 2021.

[5] D. Huang, H. El-Serag, and R. Loomba, "Global epidemiology of NAFLD-related HCC: trends, predictions, risk factors and prevention," *Nature Reviews Gastroenterology & Hepatology*, vol. 18, no. 4, pp. 223–238, 2021.

[6] W. Gan, J. Huang, M. Zhang et al., "New nomogram predicts the recurrence of hepatocellular carcinoma in patients with negative preoperative serum AFP subjected to curative resection," *Journal of Surgical Oncology*, vol. 117, no. 7, pp. 1540–1547, 2018.

[7] R. Harders, T. Morthorst, A. Lande et al., "Dynein links engulfment and execution of apoptosis via CED-4/Apaf1 in C. *elegans*," *Cell Death & Disease*, vol. 9, no. 10, p. 1012, 2018.

[8] Y. Wang, Q. Wang, X. Li et al., "Paeoniflorin sensitizes breast cancer cells to tamoxifen by downregulating microRNA-15b via the FOXO1/CCND1/β-catenin axis," *Drug Design, Development and Therapy*, vol. 15, pp. 245–257, 2021.

[9] Y. Wang, G. Luo, M. Shen et al., "The effect of meditative movement on the quality of life in patients recovering from COVID-19: a protocol for systematic review and meta-analysis," *Medicine*, vol. 99, no. 47, article e23225, 2020.

[10] G. Schiavo, L. Greensmith, M. Hafezparast, and E. Fisher, "Cytoplasmic dynein heavy chain: the servant of many masters," *Trends in Neurosciences*, vol. 36, no. 11, pp. 641–651, 2013.

[11] J. Bai, B. Yang, R. Shi et al., "Could microtubule inhibitors be the best choice of therapy in gastric cancer with high immune activity: mutant DYNC1H1 as a biomarker," *Aging*, vol. 12, no. 24, pp. 25101–25119, 2020.

[12] K. Bhat and V. Setaluri, "Microtubule-associated proteins as targets in cancer chemotherapy," *Clinical cancer research : an official journal of the American Association for Cancer Research*, vol. 13, no. 10, pp. 2849–2854, 2007.

[13] H. Tan and S. Tan, "The focal adhesion protein kindlin-2 controls mitotic spindle assembly by inhibiting histone deacetylase 6 and maintaining α-tubulin acetylation," *The Journal of Biological Chemistry*, vol. 295, no. 18, pp. 5928–5943, 2020.

[14] W. Xie, Y. Yang, S. Gao et al., "The tumor suppressor CYLD controls epithelial morphogenesis and homeostasis by regulating mitotic spindle behavior and adherens junction assembly," *Journal of Genetics and Genomics*, vol. 44, no. 7, pp. 343–353, 2017.

[15] H. Pan, W. Chai, X. Liu, T. Yu, L. Sun, and M. Yan, "DYNC1H1 regulates NSCLC cell growth and metastasis by IFN-γ-JAK-STAT signaling and is associated with an aberrant immune response," *Experimental Cell Research*, vol. 409, no. 1, article 112897, 2021.

[16] L. Wang, Z. Zhang, Y. Li, Y. Wan, and B. Xing, "Integrated bioinformatic analysis of RNA binding proteins in hepatocellular carcinoma," *Aging*, vol. 13, no. 2, pp. 2480–2505, 2020.

[17] Z. Wang, Z. Zhu, H. Wang et al., "Downregulation of circDYNC1H1 exhibits inhibitor effect on cell proliferation and migration in hepatocellular carcinoma through miR-140-5p," *Journal of Cellular Physiology*, vol. 234, no. 10, pp. 17775–17785, 2019.

[18] Z. Wang, M. Jensen, and J. Zenklusen, "A practical guide to The Cancer Genome Atlas (TCGA)," *Methods in molecular biology (Clifton, NJ)*, vol. 1418, pp. 111–141, 2016.

[19] D. Haussler, "The Cancer Genome Atlas," *Science*, vol. 320, p. 1958, 2013.

[20] S. Roessler, H. Jia, A. Budhu et al., "A unique metastasis gene signature enables prediction of tumor relapse in early-stage hepatocellular carcinoma patients," *Cancer Research*, vol. 70, no. 24, pp. 10202–10212, 2010.

[21] A. Villanueva, A. Portela, S. Sayols et al., "DNA methylation-based prognosis and epidrivers in hepatocellular carcinoma," *Hepatology (Baltimore, Md)*, vol. 61, no. 6, pp. 1945–1956, 2015.

[22] H. Woo, J. Choi, S. Yoon et al., "Integrative analysis of genomic and epigenomic regulation of the transcriptome in liver cancer," *Nature Communications*, vol. 8, no. 1, p. 839, 2017.

[23] J. L. V. Maag, "gganatogram: an R package for modular visualisation of anatograms and tissues based on ggplot2," *F1000Research*, vol. 7, p. 1576, 2018.

[24] X. Robin, N. Turck, A. Hainard et al., "pROC: an open-source package for R and S+ to analyze and compare ROC curves," *BMC Bioinformatics*, vol. 12, no. 1, p. 77, 2011.

[25] M. Love, W. Huber, and S. Anders, "Moderated estimation of fold change and dispersion for RNA-seq data with DESeq2," *Genome Biology*, vol. 15, no. 12, p. 550, 2014.

[26] D. Szklarczyk, A. Gable, K. Nastou et al., "The STRING database in 2021: customizable protein-protein networks, and functional characterization of user-uploaded gene/measurement sets," *Nucleic Acids Research*, vol. 49, no. D1, pp. D605–D612, 2021.

[27] P. Shannon, A. Markiel, O. Ozier et al., "Cytoscape: a software environment for integrated models of biomolecular interaction networks," *Genome Research*, vol. 13, no. 11, pp. 2498–2504, 2003.

[28] G. Yu, L. G. Wang, Y. Han, and Q. Y. He, "clusterProfiler: an R package for comparing biological themes among gene clusters," *Omics-a Journal of Integrative Biology*, vol. 16, no. 5, pp. 284–287, 2012.

[29] W. Walter, F. Sánchez-Cabo, and M. Ricote, "GOplot: an R package for visually combining expression data with functional analysis," *Bioinformatics*, vol. 31, no. 17, pp. 2912–2914, 2015.

[30] A. Subramanian, P. Tamayo, V. Mootha et al., "Gene set enrichment analysis: a knowledge-based approach for interpreting genome-wide expression profiles," *Proceedings of the National Academy of Sciences of the United States of America*, vol. 102, no. 43, pp. 15545–15550, 2005.

[31] T. Li, J. Fan, B. Wang et al., "TIMER: a web server for comprehensive analysis of tumor-infiltrating immune cells," *Cancer Research*, vol. 77, no. 21, pp. e108–e110, 2017.

[32] D. Aran, M. Sirota, and A. Butte, "Systematic pan-cancer analysis of tumour purity," *Nature Communications*, vol. 6, no. 1, p. 8971, 2015.

[33] A. M. Newman, C. L. Liu, M. R. Green et al., "Robust enumeration of cell subsets from tissue expression profiles," *Nature Methods*, vol. 12, no. 5, pp. 453–457, 2015.

[34] Z. Tang, C. Li, B. Kang, G. Gao, C. Li, and Z. Zhang, "GEPIA: a web server for cancer and normal gene expression profiling and interactive analyses," *Nucleic Acids Research*, vol. 45, no. W1, pp. W98–W102, 2017.

[35] M. Uhlén, L. Fagerberg, B. M. Hallström et al., "Charting the human proteome: understanding disease using a tissue-based atlas," *Science (New York)*, vol. 347, no. 6227, p. 1274, 2015.

[36] L. An, H. Zeng, R. Zheng et al., "Liver cancer epidemiology in China, 2015," *Zhonghua zhong liu za zhi [Chinese journal of oncology]*, vol. 41, no. 10, pp. 721–727, 2019.

[37] C. Frenette, "Advances in hepatocellular carcinoma," *Clinics in Liver Disease*, vol. 24, no. 4, p. xiii-xiv, 2020.

[38] Z. Gu, H. Wang, J. Xia et al., "Decreased ferroportin promotes myeloma cell growth and osteoclast differentiation," *Cancer Research*, vol. 75, no. 11, pp. 2211–2221, 2015.

[39] Y. Jiao, Y. Li, P. Jiang, Z. Fu, and Y. Liu, "High MAST2 mRNA expression and its role in diagnosis and prognosis of liver cancer," *Scientific Reports*, vol. 9, no. 1, article 19865, 2019.

[40] A. Carlisle, N. Lee, A. Matthew-Onabanjo et al., "Selenium detoxification is required for cancer-cell survival," *Nature Metabolism*, vol. 2, no. 7, pp. 603–611, 2020.

[41] C. Wang, R. Zhang, X. Wei, M. Lv, and Z. Jiang, "Metalloimmunology: the metal ion-controlled immunity," *Advances in Immunology*, vol. 145, pp. 187–241, 2020.

[42] N. Sayyadi, I. Justiniano, R. Connally et al., "Sensitive time-gated immunoluminescence detection of prostate cancer cells using a TEGylated europium ligand," *Analytical Chemistry*, vol. 88, no. 19, pp. 9564–9571, 2016.

[43] J. Xia, N. Huang, H. Huang et al., "Voltage-gated sodium channel Nav1.7 promotes gastric cancer progression through MACC1-mediated upregulation of NHE1," *International Journal of Cancer*, vol. 139, no. 11, pp. 2553–2569, 2016.

[44] Y. Wu, Z. Xu, W. Sun et al., "Co-responsive smart cyclodextrin-gated mesoporous silica nanoparticles with ligand-receptor engagement for anti-cancer treatment," *Materials science & engineering C, Materials for biological applications*, vol. 103, article 109831, 2019.

[45] K. Yan, E. Greene, F. Belga, and M. Rasenick, "Synaptic membrane G proteins are complexed with tubulin in situ," *Journal of Neurochemistry*, vol. 66, no. 4, pp. 1489–1495, 1996.

[46] B. Tang, G. Qi, F. Tang et al., "JARID1B promotes metastasis and epithelial-mesenchymal transition via PTEN/AKT signaling in hepatocellular carcinoma cells," *Oncotarget*, vol. 6, no. 14, pp. 12723–12739, 2015.

[47] M. Shen, J. Cao, and H. Shi, "Effects of estrogen and estrogen receptors on transcriptomes of HepG2 cells: a preliminary study using RNA sequencing," *International Journal of Endocrinology*, vol. 2018, Article ID 5789127, 16 pages, 2018.

[48] S. Zhu, N. Yang, J. Wu et al., "Tumor microenvironment-related dendritic cell deficiency: a target to enhance tumor immunotherapy," *Pharmacological Research*, vol. 159, article 104980, 2020.

[49] I. Lurje, L. Hammerich, and F. Tacke, "Dendritic cell and T cell crosstalk in liver fibrogenesis and hepatocarcinogenesis: implications for prevention and therapy of liver cancer," *International journal of molecular sciences*, vol. 21, no. 19, p. 7378, 2020.

[50] Y. Su, D. Wan, and W. Song, "Dryofragin inhibits the migration and invasion of human osteosarcoma U2OS cells by suppressing MMP-2/9 and elevating TIMP-1/2 through PI3K/AKT and p38 MAPK signaling pathways," *Anti-Cancer Drugs*, vol. 27, no. 7, pp. 660–668, 2016.

[51] D. Wan, C. Jiang, X. Hua, T. Wang, and Y. Chai, "Cell cycle arrest and apoptosis induced by aspidin PB through the p53/p21 and mitochondria-dependent pathways in human osteosarcoma cells," *Anti-Cancer Drugs*, vol. 26, no. 9, pp. 931–941, 2015.

[52] Y. Wang, D. Wan, R. Zhou, W. Zhong, S. Lu, and Y. Chai, "Geraniin inhibits migration and invasion of human osteosarcoma cancer cells through regulation of PI3K/Akt and ERK1/2 signaling pathways," *Anti-Cancer Drugs*, vol. 28, no. 9, pp. 959–966, 2017.

Hindawi
Disease Markers
Volume 2022, Article ID 3881310, 16 pages
https://doi.org/10.1155/2022/3881310

Research Article

lncRNA LEF1-AS1 Acts as a Novel Biomarker and Promotes Hypopharyngeal Squamous Cell Carcinoma Progression and Metastasis by Targeting the miR-221-5p/GJA1 Axis

Junda Fan,[1,2] Cheng Wang,[3] Xingyou Zhai,[2] Jianhui Li,[2] Jun Ju,[2] Yuying Zhu,[4] Shikang Zheng,[4] Nan Ren,[1] Bangqing Huang,[2] Xinying Jiang,[2] Yingli Xie,[1] Kai Zhao,[2] and Mingbo Liu[2,5]

[1]*Medical School of Chinese PLA, Beijing, China*
[2]*Department of Otolaryngology Head and Neck Surgery, Hainan Hospital of Chinese PLA General Hospital, Sanya, China*
[3]*School of Basic Medical Sciences, Weifang Medical University, Weifang, China*
[4]*School of Clinical Medicine, Weifang Medical University, Weifang, China*
[5]*The Second School of Clinical Medicine, Southern Medical University, Guangzhou, China*

Correspondence should be addressed to Kai Zhao; blue72ice@163.com and Mingbo Liu; mingbo666@vip.163.com

Received 4 February 2022; Accepted 8 March 2022; Published 25 March 2022

Academic Editor: Zhen-Jian Zhuo

Hypopharyngeal squamous cell carcinoma (HSCC) is highly malignant and extremely aggressive, making it one of the worst prognoses among all kinds of head and neck squamous cell carcinoma (HNSCC); therefore, gaining insight into molecular mechanisms of HSCC is of profound significance. In the current manuscript, we revealed the elevated expression of long noncoding RNA (lncRNA) LEF1-AS1 in HNSCC which was associated with the poor prognosis by bioinformatic analysis. Moreover, we noticed that LEF1-AS1 dramatically accelerated the proliferation, migration, invasion, and epithelial-mesenchymal transition (EMT) process in HSCC cell line FaDu. Most importantly, we illustrated that LEF1-AS1 played as a competitive endogenous RNA (ceRNA) via sponging miR-221-5p and thereby positively regulated gap junction protein alpha 1 (GJA1) expression, thus aggravated tumor progression and EMT. In conclusion, for the first time, we demonstrated lncRNA LEF1-AS1 as a novel biomarker for HNSCC and suggested LEF1-AS1/miR-221-5p/GJA1 axis as promising diagnostic and therapeutic target for HSCC treatment.

1. Introduction

Although only accounts for ~3–5% of all kinds of HNSCC, hypopharyngeal squamous cell carcinoma (HSCC) is one of the most lethal malignancies due to the grievous mortality (5 years overall survival rate less than 30% in late-stage patients) [1]. Because of the insidious onset, rapid development, and metastasis susceptibility, most patients (70% ~80%) with HSCC were at advanced stage when diagnosed, thus missed the optimal timing for surgical treatment [2]. Therefore, it is necessary to thoroughly elucidate the precise mechanisms of HSCC.

Recently, long noncoding RNAs (lncRNAs) which are identified as nonprotein-coding RNAs with over 200 nucleotides length have been revealed to play pivotal roles in molecular diagnosis and pathogenesis in almost all kinds of diseases including tumorigenesis and metastasis of cancers [3–5]. In HSCC, it has been proven that lncRNA HOXA11-AS contributed to the proliferation and migration via sponging and negatively regulation of miR-155 [6]. Moreover, lncRNA MALAT1 was found overexpressed in HSCC tissues and sponged miR-429 to stabilize the ZEB1 expression, resulting in the promotion of HSCC progression [7]. lncRNA AB209630 was shown to be decreased in HSCC

Table 1: Sequences of primers used in the study.

Gene	Sequence (5′-3′)
LEF1-AS1	
F	AAG GAC GAG AGA AAA GCA C
R	CAC ACA AAG GGG AAG ACC
GAPDH	
F	GTC TCC TCT GAC TTC AAC AGC G
R	ACC ACC CTG TTG CTG TAG CCA A
miR-221-5p	
F	ACACTCCAGCTGGGACCTGGCATACAATGT
R	CTC AAC TGG TGT CGT GGA
GJA1	
F	GGA GAT GAG CAG TCT GCC TTT C
R	TGA GCC AGG TAC AAG AGT GTG G
U6	
F	CTC GCT TCG GCA GCA CA
R	AAC GCT TCA CGA ATT TGC GT

tissues and identified as a suppressor of HSCC via inhibition of proliferation, invasion, metastasis, and survival of FaDu cells [8]. However, the functions of other lncRNAs in HSCC and potential mechanisms still remain unclear.

In the current manuscript, we illustrated the effect of lncRNA lymphoid enhancer-binding factor 1 antisense RNA 1 (LEF1-AS1) on HSCC. Bioinformatic analysis indicated that the increased expression of LEF1-AS1 in HNSCC tumors which was associated with the poor prognosis. Furthermore, we illustrated that LEF1-AS1 promoted HSCC cell proliferation, migration, invasion, and EMT process, whereas repressed cell apoptosis in both gain/loss-of-function experiments. Mechanically, LEF1-AS1 was shown to serve as a sponge for miR-221-5p to stabilize GJA1 levels. Our findings identified the oncogenic LEF1-AS1/miR-221-5p/GJA1 axis for HSCC progression and metastasis and suggested the axis as a promising target for HSCC therapy.

2. Materials and Methods

2.1. Bioinformatic Analysis. The transcriptome expression profile of HNSCC in The Cancer Genome Atlas (TCGA) database (https://cancergenome.nih.gov/) was collected. Analysis and graphics were created by *R* software (3.6.3). RNA22 (https://cm.jefferson.edu/rna22/Precomputed/) was applied to predict potential miRNA targets of LEF1-AS1, and TargetScan (http://www.targetscan.org/) was applied to seek for the candidate targets of miR-221-5p. Differentially expressed genes (DEGs) in LEF1-AS1 high or low expressed groups based on TCGA data were identified, and GSEA was performed using the Hallmark gene set (v.7.2) from MSigDB (https://www.gsea-msigdb.org/gsea/). Adjust p value<0.05, FDR < 0.25, and |NES| >1 were considered significant enrichment.

2.2. Cell Culture and Transfection. Human HSCC cell line FaDu was purchased from Chinese Academy of Sciences (Shanghai, China), and the cells were cultured in DMEM medium containing 10% FBS. The siRNA-NC, siRNA-LEF1-AS1, NC mimics, NC inhibitors, miR-221-5p mimics, and miR-221-5p inhibitors were all purchased from Genepharma (Shanghai, China) for transfection by using Lipofectamine RNAiMAX reagent (Thermo Fisher Scientific).

2.3. Proliferation Analysis and Apoptosis Analysis. The proliferation of FaDu cells was detected by CCK8 kits (Dojindo Laboratory, Japan). Briefly, the cells were seeded into 96-well plates and cultured for the indicated time, followed by the administration of CCK8 and incubation for another 4 h, and the absorption at 450 nm was examined by microplate reader (BioTek, San Diego, CA, USA). For colony formation, the transfected cells were counted, and 1000 cells were seeded into 6-well plates. 15 days later, the cell colonies were fixed with 4% paraformaldehyde and stained followed by the calculation. For cell apoptosis examination, after transfection for 48 h, the FaDu cell apoptosis was examined by using Annexin V-FITC/PI Kit (Beyotime, Shanghai, China) according to the manufacturer's instructions and detected by a flow cytometer.

2.4. Metastasis Analysis. For wound scratch assay, after transfection, scratch wounds were produced on the surface of overgrown cells by micropipette tip. After 24 h, the scratches were photographed, and the relative migrative rate was calculated by ImageJ. Basic transwell chamber (Corning) or Matrigel (BD Biosciences) precoated transwell chamber was used for the cell migration or invasion evaluation. Transwell assays were performed as previous described [9].

2.5. Quantitative Real-Time PCR (qRT-PCR) and RNA Immunoprecipitation (RIP) Assay. RNAs from FaDu cells were extracted by RNA Purification Kit (GeneJET; Thermo), and 1 μg total RNA was reversely transcribed by cDNA synthesis Kit (TaKaRa, Dalian, China) followed by qRT-PCR carried out by SYBR Green PCR Mix (TaKaRa). Results were standardized to GAPDH or U6, and the fold changes were calculated by the $2^{-\Delta\Delta CT}$ method [10]. The sequences of primers were shown in Table 1. Magna RIP Kit (Millipore, USA) was used for RIP assay, the cell lysates were incubated with Ago2 antibody or negative control IgG antibody precoated beads (Millipore), and the purified RNA was performed the following qRT-PCR analysis.

2.6. Dual-Luciferase Reporter Gene Assay. The WT or the mutant-type of LEF1-AS1 or GJA1 was inserted into pmirGLO dual-luciferase vector, respectively (Promega, Madison, WI). FaDu cells were transfected with these vectors, together with the treatment of negative control or miR-221-5p mimics. 48 h later, the activities of luciferase were examined using the dual-luciferase reporter analysis system (Promega, Madison, WI, USA).

2.7. Western Blot Analysis. After transfection, FaDu cells were harvested with RIPA Lysis reagent (Sigma-Aldrich), and protein concentrations were assessed by BCA protein assay kit (Thermo Fisher). 20 μg proteins were performed 12% SDS-PAGE then electrophoretically transferred onto

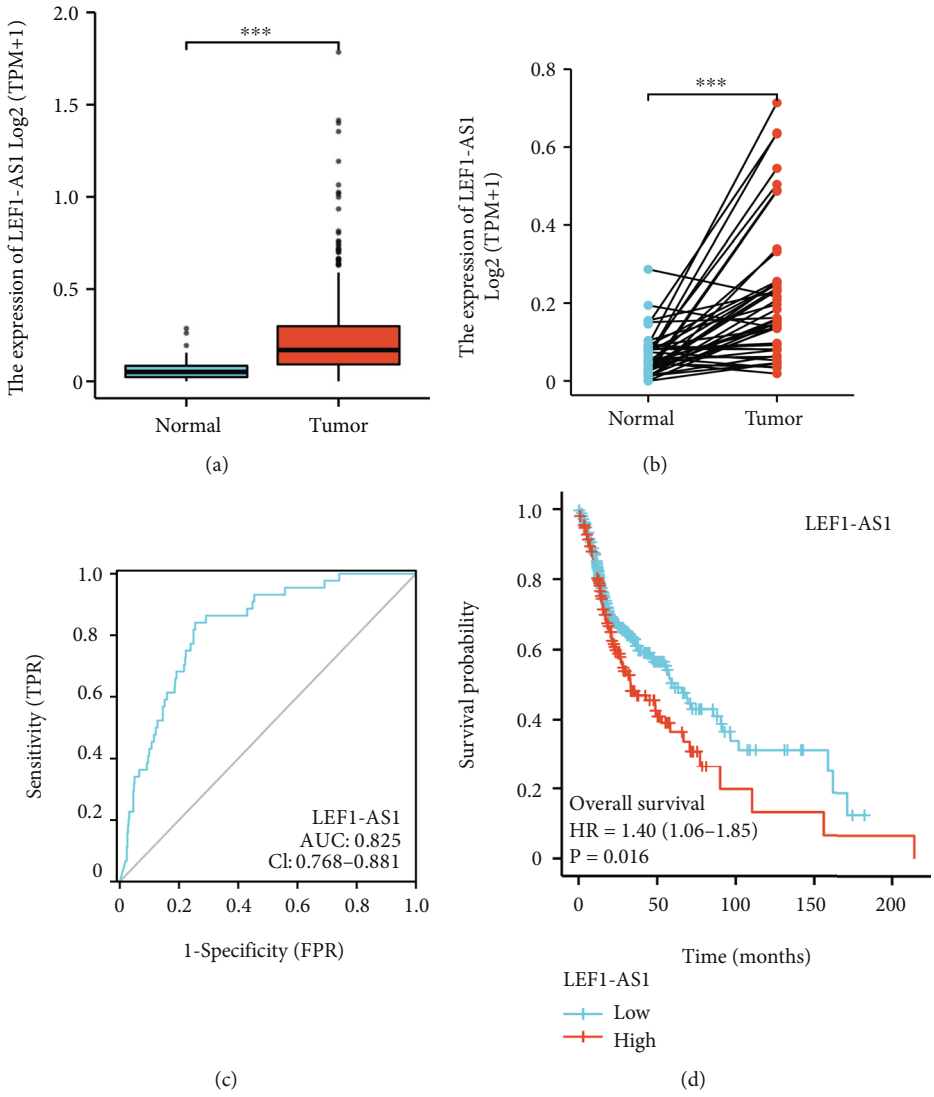

Figure 1: LncRNA LEF1-AS1 acts as a novel biomarker for HSCC. (a) The expression level of LEF1-AS1 in HNSCC tumor tissues ($n = 502$) and normal tissues ($n = 44$) from the TCGA database. (b) Comparison of the expression of LEF1-AS1 between tumor ($n = 43$) and matched normal tissues ($n = 43$) from the TCGA database. (c) ROC curve showed the diagnostic value of LEF1-AS1. (d) Kaplan–Meier curves revealed overall survival of HNSCC patients with high or low levels of LEF1-AS1 in TCGA. $^{***}p < 0.001$.

PVDF membrane followed by blocking in 1% BSA. The membranes were incubated with individual antibodies overnight at 4°C. After incubating with the corresponding horseradish peroxidase- (HRP-) conjugated secondary antibodies, the band signals were measured by using enhanced chemiluminescence kit (Thermo Fisher Scientific). Antibodies for cleaved caspase 3 (#ab2302; 1 : 500), total caspase 3 (#ab32150; 1 : 1000), GAPDH (#ab8245; 1 : 1000), N-cadherin (#ab245117; 1 : 1000), and GJA1 (#ab217676; 1 : 1000) were obtained from Abcam, and antibodies for Bax (#89477; 1 : 1000), Bcl-2 (#15071; 1 : 1000), E-cadherin (#14472; 1 : 1000), and vimentin (#5741; 1 : 1000) were purchased from Cell Signaling Technology. Appropriate HRP-tagged secondary antibodies (1 : 2000) were all bought from Santa Cruz Biotechnology.

2.8. Statistical Analysis. Statistical analysis was performed by using GraphPad Prism 8.0 (GraphPad, USA) with student's *t*-test and one-way ANOVA together with Tukey Kramer post-hoc testing. p values <0.05 were considered statistically significant.

3. Results

3.1. lncRNA LEF1-AS1 Acts as a Novel Biomarker for HNSCC. To illustrate the effect of LEF1-AS1 on HNSCC, we performed the bioinformatic analysis in TCGA datasets and explored the expression and prognosis effect of LEF1-AS1 at first. As shown in Figures 1(a) and 1(b), we observed that the LEF1-AS1 expression was obviously elevated in HNSCC tumor tissues. Furthermore, ROC data suggested LEF1-AS1 as a potential biomarker for HNSCC (Figure 1(c)). Kaplan–Meier survival analysis also indicated that aggravated LEF1-AS1 levels were associated with poorer overall survival (OS) rate in HNSCC patients (Figure 1(d)). Due to the extremely low number of HSCC cases in the

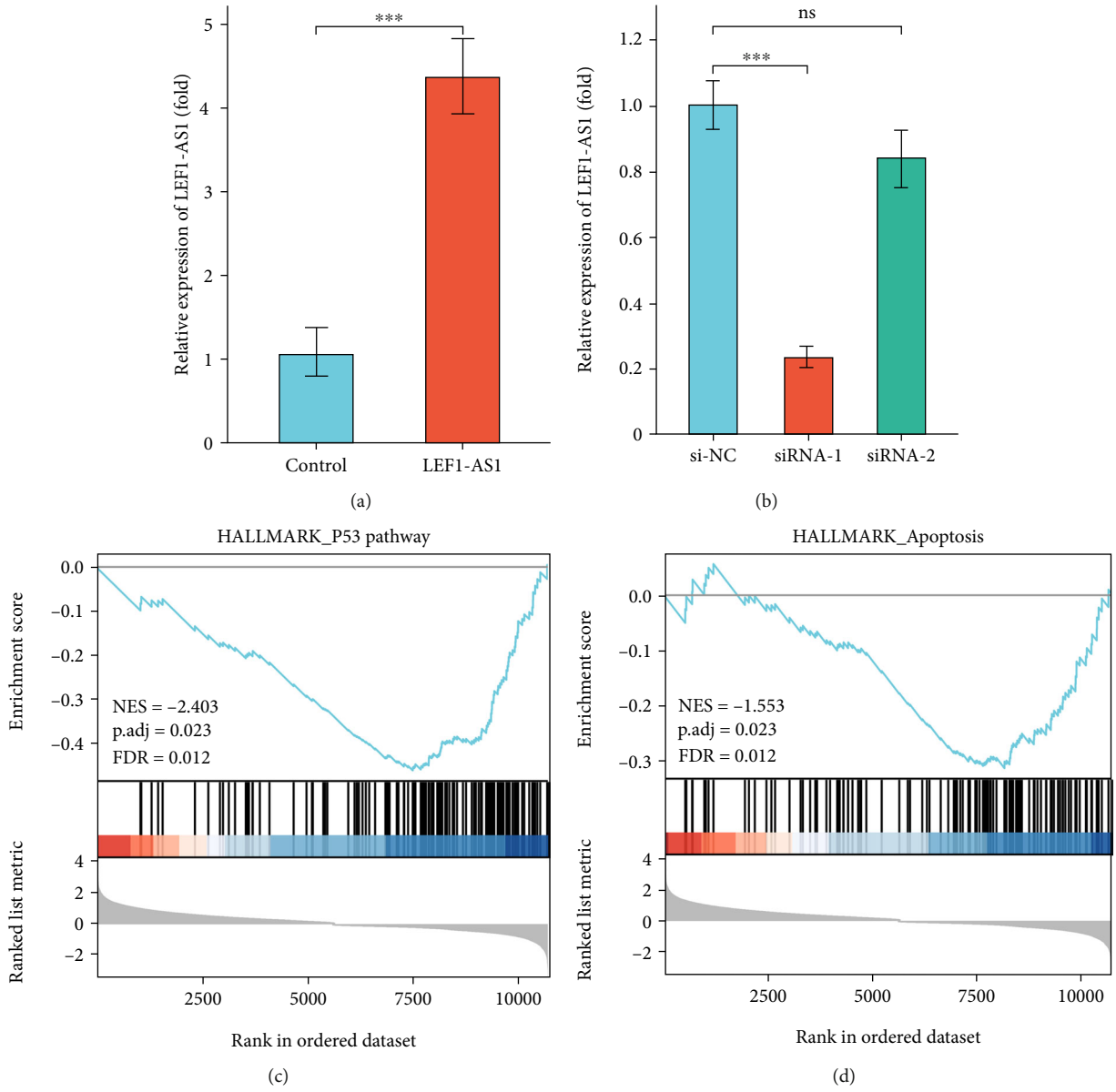

Figure 2: Continued.

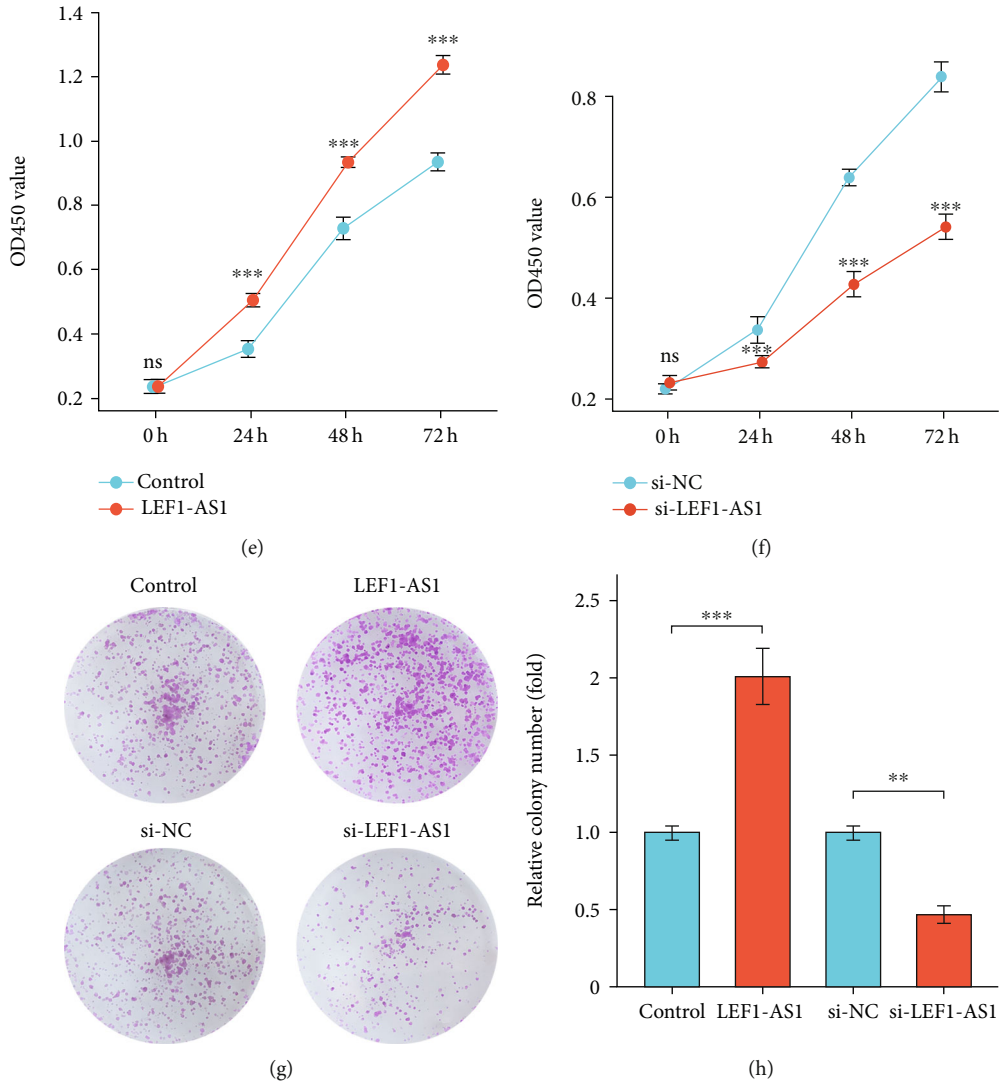

Figure 2: Continued.

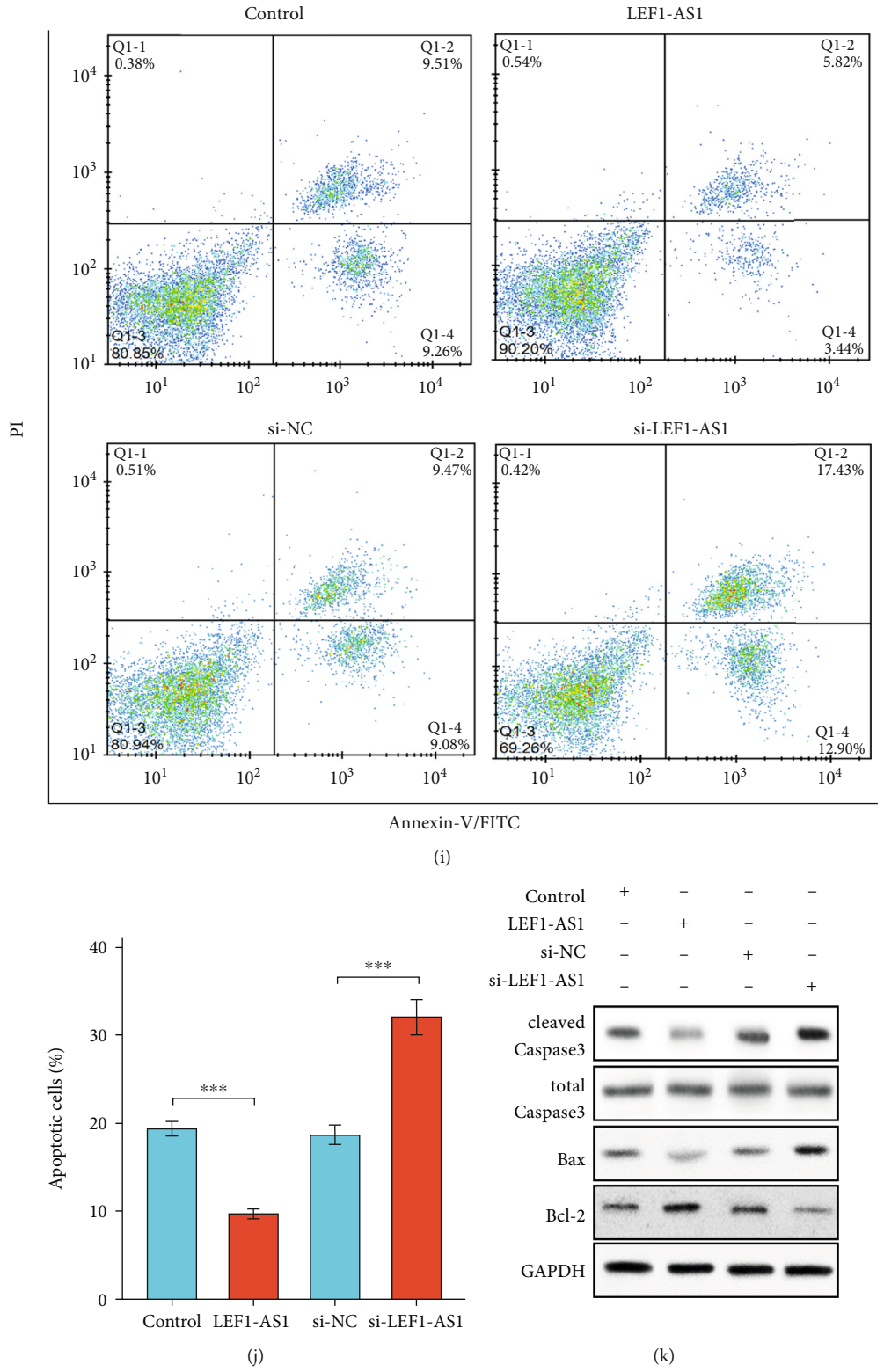

Figure 2: Effect of LEF1-AS1 on cell proliferation and apoptosis. (a, b) Efficiency of LEF1-AS1 overexpression plasmid (a) or LEF1-AS1 siRNAs (b) in FaDu cells. (c, d) GSEA analysis of P53 (c) and apoptosis (d) gene sets based on LEF1-AS1 expression information in TCGA. (e, f) CCK8 analysis in LEF1-AS1 overexpressed (e) or silenced FaDu cells (f). (g) Colony formation assay. (h) Relative colony numbers in (g). (i) Apoptosis of LEF1-AS1 overexpressed or silenced FaDu cells were detected by flow cytometry. (j) Apoptotic cell percent in (i). (k) Protein levels of apoptosis markers including cleaved caspase 3, Bax, and Bcl-2 in LEF1-AS1 overexpressed or silenced FaDu cells. Data are presented as means ± SD. $^{**}p < 0.01$; $^{***}p < 0.001$.

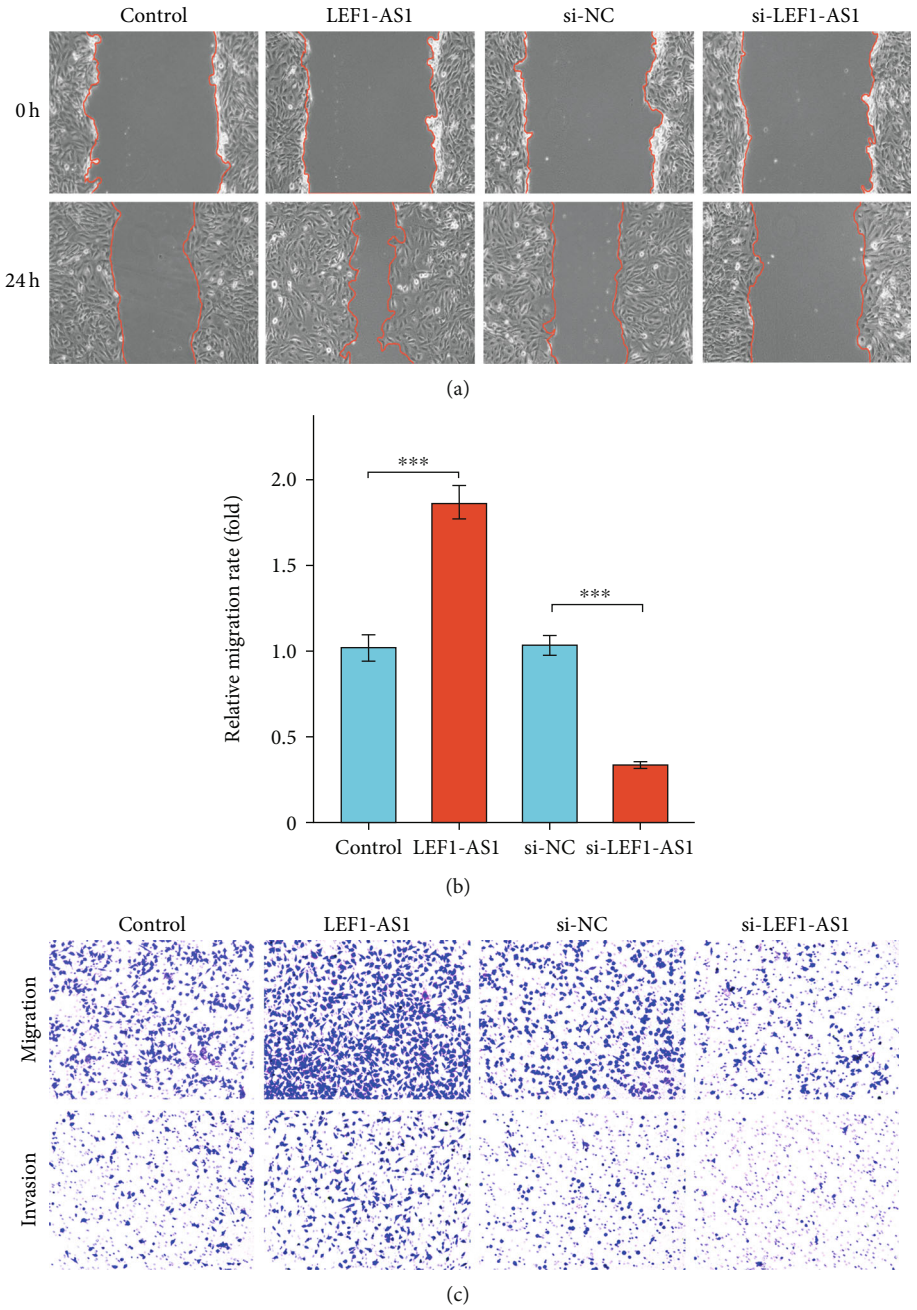

Figure 3: Continued.

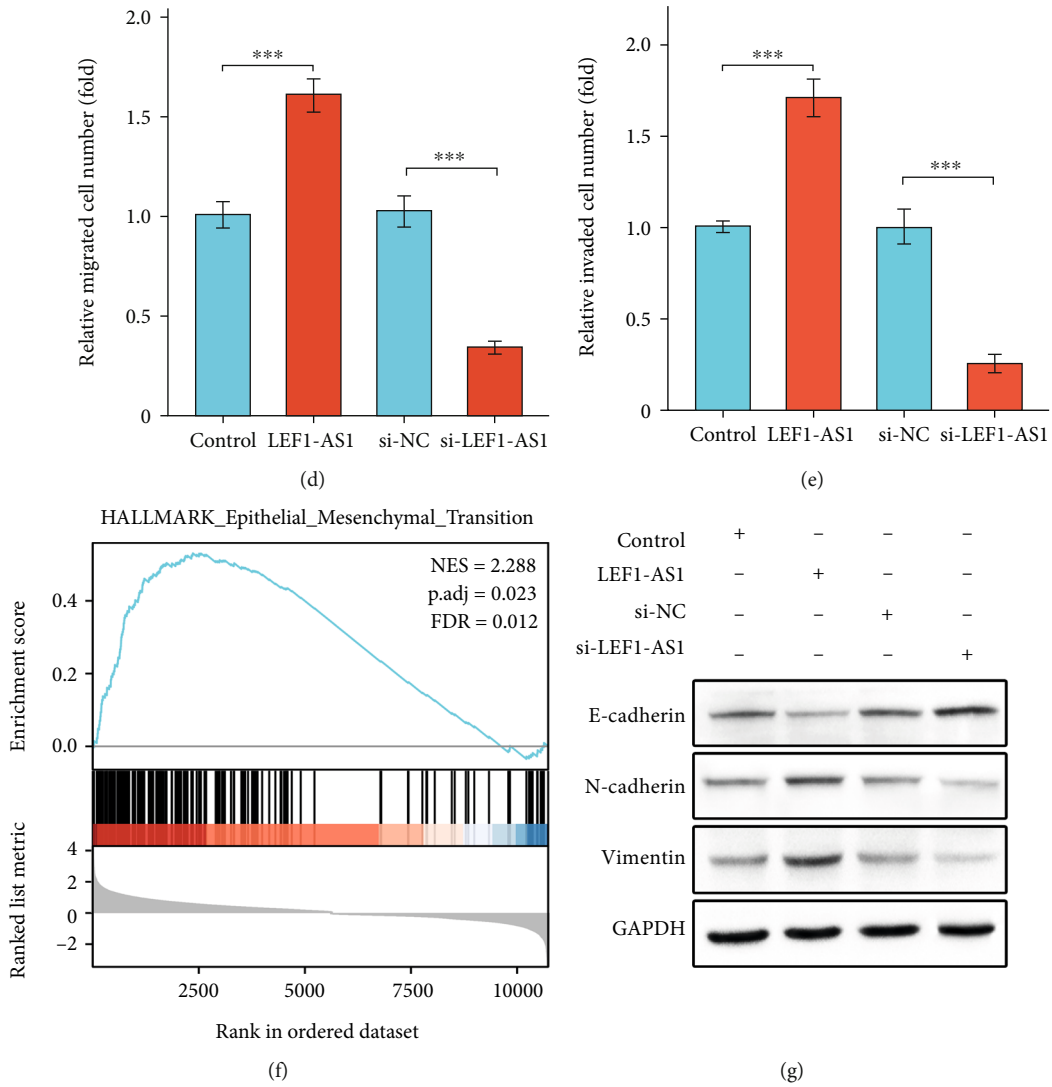

Figure 3: LEF1-AS1 positively regulates cell migration, invasion, and EMT process. (a) Wound healing assays in LEF1-AS1 overexpressed or silenced FaDu cells. (b) Relative migration rate in (a). (c) Transwell experiments for cell migration and invasion detection. (d, e) Relative migrated (d) or invaded (e) FaDu cell number in (c). (f) GSEA analysis of EMT gene sets based on LEF1-AS1 expression information in TCGA. (g) Western blot analysis of E-cadherin, N-cadherin, and vimentin in LEF1-AS1 overexpressed or silenced FaDu cells. Data are presented as means ± SD. $^{***}p < 0.001$.

TCGA database, and HSCC and other HNSCC were all squamous cell carcinomas which shared similar pathological forms, and we speculated that LEF1-AS1 may also play crucial roles in HSCC tumorigenesis and development.

3.2. Effect of LEF1-AS1 on Cell Proliferation and Apoptosis. According to the abnormal expression and prognostic value of LEF1-AS1 in HNSCC datasets of the TCGA database, we further used HSCC cell line FaDu cells to examine the effect of LEF1-AS1 on HSCC tumorigenesis abilities. We used LEF1-AS1 overexpression plasmid and siRNAs for the gain/loss-of-function experiments, and the efficiency of the overexpression or silencing of LEF1-AS1 was detected by qPCR (Figures 2(a) and 2(b)). Gene set enrichment analysis (GSEA) results showed that LEF1-AS1 associated genes were enriched in p53 pathway (Figure 2(c)) and apoptosis process (Figure 2(d)). By using CCK8 experiment, we noticed that the LEF1-AS1 overexpression obviously increased the viability of FaDu cells (Figure 2(e)), and consistent results were obtained in LEF1-AS1 silenced cells (Figure 2(f)). The overexpression of LEF1-AS1 also induced elevated colony numbers, whereas silencing of LEF1-AS1 alleviated the formation of colonies (Figures 2(g) and 2(h)). Flow cytometry analysis revealed that LEF1-AS1 contributed to the suppression of cell apoptosis (Figures 2(i) and 2(j)), as well as the altered expression of apoptosis markers such as cleaved caspase 3, Bax, and Bcl-2 (Figure 2(k)).

3.3. LEF1-AS1 Positively Regulates Cell Migration, Invasion, and EMT Process. Furthermore, we examined the effect of LEF1-AS1 on tumor metastasis. As shown in Figures 3(a) and 3(b), wound scratch assay results indicated that cell migration ability was enhanced by the LEF1-AS1 overexpression, whereas silencing of LEF1-AS1 significantly

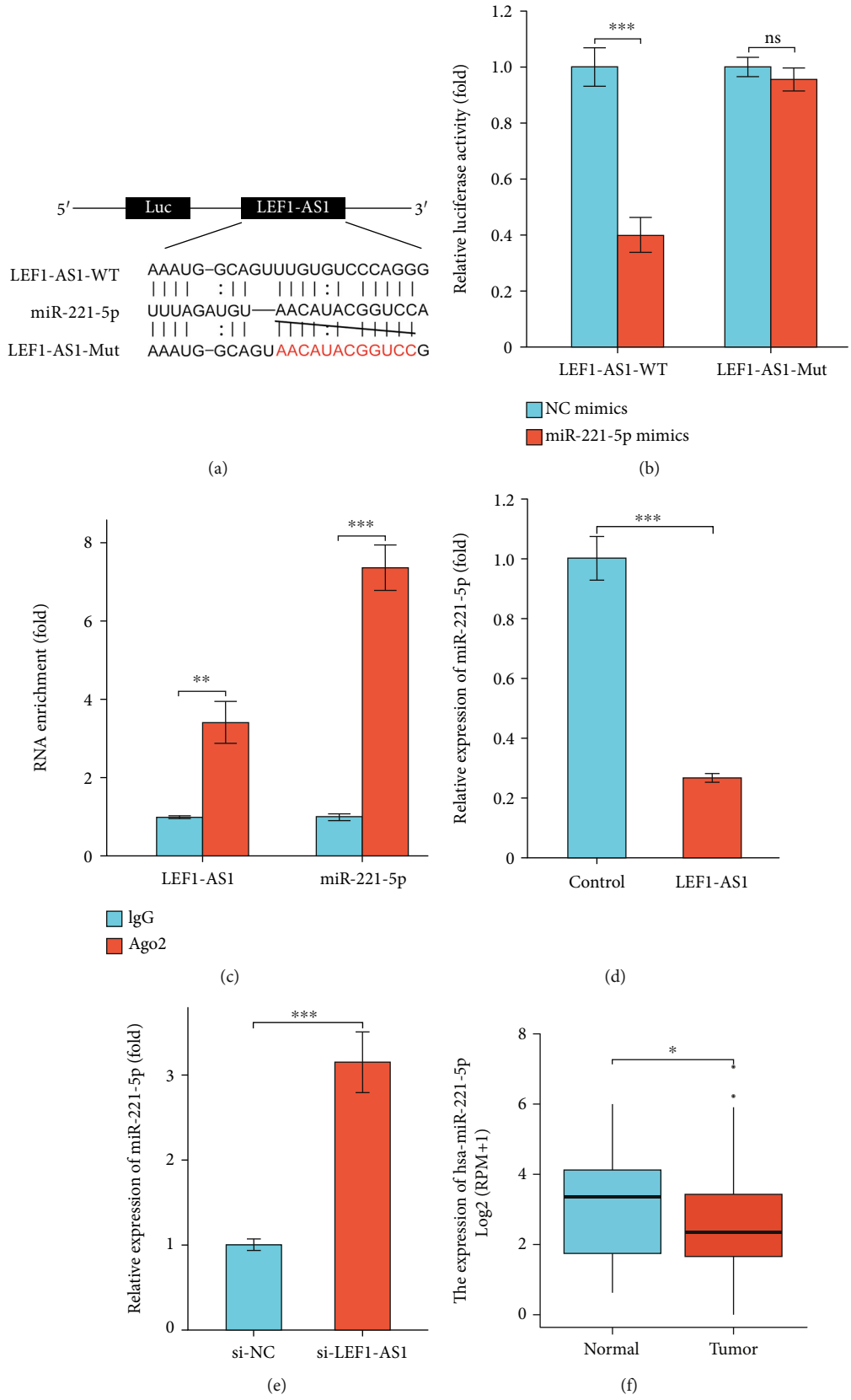

Figure 4: Continued.

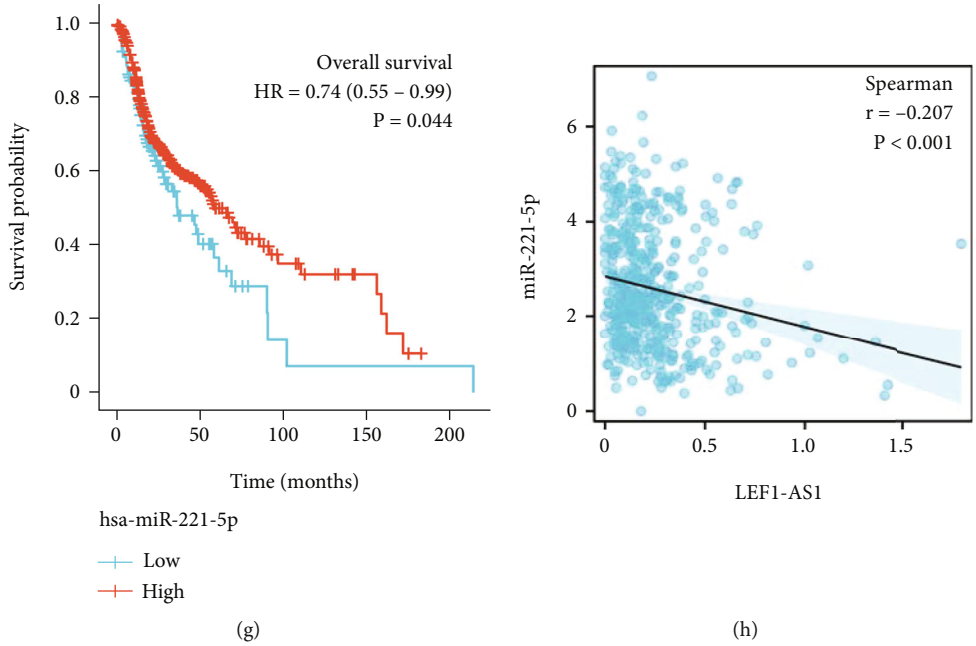

Figure 4: LEF1-AS1 acts as ceRNA to regulate the miR-221-5p expression. (a) Presentation of binding sites between LEF1-AS1 and miR-221-5p by RNA22 online tool. (b) Luciferase activity of LEF1-AS1-WT or LEF1-AS1-Mut plasmid in miR-221-5p overexpressed FaDu cells. (c) Anti-Ago2 RIP assay confirmed the combination between LEF1-AS1 and miR-221-5p. (d, e) Relative expression of miR-221-5p in LEF1-AS1 overexpressed (d) or silenced (e) FaDu cells. (f) The expression level of miR-221-5p in HNSCC tumor tissues ($n = 525$) and normal tissues ($n = 44$) from the TCGA database. (g) Kaplan–Meier curves revealed overall survival of HNSCC patients with high or low levels of miR-221-5p in TCGA. (h) Negative correlation between LEF1-AS1 and miR-221-5p in TCGA data. Data are presented as means ± SD . $^{*}p < 0.05$; $^{**}p < 0.01$; $^{***}p < 0.001$.

suppressed FaDu migration. Moreover, we found that LEF1-AS1 contributed to cell migration and invasion in transwell experiments (Figures 3(c)–3(e)). Due to the critical role of EMT process in metastasis, we also performed GSEA enrichment of Hallmark EMT-related gene set, and we found that LEF1-AS1 was obviously correlated with EMT-related genes (Figure 3(f)), and western blot data indicated that LEF1-AS1 suppressed the E-cadherin expression, whereas elevated the expression of N-cadherin and vimentin (Figure 3(g)). In brief, these data indicated that LEF1-AS1 promotes HSCC cell migration and invasion and enhanced the process of EMT.

3.4. LEF1-AS1 Serves as ceRNA to Regulate the miR-221-5p Expression. Competing endogenous RNA (ceRNA) is one of the most essential functional mechanisms of lncRNA [11]. To investigate whether LEF1-AS1 regulates tumor progression and metastasis through ceRNA mechanism, we predicted the potential candidate targets of LEF1-AS1 by using online-tool RNA22, and we identified that LEF1-AS1 existed complementary binding regions to miR-221-5p (Figure 4(a)). Dual-Luciferase reporter gene assay data demonstrated that the miR-221-5p overexpression greatly suppressed the luciferase activation of LEF1-AS1-WT plasmid but failed to repress LEF1-AS1-mutant vector luciferase activity (Figure 4(b)). To substantiate this binding relationship, we further performed RIP experiment with anti-Ago2 in FaDu cells, and the enrichment effects of LEF1-AS1 or miR-221-5p together with Ago2 were confirmed (Figure 4(c)). Moreover, the levels of miR-221-5p were significantly suppressed in LEF1-AS1 overexpressed FaDu cells, whereas silencing of LEF1-AS1 elevated miR-221-5p levels obviously (Figures 4(d) and 4(e)). In addition, miR-221-5p was observed to be downregulated in HNSCC tumor tissues in TCGA-HNSCC datasets (Figure 4(f)). Furthermore, miR-221-5p was found to be positively correlated with the favorable overall survival of patients (Figure 4(g)), and miR-221-5p levels were shown to be negatively correlated with the LEF1-AS1 expression (Figure 4(h)). In brief, these data illustrated that LEF1-AS1 negatively regulates the miR-221-5p expression in FaDu cells.

3.5. miR-221-5p Suppresses FaDu Cell Proliferation and EMT by Targeting GJA1. As shown in Figure 5(a), the efficiencies of miR-221-5p mimics and inhibitor were detected by qRT-PCR. For searching the putative targets of miR-221-5p, the TargetScan database was used which suggested GJA1 as a potential target (Figure 5(b)). Cotransfection of GJA1-3′ UTR-WT vector together with miR-221-5p mimics resulted in an attenuated dual luciferase activity, whereas miR-221-5p mimics had no affection on luciferase activity of GJA1-3(h)UTR-mutant plasmid (Figure 5(c)). Furthermore, we observed that the miR-221-5p overexpression suppressed GJA1 levels, and miR-221-5p inhibition aggravated GJA1 expression significantly (Figures 5(d) and 5(e)). In addition, miR-221-5p was shown to inhibit FaDu cell proliferation, whereas rescued the levels of GJA1 abolished the inhibitory effect of miR-221-5p on proliferation (Figure 5(f)). Consistently, inhibitory functions of miR-221-5p on EMT, cell migration, and cell invasion were all reversed by GJA1

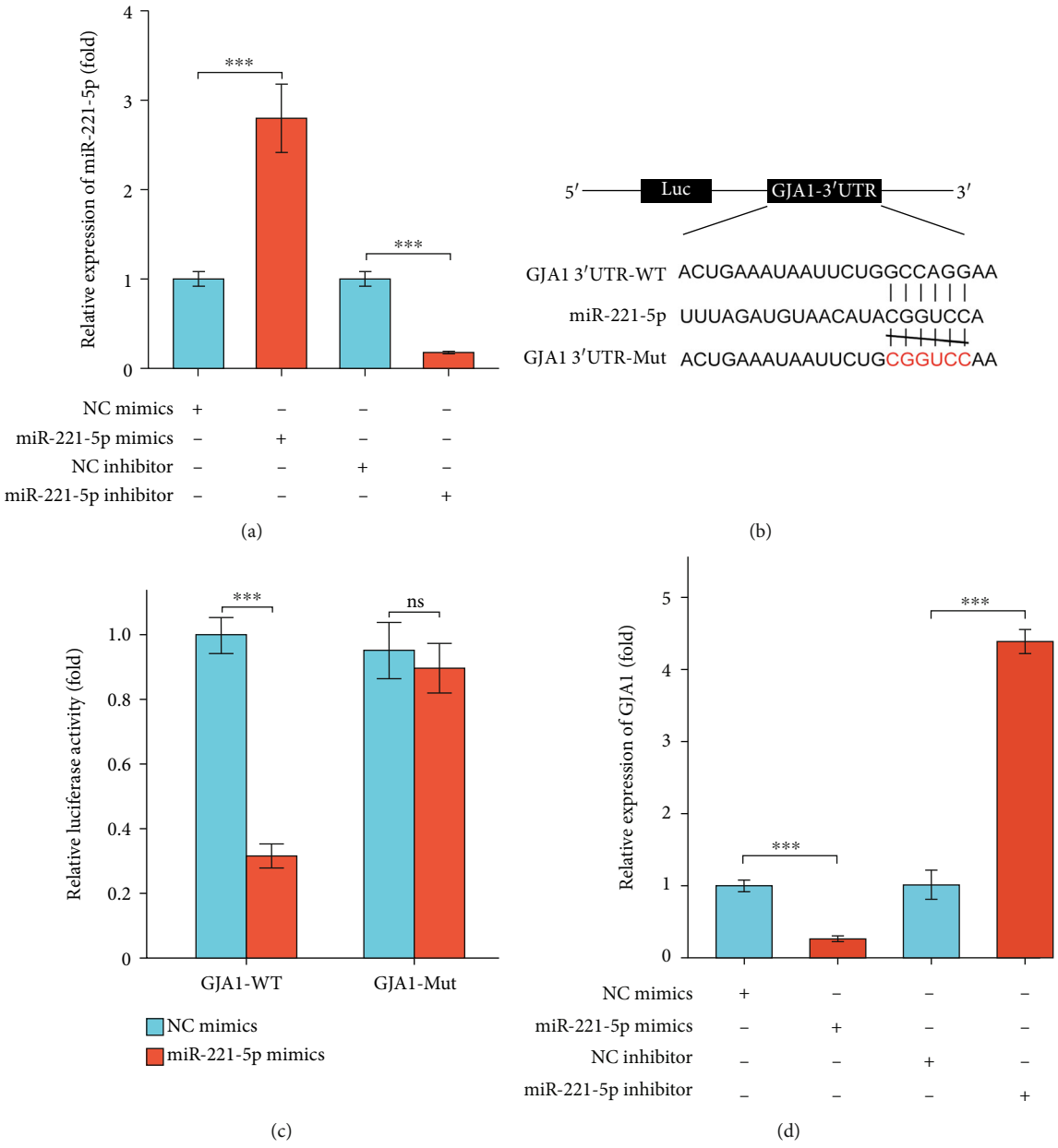

Figure 5: Continued.

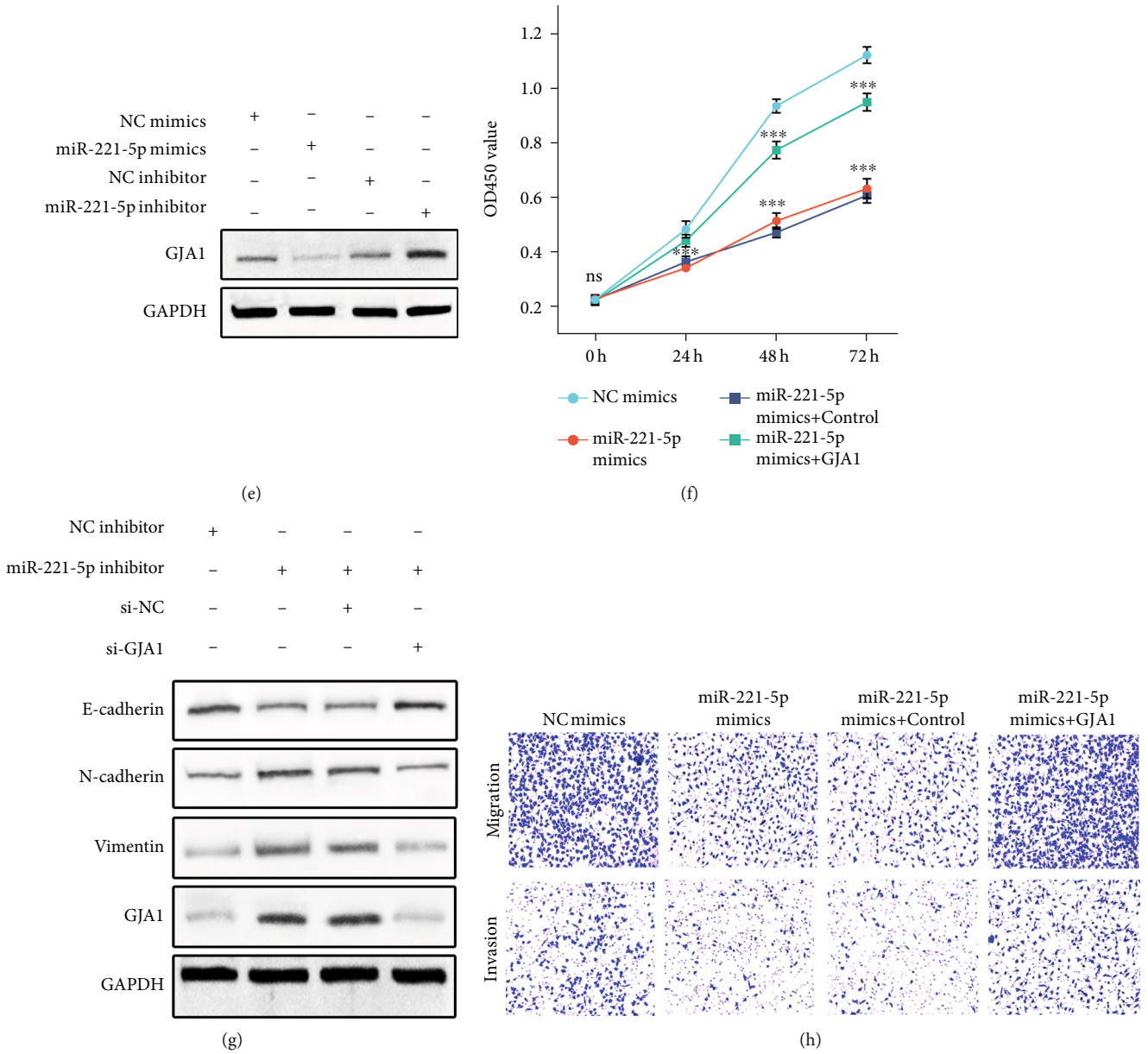

Figure 5: miR-221-5p suppresses FaDu cell proliferation and EMT by targeting GJA1. (a) Efficiency of miR-221-5p mimics and inhibitors. (b) Presentation of binding sites between miR-221-5p and GJA1 by TargetScan online tool. (c) Luciferase activity of GJA1-3′UTR-WT or GJA1-3′UTR-mutant plasmid in miR-221-5p overexpressed FaDu cells. (d, e) mRNA (d) or protein (e) levels of GJA1 in miR-221-5p overexpressed or silenced FaDu cells. (f) CCK8 results indicated that the GJA1 overexpression reversed miR-221-5p-induced inhibitory effect on cell proliferation. (g) Western blot results revealed that GJA1 silencing abolished miR-221-5p inhibitor-induced aggravation of EMT. (h) In transwell assays, the GJA1 overexpression reversed miR-221-5p-induced inhibitory effect on FaDu cell migration and invasion. Data are presented as means ± SD. $^{***}p < 0.001$.

rescue experiments (Figures 5(g) and 5(h)). In brief, these data demonstrated that miR-221-5p attenuated FaDu cell proliferation and EMT process via targeting GJA1.

3.6. LEF1-AS1 Enhances the Growth and Metastasis Abilities of FaDu Cells via the miR-221-5p/GJA1 Axis. Bioinformatic analysis revealed that the GJA1 expression was enhanced in HNSCC tumor tissues (Figures 6(a) and 6(b)), and Kaplan–Meier survival data demonstrated that the higher GJA1 expression presented a worse OS rate in HNSCC patients (Figure 6(c)). Moreover, we noticed that LEF1-AS1 dramatically enhanced the GJA1 expression (Figures 6(d) and 6(e)). Importantly, we observed that LEF1-AS1-induced FaDu cell proliferation and EMT were all reversed after transfection of miR-221-5p mimics, which mainly associated with the attenuated expression of GJA1 regulated by miR-221-5p (Figures 6(f)–6(h)). In brief, these data revealed that LEF1-AS1 acted as a ceRNA to stabilize the GJA1 expression via competing miR-221-5p, therefore, enhances the growth and metastasis abilities of FaDu cells.

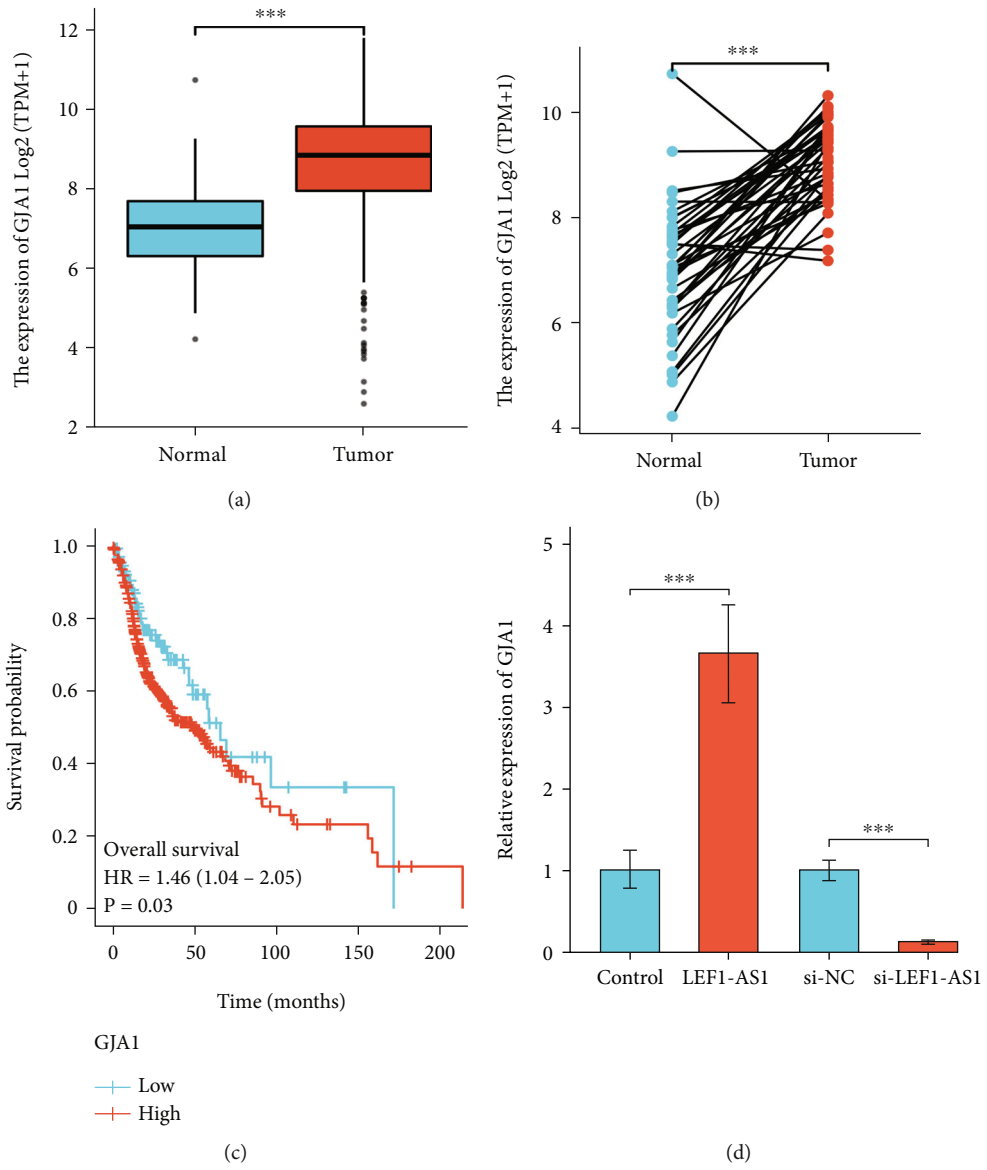

Figure 6: Continued.

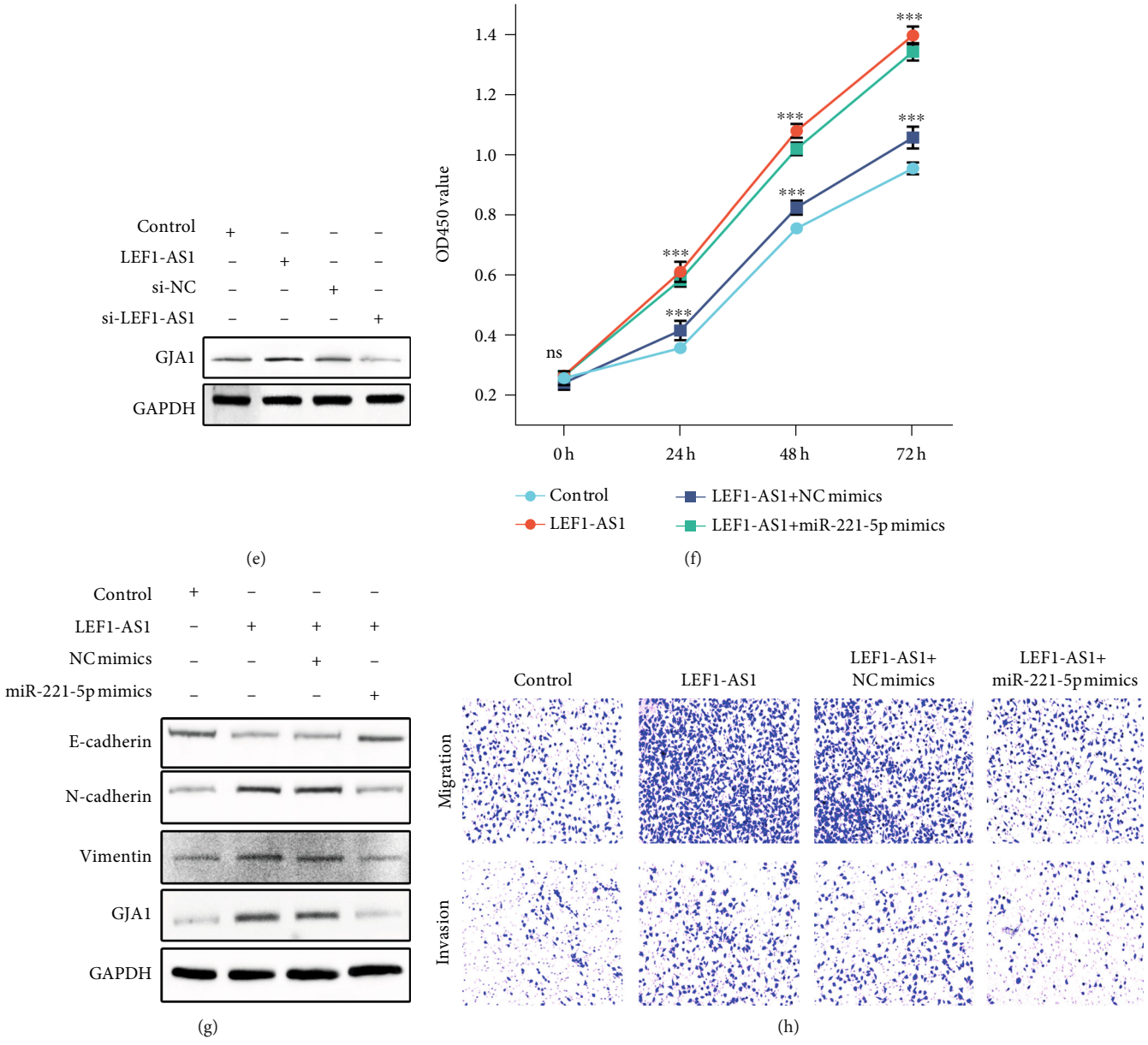

FIGURE 6: LEF1-AS1 enhances the proliferation and metastasis abilities of FaDu cells via the miR-221-5p/GJA1 axis. (a) The expression level of GJA1 in HNSCC tumor tissues ($n = 502$) and normal tissues (n =44) from the TCGA database. (b) Comparison of the expression of GJA1 between tumor ($n = 43$) and matched normal tissues ($n = 43$) from the TCGA database. (c) Kaplan–Meier curves revealed overall survival of HNSCC patients with high or low levels of GJA1 in TCGA. (d, e) mRNA (d) or protein (e) levels of GJA1 in LEF1-AS1 overexpressed or silenced FaDu cells. (f) CCK8 results indicated that the miR-221-5p overexpression reversed LEF1-AS1-induced promotion of cell proliferation. (g) Western blot results revealed that the miR-221-5p overexpression abolished LEF1-AS1-induced aggravation of EMT as well as the increased GJA1 expression. (h) In transwell assays, the miR-221-5p overexpression reversed LEF1-AS1-induced aggravation of FaDu cell migration and invasion. Data are presented as means ± SD. $^{***}p < 0.001$.

4. Discussion

In the current manuscript, we demonstrated the functions of lncRNA LEF1-AS1 in HSCC and illustrated the prooncogenic effect of LEF1-AS1 via promoting the tumor progression and metastasis. As far as we known, this manuscript is the first publication about the functions of LEF1-AS1 in HSCC and verified the role of the LEF1-AS1/miR-221-5p/GJA1 axis.

In recent time, accumulating evidences suggested that the overwhelming majority of lncRNA function as molecular sponges for miRNAs to weaken the expression of miRNAs, therefore indirectly regulated miRNAs targets levels in diverse kinds of diseases. For instance, lncRNA BCRT1 was reported to competitively bind with miR-1303 to prevent the degradation of PTBP3, which induced the progression of breast cancer [12]. In LPS-induced HK2 cells, lncRNA NKILA was observed to aggravate LPS-induced

apoptosis and inflammation via miR-140-5p sponging-associated stabilization of CLDN2 [13]. The lncRNA-PVT1/miR-619-5p/Pygo2/ATG14 axis was shown to be critical for the promotion of gemcitabine chemoresistance of pancreatic cancer [14]. The roles of LEF1-AS1 have been illustrated in other diseases in previous studies. As examples, the LEF1-AS1 expression could be induced by CREB1, and the high expression of LEF1-AS1 promoted tumorigenesis of colorectal tumor through sponging miR-489 and stabilizing DIAPH1 [15]. Moreover, LEF1-AS1 was found to aggravate the progression of ovarian cancer [16], retinoblastoma [17], and lung cancer [18]; however, the effect of LEF1-AS1 on HNSCC, especially in hypopharyngeal squamous cell carcinoma, still remains largely unknown. In this research, we illustrated the function of LEF1-AS1 in HSCC. We observed that LEF1-AS1 was upregulated in tumor tissues in the TCGA database, which was correlated with the poor prognosis. In vitro experiments revealed that LEF1-AS1 significantly enhanced cell proliferation as well as the suppression of cell apoptosis. Moreover, LEF1-AS1 was proved to enhance EMT process and improved metastasis of HSCC cells. Mechanically, it was found that LEF1-AS1 served as a sponge of miR-221-5p thereby alleviated miR-221-5p induced decreased levels of GJA1.

Antitumor effects of miR-221-5p have been illustrated previously. Jiang and colleagues demonstrated that the miR-221-5p expression was suppressed in gastric cancer tissues, overexpression of miR-221-5p reduced cisplatin chemoresistance of gastric tumor cells, and suppressed cell proliferation and migration via suppressing DDR1 [19]. Moreover, miR-221-5p was reported to inhibit prostate tumor cell proliferation and metastasis both in vivo and in vitro [20]. Consistently, we found that the miR-221-5p expression was reduced in tumor tissues in HNSCC datasets of TCGA which was negatively associated with LEF1-AS1 expression, and miR-221-5p was demonstrated as a tumor suppressor to inhibit cell growth and EMT-associated migration and invasion. By bioinformatical analysis, we identified GJA1 as the potential target of miR-221-5p. GJA1 was shown to be positively correlated with the poor overall survival of cervical cancer [21]. Moreover, GJA1 was shown to promote hepatocellular carcinoma progression via TGF-β activation and enhancement of EMT process [22]. Effect of GJA1 on proliferation and EMT ability was also confirmed in breast cancer [23], lung cancer [24], and bladder cancer [25]. Our results indicated that the GJA1 expression was increased in HNSCC tissues and correlated with the worse prognosis. In addition, we noticed that the GJA1 overexpression reversed miR-221-5p mimic-induced EMT inhibition and growth suppression, which confirmed the assumption that GJA1 was the target of miR-221-5p. At last, by performing rescue assays, we found that miR-221-5p mimic administration abolished LEF1-AS1-induced FaDu proliferation and EMT process and revealed that the function of LEF1-AS1 on FaDu progression and metastasis mainly depends upon the LEF1-AS1/miR-221-5p/GJA1 axis.

5. Conclusion

In summary, our manuscript suggested LEF1-AS1 as a novel biomarker for HNSCC, illustrated the effects of LEF1-AS1, miR-221-5p, and GJA1 on hypopharyngeal squamous cell carcinoma for the first time, and revealed that the LEF1-AS1/miR-221-5p/GJA1 axis may serve as a novel promising target for HSCC therapy. However, further exploration about the precise mechanisms by which GJA1 regulates EMT process and cell proliferation in HSCC is needed in the further studies.

Data Availability

The data used and analyzed during the current study are available from the corresponding author on reasonable request.

Conflicts of Interest

All authors declare no conflict of interest.

Authors' Contributions

Junda Fan, Kai Zhao, and Mingbo Liu designed the study and wrote the manuscript. Junda Fan, Cheng Wang, Xingyou Zhai, Jianhui Li, Jun Ju, Yuying Zhu, and Shikang Zheng carried out the experiments. Kai Zhao, Cheng Wang, Nan Ren, and Yingli Xie analyzed the data. Bangqing Huang and Xinying Jiang prepared the figures. All authors reviewed and approved the final manuscript. Junda Fan and Cheng Wang contributed equally to this work and should be considered as co-first authors.

Acknowledgments

This work was supported by the Major Science and Technology Plan Project of Hainan Province (ZDKJ202005) and supported by Hainan Province Clinical Medical Center.

References

[1] D. I. Kwon, B. A. Miles, Education Committee of the American Head and Neck Society (AHNS), and S. Neck, "Hypopharyngeal carcinoma: do you know your guidelines?," *Head and Neck*, vol. 41, no. 3, pp. 569–576, 2019.

[2] J. D. Cramer, B. Burtness, Q. T. Le, and R. L. Ferris, "The changing therapeutic landscape of head and neck cancer," *Nature Reviews: Clinical Oncology*, vol. 16, no. 11, pp. 669–683, 2019.

[3] F. Kopp and J. T. Mendell, "Functional classification and experimental dissection of long noncoding RNAs," *Cell*, vol. 172, no. 3, pp. 393–407, 2018.

[4] G. J. Goodall and V. O. Wickramasinghe, "RNA in cancer," *Nature Reviews: Cancer*, vol. 21, no. 1, pp. 22–36, 2021.

[5] Q. Xue, L. Yang, J. Wang, L. Li, H. Wang, and Y. He, "lncRNA ROR and miR-125b predict the prognosis in heart failure

combined acute renal failure," *Disease Markers*, vol. 2022, Article ID 6853939, 6 pages, 2022.

[6] J. Xu, Q. Bo, X. Zhang, D. Lei, J. Wang, and X. Pan, "lncRNA HOXA11-AS promotes proliferation and migration via sponging miR-155 in Hypopharyngeal squamous cell carcinoma," *Oncology Research*, vol. 28, no. 3, pp. 311–319, 2020.

[7] X. Liu, W. Zhao, and X. Wang, "Inhibition of long non-coding RNA MALAT1 elevates microRNA-429 to suppress the progression of hypopharyngeal squamous cell carcinoma by reducing ZEB1," *Life Sciences*, vol. 262, p. 118480, 2020.

[8] J. Zhou, M. Li, W. Yu et al., "AB209630, a long non-coding RNA decreased expression in hypopharyngeal squamous cell carcinoma, influences proliferation, invasion, metastasis, and survival," *Oncotarget*, vol. 7, no. 12, pp. 14628–14638, 2016.

[9] Y. M. Jiang, W. Liu, L. Jiang, and H. Chang, "CircLDLR promotes papillary thyroid carcinoma tumorigenicity by regulating miR-637/LMO4 axis," *Disease Markers*, vol. 2021, Article ID 3977189, 12 pages, 2021.

[10] K. J. Livak and T. D. Schmittgen, "Analysis of relative gene expression data using real-time quantitative PCR and the 2 $-\Delta\Delta$CT method," *Methods*, vol. 25, no. 4, pp. 402–408, 2001.

[11] Y. Tay, J. Rinn, and P. P. Pandolfi, "The multilayered complexity of ceRNA crosstalk and competition," *Nature*, vol. 505, no. 7483, pp. 344–352, 2014.

[12] Y. Liang, X. Song, Y. Li et al., "lncRNA BCRT1 promotes breast cancer progression by targeting miR-1303/PTBP3 axis," *Molecular Cancer*, vol. 19, no. 1, p. 85, 2020.

[13] D. Han, R. Fang, R. Shi, Y. Jin, and Q. Wang, "lncRNA NKILA knockdown promotes cell viability and represses cell apoptosis, autophagy and inflammation in lipopolysaccharide-induced sepsis model by regulating miR-140-5p/CLDN2 axis," *Biochemical and Biophysical Research Communications*, vol. 559, pp. 8–14, 2021.

[14] C. Zhou, C. Yi, Y. Yi et al., "LncRNA PVT1 promotes gemcitabine resistance of pancreatic cancer via activating Wnt/beta-catenin and autophagy pathway through modulating the miR-619-5p/Pygo2 and miR-619-5p/ATG14 axes," *Molecular Cancer*, vol. 19, no. 1, p. 118, 2020.

[15] Y. Cheng, J. Wu, B. Qin, B. C. Zou, Y. H. Wang, and Y. Li, "CREB1-induced lncRNA LEF1-AS1 contributes to colorectal cancer progression via the miR-489/DIAPH1 axis," *Biochemical and Biophysical Research Communications*, vol. 526, no. 3, pp. 678–684, 2020.

[16] Y. Zhang and F. Ruan, "LncRNA LEF1-AS1 promotes ovarian cancer development through interacting with miR-1285-3p," *Cancer Management and Research*, vol. Volume 12, pp. 687–694, 2020.

[17] H. He and M. Qin, "Long non-coding RNA LEF1-AS1 is involved in the progression of retinoblastoma through regulating the Wnt/β-catenin pathway," *Clinical and Experimental Pharmacology & Physiology*, vol. 47, no. 5, pp. 886–891, 2020.

[18] C. Xiang, Y. Zhang, Y. Zhang, C. Liu, Y. Hou, and Y. Zhang, "lncRNA LEF1-AS1 promotes proliferation and induces apoptosis of non-small-cell lung cancer cells by regulating miR-221/PTEN signaling," *Cancer Management and Research*, vol. - Volume 12, pp. 3845–3850, 2020.

[19] X. Jiang, M. Jiang, S. Guo, P. Cai, W. Wang, and Y. Li, "Promotion of miR-221-5p on the sensitivity of gastric cancer cells to cisplatin and its effects on cell proliferation and apoptosis by regulating DDR1," *Oncotargets and Therapy*, vol. Volume 13, pp. 2333–2345, 2020.

[20] M. Kiener, L. Chen, M. Krebs et al., "miR-221-5p regulates proliferation and migration in human prostate cancer cells and reduces tumor growth in vivo," *BMC Cancer*, vol. 19, no. 1, p. 627, 2019.

[21] S. Meng, X. Fan, J. Zhang, R. An, and S. Li, "GJA1 expression and its prognostic value in cervical cancer," *BioMed Research International*, vol. 2020, Article ID 8827920, 10 pages, 2020.

[22] G. Niu, X. Zhang, R. Hong et al., "GJA1 promotes hepatocellular carcinoma progression by mediating TGF-β-induced activation and the epithelial-mesenchymal transition of hepatic stellate cells," *Open Medicine*, vol. 16, no. 1, pp. 1459–1471, 2021.

[23] A. Adak, Y. C. Unal, S. Yucel et al., "Connexin 32 induces protumorigenic features in MCF10A normal breast cells and MDA-MB-231 metastatic breast cancer cells," *Biochimica et Biophysica Acta (BBA)-Molecular Cell Research*, vol. 1867, no. 12, article 118851, 2020.

[24] S. G. Zeng, X. Lin, J. C. Liu, and J. Zhou, "Hypoxia-induced internalization of connexin 26 and connexin 43 in pulmonary epithelial cells is involved in the occurrence of non-small cell lung cancer via the P53/MDM2 signaling pathway," *International Journal of Oncology*, vol. 55, no. 4, pp. 845–859, 2019.